NASA TECHNICAL TRANSLATION

NASA TT F-390

NASA TT F-390

TECH LIBRARY KAFB, NM
0068815

METHODS OF INVESTIGATING THE ATMOSPHERE WITH ROCKETS AND SATELLITES

by A. A. Kmito

Gidrometeorologicheskoye Izdatel'stvo,
Leningrad, 1966

NATIONAL AERONAUTICS AND SPACE ADMINISTRATION • WASHINGTON, D. C. • FEBRUARY 1967

TECH LIBRARY KAFB, NM
0068815
NASA TT F-390

METHODS OF INVESTIGATING THE ATMOSPHERE WITH ROCKETS AND SATELLITES

By A. A. Kmito

Translation of "Metody issledovaniya atmosfery s ispol'zovaniyem raket i sputnikov."
Gidrometeorologicheskoye Izdatel'stvo,
Leningrad, 1966

NATIONAL AERONAUTICS AND SPACE ADMINISTRATION

For sale by the Clearinghouse for Federal Scientific and Technical Information
Springfield, Virginia 22151 – Price $4.25

ANNOTATION /2

This book gives an account of the physical foundations and principles of constructing apparatus for investigating the upper atmosphere as well as the foundations of measuring techniques and preliminary processing of the data.

Particular attention is devoted to a description of the apparatus used for meteorological satellites and meteorological and geophysical rockets.

The book is intended for students of Institutes of higher learning, engineers, teachers, and scientific workers in the domains of geophysics, meteorology, radio communications, astronomy, aviation, and astronautics.

FOREWORD

/3

The practice of rocket investigations of the upper atmosphere and outer space and the launching of the most diverse artificial earth satellites and interplanetary stations has necessitated the development of methods of investigation and apparatus for measuring numerous parameters characterizing the state of the atmosphere and outer space.

Manned space flights have made it possible to expand evermore the scope of investigations and at the same time have raised a number of new problems whose solutions require the most accurate data on the state of the upper atmosphere and outer space. Experimental data are also of scientific importance since they are the starting point for the development of many sciences whose function is to study the regularities of processes and phenomena occurring in the atmospheres of planets and at various distances from the sun (geophysics, meteorology, space physics, solar physics, etc.). It is especially necessary to point out the practical and scientific value of satellite studies of processes occurring in the atmosphere that determine the weather in various regions of the earth, many of which are inadequately elucidated by ordinary meteorological information (oceans, mountains, deserts, etc.).

The equipment in use at present is characterized by great diversity, and in a number of cases the measurement of one and the same parameter is performed by essentially different instruments.

Most authors describe instruments and measuring methods in varying ways and usually in a highly abridged form. In connection with this it has become necessary to describe existing methods from a single aspect. In presenting the material, special attention was paid to a detailed description of the basic fundamentals and potentialities of the various measuring methods and to the procedure and apparatus used.

The limited volume of data and sometimes the absence of necessary material prevented the author from examining some of the presented problems with the /4
desired completeness, especially with respect to evaluating the accuracy of the methods and instruments employed.

In this book all specific data and characteristics of measuring instruments, rockets, and space vehicles are based on material from the Soviet and foreign literature which, for convenience, is broken down into Chapters.

The author expresses his sincere thanks to Candidates of Technical Sciences G.M.Zabrodskiy, N.F.Pavlov, N.A.Petrov, and Candidate of Physico-Mathematical Sciences A.A.Pokhunkov for their valuable advice on improving the manuscript.

TABLE OF CONTENTS /364

Page

Annotation ii
Foreword iii

PART I

INSTRUMENT CAPSULES AND ENVIRONMENTAL DISTURBANCES

Chapter I Types of Instrumentation Capsules 4

Section 1. Meteorological Rockets 4
Section 2. Capsules of Geophysical Rockets 8
Section 3. Space Vehicles 10

Chapter II Disturbance of the Medium by the Capsule 20

Section 1. Disturbance of the Concentration of Particles Close to a Moving Capsule 20
Section 2. Electric Field Close to the Capsule 26
Section 3. Disturbance of the Upper Atmosphere by Desorption of Molecules from the Capsule Surface 30

PART II

MEASUREMENT OF THE PARAMETERS OF THE UPPER ATMOSPHERE AND SPACE

Chapter III Measurement of Structural Parameters 35

Section 1. Measurement Principles 35
Section 2. Direct Temperature Measurements of the Upper Atmosphere 37
Section 3. Manometers for Measuring Low Pressures 42
Section 4. Pressure and Density Measurements of the Upper Atmosphere by Manometers 52

Chapter IV Measuring the Gas Composition of the Atmosphere 61

Section 1. Composition of the Earth's Atmosphere 61
Section 2. Equipment for Measuring the Composition of the Atmosphere 63
Section 3. Principle and Basic Characteristics of Radiofrequency Mass Spectrometers 68
Section 4. Radiofrequency Mass Spectrometer MKh-6401 72
Section 5. Fundamentals of Mass Spectrometer Measurements 78

Page

Section 6. Preliminary Processing of the Test Data 84

Chapter V Measurement of Cosmic Radiation and Corpuscular Flux 89

Section 1. Characteristics of Measured Quantities 89
Section 2. General Characteristics of Onboard Equipment 92
Section 3. Characteristics of the Onboard Counters 94
Section 4. Basic Components of the Electronic Circuits 109
Section 5. Equipment for Recording Cosmic Rays 118
Section 6. Radiometry Equipment 122
Section 7. Equipment for Investigating the Nuclear Component of Cosmic Rays 123
Section 8. Equipment for Measuring Corpuscular Fluxes 128
Section 9. Principles of Preliminary Data Processing 132

Chapter VI Measurement of the Concentration of Charged Particles 134

Section 1. Langmuir Probes and Ion Traps 134
Section 2. Characteristics of the Analytical Method 136
Section 3. Equipment for Ionospheric Measurements 140
Section 4. Work-Up of Ion Volt-Ampere Characteristics 142
Section 5. Measurement of Low Charged Particle Concentrations 145
Section 6. Modulation Traps 149

Chapter VII Measurements of Meteor Streams 153

Section 1. Meteors and Cosmic Dust 153
Section 2. Equipment for Recording Meteor Particles 156
Section 3. Measuring Procedure 162

Chapter VIII Measurement of Electrostatic and Magnetic Fields 163

Section 1. Basic Principles of the Atmospheric Electrostatic Field 163
Section 2. Principle and Procedure of Measuring the Electrostatic Field 164
Section 3. Equipment Used 168
Section 4. Magnetic Field in the Atmosphere and in Space 170
Section 5. Magnetometric Equipment 173
Section 6. Principles of the Nuclear-Induction Method 174
Section 7. Optical Pumping Method 177
Section 8. Method of Ferroprobes or Magnetically Saturated Sensors 179
Section 9. One-Component Ferroprobe Magnetometer 184

Page

Section 10. Measurement Procedure 186

PART III

MEASUREMENTS IN THE OPTICAL RANGE

Chapter IX Measurements of X-Ray and Ultraviolet Radiant Energy 188

Section 1. Characteristics of Emissions Subject to Measurement 188
Section 2. Instruments with Thermoluminescent Phosphor 193
Section 3. Apparatus with Ionization Sensors 197
Section 4. Filter Apparatus with Secondary-Electron Multipliers (SEM) 202
Section 5. Spectral Devices 205

Chapter X Measurements of Radiant Energy in the Visible and Infrared Spectrum Region 217

Section 1. Basic Problems of Measurement and Instrumentation 217
Section 2. Photometers 224
Section 3. Radiometers 234
Section 4. Actinometric Instruments 246
Section 5. Spectral Instruments 253

PART IV

OBTAINING THE IMAGES OF THE PLANETS AND OF THE CLOUD COVER

Chapter XI Scanning Instrumentation 258

Section 1. Optical-Kinematic Diagram 258
Section 2. Dimensions of the Scan Element and Form of the Scan Line 260
Section 3. Energy Resolution 265
Section 4. Narrow-Angle Scanning Radiometer 268

Chapter XII Photographic Instrumentation 269

Section 1. General Information on Aerial Photographic Instruments 269
Section 2. Basic Parameters and Characteristics of Photographic Instruments 272
Section 3. Requirements for the Image Sharpness and the Camera Resolving Power 276
Section 4. Photographing from Objects in Outer Space 279

Page

Chapter XIII Television Equipment 281

Section 1. Basic Principles of Television 281
Section 2. Television Pickup Tubes 287
Section 3. Principal Elements of Electrical Circuitry 299
Section 4. Basic Parameters of a Television Apparatus 303
Section 5. Television Equipment of Weather Satellites 315

Bibliography 319

NATIONAL AERONAUTICS AND SPACE ADMINISTRATION

TECHNICAL TRANSLATION EVALUATION

Budget Bureau No. 104-R037
Approval Expires: Sept. 30, 1969

TO: THE USERS OF THIS TRANSLATION →

NASA TTF NO. 390

MAINTAINING THE QUALITY OF NASA TRANSLATIONS REQUIRES A CONTINUOUS EVALUATION PROGRAM. PLEASE COMPLETE AND MAIL THIS FORM TO AID IN THE EVALUATION OF THE USEFULNESS AND QUALITY OF THE TRANSLATING SERVICE.

THIS PUBLICATION *(Check one or more)*

- ☐ FURNISHED VALUABLE NEW DATA OR A NEW APPROACH TO RESEARCH.
- ☐ VERIFIED INFORMATION AVAILABLE FROM OTHER SOURCES.
- ☐ FURNISHED INTERESTING BACKGROUND INFORMATION.
- ☐ OTHER *(Explain)*: _____

FOLD LINE FOLD LINE

TRANSLATION TEXT *(Check one)*

- ☐ IS TECHNICALLY ACCURATE.
- ☐ IS SUFFICIENTLY ACCURATE FOR OUR PURPOSE.
- ☐ IS SATISFACTORY, BUT CONTAINS MINOR ERRORS.
- ☐ IS UNSATISFACTORY BECAUSE OF *(Check one or more)*:
  - ☐ POOR TERMINOLOGY.
  - ☐ NUMERICAL INACCURACIES.
  - ☐ INCOMPLETE TRANSLATION.
  - ☐ ILLEGIBLE SYMBOLS, TABULATIONS, OR CURVES.
  - ☐ OTHER *(Explain)*: _____

FOLD LINE FOLD LINE

REMARKS

FROM

DATE

NOTE: REMOVE THIS SHEET FROM THE PUBLICATION, FOLD AS INDICATED, STAPLE OR TAPE, AND MAIL. NO POSTAGE NECESSARY.

NASA Form 1332 AUG 66

GPO 915-777

CUT ALONG THIS LINE

CUT ALONG THIS LINE

METHODS OF INVESTIGATING THE ATMOSPHERE WITH ROCKETS AND SATELLITES

A.A.Kmito

Numerous methods of investigating the upper atmosphere by scientific rockets and satellites, including ionosphere sounding probes, meteorological rockets, orbiting geophysical and solar observatories of the USSR and USA are described in detail, and underlying physical principles are reviewed, with wiring diagrams and tabulated data on the instrumentation capsules used. Photographic, telemetry, and television onboard and ground equipment is discussed, with specific reference to achievements on various unmanned and manned satellite and space probe series. Over 350 references.

INTRODUCTION *5

The most important feature of the earth's atmosphere is the inhomogeneity of its basic properties in a vertical direction, characterized by such parameters as temperature, gas composition, density, pressure, electric and magnetic field strengths, intensity and composition of corpuscular or electromagnetic radiations passing through it, etc.

In developing measurement methods it must be taken into account that, in the atmosphere, both pressure and density decrease with altitude and that the upper layers are ionized and in a plasma state. Furthermore, it is necessary to remember that at great altitudes convective and molecular heat transfer is small and radiant heat fluxes acquire the major role here.

At heights of several thousand kilometers, the upper atmosphere gradually passes over into space. This transition ends at a distance of several tens of thousands of kilometers (20 - 40,000 km), and on the dark side of the earth the extent of the atmosphere and of the transition layer is greater than on the side illuminated by the sun.

---

* Numbers in the margin indicate pagination in the original foreign text.

In space, in addition to a gas component of extremely low density (from 100 to 1 ion per cm^3) there is also a dust component (micrometeors and interplanetary dust); fluxes of corpuscular solar radiation fly by with various particle velocities and differing densities (solar wind). This is accompanied by changes in the electric and magnetic fields. Beyond the earth's atmosphere, also fluxes of primary cosmic rays are encountered which, interacting with the gas particles of the upper atmosphere, produce cosmic showers extremely rich in various particles.

The radiations penetrating and ionizing the upper atmosphere are thus its most important components, and the measurement of their parameters is one of the major problems in studying the upper atmosphere and space. Here, we also encounter the problems of investigating the radiation belts surrounding the earth, mainly outside the atmosphere. /6

The treatment of the upper atmosphere as a special area is convenient not only because of the peculiarities of its physical properties but also because of the specifics of the investigation methods used. Lifting the measuring equipment to the necessary altitudes can be accomplished only by rockets as such or by capsules launched by rockets. Capsules, carrying instrumentation and service equipment, which are inserted into satellite orbits or placed on the trajectory of interplanetary flights, are known as space vehicles (SV). The basic characteristics of rockets and SV as well as information on the measured parameters are given in Chapter I.

To date, numerous extremely diverse measurements have been made at various distances from the earth, inside the geomagnetic field and outside it as well as close to the moon and planets within the solar system. These measurements are primarily of a research nature. In the future, they will be continually improved and carried out on an ever larger scale. In particular, international collaboration of scientists should further this project.

An international program of studies of the upper atmosphere and space was worked out as early as during preparation for launching the first satellites during the International Geophysical Year (IGY). This program called for studying:

Ultraviolet and X-radiations of the sun.
Variations and composition of primary cosmic radiation.
Concentration of particles in the upper atmosphere and interplanetary plasma.
Temperature and density of the upper atmosphere.
Streams of micrometeors.
Radiation balance of the earth-atmosphere system.
Distribution and formation of the earth's cloud cover.
Magnetic and electric fields close to the earth and in space.
Radiation dose and temperature conditions within satellites.
Propagation of radio waves of various ranges.
Corpuscular fluxes and low-energy particles.
Radiation belts of the earth.
Development of structural elements of rockets and space vehicles, flight control systems, instrumentation, and other equipment.

The main purpose of the program, as we see, was to study the structure of the earth's atmosphere and the physical phenomena taking place there as well as to obtain data for solving practical problems of meteorology, astronautics, /7 radio communications and other areas of science and technology. Work according to a similar program is still continuing, in particular with the launchings of the "Cosmos" series of satellites as was stated in the TASS report on March 16, 1962.

During the first launchings of space vehicles to the moon and planets of the solar system, the mission programs were extended by projects of investigating the planetary and lunar atmospheres and studying their surfaces. The broad study program for the upper atmosphere and space will be continued in the future, at least for the duration of the International Years of the Quiet Sun (IQSY) (from January 1, 1964 to December 31,1965).

Measurement of the necessary parameters of the upper atmosphere and space forms the basis for performance of studies relative to most of the objectives of the program. The scope of these parameters, as indicated by the research program, is extremely broad.

The instrumentation must operate under the specific conditions of the upper atmosphere or space and, furthermore, must satisfy the special operating conditions in rockets or space vehicles (large linear and vibratory g-forces, effect of radiations, perturbations of the ambient medium close to the rapidly moving instrument module, etc.). In connection with this, the diverse measuring equipment used for the investigations must have a number of common properties, including sufficiently low inertia, high operating reliability, data transmission by telemetry, limited weight and size, cost effectiveness, etc.

The measurement technique also is of a specific character. The main purpose is to accomplish measurements of various parameters with minimal distortions, at maximal allowance for irremovable influences. Therefore, measurements of the parameters of the upper atmosphere and space frequently have the nature of delicate physical experiments carried out by automatic instruments under the complex flight conditions of the instrument capsule.

PART I

/8

INSTRUMENT CAPSULES AND ENVIRONMENTAL DISTURBANCES

To increase the reliability, the instrumentation is housed in special airtight containers which are designed to offer protection from such factors as vacuum, cosmic and solar radiation, meteors, etc.

The receiving devices of many measuring instruments are installed outside the capsule at points where distortions of the measured parameters, caused by the high velocity and outgassing of the capsule, as well as by its electric and magnetic fields, are minimal. To eliminate distortions caused by the launch vehicle, the instrument capsules are usually separated from the rocket at a predetermined height. The various types of launch vehicles for instrument capsules differ in flight trajectories and in scope of the problems to be solved.

To measure the parameters of the upper atmosphere up to comparatively low altitudes (50 - 150 km), small rockets with nonseparable capsules are used, known as meteorological rockets. The endeavor to conduct systematic and multiple measurements by means of meteorological rockets led to their development in the direction of maximal simplicity and economy. Meteorological rockets are widely used in the USA, USSR, France, Japan, England, and other countries.

In the Soviet Union, the blastoff of separable instrument capsules to great altitudes is accomplished by powerful rockets known as geophysical rockets. Multistage rockets, for the most part with integral capsules, known as research rockets, are used in other countries for measurements at altitudes above 100 - 150 km.

Space vehicles - satellites and interplanetary stations - are used as /9
carriers of instruments intended for measuring the parameters of near-earth and far-out space, and also of instruments for investigating the atmospheres of planets and for obtaining their images.

The diversity of the already developed instrumentation carriers, especially of space vehicles, is extensive and is continuously expanding.

Part I of the book gives a brief description of the most widely used carriers, with main emphasis on the characteristics of the instrumentation complex.

CHAPTER I

TYPES OF INSTRUMENTATION CAPSULES

Section 1. Meteorological Rockets

The world's first meteorological rocket (Type 06) was designed in 1934 by

a group of the Osoaviakhime (Society for the Assistance to Defense and Aviation-Chemical Construction) of the USSR and was launched on April 11, 1937. The rocket reached a height of 4500 m. Subsequently there were several other launchings of the Type 06 rocket (Bibl.19).

Systematic investigations of the upper atmosphere by means of meteorological rockets were begun in the USA and USSR only after the end of the Second World War.

The Soviet meteorological rocket is intended to measure the structural parameters of the atmosphere (temperature and pressure) up to heights of 80 - 100 km. It has a length of 7000 mm (without the engine starter), total weight with fuel 680 kg, diameter of the cylindrical part 435 mm, and tail span of 1200 mm (Bibl.2).

The nose cone of the rocket (Fig.1.I), representing the instrument container, is equipped with a forward-projecting thin boom (740 mm long, principal diameter 20 mm) to which the receiving devices of the measuring instruments are mounted. It is divided into three equipment bays, has a length of 1953 mm, a diameter of the cylindrical part of 435 mm, and a weight with equipment of 72 kg (Bibl.2).

The first compartment contains a membrane manometer unit (MMU) (3) whose intakes are located on the boom, a mechanical commutator (6) for the telemetry system of the rocket, and chemical power sources (batteries) (7); the second compartment carries the radio receiver (4) of the telemetry system and photographic apparatus (8); the third compartment serves for housing parachutes to return the nose to earth.

The forward part of the boom contains two small thermal manometers (1). In the center section, four wire resistance thermometers (5) for measuring the temperature of the atmosphere are stretched on steel corner plates, and the /10 temperature of the boom itself is measured by a thermometer wound on it. At the base of the boom, there are four bolometers (2) which measure the intensity of radiant energy affecting the thermometer readings.

The measuring circuits of the thermometers and manometers are Wheatstone bridge circuits with a common power supply. By means of the commutator, the output voltages of all circuits are alternately fed to the input of the transmitter whose signals are frequency-modulated. The ground-based receivers are equipped with cameras for filming the signals from the scope of a cathode-ray tube. The radio-telemetry system of the rocket is periodically calibrated with respect to frequency by transmitting control signals at the start of each cycle. The control signals are generated by connecting the bridge circuit, comprised of highly stable resistors, to the input of the transmitter.

The rocket is launched from a launching tower with spiral rails. On burnout of the booster motor the velocity of its almost vertical ascent (zenith angle about 5°) exceeds 100 m/sec, and on burnout of the liquid rocket engine (LRE) the velocity is more than 1000 m/sec (Bibl.24).

Separation of the rocket nose from the body and ejection of the recovery

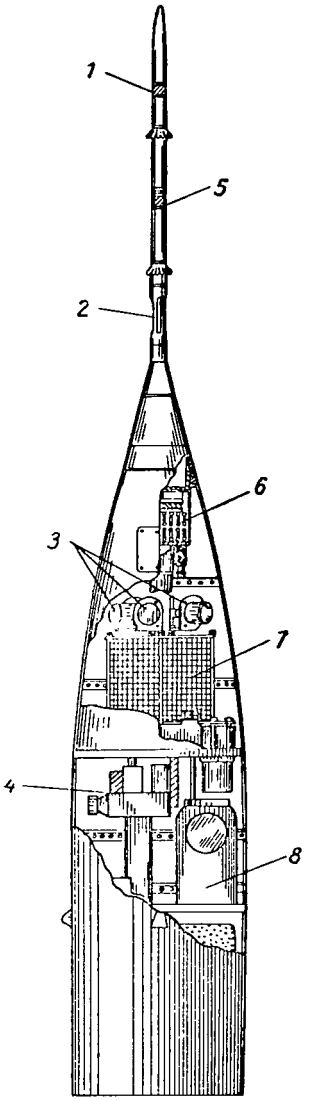

Fig.1.I Nose Cone of Meteorological Rocket.

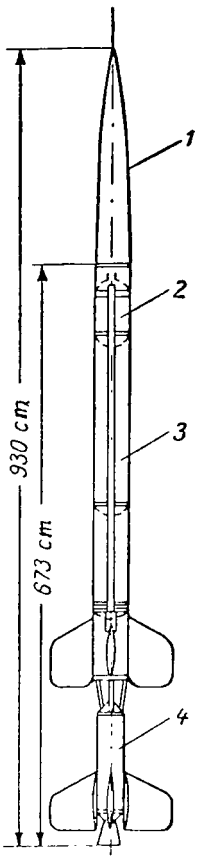

Fig.2.I Aerobee-Hi Type Rocket.
1 - Nose cone; 2 - Oxygen cylinder;
3 - Fuel; 4 - Booster motor.

parachute take place at an altitude of about 70 km. This imparts additional acceleration to the rocket nose which is boosted to a height of 80 - 100 km and then begins to fall back. At an altitude of 50 - 60 km the descent velocity, as a result of parachute braking, drops to about 100 m/sec, becoming 5 - 6 m/sec close to the earth's surface (Bibl.2). The use of parachutes lengthens the residence time of the instruments in the atmosphere and permits repeated re-use of the same rocket thus increasing the cost effectiveness of sounding missions.

The flight of meteorological rockets is tracked by optical and radar methods.

In the USA, meteorological rockets are in use that operate both on liquid and solid propellants. The former include the widely used rockets of the Aerobee type and its various modifications, and the latter include rockets of the Deacon, Nike-Cajun, Loki, etc. type (Bibl.9. 20, 21, 22, 28). The instrumentation of most rockets varies as a function of the intended mission.

Small single-stage solid rockets with a maximum altitude of 50 - 80 km are most frequently used for meteorological purposes. They carry instruments for measuring pressure, humidity, density, atmospheric wind, and also for measuring solar radiation fluxes and radiation of the earth-atmosphere system.

Measurements of various parameters of the upper atmosphere are carried out in conformity with the prescribed program on multistage research rockets with /12 a maximum altitude of several hundreds of kilometers, and onboard equipment for space vehicles is also being developed.

The basic multipurpose (research and sounding) rocket of the USA, especially during the IGY, was the Aerobee-Hi (Fig.2.1). The Aerobee-Hi rocket has a main liquid engine and a solid booster motor. Its length, including the booster, is 9.2 m, diameter 381 mm, payload 54 - 91 kg, total weight 925 kg (Bibl.24).

On burnout of the liquid engine (at a height of about 40 km) the rocket velocity reaches its maximum (2030 m/sec), corresponding to a maximum height of 265 km (Bibl.24). The ceiling of the rocket differs in other variants.

After re-entry of the rocket (at an altitude of about 6 km), the nose cone with the instrumentation separates and descends by parachute (Bibl.21, 24). As the rocket passes through the dense layers of the atmosphere the instrument capsule is heated to a temperature of about 150 - 160° (Bibl.20).

The two-stage solid sounding rocket of the Nike-Cajun class whose prototype is the surface-to-air air defense missile Nike, has found wide use for primarily measuring atmospheric pressure, composition, and density (based on the falling-ball method). This system has almost the same liftoff weight (about 700 kg) as the Aerobee but has a lower ceiling.

It should be noted that the rated G-forces of the onboard equipment of the nose section of the Cajun rocket are rather high. The maximum is 70 g and more which is typical for solid rockets, whereas the G-forces for liquid rockets are not more than 6 - 8 g (Bibl.24).

Section 2. Capsules of Geophysical Rockets

Geophysical rockets have been used in the USSR since 1949 (Bibl.19). Their instrumentation capsules are detachable from the rockets and are recovered by parachute. The instrumentation complex is not standardized and is determined by the research mission or program. The cylindrical unoriented capsule is housed in a mortar attached to the side of the rocket, and at a specified height is ejected from it at low velocity (Bibl.1).

The capsule (Fig.3.I) has four equipment bays: the parachute compartment (1); the center, openwork compartment (2) carrying the pickup devices of the instruments for investigating the atmosphere; the airtight instrument compartment (3) housing the photographic recording device, control units, and measuring circuits of the instruments; and the nose compartment (5) in which the batteries are installed. The earth's surface, cloud cover, and surrounding space are /13 photographed through the portholes (4) to fix the position of the capsule which executes a complex rotational motion with a period of several tens of seconds (Bibl.1). To the side of the compartment (6) a polished metal plate (7) for recording the impact of micrometeors is attached: The openwork compartment (2) houses devices (8) and (9) for pressure measurements at altitudes up to 200 km and for air sampling up to 110 km.

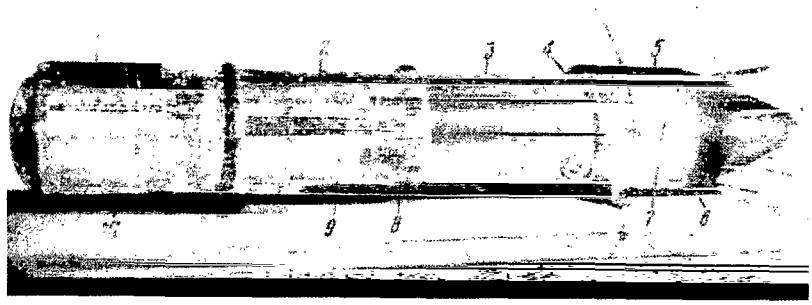

Fig.3.I Geophysical Automatic Capsule and its Equipment.

The parachute automatically deploys at a height of about 2 km above the earth's surface. After landing, the capsule is maintained in a vertical position by booms attached to the nose compartment. A nose shock absorber is used to soften the ground impact. High-altitude geophysical stations (HGS) which are still in wide use were developed during the IGY for measurements requiring steady orientation of the instrument capsule in space (Bibl.5).

The HGS consists of a spherical capsule equipped with automatic attitude controls and gyro stabilizers. The possibility of using such capsules for optical measurements in a broad spectral range is a prime requirement. For this, the capsule serving as a high-altitude optical station (HOS), is equipped with portholes.

The HGS (Fig.4.I), just as the HOS, has a diameter of 1 m and consists of two duralumin hemispheres (1) and (2) (half-shells). The half-shells are rein-

forced on the inside by stringers and ribs and are highly polished on the outside. Along the equator of the lower half-shell a shaped ring (equatorial band) is welded (3) to form an airtight connection between the half-shells. Close to the equatorial band, the lower hemisphere carries two rod antennas of the telemetry system. These are not retracted when the station is installed in the nose section of the launching rocket. In its equatorial plane, the station is provided with a platform to which the power source and the main equipment are mounted. In one variant of the high-altitude optical station, standard 80-mm portholes with flanges, to which optical instruments are attached, are welded to the upper and lower half-shells. /14

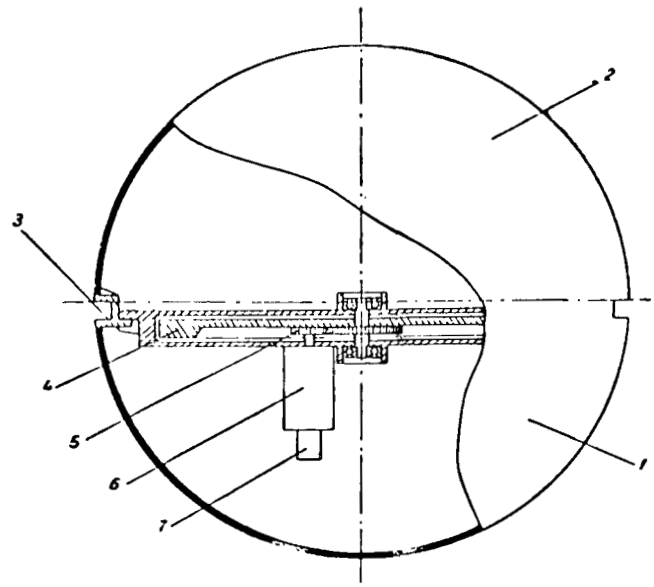

Fig.4.I Schematic Diagram of the High-Altitude Geophysical Station.

Before launching, the entire equipment is fastened to the half-shells and to the platform. The station is tested for airtightness, rinsed with an inert gas stream (nitrogen), and filled with this gas to a pressure of 1.5 atm, which prevents explosion of the gases liberated during operation of the power sources and regulates the temperature within the station.

The automatic attitude control system of the capsule is based on the gyroscopic effect. A power gyroscope (4), actuated by an electric motor (6) with the tachometer (7) over the reducing gear (5) ensures constancy of the vertical gyroscope axis during free flight of the station. During normal operation, /15 the station is oriented with respect to a prescribed azimuth by rough attitude sensors within an accuracy up to $\pm 3^{\circ}$ and maintains orientation with an accuracy to $\pm 0.5^{\circ}$, then the fine attitude sensors are brought into action (Bibl.5).

During the flight of the station, the angles of pitch, yaw, and roll are transmitted by the telemetry system. For transmission of this information three

mutually perpendicular small gyroscopes equipped with potentiometer pickoffs are installed on the station.

To control the position of the station axes relative to the sun and terrestrial horizon, optical instruments SHPS (solar halo and position sensor) and CPS (capsule position sensor) are installed on board. An all-sky camera (ASC) is mounted on the station for control observations of the type and character of the disk of the planet. The temperature in various parts of the station is measured by electric thermometers (ET). The atmospheric pressure at the boundary layer of the capsule is measured by ionization and electric discharge gages.

Launching of the rocket, carrying the station in its nose cone, is done so as to maintain a given direction with respect to azimuth and elevation. The station is separated from the rocket at an altitude of 65 - 67 km, and after fall-away of the protective cone the station is ejected from a recess, being given an additional velocity of about 1 m/sec. The station then moves as far as 1 km away from the rocket. At the moment of separation the automatic attitude control system begins to operate. Usually, after 10 - 20 sec the station will have its prescribed position. Operation of the attitude sensors ceases after the station reaches the trajectory peak where it starts falling back into the denser layers of the atmosphere, at an altitude of about 40 km. In the lower layers of the atmosphere the station falls at a velocity of 170 - 180 m/sec (Bibl.5).

Geophysical capsules are provided with devices for measuring the radiations of the sun and of the earth-atmosphere system, concentration and fluxes of charged particles, composition of the upper atmosphere, pressure up to altitudes of 200 km, electric and magnetic fields, streams of micrometeors; biomedical investigations were also carried out in conformity with the programs of the IGY and IQSY (Bibl.1).

Section 3. Space Vehicles

Based on the type of flight trajectory, space vehicles (SV) are divided into artificial earth satellites (AES) and automatic interplanetary stations (AIS). Satellites carrying a large variety of equipment for scientific investigations are known as orbiting observatories or scientific space stations.

The total of onboard equipment of space vehicles can be subdivided into /16 the following groups with respect to purpose:

1. Equipment for measurements in the upper atmosphere and space, in conformity with a prescribed program.
2. Radiotelemetry equipment, including data-storage capability. This equipment stores information obtained from all measuring instruments, including those controlling the operation of the various devices, and transmits it to the ground-based receiving stations.
3. Radio equipment to determine the motion parameters.
4. Control equipment, including programing and control devices.
5. Life support equipment for the crew and devices ensuring operational reliability of the onboard equipment. The heat-regulating system

(HRS) is one of the most important devices of this type.
6. Equipment for attitude control and stabilization of the space vehicle and flight control (trajectory correction, etc.).
7. Electric power sources.

The instrumentation and its service equipment are prescribed by the mission programs and their arrangement outside and inside the capsule is determined by the nature of the equipment. Below, we give a brief description of a space vehicle by means of which the most important scientific results were obtained.

The launching of the first three satellites in the USSR was done in accordance with the program of the IGY, and the entire program of measurements was already fulfilled with the third satellite.

The world's first artificial earth satellite launched in the USSR on October 4, 1957 had the shape of a sphere [580 mm in diameter weighing 83.6 kg (Bibl.1)] with four mutually perpendicular rod antennas. The satellite was equipped with a heat-regulating system, a system for measuring the temperature of the structural components and the inside pressure, two radio transmitters, and chemical power sources (Bibl.1).

The second satellite (November 3, 1957) was the last stage of the launching rocket. In three separate capsules, it contained measuring equipment and also the experimental animal, the dog Laika. Measurements of ultraviolet radiation, X-rays, and cosmic radiation, as well as investigations of the ionosphere and biomedical experiments were carried out on the satellite. The temperature inside and on the surface of the AES was measured (Bibl.9).

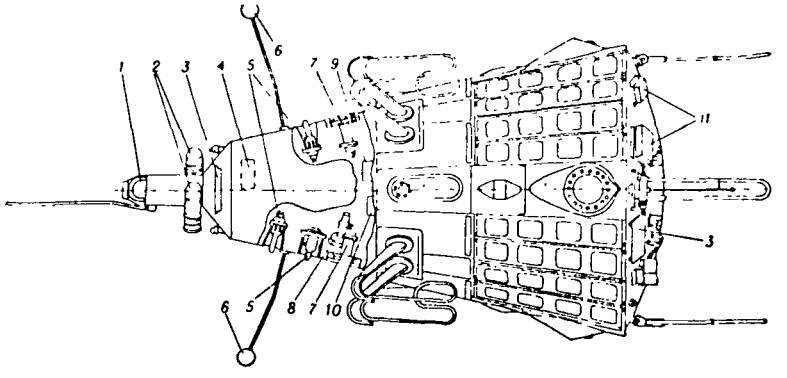

Fig.5.I Scientific Equipment of Third Soviet Artificial Earth Satellite.

The third satellite (May 15, 1958) carried different and improved equip- /17
ment (Fig.5.I). The total weight of the satellite was 1327 kg, and the weight of the scientific and measuring equipment together with the power sources was 968 kg (Bibl.1, 9). The instrumentation of the satellite included a magnetometer (1), equipment for measuring corpuscular solar fluxes (2), an instru-

ment (4) for recording photons in cosmic rays, magnetic and ionization gages (5), ion traps (6), electrostatic fluxmeters (7), a mass spectrometer (8), an instrument (9) for recording heavy nuclei, a device (10) for measuring the intensity of cosmic radiation, and equipment (11) for recording micrometeors. Electrochemical sources inside the satellite casing and solar cells (3) were used as power sources.

The Soviet space rockets launched to the moon on January 2, September 12, and October 4, 1959 were the last stages of the launching rockets from which the space vehicle was separated. The space vehicle of the first and second rockets was an airtight spherical container made of aluminum alloys. It carried scientific equipment for measuring the magnetic field, cosmic radiation, concentration of charged particles in the ambient plasma, and micrometeors.

The capsule of the first rocket passed at a distance of 5 - 6000 km from the moon, and the second descended to the lunar surface having on board a pennant with an image of the emblem of the USSR and the inscription: "USSR, September, 1959."

The space vehicle of the third rocket was an unmanned interplanetary station, made in the form of a cylindrical capsule with spherical bottoms. The maximal length of the AIS was 1.3 m, the maximum transverse dimension was 1.2 m, and it weighed 278.5 kg (Bibl.1, 9). One of the most important problems to be solved upon launching of this station was to obtain photographs of the far side of the moon and to transmit them by television apparatus to the earth. /18

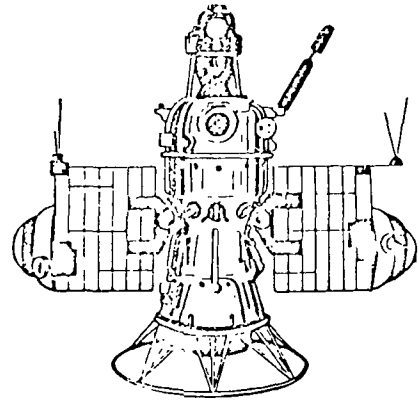

Fig.6.I Unmanned Interplanetary Station Mars-1.

The insertion into interplanetary trajectories of AIS to the planets Venus and Mars was accomplished in the USSR by a guided space rocket launched from heavy artificial earth satellites.

The interplanetary station (IS) launched toward Venus on February 12, 1961 had a weight of 643.5 kg, length of 2.035 m, and diameter of 1.05 m. This Venus probe was a space vehicle equipped with a complex of radio engineering and scientific devices, an orientation and control system, program devices, heat-

regulating system, and power sources. In design it was made in the form of a cylindrical airtight capsule carrying, on the instrument frame, the instrumentation and the buffer storage. The work program of the equipment included a check on extreme-range radio communication, measurements of cosmic radiation, micrometeor streams, magnetic field strength, concentration of charged particles in the interplanetary plasma and in corpuscular fluxes (Bibl.1).

The interplanetary probe Mars-1 (October 1, 1962) had a weight of 893.5 kg and a maximal length of 3.3 m (Fig.6.I). The diameter of the capsule was 1.1 m and the width, with consideration of the solar cells and radiators of the heat-regulating system, was 4.0 m (Bibl.18). The station was efficiently fitted with all necessary auxiliary and scientific equipment intended for measuring the parameters of both inner and outer space and in the vicinity of the planet Mars. One of the most important problems of the mission was to study the planet itself and the properties of its atmosphere.

In design, the AIS was made in the form of two airtight compartments: orbital and planetary. The orbital compartment contained equipment for operating the station during the flight to the planet. To this compartment were attached a correcting motor unit, solar battery panels, hemispherical radiators for the heat-regulating system, and the antenna of the onboard radio systems. The planetary compartment carried the measuring equipment designed for investigations near the planet.

The instrumentation of the Mars-1 probe included a phototelevision device, a spectroreflexometer for detecting the organic cover of the planet, an /19
ultraviolet spectrograph for determining the ozone content in the Martian atmosphere, magnetometric equipment, instruments for measuring cosmic radiations, a radiotelescope operating on the 150 and 1500 m wavelength, equipment for measuring meteor streams and charged particle concentration over the flight trajectory and near the planet (Bibl.18).

During the periods of radio communication with the AIS, results of the measurements were obtained over a distance of up to 8 million kilometers from the earth.

The Soviet spaceship satellites were launched (the first on May 15, 1960 and the fifth on March 25, 1961) for the purpose of operating and checking the basic life-support systems in space and the astronaut's return to earth. Biomedical and other scientific investigations were also included. Measurements of cosmic radiations, X- and ultraviolet radiations of the sun, and radiation levels within the capsule were accomplished on these spacecraft.

Beginning on March 16, 1962, in conformity with the research program of the Cosmos series of satellites (see Introduction) in the Soviet Union, systematic launchings of specialized satellites intended for a comprehensive investigation of individual problems took place. Orbits with a perigee of 200 - 300 km and apogee from 300 (Cosmos-18) to 1600 km (Cosmos-5) are characteristic for these.

Valuable scientific information was obtained from the launchings of the Vostok and Voskhod type spacecraft with astronauts on board. The effect of a prolonged stay in space on man and his performance was studied, numerous bio-

medical investigations were performed, various auxiliary systems of the SV were tested and improved, and "space sighting" was accomplished for the first time, followed by a walk in space by the first human. The launch of the controlled maneuverable space vehicle Polyot-I on October 1, 1963 was of great importance for the development of space studies.

Longer investigations of the upper atmosphere and space were started by means of the scientific stations Elektron-1 and Elektron-2 (January 30, 1964) which had the mission of detailed studies of the inner radiation belts of the earth and their physical phenomena. The experimental program of these spacecraft called for measuring the fluxes of low- and high-energy particles, magnetic fields, space radiation, chemical composition of inner space, short-wave radiation of the sun, radio emission of the galaxies, and micrometeors. These investigations were performed in conformity with the program of the IQSY (Bibl.12).

Space vehicles launched in the USA are distinguished by great diversity. /20 According to published data (Bibl.11) the USA had launched 122 space vehicles by December 31, 1962, of which 66 were for scientific research, 6 for lunar exploration, 4 were manned or carried animals, 16 were for surveillance, and 30 for military purposes.

A brief description of the US space vehicles, developed according to the research projects on the upper atmosphere and space, is given below.

The launching program of the Explorer series was started on January 1, 1958. The first American satellites were the fourth stage of the launching rocket. The nose cone of the satellite was made of stainless steel. Behind it was installed the instrument bay which was enclosed in a steel cylinder (Bibl.10). Later (beginning with Explorer-V) the satellites of this series were design-modified; for example, they were given the form of spheroids of aluminum alloys, two truncated cones of fiberglass laminate connected by the base (Explorer-VII) and an inflated plastic sphere [Explorer-XIX (Bibl.11, 26, 29, 31)].

The weight of the scientific and measuring equipment varied from 6.3 kg (Explorer-IX) to 64 kg (Explorer-VI).

Missions of the satellites of the Explorer series included measurements of atmospheric density, magnetic field, cosmic radiation, micrometeoroids, local temperatures of the satellite, charged particle concentration, electrostatic charge on the satellite skin [Explorer-VIII (Bibl.27)], fluxes of long-wave radiation and radiation balance [Explorer-VII (Bibl.26)], short-wave radiation of the sun and temperature of the gas plasma. Television pictures of the earth's surface from a height of about 31,400 km were transmitted from the Explorer-VI satellite (Bibl.30). The orbits of all satellites of the Explorer series had a large ellipticity.

Satellites of the Vanguard series were developed especially for missions of the IGY program. It was proposed to launch 12 satellites of this series; however, as a consequence of launching trouble only three were actually inserted into orbit. The satellites were made in the form of aluminum alloy spheres

about 500 mm in diameter. The weight of the first of these was only 1.47 kg (Bibl.10).

The program of measurements on these satellites included determination of the earth's magnetic field and X-radiation of the sun [Vanguard-III (Bibl.11)] and also the fluxes of visible and infrared radiation reflected by the earth into cosmic space [Vanguard-II (Bibl.8)]. The latter had an instrument capsule with equipment weighing 680 gm. It was not oriented in space and scanned the earth's surface by the field of view of the receivers as a result of rotation of the entire satellite. However, it was not possible to process the received data because of oscillations of the satellite and insufficient sensitivity /21 of the infrared receivers (Bibl.7).

A series of launchings of stabilized satellites developed for the Discoverer program was started in March 1958 to prepare manned flights into space for the Mercury project. Therefore, many of the satellites were equipped with ejection capsules and were used as test-bed for the equipment of reconnaissance satellites of the Midas and Samos types (Bibl.11). Equipment for measuring the following parameters was installed both on the ejection capsules and on the last stage of the rocket: cosmic radiation, thermal terrestrial radiation, micrometeor streams, magnetic field, and ion flux density. The effect of cosmic radiation doses on various living organisms and the propagation of radio waves were studied. The characteristic configuration of the capsule of the Discoverer satellites was a cylinder with a conical nose. The diameter was about 80 cm, length about 70 cm, and weight 130 - 140 kg. The second stage of the launching rocket went into orbit along with the satellite and then separated from it. Many of the satellites of this series were inserted into near-circular polar orbits (Bibl.11, 25).

The meteorological satellites of the Tiros series (abbreviation for Television Infrared Observation Satellite) were intended to obtain meteorological information on a global scale, mainly on the distribution of the cloud cover and radiation balance over the earth's surface. They contain television equipment for transmitting pictures of the cloud cover and underlying surface and also radiation sensors for radiation fluxes reflected and emitted by the earth in various spectrum regions. Later (in the Nimbus series) scanning infrared sensors began to be used to obtain images of the cloud cover by infrared rays during the dark time of the day.

Updating of the instrumentation for meteorological satellites was performed in the launchings of Vanguard-II and Explorer-VII.

From April 1960 to December 1963, eight satellites of the Tiros series were launched. They were all manufactured from aluminum and stainless steel alloys in the form of 18-faced cylinders (Fig.7.I). The center section of the satellite carries the receiving antenna (1) and solar cells (6) on the outer surfaces. The instrumentation is mounted to the lower base of the cylinder. It includes: a television receiving tube (9) with a wide-angle lens (10), a teletransmitter (11) with a transmitting antenna (12), a control device (14), a magnetic memory (15), a storage battery (16) with regulator (3), a receiving tube (2) with a narrow-angle lens, and a time relay (4). To maintain the rotational speed of the satellite within 9 - 12 rpm, dry-fuel rocket thrusters (8) are used.

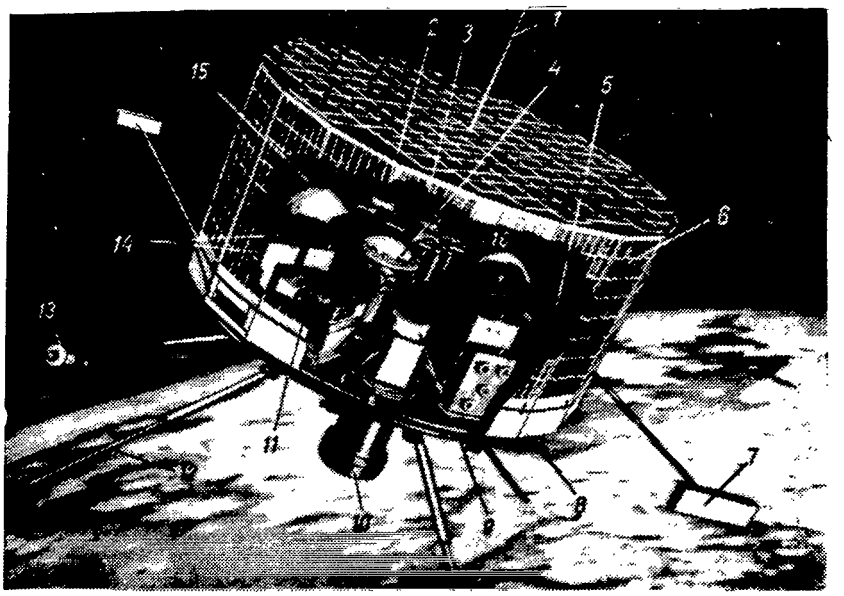

Fig.7.I Instrumentation of the Meteorological Satellite Tiros-II.

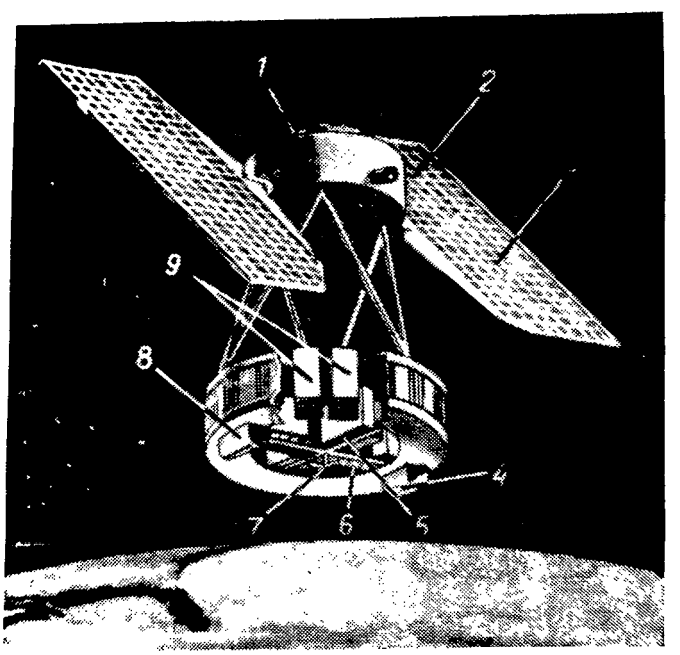

Fig.8.I Sketch of the Nimbus Satellite.

Counterweights (7) serve to slow down its rotation after separation from the launching rocket (13). /23

The Nimbus satellite (Fig.8.I) consists of two capsules connected by an open trellis. Its height is about 2.5 m, diameter [after deploying of the solar panels (3)] about 1.4 m, weight about 240 kg (Bibl.7). The satellite is stabilized in space and oriented with the bottom of the lower container directed toward the earth. Pneumatic devices and the inertia of the panels (3) are used for stabilization and orientation. The accuracy of orientation with respect to three axes is approximately $\pm 1^{\circ}$, and its rate of change is not more than 0.1° per second. The control equipment and horizon indicator (2) are situated in the upper bay (1). The lower bay (diameter 145 cm, height 33 cm) contains three television vidicon cameras (6) providing a field of view of about 105°, an electrostatic system of recording the images (5), scanning infrared radiation sensors with high (4) and medium (8) resolution, electronic equipment (9), and the antenna of the telemetry system (7).

Furthermore, spectral measurements of the infrared spectrum region and ultraviolet solar radiation were scheduled for the Nimbus series (Bibl.7, 15).

Measurements of certain parameters, in particular thermal radiation of the earth and its albedo, passage of radio waves through the ionosphere, and gravitational forces were carried out by the navigation satellites of the Transit series and also by the small simultaneously launched satellites. The latter were made in the form of spheroids, about 50 cm in diameter and 60 - 90 kg in weight. They carried instrumentation for measuring short-wave solar radiation fluxes [Greb, Solar radiation (Bibl.31)], for investigating particles of the radiation belts [Injun (Bibl.31)], etc.

Orbiting observatories have recently been launched: a geophysical (OGO) in two variants, a solar (OSO), and an astronomical (OAO) fitted with instrumentation for accommodating as many as 20 - 30 different experiments (Bibl.11). It is proposed to increase the weight of the observatories to 1400 kg (Bibl.31). The OSO launched on March 7, 1962 into a near-circular orbit at an altitude of about 600 km had a weight of about 200 kg. It consisted of two sections: an upper section oriented toward the sun and a lower section which spins for stabilization. The lower section has three brackets to whose ends gas cylinders and thrusters for maintaining rotation are mounted (Bibl.31).

With this observatory, measurements were made of the short-wave solar radiation in various spectrum regions, of the energy of cosmic dust particles, and of the character of thermal radiation of various materials attached to the outside skin.

We note that, to test the onboard equipment for orbital observatories and to investigate magnetic fields, cosmic radiation, and structural parameters of the atmosphere, satellites bearing the indexes S and P were launched. /24

Launchings of space vehicles of the Pioneer series were started on March 17, 1958 to investigate flight routes to the moon; however this mission was not completed: Of the six vehicles launched four were complete aborts and two, Pioneer-IV and Pioneer-V, did not go into the calculated lunar orbit and

became satellites of the sun.

The first of these carried an instrument capsule in the form of a glass-fiber-reinforced cone with a base diameter of 230 mm and a height of 510 mm; the second was of aluminum alloy in the form of a sphere with four paddles to which the batteries of the solar cells were mounted (the total weight of the vehicle was about 40 kg).

The research program on such space vehicles called for determining radiations, corpuscular fluxes, and propagation of radio waves at great distances. Thus, radio communication from the space vehicle Pioneer-V was accomplished over a distance up to 11.3 million kilometers (Bibl.6, 31).

At present, new spacecraft variants of the Pioneer series are being developed, weighing 50 - 60 kg and designed in the form of aluminum alloy cylinders 80 cm long and 92.5 cm in diameter (Bibl.11, 17). The side surface of the vehicle carries the solar cells with the exception of a strip 12.5 cm wide where the sensors of the various instruments are placed; the magnetometer is attached to a rod mounted to the body of the vehicle. The instrumentation includes the following units:

1) magnetometer with a sensitivity up to 1.5 gamma,
2) two traps for charged particles of interplanetary plasma,
3) two Geiger counters for measuring cosmic rays,
4) a micrometeor collision sensor,
5) an instrument for measuring electron concentration in interplanetary space (based on measurement of radio signals sent from the earth at frequencies of 50 and 400 mc).

The Ranger spacecraft series was developed for flights to the moon, since the vehicles of the Pioneer series did not achieve the prescribed cis-lunar orbit. The first two Rangers (January 1962) were intended to circumfly the moon on a geocentric orbit. Beginning with the Ranger-III vehicle, it was planned to rough-land on the moon an instrumented capsule separated at a height of 20 - 30 km. Transmission of images of the lunar surface by means of a television camera was to take place from a height of about 3000 km before ejection of the capsule.

The vehicles of the Ranger series have an openwork structure in the form of a truncated cone with a base diameter of about 1.5 m and a height of 2.5 - 3.5 m (various modifications) in an intricate arrangement. After launching the satellite, the side panels with the solar cells unfold increasing the span of the vehicle to about 5 m; and this is followed by deploying of a parabolic screen antenna. The weight of the vehicles is 306 - 349 kg and the weight of the scientific equipment, about 110 kg (Bibl.3, 15, 23). The spacecraft is provided with devices for position-fixing relative to the sun and with a correcting unit. /25

The instrumentation is designed to measure the solar radiation in various spectral ranges, cosmic radiation, magnetic fields, and accumulation of hydrogen at the boundary of the earth's atmosphere.

The ejection capsule has a spherical shape, about 0.3 m in diameter and 30 - 40 kg in weight. It contains equipment for measuring the seismic activity of the moon (seismometer and accelerometers) and the radioactivity of lunar rocks, and also power sources (mercury batteries) and a radio transmitter with a directional antenna.

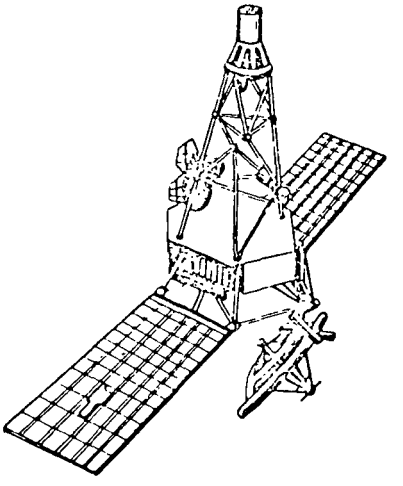

Fig.9.I Unmanned Interplanetary Station Mariner-II.

After a series of unsuccessful launchings, it became possible to obtain several thousand photographs of the lunar surface at various distances from it by means of Ranger-VII.

At present, the USA is developing space vehicles of the Surveyor type which are intended for "soft" landing on the moon of an instrument package weighing about 340 kg; the Prospector for landing a self-propelled or "roving" research vehicle; and the Greencheese for sampling and delivering to the earth specimens of the lunar surface (Bibl.11, 14, 15).

The Mariner unmanned interplanetary spacecraft were developed for scientific exploration flights to Mars and Venus. They consist of a complex open-work structure (Fig.9.I) to which the instrument capsules, parabolic screen antenna, and solar panels are mounted. In the launch position, the maximum diameter of the vehicle is 1.5 m and its height is 3 m; in orbit, the span of the panels reaches 5 m and the height increases to 3.6 m owing to raising of the antenna (Bibl.4, 11, 15).

Unmanned interplanetary spacecraft of the Mariner type had the mission to take measurements to elicit the forms of life on planets, to investigate the composition of their atmospheres, radiation level, and magnetic fields and also the character and structure of the surface of the planets. Furthermore, /26 during the flight the basic parameters of space are measured (magnetic fields, cosmic dust, concentration of charged particles, and cosmic rays).

The launch of Mariner-II toward Venus on August 27, 1962 was successful. The spacecraft had a weight of about 212 kg and accomplished the measurements called for in the program. To determine the water vapor content in the atmosphere of Venus and the temperature of its surface the equipment included microwave (13.5 and 19 mm) and infrared (in the 8 - 9 and 10 - 10.8 μ range) radiometers. Cosmic radiations were measured by equipment with gas-discharge counters and ionization chambers; micrometeorites by piezoelectric pickups, magnetic field by three-component magnetically saturated sensors, concentration of charged particles by multigrid traps with 10 voltage levels.

The Mariner-II accomplished Venus fly-by at a distance of 35,600 km (calculated: 16,000 km). Communication with the craft was maintained up to a distance of 86.7 million kilometers.

The Voyager project is being developed for launching space vehicles into satellite orbits of Mars or Venus and for ejecting an instrument package to the surface (Bibl.11, 15).

CHAPTER II

DISTURBANCE OF THE MEDIUM BY THE CAPSULE

Section 1. Disturbance of the Concentration of Particles Close to a Moving Capsule

The equipment for measuring the parameters of the upper atmosphere and space, as mentioned above, is installed in various capsules which generally move at high velocity. As a result, changes occur in the ambient plasma which must be taken into account when developing measuring techniques and also when interpreting the results, so as to obtain parameters of an undisturbed medium.

Let us take the velocity of the satellite as the characteristic velocity of the capsule at high altitudes v_0. The velocity of particles is determined by their temperature at a given level in the atmosphere.

In the undisturbed plasma of the upper atmosphere, the velocity distribution of particles can be considered Maxwellian (Bibl.1), namely:

/27

$$f(v+v_0) = n_0\left(\frac{M}{2\pi kT}\right)^{3/2}\exp\left\{-\frac{M(v+v_0)^2}{2kT}\right\}, \qquad (1.II)$$

where $f(v + v_0)$ is the distribution function with respect to the direction axis r, v is the velocity of particles having a mass M and a temperature T, n_0 is the particle concentration, k is the Boltzmann constant, v_0 is a velocity component of the capsule in the given direction r.

In a Maxwellian distribution, as is known (Bibl.5), the main velocity of the forward motion of particles of mass M is equal to

$$v = \sqrt{\frac{8kT}{\pi M}}, \qquad (2.II)$$

where T is the temperature of the plasma in thermal equilibrium.

If we take into account that the electron temperature T_e is approximately equal to the ion temperature T_i (Bibl.4, 3), then eq.(2.II) will yield

$$\frac{v_e}{v_i} = \sqrt{\frac{M}{m}}, \qquad (3.II)$$

where M and m are the ion and electron masses, respectively.

For example, at $T_i \approx T_e \approx 1000^\circ$K, eq.(2.II) yields $v_i \approx 10^5$ cm/sec for the ions of atomic oxygen, and $v_e \approx 10^7$ cm/sec for electrons.

At a velocity of the capsule of $v_0 \approx 8 \times 10^5$ cm/sec, we have

$$v_e \gg v_0 \geqslant v_i. \qquad (4.II)$$

The inequality (4.II), as is apparent from Table 1.II compiled from the data of another paper (Bibl.1) is satisfied in a wide range of altitudes of the upper atmosphere.

The mean free path of neutral molecules λ_n, of electrons λ_e, and of ions λ_i at high altitudes substantially exceeds the characteristic dimension of the capsule (radius $R \approx 10^2$ cm).

The character of flow past the capsule, and even more so the effect on the sensors of the measuring instruments (characteristic dimension $r_0 \approx 1 - 10$ cm) by the relative flow, in this case has a free molecular character in which the particles move independently of one another in conformity with their mass; there are no aerodynamic effects in the immediate vicinity of the capsule; in particular, no boundary layer is formed. Therefore, in the greatly rarefied plasma of the upper atmosphere conventional aerodynamic methods are inapplicable. To describe the behavior of particles close to the capsule, we must use the /28 kinetic theory which takes into account that the medium is an aggregate of individual particles, as was done elsewhere (Bibl.1, 4, 8); the basic results are examined below.

Let us imagine a coordinate system (r, z) referred to a spherical capsule (Fig.1.II). In this coordinate system, the capsule moving at a velocity v_0 is struck by a flux of neutral particles (molecules and atoms) whose thermal velocity, in first approximation, can be neglected with respect to v_0. After collision with the capsule surface, the neutral particles are reflected, causing the formation of a stagnation zone ahead of the capsule in which the concentration of particles is increased, and formation of a zone of rarefaction aft of the capsule.

Let us assume that the reflection of particles is of a specular nature and

TABLE 1.II

CERTAIN CHARACTERISTICS OF THE UPPER ATMOSPHERE AND SPACE

Height, km	λ_n cm	λ_e and λ_i cm	D cm	ρ_e cm	ρ_i cm	v_n and v_i cm/sec	v_e cm/sec
			Earth's Atmosphere				
100	10	50	1	~ 1	$2 \cdot 10^2$	$4 \cdot 10^4$	$9.4 \cdot 10^6$
200	$8 \cdot 10^3$	$7 \cdot 10^3$	0.2—1	~ 2	$4 \cdot 10^2$	$7 \cdot 10^4$	$1.5 \cdot 10^7$
300	10^5	$9 \cdot 10^3$	0.1—0.7	~ 3	$5.6 \cdot 10^2$	$9 \cdot 10^4$	$1.9 \cdot 10^7$
400	$7 \cdot 10^5$	$2 \cdot 10^4$	0.2—0.4	~ 3	$5.5 \cdot 10^2$	10^5	$2.2 \cdot 10^7$
500	$6 \cdot 10^6$	$4 \cdot 10^4$	0.3—0.6	~ 3	$\sim 7 \cdot 10^2$	$1.4 \cdot 10^5$	$2.5 \cdot 10^7$
700	$5 \cdot 10^7$	10^5	0.4—0.7	~ 4	$8.2 \cdot 10^2$	$1.6 \cdot 10^5$	$2.9 \cdot 10^7$
1000	$8 \cdot 10^8$	$8 \cdot 10^5$	1	~ 5	$\sim 10^3$	$2.0 \cdot 10^5$	$3.4 \cdot 10^7$
3000	$2 \cdot 10^{14}$	$3 \cdot 10^6$	4	~14	$2 \cdot 10^3$	$2.3 \cdot 10^5$	$3.9 \cdot 10^7$
			Interplanetary Gas				
3-4 Earth Radii		$3 \cdot 10^9$	30	$2 \cdot 10^2$	$4 \cdot 10^4$	$\sim 2 \cdot 10^6$	$4.4 \cdot 10^7$
			Space				
		$7 \cdot 10^{11}$	700	$\sim 3 \cdot 10^5$	$6 \cdot 10^7$	$\sim 3 \cdot 10^6$	$5.4 \cdot 10^7$

Note. The symbols λ_n, λ_e, and λ_i denote the mean free paths of neutrons, electrons, and ions respectively; B is the Debye radius, ρ_e and ρ_i are the Larmor radii for electrons and ions; v_n, v_i, and v_e are the thermal velocities of neutral particles, ions, and electrons.

that the velocities of the particles impinging on the body and of the reflected particles are identical. Let us determine the steady distribution of the /29
neutral particle concentration n_n for specular reflection which, as shown by analysis (Bibl.4), is established after a time $\frac{R_0}{v_0}$ equal to about 10^{-4} sec in the vicinity of a spherical capsule with a radius R_0 of about 100 cm.

In the case under consideration (Fig.1.II), the number of reflected particles contained in a small volume dw (r, z) situated at a point with the coordinates (r, z) will be equal to the concentration of particles in the relative flow dw (r, 0) reflected from a certain point of the capsule surface, which is determined by the angle θ. The excess concentration at the point under consideration ahead of the capsule is

$$n_n'(r, z) = n_0 \frac{dw(r, 0)}{dw(r, z)}, \qquad (5.II)$$

where n_0 is the concentration of neutral particles in an undisturbed flow.

The total concentration of particles at any point (r, z) of the stagnation zone will be

$$n_n(r, z) = n'_n(r, z) + n_0. \tag{6.II}$$

As shown elsewhere (Bibl.4), due to the fact that the velocity of particles subject to elastic collisions remains constant, the ratio of the examined volumes is equal to the ratio of their cross sections

$$\frac{dw(r, 0)}{dw(r, z)} = \frac{ada}{rdl}, \tag{7.II}$$

where

/30

$$a = R_0 \sin\theta, \quad dl = \frac{2r\left(1 - \frac{R_0}{r}\sin^2\theta\right)}{\sin^2\theta} d\theta.$$

From eqs.(5.II) and (7.II), we obtain

$$n_m(r, z) = n_0\left(\frac{R_0}{r}\right)^2 \frac{\sin^2\theta\cos^2\theta}{1 - \frac{R_0}{r}\sin^3\theta}. \tag{8.II}$$

It follows from eq.(8.II) that the excess concentration rapidly decreases (proportional to $\frac{1}{r^2}$) with distance from the capsule ($r > R_0$).

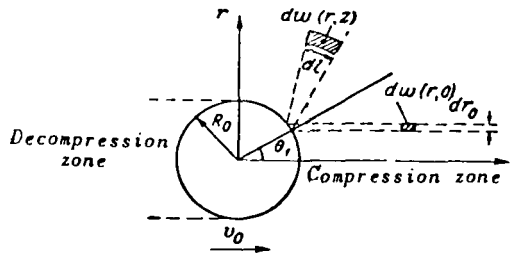

Fig.1.II Diagram of the Formation of a Disturbed Region Close to a Moving Body.

In the case of diffuse reflection, the mean velocity of the scattered particles with respect to a normal to the body surface will decrease, whereas the excess concentration, especially close to the surface, will increase. As shown by analysis (Bibl.4), at a distance of 0.01 R_0 from the surface in the front part the excess concentration (for example) is triple the particle concentration in the undisturbed relative flow n_0.

In this case, if all oncoming particles were immobile (v = 0), the space

behind the container would be completely empty. The presence of thermal agitation of the particles for the decompression (rarefaction) region is essential, since owing to the motion of the velocity component of the particles normal to the direction of flight of the capsule, this region is filled. The dimension of the highly rarefied zone is of the order of $R_0 \frac{v_0}{v}$ and, in the case of a rapidly moving body ($v_0 \gg v$), the rarefaction zone proved to be much larger than the disturbed stagnation zone ahead of the capsule. The concentration n" close to the aft surface of a rapidly moving capsule with a Maxwellian velocity distribution described by eq.(1.II) proves to be small, in conformity with the exponential relation

$$n'' \sim n_0 \exp\left[-\frac{Mv^2}{2kT} \right]. \qquad (9.II)$$

We should emphasize that the concentration of particles in the rarefied region is independent of the character of their interaction with the surface of the body. The concentration of particles moving more rapidly than the capsule, $v \gg v_0$, is evidently negligibly disturbed by it. Therefore, the rarefied region is filled mainly by particles of low mass (electrons).

The concentration distribution of neutral particles close to a spherical capsule whose velocity is by a factor of 8 greater than the velocity of the particles ($v_0 = 8v$), calculated by A.V.Gurevich (Bibl.4), is shown in Fig.2.II. Calculation demonstrates that, at a distance of 80 R_0 from the capsule, the particle concentration in the rarefied region is less than the undisturbed concentration n_0 by only 0.01 n_0. /31

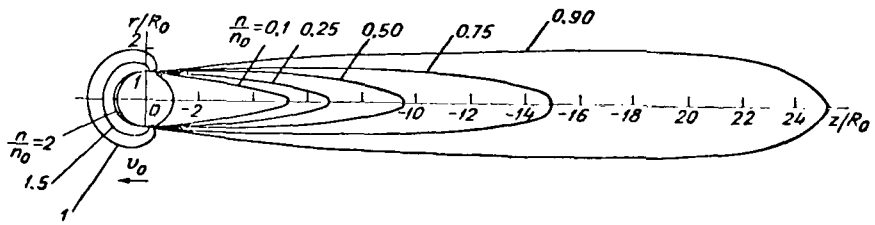

Fig.2.II Isolines of the Density of Molecules Close to a Spherical Capsule Moving at a Velocity of $v_0 = 8v$.

The concentration distribution of charged particles - ions and especially electrons - unlike neutral particles depends not only on their interaction with the capsule, but also on the electric and magnetic fields close to it.

If eq.(4.II) is satisfied and if the energy of the ions striking the body $\frac{Mv_0^2}{2}$ substantially exceeds their thermal energy kT, it can be considered in first approximation that the disturbances, especially in the compression zone, have the same character as the disturbances of the concentration of neutral

molecules examined above. This is due to the fact that the potential energy of the ion in an electric field $e\varphi$ generated as a consequence of disturbances of the plasma is usually only of the order of the thermal energy (Bibl.1).

A definite effect on the distribution of ions close to a charged capsule can be exerted by its own potential. For this reason a shielding space-charge layer is formed close to the capsule. The values of the Debye shielding distance for a fixed charge in an undisturbed plasma with a charged particle concentration N, equal to $D = \sqrt{\frac{kT}{4\pi e^2 N}}$, are given in Table 1.II for various altitudes.

In the case of a rapidly moving large body (whose size is essentially larger than the Debye radius at a given altitude $R_0 \gg D$), the field potential at a distance of the order of D from the capsule surface, as shown elsewhere /32 (Bibl.1), rapidly decreases to the value of the thermal potential of the plasma $\varphi = \frac{kT}{e}$. At the same time, usually the $e\varphi \ll \frac{mv_0^2}{2}$, and thus also, the electric charge of the capsule do not greatly affect the structure of the disturbed zone of heavy charged particles.

In the case of a slowly moving ($v_0 \ll v_i$) or small ($R_0 \leq D$) body, the effect of the electric charge, however, becomes very substantial and even determines the structure of the ionic zone of disturbance.

The distribution of the particle concentration (in our case, mainly electrons) in the steady state close to a charged body is described by the Boltzmann equation

$$N(r) = N_0 \exp\left[-\frac{e\varphi(r)}{kT}\right], \qquad (10.II)$$

where N(r) and N_0 are the particle concentrations at the point r and, in an undisturbed medium far from the body ($\varphi_0 = 0$), the quantity $\varphi(r)$ denotes the electric field potential at the point r.

The effect of the earth's magnetic field is manifested by a change in the character of motion of the ions that are able to move freely only in the direction of the field strength vector $\vec{H}_0$ and rotate in a plane perpendicular to $\vec{H}_0$. The magnitudes of the Larmor radii $\rho_i = \frac{v_i}{\omega}$ (v_i is the velocity component of thermal agitation of a particle in a plane perpendicular to $\vec{H}_0$, while ω is the angular velocity) are shown in Table 1.II. The Larmor radius for ions at high altitudes is sufficiently large so that the earth's magnetic field substantially affects the motion of the ions interacting with the capsule at sufficiently great distances from the capsule surface $z \geq \rho_i \frac{v_0}{v_i}$. Consequently, the effect of the magnetic field manifests itself mainly in an increase of the dimensions of the rarefaction zone, and the concentration of ions in this zone does not

decrease inversely proportionally to the square of the distance r^2, as in the case of neutral particles, but to the distance r (Bibl.1).

In the particular case of motion along the direction of the magnetic field, the wake of the capsule (rarefied zone) is filled only as a result of ion collisions, since in themselves the ions cannot move in a direction perpendicular to the direction of the field.

A capsule moving at a velocity v_0, which is appreciably smaller than the electron velocity, and usually having a negative potential, disturbs the equilibrium distribution of the electrons only slightly. The distribution of /33
electron concentration close to the capsule is described by the Boltzmann equation (10.II). Thus, the magnitude of the electron concentration in the disturbed zone is almost completely determined by the electric field potential φ. Disturbances of the ion concentration in the upper atmosphere differ little from disturbances of neutral particles caused by reflection of the relative flow from the capsule. There is practically no effect of shading on the electrons. Their distribution in the vicinity of the capsule is determined by the electric field.

Section 2. Electric Field Close to the Capsule

The electric field in the vicinity of the container is created both by the space charge arising in the plasma owing to the difference of concentration of charged particles of the medium in the disturbed zone and by the electric charge of the capsule itself.

The potential of the electric field φ' of a negative space charge, as follows from eq.(10.II), is equal to

$$\varphi'(r) = -\frac{kT}{e}\ln\frac{N_r}{N_0}, \qquad (11.II)$$

where N_r is the electron concentration at the point r, and N_0 is the concentration layer of particles in the undisturbed plasma.

The potential of the metal capsule φ in the plasma is determined by the balance of electric currents arising as a result of its collision with charged particles and by emission of electrons caused by irradiation of its surface.

In its general form, the current balance, according to V.G.Kurt and V.I. Moroz (Bibl.6), is written as follows:

$$I_e + I_{re} + I_i + I_{rp} + I_{ph} + I_s = \sum I \gtrless 0, \qquad (12.II)$$

where I_e is the current of plasma electrons absorbed upon collision with the capsule; I_{re} is the current of radiating electrons absorbed on passage through the radiation belts or in the corpuscular streams; I_i is the stream of plasma ions (in space, the proton current); I_{rp} is the current of radiating protons; I_{ph} is the current of photoelectron emission arising under the effect of short-wave solar radiation, I_s is the current of secondary electrons generated under bombardment of the capsule by high-energy particles.

Let us estimate the magnitudes of the components of the balance [eq.(12.II)], beginning with the most substantial at high altitudes.

If the monochromatic energy illumination of the capsule is E_ν then, at a potential of the capsule of $\varphi_0 = 0$, the flux of photoelectrons N_{ph} from unit /34 surface in unit time will be determined by the obvious relation

$$N_{ph} = \int_0^\infty \frac{E_\nu}{h\nu} k_\nu \, d\nu, \qquad (13.II)$$

where k_ν is the quantum yield of the capsule material for a radiant flux of a given frequency ν, and h is Planck's constant.

The total photocurrent from the surface of a spherical capsule with a radius R_0, neglecting the dependence of the quantum efficiency on the angle of incidence of the radiation, will be

$$I_{ph} = \pi R_0^2 N_{ph} e. \qquad (14.II)$$

It must be borne in mind that, as the positive potential of the capsule increases, a negative space-charge shielding layer forms close to it causing a decrease in the photocurrent I_{ph}.

Calculation (Bibl.6) has shown that, in the upper atmosphere, the photocurrent caused by the effect of short-wave solar radiation is approximately equal to $I_{ph} = 1.5 \times 10^{10}$ e $cm^{-2} \cdot sec^{-1} = 2.5 \times 10^{-9}$ amp/cm^2 for $\varphi_0 = 0$, while at $\varphi_0 \simeq +6$ v the photocurrent I_{ph} drops by about one order of magnitude. A further increase in the positive potential of the capsule (up to 100v) has a much smaller effect on the magnitude of the photocurrent.

Any variation in the potential of the capsule φ_0 with time is determined by the change in the current balance. The potential at the time t will be

$$\varphi_0(t) = \frac{1}{C} \int_0^t \sum I \, dt + \varphi_0(0), \qquad (15.II)$$

where C is the capacitance of the capsule (without consideration of the plasma $C = R_0$ cm).

An estimate (Bibl.6) showed that the potential $\varphi_0 = +6$v under the effect of only short-wave solar radiation is attained in the time $t \sim 10^{-5}$ sec, whereas $\varphi_0 = +100$ v is reached in the time $t \simeq 10^{-3}$ sec. After this, the increase in the potential is very slow; however, after one day the potential of the capsule in the presence of only a photocurrent would reach the appreciable value of $\varphi_0 \simeq +2$ kv.

Let us calculate the electron and proton radiation current.

The inequality of the thermal velocities of particles in the upper atmosphere (see Sect.1) causes the current of the radiation electrons impinging on the capsule to become appreciably larger than the current of protons $I_{re} \gg I_{rp}$

at close values of the concentration of electrons and protons $n_e \simeq n_p$. Furthermore, the electron fluxes in the radiation belts (see Chapt.V, Sect.1) exceed /35 the proton fluxes. Therefore, we can neglect the quantity I_{rp} for I_{re}. The current of radiation electrons striking the body of a spherical capsule at isotropic flux will be

$$I_{re} = 4\pi R_0^2 N_0 e, \qquad (16.II)$$

where N_0 is the flux of radiation electrons.

The flux N_0 includes electrons of any energy (E_e), i.e., it is in turn, determined by the equality

$$N_0 = \int_0^\infty N(E_e)\, dE_e. \qquad (17.II)$$

An estimate of the maximum possible flux N_0 (Bibl.6) yields a value of the order of $N_0 = 10^{10}$ to 10^{11} $cm^{-2} \cdot sec^{-1}$, and a current density up to $I_{re} = 10^{-8}$ $amp \cdot cm^{-2}$. Consequently, at the tops of the radiation belts (at $N_0 > 5 \times 10^9$ $cm^{-2} \cdot sec^{-1}$) the electron current may exceed the magnitude of the photocurrent so that the capsule, under its effect, may acquire an appreciable negative potential.

The secondary emission current, under the effect of radiation electrons I_{re}, leads to an increase in the potential of the capsule φ_0. Of course, its magnitude, for a secondary emission coefficient of $\eta < 1$, does not exceed the electron current I_{re} (for aluminum, for example, $\eta < 0.5$ at $E_e = 10$ Kev). Furthermore, the secondary emission current abruptly drops on an increase in the positive potential of the capsule up to several volts, since the maximum energy of secondary electrons does not exceed a few electron-volts.

The ion current I_i and the electron current I_e of the plasma are formed as a result of particle absorption upon collision and are most intense in the ionosphere.

If the thermal velocity of the ions is much lower than the velocity of the capsule $v_i \ll v_0$, we can neglect the quantity v_i and write, in first approximation, the ion current striking the capsule as the quantity of electricity contained within a cylinder, cut out by the capsule as it moves in the plasma,

$$I_i = \pi R_0^2 v_0 P_i n_{0i} e, \qquad (18.II)$$

where n_{0i} is the ion concentration in the undisturbed plasma, P_i is the coefficient of absorption (neutralization) of ions at the capsule surface.

In calculating the electron current, it is necessary to allow for the capsule potential φ_0, which determines the particle distribution close to the surface.

We note that the presence of a space charge close to the charged con- /36 tainer must be accounted for in a more rigorous calculation of the ion current, especially at great altitudes where their thermal velocity v_i is comparable to or even exceeds the velocity of the capsule v_0.

The space charge region is deformed by the motion of the capsule and by the formation of a stagnation zone ahead of it and of a rarefaction zone aft of it. As a consequence, electrons will be present only in a portion of the front hemisphere and their effective surface, as demonstrated elsewhere (Bibl.4), is equal to $\frac{\pi R_0^2}{2}$.

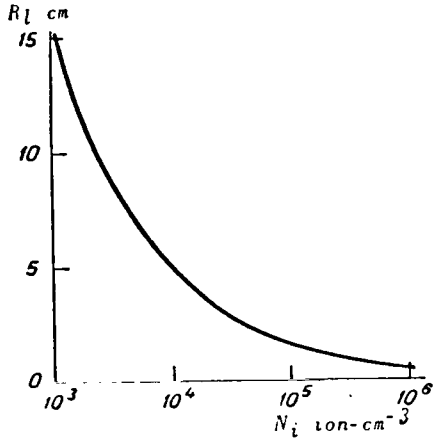

Fig.3.II Thickness of the Space Charge Layer R_l as a Function of the Ion Concentration N_i.

Taking into account the above statements, the electron current striking the negatively charged capsule in the presence of a Boltzmann distribution [eq.(10.II)] was expressed by A.V.Gurevich (Bibl.4) in the following form:

$$I_e = \frac{\pi R_0^2}{2} e v_e P_e n_{0e} e^{-\left|\frac{e\varphi_0}{kT}\right|}, \qquad (19.II)$$

where v_e is the mean thermal electron velocity in Maxwellian distribution [eq.(1.II)] and P_e is the coefficient of absorption of electrons on the capsule surface.

We note that the thickness of the spherical region of the space charge layer R_l for a stationary container can be determined analytically (Bibl.9).

The dependence of the layer thickness on the ion concentration $R_l = f(N_i)$ at $T = T_e = 300^\circ K$ is plotted in Fig.3.II from which it follows that, at the indicated temperatures, a decrease in concentration even to $N \sim 10^3$ cm^{-3} will result in an increase in the thickness of the space charge layer only to 15 cm, while on further decrease in N_i the thickness of the shielding space charge layer will increase rapidly.

In the absence of a photocurrent and a current of radiation particles, the capsule, during its travel through the plasma at $n_{0e} = n_{0i}$, will acquire a potential φ_0 whose magnitude is determined by the simple current balance $I_e = I_i$. Neglecting the space charge and using eqs.(18.II) and (19.II), we obtain

$$\varphi_0 = \frac{kT}{e} \ln\left\{\frac{v_e P_e}{2v_0 P_i}\right\} = \frac{kT}{e} \ln\left\{\frac{P_e}{P_i}\sqrt{\frac{2kT}{\pi m v_0^2}}\right\}. \qquad (20.II)$$

In the ionosphere, the potential $\varphi_0 < 0$; as shown by an estimate, it is /37 equal to approximately $(2 - 3)\frac{kT}{e}$. The magnitude of the thermal plasma potential $\frac{kT}{e}$ is small and does not exceed several volts at $T \leq 10^4$ °K.

The general equation of balance (12.II) was solved (Bibl.6) graphically for various values of u, n_{oi}, T, and N_o that are possible in the upper atmosphere and in interplanetary plasma. For the previously made estimates of the currents I_{ph}, I_{re}, and $T \sim 10^3 - 10^4$ °K, the potential of a capsule having a radius of $R_o = 65$ cm proves to be about $\varphi_0 \simeq -20$ v if $n_{oi} = 10^3$ cm^{-3}, but will be $\varphi_0 = -0.5 - 3$ v if $n_{oi} = 10^5$ cm^{-3}. Outside the radiation belts, in the illumination portion of the flight path of the capsule, its potential - as shown by calculation (Bibl.6) - should be within -2.5 v $\leq \varphi \leq +4$ v, if $n_{oi} > 10$ cm^{-3}.

This theory does not take account of the effect of the magnetic field on the motion of charged particles. Evidently, this is permissible only at high altitudes where the Larmor radii of the particles exceeds the radius of the space charge at the capsule ρ_e and $\rho_i \gg R_o$ (see Table 1.II). At heights of $h < 7000$ km, the Larmor radius for electrons is small $\rho_e < R_\ell$, so that the electron current, under consideration of the magnetic field at a low altitude above the earth, drops by about half while the potential of the capsule increases, approaching $\varphi_0 \simeq 0$, if $n_{oe} > 10^2$ cm^{-3} (Bibl.6).

Section 3. Disturbance of the Upper Atmosphere by Desorption of Molecules from the Capsule Surface

Along with the already discussed disturbances of the upper atmosphere, caused by reflection of particles of the ambient medium upon collision with the capsule, there are also disturbances caused by the liberation of gas molecules due to desorption from the surface or outgassing from within the capsule. Obviously, these effects are greatest soon after launching.

The disturbances due to molecule desorption consist of an increase in density of the ambient medium and a change in its composition. Furthermore, the molecules liberated from the capsule will have a velocity of about 8 km/sec and thus an energy of the order of 10 ev, which is sufficient for ionization of the molecules of the medium or for causing reactions of a thermochemical nature. Therefore, it is natural that, in measuring the concentration of neutral and charged particles and the density of the upper atmosphere by means of onboard instruments, these effects are taken into account.

The molecules released from the capsule surface as a result of desorption have a low density so that, in first approximation, their trajectories will /38 be rectilinear up to collision with particles of the ambient medium. Upon elastic collision of the desorbed molecule with a virtually stationary molecule of the medium, the former loses on the average half of its velocity, and in

inelastic collision the loss is even greater. As a consequence, the desorbed molecules, after collision, either remain at some distance from the capsule or return to its surface.

The molecules desorbed from the capsule surface cover a distance l before colliding with particles of the ambient medium. This distance, which B.A.Mirtov (Bibl.7) calls "withdrawal" or removal, is shorter than the mean free path of the particles of the medium λ, due to the fact that the capsule moves in the wake of the outgoing molecules.

It can be demonstrated (Bibl.7) that the distance l is correlated with the mean free path λ at a given altitude by the simple relation

$$l = \frac{v_m}{v_m + v_0}\lambda, \qquad (21.II)$$

where v_m and v_0 are the velocities of the desorbed molecules and of the capsule, respectively (if $v_0 \quad v_m$ or $v_0 \perp v_m$).

It follows from eq.(21.II) that the distance from only a stationary capsule ($v_0 = 0$) coincides with the mean free path ($\lambda = l_0$).

Let us find the excess concentration of molecules as a result of desorption n'_x at a certain distance x from the surface of a spherical capsule whose radius is equal to R_0.

The quantity n'_x in a thin spherical layer of a thickness d, located at a distance x from the surface, will evidently be equal to

$$n'_x = \frac{N_x}{w}t, \qquad (22.II)$$

where N_x is the number of desorbed molecules entering the layer in unit time; w is the volume of the layer; t is the transit time of the molecules over a distance d.

Let us substitute the quantities entering eq.(22.II) as follows:

$$w \approx 4\pi d\,(R_0 + x)^2 \quad \text{and} \quad t = \frac{d}{v'_m}. \qquad (23.II)$$

Furthermore, let us assume that the concentration of desorbed molecules decreases with distance from the capsule, both as a result of collisions with particles of the medium and as a result of an increase in occupied volume. It was shown elsewhere (Bibl.7) that

$$N_x = N_0 e^{-\frac{x}{l}}, \qquad (24.II)$$

where N_0 is the number of molecules removed from the surface of the capsule in unit time.

As a result of the substitution of eqs.(23.II) and (24.II) into eq.(22.II) we find that /39

$$n'_x = \frac{N_0}{4\pi v'_m} \frac{e^{-\frac{x}{l}}}{(R_0 + x)^2}. \qquad (25.II)$$

The resultant equation permits calculating the concentration of desorbed gases at a certain distance x from the capsule, neglecting collisions of these molecules with particles of the ambient medium.

B.A.Mirtov (Bibl.7) also derived an analogous expression for the concentration of molecules n''_x returning to the container after collision

$$n''_x = \frac{N}{4\pi v''_m l} \int_x^\infty \frac{e^{-\frac{a}{l}}}{(R_0 + a)^2} \, da, \qquad (26.II)$$

where v''_m is the velocity of the returning molecules, a is a variable of integration with respect to a column of unit cross section from x to ∞.

At the capsule surface the ratio of concentration of escaping n'_0 to returning n''_0 molecules, as follows from eqs.(25.II) and (26.II), will be

$$\frac{n''_0}{n'_0} = \frac{v'_m R}{v''_m l}. \qquad (27.II)$$

Here, we have taken into account that, at x = 0, the value of the integral in eq.(26.II) is approximately equal to $1/R_0$ if $l \gg R_0$. The results of calculation for a capsule with a radius R_0 = 100 cm at various altitudes are shown in Table 2.II (Bibl.8). It was assumed that the velocity of the molecules after collision v''_m is by one order of magnitude greater than the velocity before collision v'_m.

TABLE 2.II

DISTANCE AND RELATIVE CONCENTRATIONS OF RETURNING MOLECULES AT VARIOUS ALTITUDES H IN THE UPPER ATMOSPHERE

H km	λ_{av} cm	l cm	n''_0 / n'_0
150	2.10^3	1.10^2	1.10^{-1}
200	10^4	5.10^2	2.10^{-2}
300	10^5	5.10^3	2.10^{-3}
500	10^6	5.10^4	2.10^{-4}

It follows from Table 2.II that, in measuring the density or composition of the atmosphere by means of instruments whose receiving surfaces are at the level of the capsule skin, the effect of returning molecules can be neglected for /40

the direct flux of desorbed molecules at altitudes above 150 - 200 km. Consequently, we can do away with the direct flux of desorbed molecules if the receiving aperture of the instruments is directed along a normal to the surface of the capsule. At altitudes below 150 km, a noticeable number of desorbed molecules returning after collision will always strike the instruments.

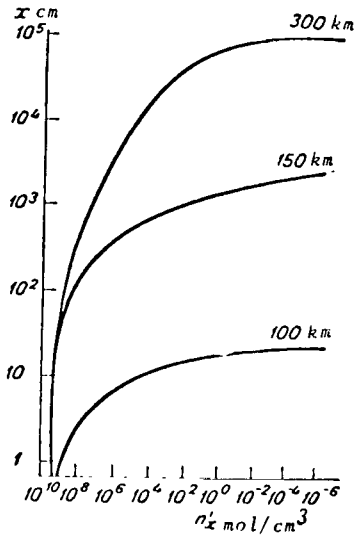

Fig.4.II Excess of Particle Concentration n'_x as a Function of the Distance x at Various Altitudes.

Based on eqs.(24.II) and (25.II), let us estimate the density of the "cloud" of desorbed molecules close to the capsule surface. We will consider, as done by B.A.Mirtov (Bibl.8), that in the case of monomolecular adsorption one square centimeter is able to hold up to 50 layers of 10^{15} molecules each. Consequently, on the surface of the capsule, equal to 10^6 cm^2, a total of $5 \times 10^1 \times 10^{15} \times 10^6 = 5 \times 10^{22}$ molecules will be adsorbed. Considering that desorption occurs uniformly during one revolution of the capsule around the earth ($t = 5000$ sec), we obtain $N_0 = 10^{19}$ molecules per sec.

The results of calculation of the excess concentration n'_x at $R_0 = 100$ cm, $v'_m = 4 \times 10^4$ cm/sec and $v_0 = 8 \times 10^5$ cm/sec, for altitudes of 100, 150, and 300 km are plotted in Fig.4.II. It is apparent from the diagram that the higher the flight altitude, the more slowly will the density of the desorbed molecules n'_x decrease with increasing distance x from the capsule surface. Under these conditions, for example at an altitude of 300 km, the concentration of desorbed molecules will remain at a maximum and be virtually constant up to a distance of about 1 m from the capsule surface (the undisturbed concentration at this altitude is $n \approx 10^8$ cm^{-3}).

On the basis of the derived relations we can also estimate the escape of gas from within the capsule (outgassing) which is permissible from the viewpoint of measuring the undisturbed structural parameters of the upper atmosphere. The estimate (Bibl.8) showed that, if the molecules of the forward flow of

desorbed gases (the axis of the instrument inlet being directed along the capsule radius) do not strike the instrument, the permissible value of outgassing for all altitudes is about 10^{19} molecules per second.

Let us now estimate the effect of disturbances caused by the flight of /41 the container on the ionization state of the ambient medium.

Naturally, those molecules that are reflected from the capsule according to the elastic collision laws have the greatest effect on the ionization of the ambient medium. The additional concentration at any distance x from the capsule, caused by reflection of molecules, can be found from eq.(25.II) by an appropriate change in the parameters entering it. For example, at an altitude of 200 km the undisturbed concentration of gas will be $n \approx 10^{10}$ cm^{-3} (Bibl.7). Here, during one second a capsule of a cross section of 3 m^2 will cause reflection of $N_0 = 10^{10} \times 8 \times 10^5 \times 3 \times 10^4 = 2.4 \times 10^{20}$ mol/sec (it is assumed here that the velocity of the molecules is equal to $v_0 = 8 \times 10^5$ cm/sec). A calculation based on this formula will yield the resultant additional concentration of molecules, which is equal to 3×10^9 cm^{-3} at the capsule surface.

The concentration of reflected molecules returning to the container after collision with particles of the medium, according to eq.(26.II) will be about 2×10^6 cm^{-3} at the surface of the satellite. With an increase in altitude, it will decrease in conformity with the decrease in density of the atmosphere.

Taking the coefficient of ionization by collision, under these conditions, to be $\alpha = 10^{-4}$, B.A.Mirtov (Bibl.7) demonstrated that the additional ionization at the capsule surface amounts to 10^2 cm^{-3}. This value is by several orders of magnitude less than the ionization of the medium (10^5 to 10^6 cm^{-3}).

The effect of thermochemical reactions on the variation in composition of the ambient medium is also negligible (Bibl.8).

PART II /42

MEASUREMENT OF THE PARAMETERS OF THE UPPER ATMOSPHERE AND SPACE

Not only the basic meteorological elements, designated as structural parameters (temperature, pressure, density, and sometimes even composition of the atmosphere), but also the parameters characterizing the fluxes of cosmic rays, corpuscles, meteor particles, and the state of the magnetic and electric fields are used for describing the state of the upper atmosphere.

The methods for measuring such diverse parameters differ greatly but the respective instrumentation used on rockets and space vehicles has a number of common circuitry elements which will be discussed in Chapter V.

CHAPTER III

MEASUREMENT OF STRUCTURAL PARAMETERS

Section 1. Measurement Principles

All structural parameters are closely correlated. This relationship has a bearing on numerous measuring methods and on interpretation of the results.

The gas pressure, which is the prime-average summary effect of collisions of particles with a given body, is

$$p = N\frac{mv^2}{2}, \tag{1.III}$$

where N is the number of particles per unit volume, m is the mass of the gas particles, and v is the most probable velocity of the particles.

Equation (1.III) contains not only a kinetic determination of the pressure but also of the temperature. Actually, /43

$$N = \frac{a}{w}, \tag{2.III}$$

where a is the number of molecules in a certain volume w.

Taking into account eq.(2.III), we obtain

$$pw_1 = A\frac{mv^2}{2}. \tag{3.III}$$

For one mole of gas the quantity a equals the Avogadro constant A. In this

case, we have

$$p = \frac{a}{w}\frac{mv^2}{2}. \qquad (4.III)$$

Taking into account that the equation of state pw = RT is rigorously valid in the field of ordinary gas dynamics, we can write

$$T = \frac{A}{R}\frac{mv^2}{2} = \frac{1}{k}\frac{mv^2}{2}, \qquad (5.III)$$

where $k = \frac{R}{A}$ is the Boltzmann constant.

Thus, the molecular temperature T, determined by eq.(5.III), characterizes only the statistical (probabilistic) kinetic energy of the molecules.

For the upper atmosphere, by analogy, concepts of ion and electron temperature are introduced depending on the energy of motion of the type of particle (electrons or ions) it characterizes.

Equations (1.III) and (5.III) yield a correlation between the pressure p, the particle concentration N, and the temperature T in the form

$$p = NkT. \qquad (6.III)$$

We note that from eq.(5.III) we also obtain a relation between the maximum velocity v at Maxwellian distribution (see Chapt.II), the temperature T, and the mass of the gas particles m, in the form of

$$v = \sqrt{\frac{2kT}{m}}. \qquad (7.III)$$

The magnitude of the structural parameters varies as a function of all possible processes in the atmosphere, with the limits of such variations being rather wide.

The average temperature distributions of the atmosphere with altitude over the middle and subpolar latitudes, in the presence of high solar activity (Bibl.29) is plotted in Fig.1.III. The diagram indicates that, at the altitude of the upper limit of the mesosphere (about 80 km), the temperature of the atmosphere is minimal (130 - 160°K). In the thermosphere, the temperature continu- /44
ously increases with height, reaching 1500 - 1800°K at a level of about 500 km and 2000 - 3000°K at a level of about 1000 km (Bibl.3, 29). At the limit of the ionosphere (about 3000 km), the temperature is estimated as being of the order of 4000°K, while in interplanetary space at a distance of 3 - 4 earth radii from the earth, it is 5000°K.

The atmospheric pressure at an altitude of about 50 km is approximately 10^3 times less than at the earth's surface; at an altitude of about 100 km it is 10^6 times less and at about 200 km, 10^9 times less than at the earth.

The density of the atmosphere at heights of 100, 200, 300 km is of the order of 10^{-10}, 10^{-12}, and 10^{-14} gm/cm^3 respectively. The concentration of neutral particles, molecules, and atoms markedly drops with altitude, for example, from 10^{13} particles/cm^3 at 100 km to 10^5 particles/cm^3 at about 1000 km.

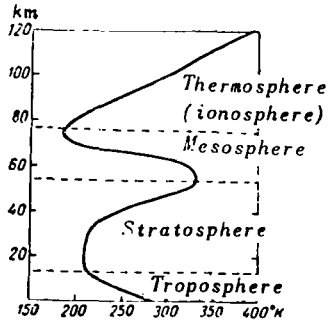

Fig.1.III Average Temperature Distribution with Height in the Atmosphere.

In the ionosphere, the concentration of ions and electrons decreases much more slowly with altitude and, at low altitudes of the ionosphere, it markedly fluctuates during the day and during the year. The concentration of ions or electrons at 100 km is (2 - 100) 10^3 particles/cm^3 and at 1000 km about 10^5 particles/cm^3 (Bibl.3). At greater altitudes, the concentration of charged particles begins to predominate over the concentration of neutral particles (see Table 1.IV).

A detailed review of available information on the structural parameters of the atmosphere and their variability is given in the monograph by I.A.Khvostikov (Bibl.29) and in a number of other works (Bibl.5, 19, 44, etc.).

The results of measurements of the structural parameters of the atmosphere are especially affected by environmental disturbances, formed close to the instrumented capsule, and by the effect of radiation fluxes on the instrument sensors, especially by solar radiation. As a consequence, the instrument readings will differ greatly from the value of the parameters of an undisturbed atmosphere. Under these conditions it is of utmost importance to allow for the methodological errors of measurements, whereas the feasibility of direct measurements of the structural parameters by some particular method is determined by the accuracy of accounting for the interaction of the instrument with the ambient medium.

Section 2. Direct Temperature Measurements of the Upper Atmosphere

Direct thermometry is widely and effectively carried out by Soviet meteorological rockets of the MR-1 series.

The boom of the rocket (see Fig.1.I), in its center portion, carries /45
electric resistance thermometers (5) made of tungsten wire 40 μ in diameter

(Bibl.2). The wire is stretched on insulated metal plates and connected to an unbalanced measuring bridge.

The thermometer is calibrated in a wide temperature range T_w under laboratory conditions. As a result of calibration, a function of the type $U_{out} = f(T_w)$ is obtained, where U_{out} is the voltage in the ratio arms of the bridge.

To determine the temperature of an undisturbed medium T_∞, based on the measured temperature of the thermometer wire T_w, distorting factors are taken into account. The method is based on an analysis of the physical aspect of the phenomena and allowance is made for factors that substantially affect the result of the measurements at high altitudes, as a consequence of the low heat exchange between the thermometer and the ambient medium.

To obtain the mathematical formula, let us write the equation of the heat balance of the thermometer wire with the following notations: ℓ = length, d = diameter, s and w = area of surface and volume, R, c_w, and ρ_w = resistance, specific heat, and density of the wire material.

The components of the heat balance of the wire will be designated in terms of dQ_n (where n = 1, 2, ...).

Using these notations, we write

$$dQ = \rho_w w c_w dT_w, \tag{8.III}$$

where dQ is the change in enthalpy of the wire on a change in its temperature by dT degrees in the time $d\tau$.

The heat gain from an internal source is

$$dQ_1 = 0.24 i^2 R\, d\tau. \tag{9.III}$$

This heat is liberated due to heating of the wire by the current of the measuring circuit during the same time interval $d\tau$.

The balance component dQ_2 takes into account the heat received by the wire from fluxes of short-wave and long-wave radiant energy striking its surface (with allowance for radiation losses). In the mathematical expression of this term of the balance, we must take into account the mutual position of the wire and the boom of the rocket. Figure 2.III shows that not the entire surface of the wire is struck by the radiant fluxes F and that the wire also receives the radiant energy reflected and radiated by the boom.

Let us introduce the following additional notations: F_1 and F_2 = densities of the short-wave and long-wave radiant fluxes, ϵ_1 and ϵ_2 = coefficients of absorption of the short-wave and long-wave radiant energy for the wire, ϵ_3 = coefficient of radiation of the wire and boom, A_1 and A_2 = coefficients of reflection by the boom of short-wave and long-wave radiant energy respectively, s_n (where n = 1, 2, ...) = effective surfaces of the wires for various radiant fluxes, /46 T_b = temperature of the boom, σ = radiation constant.

Using these notations, we write

$$dQ_2 = F_1\varepsilon_1 s_1\, d\tau + F_1 A_1 \varepsilon_1 s_2\, d\tau + F_2\varepsilon_2 s_3\, d\tau + \\ + F_2\varepsilon_2 A_2 s_4\, d\tau - [\,\varepsilon_3\sigma T_w^4 s_5 + \varepsilon_3\sigma (T_w^4 - T_b^4) s_6\,]\, d\tau = \Sigma\, d\tau, \qquad (10.III)$$

where the quantity Σ is the radiation balance of the resistance wire.

To calculate the dynamic heating of the thermometer, let us introduce into the usual equation of convective of heat transfer the average temperature T_{av} of the air stagnant at the boundary layer of the wire. In this case, the heat gain produced by the interaction of the thermometer with the gas stream will have the form

$$dQ_3 = \alpha (T_{av} - T_w) s\, d\tau, \qquad (11.III)$$

where α is the heat transfer coefficient of the resistance wire to the relative flow (whose magnitude depends on the Reynolds and Prandtl numbers).

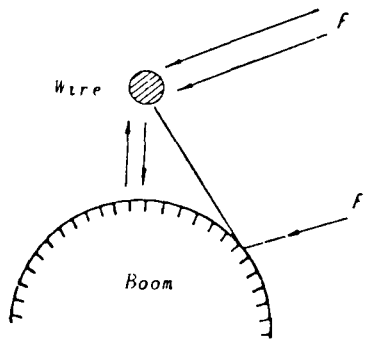

Fig.2.III Mutual Arrangement of Thermometer Wire and Rocket Boom.

The temperature T_{av} can be determined in terms of the recovery coefficient of the thermometer

$$r = \frac{T_{av} - T_\infty}{T_0 - T_\infty}, \qquad (12.III)$$

where T_0 is the stagnation temperature.

The value of the coefficient r, for different measuring conditions, can be determined experimentally.

From eq.(12.III), we obtain

$$T_{av} = T_\infty + r(T_0 - T_\infty) = T_\infty + r v_\infty^2 \frac{\gamma - 1}{2R\gamma}, \qquad (13.III)$$

where γ is the ratio of the specific heats of the gas $\frac{c_p}{c_v}$, v_∞ is the velocity

of the undisturbed flow as a result of which aerodynamic heating occurs, and R is the gas constant.

Taking into account eq.(13.III), we obtain from eq.(11.III)

$$dQ_3 = \alpha\left(T_\infty + r\frac{\gamma-1}{2R\gamma}v_\infty^2 - T_w\right)s\,d\tau. \qquad (14.III)$$

The balance component allowing for the flow of heat from the resistance wire to the boom through the holders (corner plates)

$$dQ_4 = \lambda(T_b - T_w)s'\,d\tau, \qquad (15.III)$$

where s' is the area of contact of the wire with the holders and λ is the thermal conductivity of the holders. /47

The equation of heat balance of the wire is written in the following form:

$$dQ = dQ_1 + dQ_2 + dQ_3 + dQ_4. \qquad (16.III)$$

Substituting into this formula the expressions obtained for the components, we obtain the computational equation

$$\frac{c_w\rho_w w}{\alpha s}\frac{dT_w}{d\tau} = 0.24\frac{i^2R}{\alpha s} + \frac{\Sigma}{\alpha s} - T_w + T_\infty + r\frac{\gamma-1}{2R\gamma}v_\infty^2 + \frac{\lambda s'}{\alpha s}(T_b - T_w). \qquad (17.III)$$

Considering that $\frac{c_w\rho_w W}{\alpha s}$ is the coefficient of inertia of the wire while $\frac{\lambda s'}{\alpha s} = \xi$ is the coefficient experimentally derivable for a given design of the thermometer sensor, we can write the computational formula in final form:

$$T_\infty = T_w - rv_\infty^2\frac{\gamma-1}{2R\gamma} - \frac{\Sigma}{\alpha s} - 0.24\frac{i^2R}{\alpha s} + \eta\frac{dT_w}{d\tau} + \xi(T_w - T_b). \qquad (18.III)$$

We should mention again that, during motion of the rocket, the thermometer gradually enters into ever more rarefied layers of the atmosphere in which the conditions and laws of heat transfer become complicated. This physical fact is taken into account by using various coefficients r and α in areas of ordinary gas dynamics and rarefied gas dynamics.

The terms of eq.(18.III) can be treated as corrections for possible errors in the temperature T_w measurement, produced by the measurement technique. We see that only the correction for inertia (fifth term) and inflow of heat from the holders (sixth term) can have a variable sign, whereas all other terms are essentially negative. This means that the considered factors render the

readings of the thermometer too high.

Experimental investigations by P.P.Alekseyev and others (Bibl.2) showed that, for the thermometer under consideration, all corrections except the corrections for aerodynamic heating of the thermometer (second term) are negligible up to an altitude of about 50 km where the atmosphere behaves as a continuum. /48 The correction for aerodynamic heating takes into account the effect of stagnation of the flow at the boundary layer of the wire, as a consequence of which the thermometer receives not only the energy of the thermal agitation of the molecules but also the kinetic energy of their ordered motion with a velocity v_∞. This correction is essential for all altitudes, at a sufficient velocity of motion of the thermometer.

In the 50 - 70 km altitude range, where transition to the area of rarefied gas dynamics takes place, the other corrections are not very large but markedly increase at altitudes above 70 km where it is absolutely necessary to take them into consideration.

Excessive complications in calculating the temperature T_∞ from eq.(18.III) are produced by the fact that the parameters r and α depend on the temperature of the ambient medium. To overcome this difficulty, the calculations of the temperature of the upper atmosphere are made by several (two or three) approximations. The first approximation is calculated by means of eq.(18.III) in which r and α are taken at the average temperature at a given height. The second and subsequent approximations are calculated from the parameters r and α taken at the temperature T_∞ which was found in the preceding approximation.

In deriving the computational equation for taking methodological errors into consideration, we assumed that the resistance wire is in the air flow outside the boundary layer of the boom. As the rocket moves at certain angles of attack, this condition might be disturbed. To eliminate the resultant errors, four thermometers whose wires are stretched along the boom are placed around its circumference.

To calculate T_∞ from eq.(18.III), we must know, in addition to the temperature T_w measured by the thermometer, the derivative $\frac{dT_w}{d\tau}$ obtained during the measurements; the temperature of the boom T_b measured by an auxiliary thermometer at the boom, the values of the radiant fluxes F_1 and F_2 measured by bolometers mounted to the boom (close to the body of the rocket); velocity of the rocket v_∞ which is determined from eyeball, photographic, or radar sighting of its flight.

The calculations performed by other authors (Bibl.2) showed that the mean-square error of individual temperature measurements by the described method up to an altitude of 40 km did not exceed $\pm 5^\circ$; at an altitude of 50 km, it was $\pm 10^\circ$ and at altitudes of 70 - 75 km, already $\pm 20^\circ$.

For a check, temperature calculations based on measured pressures are simultaneously performed, as was done in soundings by rockets carrying no thermometers for the ambient atmosphere, for example, in the USA (Bibl.44). The

calculations are based on the barometric formula which, according to the estimates of various authors, is valid up to an altitude of several hundreds of kilometers.

From the barometric formula /49

$$p_2 = p_1 e^{-\frac{Mgz}{RT'_\infty}}, \qquad (19.III)$$

where M is the molecular weight of the air, g the acceleration of gravity, and R the universal gas constant, it follows that the average temperature in a layer of a thickness Δz, where the pressure varies by the quantity $\Delta \ln p = \ln p_1 - \ln p_2$, will be equal to

$$T'_\infty = \frac{Mg\Delta z}{R\Delta \ln p} = \frac{Mg}{R\frac{\Delta \ln p}{\Delta z}}. \qquad (20.III)$$

Furthermore, in the USA regular thermometry up to heights of the order of 60 km is accomplished by parachute radiosondes ejected from meteorological rockets. A thermistor is used as receiver in the radiosondes (Bibl.39).

An optical method for measuring the temperature was used in the launchings of the French rocket "Véronique" (Bibl.33). This was based on measuring the width of the resonance lines of the yellow doublet of atomic sodium. A sodium cloud ejected at altitudes of 100 - 180 km was rendered luminescent by twilight solar rays. The measurements were taken over a ground-based high-transmission spectrograph, equipped with a standard cuvette filled with sodium vapors. The height of individual points of temperature measurement was determined by triangulation.

The method of detonating shells released from a rocket at certain instants of time, which is used in the USA (Bibl.7, 40, 44) to measure speed and direction permits also a calculation of the temperature of the atmosphere. The detonations of the shells are recorded by ground sound-ranging equipment. The acoustic method of measuring the temperature in this case proves useful up to a height of 80 km and even more (Bibl.29).

A widely used method is that of falling balls, containing a radio transmitter which transmits signals to a direction finder. The density is calculated from the equation of the flight of the ball (Bibl.33), under consideration of the wind.

Other methods have been developed for determining the density and temperature [observation of the diffusion of sodium vapors (Bibl.31), measurement of the fluxes of X-rays (Bibl.35, 36) and others].

Section 3. Manometers for Measuring Low Pressures

The range of pressures subject to measurement in the launch of various carriers is extremely wide: from 700 - 800 to 10^{-5} - 10^{-10} mm Hg. To cover

such a pressure range, it is necessary to use manometers with various measuring ranges or even different types of pressure gages. Let us examine the principal types, with emphasis on manometers for measuring pressures in the upper levels /50 of the atmosphere.

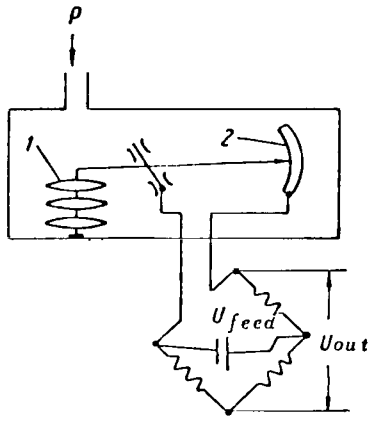

Fig.3.III Wiring Diagram of a Membrane Resistance Transducer (MRT).

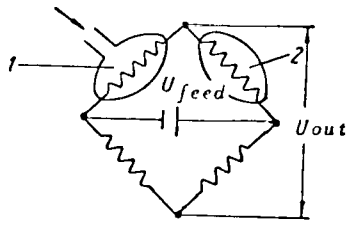

Fig.4.III Wiring Diagram of a Hot-Wire Gage (Pirani Type).

To measure high pressures on meteorological rockets, ordinary membrane resistance transducers (MRT) are used. The sensing element of the MRT is a membrane box (1) (Fig.3.III) connected with a resistance transducer (2). The latter is connected into the circuit of an unbalanced bridge. These elements of the MRT are discussed in detail in the literature devoted to meteorological and aerological measurements (Bibl.12, 13). The unbalance voltage of the bridge U_{out} is fed across the commutator to the telemetry system of the rocket (see Chapt.I, Sect.1). The limits of application of various types of MRT encompass the range from about 760 to 5 mm Hg (Bibl.2).

Hot-wire gages (Pirani type) are used in the pressure range from several millimeters to thousandths of a millimeter of mercury. The mode of operation of these instruments is based on the dependence of the heat loss of the heated body (filament) on the gas pressure in the volume of the gage if the diameter of the

wire is commensurable with the mean free path of the molecules.

The hot-wire gage is a glass cylinder communicating with the atmosphere, into which a thin tungsten filament (1) is sealed (Fig.4.III).

The equation of the heat balance of the filament in a steady state when the temperature of the filament and its resistance are constant, T_f = const and R_f = = const, will have the form

$$0.24i^2R_f = Q_1 + Q_2 + Q_3, \qquad (21.III)$$

where i is the current strength; Q_1 is the thermal flux transported by the gas particles to the walls of the cylinder; Q_2 is the heat lost by the filament /51 owing to radiant heat transfer to the walls of the cylinder; Q_3 is the heat flux arriving at the cylinder along the filament holders.

The heat transported by the gas particles from unit surface of a filament in unit time at low gas pressures (Bibl.12) is equal to

$$Q_1' = ck\alpha p(T_w - T), \qquad (22.III)$$

where c is a constant depending on the atomicity of the gas; k is the coefficient of accommodation characterizing the efficiency of the processes of energy transfer between the gas molecules and the surface of the heated filament; α is the coefficient of molecular thermal conductivity of the gas; p and T are the pressure and temperature of the gas in the volume of the gage; T_w is the wall temperature of the cylinder of the gage.

The measuring circuit of the manometer is so laid out that the effect of thermal fluxes Q_1 and Q_3, which do not depend on gas pressure, is excluded. For this, the arm (2), similar in design to the sensing element (1), does not communicate with the atmosphere (t = const) but is connected into the bridge circuit (Fig.4.III). Furthermore, the tungsten filament has a low radiation coefficient, and its temperature is low [T_f < 150 - 200°C (Bibl.12)]. Thanks to this, the output voltage of the bridge circuit U_{out} (at constant feed voltage U_{feed} and wall temperature of the cylinder T_w) depends only on the pressure p. The quantity T_w is usually measured by an auxiliary circuit so as to allow for the effect of the cylinder temperature on the instrument readings.

The limits of applicability of eq.(22.III) are determined by the mean free path of the gas molecules and by the diameter of the hot-wire gage filament. When using a filament with a diameter of 13 μ, the instrument will satisfactorily operate in the pressure range from 5 to 0.1 mm Hg. The use of a heavier filament with a diameter of 60 μ, which has a higher thermal inertia (see Sect.2) permits using hot-wire gages with a pressure range from 0.3 to 5 × × 10^{-3} mm Hg (Bibl.2), i.e., up to an altitude of about 100 km.

Equipment of this type is used in the USA, in particular on the Deacon rockets (Bibl.29). Ionization gages of various types are suitable for measuring extremely low pressures in the upper atmosphere.

Thermal ionization gages, or simply ionization gages, operate on the basis

of the pressure dependence of a current of positive ions formed through ionization of the gas in the body of the gage by electrons emitted from the heated filament. The simplest gage of this type is the triode, whose cavity is connected with the gaseous medium being measured.

It is possible to connect the ionization gage into a circuit with external and internal control. In the first case, the grid of the triode is fed an /52
accelerating potential positive with respect to the cathode (100 - 300 v), while a small potential (from -2 to -30 v) negative with respect to the cathode is supplied to the anode which serves as a collector of positive ions. The magnitude of the accelerating potential of the grid V_g should evidently be greater than the ionization potential V_i of the gas whose pressure is being measured. The negative potential of the anode V_a should not only promote the trapping of positive ions from the cavity of the gage but should also prevent the impingement of electrons. The current in the anode circuit is the quantity measured.

When the circuit is connected with internal control, the ion collector is the grid of the tube to which a negative potential is fed while the accelerating potential is applied to the anode. The circuit with external control is in much wider use since it ensures a high magnitude of the collector current. This is due to the fact that, in the first case, the distribution of the potential between the electrodes causes oscillations of the electrons close to the grid (they fly through the grid and are repelled first by the anode-collector and then by the cathode), thanks to which their mean free path and the probability of ionization of the gas increase.

Experimental and theoretical investigations (Bibl.11, 20) showed that, with both methods of connecting the gages, the ion current i_+ is proportional within wide limits to the gas pressure p and the electron emission current i_-, i.e.,

$$i_+ = ki_-p, \tag{23.III}$$

where k is a constant depending on the design of the gage (on shape, material, placement, and size of the electrodes) and also on its operating conditions (magnitudes of the potentials applied to the electrodes).

The sensitivity of the gage S is represented by the ratio of the collector current to the pressure

$$S = \frac{di_+}{dp} = ki_- = \frac{i_+}{p}. \tag{24.III}$$

The theory of ionization gages (Bibl.20, 21), based on the assumption that the electrodes are in the form of concentric cylinders (without consideration of recombination), leads to the following expression for the sensitivity in the case of a circuit with external control:

$$S = \frac{\beta Bp}{V_g}\left[\beta - (V_g - V_i + \beta)e^{-\frac{V_g - V_i}{\beta}}\right], \tag{25.III}$$

where V_g and V_i are the grid and gas ionization potentials, respectively; β is a

constant depending on the gas properties (for example, for molecular nitrogen, $\beta = 160$, and for neon $\beta = 300$); B is a constant taking into account the potential distribution between the electrodes of the gage and the absorption of electrons by the grid during their oscillation near it. This can be determined upon calibration of the gage. /53

Consequently, the sensitivity of ionization gages depends on the properties of the gas filling the cavity and also on their design features and operating conditions. Experiments have shown that the sensitivity S is approximately proportional to the total number of electrons contained in a molecule of gas or vapor [the sensitivity for helium is low, being about 0.18 in comparison with air (Bibl.11)]. The upper limit of the measured pressures can be raised to 10^{-2} - 10^{-1} mm Hg (Bibl.22). This limit is given by the occurrence of cathode "poisoning" and cathode cooling as a result of increased heat transfer upon increase in pressure (this leads to an appreciable drop of the emission current) and also by possible overheating of the cathode or of the heating element.

The lower limit is given by the decrease in the signal-to-noise ratio. Noises arise mainly as a consequence of photoionization of the material in the collector under the effect of soft X-radiation emitted by the grid under bombardment by electrons. The photocurrent from the collector increases the measured current i_+, leading to a distortion of the measurement results. The lower limit of measurements is the pressure p at which the ion current becomes comparable with the photocurrent of the collector. To reduce the lower limit, the ionization gages are designed so that the hot cathode is located outside the cylindrical grid (on the side) rather than inside it. Inside the grid is placed the collector made in the form of a thin filament (to reduce the photosensitive surface). The grid is made of a material with a low atomic number (to reduce the bremsstrahlung). The path of the electrons in this gage design is sufficiently long and its sensitivity is not reduced.

The liberation of tungsten vapors heated by the cathode, having a tension of about 10^{-12} mm Hg, restricts the lower limit of pressures measurable by a gage of this design to a magnitude of the order of 10^{-11} mm Hg (Bibl.8).

For the ion current i_+ to be related with the gas pressure by a linear dependence [eq.(23.III)] it is necessary to stabilize the magnitude of the anode current i_- and the work function of the electrodes of the gage. A sufficient degree of stabilization of the latter is provided by using gas-discharge stabilizers or by using galvanic cells. The problem of stabilizing the current i_- in a wide range of measured gas pressures and in the presence of its variable composition is much more difficult since in this case the emissivity of the cathode will vary.

Numerous circuits are in existence for stabilizing the anode current (Bibl.11), based on introducing a negative feedback between the anode current /54 and the filament current of the cathode. All of these are of excessive weight, size, and power consumption. To eliminate these shortcomings, tetrode ionization gages such as the IM-7 have been developed in the USSR (Bibl.23), which are used for measuring pressures up to altitudes of 500 km (Bibl.15).

In this gage, stabilization of the emission current is accomplished by an

auxiliary flat grid (4) (Fig.5.III) placed between the anode grid (1) and the cathode (3). The latter is made of a tungsten wire 0.05 mm in diameter and is arranged asymmetrically (on the periphery). The cylindrical anode grid (1) is made of nickel wire 0.2 mm in diameter. The collector of the gage (2) is made

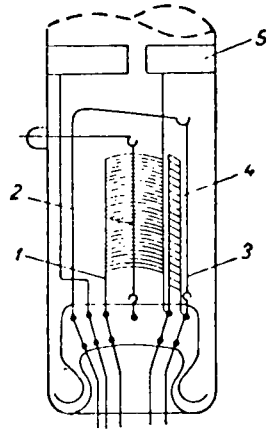

Fig.5.III Schematic Diagram of Tetrode Ionization Gage.

in the form of a tungsten wire 0.1 mm in diameter, mounted along the axis of the anode grid. To reduce leakage in the collector circuit its lead-out is placed on the cylinder of the gage. The input of the gage carries a vapor-deposited guard ring (5) which is under a sufficiently high potential to prevent penetration of positive ions from the ambient medium into the working volume. The /55

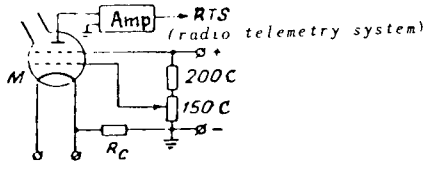

Fig.6.III Wiring Diagram of Tetrode Ionization Gage.

operating conditions of the IM-7 gage are characterized by the following voltages: anode-cathode +240 v, collector-cathode -60 v, control grid-cathode from -10 to +20 v, cathode filament 6.7 v. The anode current is equal to 3 ma, while the filament current of the cathode is 0.55 amp. The sensitivity of the gage under these conditions is S = 0.025 amp/mm Hg (with respect to air). The limits of its use are from 10^{-4} to 10^{-9} mm Hg (Bibl.8).

A circuit (Fig.6.III) with a negative feedback is used to stabilize the anode current of the tetrode gage M. The coefficient of stabilization of the anode current in this circuit is determined mainly by the transconductance of

the triode portion of the gage and by the magnitude of the feedback resistance R_c. The latter simultaneously determines the negative bias at the collector.

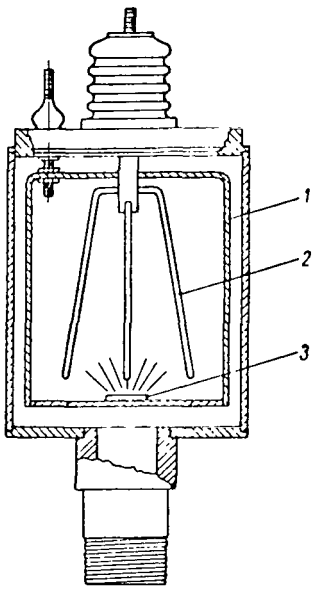

Fig.7.III Schematic Diagram of Alphatron.
1 - Control electrode; 2 - Collector;
3 - α-particle source.

The ion current of the gage at low gas pressures and at the indicated value of S is low (at $p = 10^{-6}$ mm Hg, the current $i_+ = 2.5 \times 10^{-8}$ amp). Therefore, direct-current amplifiers are used with a sufficiently high input resistance and a high amplification factor. The output voltage of the amplifier A is fed to the telemetry system of the carrier. Reference voltages are periodically supplied to the amplifier input for calibration. The instrument scale is usually divided into several subranges (Bibl.22).

Radioactive ionization gages of the alphatron type (Bibl.5, 41, 42), which are a variant of the cold-cathode ionization gage, are used in the USA to measure the pressure of the upper atmosphere on rockets. In alphatrons (Fig.7.III), ionization of the gas is accomplished by α-particles, emitted by radium and by its decay products at a constant rate.

To obtain a linear dependence of the ion current on the gas pressure, it is necessary to have the size of the cavity of the gage appreciably smaller than the length of the mean free path of the particles (before recombination at a given gas pressure). Therefore, the upper limit of pressure measurable by the alphatron is determined by the size of its cavity. This limit is usually several millimeters of mercury. The lower limit of the alphatron is determined by the background current of secondary electrons knocked out from the grid by the α-particles. For this reason, the grid is made in the form of thin wires (Fig.7.III). Between the grid (1) and the collector (2), a potential of

30 - 40 v is applied; the ion current flowing in this circuit is the measured quantity. At a pressure of the order of 10^{-4} mm Hg the magnitude of the ion current of this manometer (of the order of 10^{-14} amp) becomes comparable with the background current (Bibl.11).

At a sufficiently low air pressure ($p < 10$ mm Hg), when ion recombination can be disregarded, the following expression can be theoretically obtained for the ion current in the alphatron chamber: /56

$$i_+ = \frac{eq_0p}{760}\eta LA, \qquad (26.III)$$

where e is the electron charge; q_0 is the specific ionization for a given gas at $p = 760$ mm Hg (for air $q_0 = 4 \times 10^5$ cm^{-1}); η is a constant depending upon the design of the alphatron; L is the average linear dimension of the cavity of the manometer; A is the activity of the α-radiation source.

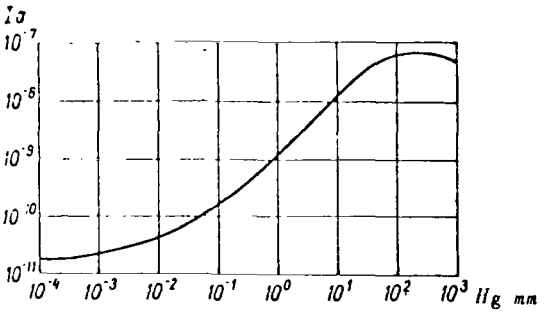

Fig.8.III Calibration Curve of Alphatron.

The dependence of the readings of the alphatron on the gas properties and design data of the manometer follows from eq.(26.III). The calibration curve of the alphatron (as shown by Fig.8.III) is nonlinear. The operating principle of manometers with a β-source (betatrons) is analogous. An important advantage of ionization gages with a cold cathode is their great reliability and the impossibility of chemical reactions between the gas and the incandescent cathode; in certain cases, however, it is necessary to take into account that absorption of gases (evacuation), which has been noted for ionization gages (Bibl.22, 11), occurs here also.

Magnetic electric discharge gages (Penning gages) operate on the principle of dependence of the current of the electric discharge in the gas i on the gas pressure p. The anode of the gage is designed as a ring (1) (Fig.9III) attached to a rod electrode while the cathode is in the form of plates (2). The guard ring (3) which prevents penetration of positive ions of the ambient medium into the cavity of the gage, is connected with the anode.

Gages of this design were specifically used in measurements by the third satellite (Bibl.15). In other designs, the anode is placed in a metal box which serves as the cathode.

To increase the discharge current and to maintain a continuous discharge at low pressures, the cavity of the manometer is placed in a strong magnetic /57 field directed along the axis of the ring-shaped anode (Fig.9.III). In this case, the electrons ionizing the gas under the effect of the accelerating electric field, move along curvilinear trajectories similar to spirals wound on the magnetic lines of force. This substantially increases the probability of gas ionization by each electron.

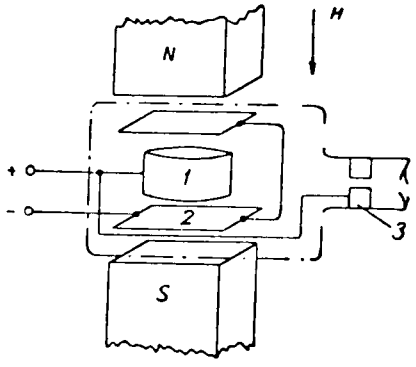

Fig.9.III Diagram of the Magnetic Electric Discharge Gage.

The discharge chamber and a permanent N - S magnet are combined into a single unit by a casing, not shown in the sketch of Fig.9.III. Between the cathode and the anode of the gage, a high voltage U (several kilovolts) is applied. A ballast resistor R_b is connected into this circuit and limits the discharge current i, in order to eliminate the possibility of an arc discharge at a sufficiently high pressure p. The voltage drop across the resistor R_b is sufficiently high. It is usually fed directly to the telemetry system across a matching cathode follower. The dependence of the discharge current i on the pressure p will obviously have the following form:

$$i = \frac{U - U_0}{R_6 + R_p} \qquad (27.III)$$

where U_0 is the minimal discharge voltage (at a maximal measured pressure); R_p is the equivalent resistance of the discharge gap depending upon the pressure of the gas and its properties.

With an accuracy sufficient for practical calculations we can write the dependence of R_p on the pressure p in the form of

$$R_p = \frac{k}{p^n}, \qquad (28.III)$$

where k is a coefficient determining the sensitivity of the gage; n is a constant depending on the gas properties [its value varies within limits from 0.9 to 1.15 (Bibl.17)].

The dependence of the readings of the electric discharge gage on the gas properties has the same character as that of the ionization gages, except that it varies with a change in gas pressure. Therefore, discharge gages require individual calibration within wide limits for different gas compositions. In strong magnetic fields, measured in kg-oersteds, the characteristic curve of the electric discharge gage is close to linear (Bibl.22), i.e.,

$$i = Cp, \qquad (29.III)$$

where C is a constant depending mainly on the electrode area and on the gas properties. /58

The lower limit of application is determined by a decrease in the ion discharge current i to a value comparable with the background current of electrons emitted from the cathode under the effect of a strong electric field. For various gages of this design, the maximum measurable pressure is 10^{-7} to 10^{-6} mm Hg (Bibl.11).

It follows from eq.(27.III) that an increase in pressure to a value where $R_p \ll R_b$ constitutes the upper limit of measurement. Obviously, two methods are possible for raising this limit: 1) the use of small values for the resistance R_b and 2) a decrease in the magnitude of the discharge current by reducing the electrode surface. However, both these methods cannot be realized in full since, to eliminate the arc discharge at $p > 10^{-3}$ mm Hg, a value of $R_b \simeq 10^6$ Ω is required, and any decrease of the electrode surface will lead to a drop in sensitivity of the gage and to cessation of its operation at low pressures (about 10^{-5} mm Hg) as a consequence of the instability of the discharge.

As a result, the general operating range of the magnetic electric discharge gage is restricted to limits from 10^{-3} to 10^{-6} mm Hg (Bibl.9).

We note that the lower limit of application of the Penning gage whose design provides for measures to eliminate emission from the cathode, could be brought to 5×10^{-14} mm Hg under laboratory conditions.

Furthermore, designs of multichamber and multisection electric discharge manometers (with electrodes of different size) have been developed, which operate in the range from 10^{-1} to 10^{-7} mm Hg or from 1 to 10^{-5} mm Hg (Bibl.9).

Magnetic electric discharge manometers have some advantage over the ionization gage owing to the absence of a hot cathode. Drawbacks include the comparatively large weight of the permanent magnet and the adsorption of ions on the surface of the continuously sputtering electrodes (pumping effect).

The errors of measurement of gas discharge gages are mainly due to instability of the discharge. At pressures of 10^{-4} to 10^{-5} mm Hg they reach ±10%, which is somewhat higher than for ionization gages (Bibl.22).

The sensitivity of ordinary gas discharge gages is 1 - 3 amp/mm Hg.

The onboard manometric equipment of the third satellite (Bibl.15) is shown in a block diagram in Fig.10.III. The ionization gages with traps (IM-7L),

operated in the range of 10^{-5} to 10^{-9} mm Hg, and their amplifiers (UPT) had two ranges of amplified currents each. The electric discharge gage (MME-S1) operated in the range from 10^{-5} to 10^{-7} mm Hg (Bibl.16). The operation of the equipment was controlled by a programmer-timer (PVM) through a coupler system (KSU) which also calibrates the amplifiers UPT. /59

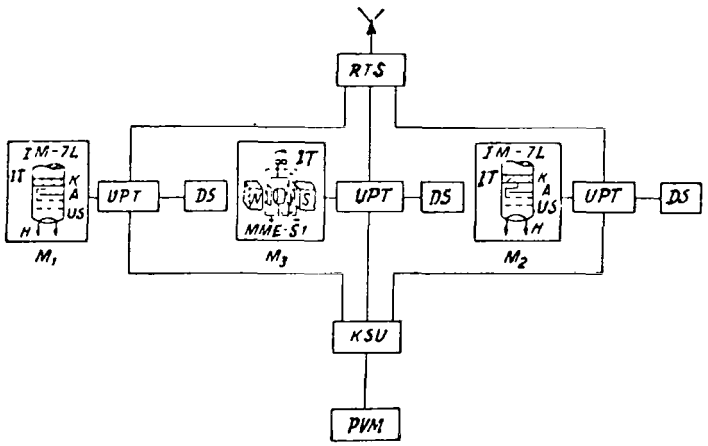

Fig.10.III Block Diagram of Manometric Equipment of the Third Satellite.

US = Amplifier; RTS = Radio telemetry system; IM-7L = Ionization gage; MMES1 = Electr. discharge gage; UPT = Amplifier; DS = Drum switch; IT = Indicator tube; KSU = Coupler system; PVM = Programer-timer.

The main instrument errors in measuring low pressures or densities by equipment of this type are due to a change in composition of the atmosphere with height. An estimate shows that, when calibrating the equipment in the earth's atmosphere, the possible error due to a change in composition amounts to ±20% at a height of 200 km and ±60% at 500 km (Bibl.16).

Section 4. Pressure and Density Measurements of the Upper Atmosphere by Manometers

The method of determining the static pressure of an undisturbed flow p_∞, based on the pressure measured by a pressure gage p_1, depends on the regularities of the interaction of the measuring instrument with the atmosphere and its installation on the carrier. In the domain of ordinary gas dynamics and slip flow, encompassed by meteorological rockets, calculations are performed with allowance for methodological errors introduced in the pressure-gage readings by the high-velocity flow, just as is done in direct temperature measurements. In the domain of molecular gas dynamics, the calculations are performed on the basis of correlations between the number of particles striking the cavity of the manometer and the number of particles in the undisturbed atmosphere. If the composition of the atmosphere is known, the gage readings can be interpreted by calculating the density; this method is used in measurements on high-altitude rockets, geophysical capsules, and artificial earth satellites. /60

Let us examine the methodological errors and the procedure for taking them into account in pressure measurements by meteorological rockets.

1. Evolution of gas adsorbed in the lower atmosphere by the surface of the carrier. To eliminate this error, the pressure gages are installed on the nose of the rocket where the pressure of the liberated gases is not more than 10^{-5} mm Hg (Bibl.2). Soviet meteorological rockets are equipped with a boom of small surface (see Chapt.I, Sect.1) and thus have less outgassing.

As indicated before (see Chapt.II, Sect.3), the effect of outgassing of a satellite, not exceeding 1 cm^3/sec at atmospheric pressure, can be disregarded.

The cavities of low-pressure gages are carefully evacuated and sealed; at a given altitude they are sprung open by mechanical percussion devices. When taking measurements in the ionosphere, protective metal shields connected with the body of the capsule are sometimes installed at the inlet of the electric manometers, in addition to guard rings, for protection from charged particles.

We note that outgassing of the satellite surface practically ceases after several (up to 3 - 5) days of flight in the upper atmosphere; their outer skin is made from materials with a low vapor pressure. The background of gas liberation can be estimated from the gage readings in the area of the molecular shadow of an unoriented capsule (see Chapt.II, Sect.1).

2. Dynamic pressure. Gas enters the intake orifices of the manometer tubes from the boundary layer of the carrier; the pressure in the boundary layer p_1 can be greater or less than the undisturbed pressure p_∞ (depending on the point of installing the manometer, angle of attack α, and Mach number). The relation between the pressures p_1 and p_∞ is introduced in terms of the pressure coefficient a which is defined as the ratio of the difference of these pressures to the dynamic pressure

$$a = \frac{p_1 - p_\infty}{\frac{1}{2}\rho_\infty v_\infty^2}, \qquad (30.III)$$

where ρ_∞ is the density of the undisturbed atmosphere. The coefficient a can be found experimentally.

Testing of rocket nose cones in wind tunnels showed that the pressure /61
coefficient depends primarily on the distance of a given point on the rocket surface from the rocket nose l (Bibl.24). The dependence of the coefficient a on the distance along the rocket, expressed in diameters l/d for different Mach numbers and angles α, is plotted in Fig.11.III. The diagram shows that, at a distance of about 6 - 7 diameters from the rocket nose $\left(\frac{l}{d} = 6 - 7\right)$, the pressure coefficient a at high velocities is close to zero, which means that an efficient placement of the pressure sensors may substantially reduce the correction for dynamic pressure.

Making allowance for the characteristics of the pressure coefficient distribution and the flight velocity of the meteorolocical rockets of the MR-1 type,

the intake orifices of the heat gages are located on a boom at a distance of 6.5 diameters from the nose. The value of a for the conditions of flight can be determined experimentally and can be calculated theoretically (Bibl.30).

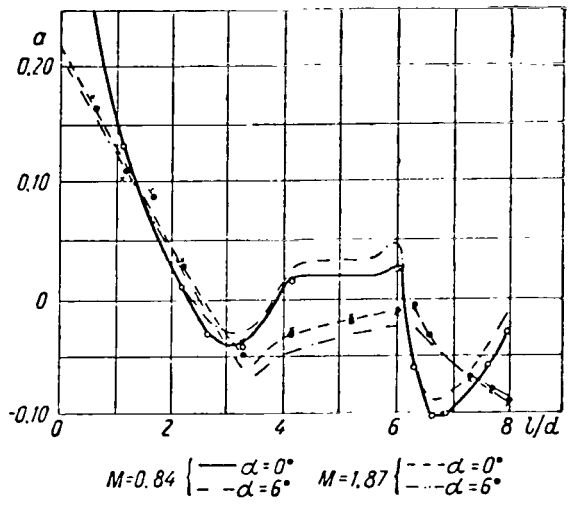

Fig.11.III Pressure Coefficient a as a Function of the Distance ℓ/d, the Mach Number, and the Angle of Attack α.

Thus, to eliminate the effect of dynamic pressure on the result of pressure measurements, we can introduce a correlation determined from eq.(30.III), namely,

$$p_\infty = p_1 - \frac{1}{2} a \rho_\infty v_\infty^2. \qquad (31.III)$$

3. Thermal effusion. The phenomenon of thermal effusion consists in /62 that the pressure at a given point of a rarefied gas is directly proportional to the temperature at this point. The thermal effusion in a manometer is described by an equation of the type

$$\frac{p_1}{p_2} = \left(\frac{T_1}{T_2}\right)^h, \qquad (32.III)$$

where p_1, T_1, and p_2, T_2 are, respectively, the pressure and temperature at the points 1 and 2, and h is the effusion coefficient.

The magnitude of the effusion coefficient, based on the data of other authors (Bibl.2), is determined by the dimensions of the tubing b and the mean free path of molecules in the gas λ, over the equation

$$h = \frac{1.8741\left(\frac{\lambda}{b}\right)^2}{1 + 3.49\left(\frac{\lambda}{b}\right) + 3.75\left(\frac{\lambda}{b}\right)^2}. \qquad (33.III)$$

Equation (33.III) shows that, in the lower atmosphere where $\lambda \ll b$, the quantity $h \approx 0$ so that the effect of thermal effusion on the pressure is virtually nonexistent. In the upper atmosphere where $\lambda \sim b$ as a result of the fact that the temperature in the boundary layer of the carrier T_1 is not equal to the temperature in the cavity of the manometer T_2, the pressure measured by the instrument p_2 will differ from the pressure in the boundary layer p_1.

To account for the error introduced into the results by thermal effusion, we will introduce still another correction into eq.(31.III). For this purpose, p_1 is substituted by the expression (32.III). The computational equation then acquires the following form:

$$p_\infty = p_2\left(\frac{T_1}{T_2}\right)^h - \frac{1}{2}a\rho_\infty v_\infty^2. \qquad (34.III)$$

4. Inertia of the pressure gage. Heat gages installed on the MR-1 meteorological rockets have a comparatively high thermal inertia in the upper atmosphere: at heights of 60 - 80 km, the time constant reaches 4 - 4.5 sec. During this time the rocket covers several kilometers. In processing the observations, this is taken into account on the basis of experimental determinations of the time constant of the gages under laboratory conditions. The magnitude of the correction for inertia depends on the law of the time rate of change of the temperature. At a linear dependence, it obviously is equal to the product of the coefficient τ multiplied by the time derivative of the pressure.

In pressure calculations based on eq.(34.III) the temperature of the flow in the boundary layer near the intake orifice of the manometer T_1 is calculated from eq.(13.III). The necessary values of the recovery coefficient for the static tube are determined with consideration of the characteristics of the gas flowing past the body at various altitudes. Since the quantities λ, p_∞, and r depend on p_∞, several approximations must be made in calculating by means of /63 eq.(34.III), just as is done in calculations of the temperature T_∞ (see Sect.3 of this Chapter). The quantities v_∞, T_∞, and T_2 are measured directly during the rocket flight.

The mean-square error of a single measurement by the described method is estimated as ±4% (Bibl.2).

In the more rarefied regions of the upper atmosphere, the interaction of the gage with the ambient medium takes place in accordance with the law of free molecular flow. In this case, the mean free path in the boundary layer is of the order of, or greater than, the diameter of the intake orifice of the pressure gage and the pressure inside it will not be related by the equation of thermal effusion with the pressure in the boundary layer. The computational equation should then have a different form. Let us derive it.

Let us assume that a rocket or satellite is moving with a velocity v_0 relative to the earth, that the area of the intake of the manometer is s, and that the angle included by the plane s and the velocity v_0 is equal to θ (Fig.12.III).

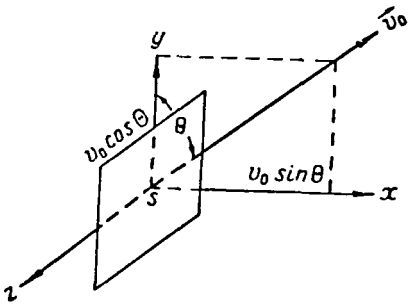

Fig.12.III Relative Position of the Manometer Intake s and the Velocity Vector v_0.

Considering that the velocity distribution of the molecules obeys Maxwell's law, i.e., that the gas is in thermodynamic equilibrium, Kh.Sh.Tzyan (Bibl.27) and E.Zenger (Bibl.30) found that the number of molecules n_{in} flowing through unit surface s in unit time into the cavity of the manometer is equal to

$$n_{in} = \frac{Nv}{2\sqrt{\pi}} \{e^{-\beta^2} + \beta\sqrt{\pi}\,[1 + \Phi(\beta)]\}, \qquad (35.III)$$

where v is the most probable velocity of the molecules, N is the number of molecules in unit volume of the atmosphere, $\beta = \frac{v_0 \sin\theta}{v}$ is a parameter, $\Phi(\beta) = \frac{2}{\sqrt{\pi}} \int_0^\beta e^{-t^2} dt$ is the error integral.

The number of molecules n_{out} escaping from the manometer under the same conditions is equal to

$$n_{out} = \frac{N_1 v_1}{2\sqrt{\pi}} \{e^{-\beta^2} - \beta\sqrt{\pi}\,[1 - \Phi(\beta)]\} \approx \frac{N_1 v_1}{2\sqrt{\pi}} \quad (\beta \leqslant 0{,}1), \qquad (36.III)$$

where N_1 and v_1 are, respectively, the number and most probable velocity of molecules in the manometer cavity. At a sufficiently large accommodation coefficient, the quantities N_1 and v_1 are determined by the wall temperature of the manometer T_1 since the molecules escape after multiple collisions. /64

As before, the pressure and temperature in the undisturbed atmosphere will be denoted by p_∞ and T_∞ and that in the cavity of the manometer, by p_1 and T_1.

On the basis of eq.(6.III) which relates the pressure to the temperature,

we obtain the following expression for measuring the pressure in the cavity of the manometer dp_1 during the time interval $d\tau$:

$$\frac{dp_1}{d\tau} = kN_1 \frac{dT_1}{d\tau} + kT_1 \frac{dN_1}{d\tau}. \tag{37.III}$$

On the basis of eqs.(35.III) and (36.III) we find that the change in the number of particles per unit volume of the manometer during the time $d\tau$ is equal to

$$dN_1 = \left(\frac{Nv}{2\sqrt{\pi}} \{ e^{-\beta^2} + \beta\sqrt{\pi} [1 + \Phi(\beta)] \} - \right.$$
$$\left. - \frac{N_1 v_1}{2\sqrt{\pi}} \right) \frac{s}{w} d\tau, \tag{38.III}$$

where w is the volume of the manometer cavity.

In the steady state $\frac{dp_1}{d\tau} = 0$, so that

$$kN_1 \frac{dT_1}{d\tau} + \frac{s}{w} kT_1 \left(\frac{Nv}{2\sqrt{\pi}} \varkappa(\beta) - \frac{N_1 v_1}{2\sqrt{\pi}} \right) = 0, \tag{39.III}$$

where the designation $\varkappa(\beta) = e^{-\beta^2} + \beta\sqrt{\pi} [1 + \Phi(\beta)]$ is introduced.

We will next transform eq.(39.III) into

$$\frac{skT_1 N_1 v_1}{2w\sqrt{\pi}} \left(\frac{Nv\varkappa(\beta)}{v_1 N_1} - 1 + \frac{2w\sqrt{\pi}}{sT_1 v_1} \frac{dT_1}{d\tau} \right) = 0. \tag{40.III}$$

The first factor in eq.(40.III) is known not to equal 0, and the last term in the second factor is obviously quite small since the temperature of the manometer cavity does not undergo abrupt fluctuation, i.e.,

$$\frac{2w\sqrt{\pi}}{sT_1 v_1} \frac{dT_1}{d\tau} \approx 0.$$

Taking this into account, we obtain the computational formula in the form of

$$N = \frac{v_1 N_1}{v\varkappa(\beta)} \tag{41.III}$$

At high flight velocities and in an almost head-on flow when the quanti- /65
ty β is sufficiently large ($\beta \geq 1.5 - 2$), the function $\Phi(\beta) \approx 1$ and thus $\varkappa(\beta) \approx 2\beta\sqrt{\pi}$. Substituting this expression into eq.(41.III) and substituting the most probable velocity of the molecules for the terms of the molecular temperature in conformity with eq.(7.III), it will be found that the number of particles per unit volume (density of the upper atmosphere) determinable by eq.(6.III) will be equal to

$$N = \frac{p_1}{\sqrt{T_1} v_0 \sin\theta} \sqrt{\frac{1}{2\pi m k}}. \qquad (42.III)$$

Using eq.(6.III) for calculating the pressure p_∞ from the measured value of p_1, we obtain the expression

$$p_\infty = \frac{p_1}{v_0 \sin\theta} \sqrt{\frac{k}{2\pi m}} \frac{T_\infty}{\sqrt{T_1}}. \qquad (43.III)$$

It is obvious that, to calculate the density ρ_∞ of the upper atmosphere, it is necessary to know not only the measured value of the pressure p but also the temperature in the manometer cavity T_1, the velocity of the rocket or satellite v_0, the orientation of the pressure gage intake with respect to the flow θ, and the mass m of the particles (molecules or ions), i.e., the gas composition of the atmosphere at the altitude of measurement. Furthermore, to calculate the pressure, the temperature of the medium T_∞ must be known.

The hydrodynamic time constant of the gage is determined by the change in its orientation with respect to the flow. This has an influence, for example, when the carrier is not stabilized in space.

If the manometer intake faces the rear of the carrier the quantity β increases, and the function $\varkappa'(\beta) = e^{-\beta^2} - \beta\sqrt{\pi}[1 - \Phi(\beta)] \approx 0$ (at $\beta \geq 2$). Consequently, the number of particles entering the gage from the rear cone will be quite small. At the same time, the counterflow of particles dN_- which had entered the manometer when it was at the front and which leave it during the time $d\tau$, will be determined as usual by the wall temperature of the manometer T_1, i.e.,

$$dN_- = \frac{N_1(T_1) v_1 s}{2\sqrt{\pi}} d\tau. \qquad (44.III)$$

The corresponding pressure change in the cavity of the manometer will then be

$$-\frac{dp_1}{p_1} = \frac{v_1 s d\tau}{w \cdot 2\sqrt{\pi}}. \qquad (45.III)$$

It follows from eq.(45.III) that, upon any change in orientation of the /66 manometer, the pressure in it will decrease in accordance with the law

$$p_1(\tau) = p_{1,0} e^{-a\tau}, \qquad (46.III)$$

where $p_{1,0}$ is the pressure in the manometer cavity at the instant ($\tau = 0$) when the particles cease to flow into the manometer.

The time constant of the manometer is

$$\eta = \frac{1}{a} = \frac{2w\sqrt{\pi}}{v_1 s} = \frac{w}{s} \sqrt{\frac{2\pi m}{k T_1}}. \qquad (47.III)$$

At $s = 3.14$ cm^2, $w = 100$ cm^3, $T_1 = 300^\circ$K, and $m = 2.66 \times 10^{-23}$ gm (atomic oxygen) we obtain the hydrodynamic time constant of the manometer as $\tau \approx 2 \times \times 10^{-3}$ sec (Bibl.10).

Thus, the pressure in the manometer cavity facing the rear of the carrier will drop off rapidly to values that can no longer be measured.

In measuring the pressure of the upper atmosphere and space by pressure gages installed on rapidly moving carriers, in particular on satellites ($v_0 \approx \approx 8$ km/sec), there are a number of additional sources of methodological errors. We will indicate the most important of these.

Ionizations by collision and dissociation of the gas in the chamber of the manometer are possible since the kinetic energy of the oncoming particles at a velocity of the order of 8 km/sec is 10 ev for a gas like nitrogen N_2. Calculations (Bibl.10) have shown, however, that these effects result only in negligible errors of measurement (less than 1%). A greater influence is exerted by the phenomenon of mass selection in a free molecular flow, which manifests itself in that an intake facing against the flow will primarily trap heavy gas particles while an intake facing toward the rear will trap light particles. The method of allowing for this effect as well as for the variation in gas concentration, produced by collisions and interaction with the wall of the cavity, will be discussed later in the text in connection with mass-spectrometer measurements (see Chapt.IV).

Substantial errors may arise in pressure measurements owing to inaccurate knowledge of the altitude- and time-variant parameters required in the calculation, and owing to errors of telemetry in transmitting data to the ground as well as to outgassing of the carrier surface. To eliminate the latter, the intakes can be extended forward. Calculations (Bibl.10) have shown that, for a satellite, a 10-cm forward projection of the intake almost completely eliminates the effect of the adsorbed gases liberated from the surface.

In pressure measurements by capsules of geophysical rockets, the mean- /67
square error is estimated as ±10% and increases with height, especially if $p < < 10^{-7}$ mm Hg.

The total error of the pressure or density measurements on a satellite, with consideration of the errors in determining altitude, velocity, calibration of the equipment, telemetry, and basic assumptions of the analysis, may go as high as 200% at altitudes up to 200 km (Bibl.16).

We note that, if the gage is not a cavity with an orifice but a cylindrical tube covered on one end, it will be necessary to allow for the dynamic resistance of the tube when determining the pressure p_∞ from the measured pressure p_1. This resistance will differ for the incoming flow and for the outgoing flow. The particles of the incoming flow will strike the inside of the tube as a narrow beam, almost without colliding with the wall; in other words, they will have a narrowly directed velocity indicatrix in the coordinate system fixed with respect to the instrument. In the outgoing flow at total accommodation of the particles to the wall temperature, all directions of particle motion are equally probable and the velocity indicatrix will have a spherical shape. It follows from the

character of these indicatrices that the impingement of particles inside the tube is facilitated, resulting in a positive pressure ($p_1 > p_\infty$) there.

A.I.Ivanovskiy and a number of other authors (Bibl.12), in investigating this effect, arrived at the conclusion that, if the relative flow is directed along the tube axis, the formula $p_\infty = p_1 \frac{1}{\varkappa(\beta)} \cdot \sqrt{\frac{T}{T_1}}$ which follows from eq.(41.III), must be replaced by the more general formula

$$p_\infty = \frac{p_1}{\varkappa(\beta)} \frac{K(0, l/r)}{K(\beta, l/r)} \sqrt{\frac{T}{T_1}}, \qquad (48.III)$$

where $K\left(\beta, \frac{l}{r}\right)$ is the value, averaged for the tube cross section, of Klausing's factor which characterizes the probability that particles of the relative flow are within a tube of radius r at a distance l from the inlet; $K(0, l/r)$ is Klausing's factor for particles of the outgoing flow. The values of Klausing's factor for various conditions are given elsewhere (Bibl.12) where it is shown that, in the particular case where the manometer is a cavity with an orifice $\left(\frac{l}{r} = 0\right)$ the factor $K(\beta, 0) = 1$ for all β. In this case, eq.(41.III) is valid.

In conclusion, we should mention an interesting method of thermometry by using two manometers (or mass spectrometers) proposed by A.R.Repnev (Bibl.25). /68 The method is based on the use of the phenomenon of thermal diffusion. On substituting, in eq.(32.III), the pressure p by the concentration of particles N according to eq.(6.III) for two volumes filled with gas of different temperature T and T_1, we obtain

$$N = N_1 \sqrt{\frac{T_1}{T}}. \qquad (49.III)$$

Equation (49.III) is fully valid in the case of a free molecular flow if the normal to the plane of the manometer intake is perpendicular to the velocity vector of the satellite v_0. Actually, the inflow of gas into the cavity of this manometer is determined only by the gas temperature T in the atmosphere, while the outflow is defined by the wall temperature of the manometer T_1. If a second manometer is so installed that its intake is directed against the flow, the inflow into the instrument will be determined by the velocity of the satellite v_0. In the case of a sufficiently high velocity v_0, when the parameter $\beta \geq 1.5 - 2$ (see Sect.4 of this Chapter), the formula for determining the concentration of particles in the atmosphere N_1, as follows from eqs.(42.III) or (43.III) will have the form

$$N = N_1' \frac{1}{v_0 \sin\theta} \sqrt{\frac{kT_1'}{2\pi m}}. \qquad (50.III)$$

From eqs.(49.III) and (50.III) we obtain

$$T = \left(\frac{N_1}{N_1'}\right)^2 \frac{T_1}{T_1'} \frac{2\pi m v_0 \sin\theta}{k} \qquad (51.III)$$

Thus, by measuring N_1 and N_1' by two manometers (pressure and effusion) installed as indicated above, it becomes possible to determine the temperature of the atmosphere at great altitudes. For this, it is necessary to measure the wall temperature of the manometers T_1 and T_1', the velocity of the satellite v_0 and its orientation θ, and to know the mass of the gas molecules m. This method has not yet been put into practical use, but it evidently holds promise.

CHAPTER IV

MEASURING THE GAS COMPOSITION OF THE ATMOSPHERE

Section 1. Composition of the Earth's Atmosphere

The gas composition of the atmosphere is characterized by a high degree of constancy in a broad layer of intensive convective and turbulent mixing, extending from the surface of the earth to heights of 100 - 110 km. The data cited by B.A.Mirtov (Bibl.16) on the percentage composition of dry air in this layer are given in Table 1.IV. The Table shows that the atmosphere up to great altitudes is mainly composed of nitrogen and oxygen. The relative concentration of the basic atmospheric constituents, indicated in Table 1.IV, does not change on variations in the meteorological conditions (temperature, pressure, humidity, and intensity of solar radiation). The variable components, ozone and water vapor, undergo noticeable fluctuations on any change in meteorological conditions. /69

TABLE 1.IV

COMPOSITION OF THE ATMOSPHERE UP TO 100 - 110 km

Gas	Percent by Volume	Gas	Percent by Volume
N_2	78.084 ± 0.004	He	$(5.239 \pm 0.05)\ 10^{-4}$
O_2	20.946 ± 0.002	Kr	$(1.14 \pm 0.01)\ 10^{-4}$
Ar	0.934 ± 0.001	Xe	$(8.7 \pm 0.1)\ 10^{-6}$
CO_2	0.030 ± 0.003	H_2	5.10^{-5}
NO	$(1.821 \pm 0.004)\ 10^{-3}$		

A characteristic feature of atmospheric ozone is the appreciable increase in its concentration at heights from 15 to 50 km, with a maximum reached near 20 - 25 km. The formation of this layer is explained by the photochemical theory (Bibl.17). The concentration of ozone here reaches 2.7×10^{12} molecules per cubic centimeter or 10^{-5}% by volume (Bibl.16).

Water vapor is concentrated mainly in the lower atmosphere. Its content by volume fluctuates within wide limits: from values close to zero at very low temperatures over land to 4% at high temperatures over the sea (Bibl.14). At heights of 10 - 15 km, the concentration of water particles usually does not

exceed 7×10^{13} to 1.5×10^{14} cm^{-3} (Bibl.31). From data reported by several foreign researchers, as I.A.Khvostikov indicates (Bibl.33), it follows that there usually is an increase in water vapor content of the upper levels of the stratosphere with height (the measured specific humidity at an altitude of about 27 km reaches a value on the order of 10^{-4} gm/gm, whereas the total water content of the atmosphere above 28 km is about 20 μ of precipitated water). Rocket measurements carried out with mass spectrometers in the USA indicate the presence of water molecules in noticeable quantities up to heights of the order of 100 km; however, these data are not reliable and may be due to methodological errors of measurement.

At heights above 100 - 110 km, molecular oxygen O_2 under the effect of radiant energy of wavelength $\lambda < 1750$ Å intensely dissociates into atomic /70 oxygen which, combining with nitrogen, forms new atmospheric components, namely, molecules of NO, N_2O, etc. Furthermore, at these altitudes gravitational separation of the gases begins. This is manifested by a noticeable decrease in the partial pressure of argon with respect to the pressure of neutral nitrogen (Bibl.16). No increase in the concentration of light gases - helium and hydrogen - has been detected by the most modern equipment, up to appreciable altitudes. Thus, from mass spectrometer measurements of the composition of the atmosphere, performed by V.G.Istomin (Bibl.8) and A.A.Pokhunkov (Bibl.23, 24), we know that helium ions, within the limits of instrument sensitivity of $(1.7 \pm \pm 0.8)\ 10^3$ cm^{-3}, are found only above a height of 370 km and that their concentration increases with altitude according to a quasi-linear law [up to $(7 \pm 2)\ 10^3$ cm^{-3} at an altitude of 430 km]; above 500 - 600 km, they apparently are the dominating component of the ionosphere. Neutral helium molecules could not be detected up to a height of 370 km by equipment with a sensitivity of 10^8 cm^{-3} (Bibl.23). Molecular hydrogen above 130 km has not been noted by existing equipment with a threshold sensitivity of 3×10^7 particles/cm^3 (Bibl.25).

TABLE 2.IV

CONCENTRATION OF PARTICLES AND AVERAGE MOLECULAR WEIGHT OF THE ATMOSPHERE

Altitude, km	N_o cm^{-3}	n_e, n_i, cm^{-3}	M_o
100	$(2.5 \div 4)\ 10^{13}$	$(2 \div 100)\ 10^3$	28
200	$3 \cdot 10^{10}$	$(3 \div 50)\ 10^4$	24
300	$3 \cdot 10^9$	$(1 \div 20)\ 10^5$	24
400	$5 \cdot 10^8$	$(5 \div 15)\ 10^5$	~20
500	$5 \cdot 10^7$	$(1 \div 10)\ 10^5$	~20
700	$6 \cdot 10^6$	$(2 \div 5)\ 10^5$	~16
1000	10^5	10^5	~14
3000	1	$(5 \div 7)\ 10^3$	~14

The relative concentration of hydrogen increases at great distances from the earth, with the interplanetary gas (at a distance of more than 3 - 4 earth radii) consisting practically only of hydrogen ions (Bibl.1). Present-day data on the concentration of neutral particles N_o, concentration of ions (or

electrons) $n_i n_e$, and on the molecular weight M_0 of the atmosphere at high altitudes are given in Table 2.IV, based on the data of the author (Bibl.1).

Table 2.IV shows that the relative number of ions n_i/N_0 is quite small in the upper atmosphere. At 300 km, this ratio amounts to not more than 0.1% and at about 700 km does not exceed 10%. Only above 1000 km does the atmosphere /71 become noticeably ionized. At heights of about 3000 km, the ratio n_i/N_0 reaches almost 10^4, i.e., the atmosphere becomes almost completely ionized.

In the lower ionosphere (at 60 - 100 km), the predominant ions are NO^+ and O_2^+. At high altitudes, O_1^+ ions appear. The latter begin to predominate in the ion composition at altitudes above 200 km, with a rather sharp peak of the concentration of O_1^+ ions (about 6×10^5 cm^{-3}) being observed at a level of about 250 km (Bibl.24). A noticeable increase in the relative concentration of N_1^+ ions begins at 250 - 300 km, and at 800 - 900 km it already reaches 7 - 9% of the concentration of O_1^+ ions.

At heights above 100 km, H_2O, OH, NO, CO_2, and N_2O have been recorded as small admixtures of the atmosphere. At 100 - 120 km, the maximum content of H_2O does not exceed 0.6%, OH is 6×10^{-3}%, NO is 0.1% and the mixture of CO_2 + + N_2O, having a mass number of 44, is about 1% (Bibl.25). At heights of 103 - - 126 km, magnesium oxide $Mg^{26}O$ is found which is apparently formed by the burning up of meteorites. The ions Mg^+, Ca^+, and Fe^+ of meteor origin were found at these heights also by V.G.Istomin (Bibl.6).

The physical reason for the formation of complex compounds of the type O_3, NO, OH, N_2O, etc. in the atmosphere is the occurrence of chemical reactions upon collision of dissociated and ionized molecules of oxygen, nitrogen, and hydrogen. The course of these reactions evidently depends largely on the influence exerted by electromagnetic and corpuscular solar radiations and micrometeorites on the atmosphere. The gas composition of the atmosphere, in turn, has a definite effect on almost all processes occurring in it.

Section 2. Equipment for Measuring the Composition of the Atmosphere

Rocket studies of the composition of the upper atmosphere were initiated in the USA in 1947 (Bibl.16). Samples were collected in evacuated steel cylinders whose intakes were provided with opening and closing devices which came in numerous variants. The most effective opening device was a piston knocked out by means of a powder charge (Bibl.16). Closing in most cases was accomplished by flattening the intake with another powder charge.

The sampling cylinders were mounted in the nose of the rockets so that the ends of the intake nozzles projected into a chamber which communicated through /72 lateral holes with the ambient atmosphere.

For analyzing the samples, physicochemical methods are primarily used. In the widely used Glückauff and Paneth device (Bibl.16), H_2O and CO_2 are frozen out of the samples at the temperature of liquid nitrogen. The quantity of oxygen in the sample is then determined by absorption on a clean hot copper

surface. For determining the oxygen by this method with an error of ±0.3%, a sample of 0.3 - 0.5 cm^3 is needed (under normal conditions). The mixture of nitrogen and inert gases is separated from helium by cold traps filled with activated charcoal. The helium is not adsorbed by the charcoal and is pumped out of the traps. Barium heated to 700°C is used for absorbing the nitrogen. The remaining mixture of argon, hydrogen, and other gases is also separated by means of absorbents.

The major shortcoming of the physicochemical method is the need for sufficiently large gas samples. As a result, the practical application of the method is limited to heights of 70 - 90 km. The attempt by McQueen to use a ground-based magnetic mass spectrometer for analysis of the air samples did not produce favorable results (Bibl.16).

Rocket investigations of the chemical composition of the atmosphere in the Soviet Union began in 1949 (Bibl.16). A more improved procedure of sampling by glass cylinders with a capacity of 400 and 3000 cc, installed in the openwork compartment of a recoverable strap-on capsule, which separates from the rocket, is used (Chapt.I, Sect.1). The use of glass cylinders permits a better preservation of the air sample composition. However, even in this case unstable components such as O, N, OH, NO, etc. as well as various ions colliding with one another and with the walls of the cylinder pass into their ground states, forming stable molecules O_2, N_2, H_2O. This increases the error of measurement.

Cylinders with a capacity of three liters deliver a volume of gas less than 1 mm^3 for analysis from a height of about 100 km (under normal conditions). An increase in the sampling height by as little as 10 - 12 km leads to a decrease in the gas volume by about one order of magnitude. As a consequence, the applicability of this sampling method is limited and depends on the sensitivity of the equipment used for the analysis.

The spectral method developed by S.E.Frisch et al. (Bibl.3) is used in the USSR for gas analysis. This method permits determining the main components (oxygen, nitrogen, argon) of small quantities of gas (10^{-1} to 10^{-2} cm^{-3} under normal conditions) with an error of less than 5 - 8%. Thanks to this, the ceiling of investigations is raised to an altitude of about 110 km (Bibl.16).

The Frisch method is based on the use of a high-frequency gas discharge /73
excited by electrodes installed outside the discharge tube (capillary analyzer) which thus does not react with the gases of the sample. The principle of this technique is to photograph the fluorescent spectrum of the investigated mixture and the spectra of three standard mixtures of gases of known concentration in the 7000 - 8000 Å range. This is followed by a photometric analysis to determine the quantity of the basic components. A spectrometer with a glass optical system, for example the ISP-51, is used in the analysis (Bibl.16).

Losses of unstable atmospheric components and the marked decrease in the feasibility of the sampling method above 100 km necessitated a search for suitable mass-spectrometer equipment for analyzing the gas composition of the upper atmosphere. The basic feature of this equipment, which ensures its wide use on rockets and satellites, is the fact that the analysis can be made directly at the site of sample collecting, at a high sensitivity and resolution.

Magnetic mass spectrometers with static fields have good sensitivity and high resolution (up to 6×10^4); however, they are heavy and large, require complex adjustment of the mass analyzers and, furthermore, need considerable time for recording the spectrum [more than 5 - 10 min (Bibl.2)]. Attempts to use them on rockets in the USA were unsuccessful (Bibl.13).

In the last 15 - 20 years both magnetic and nonmagnetic dynamic instruments have been developed for investigating the upper atmosphere. The former include instruments of the omegatron type, and the latter comprise radiofrequency and time-of-flight mass spectrometers.

The principle of the omegatron is based on using the characteristics of ion motion in a direct-current magnetic field and, perpendicular to it, an alternating-current electric field. At resonance, when the frequency of the electrical field is equal to the Larmor precession of ions of determined mass $\left(\omega = \frac{eH}{2mc}\right)$, the trajectory of their motion in the instrument chamber approaches an Archimedes spiral. The ion receiver is located at a certain fixed distance from the center of the spiral in such a manner that only resonance ions are able to reach it. In the omegatron chamber, the ions are accelerated regardless of the initial phase, thus avoiding acceleration at harmonics producing false peaks of the ion current. Therefore, the peaks on the recording of the ion current are single-valuedly determined by the frequency of the electric field. The most suitable receiver for recording ion current peaks in the omegatron is an open-type secondary electron multiplier (Bibl.32).

Simplicity and reliability, as well as high sensitivity are features of /74 the omegatron.

The lower limit of the measurable partial pressures of gas for instruments of this type is estimated as of the order of 10^{-10} mm Hg (Bibl.13).

The resolution R of the mass spectrometer is determined by the relation

$$R = \frac{M}{\Delta M}, \qquad (1.IV)$$

where M is the mass number of ions for a given peak, while ΔM is the difference of the mass numbers of two adjacent peaks recorded separately.

We note that the quantity ΔM is usually determined at zero recording level of the ion current.

The resolution, as indicated by eq.(1.IV), is characterized by the type of recording of the ion current of the mass spectrometer. For example, if the resolution close to a peak with a mass number M = 20 atomic mass units (a.m.u.) is R = 20, then the peaks of ions with mass numbers $M' = 19$ or $M'' = 21$ will differ (beginning with the zero level) since, in our example, $\Delta M = 1$.

The resolution R of omegatrons is not constant with respect to the scale of the mass spectrograph; it decreases for heavier ions. Thus, for the instrument

described elsewhere (Bibl.11), the resolution for hydrogen atoms $M' = 1$ is $R' = 443$; for helium atoms of $M'' = 4$, $R'' = 111$; and for carbon dioxide or nitrogen peroxide of $M''' = 44$, $R''' = 10$. The resolution of omegatrons in the region of large masses is substantially improved upon a decrease in the high-frequency voltage, but in this case the amplitude of the peaks drops and the sensitivity becomes less.

An important feature of omegatrons is the small size of the mass analyzer. For example, the chamber of the omegatron whose parameters were indicated above, measures 48 × 36 × 36 mm, and it simultaneously performs the functions of both ion source and ion analyzer (Bibl.11). Numerous investigations (Bibl.11, 34, etc.) show that the use of these instruments for measurements in the upper atmosphere is promising.

The principle of the time-of-flight mass spectrometer is based on the dependence of the transit time during the drift interval of ions with definite energy, on their mass. At a large drift length, i.e., when the time of flight of the ions is sufficiently long, the peaks of ions of different mass are recorded separately in time, meaning that the resolution is increased. Short voltage pulses serve to knock the ions out of the ionization chamber. The secondary electron multiplier is the most widely used receiver.

Investigations by G.M.Martynkevich (Bibl.12) demonstrated that a shortening of the drift space of the time-of-flight mass spectrometer to 150 mm permits /75 obtaining sufficiently good results under laboratory conditions, although the resolution of the instrument is not high (about 10 - 14 in the region of 30 a.m.u.).

The main advantage of the time-of-flight mass spectrometer is its rapid response, reaching 10^{-4} sec and less (Bibl.12, 13). Instruments of this type are of simple design, have an uncomplicated electric circuit, and low weight. In connection with this, various attempts are being made to use this instrument for measurements in the upper atmosphere (Bibl.13).

However, radiofrequency mass spectrometers of the Bennett type, in which electric fields are used for mass separation of the ion, have proved most suitable for solving the problems under consideration. These instruments are comparatively light and small at sufficiently high sensitivity and resolution, which ensures their wide use in measurement techniques both in the USSR and in the USA. The field of application of mass spectrometers is limited both downward and upward.

The lower limit is determined by the mean free path of the particles λ. The value of λ should obviously be greater than the path of ions L in the analyzer. When L is equal to 10 - 15 cm, the lower boundary of application is close to 100 km since the mean free path of the neutral particles λ_n at this level is 10 cm while of electrons λ_e and of ions λ_i it is 50 cm each (Bibl.1, 18).

The upper limit of the application range for the mass spectrometer is determined by its sensitivity, i.e., by the value of the minimum ion current recordable by the instrument. According to data by B.A.Mirtov (Bibl.16), we can

consider that the ion concentration of the order of 10^3 cm^{-3}, created by the ion source, still permits reliable measurements, for example, with a radiofrequency mass spectrometer. When analyzing the ion composition of the atmosphere, this limit is higher since the natural ionization of the upper atmosphere provides the necessary ion concentration (see Table 2.IV) up to heights exceeding 1000 km.

Consequently, limits of applicability of an instrument substantially depend on the design data. Thus, to measure the atmosphere components below the critical level produced by the mean free path L of the ions in the analyzer, a pumping system can be used. This system should provide a pressure drop of the sample to the required value, after which the gas is allowed to enter the analyzer. The pressure in the analyzer can be calculated from the pumping rate and from the measured outside pressure. The use of this system, according to the calculations by other authors (Bibl.10), permits reducing the lower limit to 50 km and even higher.

The radiofrequency Bennett mass spectrometer was first proposed for research of the upper atmosphere in 1952. The first successful launch of a /76
mass spectrometer installed in the nose cone of an Aerobee rocket was made in 1953 (Bibl.16). The intake of the analyzer communicated with the atmosphere through a number of narrow slits made in the nose skin of the rocket. Subsequently, the accuracy of measurement in the USA was appreciably increased by separating from the rocket the nose cone, which shrouded the analyzer during flight through the dense layers of the atmosphere. The analyzer was uncovered by means of a percussion mechanism. The intake of the analyzer was mounted along the axis of the rocket and was made to project slightly beyond the leading edge of the nose section. The RMS-1 radiofrequency mass spectrometer was first used on geophysical rockets in the Soviet Union by V.G.Istomin in 1957 (Bibl.16, 35). The equipment developed in the USSR is based on the usual principles; however, substantial modifications were made in its design, leading to improvement in its characteristics and reliability. An especially important improvement is filling the analyzer with a control mixture before opening. This permits periodic check calibration of the apparatus on the ground and during flight (before opening the analyzer).

Later (in 1959) a series of improved mass spectrometers, such as the MKh-6401, MKh-6403, and MKh-6405 designed on the basis of the RMS-1 mass spectrometer used on the third Soviet artificial satellite, was developed and used extensively in subsequent measurements (Bibl.19). Unlike the American method, the analyzer of the mass spectrometer is installed, as a rule, in a sufficiently wide receptacle on the side of the detachable capsule. The intake, after opening, communicates with the atmosphere. The point of installation is selected so that the elements of the capsule do not block the "field of view" of the analyzer. Before the flight, the capsule is carefully cleaned and washed with alcohol. Ejection of the capsule from the rocket occurs at an altitude of about 90 km, a relative velocity of the order of 1 m/sec being imparted to it (Bibl.8). At the separation altitude, the mean free path is about 4 cm; the capsule immediately moves away to a distance of many mean free paths from the rocket, into the undisturbed atmosphere which is free from contamination.

We note that a special capsule without openwork bay (Bibl.16) was used in the USSR in the mass spectrometer measurements. This bay was replaced by a

pressurized compartment housing the telemetry system, the backup loop oscillograph for telemetry recording, and the mass spectrometer. Outside the compartment, the antennas of the radio receiver were mounted. In all other respects, the design of the capsule is analogous to that described above (see Chapt.I, Sect.2). Use of this mass spectrometer on board the third satellite made it /77 possible to obtain a vast amount of data on the composition of the ionosphere at heights from 225 to 980 km (during the operating period of the equipment from May 15 to 25, 1958, about 15,000 mass spectra of positive ions were recorded).

Section 3. Principle and Basic Characteristics of Radiofrequency Mass Spectrometers

The operating principle of the RF mass spectrometer proposed by Bennett in 1948 (Bibl.19) consists in the mass separation (selection) of ions relative to their energy increment in the HF electric field of triple-grid cascades. The circuit of the analyzer operating on this principle (Fig.1.IV) consists of an ion source [cathode (1) and ionization chamber (2)] and a three-grid selecting cascade and ion collector (7), there being no need for the ion source when analyzing ionized gases. In front of the plate of the collector (7), the grid (6) is installed, fed with a stopping potential U_t.

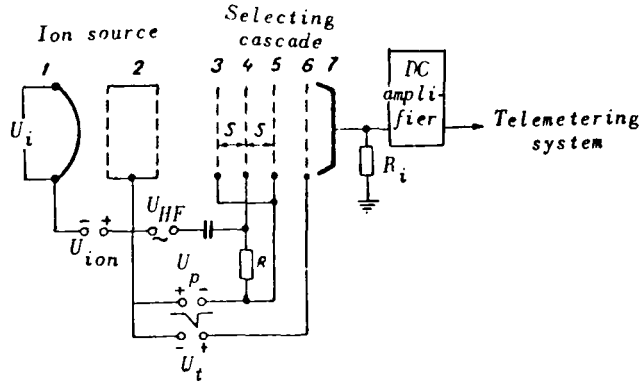

Fig.1.IV Wiring Diagram of the Analyzer of the Mass Spectrometer with One Triple-Grid Cascade.

A uniformly rising (sawtooth) negative sweep voltage U_p is fed to the system consisting of three grids (3), (4), and (5) spaced by identical distances s. In addition, a sinusoidal alternating voltage is supplied to the center grid (4) of the cascade

$$U_{HF} = \pm U_0 \sin(\omega t + \theta), \qquad (2.IV)$$

whose frequency $\omega = 2\pi\nu$ is sufficiently high and whose amplitude is low ($U_0 \ll U_p$).

The positive ions formed in the ion source or ions of the ambient medium

are accelerated by the negative potential U_p and, passing through the first grid (3) of the selecting cascade, impinge under the effect of the high- /78
frequency voltage applied to the grid (4). The HF field imparts an additional acceleration to the ions, with the greatest energy increment shown by the ions drawn into the selecting cascade at a negative voltage U_{HF}, passing through the center grid (4) at the instant of change in sign by the HF voltage, and then ejected from the cascade. The ions that are given the greatest energy increment in the selecting cascade are known as synchronous ions. The mean velocity v_0 of the synchronous ions in the gap between the grids (2) and (3) is a constant for a given instrument. As the sweep voltage U_p increases, this velocity v_0 is acquired by ions of ever greater mass. The stopping potential U_t supplied to the grid (6) is so selected that only synchronous ions pass through it to the collector. Consequently, the recording of the ion current of the collector shows a number of peaks corresponding to ions of ever greater mass (see Fig.5.IV).

The correlation between the sweep voltage U_p and the mass of singly charged ions can be determined from the following considerations:

The velocity imparted to a positive ion with a mass number M in the accelerating axial sweep field U_p obviously is equal to

$$v = \sqrt{\frac{2eU_p}{Mm_0}}, \tag{3.IV}$$

where e is the electron charge, $m_0 = 1.66 \times 10^{-24}$ gm is the atomic mass unit.

The magnitude of the increment of ion energy obtained in the high-frequency field of the three-grid cascade is

$$\Delta W = \Delta\left(\frac{mv^2}{2}\right). \tag{4.IV}$$

If we take into account the smallness of this quantity determined by the condition $U_0 \ll U_p$, we can transform eq.(4.IV) in the following manner:

$$\Delta W = \frac{v}{2}\Delta(mv) = v\int_0^{\tau}\frac{U_{HF}}{s}e\,d\tau, \tag{5.IV}$$

where $\tau = \frac{2s}{v}$ is the transit time of the ion into the three-grid cascade, $\frac{U_{HF}}{s}$ is the axial electric HF field strength.

Using eq.(2.IV) and substituting the integration limits, we obtain /79

$$\Delta W = \frac{v_e U_0}{s}\left[\int_0^{\frac{s}{v}}\sin(\omega t+\theta)\,dt - \int_{\frac{s}{v}}^{\frac{2s}{v}}\sin(\omega t+\theta)\,dt\right] = \tag{6.IV}$$

$$= \frac{v_e U_0}{\omega s}\left[\cos\theta - 2\cos\left(\frac{\omega s}{v}+\theta\right)+\cos\left(\frac{2\omega s}{v}+\theta\right)\right].$$

The initial phase angle of the HF voltage at which the ions receive a maximum energy increment, as is apparent from the expression derived for ΔW, will then be

$$\frac{s\omega}{v_0}+\theta = 180^\circ, \qquad (7.IV)$$

where $\frac{s\omega}{v_0}$ is a parameter of instrument tuning and v_0 is the ion velocity.

The tuning parameter is so selected that the magnitude of the phase angle θ is approximately equal to -46° at the entrance of the ion into the cascade and $+46^\circ$ at its exit.

From condition (7.IV) and eq.(3.IV), we find that the mass number of the synchronous ions is determined by the formula

$$M = \frac{0.266U_p}{\nu^2 s^2}, \qquad (8.IV)$$

where ν is expressed in megacycles, s in centimeters, and U_p in volts.

Equation (8.IV) is the basic formula for the radiofrequency mass spectrometer. From this, knowing the values of ν, s, and U_p for a definite peak of the ion current, the mass of the ions can be directly determined.

The amplitude of the ion current peaks will evidently be proportional to the ion concentration if the sensitivity of the instrument is kept constant.

In connection with this, the sensitivity of mass spectrometers is characterized by the magnitude of the change in concentration corresponding to the variation in output signal by one percent of the telemetry scale.

A variation in the stopping potential U_t causes a change of the zero level of the signal and, consequently, of the basic instrument parameters. Upon an increase in the potential U_t, the resolution increases (narrowing of the ion current peaks) and the sensitivity decreases (decrease in amplitudes of the peaks with increase in zero level). Thus, the magnitude of the stopping /80
potential U_t in mass spectrometers is established by the required sensitivity (collector current); to increase the resolution several three-grid cascades, separated by equipotential drift spaces, are used in analyzers instead of only one.

The extent of the drift space - distance L between the center grids of the cascade - is so arranged that the transit time of synchronous ions along these intervals is equal to the total number of periods T of the HF field,

$$L = v_0 bT, \qquad (9.IV)$$

where v_0 is the velocity of the synchronous ions in the analyzer, b is a

constant coefficient selected in accordance with the required resolution.

If eq.(9.IV) is satisfied, only synchronous ions will pass through the center grids of all cascades at the instant of sign reversal of the HF field. The cloud of synchronous ions drifting along the analyzer axis is more sharply separated from the nonsynchronous ions and the peaks of the ion current are more narrow. Thus, the resolution of the instrument is increased (by a decrease in the quantity ΔM).

It is important to note that an increase in the number of selecting cascades of the analyzer leads to a decrease in ghost harmonic peaks which are secondary maxima of ion-energy increment. The presence of harmonic peaks would interfere with the interpretation of mass spectra. The level of the harmonic peaks, naturally, changes with any change in magnitude of the stopping potential U_t, but an increase in U_t in order to decrease the amplitude of the harmonics is not expedient since this would lead to a decrease in sensitivity. An analysis (Bibl.4) showed that the level of harmonics, permissible with respect to sensitivity, should not exceed 0.85 - 0.87 of the fundamental peak.

We note that the resolution is approximately proportional to the total length of the drift spaces. The use of an analyzer with small drift spaces would require an appreciably greater number of three-grid cascades to achieve the necessary resolution.

As a parameter characterizing the design of the analyzer of a mass spectrometer, it is common to indicate the number of drift spaces and the number of corresponding periods of HF voltage. For example, a high resolution can be achieved for 5 - 9 - 4 - 7 = cyclic instruments. This means that the analyzer contains five cascades and that, for the first drift space, the value of the coefficient b in eq.(9.IV) will be equal to 5, for the second drift space 9, etc.

To ensure constancy of the synchronous ion velocity v_0 at all drift spaces between the extreme grids of the cascades of the multistage analyzers, a positive bias voltage U_b is applied. This voltage compensates the energy increment imparted to the synchronous ions in the selecting cascades. At the same /81 time, it correspondingly reduces the velocity of the nonsynchronous ions, without lessening the resolution of the instrument.

The optimum value of the bias voltage U_b for each multistage analyzer is selected when tuning the instrument for maximum sensitivity. If the value of U_b deviates from optimum in any direction, the phase angle at the instant of arrival of the synchronous ions at the cascades will differ from optimum ($\theta = -46^\circ$), causing a drop in sensitivity of the instrument.

We note that subranges of the mass scale are usually provided in instruments, resulting in a broad common range with a comparatively simple sweep-voltage U_p oscillator. The change from one mass range to another is accomplished by changing the frequency ν of the HF oscillator. Simultaneously, the sweep oscillator is switched.

The values of ν and U_p should match. For example, for the subranges of

1 - 4 and 12 - 56 a.m.u. used in our instruments and an intergrid distance of s = 0.15 cm at a minimal sawtooth sweep voltage $U_{p\,min}$ = -70 v, the high-frequency of the first subrange, as follows from eq.(7.IV), should be equal to about 30 mc ($\nu_1 = \sqrt{\frac{0.266 \times 70}{1 \times 2.25 \times 10^{-2}}} = 30$) and for the second subrange $\nu_2 = \sqrt{\frac{900}{12}} =$ = 8.6 mc. In our case, the maximum value of the sawtooth voltage should be $U_{p\,max_1}$ = -280 v for the first subrange and $U_{p\,max_2}$ = -350 v for the second. These frequencies and voltages are generated in the mass spectrometer of the MKh-6403 type during a sweep time of the subranges of 0.6 and 2.4 sec, respectively. In the MKh-6401 mass spectrometer, the frequencies ν_1 and ν_2 were selected to be half those indicated above.

The comparative characteristics of the RF mass spectrometers used for investigating the composition of the upper atmosphere (Bibl.19, 35) are given in Table 3.IV.

Section 4. Radiofrequency Mass Spectrometer MKh-6401

The small automatic MKh-6401 radiofrequency mass spectrometer (Bibl.18) is designed for measuring the ion and molecular composition of the upper atmosphere. The block diagram of the instrument is given in Fig.2.IV. The electronic measuring unit generates the supply voltage for the analyzer, amplifies the ion currents, and reads out to the telemetry system all parameters needed for monitoring the operation of the instrument and for interpreting the mass /82 spectra. It incorporates an ion-current amplifier, high-frequency and sawtooth voltage oscillators, a device for switching the mass ranges, and a stabilized feed-voltage converter for all elements of the instrument.

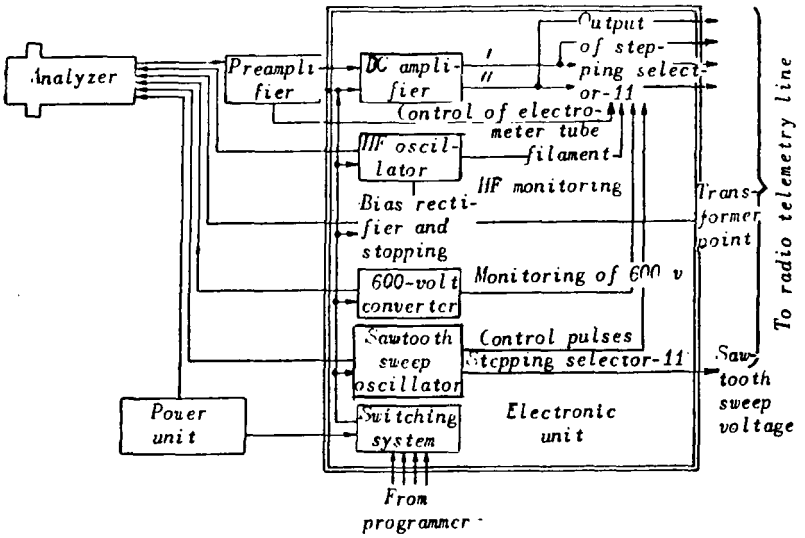

Fig.2.IV Block Diagram of Mass Spectrometer.

TABLE 3.IV

BASIC CHARACTERISTICS OF MASS SPECTROMETERS

Characteristic	Townsend Instrument	RMS-1	MKh-6401	MKh-6403	MKh-6405
Number of cycles of the analyzer	5 - 7	5 - 7	5-9 - 4-7	5-9 - 4-7	5-9 - 4-7
Mass range, a.m.u.	5 - 48	6 - 48	1-4/12-56	1-4/12-56	1-2/12-36
Resolution R (with respect to the base of the peak) maximum	25	30	50	50	20
at M = 20 under laboratory conditions	-	20	20	20	-
Sensitivity per 1% of the telemetry scale in ion analysis					
On a rocket, ion/cm^3	-	4×10^2	5×10^2	1×10^2	-
On a satellite, ion/cm^3	-	80	-	-	-
Sensitivity in neutral analysis (with respect to argon), particles/cm^3	-	-	1.6×10^8	1.6×10^7	-
Same, mm Hg	-	-	5×10^{-9}	5×10^{-10}	1×10^{-10}
Weight without power source, kg	6.0	6.0	3.3	2.0	2.0
Power input, w	> 30	25	6	4	4

The five-stage analyzer of the instrument (Fig.3.IV) is designed on a 5 - 9 - 4 - 7-cycle circuit. The ion source of the analyzer is arranged so that it can be removed when measuring the ion composition of the atmosphere. An economic thorium oxide cathode, using a current of not more than 0.5 amp at a voltage of 1.5 v, is used here.

All 23 grids of the analyzer are made of a one-layer winding of tungsten wire. The casing of the analyzer, having a length of 270 mm without the ion source and 410 mm with it and a diameter of 50 mm, is made of stainless steel. Its front part is provided with a glass sphere which, before start of operation in the atmosphere, is broken by a striking mechanism attached to the casing of the ion source. /83

The collector is directly connected with the input of the pre-amplifier which is housed in a removable head attached to the base of the analyzer. The ionization chamber of the ion source consists of two grids connected in parallel

and fed with a voltage of 40 v (relative to the cathode), for accelerating the electrons. Beyond the chamber are two grids supplied by a negative voltage of 70 - 100 v which extracts the ions from the ionization chamber. /84

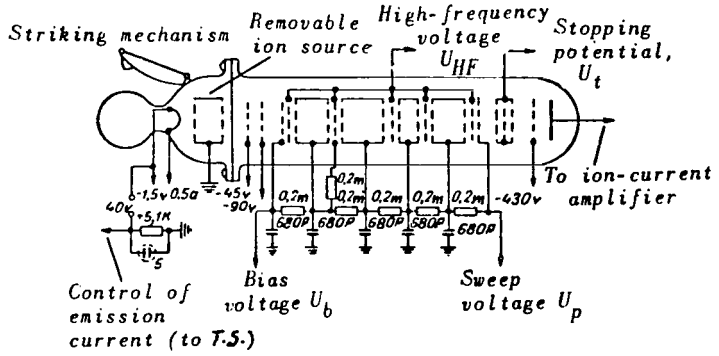

Fig.3.IV Wiring Diagram of the Analyzer of the MKh-6401 Instrument.

A positive stopping potential U_t is supplied to the three parallel-connected grids, which provides a pronounced cut-off of ions by energies. The negatively charged grid at the ion collector prevents the occurrence of a dynatron effect. The weight of the analyzer, with preamplifier and ion source, is 2.1 kg.

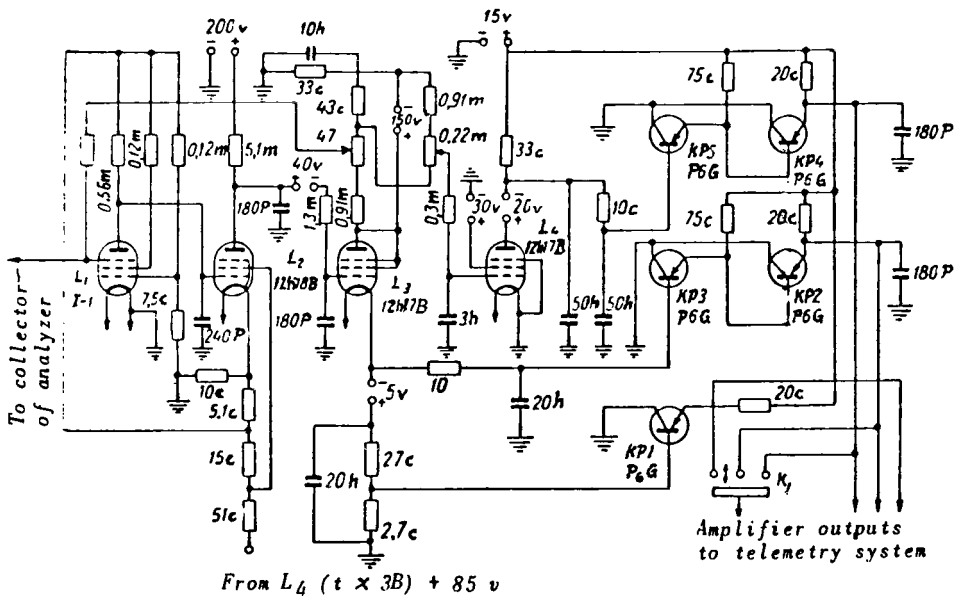

Fig.4.IV Basic Diagram of the Ion-Current Amplifier.

The elements of the electronic unit are mounted to two connected panels which can be moved in an aluminum casing of 210 × 90 × 70 mm dimensions. The weight of the unit is 1.2 kg.

The circuit of the ion-current amplifier (Fig.4.IV) consists of four DC amplifier stages. The first three stages are enveloped by a negative voltage feedback. An electrometer pentode of the I-1 bar type (L_1) is used in the first stage which is the preamp. The plate voltage of the tube I-1 (about 15 v) is tapped from the voltage divider which is connected into the cathode circuit of the second stage, composed of the tube 1 Zh18B (L_2). The third stage is composed of the tube 1 Zh17B (L_3) in a triode in connection with distributed loads. The voltage of the negative feedback is tapped from the load in its plate circuit across a potentiometer, which permits regulating the zero level of the output signal.

We note that generally electrometer amplifiers are used for measuring small currents that slowly vary with time. Their input resistance R_1 is large, /85 of the order of 10^{11} - 10^{12} ohms at a negligible magnitude of the shunting stray capacitance $C_s \approx 0.1 - 0.2$ μμf. The time constant of the input circuit therefore is large, $\tau = R_1 C_s \simeq 10 - 200$ sec (passband from 0 to 1 - 20 cps). In a mass spectrometer and in certain other instruments, it might become necessary to measure high-speed events which requires a reduction in the time constant τ to milliseconds or, in other words, a broadening of the frequency band to hundreds of cycles.

The sensitivity of narrow-band electrometer amplifiers is limited by the intrinsic noise of the tube, primarily by its flicker noise (Bibl.21). In broad-band circuits built of modern electrometer tubes, for example of type I-1 tubes, the thermal noise of the high input resistance (R_1 of the order of 10^{10} ohms) predominates and the sensitivity is close to the theoretical threshold.

Recently, the circuit of a transistorized broad-band electrometer amplifier with the use of a single I-1 tube in the first stage has been developed for on-board equipment (Bibl.30), with the control accomplished with respect to the first grid. At a sufficiently large negative bias, the electron current of this grid is almost completely absent. The thermionic current of the cathode, which also furnishes a considerable contribution to the magnitude of the grid current of the electrometer tubes, is not large because of the low temperature of the cathode and the low power dissipation (0.01 w). Therefore, it was possible to increase the voltage across the plate and the screen grid of the tube and to obtain from the electrometer stage a high amplification factor with respect to voltage (up to 100). The time constant of the input circuit of this amplifier is 0.01 sec at an input resistance of 10^{12} ohms, while the range of measurable currents is from 10^{-11} to 10^{-14} amp. The total voltage amplification factor (without feedback) of the first three stages of the circuit in Fig.4.IV is equal to 400.

Within the high-sensitivity channel there is an additional fourth stage in the tube 1 ZH17B (L_4) with a voltage amplification factor of 10.

The low-sensitivity channel output is taken only from a part of the load resistance which is connected into the cathode circuit of the tube L_3. Thanks to this, the amplification in the low-sensitivity channel is one order of magnitude less than in the moderate-sensitivity channel.

To obtain a low output resistance and matching with the telemetry system, all three outputs of the amplifier have P6G transistorized emitter followers. The output voltages have positive polarity. The outputs of the amplifier can be fed simultaneously to the three channels of the telemetry system or alternately to one channel across an electromechanical commutator K_1. The dynamic range of all amplifier channels reaches 10^5 (the measurable currents of the collector are from 10^{-8} to 10^{-13} amp in order of magnitude). The time constant of the amplifier does not exceed 1.5 msec because of the use of a correction system. This permits an undistorted recording of the entire mass spectrum from 1 to 56 a.m.u., within 3 sec. /86

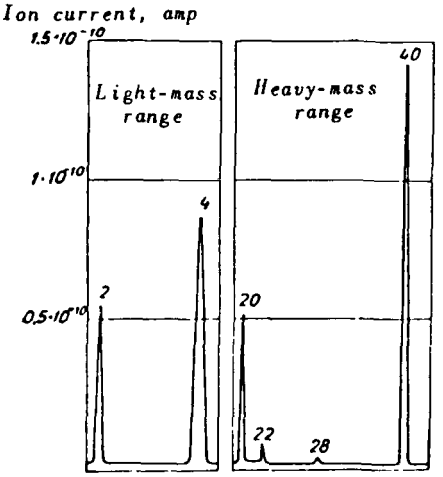

Fig.5.IV Mass Spectrum of Control Mixture of the Analyzer Filling Gas.

The analyzer of the mass spectrometer is pre-evacuated at a high temperature and then filled with a mixture of hydrogen, helium, neon, and argon at a pressure of about 10^{-5} mm Hg at a definite percentage ratio. This permits periodic monitoring of the operation of the entire instrument, by recording a calibration spectrum of the gas mixture of the analyzer. The configuration of the mass spectrum obtained from the moderate-sensitivity channel of the amplifier is shown in Fig.5.IV. The diagram indicates that the resolution of the instrument is readily determined from the peaks of the neon isotopes (20 and 22).

The HF oscillator (Fig.6.IV) generates a voltage of about 6.5 v at frequencies of 4.3 and 15 mc and also a constant voltage of positive polarity up to 80 v, which is supplied to the suppressor electrode. The oscillator is designed as a self-oscillating circuit with a pentode 1P22B (tube L_5). The circuits L_1 and L_2 mounted in the plate circuit of the tube L_5 are tuned to frequencies of 4.3 and 15 mc, respectively. The switch-over from generation of a frequency of 4.3 mc to a frequency of 15 mc is accomplished by closing, with respect to high frequency, the circuit of L_1 across the contact of the relay K_{4-1}. The oscillator is frequency-stabilized by means of the crystals KB_1 and KB_2 and also with respect to amplitude. The amplitude stabilization system is based on a comparison of the rectified HF voltage with a stabilized reference

voltage and on an amplification of the difference of these voltages for regulation. The HF voltage, rectified by the diode L_6, is fed to the input of the two-stage DC amplifier consisting of the tubes L_7 and L_8. The reference voltage from the stabilitron tube, for which a cold thyratron TKh3B is used, is fed to the cathode of the first stage of this amplifier. The amplitude is regulated by varying the voltage across the screen grid of the tube. As a result of /87 these measures, the circuit of the HF oscillator is noncritical to mismatch of the circuits, to fluctuations in temperature and humidity, and to other factors. The stopping potential U_t is tapped from the load resistance in the circuit of the rectifier diode.

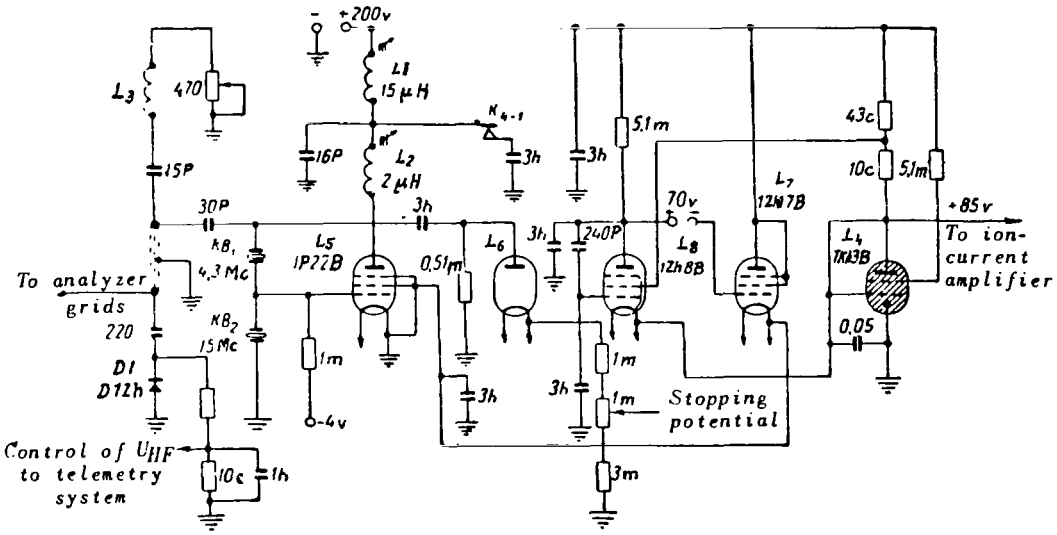

Fig.6.IV Principal Wiring Diagram of the High-Frequency Oscillator.

The mode of operation of the circuits of the sawtooth sweep generator (Fig.7.IV) is based on charging the capacitors by a direct current across the pentode L_9. Thanks to this, the time rate of change of the voltage is linear (deviations from linearity are not more than 3 - 4%). The different charging rate, needed to ensure sweeping of the ions in the subranges of the mass scale, is obtained by connecting the capacitors of differing capacitance by means of contacts of the relay K_{2-2}. For the light-mass subrange the charging time is 0.5 sec and for heavy masses, 2.5 sec (capacitances of 0.25 and 1 μf, respectively). The energy stored upon charging the capacitor which generates the negative sweep voltage in the heavy-mass subrange is used to switch the electromechanical commutator of the amplifier outputs P_1, which is connected into its /88 discharge circuit. At the same time, the bias voltage which has been increased owing to the 70-volt DC source, is tapped from the plate of the tube L_9.

The switching circuit, designed on the principle of a relaxation oscillator, operates for 0.5 sec with an interval of 2.5 sec. This causes flopover of the relay contacts switching the circuits of the HF oscillator and the capacitor of the sawtooth generator simultaneously.

The instrument is powered by a DC transformer assembled from semiconductor instruments with input stabilization. The instrument switches on and off the delivery of a short pulse to the winding of the relay in the transformer feed circuit. The signals from the three outputs of the amplifier and the monitored parameters are fed to the telemetry system.

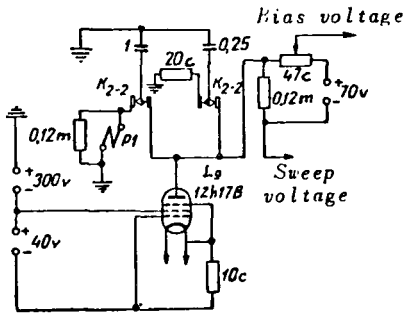

Fig.7.IV Principal Wiring Diagram of a Sawtooth Sweep Voltage Generator.

Independent checking, tuning, and calibrating of the MKh-6401 mass spectrometer, just as for other types of instruments, are carried out from the ground control unit (console) by means of which the fundamental regimes of the mass spectrometer can be established and measured, the mass spectrum can be observed on the screen of a cathode-ray tube or can be displayed on a loop oscillograph. To calibrate the amplifier, the console is provided with a constant-voltage source, feeding the input of the amplifier across a step divider. The variable voltages are measured by a cathode voltmeter mounted on the console.

On the basis of recording the spectrum of the control mixture (see Fig.5.IV) a calibration curve of the dependence of the gas mass on the time that has passed since the start of scanning a given mass range is plotted. The error of laboratory calibration of mass spectrometers in the USA is estimated as 20% (Bibl.38).

Section 5. Fundamentals of Mass Spectrometer Measurements

Mass spectrometry permits determining not only the chemical composition of the investigated gas but also, by measuring the amplitude of the ion current peaks, determining the distribution of partial concentrations of the components of the free atmosphere with respect to height. For this, it is necessary to use a measuring method in which the effect of all factors distorting the results is reduced to a minimum and taken into account. This necessitates investigating the problems of the interaction of the mass spectrometer analyzer with the ambient atmosphere during flight and to estimate the possible distortions of the compositions and concentrations of the investigated gas.

Outgassing of the capsule is an important source of error. Additional

methodological errors are produced by installation of instruments on rapidly moving capsules. The result of the measurements is here affected by the distortion of the concentration near the capsule, by orientation of the analyzer with respect to the relative flow, by the charge of the capsule, and by other factors. /89

In measuring the ion composition of the upper atmosphere, fewer methodological difficulties arise than in measuring the neutral components. Owing to the high rate of gas exchange after opening the analyzer (after 1 - 1.5 sec), dynamic equilibrium of the fluxes of incoming and outgoing particles is established. The latter pass through the ion source of the analyzer, with some of them undergoing ionization and again being analyzed. However, there is a considerable difference between the incoming and outgoing fluxes: the particles of the incoming flux strike the ionization region for the most part directly from the atmosphere, whereas the particles of the outgoing (reflected) flux undergo one or several collisions with the walls or components of the analyzer (grids, collector, etc.). When the particles collide with the walls or with each other, different reactions may occur which change the composition of the mixture.

Let us examine the perturbing processes and a method for taking them into account.

a) Exclusion of outgassing background. The measuring method based on the use of separable capsules greatly reduces the effect of outgassing of the rocket and capsule on the data; however, in this case the mass spectrometer records ions of contaminants detected from the character of the recording of the ion current. As a result of tumbling of the unoriented capsule or satellite the intensity of the peaks on the ion-current recording varies (is modulated), with the period of rotation of the container depending on whether the intake is located in the compression or rarefaction zone. The intensity of the background of outgassing (water vapor, nitrogen, oxygen, carbon dioxide, etc.) is virtually independent of the capsule orientation (Bibl.7, 26).

In certain measurements (Bibl.23), the outgassing background was taken into account based on measurements at the time when the analyzer intake was in the region of the molecular shadow. The pressure of the gas background in the cavity of the analyzer p_b was determined by the formula

$$p_b = k_e I_t , \qquad (10.IV)$$

where I_t is the amplitude of the peak of a given gas on variation in the molecular shadow, and k_e is the calibration coefficient of the mass spectrometer whose magnitude depends on the emission current of the thermionic cathode.

For example, for the MKh-6401 instrument we have $k_e = 4 \times 10^4$ mm Hg/amp at an emission current of 1 ma (Bibl.23).

b) Consideration of the effect of the charge and velocity of the capsule. If the capsule to which the mass spectrometer is mounted has a potential φ relative to the undisturbed plasma, this is equivalent to the sweep voltage U_p changing by the same magnitude /90

$$U'_p = U_p \pm \varphi. \qquad (11.IV)$$

The motion of a carrier with a high velocity v_0 exceeding the mean velocity of the gas particles results in the particles entering the analyzer as an ordered flow with the velocity of the carrier. This is equivalent to an increase in the negative sweep voltage by a certain magnitude ΔU_v. The law of the conservation of energy states that

$$\Delta U_v = \frac{300mv_0^2}{2e} = \frac{150m_0Mv_0^2}{e}, \qquad (12.IV)$$

where Δv_0 is the velocity component along the axis of the analyzer, e is the electron charge in electrostatic units, M is the mass number of the ion, and m_0 is the atomic mass unit.

Equation (12.IV) indicates that a change in the effective sweep voltage due to the velocity effect ΔU_v depends on the ion mass; for light ions it is less. For example, the value of ΔU_v, when the instrument is mounted on a satellite moving with a velocity of $v_0 = 8 \times 10^5$ cm/sec, for ions with M = 16 is 5.35 v and for ions with M = 30, about 10 v. Thus, the effective sweep voltage with consideration of both factors in question here is

$$U_p'' = U_p \pm \varphi + \Delta U_v. \qquad (13.IV)$$

The real mass number corresponding to the ion current peak on the telemetry recording, in conformity with the basic formula (8.IV), will be

$$M_{real} = \frac{1}{k}(U_p \pm \varphi + \Delta U_v) = M_{dec} \pm \Delta M_\varphi + \Delta M_v, \qquad (14.IV)$$

where $k = \frac{r^2 f^2}{0.266}$ is the instrument constant, M_{dec} is the mass number of the peak determined upon decoding the recording with respect to the magnitude of the sweep voltage U_p or from a calibration curve, ΔM_φ is the correction for the charge of the capsule, ΔM_v is the velocity correction determined by mapping the velocity of the space vehicle v_0 onto the axis of the analyzer.

It is apparent from eq.(14.IV) that the mass number of the ion current peak M_{dec}, determined by decoding the telemetry recording on the basis of laboratory data, is usually less than the real value of the mass number M_{real}; in other words, when measurements are taken on a rapidly moving capsule the instrument scale shifts toward light masses, with the magnitude of this shift depending on the mass of the ions. Using eq.(12.IV), we finally obtain

/91

$$M_{real} = \frac{1}{k}\left(\frac{U_p \pm \varphi}{1 - 150\frac{m_0v_0^2}{ek}}\right) = \frac{M_{dec} \pm \Delta M_\varphi}{1 - 150\frac{m_0v_0^2}{ek}}. \qquad (15.IV)$$

For example, the RMS-1 mass spectrometer installed on the third Soviet satellite had an instrument constant of k = 7.2 a.m.u./v (Bibl.7) and a sufficiently stable negative potential of about $\varphi = -3$ v (Bibl.6). In this case, the correction $\Delta M_\varphi = 0.42$ a.m.u. and a maximum shift of the mass peaks produced by the velocity effect, as follows from eq.(15.IV) at $v = 8 \times 10^5$ cm/sec, was

0.74 a.m.u. for mass 16 and 1.39 a.m.u. for mass 30 (nitric oxide). There is no velocity correction when the axis of the analyzer is along a normal to the velocity vector of the capsule.

It must be borne in mind that the presence of the negative capsule potential φ and of the ordered velocity of the ion flux v leads to a decrease in the effective stopping potential $U_t' < U_t$ by a value of $\varphi + \Delta U_v$. As a result of the drop in stopping potential, the sensitivity of the mass spectrometer in flight increases, more for heavy ions than for light ions, i.e., the discrimination effect occurs. The mass resolution correspondingly drops in comparison with the adjustment parameters. The increase in sensitivity, in turn, leads to the appearance or enhancement of harmonic peaks on the recording. Thus, the RMS-1 instrument, adjusted to a resolution of $R \simeq 20$ in the region of mass numbers M = 20 a.m.u., actually had a resolution of $R \simeq 10$ in the region of M = 16 a.m.u. (Bibl.6). As a result, the mass peaks in the region of light masses were completely resolved if their mass numbers differed approximately by 2 a.m.u. or more, whereas in the region of heavy masses ($M \approx 30$) the peaks for ΔM = 2 a.m.u. were resolved incompletely at the zero level.

However, the presence of harmonic peaks made it possible to broaden the dynamic range of the instrument toward higher sensitivities since, upon saturation of even the low-sensitivity output (ion current above 10^{-8} amp), the amplitudes of the peaks could be estimated by the harmonics, the light harmonic for atomic oxygen M = 16 being on the average 0.1 of the amplitude of the main peak (Bibl.6).

c) Role of processes in the analyzer. The gas mixture taken into the analyzer undergoes various changes produced during the inflow of gas into the /92
analyzer and within it, during various interactions between the neutral particles, ions, electrons, and walls of the instrument. Certain of these processes may noticeably change the gas composition or the concentration of the individual components.

Enrichment of the gas taken into the analyzer, by heavy or light components, may take place while the gas passes the intake, as a function of its orientation. This phenomenon, known as mass selection, is observed [as mentioned by A.I.Repnev (Bibl.27)] in a free molecular stream in the presence of unsteady processes and a density gradient in the instrument. The method of allowing for the mass selection phenomenon is analyzed in the discussion on gas component analyses in processing the data.

The inelastic collisions of neutral particles of the gas mixture may cause excitation of the electronic, vibrational, and rotational levels of the molecules, transfer of electron excitation, vibrations, or rotation, and ionization, recombination, dissociation, etc. There also may be collisions of photons with neutral particles, resulting in excitation and ionization of ions and in excitation of ionization and dissociation of molecules. The atoms may recombine upon collisions with third particles on their travel to the ion source, if this path is sufficiently long. An estimate shows, however, that the efficiency of these processes in the presence of the necessary design characteristics of the analyzer is not high and that, at variations in the gas composition under their effect, they can be disregarded in first approximation (Bibl.28).

Inelastic collisions of charged particles with neutral particles, in addition to dissociation, ionization, and excitation, may result in the formation of heavy ions and in charge transfer. Collisions with electrons, leading to the production of positive ions, specifically take place in the ion source of the analyzer. The ion current I generated under the effect of a focused cylindrical electron beam (Bibl.2) is determined by the expression

$$I = iN_nQd, \qquad (16.IV)$$

where i is the electron current of the source, N_n is the density of neutral particles in the ionization space, Q is the effective ionization cross section, and d is the dimension of the ion source over the path of the electron beam.

The effective cross section Q depends on the type of molecule or atom and on the electron energy, which reach a maximum for most gases in the energy range of 70 - 100 ev. These energies of the ionizing electrons are generally utilized in mass spectrometers. The effective cross sections for the production of negative ions of the basic components of the atmosphere in this case are much smaller than the cross sections for the production of positive ions /93 (Bibl.28); therefore, the effects of the action of negative ions are usually disregarded. The fact that the cross section is dependent on the type of gas causes the ratio of the ion currents of two given components to differ from the ratio of their partial pressures in the ion source. At present, it is difficult to take this effect into account because of the lack of reliable data on the effective cross sections of gas ionization. For example, according to available data (Bibl.28), the cross section of maximum ionization for He and Ar differ by one quarter magnitude (approximately 3×10^{-17} and 3×10^{-16} cm^2).

The probability of molecule dissociation on collision with electrons of the ion source is not great. For nitrogen molecules, this effect is virtually absent whereas the number of dissociating events of hydrogen molecules does not exceed $\frac{1}{200}$ of the ionizing events of these molecules (Bibl.28).

The effect of charge transfer may lead to the production of ions of new sorts, which are absent in the free atmosphere. This must be borne in mind when analyzing the ion composition. The extent of the charge transfer effect is small. Thus, the relative number of ions H^+, undergoing charge transfer over a path of 1 cm at a pressure below 10^{-3} mm Hg, does not exceed 0.1%. This means that the production of not more than 0.1% H_2^+ ions with respect to primary H^+ ions is possible (Bibl.28).

The effective cross sections for multiple ionization, at an electron energy of about 100 ev, are much smaller (by one to three orders of magnitude) than the cross sections for single ionization (Bibl.15). In some cases, the possibility of double ionization and dissociation of molecules must be considered (for O_2, CO_2, N_2O, etc.).

Processes of interaction of particles with the walls and electrodes of the analyzer play the most important role in the formation of the gas mixture composition.

Recombinations of atoms (O, N, H, etc.) as they take place in the upper atmosphere are compensated by the photodissociation reactions. After striking the instrument, the equilibrium is disturbed and the number of atoms decreases under the effect of recombination processes.

As a result of the collision of particles with the wall, they are adsorbed or absorbed (in the latter case, the particle penetrates inside the body). On the surface, chemical reactions may take place, specifically recombinations of the absorbed atom with an atom impinging on the surface.

Upon collision, the particle remains on the surface for a certain time, exchanging energy with the atoms of the crystal lattice. The particles adapt themselves to the temperature of the instrument walls. The accommodation coefficient, characterizing the degree to which the particles absorb the temperature of the wall if the surface is covered with a layer of adsorbed gas, reaches /94 a value of 0.8 - 0.9 (Bibl.28). In the technique of mass spectrometer measurements it is usually considered that complete accommodation of the particles to the wall temperature occurs during the residence time in the instrument, when there are many collisions.

The sorption phenomena on the hot filaments of the ion source in a neutral analysis lead to an interaction of oxygen and carbon of the filament, which results in the formation of CO and CO_2 molecules and in a decrease in the oxygen content of the mixture.

Recombination in the analyzer is especially extensive for oxygen which is the main atmosphere component at heights of 200 - 400 km. An analysis of these effects, as it was performed by A.I.Repnev (Bibl.29) on the assumption that only oxygen atoms whose concentration is equal to N_0 are present in the atmosphere, leads to the following simplified equation for the rate of formation of O_2 molecules:

$$\frac{dN_{O_2}}{dt} \approx k_1 N_{O_2}^2 N + b_1 N_{O_2} \sqrt{T_1} \frac{A_1}{w} + \\ + b_2 N o \gamma \sqrt{T_1} \frac{A_1}{w}, \qquad (17.IV)$$

where N_{O_2} and N are the concentrations of oxygen molecules and third particles that entrain the excess energy in collisions, k_1 is a constant of the reaction velocity of triple collisions, b_1 and b_2 are constants of the reaction velocity of recombination upon collisions of two atoms with the wall and with the adsorbed molecules where the wall plays the role of a third body, T_1 is the temperature of the inside surface of the analyzer, A_1 is the area of the surfaces on which recombination takes place, w is the volume of the analyzer, and γ is a coefficient characterizing the probability of recombination on the wall.

An analysis of eq.(17.IV) shows that the efficiency of the recombination processes at the walls of an ordinary analyzer exceeds the efficiency of other recombination processes by more than a factor of 100 at a low atomic oxygen pressure $p_o < 10^{-3}$ mm Hg (above the level of about 90 km in the atmosphere). The effect of recombination can substantially decrease provided the product

$\gamma \frac{A_1}{A}$, where A is the area of the inlet of the analyzer, has a low value. This is low, in particular, for glass analyzers (for glass, $\gamma \approx 10^{-4}$). If there are heated surfaces in the analyzer, the atomic particle concentration of many gases will decrease and the molecule concentration will increase. This effect must be taken into account in determining the gas concentration when processing the mass-spectrometer data (see Sect.6). Bombardment of the inside surfaces and /95 electrodes of the analyzer by charged particles or by high-energy quanta radiated by the sun leads to the production of secondary electrons which, according to data by Bernard (Bibl.2), may noticeably change the total current passing through the instrument. There is an especially severe distorting effect of secondary emission when a secondary emission amplifier is used as the ion receiver. In making relative measurements, these defects are disregarded (Bibl.28).

Section 6. Preliminary Processing of the Test Data

The telemetry recordings of the mass spectrometer data for all amplifier outputs of different sensitivities are processed together since minor admixtures of gases are noticeable only at the output of maximum sensitivity, whereas the main gas components at this output yield broad overshoots which can be localized only with respect to the low-sensitivity output. For example, the recordings obtained from the third satellite on May 23, 1958 [height 230 km, latitude 55°N (Bibl.7)] are shown in Fig.8a.IV. As we see, there are numerous harmonic peaks on the recording of the mass spectrum for the high-sensitivity channel, while the resolution in the region of large mass numbers is substantially lowered (owing to a decrease in U_t).

Processing of the recording begins with separation into subranges and determination of the mass numbers corresponding to the peaks on the recording from the instrument calibration curve. The time from the start of recording of each subrange is determined by markers on the recording. The separation of the fundamental and harmonic peaks (if there are any) in the spectra is done by comparing their amplitudes and the character of change in relation to the flight altitude and orientation of the instrument. The loci of the harmonic peaks and their width are determined from the data of laboratory tests of the instruments.

After introducing the velocity correction in accordance with eqs.(12.IV) and (14.IV), the mass numbers of the peaks taken as the fundamental peaks will differ from whole even numbers by a fraction of an atomic mass unit. This difference is usually due to the effect of the negative charge of the satellite and is used in conformity with eq.(14.IV), for determining the negative potential of the satellite. For example, on the recordings of the third satellite on May 22, this difference was 0.3 a.m.u., which for k = 7.2 a.m.u./v yields φ = = -2.2 v (Bibl.7).

The curves in Fig.8a.IV were obtained at a potential φ of about zero. The mass peaks, given here with consideration of the velocity correction, were identified as follows: 16 - O^+, 14 - N^+, 18 - oxygen isotope, 30 - NO^+, 32 - O_2^+, and 28 - N_2^+. All other peaks in Fig.8a.IV are harmonic (spurious). /96

Thus, peaks with mass numbers of 10, 5, and 12 are "light" harmonics with peaks of 14 and 16 respectively, whereas the peak with the mass number 22.5 (at the center) consists of light harmonics with peaks of 28, 30, and 32. The peaks with the mass numbers 40 and 43 are "heavy" harmonics with peaks of 28 and 30.

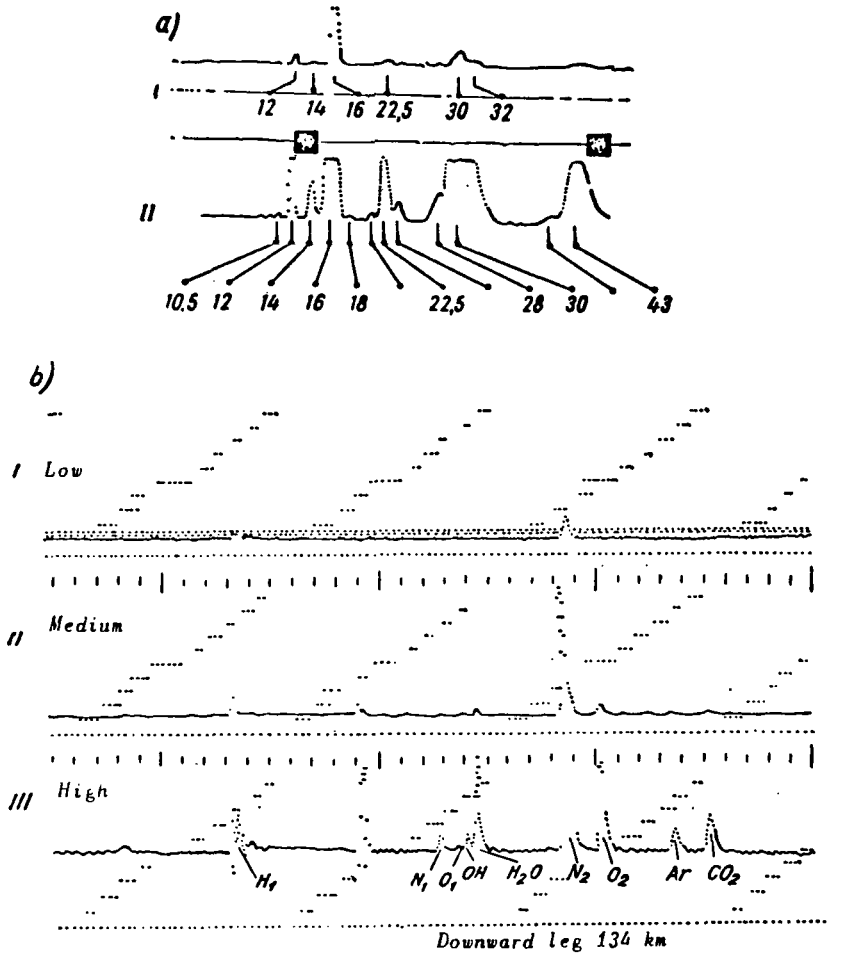

Fig.8.IV Examples of Recordings of Mass Spectrometer Signals, Used on the Third Satellite (a) and on a Geophysical Rocket (b).
I - Output of low-sensitivity channel; II - Medium; III - High.

The concentration of particles is determined from the amplitude value, defined from markers of reference voltage on the telemetry scale on the recording, of which an example is shown in Fig.8b.IV. /97

In the ion analysis, the amplitude of the peak in a channel of given sensitivity i_M is related with the concentration of corresponding ions n_M. For a rapidly moving capsule, when the thermal velocities of the ions are much less than its velocity v_0, this relation will obviously have the form

$$i_m = n_m e v s_{eff}(e, M, \varphi)\ \eta\ (M, \varphi, \vec{v}_0), \qquad (18.IV)$$

where e is the ion charge; s_{eff} is the effective cross section of the analyzer inlet depending on the angle θ with the velocity vector $\vec{v}_0$, on the mass number of the ions M and on the capsule potential φ; η is the current efficiency of the analyzer equal to the ratio of the current of ions of mass M entering the analyzer to the current of these ions at the collector i_M.

To determine the concentration n_M, the dependence of the parameters s_{eff} and η on the capsule potential, ion mass, and angle θ or velocity v_0 must be known. However, these parameters were not determined in the discussed experiments.

In processing the data collected by the third satellite (Bibl.6), a number of important conclusions as to the change in relative concentration of positive ions were drawn on the basis of eq.(18.IV) for an identical orientation of the instrument $\theta = 0$ and at a certain satellite potential φ. The constancy of the latter was checked on the constancy of the relative level of the harmonic peaks on the recording, since this level is highly sensitive to the magnitude of the effective stopping potential U_t. The effects of mass discrimination are substantial only for groups of ions with greatly differing masses. Therefore, the ratios of adjacent peaks i_M should be equal to the ratio of the concentration of given groups of ions n_M in the atmosphere

$$\frac{i_{m_1}}{i_{m_2}} = \frac{n_{m_1}}{n_{m_2}}. \qquad (19.IV)$$

In addition, V.G.Istomin (Bibl.9), in processing the test data, made the following assumptions: a) The sum of the concentration of positive ions is equal to the electron concentration $\Sigma n_M = n_e$, i.e., the value of negative ion concentration can be disregarded; b) the sum of the amplitudes of the ion peaks on the mass spectrogram is proportional to the total positive ion concentration $\Sigma i_M = k\Sigma n_M$. In this case, as follows from eq.(19.IV), the absolute concentration of ions with mass number M_1 can be determined from the relation

$$n_{m_1} = i_{m_1} \frac{n_e}{\Sigma i_m}. \qquad (20.IV)$$

The values of electron concentration n_e were taken from data obtained by other methods, while the values of the peak amplitude i_{M_1} and the sum Σi_M were determined from the recording. /98

The potential of the capsule φ has no effect on the results of measuring the neutral particle concentration; however, it is then necessary to allow for the effects of mass selection and distortions caused by the reflected flux.

Mass selection is caused by the fact that the moving mass-spectrometer analyzer is struck by a mixture of gases rarefied so much that the particles of each component move independently of one another. If the oncoming flow enters the analyzer, the mixture will be enriched by heavy components and, at opposite orientation, by light components.

Let the analyzer have a volume w and an intake of an area s. If, at the instant t = 0, the evacuated cavity of the capsule moving at a velocity v_0 is opened, then $\frac{N_0 v}{2\sqrt{\pi}} \varkappa(\beta) s\, dt$ particles will enter the volume during the time dt (see Chapt.III, Sect.4). As a result, the particle density in the instrument N_1 increases by a value dN_1 equal to

$$dN_1 = \frac{N_0 v}{2w\sqrt{\pi}} \varkappa(\beta) s\, dt \qquad (21.IV)$$

During the same time, a stream of particles which has acquired the wall temperature T_1 as a result of collisions, will escape from the volume of the analyzer. This leads to a decrease in particle density N_1 in the volume by $\frac{N_1 v_1}{2\sqrt{\pi}} \frac{s}{w} dt$ where v_1 is the velocity and N_1 the density of the particles at a temperature T_1.

Considering that N_0 depends on time, in consequence of the ascent of the capsule at a vertical velocity component v_0 in the atmosphere where the pressure drops with altitude according to the barometric formula and that v and $\varkappa(\beta)$ do not depend on time, A.I.Repnev (Bibl.27) after certain simplifications solved the equation of particle balance in the form of

$$N_1(t) = N_0 \varkappa(\beta) \frac{v}{v_1} \left(1 - e^{-\frac{t}{\tau_1}}\right), \qquad (22.IV)$$

where $\tau_1 = \frac{2w\sqrt{\pi}}{v_1 s}$ is the time after which (after opening) the mass selection effect begins to appear.

Using eq.(22.IV) the ratio of particle concentrations of two atmospheric /99 gases differing by the molecular weights M and M' will be obtained in the form of

$$\frac{N_0}{N_0'} = \frac{N_1 \varkappa'(\beta')}{N_1' \varkappa(\beta)} \frac{\left(1 - e^{-\frac{v_1' s t}{2\sqrt{\pi} w}}\right)}{\left(1 - e^{-\frac{v_1 s t}{2\sqrt{\pi} w}}\right)} = \frac{N_1}{N_1'} \mu, \qquad (23.IV)$$

where N_1 and N_1' are the concentrations of the corresponding gases in the analyzer volume.

The coefficient μ by which the measured gas concentration ratios must be multiplied to obtain their ratio in the atmosphere is known as the coefficient of mass selection.

Under equilibrium conditions, when the time terms cease being a factor, the selection is determined by the ratio

$$\mu_0 \approx \frac{\varkappa'(\beta')}{\varkappa(\beta)}. \qquad (24.IV)$$

In this case, when the velocity of the capsule is high ($\beta > 1.5 - 2$), the function $\varkappa(\beta) \simeq 2\beta\sqrt{\pi}$ and the coefficient μ_0 are transformed into

$$\mu_{00} \approx \sqrt{\frac{M'}{M}}. \qquad (25.IV)$$

The values of μ_0 and μ_{00} were calculated by Repnev (Bibl.27) for various conditions. For example, in measuring the concentration ratio of molecular nitrogen N_2 to atomic oxygen O the correction coefficient is $\mu_{00} = 1.323$ and for N_2 and He, $\mu_{00} = 0.266$.

An analysis of the distortions introduced by the effect of the reflected flux, made by A.A.Pokhunkov (Bibl.26), confirms that mainly recombinations of chemically active atomic components of the atmosphere on the analyzer surfaces must be allowed for. To take this effect into consideration, Pokhunkov introduced the correction coefficient K_c. A calculation shows that, if the inside surfaces of the analyzer are gold-plated, the correction for recombination - even for atomic oxygen - is negligible ($K_c \simeq 1.1$).

Thus, mass-spectrometer data can be used also for obtaining information on the concentration not only on inert but also on chemically active components of the atmosphere.

Consequently, it is possible to determine the temperature of the atmosphere under conditions of a free molecular flow past the capsule (see Chapt.III, Sect.5).

The computational formulas (24.IV) and (25.IV) are valid under the assumption of a free molecular stationary flow and the presence of a local Maxwellian velocity distribution in the atmosphere. The condition of a free molecular flow past the instrument $\lambda \geq 10$ L (where λ is the mean free path of the molecules, and L is a characteristic dimension of the instrument) is satisfied at heights of about 150 km and more, where $\lambda \geq 5$ m. A steady state of the flow (equality of the number of incoming and outgoing particles) is ensured if the time constant of the instrument τ is much less than the time during which the density along the orbit changes noticeably. /100

It follows from the previously derived formula [eq.(47.III)] that the magnitudes of τ, for the mass spectrometers in present use, are of the order of tens or one millisecond. Thus, in the case of $w = 250$ cm^3 and $s = 0.8$ cm^2 at a height of about 150 km we obtain $\tau = 1.5 \times 10^{-2}$ sec. At a distance of about 120 m, which the satellite will traverse during this time on a circular orbit, the density changes are not great.

In estimating the errors of determining the temperature, M.N.Izakov (Bibl.5) started from the error in measuring the partial pressure $\delta p/p = 5\%$. With an error of measurement for the wall temperature of the analyzer of not

more than $\pm 1^{\circ}$ at the temperature level $T_1 \approx T_2 \approx 300 - 400^{\circ}K$, the error introduced by the temperature terms will not exceed 1%. The error in determining the velocity of the satellite, with consideration of wind, may reach 2.5%. The error in determining the angle φ is estimated as being $\delta\varphi \simeq +0.5R$. In this case, the mean-square error of an individual measurement for $\varphi = 0$ is estimated to be 14 - 19% (depending on height) while for $\varphi \leqslant -5^{\circ}$ the error drops to 7-8%.

The error of the method will decrease by a factor of 3 if a total of ten measurements are made during the time of a small temperature change (about 1 sec).

CHAPTER V

MEASUREMENT OF COSMIC RADIATION AND CORPUSCULAR FLUX

Section 1. Characteristics of Measured Quantities

In the flux of cosmic radiation, primary and secondary components are distinguished.

The primary flux (outside the earth's atmosphere) contains rays of galactic and solar origin.

The primary flux of galactic origin is isotropic and consists of the nuclei of various elements, accelerated to very high energies (up to $E = 10^{19}$ ev). The flux is composed mainly of protons which account for about 80% of the total number of particles (Bibl.71). The density of the isotropic proton flux in space changes little and averages 2 - 2.5 $cm^{-2} \cdot sec^{-1}$ (Bibl.27, 46), with /101
protons of very high energies (more than 10^{16} ev) rarely encountered (at $E_p = 10^{15}$ ev, the average intensity is 10^{-6} $cm^{-2} \cdot sec^{-1} \cdot steradian^{-1}$). In addition to protons, α-particles (approximately 0.3 $cm^{-2} \cdot sec^{-1}$) and nuclei of heavier elements [accounting for only 1 - 2% of the total flux (Bibl.30)] are observed in the primary flux. The primary fluxes are usually measured with respect to groups of nuclei of light elements L (Li, Be, and B), medium elements M (C, N, O, and F) and heavy elements H (with an atomic number $z \geq 10$).

The fluxes of primary cosmic rays of solar origin are associated with chromosphere flares, but not in all flares are the particles accelerated to high energies. Thus, flares in which protons are emitted with an energy to 10 Bev (10^{10} ev) are observed once every three to four years (Bibl.58). In rays of solar origin, as in galactic, protons predominate but their energy is less (from 10^{3} to 10^{11} ev), while the flux in the region of the earth's orbit reaches very high values [up to $10^{9} - 10^{12}$ $cm^{-2} \cdot sec^{-1}$ (Bibl.45 - 72)].

The flux of low-energy electrons ($E_e \simeq 1 - 10$ ev) may exceed the proton flux by several tens of times (Bibl.27, 66, 72). Furthermore, nuclei of He, (15%), O, C, (0.1% each), N (0.01%), and of other elements (in still smaller quantities) are observed in the solar corpuscular flux.

The stream of electrons emitted by the sun under normal conditions reaches

$10^7 - 10^{10}$ $cm^{-2} \cdot sec^{-1}$, with a particle energy from 2 ev to 10 Kev (Bibl.58, 73).

The sun also emits a high-energy flux of electromagnetic penetrating radiation (X- and γ-radiation). According to data by W.O.Roberts (Bibl.58) the flux of soft X-radiation of the sun amounts to $10^{-3} - 10^{-4}$ $erg \cdot cm^{-2} \cdot sec^{-1}$* but it is subject to wide fluctuations. The magnitude of the flux of gamma-radiation quanta (energy $E \geq 1$ Mev) is usually by one to two orders less than the X-radiation.

An important characteristic of primary cosmic rays is the dependence of the flux density and particle energy on the latitude of observation, the flux being enriched by lower-energy particles with an increase of the geomagnetic latitude beyond a certain limit [effect of latitude cutoff (Bibl.27)].

On interaction of the particles of the primary cosmic radiation flux with atmospheric gases, a secondary flux of increasing density is formed. Maximum development of this flux is observed at heights of 20 - 22 km, and all known particles [secondary protons, mesons, neutrons, etc. (Bibl.24)] are present /102 in it. On approaching the earth's surface, the intensity of the flux of cosmic rays decreases, from a maximum level, by a factor of 50 - 150, depending on latitude.

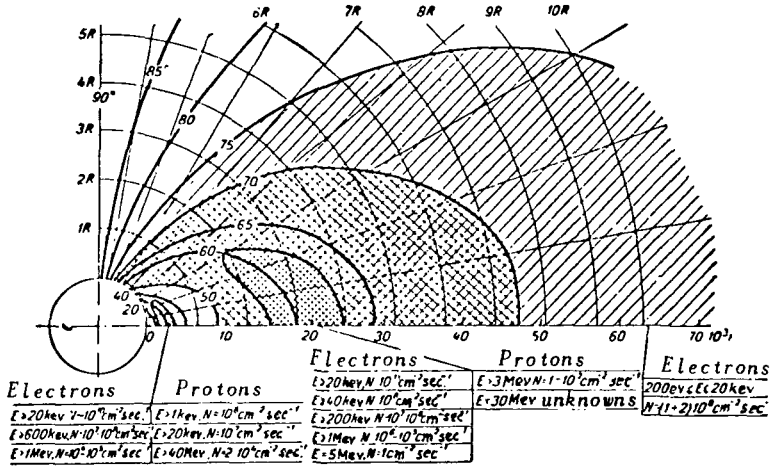

Fig.1.V Radiation Belts of the Earth.

Secondary cosmic rays are usually divided into a soft component which is stopped by a layer of lead of 10 cm thickness, a hard component penetrating through such a filter, and a nucleonic component.

The soft component consists mainly of electrons, positrons, and photons. The hard component contains heavier particles, mainly mesons. The relationship between the fluxes of the various components varies with height and depends on

* On converting the flux to energy units, we are assuming that 1 ev ≈ 1.6 × × 10^{-12} erg.

the geophysical conditions. At sea level, for example, the proportion of the soft component is about 30% of the total flux (Bibl.20, 24).

Cosmic rays undergo variations (change in intensity) caused by changes in the atmospheric conditions, the earth's magnetic field, or the conditions of space. The variations may have a regular character caused, for example, by periods of solar activity, or a random character. Low-energy particles undergo the greatest variations (Bibl.27).

Investigations of cosmic rays in the upper atmosphere, by means of equipment installed on board rockets and satellites, led to the recent discovery of the earth's radiation belts.

An idea as to the streams of particles and energies, subject to measurement in the radiation belts of the earth, can be obtained from Fig.1.V where the position of the belts in the geomagnetic field is given and the particle fluxes are indicated in maximum intensities based on the data of a number of authors (Bibl.6 - 16, 38 - 44, 57, 58, 72 - 79). Taking into account the axial sym- /103 metry of the belts and the symmetry relative to the geomagnetic equator, a cross section of only one-fourth of the space occupied by the belts can be shown here. Concentric circles are drawn at a distance which is a multiple of the earth's radius R. The lower portion of the sketch gives the energies and fluxes of particles in the regions of maximum intensity of the belts.

We note that at high latitudes (about 65°), as established by Soviet researchers (Bibl.61), the outer belt dips to low heights (about 200 km), with the extent and intensity of this belt strongly depending on the solar activity (the intensity varies by a factor of 10 - 100). Anomalous dips of the inner belt also have been observed (Bibl.57).

As soon as a space vehicle enters the radiation belts, appreciable radiation levels are created inside the capsule which are measured by dosimeter whose design is similar to that of the equipment for measuring the intensity of cosmic rays, which also play a part at the high radiation levels.

The radiation doses, subject to measurement, are produced not only by penetration of the energy particles into the capsule but also by bremsstrahlung and secondary particles which arise under irradiation of the capsule skin. The integral intensity of bremsstrahlung I_e Mev/electron, with total stopping of monoenergetic electrons, is determined by their energy E_e Mev and the mass of the substance in conformity with the formula

$$I_e = 5.77 \cdot 10^{-4} z E_e^2, \qquad (1.V)$$

where z is the atomic number of the element with which the electrons interact.

Bremsstrahlung has a continuous spectrum, sharply limited on the short-wave end by the quantity λ_g which, for electrons, is determined from the relation $\lambda_g = \frac{12\,345}{U}$ (Å), where U is the accelerating potential in volts corresponding to the particle energy. For example, at an electron energy E_e = 50 Kev the

quantity $\lambda_g \simeq 0.25$ Å.

The energy peak in the bremsstrahlung spectrum lies close to λ_g [corresponding to the wavelength maximum λ_{max} approximately equal to 3/2 λ_g (Bibl.17, 58)].

An estimate of the total radiation doses inside a spacecraft with an aluminum skin of 2 - 5 gm/cm^2 thickness* (Bibl.30) yields a value from 14 mrad/day for a flux of primary cosmic rays to several tens of rad/hr in the zone of maximum intensity of the inner belt (at a quiet sun). /104

At the intensity maximum of the outer belt and for a small thickness of the protective skin (less than 1.0 gm/cm^2) hard electrons penetrating the skin furnish the main contribution to the radiation dose which reaches 29.5 rad/hr. At a greater thickness of the protection, the bremsstrahlung furnishes the main contribution to the dose reaching 13.8 rad/hr (Bibl.58).

Of greatest interest at present is an investigation of the correlation of cosmic rays and corpuscular fluxes with geophysical and solar processes, their effect on the crew of a spacecraft and on the performance of various onboard devices, and an elucidation of their role in the thermal regime and ionization of the upper atmosphere. Toward this end, measurements are made of the intensity of fluxes of various particles, their energy distribution in time and space, and the radiation dose inside and outside the capsule.

Measurements on the characteristics of cosmic rays, to obtain information on processes in outer space and on the structure of space itself, are also of considerable interest (Bibl.26).

The energy range of particles subject to measurement, as demonstrated, is rather broad (from a few units to 10^{18} - 10^{19} ev). This necessitates the use of diverse equipment, especially when measuring particles of low and very high energies.

Section 2. General Characteristics of Onboard Equipment

The onboard instrumentation of most space vehicles launched in the Soviet Union and in the USA includes equipment for measuring the intensity of cosmic rays (Bibl.27, 57, 58, and others). This comprises mainly gas-discharge and scintillation counters and electronic circuits for measuring the repetition rate of particles of various energies. In particular, such equipment was used in the renowned flights of the interplanetary probes Mars-1, Luna-4 (Bibl.13), and Mariner-2 (Bibl.47).

The radiation level in near-earth space at heights of 180 - 340 km was measured by radiometric instruments designed on the same principle as equipment

---

* Here and below, "thickness" is to mean the product of the geometric thickness multiplied by the density of the substance. Occasionally, this quantity is called "mean free path".

for measuring cosmic radiations (Bibl.14, 51). This type of instrumentation was later used extensively in measurements on the Cosmos satellite series (Bibl.51, 62).

Spherical electrostatic analyzers of the soft component (from 0.1 to 30 Kev), developed by V.V.Mel'nikov and coworkers, were used to obtain the energy spectrum of the particles (Bibl.48).

Measuring equipment for investigating cosmic radiations by gas-discharge /105 counters (such as Anton-302) and multichannel scintillation counters developed by Van Allen and coworkers, were most widely used in the USA, in particular on the Explorer series, the Pioneer spacecraft, and other space vehicles (Bibl.45, 58, 57, 77). Magnetic spectrometers which analyzed electrons of different energies (2 - 5 channels each) were used in certain experiments. End-window counters [such as Anton-312 (Bibl.46)] or scintillation counters of various types (Bibl.31, 57) were used as receivers.

Semiconductor counters have recently found greater use in onboard equipment (Bibl.36, 77). Ionization chambers which permit determination of the total ionization (Bibl.27) and also pulse chambers (Bibl.77) have been used in certain measurements.

The composition of cosmic rays was measured by Cerenkov counters with multichannel electric circuits.

It should be mentioned that the Cerenkov counters, which recorded all nuclei with a charge exceeding a prescribed value ($z \geq 2$, $z \geq 5$, $z \geq 15$, etc.) were designated as integral counters by the authors (Bibl.41) and those intended for measuring the nuclear spectrum by charges, which measured the amplitude of the pulse caused by the passage of each nucleus through the detector, are called differential counters. In the latter case, the selection of the nuclei passing through a narrow solid angle was accomplished by two banks of gas-discharge counters connected into a coincidence circuit (so-called cosmic-ray telescope). The pulse of the Cerenkov counter was recorded only when the telescope was operating (Bibl.41).

Classical methods based on the use of thick-walled photographic emulsions were also widely used in rocket research. Geoactive corpuscles having comparatively low energies were measured by semiconductor or scintillation counters with thin crystals (Bibl.31) and by special soft-electron indicators equipped with fluorescent screens (Bibl.32 - 36).

The main elements of the counter circuits are amplifier-shaping stages, scaling flip-flop loops, and output devices of the counting-rate meter type (CRM) or resistance-coupled adders. The electronic circuits are usually powered from the onboard network, in which silicon solar cells are used as power sources. The high voltage for feeding the counters is tapped from storage batteries or transistor-stabilized transformers which, on temperature fluctuations of -20° to $+50^{\circ}$C, ensure a counting error of not more than 0.25% (Bibl.10).

Section 3. Characteristics of the Onboard Counters /106

Gas-discharge cylindrical counters of the type STS-5 or Anton-302 with a filament anode are most widely used in space vehicles. In such counters, the electric field strength E increases with approach to the anode in accordance with the formula

$$E = \frac{U}{r \ln \frac{r_2}{r_1}}, \qquad (2.V)$$

where U is the voltage applied to the counter, r_2 and r_1 are the radii of the counter casing (cathode) and filament (anode) respectively, and r is the distance from the axis of the counter.

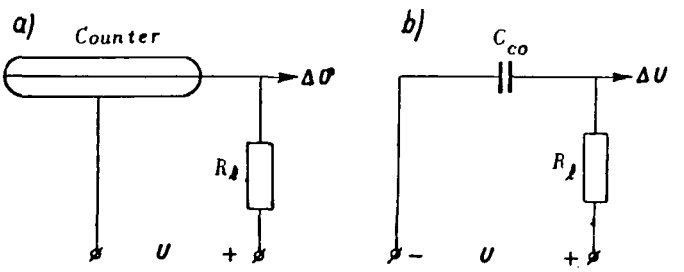

Fig 2.V Wiring Diagram of a Gas-Discharge Counter (a) and its Equivalent Circuit (b).

This permits increasing the ionizing power of the electrons moving toward the anode.

The variation in voltage ΔU across the filament of the counter (relative to the cathode) wired as shown in Fig.2a.V, when an ionizing particle strikes its working volume will be, in conformity with the equivalent circuit in Fig.2b.V,

$$\Delta U = \frac{ekN}{C_{co}}, \qquad (3.V)$$

where k is the gas amplification factor, N is the number of pairs of primary ions, e is the electron charge, and C_{co} is the capacitance of the counter.

Calculation shows that, for a particle producing ionization of $N = 10^3$ pairs of ions in the working volume of the counter at $k = 10^5$ and $C_{co} = 10$ μμf, the quantity $\Delta U \simeq 1.6$ v, i.e., ΔU is sufficiently large.

The shape of the voltage pulse of the gas-discharge counter is determined by the physical processes occurring in it.

The positive potential U_0 of the counter filament, corresponding to the operating voltage across it, does not change in the absence of ionizing /107

particles, as is shown in the segment 1 - 2 (Fig.3.V), for a counter with a grounded casing. If, at the instant t_2, a particle enters the counter, a discharge is initiated and persists to time t_3 (approximately 10^{-6} sec). The potential of the filament by this time drops markedly, due to an accumulation of electrons which are retained there by the "sheath" of positive ions. Termination of the discharge is followed by the recovery stage (lasting about 10^{-4} sec), since the velocity of the positive ions toward the cathode of the counter is comparatively low. The leading edge of the pulse consequently is steep and the trailing edge is extended.

The impingement of other particles at the instants t_4 and t_6 cause the appearance of similar pulses but of lower amplitude, if they are separated by a time interval commensurable with the resolving (dead) time of the counter $\tau_1 = t_d$. In this case, if this interval is less than the quantity t_d, such as occurs for a particle entering at the instant t_5, the particle will not be recorded. This is due to the fact that discharge ($k > 1$) takes place only when the voltage across the counter is not less than the voltage corresponding to the start of the gas amplification region (voltage of the start of counting U_a in Fig.3.V).

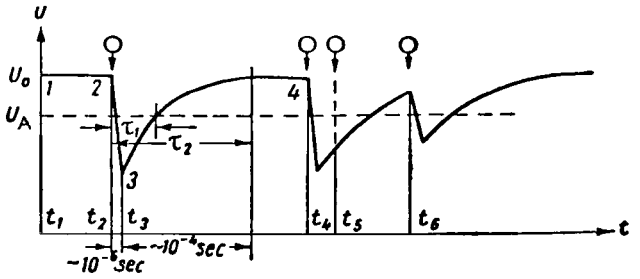

Fig.3.V Scheme of Pulse Shaping of the Counter.

The time of complete recovery of the filament potential is equal to τ_2. If the time interval between particles is not less than this value, the amplitude of the impulse caused by any particle will have the same (nominal) value.

The voltage pulse entering the measuring circuit is taken from the counter load R_ℓ (see Fig.2.V). The duration of its trailing edge is determined by the charging time of the stray capacitance C_s which includes the self-capacitance of the counter C_{co} and the wiring capacitance across the resistance R_ℓ. To reduce the pulse duration, it is desirable to have a low value of $R_\ell C_s$. On the other hand, to increase the amplitude of the voltage pulse the resistance R_ℓ /108 should be sufficiently large. In wiring diagrams, the resistance R_ℓ is usually taken so that the time resolution provided by the gas-discharge counters themselves does not decrease.

The dose rate of stopping X-radiation and gamma radiation, produced in the casing of the counter and in its components, is measured by counting the number n of pulses in the counter per unit time.

The relation between the number of pulses n and the dose rate of radiation P acting on the counter is found in the following manner:

If the flux density is denoted by F and the area of effective cross section of the counter by s, then

$$n = \varepsilon F s, \tag{4.V}$$

where ε is the effectiveness of the counter relative to the quanta being recorded.

The dose rate of the bremsstrahlung is

$$P = \mu F E, \tag{5.V}$$

where μ is the linear absorption coefficient of quanta in air under normal conditions, and E is the quantum energy of the monoenergetic flux.

It follows from eqs.(4.V) and (5.V) that the quantities n and P are related by

$$P = \frac{\mu E}{\varepsilon s} n. \tag{6.V}$$

It is obvious that under loads exceeding the permissible value, with respect to the resolving time t_d, counting errors will occur. If the actual number of statistically distributed particles striking the counter is n_1, then the number of particles recorded by it, as follows from the theory (Bibl.2), will be n_2, where

$$n_2 = \frac{n_1}{1 + n_1 t_M}. \tag{7.V}$$

The error of measurement, in this case, will be

$$\Delta n = \frac{n_1 - n_2}{n_1} 100\%. \tag{8.V}$$

The counting errors of equipment using counters, occurring under large loads, for example in the radiation belts, can be taken into account by a previously recorded load characteristic. For this, the counter connected into the measuring circuit is subjected to an ever increasing load (usually by irradiation from a uniformly approaching isotope).

The load characteristic is obtained in the form of a curve of the dependence of the recorded number of particles n on the number of particles actually irradiating the counter n_a. This curve is characterized by the presence of a saturation section which begins at values of n_a equal to 10^{-4} - 10^{-5} counts/sec for the halogen counters used on board space vehicles (Bibl.44). /109

Self-quenched halogen counters with a steel casing of the STS-5 type have a working (effective) diameter of 10 ± 0.1 mm and a length of 100 ± 1 mm. To provide mechanical strength, the thin counter casing (thickness, about 65 μ or 50 mg/cm^2) is equipped with stiffeners. Calculation shows that the energy necessary for passage of particles through the casing is about 0.5 Mev for electrons

and about 5 Mev for protons.

The counter is filled with neon, with a small addition of argon and 5% bromine. The rated operating voltage is 400 v and the start-of-counting voltage, 300 v. The capacitance of the counter is about 10 μμf. The resolving time of the counter t_d is of the order of 10^{-4} sec (optimal load of about 10^4 counts/sec). The service life is 10^9 counts (Bibl.44, 64).

Gas-discharge counters of smaller dimensions [working length 50 mm, diameter 10 mm (Bibl.13)] were used in the instrumentation of the interplanetary probes Mars-1 and Luna-4.

Counters of the Anton-302 type are also made of stainless steel, but are larger [filament length 101.6 mm, inside diameter 19.8 mm (Bibl.65)]. The wall thickness varies from 0.5 to 1.25 mm (Bibl.77). With a shielding layer of magnesium (265 mg/cm^2) and steel (400 mg/cm^2), as was used in the instrumentation of Explorer-XII (Bibl.46), the counters directly recorded electrons with an energy of at least 1.6 Mev and protons with an energy of at least 20 Mev. Bremsstrahlung was recorded with a low efficiency.

The efficiency of the Anton-302 counters installed on Explorer-XII, according to investigations by O'Brian, Van Allen, Laughlin, and Frank (Bibl.46) is characterized by the curve shown in Fig.4.V. The graph gives the variation in the ratio of the counting rate N counts/second to the flux density from all directions of monoenergetic electrons F cm^{-2} · sec^{-1} as a function of the electron energy E_e. The curve in Fig.4.V shows that the efficiency of gas-discharge counters is practically 100% for particles penetrating into the casing. Accordingly, halogen counters are used mainly for counting the total number of particles. The counters also record (although at low efficiency) those particles which do not penetrate inside but produce X-radiation on deceleration within the walls.

Scintillation counters operate on the principle of recording light scintillations produced on interaction of the particles with a phosphor. The counter constitutes a system consisting of a crystal, light conductor, and photomultiplier (PM) receiving the radiation of the scintillations.

The scintillators in present use have a very short glow time (10^{-6} sec and less). The transit of the pulse in the multiplier is of the same order, so that the resolving power of scintillation counters is much higher than that of /110
gas-discharge counters. The practical counting rate is limited only by the resolving power of the electronic recording circuits.

An extremely important characteristic of scintillation counters is the proportionality between the pulse height and the energy liberation in the crystal. This forms the basis for the separation (selection) of particles by energy, in multichannel instruments where each channel is tuned to a certain operating threshold. A deviation from proportionality between the light yield and energy released by the particle in the scintillator has been observed only for particles with low energies.

Scintillation counters record fast ionizing particles (electrons, α-

particles, protons, etc.) and also electromagnetic radiation whose quantum energy in the scintillator, owing to the Compton effect and to photoeffects, is converted into energy of secondary electrons, producing ionization and excitation of atoms and molecules of the scintillator material. The spectral dis- /111
tribution intensity and the duration of scintillation of the excited atoms differ for different substances. Therefore, the scintillator substance should be selected with respect to its characteristics, for optimum solution of the problem in question.

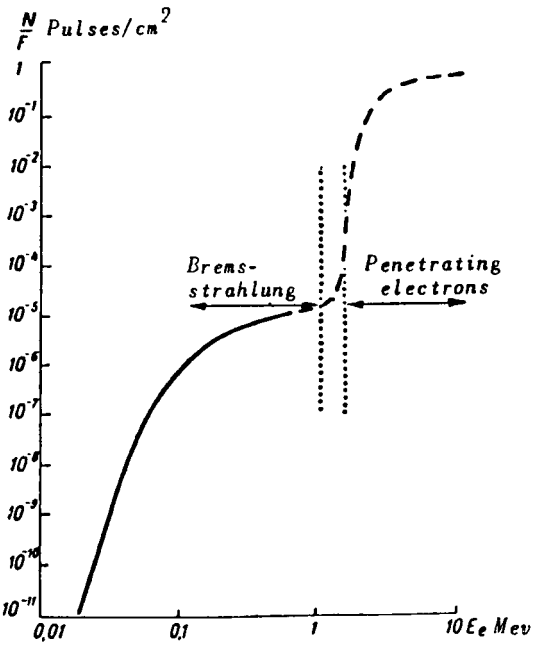

Fig.4.V Efficiency of Gas-Discharge Counter for Electrons.

A most important characteristic of scintillators is the light yield for conversion efficiency η, characterizing the conversion of energy absorbed in the scintillator ΔE into light energy

$$\eta = \frac{\bar{a}}{\Delta E} b, \qquad (9.V)$$

where $\bar{a}$ is the mean number of light quanta emitted per scintillation, and b is a coefficient allowing for the loss of light along the path to the photocathode of the photomultiplier.

Occasionally, the relative scintillation efficiency η_{rel} is used, which is determined by comparison with the scintillation efficiency of a standard,

$$\eta_{rel} = \frac{\eta}{\eta_{st}} 100\%.$$

The shape of the scintillation pulse is characterized by a rapid rise of the leading edge and a comparatively slow exponential drop. Therefore, a time

constant (attenuation constant) τ, defined as the time during which the maximum pulse peak decreases e times (or by 63%), is used for the characteristic of the scintillation (pulse) duration. The luminous intensity I, observed after a lapse of time t from the start, is thus determined by an exponential relationship of the type

$$I = I_0 e^{-\frac{t}{\tau}}, \qquad (10.V)$$

where I_0 is the maximum luminous intensity.

The photomultiplier of the scintillation counter should be matched both with the scintillator and with the measuring circuit and should satisfy the specific demands of operation onboard space vehicles.

A highly important parameter characterizing the possibility of matching the PM with the scintillator is the spectral quantum efficiency of its photocathode. This parameter, however, varies greatly from specimen to specimen so that, in practice, the integral sensitivity of the PM related with the quantum efficiency by a linear dependence is generally used (Bibl.49).

The quantum efficiency of antimony-cesium (SbCs), oxygen-antimony-cesium (SbCsO) and the recently developed multi-alkali (SbNaKCs) photocathodes (Bibl.49) is shown in Fig.5.V. The integral sensitivity of the PM with these photocathodes is indicated on the curves. Figure 5.V indicates that the maximum quantum efficiency of antimony-cesium photocathodes does not exceed 10% on the average. For the best specimens, it reaches 25 - 30%. Therefore, a special selection of multipliers for scintillators is usually made. /112

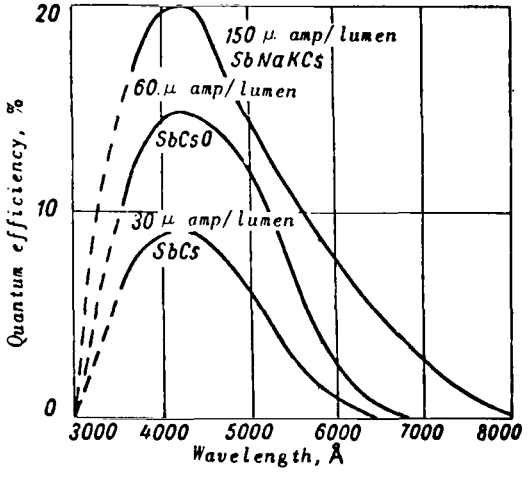

Fig.5.V Quantum Efficiency of the Photomultiplier Photocathodes.

Furthermore, for the PM used in scintillation counters, it is necessary to have linearity of the light characteristic within the limits of variation in the light flux of the scintillator. Deviations of the light characteristic of the PM from linear in the region of low light fluxes are due to the effect of

the dark current of the multiplier and, in the presence of large light fluxes, to "fatigue" of the emitters and to the appearance of a space charge in the region of the last cascades of the multiplying system, which cause defocusing of the electron beam. Therefore, the region of linearity of the light characteristic essentially depends on the magnitude and distribution of the feed voltage. For practical purposes, it is necessary to ensure linearity of the characteristic in the region of light fluxes from approximately 10^{-13} to 10^{-4} lumen (Bibl.70).

The noise level of the PM and the parameters of the scintillator determine the lower limit of energies and intensities of the radiation recorded by the counter. The signal-to-noise ratio at the output of the PM is determined not only by its design parameters but also by the operating temperature on which /113 depends the dark current, the passband of the measuring circuit, and the effect of radiations on the dynodes and the casing of the PM.

The amplitude of the output pulse (Fig.6.V), formed at the scintillation counter, is determined by the counter parameters and by the elements of the wiring circuit - the load resistance R_ℓ and the stray circuit capacitance C_s.

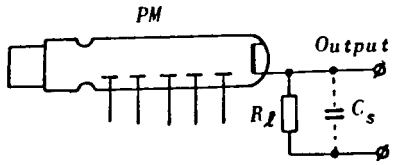

Fig.6.V Wiring Diagram of the Scintillation Counter.

An analysis (Bibl.49) shows that the maximum value of the signal at the output of the scintillation counter will occur at an optimum value of the load resistance determined from the formula $R_\ell C_s = \tau$, where τ is the attenuation constant of the scintillator. In this case, a time change in pulse height is described by the equation

$$U(t) = \frac{Q}{C_s}\frac{t}{\tau}e^{-\frac{t}{\tau}}, \qquad (11.V)$$

where Q is the anode charge occurring at the initial instant (t = 0) at which the luminescence of the scintillator strikes the PM.

The maximum pulse height is

$$U_{max} = \frac{1}{e}\frac{Q}{C_s} \approx \frac{M\bar{\eta}\beta N_0}{C_s}, \qquad (12.V)$$

where e is the electron charge, M is the amplification factor of the PM, $\bar{\eta}$ is the mean quantum efficiency of the photocathode of the PM, β is the photon collection coefficient at the photocathode, and N_0 is the number of photons emitted by the scintillator at the initial instant (t = 0).

As follows from the equations and from a qualitative analysis, the design of the scintillation counter and the supply regime of the PM should provide for maximum collection of photons and electrons, i.e., for a maximum charge Q at its anode. The shape of the pulses of the counter is determined primarily by the time constant τ of the scintillator. By changing the amplification factor of the PM and the parameters of the anode circuit, it is possible to vary both the amplitude and the duration of the edge of the output pulse of the counter, matching it to the measuring program and to the recording electronic circuit.

In equipment for measuring the intensity of cosmic rays and also the radiation doses on board space vehicles, sodium iodide crystals NaI, activated with thallium NaI (Tl), and cesium iodide with the same activator CsI (Tl) are used as scintillators.

The scintillator NaI (Tl) has a radiation spectrum in the region from 0.30 to 0.55 μ with a peak of about 0.45 μ, a time constant $\tau = 2.5 \times 10^{-7}$ sec, /114 and a conversion efficiency for electrons of about 8%. The output amplitude of scintillations is linear for electrons with an energy of 1 - 6 Mev, deuterons, and protons of all recordable energies. The crystal is able to record α-particles; however, in this case the relation between the scintillation amplitude and the energy of the particles is nonlinear up to a particle energy of 10 Mev. The density of the crystal is 3.67 gm/cm^3, and the melting point is 651°C. A shortcoming of this scintillator is its hygroscopicity, which causes it to become turbid in time and thus become useless. Therefore, NaI (Tl) is used for inside counters situated in the pressurized capsule of spacecraft, with a low moisture content of the filling gas (Bibl.51).

Moisture-resistant crystals CsI (Tl) having, however, a lower conversion efficiency [$\eta_{rel} = 0.3$ with respect to NaI (Tl) taken as the standard] are used as scintillators for outside counters. The duration of luminescence is $\tau \simeq \simeq 10^{-6}$ sec, and its spectrum is located within 0.4 - 0.7 μ at a maximum of about 0.6 μ (Bibl.49, 51).

Photomultipliers with flat-end photocathodes are used as converters. As a typical example, we are giving the main parameters of a PM-35 multiplier used in combination with the NaI (Tl) crystal. The diameter of the container is 34 ± 0.6 mm at a photocathode diameter of 30 ± 1 mm. The region of spectral sensitivity is from 0.3 to 0.6 μ, with a peak near 0.4 μ. The sensitivity of the photocathode (integral) is 20 μ amp/lumen. The photocathode and dynodes (eight U-shaped dynodes) have antimony-cesium emitting surfaces. The operating voltage is 700 - 1750 v. The integral sensitivity is 1 - 30 amp/lumen, at an amplification factor of 10^5 - 10^6, a dark current of 10^{-2} μ amp, and an output capacitance of 3 $\mu\mu$f (Bibl.23, 70).

An important condition for the high-quality and reliable operation of a scintillation counter is its efficient design. The basic design features of scintillation counters are the effective collection of the light of the scintillations at the photocathode of the PM, tightness for extraneous light, and sufficient resistance to linear and vibratory stresses.

Scintillation counters with a NaI (Tl) crystal and a PM-35 photomultiplier installed inside the capsule were enclosed in an aluminum casing with a wall

thickness of about 0.5 mm (Bibl.15). The crystal was clamped to the end of the PM by the casing cover over a rubber gasket. The free space was filled with mineral oil to ensure good optical contact. The inside surface of the cover was coated with magnesium oxide reflecting 98% of the light.

By recording all cases of energy liberation of more than 5 Mev in a crystal of about 40 mm thickness (Bibl.6 - 16, 59 - 62) it was possible to count practically all high-energy particles (an energy of 5 Mev is liberated if the /115 relativistic particle covers a path of at least 10 mm in the crystal.

The design of counters installed outside the capsules took into account the necessity of recording less energetic particles and quanta. The cesium iodide crystal (1). (Fig.7.V) was cemented or tightly ground into the end (3) of the box of the PM. The crystal was protected from extraneous light by a thin aluminum foil (2). Its diameter was 30 and height 2.2 mm (Bibl.60). The dimensions of the main elements of the counter are shown in the diagram.

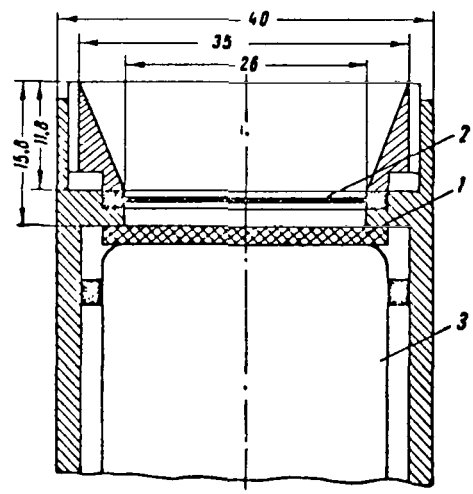

Fig.7.V Structural Elements of the Scintillation Counter.

In the equipment of the second satellite (Bibl.60), the crystal of the counter was protected, within the limits of a solid angle of 0.15 of 4π, by an aluminum coating of 2 mg/cm^2 thickness. The counter was able to record X-radiation at an efficiency close to unity, gamma-radiation at a low efficiency, electrons with an energy of more than 0.3 Mev, and protons with an energy of more than 1 Mev.

The design of the scintillation counters in the USA (Bibl.31, 77) is virtually the same as our own designs described above.

Wide use is made of the possibilities of measuring the spectrum of recorded particles by varying the type of scintillator, its thickness, and threshold amplitude recording levels.

To illustrate the point, Fig.8.V, based on data by Ludwig and McDonald

(Bibl.77), shows the curve of energy liberation by protons E_p in a CsI (Tl) crystal of 0.5 gm/cm^2 thickness (about 1 mm), absorbed (A) and transmitted (B). The diagram indicates the levels of recording amplitudes (1 - 8) in the equipment of the Explorer-XII satellite.

The silicon (n - p) counter comprises a small silicon plate on whose surface a (n - p) junction is formed; for this reason, they are also known as surface-barrier counters. The space-charge region of the (n - p) junction is the sensitive layer of the counter. On switching the counter in a barrier direction (Fig.9.V), when the plus terminal of the source is applied to the n-silicon, /116 the sensitive layer of the junction broadens. Its thickness for our own model, 5 × 5 mm in cross section, is about 60 μ at an operating voltage of 40 v (Bibl.37). The silicon counters developed in the USA have similar parameters (Bibl.55).

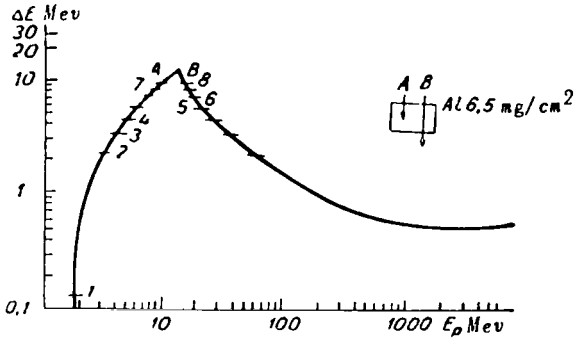

Fig.8.V Energy Liberation of Protons in a Cesium Iodide Crystal of 1 mm Thickness, and Amplitude Recording Levels of Particles with Different Energy Liberation.

The passage of the current carriers, produced by the ionizing particle, through the energy barrier is equivalent to the current pulse through the (n - p) junction with a voltage amplitude at the output of

$$\Delta U = \frac{eN}{C_s}, \qquad (13.V)$$

where N is the number of electron-hole pairs formed by the particle, C_s is the stray capacitance of the wiring and of the (n - p) junction at which the charges released by the particle are collected.

This voltage pulse ΔU is recorded by the counting circuit. The time during which the charge at the capacitor C_s is collected is about 10^{-9} sec for the /117 counters used [the capacitance of the counter C_{co} = 400 μμf • cm^{-2} at a voltage of U = 30 v (Bibl.65)]. This time determines the duration of the leading edge of the pulse. The duration of the trailing edge depends on the time of diffusion of the minority carriers t_o from the point of their formation to the (n - p) junction as well as on the time constant of $R_\ell C_s$ of the circuit.

The quantity t_o determines the time of accumulation of the charges at the

capacitor of the (n - p) junction. This is related with the thickness of the sensitive layer d and the diffusion coefficient of the carriers D by the equation

$$t_0 = \frac{d^2}{2D}. \qquad (14.V)$$

It is obvious that the accumulation time t_0 should be appreciably less than the lifetime of the carriers.

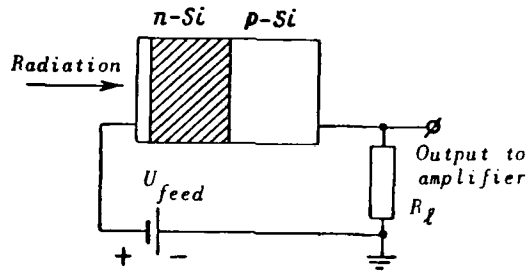

Fig.9.V Wiring Diagram of (n - p) Counter.

The quantity d, in turn, depends upon the resistivity of the P region ρ and on the reverse bias U (Bibl.55).

If the path of the particle in the counter does not extend beyond the limits of the sensitive layer d, the pulse amplitude will be proportional with a high accuracy to the energy of the particle since it is proportional to ionization in the space-charge region of the counter.

Silicon detectors with the above-indicated thickness of the sensitive layer (d = 60 μ) have linearity when recording α-particles with an energy up to 10 Mev and protons up to 2.5 Mev (Bibl.37).

Investigations (Bibl.55) have shown that, for each ionizing event, a proton loses on the average 3.5 ev in silicon [an electron, about 1 ev (Bibl.80)], whereas approximately one order of magnitude more energy is required per ionizing event of a gas. Therefore, silicon counters are much more sensitive (effective) detectors than gas-discharge counters.

Semiconductor detectors for investigating cosmic radiation, developed for example by Phillius and McIlwein (Bibl.77), are characterized by an energy liberation ΔE which varies with any variation in the proton energy E, as shown in Fig.10a.V. The diagram indicates the recording thresholds for protons with respect to the channels I, II, and III.

Of interest is the use of silicon (n - p) detectors in the instrumentation of the Telstar satellite [July 10, 1962 (Bibl.80)]. Here, in addition to the recording of protons of various energies (above 50 Mev, in the region of 26 - 34 Mev and 2.4 - 25 Mev) the silicon detectors were used to record the spectral distribution of electrons (in the range from 200 Kev to 1 Mev by four channels). To limit the angle of the field of view, the counters were placed

in massive casings with receiving apertures. The selection of particles by energy was accomplished with the use of metal and magnetic filters, by connecting the discriminators into the measuring circuit, and by selecting the feed voltage of the detectors. The electron efficiency of the silicon detector for 1 - 4 channels is illustrated in Fig.10b.V. The diagram demonstrates that, /118 even at an electron energy greatly exceeding the energy corresponding to the recording maximum in a given channel, the detector will remain sufficiently sensitive.

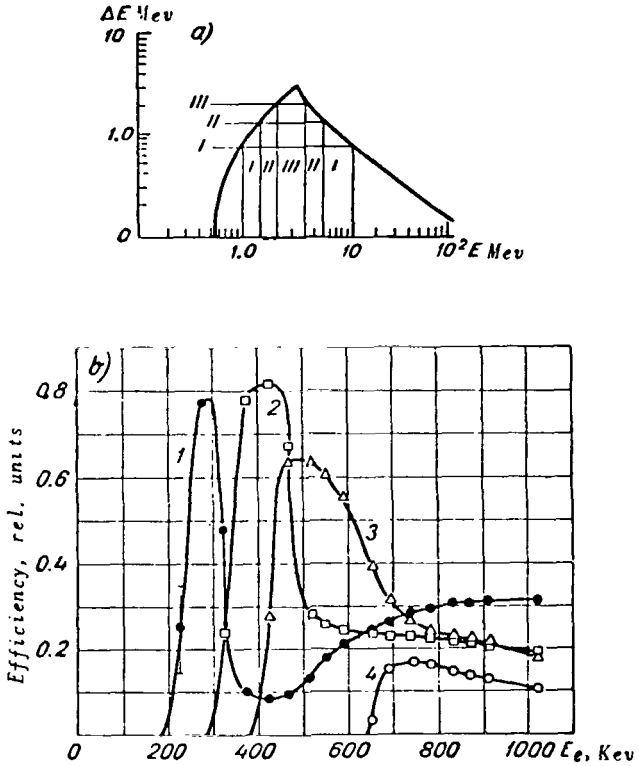

Fig.10.V Proton (a) and Electron (b) Efficiency of the (n - p) Counter.

Investigations as to the effect of high-energy protons on surface-barrier silicon detectors (Bibl.5) showed that their properties are retained at doses up to 10^{11} - 10^{12} protons $\cdot$ cm^{-2}, which ensures reliable operation for about 10^6 sec in the zone of maximum intensity of the inner radiation belt.

The onboard instrumentation of the American spacecraft employed semiconductor particle detectors made of cadmium sulfide CdS, which changes its conductivity under the effect of irradiation in proportion to the release of /119 energy in the volume of the substance (Bibl.57, 77). The onboard equipment of the Explorer XII used cadmium sulfide detectors, for example, to record electrons with an energy with more than 0.5 - 4 Mev and protons with an energy of at least 20 - 40 Mev [in combination with various shields (Bibl.46)].

Cerenkov counters will be briefly examined in conclusion.

One of the most important features of Cerenkov radiation is its directivity along the movement of the particle. The theory of the phenomenon (Bibl.22, 68) shows that radiation is concentrated in a cone (Fig.11.V), half of whose aperture angle θ is determined by the ratio of the speed of light in a given medium c_1 to the speed of the particle in the same medium v:

$$\theta = \cos^{-1}\frac{c_1}{u} = \cos^{-1}\frac{1}{n\beta}, \qquad (15.V)$$

where c_0 is the velocity of light in vacuum, $\beta = \frac{v}{c_0}$ is a dimensionless parameter, and n is the refractive index of the medium.

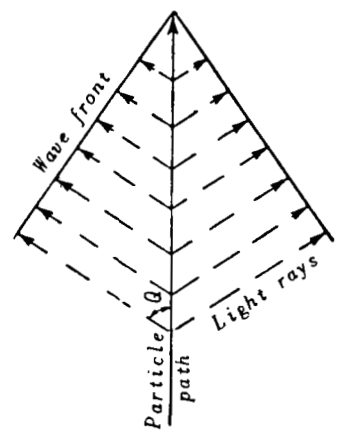

Fig.11.V Schematic of Propagation of Cerenkov Radiation.

From eq.(15.V), the following conclusions on the properties of Cerenkov counters can be derived:

1. For each substance (counter) there is a critical particle speed v_{min} below which the radiation cone contracts into a line ($\theta = 0$). In that case, radiation is absent and $v_{min} = \beta_{min} c_0 = \frac{1}{n} c_0 = c_1$.

2. For each substance there also exists a maximum aperture angle of Cerenkov radiation θ_{max}, corresponding to ultrarelativistic particles $v \simeq c_0$, i.e., $\theta_{max} \simeq \cos^{-1}\frac{1}{n}$.

3. The occurence of Cerenkov radiation in a substance takes place when the condition $n\beta \geq 1$ or $n > 1$ is satisfied, since $\beta \leq 1$ always. This means that short-wave rays for which $n < 1$, for example X-rays, cannot form part of the

composition of Cerenkov radiation. The spectral region of radiation is not limited at the long-wave end.

Only detectors whose Cerenkov radiation maximum lies in the visible region sensed by the PM have found practical use in the equipment under consideration. From the theory of the phenomenon (Bibl.22), we derive the following expres- /120 sion for the intensity of Cerenkov radiation expressed in terms of the number of photons N in the wavelength range from λ_1 to λ_2,

$$N = \frac{4\pi^2}{hc_0^2}(ze)^2\left(\frac{1}{\lambda_2} - \frac{1}{\lambda_1}\right)\left(1 - \frac{1}{n^2\beta^2}\right)L, \qquad (16.V)$$

where h is Planck's constant, z is the atomic number of the element, e is the elementary charge, and L is the length of path of the particle in the substance.

Consequently, by measuring the intensity of Cerenkov radiation in the visible spectrum region, it is possible to determine the atomic number of the element z if the path of the particles in the substance of the detector is constant, L = const. This forms the basis for the use of Cerenkov counters in analyzing the composition of cosmic rays. The pulse amplitude of the counter, which comprises a system of detectors and a photomultiplier, according to eq.(16.V) is proportional to the square of the particle charge $(ze)^2$.

The duration of the flash of Cerenkov radiation is determined by the transit time of the particle through the detector, i.e., by the thickness of the detector. This can easily be reduced to 10^{-11} - 10^{-13} sec; however, the comparatively short resolving time of modern PM (10^{-7} - 10^{-9} sec) does not permit complete realization of the possibility of a rapid count of particles by means of such counters. As a result the dead time t_d of the conventional Cerenkov counters is at least 10^{-9} sec (Bibl.22).

The Cerenkov counter is connected into the measuring circuit in the same manner as a scintillation counter. Plexiglas (polymethylmethacrylate resin) which has a number of valuable properties [large refractive index, low light attenuation, absence of fluorescence, stability of physical and chemical properties, and ease of handling (Bibl.25)], is used as the detector in Cerenkov counters for spacecraft.

The refractive index of Plexiglas in the visible region is n = 1.50, which determines the normal speed of the recorded particles $v_{min} = \frac{1}{1.5} c_0 = 0.7\, c_0 =$ 200,000 km/sec.

We note that all liquids and solids have values of n for the visible region from 1.3 to 1.8, which determines the minimum speed v_{min} of particles recorded with respect to Cerenkov radiation (from 0.56 c_0 to 0.77 c_0). The threshold energies of particles having a different mass can be determined over the known value of v_{min}. When using a Plexiglas detector, these energies will be $E_e \simeq$ $\simeq$ 0.2 Mev for electrons, $E_p \approx$ 300 Mev for protons, $E_\alpha \simeq$ 1 Mev for α-particles, and $E_{\pi\mu} \approx$ 30 - 40 Mev for π-mesons and μ-mesons.

A Cerenkov counter with a Plexiglas detector can also be used for recording γ-quanta and neutrons with energy of 400 - 900 Mev (in this case secondary electrons are the radiation excitation agents). The efficiency of recording neutrons is comparatively high, being 1 - 2% (Bibl.22). /121

The maximum aperture of the radiation cone in Plexiglas for singly charged particles is $\theta_{max} = 52^{\circ}$. The character of the dependence $\theta = f(E)$ is such that, at low energies of the particles E close to the recording threshold with respect to Cerenkov radiation, the value of the angle θ varies rapidly while, at large energies, it varies slowly. Thus, for electrons with an energy $E_e = 10$ Mev the angle will be $\theta = 52^{\circ}$, for $E_e = 1$ Mev, $\theta \sim 45^{\circ}$, and for $E_e \approx 0.2$ Mev, $\theta = 0$.

The light yield $\frac{dN}{dL}$, as follows from eq.(16.V) depends on the angle θ, being proportional to the quantity $(1 - \cos^2\theta)$. For example, for electrons with an energy of $E_e = 1$ Mev in the sensitivity range of the antimony-cesium photocathode (0.3 - 0.6 μ) the light yield is about 250 photons per centimeter of path.

Any singly charged particle z = 1 (electron, meson, proton) produces in Plexiglas a maximum number of quanta $N_{max} = 270$ cm^{-1} (Bibl.25). The transmission coefficient of Plexiglas in the visible region is about 90%. Consequently, a singly charged particle on a path equal to 26 mm [usual thickness of a detector (Bibl.25, 43)] causes the appearance of a light flash consisting of approximately 700 photons. Taking the efficiency of the photocathode $\eta = 5\%$ into consideration, approximately 35 electrons will be emitted from the photocathode in this case which, at an amplification factor of the photomultiplier $M = 10^5$ and at an output capacitance $C_s = 10$ μμf, will produce a voltage pulse with an amplitude equal to $\Delta U = \frac{10^5 \times 35 \times 1.6 \times 10^{-19}}{10^{-11}} = 50$ mv. In practice, the amplitude at the counter output is somewhat less, since there is a certain loss of light quanta and electrons. Therefore, it is necessary to ensure optimum light gathering power of the detector in designing the PM and a selection of feed conditions that permits measuring the lowest possible luminous fluxes.

In design, the Cerenkov counter is a Plexiglas detector cemented to the end of the box of the PM and placed in a light-tight metal casing.

It should be noted that a Cerenkov detector of Plexiglas cannot be made very large, because of the fact that, as soon as the path of the nuclei exceeds 40 mm, the heavy nuclei are split into light nuclei which can be recorded, thus distorting the result (Bibl.22).

When installing Cerenkov counters on space vehicles, the effect of stopping X-radiation and particles directly on the PM leads to an increase in background. This phenomenon was specifically noted during operation of the equipment in the radiation belts on board the first space rocket and was later used to determine the total count of particles in the channel with minimum threshold (Bibl.42). /122

Section 4. Basic Components of the Electronic Circuits

Wiring diagram. The basic purpose of the circuit is to supply power to the counters. In this case, the width of the spectrum of the recorded pulses should coincide with the passband of the subsequent electronic circuit.

It is common practice to consider that the passband of the circuit $\Delta\nu_{opt}$ (or its time constant τ_{opt}) and the width of the signal spectrum $\Delta\nu_s$ are related by the expression

$$\Delta\nu_{OPT} = \frac{1}{\tau_{OPT}} \approx 1.37\,\Delta\nu\,. \qquad (17.V)$$

The output voltage taken from the load resistance of the counter R_ℓ, as indicated by the above-discussed wiring diagrams, is equal to

$$U_{out} = R_\ell C_s \frac{dU}{dt}, \qquad (18.V)$$

where $\frac{dU}{dt}$ is the time rate of change in voltage at a total capacitance of the circuit C_s.

The product of $R_\ell C_s$, which is the time constant of the circuit, is usually made sufficiently small to ensure the required passband.

Frequently, this is so small that the condition of discrimination of pulses with durations τ recorded from the counter ($R_\ell C_s < \tau$) is satisfied, which permits standardization of the pulses in shape and duration, facilitating operation of the following scaler. Pulse discrimination by the circuit necessitates their subsequent amplification.

Pulse amplifiers. The most important requirements on pulse amplifiers are high operating stability and uniformity of amplification in a wide frequency band. In the equipment in question, the amplifier circuits are assembled of semiconductor elements, providing sufficiently high reliability, stability, compactness, and low power consumption.

Two variants of connecting the transistors are most widely used in amplifier circuits: with a common collector (emitter follower) and with a common emitter. A characteristic feature of the amplifier circuit with a common collector is a high input (10 - 100 kΩ) and low output (10 - 500 Ω) resistance. This permits using such amplifiers as matching or output devices. The passband of the emitter follower is determined mainly by the frequency properties of the transistor and is numerically equal to its cutoff frequency ($\Delta\nu \approx \nu_c$). Amplifiers with a common emitter are primarily used for amplifying voltage. The passband of such amplifiers is determined by the cutoff frequency of the transistor ν_c and by its amplification factor with respect to the current α /123

$$\Delta\nu \approx \nu_c(1-\alpha).$$

Unified amplifiers, designed under consideration of the specific operating

characteristics (large overloads, broad temperature range of the medium, etc.) have found wide use in equipment.

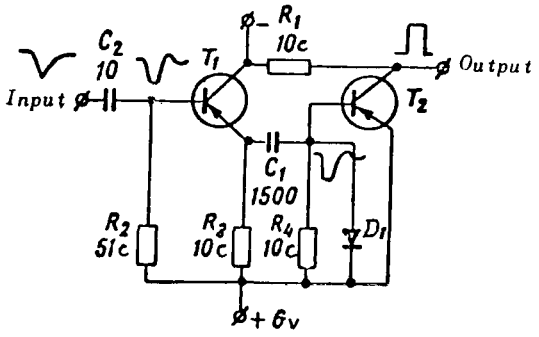

Fig.12.V Wiring Diagram of Amplifier-Shaper Cascade of a Gas-Discharge Counter.

Amplification and shaping of the pulses taken from the gas-discharge counters was accomplished by a two-stage amplifying-shaping cascade (Fig.12.V) designed to operate on negative input pulses with an amplitude from 2 to 50 v. To increase the input resistance, the first stage consists of a transistor T_1 connected in the circuit with the common collector. Amplification and shaping of the pulses (owing to saturation of the collector current) is accomplished by the second stage of the cascade, consisting of a transistor T_2. The catcher diode D (type D9Zh) is connected into this stage. The output pulses of the cascade have sufficiently steep leading edges, an amplitude of about 6 v, and a duration of the order 10 μsec (Bibl.15, 51).

One of the most widely used variants of the pulse amplifier of a scintillation counter is shown in Fig.13.V. The device comprises two amplification stages assembled in a circuit with a common collector consisting of the transistors T_1 and T_3, and two stages in the circuit with a common emitter consisting of the transistors T_2 and T_4. Stabilization of the operating conditions of /124 the transistors in this circuit is provided by direct-current feedback in each cascade. The circuit of the transistor base T_2 of the second amplifier stage is connected with the resistance R_4 which serves to decrease the fluctuation of the constant voltage component at the transistor base T_2 in the case of large pulse amplitudes at the input when the transistor T_4 changes to saturation condition. The resistance R_{11} limits the current of the transistor base T_4. As a result, the amplifier is insensitive to overloads created by switching it into the anode of the PM or the last dynodes. When using a P402 transistor, the total amplification of all four stages varies within the limits from 50 to 150 (depending on the magnitude of the resistance R_4) or positive input pulses occur with an amplitude of 5 - 50 mv and a duration of about 10 μsec (Bibl.15, 51).

Current discharger (CD). The discharger (Fig.14.V) converts the direct /125 current flowing in the circuit of the anode or dynode of the PM of the scintillation counter into a pulse train. The CD operates on the principle of a relaxation oscillator with a neon tube L_1. The number of pulses n tapped from the resistance R_2 in unit time is determined by the time average of the current i

of the capacitor charge C_1 in the interval between cutoff and ignition of the tube L_1:

$$i = \frac{q}{t} = \frac{C_1 (U_{ig} - U_c)}{t} n, \qquad (19.V)$$

where U_{ig} and U_c are the potentials of ignition and cutoff of the neon tube, and q is the charge received by the capacitor C_1 in the time t.

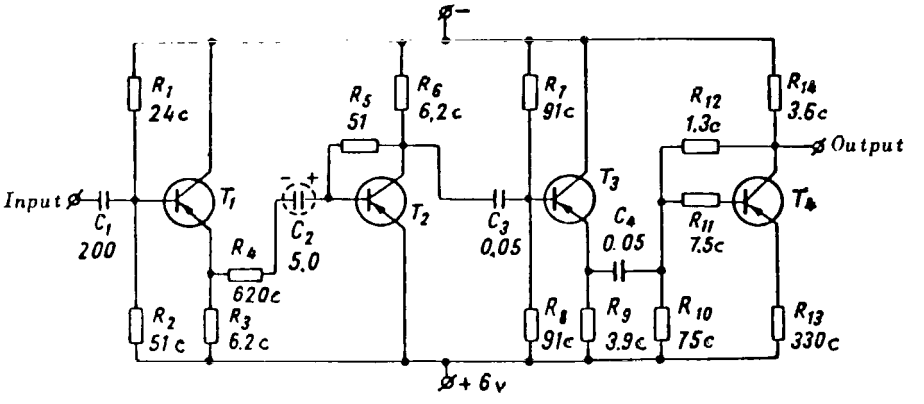

Fig.13.V Wiring Diagram of Pulse Amplifier of Scintillation Counter.

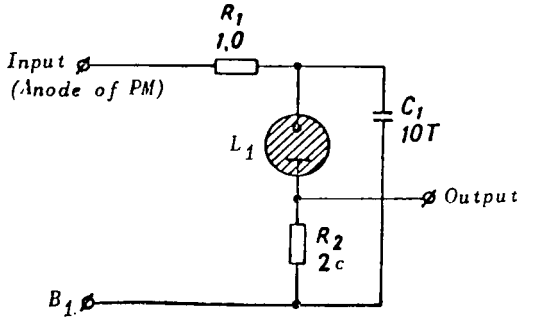

Fig.14.V Wiring Diagram of Current Discharger.

The resistor R_1 limits the current flowing through the capacitor C_1, to maintain linear dependence [eq.(19.V)].

The pulses of the CD used in the equipment for cosmic ray measurements (Bibl.15) had an amplitude up to 30 v and were delivered directly to the first flip-flop of the scaling circuit across the blocking capacitor.

Flip-flop Circuits. The flip-flops used in the scaling circuits should have high response and operational stability.

The response of a flip-flop is characterized by the cutoff trigger fre-

quency ν_c which is determined mainly by the frequency parameters of the transistors and their operating conditions. The response, of course, drops if open transistors operate under saturation conditions.

The stability of the flip-flop is characterized by its operational stability when the parameters deviate from normal, which usually occurs on any variation in the reverse current of the collector I_{co} and in the amplification factor of the transistors β with temperature. Circuits in which the open transistor operates exactly under saturation conditions evidently have the greatest stability. Therefore, flip-flops with a moderately large load (medium-frequency) operate as a rule under saturation conditions.

The input trigger pulses of positive polarity to the transistor bases of the flip-flop T_1 and T_2 (Fig.15.V) are fed across the blocking diodes D_1 and D_2 rather than across the blocking capacitors as usual. As a result, the feedback of transients of the flip-flop to the oscillator (preceding flip-flop) is eliminated, transition to a new stable state is facilitated (the capacitance, connected in parallel with the input, is small), and the possibility of spurious operation of the flip-flop under the effect of negative noise pulses is reduced.

The conditions of symmetry of the flip-flop, required for optimum reliability and throughput, are indicated in Fig.15.V.

/126

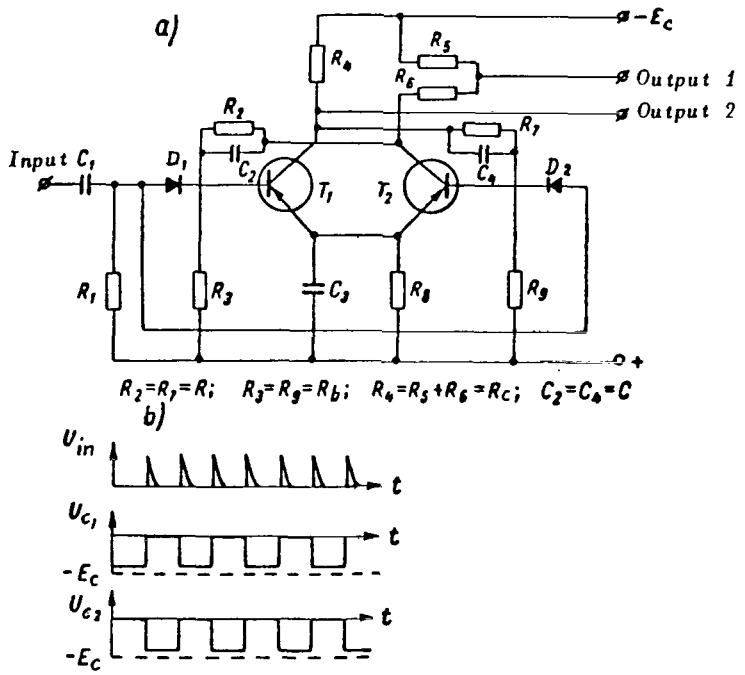

Fig.15.V Wiring Diagram of a Symmetric Flip-Flop (a) and Voltage Diagram at its Input and Outputs (b).

The condition of saturation of the open transistor (the base current exceeding the saturation threshold, i.e., $I_b \geq I_{b,s}$) and also the condition of

reliable blocking of the second transistor (the voltage across its base U_b being positive and greater than the critical cutoff voltage $U_{b.t}$) are ensured by proper selection of the resistances of the circuit (R, R_c, and R_b) and the feed voltage E_c.

The amplitude of the output pulse of the flip-flop U_{out} can be determined by the approximate formula, which is obvious from Fig.15.V

$$U_{out} \approx \frac{E_c R}{R_c + R}. \qquad (20.V)$$

Such an estimate disregards the voltage drop across the collector load, due to the flow of the collector current of the blocked transistor I_{co}.

The value of the triggering threshold of the flip-flop, whose wiring diagram is given in Fig.15.V, together with its stability according to investigations by G.S.Dragun et al. (Bibl.25), are plotted in Fig.16.V. The graph /127 shows that, on variation in the feed voltage from 14 to 6 v and in the temperature from 0° to 60°C the threshold changes by not more than 25%.

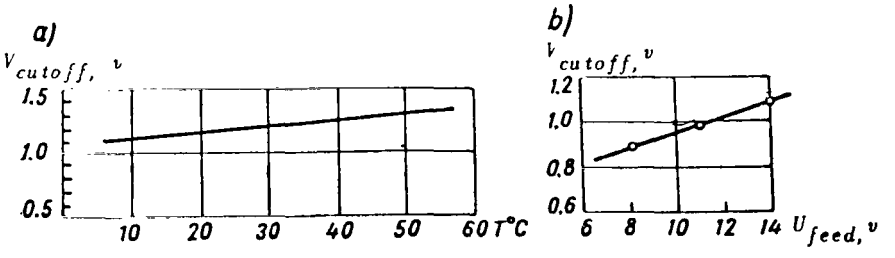

Fig.16.V Operating Threshold of the Flip-Flop as a Function of Temperature (a) and Feed Voltage (b).

The stability of the threshold is especially important when using flip-flops as discriminators in the channels of scintillation or Cerenkov counters. The cutoff frequency of flipping the flip-flop ν_c, composed of transistors with a threshold frequency of ν_t not exceeding 10 mc can be estimated (Bibl.63) from the inequality $\nu_c \leq 0.2\,\nu_t$.

To increase the response it is necessary to use high-frequency transistors and to provide for an unsaturated regime in which the time of dissipation of the minority carriers in the base of the open transistor decreases. For this purpose, additional shunting diodes are connected in the circuits of the high-frequency flip-flops installed in the channel of the scaling circuit, or other methods of limiting the collector current of the transistors are used.

The wiring diagram of a high-frequency flip-flop serving as pulse discriminator of the PM in onboard radiation measuring equipment in rockets and satellites (Bibl.51) is shown in Fig.17.V. The flip-flop is actuated by positive pulses that pass through the blocking diodes D_1 and D_2 only when their amplitude

exceeds the trigger voltage of the diodes. The latter can be regulated by means of a divider at the resistors R_1 and R_2. As a result, the pulses are selected with respect to the threshold of recording particles. The divider at the resistors R_3, R_4 and the diodes D_3 and D_4 serve to prevent the transistors from entering into the saturation regime of the collector current.

The cutoff trigger frequency ν_c of the high-frequency threshold flip-flop (HTF), composed of P406 transistors according to the above circuit, for periodic standard pulses (strays) is 3×10^5 cps for statistically distributed pulses. The stability of the threshold is not less than 10% on fluctuations in the ambient temperature from -30° to $+50^\circ$ C at variations in the feed voltage by ±20% (Bibl.15). The value of the operating threshold can be varied, by means of a divider (R_1, R_2), from 0.6 to 2.5 v at a duration of the trigger pulses of 2 - 10 μsec (Bibl.51). /128

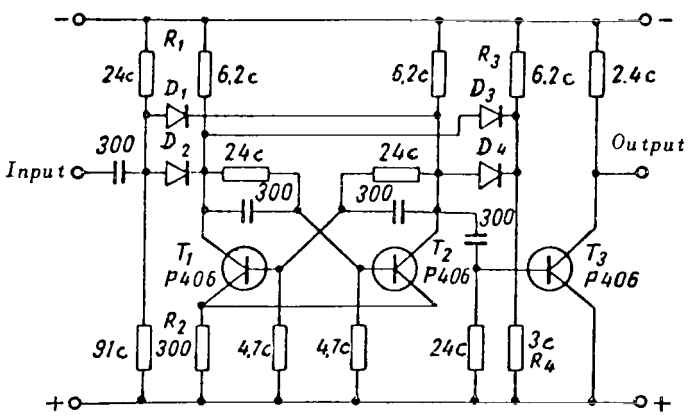

Fig.17.V Wiring Diagram of High-Frequency Flip-Flop with Amplifier.

The amplitude at the output of the flip-flop reaches 3 - 4 v, which permits their interconnection in the scaling circuits. The interrogated flip-flops, whose output pulses were fed across an adder directly to the telemetry system, were made up of P16B transistors and were equipped with a T_3 transistor output power amplifier (Fig.17.V). The circuit R_3, D_3, R_4, and D_4 was not set up at low loads of the flip-flop.

Monostable multivibrators (MMV), or driven multivibrators with emitter coupling, are used in the equipment under consideration for standardizing (normalizing) the counter pulses.

The circuit of the MMV (Fig.18.V), as a result of it being triggered by an external pulse U_n, produces one pulse $U_{out} = U_{c_2}$ whose amplitude and duration are always the same. Thus, the pulse train whose amplitude and duration are sufficient for triggering the monostable multivibrator is transformed into a sequence of standard pulses needed for feeding to an output device of the counting-rate meter type.

In the starting (stable) condition, the transistor T_1 is closed and T_2 is open. This is ensured by selecting the resistances constituting the circuit in Fig.18a.V, while the operating conditions of the open transistor are determined mainly by the magnitude of R_b.

The trigger pulse of negative polarity, on entering the base of the cut-off transistor T_1, opens it and thus causes the development of a cascading process of reversing the circuit, as a result of which the transistor T_2 is cut off. /129 On reversing the circuit at the collector of the transistor T_1, the potential rises steeply to a value of $E_c - I_cR_c$ and, at the collector of the transistor T_2, drops to E_c. Consequently, a positive pulse can be taken from the former and a negative pulse from the latter.

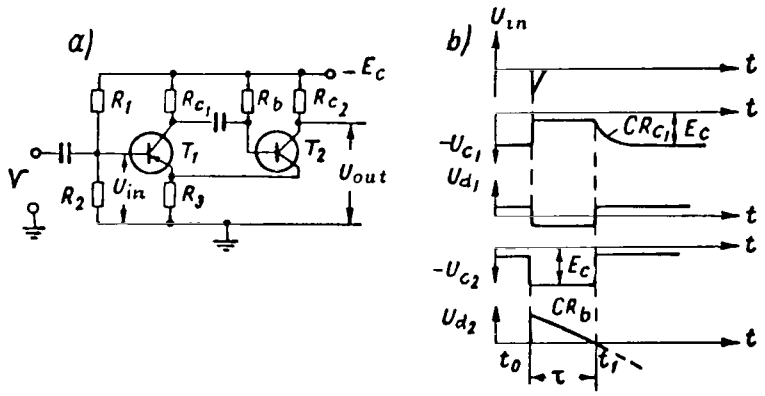

Fig.18.V Wiring Diagram of a Monostable Multivibrator (a) and Voltage Diagrams at its Characteristic Points (b).

The basic process determining the duration of the shaped pulse τ is the discharge of the timing capacitor C_1 across the resistor R_b, the internal resistance of the voltage source E_c, the resistor R_e, and the open transistor T_1. We can demonstrate (Bibl.63) that $\tau = 0.7\ R_bC_1$.

The amplitude of the output pulse U_{out} taken from the load of the transistor T_2 evidently (Fig.18.V) is equal to

$$U_{out} = E_c \frac{R_{c_2}}{R_e + R_{c_2}}. \qquad (21.V)$$

The duration of the leading edge of the output pulse t_e is determined by the threshold frequency of the transistors ν_t and is approximately equal to

$\frac{1}{\nu_t}$ (Bibl.52).

The monostable multivibrator assembled according to the above wiring diagram from P14 transistors (for example, in the equipment for measuring heavy nuclei) formed quasi-square pulses of a duration of $\tau \approx 20$ μsec with high stability (Bibl.25).

Output devices. In many space instruments either output adders or counting-rate meters (CRM) are used to increase the quantity of information transmitted /130 over a given channel of the telemetry system.

The adders are made up of resistors in such a manner that the output voltage taken from several (usually, three) flip-flops is summed, forming, at the output of the device, a single signal whose amplitude varies in steps from zero to maximum.

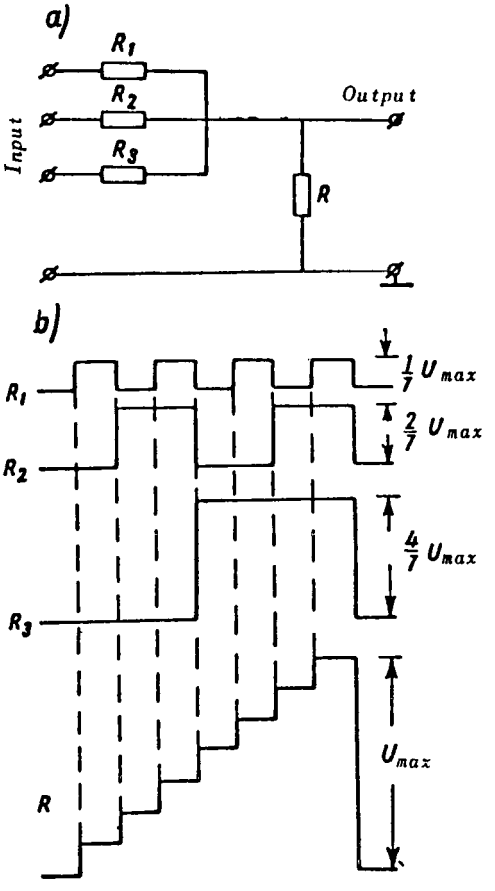

Fig.19.V Wiring Diagram of Adder (a) and Voltage Diagram Across its Resistors (b).

The simplest circuit of an adder operating on three flip-flops is shown in Fig.19a.V. The trigger pulses are fed to the resistors R_1, R_2, and R_3 and the output voltage is tapped from the resistor R. Thus, this circuit is a divider with a variable resistance R_k (where k is equal to 1, 2, or 3) whose voltage /131 at the output is

$$U_{out} = U \frac{R}{R_k + R}, \qquad (22.V)$$

where U is the amplitude of the pulses arriving from the flip-flops.

Equation (22.V) shows that the larger R_k, the smaller the voltage U_{out}. If the flip-flops, connected in series into the circuit, produce pulses with the same amplitudes U and the resistors are selected so that $R_1:R_2:R_3 = 4:2:1$, then with a uniform load of the counting circuit the time diagrams of the voltages across the resistors of the adder will have the shape shown in Fig.19b.V. In constructing the diagrams it was necessary to make allowance for the number of steps equal to seven, since $\sum_{k=1}^{3} R_k = 7$ relative units and the variation in the output voltage at one step is equal to $1/7\ U_{out\,max}$. Hence, it follows that the magnitude of the output voltage of the adder U_{out} can be used for determining the state of all three flip-flops connected with the adder since the amplitude of the output voltage drops practically to zero after each operation of the third flip-flop. The operation of the CRM (Fig.20.V) is based on an accumulation by the capacitor C_r of the charges produced by each pulse arriving at the input. During the intervals between pulses, the capacitor C_r is discharged to the load resistor R_l from which the constant output voltage U_{out} entering the telemetry system is taken.

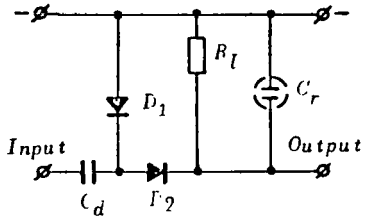

Fig.20.V Scheme of the Third Flip-Flop.

Under stable conditions when the rate of the pulses of similar duration N pulses/sec arriving at the CRM is constant, the discharge q produced by the dosing capacitor C_d and transmitted by it to the reservoir capacitor C_r will be equal to

$$q = C_d(U_{in} - U_r)Nt, \qquad (23.V)$$

where U_{in} is the voltage amplitude of the input pulses, U_r is the voltage across the reservoir capacitor C_r, t is the operating time of the circuit. The magnitude of the charge lost by the capacitor C_r as a result of the discharge current through the resistor R_l is

$$q_{dis} = \frac{U_r}{R_l} t. \qquad (24.V)$$

It follows from eqs.(28.V) and (29.V) that the output voltage, equal to the voltage across the capacitor C_r, will be

/132

$$U_{out} = U_r = \frac{C_d R_l N U_{in}}{1 + C_d R_l N}. \qquad (25.V)$$

It is evident from eq.(25.V) that, provided $C_d R_l N \ll 1$, the characteristic

curve of the counting-rate meter, will have a linear segment within whose limits the correlation

$$U_{out} \approx C_d R_\ell N U_{in} \qquad (26.V)$$

exists, if $N \leq N_{max}$, where N_{max} is the maximum counting rate on the linear segment of the characteristic curve.

The output voltage of the CRM, as indicated by eq.(25.V), does not depend on the magnitude of the reservoir capacitor C_r. The latter is selected on the basis of the permissible error of measuring the counting rate of statistically distributed pulses. As shown by analysis (Bibl.4), the relative probable error obtained upon measuring the mean pulse rate $\bar{N}$ with respect to the output voltage of the integrating circuit is

$$\varepsilon = \frac{0.67}{\sqrt{2\bar{N}R_\ell C_r}}. \qquad (27.V)$$

From the equality (27.V), expressing the quantity ε in percent, we find that the relative probable error of measurement will not exceed the prescribed quantity $\varepsilon\%$ if the inequality

$$C_r \geqslant \frac{2300}{\varepsilon^2 R_\ell N}. \qquad (28.V)$$

is satisfied.

For example, to ensure linearity up to N_{max} = 500 pulses/sec with an error of measurement of not more than 10%, we must have a time constant of the discharge of the integrating circuit of $R_\ell C_r \geq 5 \times 10^{-2}$ sec. To ensure measurements by the CRM of the average rate of statistically distributed pulses with a standard deviation of σ = 3% ($\varepsilon \approx 0.67\,\sigma$) we must have $\bar{N}R_\ell C_r$ = 500 while with an error of σ = 1% we already need $\bar{N}R_\ell C_r$ = 5000.

Since the magnitude of the output voltage of the CRM depends not only on the average rate of the input pulses $\bar{N}$ but also on their amplitude U_{in}, a normalizing device, usually a monostable multivibrator, is installed in front of the CRM (Bibl.25).

Section 5. Equipment for Recording Cosmic Rays

The principles of grouping the elements of counters in equipment for measuring the intensity of cosmic rays are illustrated by the circuits of one /133 of the variants (Bibl.15) shown in Figs.21a.V and 21b.V.

These principles are retained in the layout of other instruments used both in the USSR and in the USA; however, the number of channels and their parameters are modified (Bibl.27, 45).

The equipment under consideration consists of one gas-discharge counter of the STS-5 type and one scintillation counter, with their electronic circuits.

The circuits of the counters are made up of the discussed standard components: amplifier (A), medium-frequency flip-flops (T), high-frequency flip-flops (HT) tuned with respect to threshold (HTT) or equipped with output amplifiers (HTA), and also of output adders (OA) operating from the flip-flops with amplifier (TA).

The STS-5 counter is connected into a circuit with a grounded casing (Fig.21a.V). The supply battery, together with the resistor R_1 limiting the current, is enclosed in a metal box and sealed with a composition of equal parts of wax and rosin. The resistor R_1 serves to protect the batteries against damage during a corona discharge appearing at a pressure of the order of 1 mm Hg (Bibl.15).

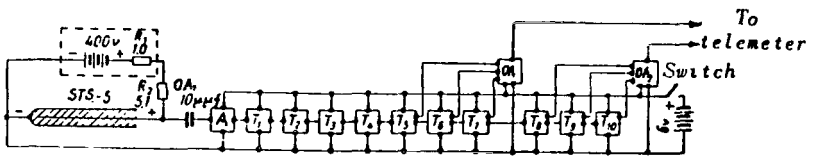

Fig.21a.V Block Diagram of One Variant of a Device with a Gas-Discharge Counter.

In the scintillation counter (Fig.21b.V) the pulses for counting particles of different energy liberation in the NaI (Tl) crystal were recorded from the 11^{th}, 9^{th}, and 8^{th} dynodes of the PM-1S (thresholds I, II, and III, respectively). An energy liberation exceeding 50 Kev corresponded to the threshold I, 500 Kev to the threshold II, and 5 Mev to the threshold III.

The total energy liberation (ionization) was determined by the average current of the anode and of the 7^{th} dynode. This was done in order to determine the energy emission during extensive radiation of the crystal when the anode current of the PM is saturated, by comparing the readings of these channels. Current dischargers, whose sensitivity limit with respect to the average discharge current of the capacitor was 10^{-10} amp, were used in the ionization channels (Bibl.15). The circuit of the current discharger, coupled with the 7^{th} dynode, contained an additional neon tube L_2 which protected the dynode against appreciable variations in potential owing to leakage (of opposite polarity in comparison with the ionization current). The tube L_2 was fed with a voltage such that it was fired upon a potential drop of the dynode by 30 - 40 v, /135 which stopped a further drop in potential.

The presence of several channels of the scintillation counter permits obtaining diverse parameters of cosmic rays at small weight and energy consumption of the equipment [the energy consumption of one flip-flop is about 4 mw (Bibl.15)].

Calibration of the instruments is done under laboratory conditions to determine the basic characteristics of the measuring channels.

The basic characteristic of the total ionization channels is the energy release in the crystal η, corresponding to one pulse of the current discharger.

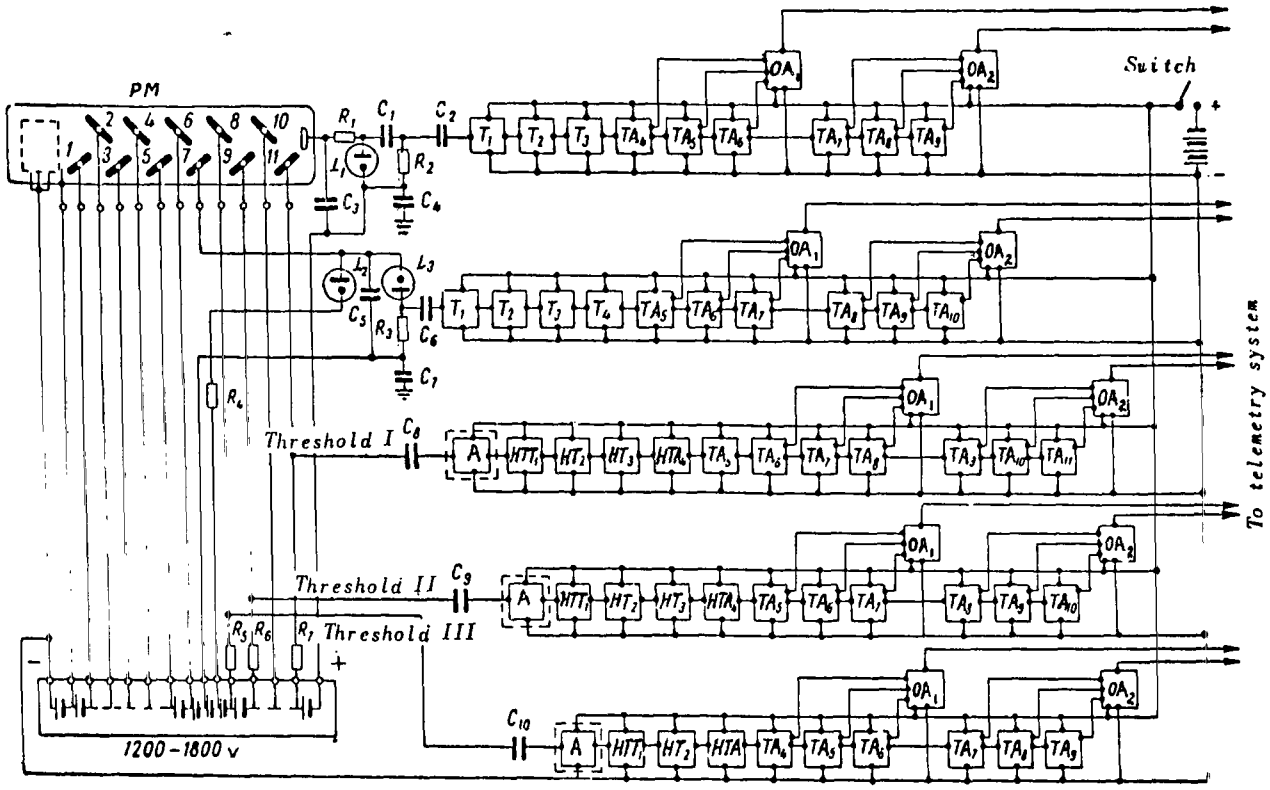

Fig.21b.V Block Diagram of One Variant of an Instrument with a Scintillation Counter.

For calibration of the channel, the scintillation counter is irradiated with gamma-rays emitted by radioactive isotopes Co^{60} or Hg^{203} (Bibl.15, 51). The count of the recorded pulses is done simultaneously with respect to the total energy release channel n and with respect to the threshold channel recording the number of quanta with a given energy N. If we designate the energy release of one quantum by $\bar{\eta}$, for the total energy release in the crystal ΔE, we obtain the expression

$$\Delta E = N\bar{\eta}. \tag{29.V}$$

On the other hand, if η is the energy released in a crystal during one operation of the current discharger, the energy release during the time of measurement will be

$$\Delta E = n\eta. \tag{30.V}$$

From equalities (29.V) and (30.V) it follows that the unknown quantity is equal to

$$\eta = \frac{N}{n}\bar{\eta}. \tag{31.V}$$

We note that the quantity $\bar{\eta}$ is the average energy release of one quantum of γ-radiation of the isotope used, which is determined from the energy spectrum of the pulse amplitudes at the output of the photomultiplier.

The average energy release in the NaI (Tl) crystal for equipment of the discussed type, upon irradiation with the gamma-quanta of Co^{60} is equal to 530 Kev (Bibl.51). The quantity $\bar{\eta} = 4 \times 10^{10}$ ev/pulse. This means that one pulse in the channel of total energy release corresponds to the transmission of approximately $\frac{4 \times 10^{10}}{5.3 \times 10^{4}} \approx 8 \times 10^{5}$ pulses in the first threshold channel of the instrument.

For an external scintillation counter with a CsI (Tl) crystal, with analogous calibration of the first channel, a value of $\bar{\eta} \simeq 10^{10}$ ev was obtained /136 (Bibl.51), and the constancy of this coefficient was checked in a wide range of energy release (Bibl.15).

The minimum energy release in the crystal η_t, beginning with which the particle is recorded in a given channel (counting threshold), is determined upon calibration of the threshold channels. For this purpose, the counter is irradiated with gamma-quanta of the radioactive isotope Co^{60} or Cs^{137} [the former emits gamma-quanta with an energy of 1.1 and 1.3 Mev while the latter emits 661 Kev (Bibl.29)]. The counting threshold η_t is calculated on the basis of the linear dependence of the pulse amplitude of the counter U on the energy release in the crystal. First, the linearity of the amplifier A at the input of a given channel is checked by means of an oscillograph and a reference signal generator. Then, the magnitude of the pulse U_1 at the output of the amplifier A upon irradiation of the counter is measured by an oscillograph. From the proportionality of the energy release and pulse it follows that

$$\eta_t = \frac{U_t}{U}\eta, \qquad (32.V)$$

where $\overline{\eta}$ is the mean energy release of gamma-quanta emitted by a given isotope. We note that eq.(32.V) can be used also for establishing the necessary operating threshold of the flip-flop U_t if it is necessary to adjust the channel for operation with respect to a given magnitude of η_t (Bibl.51).

Calibration of the channels of the gas-discharge counters consists in determining the load characteristics by the method proposed earlier (see Sect.3). This permitted broadening the range of measurable intensities by about one order of magnitude. Thus, a true counting rate of up to 10^6 pulses/sec was reliably recorded by the scintillation counter and up to 10^5 pulses/sec by the gas-discharge counter (Bibl.15).

Section 6. Radiometry Equipment

Radiometry (dosimetry) equipment is designed to measure the intensity of ionizing radiations and to determine the absorbed doses of radiation on space objects. The instrumentation comprises the same type of basic elements as described above.

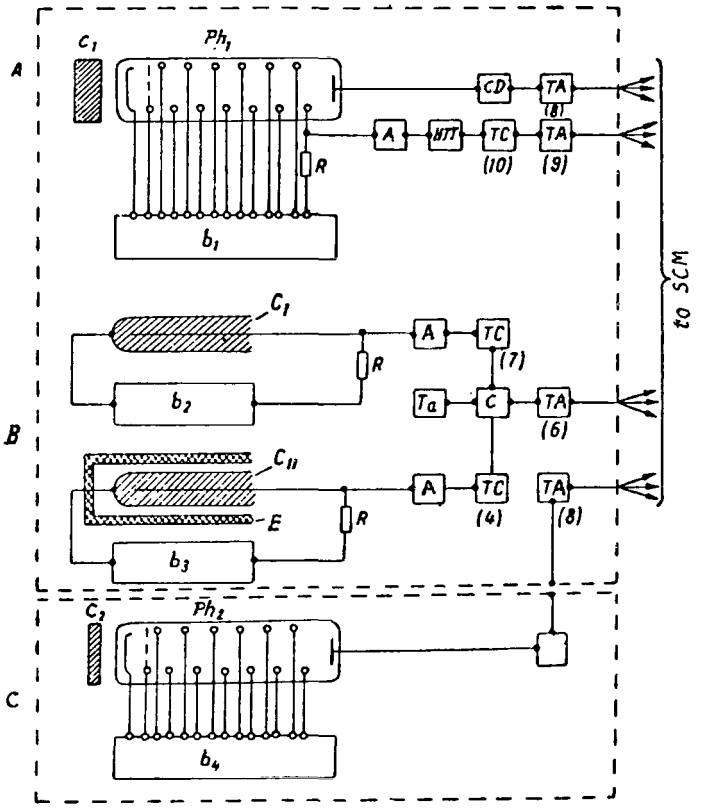

Fig.22.V Block Diagram of Radiometry Equipment.

As a typical example, let us examine the radiometry equipment (Fig.22.V) installed on the second Soviet satellite [August 1960 (Bibl.51, 59)]. This equipment included:

one internal scintillation counter with a sodium iodide crystal (diam. 30 × 14 mm) and a PM-16 photomultiplier;
two gas-discharge counters STS-5, one of which was shielded with brass and steel, each 1 mm thick;
one external scintillation counter with a cesium iodide crystal (diam. /137
30 × 2.2 mm) and a PM-15.

The inside counters with their measuring circuits (as shown in the block diagram of Fig.22.V) were designed as an integral instrument. The internal scintillation counter had two channels: 1) a channel for measuring the total energy release by means of a current discharger CD, 2) a threshold channel with a threshold η_t = 25 - 30 Kev [the threshold operating voltage of the HTT was U_t = 0.75 v and the amplification factor of the three-stage amplifier A was 100 (Bibl.51)].

The outside-counter, designed as an individual instrument, had only one channel of total energy release. This counter was mounted to the outside skin of the spacecraft to measure the energy flux of soft charged particles, for /138 example electrons of the radiation belts. Within the limits of a solid angle equal to 0.15 steradians, it had a protection of aluminum foil of 1 mg/cm^2 thickness; in other directions, the shielding of the counter varied from 1 to 150 gm/cm^2 (Bibl.51).

The designations of the building blocks (elements) in Fig.22.V correspond to those adopted earlier (see Sect.5).

A special feature of the equipment was that both gas-discharge counters had the scaling circuit in common. Their switching was accomplished alternately by the commutator C controlled by a multivibrator (timer) T_a (at a time interval of 16 min). The counter, surrounded by a shield, had a smaller number of preliminary flip-flops (four).

All output signals were stored by an onboard self-contained memory SCM with a 24-hour storage capacity.

The counters were supplied from storage batteries B_1 - B_4 (type GB-400) and a voltage of 1600 v was delivered to the PM. The radiometers were calibrated with respect to the same characteristics as in the method described earlier (see Sect.5).

Section 7. Equipment for Investigating the Nuclear Component of Cosmic Rays

As an example, let us examine the equipment designed for recording heavy nuclei in the flux of cosmic rays and the total count of particles striking on the receiver. This equipment was installed on the second spacecraft launched to the moon on September 12, 1959 (Bibl.25).

The equipment, of which a block diagram is shown in Fig.23.V, consists of a Cerenkov counter with a cylindrical Plexiglas detector (26 × 26 mm) combined with a PM-25 and an electronic counting circuit with two threshold channels ($z \geq 5$ and $z \geq 15$).

To separate the output pulses by counting thresholds, a voltage divider on resistors R_1 and R_2 and threshold flip-flops of the scaling circuits are used. The scaling circuits contain six flip-flops TC in the first channel and two flip-flops in the second channel.

The state of the three flip-flops (of the third and sixth in the first channel and the second in the second channel) was transmitted to the radiotelemetry system (RTS) over an adder with a matching amplifier MA. The third channel (of the total count) contains the amplifier stages A, the monostable multivibrator MMV, and the CRM. The high-voltage power sources (900 v) consist of sealed dry cells.

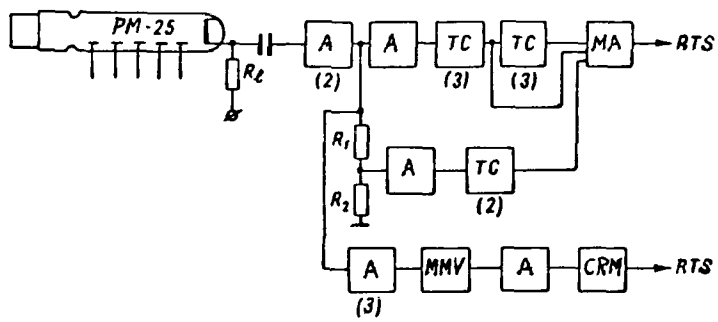

Fig.23.V Block Diagram of Equipment Variant for Recording Heavy Nuclei in Cosmic Rays.

The principal wiring diagram of this equipment (Bibl.25) is shown in Fig.24.V. Here, the output signal is taken from the plate load of the PM (110 kilohms) whereas in other instruments of this type, designed to measure /139 heavier nuclei, the outputs to the counting circuit are taken from the loads in the circuits of the intermediary dynodes. Between the last dynodes of the PM, capacitors (each of 10^{-9} f) are installed which prevent a drop in potential if the PM are heavily irradiated.

The amplifier stages, flip-flop loops, and output devices are assembled on the basis of the previously discussed standard circuits. The signal to the radiotelemetry system is delivered from the resistance-coupled adder (39, 75, and 130 kilohms) across the P101 transistor amplifier and the compensating source U_{comp} which ensures readout of positive voltage.

The total-count channel has five amplification stages since it is laid out to measure the weakest pulses produced under the effect of heavy particles on the detector and under the effect of various particles directly on the PM (on the cylinder, dynodes, etc.). The dependence of the output voltage of this channel U_{out} on the load ν cps at the input of the CRM for periodic pulses is shown in Fig.25.V. This diagram shows that the characteristic curve of the

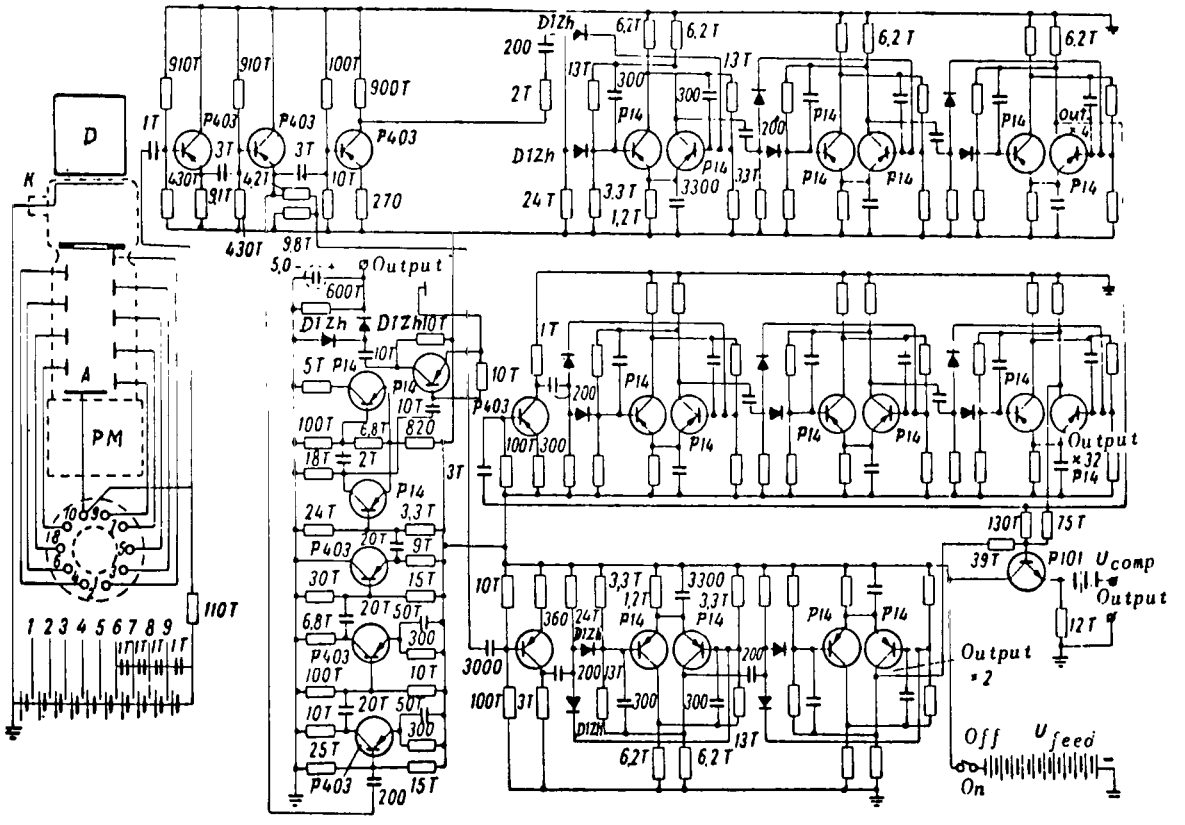

Fig.24.V Principal Wiring Diagram of Equipment for Recording Heavy Nuclei in a Cosmic Ray Flux.

channel at loads of more than 500 - 600 pulses/sec passes into the saturation region and then starts drooping [owing to the dead time of the monostable multivibrator (Bibl.25)].

The linearity of the Cerenkov counter is tested by checking the linearity of the PM in the working range of the output signal amplitudes. For this, light flashes of a spark source are used whose duration [about 10^{-9} sec (Bibl.25)] is close to the flash duration of Cerenkov radiation in the detector ($\sim 10^{-10}$ sec) and less than the transit time of the electrons of the dynode system of the PM-25 ($\sim 5 \times 10^{-8}$ sec).

By measuring the intensity of the flashes with an iris diaphragm and measuring the amplitude U of the pulses at the output of the PM with a vacuum-tube voltmeter, a dependence of the type of U = f(s) is obtained where s is the /141 area of the iris of the diaphragm. The linear segment of this dependence is the operating segment.

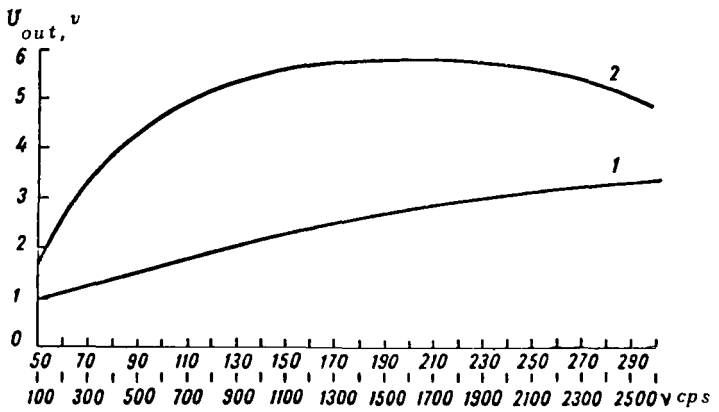

Fig.25.V Characteristic Curves of the CRM of the Total-Count Channel for Loads up to 300 pulses/sec (1) and up to 2600 pulses/sec (2).

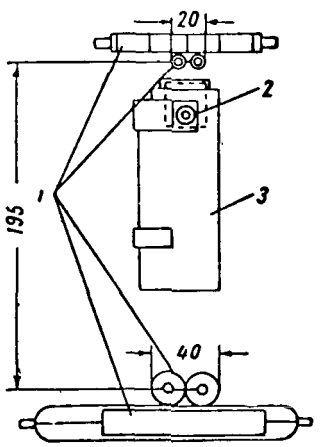

Fig.26.V Schematic of Device for Checking and Tuning Equipment with Cerenkov Counter.

A check of the operating stability of the equipment and its tuning and calibration is carried out by making use of the μ-mesons of cosmic rays reaching the earth's surface.

The amplitude distribution of the pulses from such muons is periodically checked to determine the stability of the equipment. A Cerenkov counter with a detector placed in a light-proof housing (3) is arranged between gas-discharge counters (1) (Fig.26.V) forming a cosmic-ray telescope. This permits separating a definite solid angle of the field of view of the counter ω. The quantity ω is selected such that the effective area of the detector is cut out, i.e., the path of the particles is approximately equal to the height of the detector (26 mm). The pulses of all four groups of the counters of the telescope are set to the coincidence circuit with a resolving time of $\tau \approx 10^{-6}$ sec. Upon operation of this circuit, the pulse at the output of the PM is measured. Thus, only μ-mesons passing through the solid angle ω are selected. The pulses of the PM are /142 measured by photographing the screen of the oscillograph. From the obtained results, a curve is plotted of the pulse amplitude distribution of the μ-mesons, from which the average pulse from a μ-meson at the output of the PM of this instrument is determined.

Investigations (Bibl.7) show that the stability of the instruments is characterized by a variation in the average pulse not exceeding 10 - 20% over a period of several months. Such a stability of the amplification factor of a PM is considered sufficient to estimate the fluxes of various groups of nuclei.

Calibration of each channel of the instrument is done in the following manner: Short pulses are delivered from a generator across the RC matching circuit to the input of the channel which is disconnected from the PM. The pulse amplitude for a channel tuned to count singly charged particles is made equal to the average amplitude of the pulse from the μ-meson $\bar{U}_\mu$. The threshold channels tuned to count particles with different z, as indicated by eq.(16.V), should operate only at an amplitude at its input exceeding $\bar{U}_\mu$ by z^2 times. For example, to tune and calibrate a channel of $z \geq 5$, an amplitude equal to 25 $\bar{U}_\mu$ is supplied and for a channel of $z \geq 15$, a threshold amplitude at the input equal to 225 $\bar{U}_\mu$.

The threshold of the total-count channel (indicator of intensity) in this instrument is tuned to operate from a pulse corresponding to 1/3 $\bar{U}_\mu$.

To check the performance of the instrument before launching, a neon tube (2), shown in Fig.26.V, is mounted in the light-proof housing of the counter opposite the Plexiglas detector. When checking the performance of the instrument, the circuit of the relaxation oscillator, mounted in the console for independent checking, is connected to this tube. The readings from the adder output appear on the needle indicator of the console during flashing of the tube.

The total-count channel is checked by means of the isotope Co^{60} in the same manner as that used for the above-discussed instruments (see Sect.5 of this Chapter).

Section 8. Equipment for Measuring Corpuscular Fluxes

The intensity of particles of various energy in the corpuscular fluxes at various heights of the upper atmosphere was measured in the USA (Bibl.31, 77) mainly by means of scintillation counters, with a thin (of the order of 0.1 gm/cm^2) CsI (Tl) crystal. To reduce the irradiation of the PM, a layer of aluminum (foil) of a thickness of (3 - 4) 10^{-2} mg/cm^2 was vacuum-deposited on the outer surface of the crystal. In this case, the sensitivity to irradiation from the sun is decreased approximately by a factor of 10^4, but particles /143 with a very small mean free path are not recorded. On the other hand, energetic particles of cosmic rays as well as X-rays and γ-radiation are not recorded by the thin crystal. For example, of the two scintillation counters used by L.G. Meredith et al. (Bibl.31), one recorded electrons with an energy in the range from 3 to 100 Kev at a sensitivity from 10^{-2} to 10^3 erg·cm^{-2}·sec^{-1}, protons with an energy from 30 Kev to 1.5 Mev, and heavier ions at a sensitivity from 10^3 to 10^5 cm^{-2}·sec^{-1} steradian^{-1}. The recorded particles are separated by their deflection in magnetic or electric fields and by varying the layout of the counters.

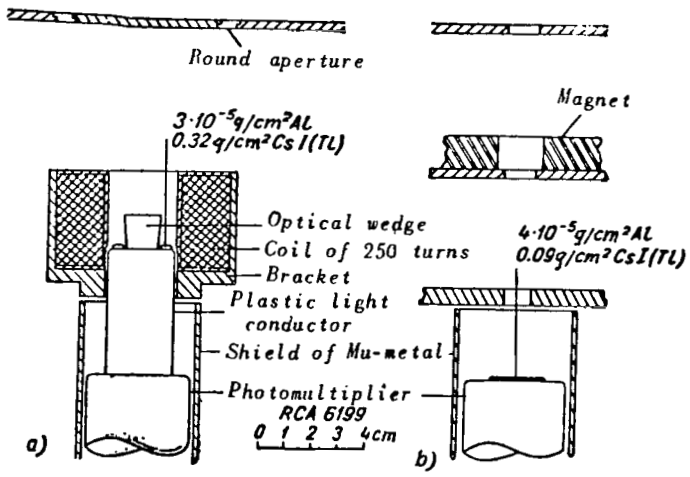

Fig.27.V Scintillation Counters for Recording Electrons (a) and Protons (b) in Corpuscular Fluxes.

The counters used by McIlwein (Bibl.31), for investigating corpuscular fluxes that are responsible for polar auroras, are of interest.

The input of the electron receiver (Fig.27a.V) is provided with a diaphragm having a round aperture and a focusing coil, whose current is varied in steps from 0 to 15 amp. Thanks to this, electrons with an energy from 3 to 100 Kev were collected on the thin annular scintillator CsI (Tl). The lower limit is determined by the thickness of the aluminum foil and the upper limit by the maximum focusing current. Protons with an energy of $E_p > 45$ Kev, for all practical purposes, are not deflected by the magnetic field of the coil and are not recorded. The change in current of the PM is judged from the energy spectrum of the recorded electrons. The geometry factor of the receiver was equal

to 8.5×10^{-2} cm^2 • ster.

In the proton receiver (Fig.27b.V), the scintillator was made in the form of a disk of CsI (Tl) attached directly to the cylinder of the PM. The angle of view of the counter is determined by a diaphragm and by the inside hole of an annular magnet whose field (400 gauss at the hole center) prevents electrons with an energy below 1 Mev from striking the indicator. The geometry factor of this receiver was 3.5×10^{-3} cm^2 • ster. /144

Receivers similar to scintillation counters are most widely used in Soviet equipment, but the scintillators themselves consist of thin layers of zinc sulfide activated with silver ZnS (Ag) or strontium phosphate activated with europium $Sr_3(PO_4)_2(Eu)$. A fluorescent substance (5) (Fig.28.V) several mg/cm^2 in thickness is deposited on a glass plate (6) installed in front of the PM (Bibl.19).

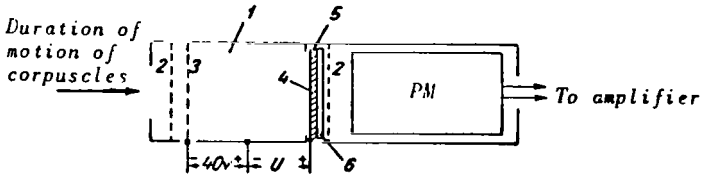

Fig.28.V Diagram of the Electron Indicator.

In the simplest instrument (electron indicator) the fluorescent screen is installed inside an aluminum tube (1) with a certain angle of view, limited by the entrance diaphragm. In this case, it must be remembered that particles of sufficiently high energies can pass through the body of the tube and that, furthermore, bremsstrahlung can be recorded. This creates a background which must be taken into account.

The ZnS (Ag) scintillator exhibits fluorescence in the visible region (λ_{max} = 0.45 - 0.52 μ). The light yield for electrons relative to NaI (Tl) reaches 3 - 3.5 sec and a radiation time of 10^{-3} - 10^{-5} sec (Bibl.49). The scintillator also is sensitive to X-radiation, the light yield in this case reaching 20% (Bibl.67).

Investigations (Bibl.36) show that the radiation of the scintillator is directly proportional to the flux of energy of the irradiating particles if their energy is not very high (for electrons E_e < 100 Kev).

To investigate the distribution of particles by energies, light-proof foils of various thickness are used.

The absorption of electrons in the substance depends on the atomic number z, on the energy of the electrons, and on the geometry of the beam. In addition to absorption, there occurs deflection of an individual electron in the field of force of the atomic nucleus which leads to a random distortion (bend) of its trajectory. As a result, the beam undergoes scattering in various directions, including backward. This causes additional attenuation of the flux which /145

is especially noticeable upon an increase in the thickness of the foil (more than 1 - 2 μ for aluminum). As a result mainly of the second effect, the flux of electrons having, for example, an energy of 25 Kev is attenuated by about 10% in aluminum foil of 0.6 μ thickness (0.18 mg/cm^2) and by about 99.9% in foil of 8 μ thickness (2.38 mg/cm^2) (Bibl.29). The length of the mean free path of electrons of various energy E_e in aluminum foil (Bibl.28) is given below:

Energy E_e, Kev	10	20	30	40	50	100	500	1000	2000	5000
Mean free path, mg/cm^2	0.16	0.68	1.5	2.6	4.0	13.5	165	420	950	2540

In the equipment of the Cosmos-3 and Cosmos-5 satellites aluminum foil of 0.4, 0.6, and 1.1 mg/cm^2 was used (Bibl.19) and on the third satellite, 0.4 and 0.8 mg/cm^2 (Bibl.34). The indicators reacted to electrons whose mean free path exceeded the indicated values.

An important improvement of the electron indicators installed on the satellites of the Cosmos series (Bibl.19) was the use of an accelerating step potential U applied to the aluminum foil relative to the center point of the tube (1) (Fig.28.V). This voltage was slowly varied from 0 to 11 kv (the duration of the steps was about 4 sec) on the Cosmos-5 satellite and from 0 to 4.3 kv on the Cosmos-3, with three intermediate steps (0.15, 3.0, 5.5 and 0.1, 1.6, 2.3 kv, respectively).

The accelerating chamber was shielded from the surrounding space by means of grids (2) connected with the tube. The receiving screen was protected from thermal electrons of the external plasma by a constant negative potential (-40 v) applied to the input grid (3) relative to the center point of the casing (1). The magnitude of this potential was selected with consideration of the possible potential of the container relative to the plasma and the contact potential difference between the grid (3) and the casing.

The use of an accelerating potential permits an appreciable decrease of the threshold energy of recordable particles: at a voltage U = 11 kv, the energy threshold is equal to 40 ev, i.e., is determined by the potential applied to the input grid (3). On the other hand, electrons with an energy of 40 - 50 Kev are not modulated at all by this accelerating potential, which permits estimating the contribution of these particles. On analyzing the energy spectrum of /146 electrons in a corpuscular flux, both in the modulated region of particle energies (from 40 ev to 40 - 50 Kev) and outside it, the readings of indicators with foil of different thicknesses were used (Bibl.19).

The measuring circuit of the electron indicators contains an amplifier with outputs of low and high sensitivity. Thanks to this, the range of measurable flux intensities exceeded three orders of magnitude. The threshold flux recordable by the circuit for electrons with an energy of E_e = 40 ev was equal to 2 × × 10^8 electrons·cm^{-2}·sec^{-1}×ster^{-1}, while for E_e = 7 Kev it was 2 × 10^6 electron·cm^{-2}·sec^{-1} × ster^{-1} (in an isotropic flux). For electrons with an energy of more than 20 Kev the sensitivity did not depend on the energy of the particles (Bibl.19, 33).

During flight, the equipment was calibrated by means of an electron beam emitted by a tritium target which was periodically traced at the input of the indicator (at an accelerating potential of 11 kv). The results obtained indicate the operational stability of equipment of this type.

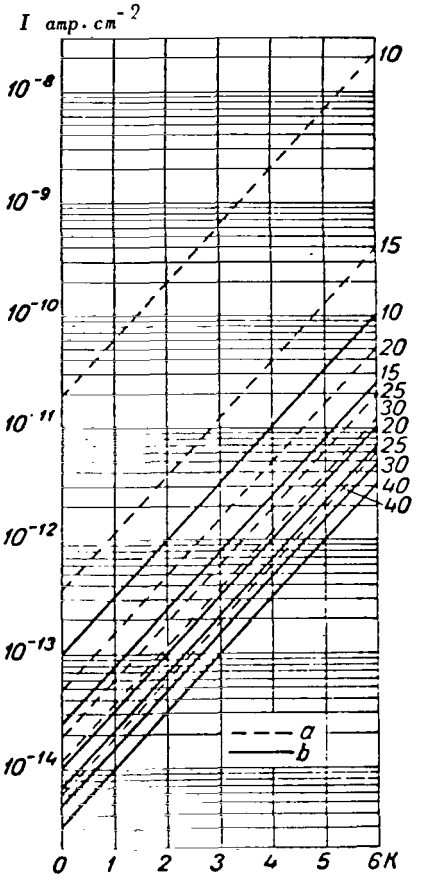

Fig.29.V Calibration Curves of Electron Indicators with Foil of Different Thicknesses.

Investigations (Bibl.36) have shown that electrons with an energy of about $E_e \geq 1$ Mev act on the screen and dynodes of the PM both directly by penetrating through the tube and by the bremsstrahlung caused by them. For particles of smaller energies, the angle of view of the indicators is determined by the entrance diaphragm and is equal to 1/12 steradian.

The electron indicators were calibrated in a flux of monoenergetic electrons.

Figure 29.V shows, for example, the calibration curve of the equipment installed on the third satellite (Bibl.34). Divisions of the radiometric scale K proportional to the logarithm of the photocurrent of the indicator are plotted

on the x-axis and the current density of the electrons I in a logarithmic scale for foil of 0.8 mg/cm^2 (a) and 0.4 mg/cm^2 (b) thick are plotted on the y-axis. The numerals entered next to the curves indicate energy (Kev) in the axial flux of electrons. /147

Since the configuration of the energy spectrum of the recorded electrons is not known, we determined - in analyzing the results of the measurements - the equivalent energy E_{eq} of a monoenergetic flux of electrons corresponding to the observed relationship of the photocurrents of the indicators. The equivalent current I_{eq} and the energy flux E_{eq} were determined from the value of E_{eq}, on the basis of the calibration curve. These quantities, as indicated by V.I. Krasovskiy et al. (Bibl.34), constitute the lower limits of the actual values.

When analyzing the results obtained by means of indicators with a variable accelerating field, the depth of modulation of the photocurrent, which permits estimating the energy of the recorded particles, was taken into account (Bibl.19).

Section 9. Principles of Preliminary Data Processing

The telemetry recordings of the results contain the readings of the adders or CRM installed in various channels of the equipment. In interpreting the recording of the adders, one proceeds from the fact that the transition from the first step of the recording to the second takes place at initial operation of the first flip-flop; from the third step to the fourth at initial operation of the second flip-flop; from the seventh step to the zero level at operation of the third flip-flop connected with a given adder (see Sect.4).

If the time of recording a complete cycle of the adder is short, it is obviously possible to use the complete operating cycles of the adder to determine the instantaneous intensity during a given averaging interval.

Let the number of flip-flops up to the adder be equal to k; then, at the instant of completion of the recording a complete cycle t_2, $n = 2^{k+3}$ pulses will pass through the circuit, while from the instant of start of the cycle t_1 (during the time $\Delta t = t_2 - t_1$) $\Delta n = 2^{k+3} - 2^k$ pulses will pass through.

If the required averaging interval should be smaller than the time of recording a complete cycle of the adder, processing of the data must be done with respect to incomplete cycles. We see from Fig.19.V that, for example, at the moment of operation of the first flip-flop of the adder t_{k+1} the number of pulses passing through the scaling circuit will be $n_1 = 2^{k+1}$, whereas at the onset of operation of the second flip-flop t_{k+2} the number will be $n_2 = 2^{k+2}$. Consequently, the number of pulses, passing during such an averaging interval $\Delta t = t_{k+2} - t_{k+1}$, will be equal to $\Delta n = 2^{k+2} - 2^{k+1}$. The number of particles counted in a given channel of the instrument during unit time will be $\frac{\Delta n}{\Delta t}$.

Preliminary processing of the data with respect to all channels comprises:

1. With respect to the total-count (ionization) channels, the total /148

energy release of the particles in the crystal is calculated, being equal to

$$E = \frac{\Delta n}{\Delta t}\eta, \qquad (33.V)$$

where η is the energy release corresponding to one pulse of the current discharger.

2. With respect to the threshold channels, the number of particles released in the crystal and the energy exceeding the threshold energy, equal to $\frac{\Delta n}{\Delta t}$, are calculated.

3. With respect to the threshold channels and channels of the gas-discharge counters, the instantaneous intensities I of the recorded particles is determined

$$I = \frac{\Delta n}{\Delta t s_{eff}}, \qquad (34.V)$$

where Δt is a sufficiently small interval close to the time t to which the intensity I pertains, and s_{eff} is the effective area of the counter.

In processing the information of the dosimeter equipment (on the basis of the data of the channel of total energy release), we determined the absorbed radiation dose rate R. For this, we used the formula

$$R = \frac{E}{6.24 \cdot 10^{13} m}, \qquad (35.V)$$

where m is the mass of the crystal in grams and the numerical multiplier serves to convert the total energy release from electron-volts to hundreds of ergs (when expressing the dose R in rads).

Preliminary processing of the data obtained from the equipment with Cerenkov counters consists in determining the flux of nuclei N whose atomic number exceeds the threshold of a given channel. The magnitude of the flux is calculated by the formula

$$N = \frac{\Delta n}{G \Delta t}, \qquad (36.V)$$

where G is the geometry factor of the instrument.

Interpretation and processing of the recordings of the channels equipped with CRM, for example the total-count channel, are accomplished from the calibration curve of the CRM [$U_{out} = f(\nu$ cps)] recorded in the laboratory when calibrating a given channel of the instrument (see Fig.25.V).

The errors of measuring the parameters of cosmic rays on space vehicles are composed of errors introduced by the measuring instrument itself, errors of the telemetered information, errors of calibrating the instruments, and errors of processing. The statistical errors of counting pulses do not exceed 1 - 10%. The energy spectrum of the particles, however, can be determined with an appreci- /149

ably greater error.

CHAPTER VI

MEASUREMENT OF THE CONCENTRATION OF CHARGED PARTICLES

Section 1. Langmuir Probes and Ion Traps

The essence of the method of probe analysis consists of measuring the current of ionized gas particles on a conductor (collector) placed in the investigated medium. The collector is connected with the case of the carrier across a sufficiently large resistance, whose voltage drop is recorded by the measuring circuit. One of the most important conditions of using a probe is smallness of its surface with respect to the area of the hull of the carrier [approximately by three orders of magnitude (Bibl.1)].

The stream of particles on any body in the upper atmosphere, as indicated earlier (see Chapt.II, Sect.2) contains electron and ion components; depending upon the potential of the body relative to the plasma (or to the capsule), either one may predominate substantially. In this connection, the method of probe analysis is based on obtaining the dependence of the probe current on its potential, which is called the probe characteristic. An analysis of the probe characteristics permits determining the concentration of charged particles (electrons or ions) and a number of other parameters of the medium, in particular the electron temperature T_e [based on the slope of the characteristic curve (Bibl.2)]. Devices of this type are known as Langmuir probes and have been used rather widely. Thus, Smith used a steel cone attached to the nose of the rocket as a probe (Bibl.1). To lessen the electron photoemission current from the surface of the probe, which distorts the analytical results, Japanese researchers have used latticed spherical Langmuir probes with a diameter of 2 cm (Bibl.16).

More widely used are probes with a controlled potential applied to an additional grid, placed in the particle path to the collector. This permits a better selection of the recorded particles with respect to the sign of the charge and to energy. Inside the probe, an electric field is generated which /150 ensures total collection of the charged particles that have passed through the grid on the collector. In certain cases, one more grid is placed near the collector which is fed with a sufficiently large negative (relative to the collector) potential, preventing the emission of photoelectrons. Devices of this type are known as two- or three-electrode ion traps.

The basic problems solved by means of traps include: determination of particle concentration in the stationary plasma of the upper atmosphere and interplanetary medium, its variations in time and space under the effect of various factors, and measurement of the intensity of soft corpuscular fluxes.

Two-electrode traps for measuring the concentration of positive ions in the upper atmosphere were used with excellent results by K.I.Gringauz, V.V.Bezrukikh and V.D.Ozerov (Bibl.6) in the Soviet Union on the third artificial earth satellite. These traps operated from May 15 to June 3, 1958 in daytime at heights

up to 1000 km. During this time it was possible to obtain more than 10,000 measurements of the ion concentration localized in space and time (Bibl.4).

Three-electrode traps designed to measure the concentration of positive ions and electrons were installed on a number of space vehicles, including the unmanned interplanetary spacecraft launched in the USSR (Bibl.7).

This led to the discovery of the third, outermost belt of charged particles (see Fig.1, Chapt.V), permitted measurements of solar corpuscular fluxes outside the geomagnetic field for the first time, and yielded estimates on the possible concentration of interplanetary ionized gas (Bibl.2, 8). As derived from the measurements on the unmanned interplanetary Venus probe, the concentration of electrons in the corpuscular flux apparently is 20 cm^{-3} at a distance of about 1.9 million kilometers from earth (Bibl.7). The concentration of stationary gas in space at a distance of about 126,000 km was approximately 1.5 cm^{-3} [based on measurements by the capsule of the third space rocket which photographed the far side of the moon (Bibl.6)].

Similar equipment was installed on rockets and satellites in the USA and Japan (Bibl.10, 16). For example, a flat three-electrode ion trap, whose outer grid was attached at the level of the rocket skin, was used by R.Ye.Bourdo (Bibl.1). Subsequently, Bridge et al. (Bibl.11, 12) developed an improved multigrid trap known as plasma probe or trap with modulation (Bibl.7). This device contained an additional grid to which a variable voltage was applied, which increases the selectivity of the trap and its sensitivity.

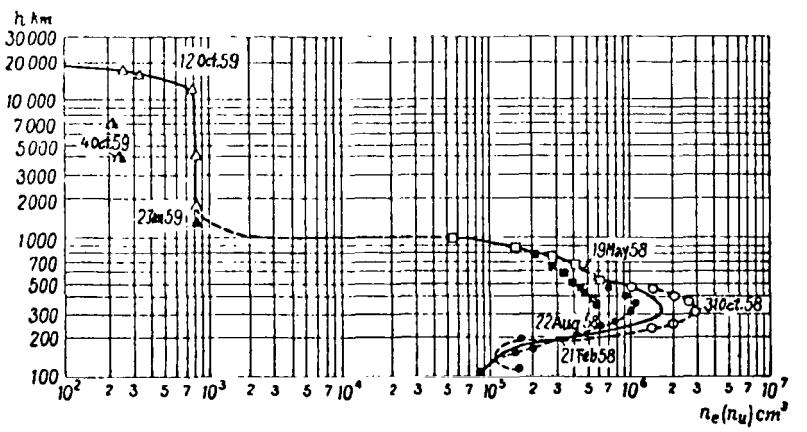

Fig.1.VI Vertical Distribution of Electron n_e (or Ion n_1) Concentration in the Atmosphere at Heights above 100 km, Based on Experimental Data.

Thus, the trend in the development of probes was to make them similar to the analyzers of mass spectrometers (see Chapt.IV). For measuring the concentration of individual gas components, simple two-stage one-cycle radio-frequency mass spectrometers, having a sensitivity up to 10 cm^{-3} at a power consumption /151 of 2 w and a weight of less than 2 kg, have been proposed (Bibl.15).

It must be remembered that there are other probe variants in existence which have not found wide use (Bibl.1).

The magnitudes of the concentrations subject to measurement at altitudes up to 20,000 km can be estimated from a summary graph of the vertical distribution of free electrons n_e or ions n_i in the gaseous envelope of the earth, on the side illuminated by the sun at a period close to maximum solar activity (Fig.1.VI). The launching dates of spacecraft and geophysical rockets, whose data were used by G.I.Gringauz in plotting the graph (Bibl.6) are also indicated in the diagram.

Section 2. Characteristics of the Analytical Method

The characteristics of the method of measuring by means of traps are ruled by the presence of perturbations in the ambient medium, both near the instrumented capsule and near the traps themselves which are co-moving with the plasma. Perturbations produced by the presence of bodies were discussed earlier (see Chapt.II). There it was shown that the motion of a body in the plasma sets up a potential determined by the balance of inflowing currents. In the upper atmosphere (ionosphere), under ordinary conditions, a spherical capsule should have a slight negative potential.

Furthermore, it was noted that the particle stream of different sign on /152 a charged body is expressed differently: If the signs of the particle and body charges coincide, the dependence of the current on the potential has an exponential character; otherwise the current depends linearly on the radius of the space charge region R_c. It can be shown in the latter case that the dependence of the current on the potential of the body φ is practically linear (Bibl.4). By following the concepts given elsewhere (Bibl.2, 4), this dependence for a spherical trap can be defined.

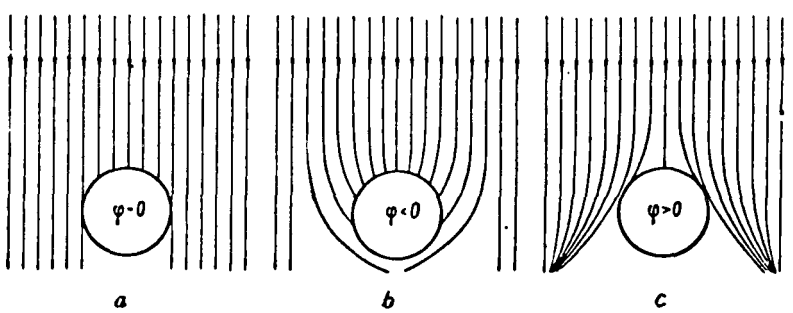

Fig.2.VI Schematic Drawing of the Flow of Ions Past a Trap whose Sheath Potential is Equal to (a), Less than (b), or Greater than (c) the Potential of the Ambient Plasma.

The current $I_{c,i}$ generated by positive ions in the collector circuit and equal to the ion current through the sheath of the trap, at complete collection inside the trap, can be written as follows, just like the conduction current in

a gas (Bibl.2):

$$I_{c,i} = \alpha e n_i v_0 s_{eff}, \qquad (1.VI)$$

where α is the transmission coefficient of the latticed case of the trap, e is the electron charge, n_i is the concentration of positive singly charged ions; v_0 is the velocity of the trap; $s_{eff} = sf(\varphi)$ is the effective cross section of the trap depending upon its potential φ relative to the undisturbed plasma and the geometric cross section s of the trap casing.

Thus, our task reduces to determining the dependence of the effective cross section of the trap s_{eff} on its potential φ, i.e., to determining the form of the function $f(\varphi)$.

The variation in the character of motion of positive ions in the upper atmosphere close to a trap with a variation in its potential φ is shown schematically in Fig.2.VI. In the case (Fig.2a.VI) when $\varphi = 0$ (the potential of the trap does not differ from the potential of the undisturbed plasma), all ions confined in a cylinder of a height equal to the velocity v_0 and of a cross section equal to s will strike the trap sheath in unit time. This case is the simplest and thus is desirable for taking measurements since the effective /153 cross section is then determined simply as $s_{eff} = s$ and the unknown function will be $f(\varphi) = 1$.

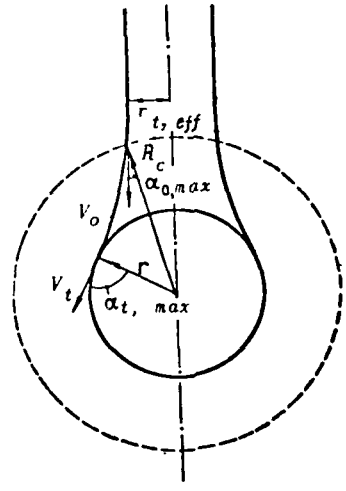

Fig.3.VI Diagram of Motion of an Ion Near a Trap.

In the presence of a negative potential on the trap envelope ($\varphi < 0$) a positive space-charge layer is created around it. The number of particles impinging inside the trap increases in comparison with the first case (Fig.2b.VI). Consequently, if $\varphi < 0$, then the quantity $s_{eff} = sf(\varphi)$, and $f(\varphi) > 1$.

In the presence of a positive potential on the trap casing ($\varphi > 0$) certain particles will be repulsed by the field of the trap and its effective cross section will decrease ($f(\varphi) < 1$). At a sufficiently large positive potential φ_{st},

known as the stopping potential (Fig.2c.VI), all atmospheric ions will be repulsed by the trap and there will be no ion current. In this case, $f(\varphi_{st}) = 0$.

Let us assume that the boundary of the negative space-charge layer (for $0 \leq \varphi \leq \varphi_{st}$) in the direction of the oncoming ion flux has a spherical shape as shown in Fig.3.VI. Let us write the law of the conservation of momentum, in a field of central forces for ions at the boundary of the space-charge layer of radius R_c and at the surface of the casing of a trap of radius r, in the form of

$$v_0 R_c \sin \alpha_0 = v_t r \sin \alpha_t, \tag{2.VI}$$

where v_0 and v_t are the velocities of the ions at the boundary of the undisturbed zone and at the surface of the trap; α_0 and α_t are the angles between the velocity direction of the ion and its radius vector (from the center of the trap) at the surface of the layer and at the surface of the trap, respectively.

It is apparent from Fig.3.VI that the condition of an ion striking the surface of a trap has the form

$$0 \leqslant \alpha_t \leqslant \frac{\pi}{2}. \tag{3.VI}$$

From eq.(2.VI) and condition (3.VI) it follows that the surface of a trap will be struck only by those ions which enter the space-charge layer at an angle of α_0, determined from the condition

$$\sin \alpha_0 \leqslant \frac{v_t r}{v_0 R_c}. \tag{4.VI}$$

The potential energy of an ion at any point of the electric field with /154 a potential φ is equal to $e\varphi$. Consequently, using the law of the conservation of energy we can write

$$\frac{m_i v_0^2}{2} = \frac{m_i v_t^2}{2} + e\varphi, \tag{5.VI}$$

where m_i is the mass of ions of the i-th group if the atmosphere is inhomogeneous in composition.

It follows from eq.(5.VI) that

$$v_t = v_0 \sqrt{1 - \frac{2e\varphi}{m_i v_0^2}}. \tag{6.VI}$$

Hence, the maximum value of the angle of incidence $\alpha_{0\,max}$ can be rewritten, by using eq.(4.VI), as

$$\sin \alpha_{0\,max} = \frac{r}{R_c} \sqrt{1 - \frac{2e\varphi}{m_i v_0^2}}. \tag{7.VI}$$

The effective cross section of the trap is

$$s_{eff} = \pi (R_c \sin \alpha_{0\,max})^2 = \pi r^2 \left(1 - \frac{2e\varphi}{m_i v_0^2}\right). \tag{8.VI}$$

The form of the unknown function thus becomes

$$f(\varphi) = 1 - \frac{2e\varphi}{m_i v_0^2}. \qquad (9.VI)$$

In the case of equality of the potentials of the trap and of the plasma ($\varphi = 0$) we find from eq.(9.VI), in conformity with the qualitative discussions given earlier, that $f(\varphi) = 1$. At total stopping of the oncoming ion flux, when the energy of the field $e\varphi_{st}$ is equal to the energy of the oncoming ion $\frac{m_i v_0^2}{2}$, we obtain $f(\varphi_{st}) = 0$. Consequently,

$$\varphi_{st} = \frac{m_i v_0^2}{2e}. \qquad (10.VI)$$

In accordance with eq.(1.VI) for a positive ion current across the collector of the trap we obtain the final expression

$$I_{c,i} = \alpha n_i e v_0 \pi r^2 \left(1 - \frac{2e\varphi}{m_i v_0^2}\right), \qquad (11.VI)$$

where v_0 is the velocity of the oncoming ion flux which is practically equal to the velocity of the capsule (or trap attached to it) in the medium.

An analysis (Bibl.4) shows that the linear relation (11.VI) between the /155 current $I_{c,i}$ and the potential φ is not disturbed when φ passes through zero into the region of negative values, as long as the condition $R > \sqrt{\frac{S_{eff}}{\pi}} = r_{eff}$ is satisfied, where r_{eff} is the effective radius of the trap.

At an even greater increase in negative potential of the trap, the effective cross section s_{eff} at first increases rapidly and then markedly slows down, as follows from eq.(11.VI).

The described analysis method is based on the use of eq.(11.VI) for a positive ion current $I_{c,i}$, which is ensured by the design features of the trap. The concentration of free electrons in this case is estimated by assuming neutrality of the plasma ($n_e \simeq n_i$), which is valid at least for the outer ionosphere (Bibl.4).

As noted above, the state in which we have $\varphi = 0$ is the most favorable state for measuring the undistorted concentration of positive ions in the upper atmosphere (ionosphere). To ensure such a state there during the measurements, in other words, to have the potential of the trap envelope φ_t always pass through the potential of the plasma φ_{pl} during the measurement, bipolar voltage pulses of a sufficiently high amplitude U are periodically fed to the trap shell, relative to the capsule. Now, the collector current I_c is recorded as a function of the voltage U. The obtained recording, known as the ion volt-ampere characteristic, is then analyzed.

By analyzing the ion volt-ampere characteristic we can find a point where $\varphi = \varphi_t - \varphi_{pl} = 0$. Interpretation of the measurements at this point is the simplest and most reliable. A second feature of the method has to do with the dependence of the thickness of the space-charge layer on the concentration of charged particles in the ambient medium.

A calculation (Bibl.4) shows that the thickness of the space-charge layer in the front section of a given capsule does not exceed 15 cm even at the comparatively great heights of the upper atmosphere where the concentration of charged particles is low ($n_i \approx 10^4$ cm^{-3}). As a consequence, it is possible to extend the traps beyond the space-charge layer of the capsule when taking measurements in the ionosphere. This is done by installing them on rods more than 15 cm long. Obviously, on an unoriented capsule several traps must be installed, in such a manner that at least one of these will be directed forward in the direction of flight of the capsule at the time of measuring.

On a decrease in the charged particle concentration, upon passing into interplanetary space, the thickness of the space-charge layer increases and /156
reaches several meters. As a consequence, the traps designed for measuring small concentrations of interplanetary gas cannot be extended beyond the space-charge region of the capsule and must be attached almost at the level of the capsule skin.

A third characteristic feature of measurements by traps is the presence of a stray collector current I_{c0}. This current is generated under the effect of various radiations (mainly short-wave solar radiation) striking the collector. Radiations that cause emission of electrons from the collector produce the positive component of the stray current I_{c0}. This current flows in the measuring circuit when access of positive ions from the ambient medium to the collector is totally stopped. Thus, the measured value of the collector current I_c has two basic components and can be written as the sum

$$I_c = I_{c,i} + I_{c,0}. \qquad (12.VI)$$

The presence of a stray current $I_{c,0}$ and its time-variance substantially reduces the possibilities of measuring small charged particle concentrations by two-electrode traps, since the quantity $I_{c,i}$ cannot be separated from a background of $I_{c,0}$.

To produce the stray current $I_{c,0}$ in traps intended for measurements in interplanetary space, an additional antiphotoelectronic grid is introduced.

Section 3. Equipment for Ionospheric Measurements

The equipment for measuring the concentration of positive ions at heights up to 1000 km, as indicated above, had been in successful operation for a long time on the third artificial earth satellite (Bibl.4). The equipment included 2 two-electrode traps installed diametrically opposite on adjustable rods (see Fig.5.I) of 65 cm length. Each trap had a spherical perforated shell of a radius of r = 5 cm (transmission coefficient of the shell, $\alpha \approx 0.63$) and a spherical hollow collector of a radius of 1.5 cm. The grids and the collectors of the

traps were made of brass and were chromium-plated. The grids (2) (Fig.4.VI) of both traps were connected with the satellite body (5) across a resistance of the order of 10 kilohms, and the collectors were connected across a resistance of the order of 1 megohm.

To create an electric field within the traps, a potential E_c = -150 v was applied from a special battery to the collector relative to the satellite body. As a result, positive ions of the plasma having an energy of the order of one electron-volt were completely taken up by the collector, whereas electrons with an energy below 150 ev were repulsed.

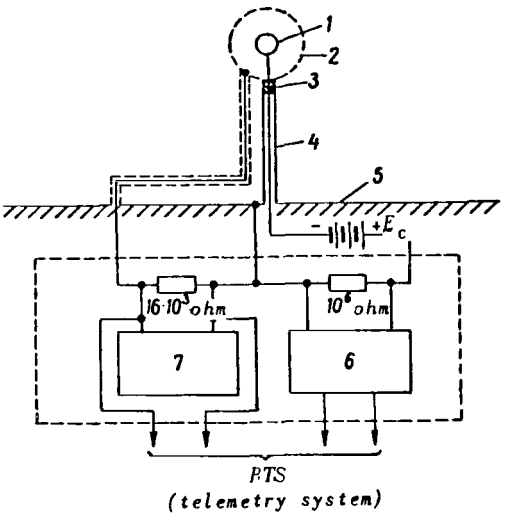

Fig.4.VI Block Diagram of Two-Electrode Trap.

To vary the potential of the trap φ_t relative to the plasma and to make /157 φ pass through zero, sawtooth pulses with an amplitude U varying from +28 to -14 v (relative to the satellite body) were periodically (every 2 sec) fed to the traps from a bipolar pulse generator (7). The magnitude of this voltage was transmitted over the telemetry system.

The shell of the trap (2) was isolated by polyfluoroethylene resin (3) from the tubular telescope rod (4) and the collector (1).

The stream of charged particles striking the collector creates a potential difference and a current in the collector-casing circuit. The voltage drop across the resistance of 1 megohm is transmitted by the cathode follower (6) to the telemetry system. The magnitude of the voltage on the shell of the trap and its collector current, which are recorded on the ground, made it possible to plot for each trap the ion volt-ampere characteristic corresponding to each bipolar voltage pulse.

At a trap potential of $\varphi \approx 0$ and a positive ion concentration of $n_i \approx \approx 10^7$ cm^{-3}, the magnitude of the collector current was approximately 3×10^{-5} amp and, at $n_i = 10^4$ cm^{-3}, about 5×10^{-8} amp. Amplification of the currents within these limits was accomplished by cathode followers with tubes of the 6N16B type

(Bibl.4). To broaden the dynamic range of the follower, a diode cut off by a special bias was connected into the circuit parallel to the input resistance. When the collector current exceeded 10^{-6} amp, the voltage drop across the /158 input resistance compensated the voltage of the C battery, the diode opened and shunted the input resistance, reducing the amplification factor of the cascade.

During the flight, periodic checks were made (every 30 sec) whether the condition of total collection of ions entering the trap on the collector was satisfied. This was done by switching into the collector circuit resistances selected so that the voltage drop across them substantially lowered the negative voltage across the collectors. In this case, the magnitude of the collecting field (between the collector and shell of the trap) also decreased. The constancy of the collector current, when connecting these resistances, was used as criterion for total collection of the ions.

Two independent driven sawtooth voltage generators (Bibl.7) were used for shaping the bipolar pulses. These generators were triggered by pulses from an asymmetric multivibrator that generated square pulses with a duration of 130 msec with a frequency of 0.5 cycles. This duration determined the time shift in the generation of positive and negative pulses. The shaped pulses were fed to the grids of the traps through the cathode followers (Bibl.4).

Section 4. Work-Up of Ion Volt-Ampere Characteristics

The ion volt-ampere characteristics of the type $I_c = f(U)$ (Fig.5.VI) are plotted from the data of the telemetry recordings of the collector currents I_c at various values of the sawtooth voltage on the trap shell $U = \varphi_t - \varphi_0$.

We note that, at large electron currents across the latticed shells of the traps, it was impossible to plot the total volt-ampere characteristic with a saturation segment, formed at a sufficiently large positive potential of the trap shell as a consequence of complete stopping of the positive ions. The magnitude of the current along the saturation segment is rather high, since it is equal to the stray current of the collector $I_{c,0}$ and permits taking this into account when analyzing the observations.

The volt-ampere characteristics can be analyzed to obtain the positive ion concentration n_i by two methods (Bibl.4).

First method. The equation of the ion volt-ampere characteristic when measuring the concentration of positive ions, according to eqs.(12.VI) and (1.VI), can be written as follows:

$$I_c = \alpha n_i e v_0 s_t f(\varphi) + I_{c,0}, \qquad (13.VI)$$

where $s_t = \pi r^2$ is the cross-sectional area of a spherical trap of radius r;

$f(\varphi) = 1 - \frac{2e\varphi}{Mv_0^2}$ is a factor allowing for the effect of the trap potential φ on the effective cross section for ions of mass M. /159

It follows from the expression for the characteristic [eq.(13.VI)] that, at the instant that $\varphi = 0$, the measured magnitudes can be used for determining the ion concentration:

$$n_i = \frac{I_c - I_{c,0}}{\alpha e v_0 \pi r^2}. \qquad (14.VI)$$

This constitutes the essence of the first method of interpreting the volt-ampere characteristics.

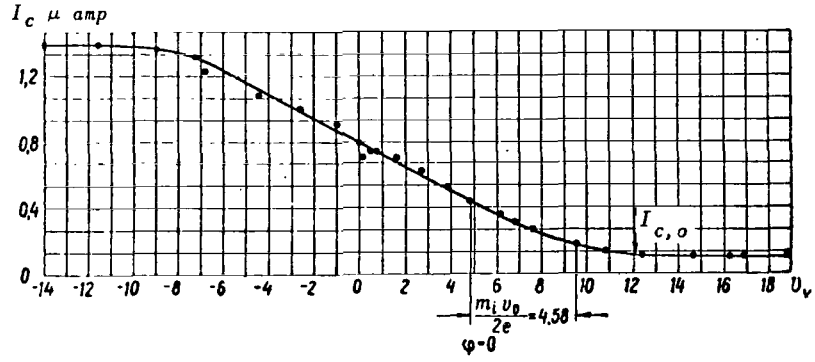

Fig.5.VI Ion Volt-Ampere Characteristic of a Trap Installed on the Third Satellite (May 19, 1958, h = 976 km).

The instant $\varphi = 0$ is determined by calculating the stopping potential φ_{st} (relative to the undisturbed plasma) and finding the decelerating voltage on the trap shell U_d (relative to the capsule). The latter is determined from the start of the saturation segment on the total ion volt-ampere characteristic. The point on the characteristic curve with the abscissa $U_0 = U_d - \varphi_{st}$ exactly corresponds to the unknown instant at which the potential of the trap relative to the plasma becomes equal to zero, $\varphi_t = 0$. Actually, by using the previously adopted notations, we can write two equalities:

$$\text{and} \quad \begin{aligned} U_0 &= -\varphi_0 \quad (\text{for } \varphi = 0) \\ U_d &= \varphi_{st} - \varphi_0 \quad (\text{for } \varphi = \varphi_{st}), \end{aligned} \qquad (15.VI)$$

where φ_0 is the potential of the capsule relative to the plasma.

It follows from equalities (15.VI) that

$$U_0 = U_d - \varphi_{st}. \qquad (16.VI)$$

From the current at this point we calculate the concentration of positive ions [see eqs.(10.VI) and (14.VI)].

We note that, if the plasma contains positive ions of different mass, /160 a calculation of φ_{st} by eq.(10.VI) must successively take as m_i masses of different ion groups corresponding to the composition of the atmosphere at a given height. However, as mass spectrometer has shown, oxygen ions predominate in the earth's ionosphere. The smoothness of the experimental volt-ampere character-

istics (see for example, Fig.5.VI) indicates a practically homogeneous ionosphere since otherwise sharp breaks in the characteristic curves, caused by alternate stopping of various ion groups, would be observed upon an increase in the positive potential of the traps. It is also necessary to bear in mind that eq.(10.VI) is rigorously valid only at not relatively moderate temperatures of the plasma T, when $v_i \ll v_0$. On a rise in the plasma temperature T, as shown by analysis (Bibl.4), the volt-ampere characteristic shifts to the right and moves upward, increasing its curvature, since I_c increases nonlinearly in this case. At plasma temperatures of the order of thousands of degrees we can use the approximate formula (10.VI). The method of analysis by the first method can be illustrated on the basis of the characteristic curve shown in Fig.5.VI. Under the test conditions indicated here for oxygen ions ($M = 16 \times 1.66 \times 10^{-24}$ gm), eq.(10.VI) demonstrates that $\varphi_{st} = 4.5$ v. The point where the stopping segment begins on the characteristic curve is determined by the abscissa $U_d = 9.4$ v. The magnitude of the voltage across the trap shell U_0 at which its potential with respect to an absolute value is equal to the potential of the plasma φ_{pl} and opposite to it in sign, i.e., at which $\varphi = 0$, will be equal - in conformity with eq.(16.VI) - to $U_0 = 9.4 - 4.5 = 4.9$ v. From the value of the collector current at this point $I_c = 0.44$ μamp and of the current along the saturation segment $I_{c0} = 0.09$ μamp we find, by using eq.(14.VI), that the ion concentration at this point of the upper atmosphere is $n_i = 10^5$ cm^{-3}.

Second method. This method is based on determining the slope of the volt-ampere characteristic to the axis of the abscissa which, as is apparent from Fig.5.VI, is equal to $\frac{dI_c}{dU}$.

If we take into account that the potential of the object during the time of recording the characteristic curve (about 0.2 sec) is practically unchanged $\varphi_0 = \text{const}$, then the general expression for the voltage across the trap $U = \varphi - \varphi_0$ will show that $dU = d\varphi$. Thus, using eq.(13.VI) [or eq.(11.VI)] we find that

$$\frac{dI_c}{dU} = \frac{dI_c}{d\varphi} = -2e^2\alpha n_i \frac{\pi r^2}{Mv_0^2} \qquad (17.VI)$$

or

$$\frac{dI_c}{dU} = Bn_i, \qquad (18.VI)$$

where $B = -2e^2\alpha \frac{\pi r^2}{Mv_0^2}$ is a constant for a trap of the given design, operating /161 in a homogeneous plasma and installed on a capsule moving in the plasma with a constant velocity v_0.

The second method obviously is more universal, since it permits analyzing complete ion volt-ampere characteristics.

The first method, however, additionally yields the magnitude of the potential of the object φ_0 during measurements, from which the temperature of the plasma can be estimated.

The plasma temperature is estimated on the assumption that the velocity distribution of electrons obeys Maxwell's law and that the plasma is neutral.

Then the plasma temperature, as follows from a determination of the thermal potential (see Chapt.II), is given by the relation

$$T = \frac{e\varphi_{pl}}{k} \approx \left|\frac{e\varphi_0}{k}\right| = \frac{eU_0}{k}, \qquad (19.VI)$$

where k is the Boltzmann constant.

For example, at $U_0 = +2$ v and a height of about 240 km where $n_i = 5 \times 10^5$ cm^{-3}, we obtain $T_e \approx T_i \approx T = 7 \times 10^3$ °K, whereas at a height of about 800 km, where $n_i = 1.9 \times 10^5$ cm^{-3} and $U_0 = +6.5$ v (in this case, the potential of the capsule is $\varphi_0 = -6.5$ v) we already have $T \approx 15{,}000$°K (Bibl.4).

The total error of measurement, in comparison with the data of the ionospheric probes does not exceed ±25% on the average. The results obtained in analyzing the characteristics by the first and second methods coincide with an accuracy to within a few percent (Bibl.4).

Section 5. Measurement of Low Charged Particle Concentrations

At distances from the earth where the concentration of ions is so low ($n_i < 10^3$ cm^{-3}) that the magnitude of the current of the useful signal I_c is comparable with the stray currents I_{c0}, measurements become impossible. Furthermore, it was previously indicated that at a low ion concentration the positive space-charge layer surrounding the space object becomes so great (more than 1 m) that it is difficult to extend the traps beyond its limits (even at the front of the object).

Therefore traps designed to measure small charged particle concentrations (Fig.6.VI), in addition to an external grid (1) and a collector (3), have an internal (photoelectric) grid (2) which is under a sufficiently large negative potential. The traps are fastened directly to the skin of the space object /162 by means of the base (7) with a rubber gasket (8). The grid (1) is attached to the aluminum shell of the trap (5) over a polyfluoroethylene insulator (4). The connection of all three electrodes of the trap with the measuring circuit is accomplished through airtight leads (6).

Below, we will give the technical data of the three-electrode traps installed on the spherical capsule of the second space rocket launched to the moon on September 12, 1959 (Bibl.6). The hemispherical outer grid (1) of a radius of 3 cm was made of nickel wire mesh. The collector (3) is a nickel disk of 0.4 mm thickness of a radius of about 2 cm. The inside grid (2) was flat and made of tungsten wire mesh. This was done because the use of woven grids ensures greater uniformity of the proximity field than that of perforated grids.

Similar equipment was installed on the Venus probe launched on February 12, 1961 (Bibl.3). Its most important improvement was an increase in transmission of the inside grid, in order to reduce the collector current component generated by photoelectronic and secondary emission from this grid.

A different number of traps, with various orientation relative to the direction of flight and to the sun was installed on various spacecraft. For

example, on the capsule of the second spacecraft the traps were installed at the vertices of a tetrahedron inscribed in the capsule, so as to ensure measurements in the solar shadow by at least one trap at any instant of time (Bibl.9).

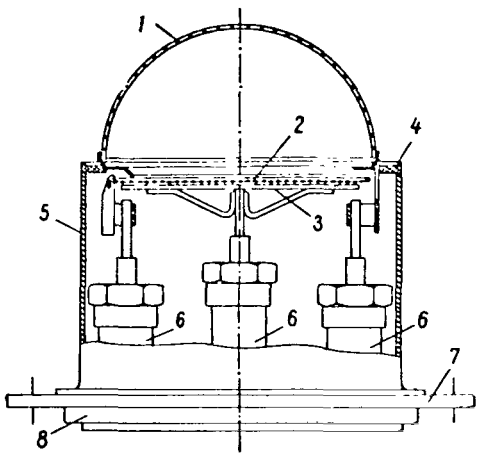

Fig.6.VI Diagram of a Three-Electrode Trap.

The circuit for feeding voltage to the electrodes of the space trap is shown in Fig.7a.VI. The electrode potentials of the traps relative to the capsule of the second spacecraft (Bibl.6) were as follows: at the collectors $U_c = -(60 - 90$ v), on the inside grids $U_{g2} = -200$ v, and on the outside grids of each of the four traps $U_{g1} = -10, -5, 0, +15$ v, respectively.

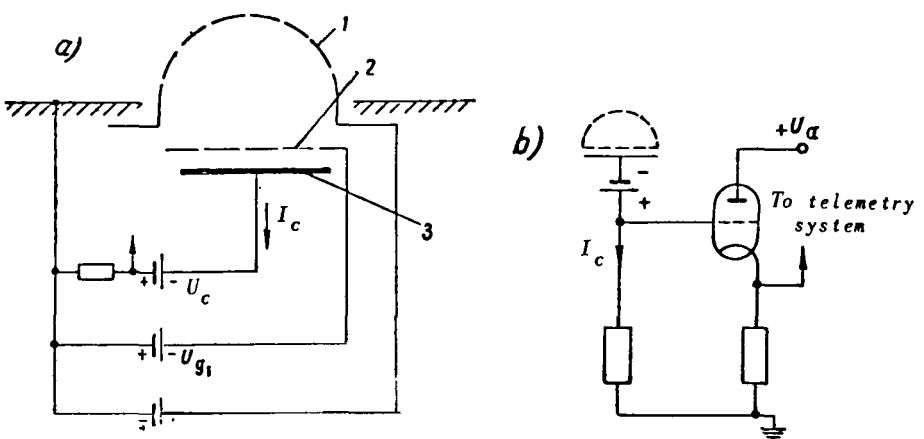

Fig.7.VI Wiring Diagram (a) and Ion-Current Amplifier (b) of a Three-Electrode Trap.
1 - Outer grid, 2 - Inner grid, 3 - Collector.

The amplifiers for the collector currents were designed so as to permit measurement of currents caused both by positive and negative particles. In the described equipment, the amplifiers measured positive currents from $+10^{-10}$ /163

to $+5 \times 10^{-9}$ amp and negative currents from -10^{-10} to -1.5×10^{-9} amp.

The instantaneous values of the collector current of each trap were recorded twice every minute. The principal wiring diagram of the amplifier cascade for the collector currents of the traps is shown in Fig.7b.VI. The cathode followers with a broadened range and the telemetry system of the equipment installed on the second Soviet spacecraft (Bibl.9), for example, ensured the possibility of recording positive collector currents from 10^{-10} to 1.5×10^{-9} amp. The instantaneous values of each collector current in this equipment were recorded twice every minute.

An interpretation of the measurements basically amounts to an estimate. Let us examine its principles for the described equipment (Bibl.6).

The potentials of the outer grids of all traps were different, in order to permit estimating the energy of particles striking the collector. Their magnitudes were so selected that it was possible to separate currents I_c generated by protons of the interplanetary plasma, whose energy is of the order of one electron-volt, from currents generated by the protons of corpuscular fluxes, whose energy measures in ones and tens of Kev.

In a stationary plasma, the positive (ion) current of the trap with a voltage across the outer grid of $U_{g1} = +15$ v should obviously be equal to zero, and in corpuscular fluxes it should not depend on the potential of the outer grids. In this case, if the corpuscular flux acts against a background of /164
the positive plasma current, the positive current of the collector I_c will slightly vary depending upon U_{g1}.

Low-energy electrons are unable to overcome the retarding field between the outer and inner grids of the traps ($U_{g2} - U_{g1} \approx 200$ v), but electrons with an energy exceeding 200 ev are able to produce negative collector currents $-I_c$ from which it is possible to judge the flux of such electrons.

When the trap was illuminated by the sun, photoelectrons impinged on the collector from the inside grid. The magnitude of this stray photocurrent during flight could reach values as high as 5×10^{-10} amp (Bibl.7). Therefore, placing the trap in the sun's shadow is preferable for measurements.

A positive stray current may be produced by electron emission from the collector, irradiated by a flux of soft electrons with an energy up to several tens of Kev. Special investigations of this effect (Bibl.8) showed that it causes a noticeable decrease in the efficiency of recording electrons by means of three-electrode traps of the design under consideration. The dependence of the ratio of the negative current of the trap collector I_c to the current of the incident flux of electrons I_0 at various electron energies E is shown in Fig.8.VI. The diagram indicates that the average efficiency of recording an electron flux of an energy from 0.2 to 40 Kev is 50% (in the absence of solar radiation and at a voltage across the inside grid of $U_{g1} = 200$ v). The maximum energy of recordable electrons and protons is of the order of several million electron-volts (Bibl.8).

Unoriented capsules, moving along a trajectory, perform complex rotational

movements. As a consequence, the orientation of the traps installed on them relative to the sun and direction of flight changes continually. This causes continuous fluctuations of the collector current I_c. Here, the processing of the data from three-electrode traps is done by analyzing the curves envelopes of the maximum and minimum values of the current I_c. The concentration of charged particles, generating a collector current I_c of given sign and magnitude, was calculated (Bibl.5) in first approximation, without consideration of the stray current I_{c0} and the potential of the capsule φ. In this case, the computational formula (14.VI) is simplified and assumes the form of an estimating inequality

$$n_i \leqslant \frac{I_{c,min}}{\pi \alpha v_0 e r^2}, \qquad (20.VI)$$

where $I_{c,min}$ is the minimum measurable value of the collector current.

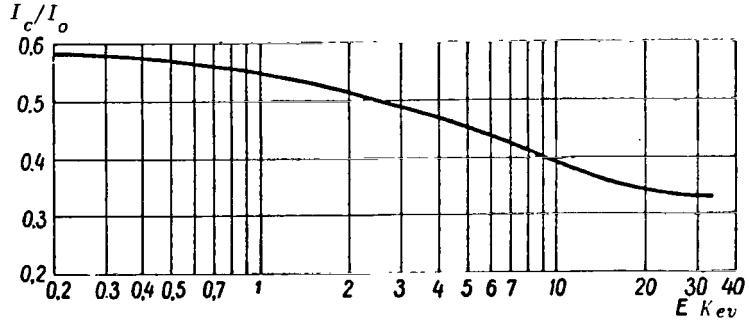

Fig.8.VI Dependence of Relative Collector Current on Electron Energy E.

In certain cases (Bibl.5), the intensity I of the measured corpuscular flux was calculated from eq.(20.VI). For this, the current I_c was expressed as the number of singly charged particles passing through the cross section of the trap in unit time. The computational formula is then written as /165

$$\lambda = \frac{I_c}{\alpha \pi r^2}. \qquad (21.VI)$$

As a result of calculation, we obtain approximate characteristic curves for the concentration of interplanetary plasma, for energetic electrons, and also for the intensity of corpuscular fluxes in space.

For example, during the flight of the second spacecraft to a distance of more than 330,000 km until the capsule impacted on the moon (Bibl.9), the upper (1) (Fig.9.VI) and the lower (2) limits of the collector currents in traps with U_{g1} equal to -10, -5, and 0 v as well as the upper limit (3) of the currents in the trap with U_{g1} = +15 v indicated the presence of almost identical positive collector currents in all traps. Consequently, the object passed through a flux of positive ions [as suggested elsewhere (Bibl.9), through a flux of solar corpuscular radiation] with energies of more than 15 ev. The intensity of the flux corresponding to the current $I_c = 5 \times 10^{-10}$ amp proved to be of the order of 10^8 $cm^{-2} \cdot sec^{-1}$.

In this lunar probe, recording of electron fluxes of the order of 10^7 $cm^{-2} \cdot sec^{-1}$ with energies exceeding approximately 200 ev continued, after having /166 been initiated in all traps (whose current is shown by curve 2) when the capsule was more than 10,000 km from the earth (Bibl.9).

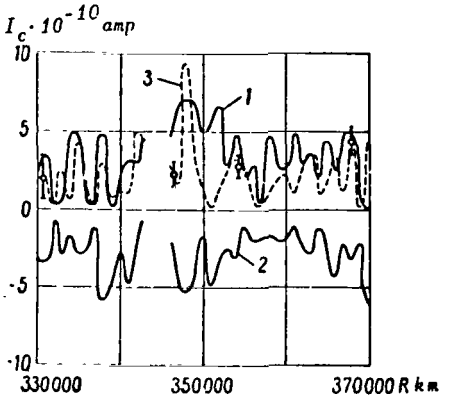

Fig.9.VI Example of a Recording of Collector Currents for Three-Electrode Traps.

The error of the charged particle fluxes determined by this method is of the order of measurable magnitudes (Bibl.8).

Section 6. Modulation Traps

As indicated above, measurements of charged particle concentrations by means of traps are hampered by the presence of a stray collector current $I_{c,0}$. This mainly constitutes the photocurrent generated on illumination of the collector by the sun. The density of this current was estimated as of the order of 10^{-8} amp/cm^2 (see Chapt.II). The direction of the photocurrent coincides with the direction of the current of positive ions to the collector. If an antiphotoelectronic grid is used in the trap, photoelectrons may also be emitted from the latter, which generate an appreciably smaller stray current component $I_{c,0}$ which is subtracted from the recorded current of positive ions. The density of this reverse current, according to an estimate by other authors (Bibl.11), may reach 10^{-9} amp/cm^2. At the same time, the density of the collector current subject to measurement at a concentration of about 1 cm^{-3} amounts to only 10^{-13} - 10^{-4} amp/cm^2. Therefore, in designing equipment for measurements in interplanetary plasma and for investigations of highly rarefied planetary atmospheres, further improvements were made in the method of traps with the purpose of decreasing the stray current $I_{c,0}$. This is accomplished by modulating the collector current I_c without modulating the stray current $I_{c,0}$ and by measuring the variable component of the output signal.

The wiring diagram of a plasma detector or trap with modulation, developed by Bridge, Dilworth, et al. (Bibl.11, 12) is shown in Fig.10.VI. A square modulating voltage with an amplitude E_0 and a frequency of about 1500 cps is fed to

the grid (2) from a special generator. The grids (3) and (1) are connected with the shell of the capsule and serve as electrostatic shields for the modulating grid. Especially important is the screen grid (3) which prevents capacitive coupling of the modulating grid (2) with the collector (5). The antiphotoelectronic grid (4) is under a negative potential of 100 - 130 v with respect to the collector (5). This voltage is time-invariant, for which reason the photoelectronic current is not modulated.

The casing of the detector and collector (area about 20 cm^2) is made of magnesium, and the grids are of tungsten wire with a transmission coefficient of $\alpha = 0.95$, except for the grid (4) which is made of phosphor bronze (Bibl.11).

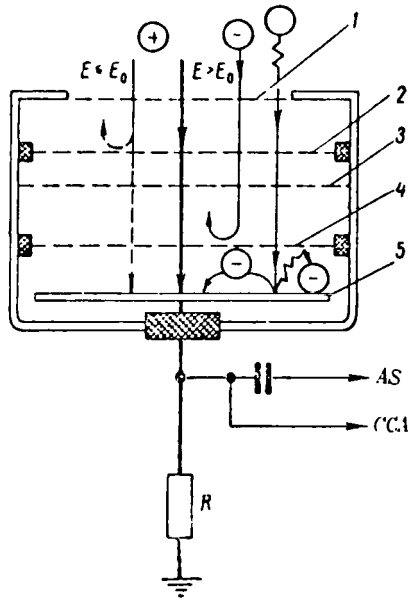

Fig.10.VI Diagram of Modulation Trap.

For a detailed energy analysis of the recorded particles, the level of the modulating voltage E_0 is varied stepwise. In the latest version of the modulation trap (Bibl.12), the level of E_0 during the measuring cycle lasting 19 min 44 sec is varied seven times from zero to 2300 v, with intermediate values of 5, 20, 80, 250, 800, and 2300 v (every 2 min 28 sec). /167

The detector operates in the following manner: At a zero potential across the grid ($E_0 = 0$), protons of all energies pass to the collector. When the amplitude of the modulating voltage exceeds $\frac{Mv^2}{2e}$, protons of a given energy are not passed to the collector. Thus, a variable-current signal arises in the collector circuit, corresponding to alternating penetration and stopping of the plasma protons. The smaller the energy of the recorded protons, the shorter will be the duration of the step signal at the output of the trap in each measuring cycle.

The outer electrons that are not retarded by the grid (4) at $E_o = 0$, and after their acceleration by the grid (2) when $E_o > 0$, produce the constant component of the collector current.

The current of the inner electrons, emitted under the effect of electromagnetic radiations and ions on the collector of the detector, is also not modulated since the field of the grid (2) is screened by the grid (3).

The presence of an antiphotoelectronic grid (4) in the ion detector makes it possible to record the flux of energetic protons by measuring the constant current from the collector across the shell of the capsule whose potential is assumed constant during the measuring cycle. Actually, at a temperature of not more than 1 million degrees (°K) the electrons of the outer plasma cannot overcome the energy barrier of the grid (4). Furthermore, the energy of the protons is determined by the velocity of the capsule rather than by the temperature.

Thus, the current flowing across the collector of the detector has one constant and one variable component. The former is due to the current of protons /168 with an energy of $E_p > eE_o$ and of photoelectrons from the grid (4) to the collector, while the latter is due to the current of protons with an energy of $E_p < eE_o$.

The authors (Bibl.11) note that the potential of the modulating grid E_o, needed for stopping the protons, decreases in proportion to $\cos^2\theta$ if the beam enters at an angle θ to the axis of the detector. This is explained by the fact that the velocity component in the direction of the field depends upon the angle θ. As a consequence, the energy of the protons E_p determined from measurements by the method under consideration in a disordered flux contains an error of

$$\Delta E_p = E_p \tan^2 \theta_m, \qquad (22.VI)$$

where θ_m is the angle of view of the detector.

For a model, for example as that described by other authors (Bibl.11), we have $\tan^2 \theta_m = 3$. For the very same reason, the sensitivity of the detector depends on the angle of incidence of the flux to the cut-off plane of the receiving aperture, and the maximum sensitivity is retained almost unchanged upon deflection through an angle of up to 15° in all three planes from the axis of the detector (Bibl.12). The plane field of view of the detector (Bibl.12) is about 130°. Furthermore, it is necessary to consider the possibility of reflection of protons of energy $E_p > eE_o$ when they strike obliquely (Bibl.12).

The plasma detector of the above-described design was installed, in particular, on the Explorer-X (Bibl.11). The device was attached so that the inlet aperture came to lie on the lateral surface of the satellite. Scanning of space was done by rotating the capsule. Orientation of the detector in this case was continuously determined by an optical sensor.

Two modulating grids were used in the detector installed on this satellite. A high voltage from a high-voltage modulator was fed to one grid and a low voltage from another modulator to the other grid. When no voltage was fed to the grid, it was grounded. The block diagram of the plasma detector system,

installed on Explorer-X (Bibl.12), is shown in Fig.11.VI. Measurements of the constant current by a constant-current amplifier (CCA) and of the variable component of the collector current were accomplished. In the latter case, the signal, coming from the preamplifier PA, passed through the filter (1) (double T-shaped bridge) tuned to the modulation frequency (about 1400 cps) to the end amplifier (A) and then to the telemetry system RTS as a constant voltage, fluctuating by not more than 0 - 5 v. The limit of sensitivity of the variable-current amplifier (with respect to noise) was about 2×10^{-11} amp, and the saturation limit was approx. 10^{-7} amp. When measuring the unmodulated signal after the CCA, the signal was read out directly to the RTS. The maximum sensitivity of the amplifier CCA was about 10^{-7} amp.

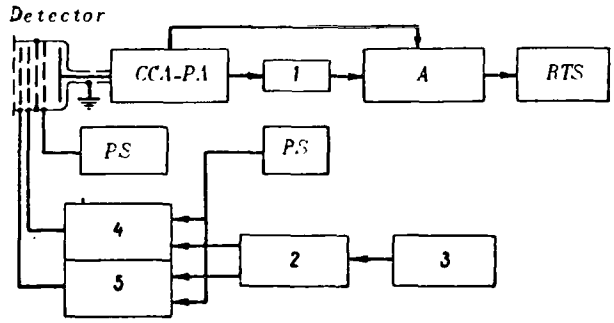

Fig.11.VI Block Diagram of Equipment with Modulation Trap.

Delivery of the modulating voltage to the grids from the low-voltage (4) /169 and the high-voltage (5) modulators was regulated automatically by means of the device (2) connecting the flip-flop generator (3). The antiphotoelectronic grid and the electronics were fed from various power sources PS. The weight of the entire equipment of the plasma detector (without telemetry) was 1.2 kg at a power consumption of less than 40 mw (Bibl.12).

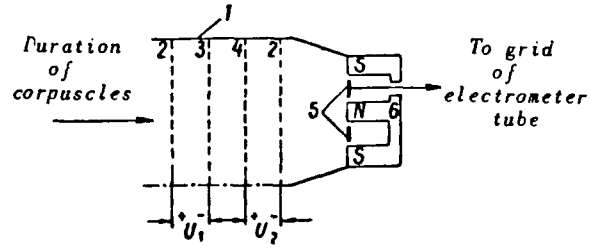

Fig.12.VI Diagram of Trap for Measuring the Intensity of Corpuscular Fluxes.

Traps for measuring the intensity of corpuscular fluxes are similar in design to modulation traps. Such traps were first used on the specialized satellites Cosmos-3 and Cosmos-5 (Bibl.3). The principal wiring diagram of the trap for charged particles of corpuscular fluxes developed by V.V.Krasovskiy

et al. (Bibl.3) is shown in Fig.12.VI. The device consists of an aluminum casing (1) housing the metal grids (2), (3), (4) and the ring collector (5). The current from the collector to the container is measured by an electrometer-type amplifier.

The grids (2) are connected directly with the casing (1) and serve as electrostatic shields. Voltages U_1 and U_2 are fed to the insulated metal grids. A constant negative voltage U_1 is used for limiting the energy spectrum of electrons passing to the collector, to a magnitude eU_1 ev. In the equipment installed on these satellites (Bibl.3), the magnitude of the electron energy cut off by this grid was 40 ev. /170

A positive step voltage U_2 is supplied to the grid (4), which prevents penetration of protons with an ever increasing energy into the trap. For example, in the investigated equipment (Bibl.3), this energy increased by four steps from 0.15 to 11 Kev (over 3 and 6 Kev).

The ring collector (5) is placed in the gap of the permanent magnet (6) whose field prevents electron emission from the collector under the effect of various radiations. Simultaneously, this magnetic field prevents penetration of low-energy electrons (with an energy less than 5 Kev in our example) and ions (with an energy less than 30 ev for O^+ ions) into the collector.

For high-energy ions and electrons, the effective solid angle of the trap had a magnitude of about one steradian. For particles moving at an angle of 30° to the axis of the trap, its sensitivity decreased by about 50%.

The scale of the amplifier permitted recording positive currents, isotropic within the field of view, in the range of 3×10^5 to 5×10^6 $cm^{-2} \cdot sec^{-1} \cdot ster^{-1}$, and anisotropic with a narrow disk-like distribution in the range of 3×10^6 to 5×10^7 cm^{-2} sec^{-1} $\cdot$ $ster^{-1}$. In other variants of traps, different potentials that ensure selection of recordable particles were fed to the grids (Bibl.3).

Thus, traps of this type continuously record the total electron current whose energy exceeds an established threshold and of protons whose threshold of recording varies stepwise. The interpretation of the measurements is of an approximate character and is based on previously discussed principles (Sect.5 of this Chapter).

CHAPTER VII

MEASUREMENTS OF METEOR STREAMS

Section 1. Meteors and Cosmic Dust

Bodies of the solar system invading the earth's atmosphere at cosmic velocities are known as meteors; the smallest are called micrometeors or cosmic dust and the largest are called bolides. Meteors are divided into periodic and sporadic, the recurrence of the latter being appreciably greater. /171

The bodies of meteor material falling on the earth are known as meteorites. Their number reaches several thousands a year, and the mass of the largest ever recorded was 100 tons (total mass of the fragments of the Sikhote-Alin meteorite).

The velocity at which meteors enter the atmosphere is about 10 - 70 km/sec and depends on the direction of the meteor with respect to the earth.

The average recurrence of meteors entering the earth's atmosphere during a 24-hour period rapidly increases as their mass decreases (Table 1.VII).

TABLE 1.VII

RECURRENCE OF METEORS OF VARIOUS MASSES

Method	Mass, gm	Number per Day
Extrapolation	500—100	300
	100—10	2500
	10—1	1.8×10^4
	1—0.1	$4 \cdot 10^5$
Photographic and radar	100—10	10^6
	10—1	3.6×10^7
	1—0.1	1.9×10^8
	0.1—0.01	3.3×10^9
	0.01—0.001	6.5×10^{10}
Extrapolation	10^{-9}—10^{-13}	10^{14}
	10^{-13}—10^{-17}	10^{18}

Calculations (Bibl.10) show that particles of meteoric material with a diameter below 0.25 μ should be absent in meteor streams since they are repulsed beyond the limits of the solar system by light pressure. Micrometeors (or dust) measuring 0.25 - 1 μ have the greatest recurrence (about 99%).

According to investigations by a number of authors, the quantity of meteoric matter falling on the earth's surface per day is from 24 to several thousands of tons, which corresponds to an energy of at least 10^{20} erg applied to the earth. However, the thickness of the meteorite deposit on the earth during the entire geological period (2×10^9 years) does not exceed 2 m (Bibl.10).

The average spatial density of meteor matter near the earth is estimated to be 10^{-21} - 10^{-24} gm/cm^3 (Bibl.5). The character of the interaction of a meteor with the atmosphere largely depends on its size. Collisions with air /172 molecules impart momentum and energy to it. This leads to a deceleration and burn-up of the meteor. Small bodies (of mass less that 10^{-9} gm), characterized by a relatively large surface area, are rapidly decelerated and all of the generated energy is expended for radiation. For a long time, these remain suspended

in the upper atmosphere as cosmic dust and then settle out on the earth. Mixing of dust of cosmic and terrestrial origin occurs at a height of 80 - 90 km (Bibl.10). Large particles are decelerated appreciably less.

Meteors whose mass exceeds 10^{-9} gm are vaporized (burned up) at heights below 160 - 120 km, at a temperature of 2000 - 3000°K. Dissociation of the vaporized molecules leads to an additional ionization of the atmosphere along the meteor trail. As the result, meteors of the masses indicated in Table 1.VII can be observed from the earth by photography and radar. Particles whose mass is less than 10^{-3} to 10^{-4} gm are seen at night from the earth by the unaided eye, and particles with a mass more than 1 gm are able to reach the earth's surface (Bibl.2).

We note that observations of the character of meteor trails and their shifting permit indirect soundings of the atmosphere at heights of 80 - 120 km, to obtain information on winds, turbulence, and density of the upper atmosphere. Some data on cosmic dust can be obtained by astronomic methods (twilight observations).

Direct measurements of meteor streams by means of equipment installed on rocket and satellite capsules indicate a large scattering of the measured intensities of meteor streams. Figure 1.VII shows the dependence of the frequency of recorded impacts N on the height above the earth's surface, based on the data of geophysical rockets of the USSR (1 - 3), rockets of the USA (4 - 9), third Russian satellite (10, 11), Explorer-I (12) and Vanguard III (13), second spacecraft (14), third spacecraft (15), Pioneer-1 (16) and Explorer-IV (17). All data used in constructing Fig.1.VII have been reduced to equal sensitivity of the equipment $m_{min} = 10^{-8}$ gm with respect to $N(m) = m^{-1}$, where m is the mass of the meteor (Bibl.11). The recorded frequency of impacts N is referred to the average height for each case of measuring.

It is apparent from these data that close to the earth (h = 100 - 300 km) there is a zone of high density of dust particles. At heights of h = 400 - - 2000 km, the frequency of impacts N is about 10^{-3} impacts$\cdot m^{-2} \cdot sec^{-1}$. Measurements at significant distances from the earth ($h > 10^4$ km) are characterized by a large standard deviation of the obtained results: The equipment installed on the Explorer-VI and Pioneer-1 gave values of 5×10^{-6} and 4×10^{-5} $m^{-2} \cdot sec^{-1}$, while those recorded on the second and third space rockets yielded 9×10^{-4} /173 and 10^{-3} m^{-2} sec^{-1}, respectively (for $m = 10^{-8}$ gm). At 400 - 2000 km, sporadic increases in the frequency of impacts N by one order of magnitude and more were noted (up to 11 $m^{-2} \cdot sec^{-1}$ on the third satellite).

It was assumed in various calculations (Bibl.17) that the intensity of the stream of particles with mass 10^{-6} gm is at least 10^{-9} m^{-2} sec^{-1} and with mass 10^{-10} gm, at least 10^{-4} m^{-2} sec^{-1}.

Meteor streams are studied to evaluate their effect on the reliability of all types of equipment during flight and to elucidate the role of meteors in various geophysical processes (ionization, change in atmospheric composition, etc.) and in the solar system.

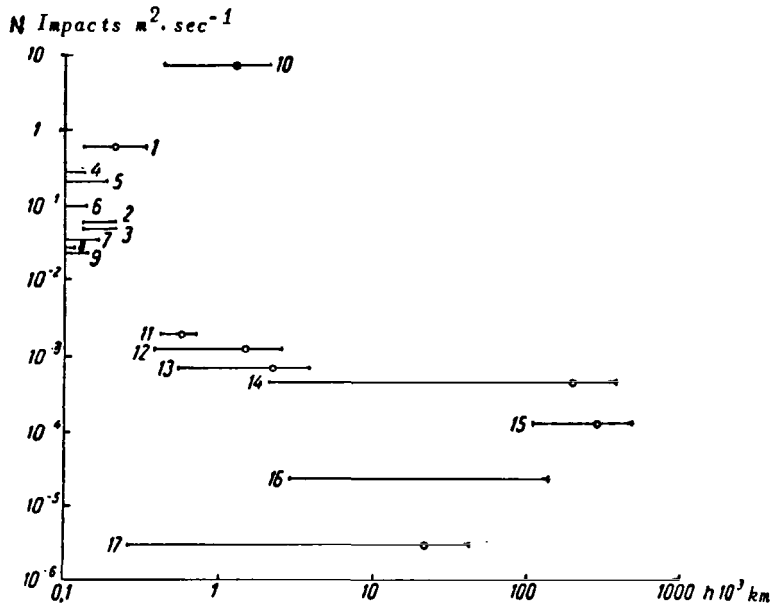

Fig.1.VII Frequency of Collisions with Meteors N as a Function of the Height h above the Earth's Surface, according to Experimental Data.

Section 2. Equipment for Recording Meteor Particles

Many different methods, based on the use of various collision effects, have been proposed and employed to measure the number of collisions of a certain surface with meteor particles. For example, the following have been recorded: glow produced in Plexiglas; change in conductivity of a thin wire mesh [diameter 10 μ on Explorer-III (Bibl.8)] torn by impact of a meteor; change in illumination of a cadmium-sulfide photoresistor whose photosensitive surface is covered by a shield of Mylar film coated with a vacuum-deposited aluminum layer which is ruptured under the impact of micrometeors (Bibl.3), etc. /174

A specialized satellite of the USA (S = 55, or Explorer-XIII), developed especially for investigations of micrometeor streams, was equipped with gas-filled cells as the main sensors (Bibl.3). The cells were made of a copper alloy with beryllium in the form of cylinders. The flat part of the cell measured 50.8 × 180 mm. The thickness of the walls was differed for different groups of sensors and varied within 0.025 - 0.125 mm. The cells were filled with nitrogen and helium. When the cells were pierced by micrometeors, the gas escaped and threw a baroswitch mounted to the end of each cell. Information on triggering of the switch of each cell was transmitted by telemetry. The cells were installed in rows on the surface of the satellite, with the convex portion outward.

The most valuable information, however, can be obtained by piezoelectric sensors (crystal microphones) whose action is based on recording the reactive pulse generated when a meteor strikes the obstacle. Investigations have shown that collisions of meteor particles with a solid wall have the character of an

explosion because the energy released is greater than the binding energy of the crystal lattice. According to calculations (Bibl.14), the depth of penetration of a small meteor particle is of the order of its radius r. If we assume the funnel, formed as a result of the explosion of the particle upon impact, to be of hemispherical shape, we can find the dependence of the funnel radius R on the particle energy $E = \frac{mv^2}{2}$.

Provided that the energy E of the particle is expended only for its own melting and for that of a certain volume of the obstacle, we can write the equation of energy balance in the following form:

$$\frac{mv^2}{2} = mP_m + MP_o, \qquad (1.VII)$$

where M is the mass of the obstacle melted in the volume of the funnel, P_m and P_o are the energy densities needed to melt the substance of the meteor and obstacle.

Provided that $P_m \simeq P_o = P$ and $m \ll M$, it follows from eq.(1.VII) that

$$M \approx \frac{mv^2}{2P}. \qquad (2.VII)$$

Substituting into eq.(2.VII) the density of the obstacle substance ρ and the radius of a hemispherical funnel R, we obtain

/175

$$\frac{2\pi}{3} R^3 \rho \approx \frac{mv^2}{P}. \qquad (3.VII)$$

Hence it follows that

$$R(m, v) \approx \sqrt[3]{\frac{3}{\pi\rho P}\frac{mv^2}{2}}. \qquad (4.VII)$$

For example, for aluminum we have $\rho = 2.7$ gm/cm^3, $P_o = 10^{10}$ erg/gm (Bibl.14) and $R \simeq 2.8 \times 10^{-4} \sqrt{E}$.

This relation forms the basis of one of the methods of estimating the energy of meteors in rocket experiments, when the radius of the funnel formed in an aluminum or copper plate is measured and the number of particles is counted from the number of funnels present.

The character of the dependence of the magnitude of the reactive momentum I created in the obstacle upon explosion, on the meteor energy E has been studied with insufficient reliability. In agreement with the investigations by K.P. Stanyukovich (Bibl.14) the existence of a direct proportionality is proposed

$$I = AE, \qquad (5.VII)$$

where A is the proportionality factor depending on the energy densities P_m and P_o, on the angular distribution of the ejected mass, and on the degree of in-

stability of the process.

From other investigations (Bibl.9, 16) follow postulated dependences of the type $I \sim mv^{1.6}$ or mv. Consequently, the use of a piezoelectric transducer, mounted to the receiving plate does not permit a direct measurement of the mass m or the velocity v of a given meteor (since the momentum of impact of the particle against the receiving plate is appreciably smaller than the instantaneously following reactive momentum I caused by ejection of a certain mass of the transducer upon explosion). The measurements can be interpreted on the basis of a dependence of the type $I \sim mv^k$, where k is a certain coefficient subject to refinement.

The sensors reacting to the reactive momentum are known as ballistic sensors or pickups.

A ballistic sensor, in addition to a transducer, contains elements of mass and elasticity. Bending of the elastic element causes deformation of the piezoelectric transducers, which generates an electric pulse. The mass element should have a low elasticity so that the oscillations are damped within a time shorter than the time constant of the recording circuit.

To have the operating conditions of the ballistic sensor depend little on where the particle strikes the mass element, it is necessary to use a sufficiently large number of quartz crystal transducers attached along the perimeter of the mass element and connected in parallel (Bibl.4).

The quality of the piezoelectric transducers is characterized by the /176
piezoelectric modulus d. The piezoelectric modulus is the proportionality factor between the charges q generated at the faces perpendicular to the electric axis of the crystal and the strain force F. If the piezoelectric transducer has the shape of a parallelepiped and a homogeneous tensile force F_x acts on it along the electric axis x (longitudinal piezoelectric effect), then the magnitude of the charges in conformity with the theory developed for quartz (Bibl.15), will be

$$q = F_x d. \qquad (6.VII)$$

The magnitude of the charges in this case, as indicated by eq.(6.VII), does not depend on the geometry of the transducer.

Under the effect of a tensile force acting along the mechanical y-axis of the crystal (transverse piezoelectric effect), the charges created on these faces are

$$q = -F_y \frac{b}{a} d, \qquad (7.VII)$$

where b and a are the width and thickness of the transducer, respectively.

The negative sign in eq.(7.VII) shows that the sign of the charges is opposite, in comparison with the longitudinal piezoelectric effect.

Thus, in the transverse piezoelectric effect the sensitivity of the transducer can be increased by the ratio $\frac{b}{a}$.

In the absence of leakage, the charges q are retained during the entire time of the effect of the force F. Consequently, to obtain the maximum charge, a high degree of insulation of the quartz crystal transducer is required.

An explosion of meteor particles on the surface of the mass element of the ballistic sensor causes damped oscillations of the latter with a frequency ω equal to the frequency of the natural oscillations of the entire transducer. The transducer will be subject to a variable force with a decreasing amplitude. Under the effect of a variable force on the piezoelectric transducer

$$F(t) = F_m e^{-nt} \sin \omega t, \tag{8.VII}$$

charges q will appear on its faces which are determined by the relation

$$q = q_m e^{-nt} \sin \omega t, \tag{9.VII}$$

where F_m and q_m are the amplitude values of the force and charge, respectively; n is the damping factor.

The current i discharging from the transducer through the leakage resistance and input resistance of the measuring circuit R_{in} is determined by the formula /177

$$i = \frac{dq}{dt} = q_m e^{-nt} (n \sin \omega t + \cos \omega t). \tag{10.VII}$$

On using the transverse piezoelectric effect, when eq.(7.VII) is satisfied, we obtain

$$i = dF_{y\ max} \frac{b}{a} e^{-nt} (n \sin \omega t + \cos \omega t). \tag{11.VII}$$

The voltage taken from the load of the wiring circuit is

$$U = \frac{d}{Z} F_{y\ max} \frac{b}{a} e^{-nt} (n \sin \omega t + \cos \omega t), \tag{12.VII}$$

where Z is the impedance of the input of the measuring circuits. Thus, the amplitude of the measured voltage will depend linearly on the applied force $F_{y\,max}$ and will decrease with the damping factor n, the quantities $F_{y\,max}$ and n being inversely proportional to the elasticity of the springs to which the mass element of the ballistic sensor is attached.

To keep the dead time of the sensor small and to prevent spurious damped pulses from being recorded by the measuring circuit, it is necessary to ensure a sufficiently rapid damping of the oscillations (the springs and transducers should be made of a material with a low modulus of elasticity ε).

Crystals of Rochelle salt $NaKC_4H_4O_6 \cdot 4H_2O$ have the highest piezoelectric modulus ($d = 3 \times 10^{-9}$ C/kg); however, they have low mechanical strength and high hygroscopicity, which interferes with their practical application (Bibl.15).

The next best piezoelectric transducers are barium titanate $BaTiO_3$ and ammonium phosphate $NH_4H_2PO_4$. Barium titanate has a piezoelectric modulus of d =

$= 1.07 \times 10^{-9}$ C/kg and a modulus of elasticity of $\epsilon = 1.15 \times 10^{12}$ kg/m^2 (Bibl.15) while the values for ammonium phosphate are $d \simeq 3 \times 10^{-10}$ C/kg and $\epsilon \simeq 5 \times 10^{10}$ kg/m^2 (Bibl.13). These piezoelectric transducers have a sufficient water resistance and stability of the piezoelectric modulus in a wide range of temperatures; however, the smaller elasticity of ammonium phosphate permits its wider use in sensors where the transducer is attached to springs and should play the role of a damping element.

The equivalent circuit of a piezoelectric transducer (Fig.2.VII) contains a transducer capacitance C_0, input capacitance of the measuring circuit C_{in}, transducer resistances (volume and surface) R_0, and an input resistance of the measuring circuit R_{in}. The quantity of electricity produced by the piezoelectric transducer at the instant of applying a constant force F is

$$q_0 = U_0(C_0 + C_{in}). \qquad (13.VII)$$

The time rate of change of the output voltage under the continuous effect /178 of the force F will be determined by the time constant of the transducer circuit, namely,

$$U(t) = U_0 e^{-\frac{t}{RC}} \approx \frac{q_0}{C}\left(1 - \frac{t}{RC}\right), \qquad (14.VII)$$

where $C = C_0 + C_{in}$ and $R = \frac{R_0 + R_{in}}{R_0 R_{in}}$.

By assigning a measurable value of the ratio $\frac{U(t)}{U_0}$ during the time t, counted from the moment of applying the force, we can determine the necessary parameters R and C. The value of R_0, however, should be sufficiently large to reduce the charge leakage from the sensor, so that the inequality $R_0 \gg R_n$ is usually satisfied.

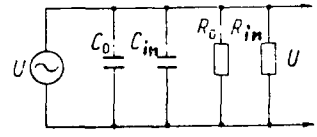

Fig.2.VII Equivalent Circuit of Piezoelectric Transducer.

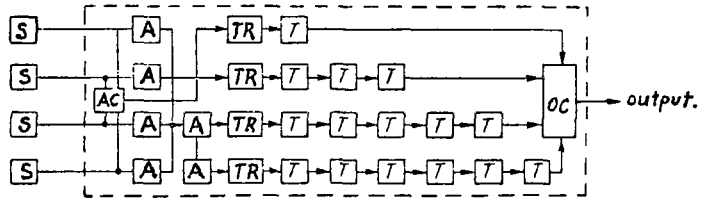

Fig.3.VII Block Diagram of Equipment for Measuring Micrometeors.

When measuring short pulses, the value of RC should be small; however, the requirement of a sufficiently large value of R_o (for insulation) is retained. As a consequence, there is a tendency to make the self-capacitance of the sensor increasingly smaller, for which purpose its area is also made smaller. If it becomes necessary to increase the receiving surface of the equipment, several sensors connected in parallel are used.

The block diagram of the Soviet equipment for investigating micrometeors on rockets and satellites (Bibl.1, 7) is shown in Fig.3.VII. Here, four ballistic sensors S are used, whose signals are recorded over four channels (ranges) of different sensitivity. The signal from each sensor is fed to individual amplifiers A which are elements of the adder circuits.

Pulse height selection is accomplished by threshold counting circuits, which are switched on after passage of various number of stages of the amplifier A. The signal corresponding to the first range is taken directly from two /179 sensors across the resistance-coupled adder circuit AC. The number of pulses in each amplitude range is counted by means of the flip-flops T.

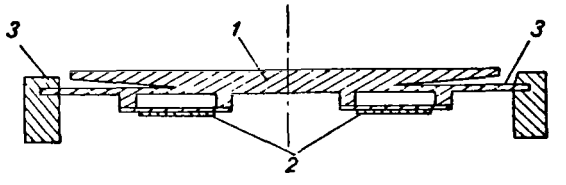

Fig.4.VII Diagram of the Ballistic Sensor.

So that repeated operation of the counting circuit under the effect of damped oscillations of the strong signal of the ballistic sensor is eliminated, a trip relay (monostable multivibrator) TR with a dead time of 0.06 - 0.08 sec is installed at the input of each circuit. As a consequence, the dead time of the counting circuit τ is high, and its resolving power $1/\tau$ is only 12 - 17 impacts per sec (Bibl.7). This counting rate, as follows from the characteristics of the recurrence of meteors (see Sect.1 of this Chapter) is sufficient. The TR circuits simultaneously act as threshold devices.

The counting circuit of the most sensitive (fourth) range has six flip-flops and performs scaling to 32. The trigger pulse of the trip relay of this range is taken from the last stage of the amplifier and permits recording of the sensor signals of a magnitude of 0.001 v and higher, without limitation (Bibl.7).

The output circuit OC which is fed with the outputs of all four ranges, is a resistance-coupled adder with a ratio of 1:2:4:8.

The ballistic sensor used in this equipment is a plate (1) (Fig.4.VII) mounted on supports by means of springs (3). The lower portion of the plate carries four ammonium phosphate piezoelectric elements (2). The eigenfrequency of the sensors is about 400 cps (Bibl.7). The equipment is able to record meteor particles with a mass up to 1 billionth of a gram moving at a velocity

of about 40 km/hr (Bibl.1).

The equipment with piezoelectric transducers, used in the USA, is designed along the same principles (Bibl.3). The basic difference of the sensor lies in the use of only one transducer (microphone) attached at the center of the /180
aluminum sensor surface with an area of 0.038 m^2 mounted on rubber shock absorbers.

The instrument installed on the Explorer-I had one recording channel with a linear dependence of the recorded signal amplitude on the momentum of the particle (from 10^{-2} to 50 dyne/sec).

The instrument installed on the lunar probe Pioneer-I had two channels tuned to different levels of pulse recording. These levels were obtained by tapping one channel after the second stage of the amplifier and the second channel after the third stage (Bibl.16).

Section 3. Measuring Procedure

Equipment with ballistic sensors permits measuring the total stream of meteor particles and determining, within a limited range, the spectrum of recorded pulses. On the basis of the latter, it is possible to estimate the distribution of particles by energy and to calculate their mass if a certain flight velocity of the particles is given. Equipment of this type was widely used in various modifications, both on geophysical rockets and on spacecraft (see Fig.1.VII). Ballistic sensors, combined in groups, were installed directly on the shell of the capsule.

In the first rocket flights, it was found that at low thresholds of recording pulses in the high-sensitivity channel, particles impinging not only directly on the sensing surface but also on the casing of the sensor or on components of the rocket were recorded (Bibl.11). Therefore, in later equipment the recording thresholds were increased so as to reduce these effects. Thus, in the equipment installed on Soviet spacecraft the high-sensitivity range was adjusted to count the pulses of the sensor with an amplitude of at least 1 mv. Taking into account that the recorded pulse is proportional to the energy of the particles, then at their velocity of v = 40 km/sec this corresponds to recording particles with a mass of at least 10^{-9} to 10^{-8} gm. The medium-sensitivity channel was adjusted to record particles with a mass of at least 10^{-8} to 10^{-7} gm, and the low-sensitivity channel of at least 2×10^{-7} gm (Bibl.12).

The instrument is calibrated under laboratory conditions. The procedure is the same in the USSR and in the USA (Bibl.7, 16). It consists of measuring the amplitude of pulses obtained at the output of the instrument when steel balls of a known mass M are dropped on the working surface of the sensor. The height of drop h_1 and the height of rebound h_2 are measured. The momentum imparted to the sensor is determined by the known formula

$$mv = m\sqrt{2g(h_1 - h_2)}, \qquad (15.VII)$$

where g is the acceleration of gravity at a given latitude.

The calibration curve is plotted as the dependence of the output voltage U_{out} on the moment of momentum $U_{out} = f(mv)$. The curve is practically linear within a wide range from 10^{-1} to 10^{3} dyne/sec, and the equipment records vibrations of the carrier only in the outgoing section (Bibl.7, 16). Processing of the telemetry data consists in determining U_{out} for various instants of time, and from this the moment of momentum mv. If we consider that the reactive momentum is proportional to the particle energy or moment of momentum, then - if a definite velocity is assumed [v being equal to 40 or 50 km/sec in the USSR or 30 km/sec in the USA (Bibl.11, 16)] - the minimum recordable particle mass can be determined. /181

The error of counting the particles and determining their flux through unit cross section is small; it is determined by statistical functionals which were discussed above for similar circuits (see Chapt.V). As we mentioned there, the mass is estimated in first approximation with an uncertainty factor of the order of 3 (Bibl.11).

CHAPTER VIII

MEASUREMENT OF ELECTROSTATIC AND MAGNETIC FIELDS

Section 1. Basic Principles of the Atmospheric Electrostatic Field

Electrostatic fields in the atmosphere are generated upon the formation of space charges. In the upper atmosphere, by virtue of its excellent conductivity, protracted existence of high stationary space charges is improbable, whereas space charges forming in the troposphere may reach tens of Coulombs. Close to thunderclouds, the electrostatic field strength, for example, may be quite high (up to $10^{3} - 10^{4}$ v/cm).

An electrostatic field is observed also close to all charged bodies existing in the atmosphere. Close to the earth, in particular, an electrostatic field caused by its negative charge is active.

The strength (potential gradient) of the electrostatic field close to the earth during clear weather is different at different points. It changes from several tenths of volts to several volts per centimeter and its vector is directed toward the earth. The average value of the strength of the normal earth field is $E_{on} = 1.3$ v/cm. The surfaces of a normal field of the earth are caused by space charges of clouds, precipitation, etc.

The normal field of the earth decreases with the height h by an exponential law of the type

$$E_n = E_{0n} e^{-ah}, \qquad (1.VIII)$$

where E_{on} is the strength of the normal field close to the earth, and a is a constant. /182

At a height of about h = 10 km the normal field, as we see, is already very

weak. There is little information available at present on electrostatic fields and thus also on space charges in the upper atmosphere, since development of direct measurement methods started only recently both in the USSR (Bibl.14, 3) and in the USA (Bibl.21).

Measurements carried out on geophysical rockets of the USSR since 1957 (Bibl.3, 12) showed that the electrostatic field near the surface of a rocket mainly corresponds to its negative charge and, on the average, is equal to 0.2 - 2 v/cm . The maximum value of the field strength reached 6 v/cm, and trajectory segments were observed where the rocket acquired a positive charge. Comparatively weak external electrostatic fields, not associated with the charge of the rocket, have also been recorded. The external field strength was found to be of the order of $E \approx 10^{-3}$ v/cm, and its magnitude did not change by more than a factor of 3 - 5 within heights of 100 - 440 km.

The electric field near the third satellite was also small. The field strength did not exceed a value of E = 3 v/cm; however, in these measurements the results were substantially distorted by the presence of noise (Bibl.11).

The necessity to measure the electrostatic field near the surface of the carrier is due primarily to the effect of the field on the measurements of various environmental parameters (see Chapt.II). These measurements help to define the causes of magnetic storms and polar auroras, the causes of electrification of the earth and atmosphere, etc.

Measurements of the electrostatic field strength near the surface of a space vehicle are also important for solving technical problems, in particular for determining the operating conditions of ion devices.

Section 2. Principle and Procedure of Measuring the Electrostatic Field

Measurements of electrostatic field strength are based on the correlation between the surface density of an electric charge of a conducting body in this field and its strength. The surface density of a charge σ induced on the surface of a conductor, as follows from the known theorem of Ostrogradskiy-Gauss, is associated with the normal component of the field strength at a given point E by the relation

$$\varepsilon E = 4\pi\sigma, \tag{2.VIII}$$

where ε is the dielectric constant of the medium.

If, in a uniform field of strength E, a conducting plate with a surface s normal to the field is inserted, then the charge induced on it

$$q = \frac{\varepsilon E s}{4\pi}, \tag{3.VIII}$$

and the potential of the plate caused by this charge, will be /183

$$V = \frac{\varepsilon E s}{4\pi C}, \tag{4.VIII}$$

where C is the capacitance of the plate.

Measurements of the field strength E, based on these relations, can be accomplished by static and dynamic methods. In the former case, the quantity E is determined by measuring the charge of a certain body in a field by means of eq.(3.VIII). This method, however, is more difficult to use in the upper atmosphere since, for such measurements, highly sensitive electrometers are needed and rather high requirements for insulation must be met.

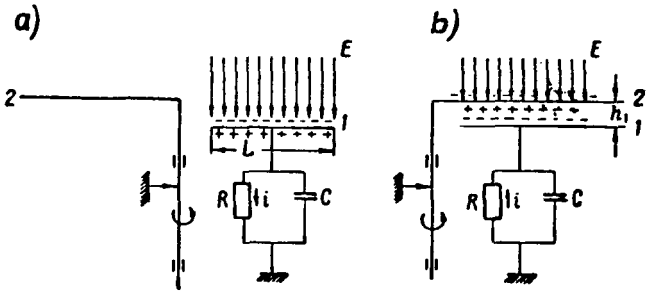

Fig.1.VIII Principle of Action of an Electrostatic Generator.
a - With exposed plate; b - With shielded plate.

The dynamic method, based on the use of so-called electrostatic generators or fluxmeters, is more reliable. The mode of action of the fluxmeter consists in converting the electrostatic field to an alternating voltage or current by periodic exposure and shielding of the conducting body in the field being measured. In this case, movement of the charges induced in the body creates a measurable alternating electric current. The magnitude of the current is directly proportional to the magnitude of the field strength (Bibl.13).

The electrostatic generator, representing the receiving element of the instrument, contains a measuring plate (1) (Fig.1.VIII) and a rotating shield (2). The shield and plate are connected with the casing of the object (capsule), and a load resistance R, shunted by the capacitance C, is connected into the plate circuit (1). When the plate (1) is exposed (Fig.1a.VIII) a negative charge /184 will be induced on its upper surface under the effect of the field E being measured and a positive charge on the lower surface. As a consequence, a current i will flow through the resistance R to the skin of the capsule. When the plate (1) is shielded, a current of opposite direction will flow through the resistance R, compensating the negative charge of the plate. At alternating exposure and shielding of the measuring plate, an alternating current i will flow through the load resistance R, whose magnitude, according to eq.(3.VIII), will be equal to

$$\pm i = \pm \frac{\varepsilon E}{4\pi} \frac{ds}{dt}, \qquad (5.\text{VIII})$$

where $\frac{ds}{dt}$ is the rate of change of the surface area of the plate.

The instants of the change in sign of the current i coincide with the start

of shielding or exposure. At a constant rate of change of the area s, as follows from eq.(5.VIII), the absolute value of the current i will not change in a constant field.

In the equipment being used, the frequency of exposing the plate ν is of the order of 10^3 cps. The rate of change of the plate area in this case is of the order of $\frac{ds}{dt} \approx 10^4$ cm^2·sec^{-1} (Bibl.12). Based on this quantity, eq.(5.VIII) makes it possible to estimate the magnitude of the current of the measuring plate i. For example, in a field of E = 1 v/cm this current will be $i \approx 10^{-9}$ amp. The voltage drop across the resistance $R = 10^5$ ohm will be $U \approx 10^{-4}$ v. This voltage should be amplified and measured by the electronic circuit of the instrument. We note that the load resistance R in the upper atmosphere may be shunted by the resistance of the ambient medium. To avoid this, the value of R should be sufficiently small.

It follows from the operating principle of the electrostatic generator that a reversal of direction of the vector of the field strength E will result in a phase shift of the current i or of the voltage U by 180°. This can be recorded by the measuring circuit whose output is provided with a phase detector.

The block diagram of the instrument (Fig.2.VIII) shows the above-mentioned basic elements.

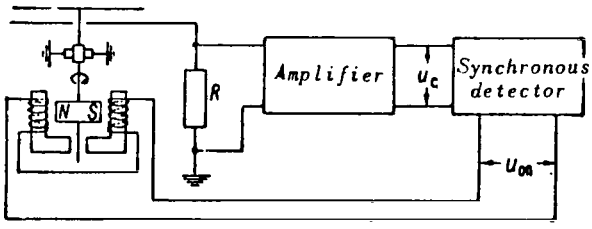

Fig.2.VIII Block Diagram of Instrument for Measuring Electrostatic Field Strength.

Measurements in the upper atmosphere, however, are accompanied by the appearance of a noise current i_2, which can be reduced by modifying the described circuit. Let us examine the antinoise measures proposed by Ya.M.Shvarts (Bibl.18).

The generation of noise is due to the following basic causes:

a) currents on the surface of the measuring plate, owing to its motion in the plasma;
b) photoemission from the plate under the influence of solar short-wave radiation;
c) induction of charges, owing to motion in a magnetic field. /185

The magnitude of the total noise current i_2 evidently is determined by the

exposed surface of the plate s

$$i_2 = j_2 s, \qquad (6.VIII)$$

where j_2 is the noise current density.

The time diagrams of the useful current of the signal i_1 and of the noise current i_2 at a constant rate of change of the exposed surface $s\left(\frac{ds}{dt} = \text{const}\right)$ are shown in Fig.3.VIII.

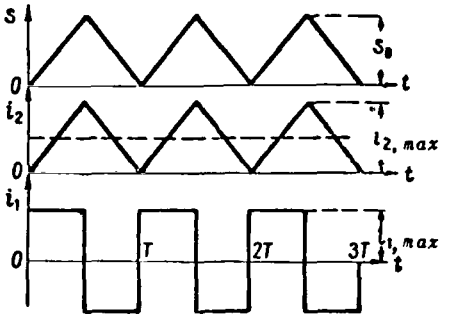

Fig.3.VIII Time Diagrams of the Currents of an Electrostatic Generator.

The total voltage entering the measuring circuit from the output of the electrostatic generator will be the result of the effect of the signal current i_1 and noise current i_2 on the output RC-loop of the generator (see Fig.1.VIII).

A harmonic analysis (Bibl.18) showed that the phase shift between corresponding harmonics of the voltages of the signal U_1 and of the noise U_2 is equal to the phase shift between the currents i_1 and i_2, i.e., 90°, where the form of the voltages and currents differs. The signal-to-noise ratio $\frac{U_1}{U_2} = m$ at the output of the electrostatic generator (or at the input of the measuring circuit), operating in a medium with a dielectric constant ε, is equal to

$$m = \frac{\varepsilon E \nu}{2 j_2}. \qquad (7.VIII)$$

When taking measurements in the plasma of the upper atmosphere, where /186 the noise current density reaches a value of $j_2 = 10^{-6}$ to 10^{-7} amp/cm^2 (Bibl.18), the signal-to-noise ratio becomes appreciably less than unity ($m \approx 10^{-2}$ for an instrument with an exposure frequency of $\nu = 10^3$ cps in a field of E = 1 v/cm^2).

Several methods of suppressing the noise current are possible. One is to use a phase-sensitive element at the output of the measuring circuit, exactly tuned to the first harmonic of the signal voltage.

Noise suppression at the output of the instrument may lead to overloading of the amplification circuit. Therefore, antinoise measures must also be taken at the input of the measuring circuit.

A method of modulating the electrostatic field without modulating the noise current, by using latticed electrodes, has found practical use in the instrumentation of geophysical rockets (Bibl.12).

An estimate (Bibl.18) shows that the overall increase in sensitivity of the instrument obtained with the use of all possible antinoise measures may become 10^5 to 10^6-fold. This means that, against a background of maximum possible noise current in the ionosphere, it is possible to measure fields close to the surface of the carrier with a strength of at least $E_i \approx 3 \times 10^{-2}$ v/cm (at an exposure frequency of $\nu = 1500$ cps).

Section 3. Equipment Used

The equipment developed by G.L.Gdalevich, I.M.Imyanitov, and coworkers was used to measure the magnitude and sign of the electrostatic field at two diametrally opposite points of the capsules of geophysical rockets (Bibl.3) and on the third satellite (Bibl.11). Similar equipment, as far as we can judge from another paper (Bibl.21), was used also in the USA.

The placement of the sensors (electrostatic generators) and measuring unit MU on the third satellite (Bibl.11) was shown in Fig.5.I.

The block diagram of the equipment was described earlier (see Fig.2.VIII).

The measuring and shielding plates were made in the form of flat nickel-plated brass disks with six uniformly arranged sector cutouts.

The output voltage of the reference voltage generator (RVG) had a frequency of 900 cps (equal to the signal frequency) and an amplitude of about 100 v. It was driven by a motor M having a stabilized rotational speed of 9000 rpm within an accuracy of ±2 - 3%.

The measuring circuit consists of two channels, each of which is connected with its own electrostatic generator (one channel is shown in Fig.4.VIII). Both channels are designed in the same manner and include an amplifier, a synchronous detector, an output (matching) cathode follower, and a device for automatic /188 sensitivity switching. The channels are supplied from a common diode (D_6 - D_9) rectifier.

The three-stage AC amplifier is composed of 6Zh1B tubes L_1, L_2, and L_5; it also contains a 900-cycle frequency filter. The passband of the amplifier with respect to the 0.95 level is equal to 100 cps. The amplification factor at maximum sensitivity is $K_U = 5 \times 10^5$. The automatic sensitivity switch is a two-stage amplifier composed of 6Zh1B tubes L_3 and L_4 which controls operation of the relay P1. The latter, at a sufficiently high signal voltage, reduces the sensitivity by switching the resistance-coupled (R_{25} and R_{26}) divider into the circuit.

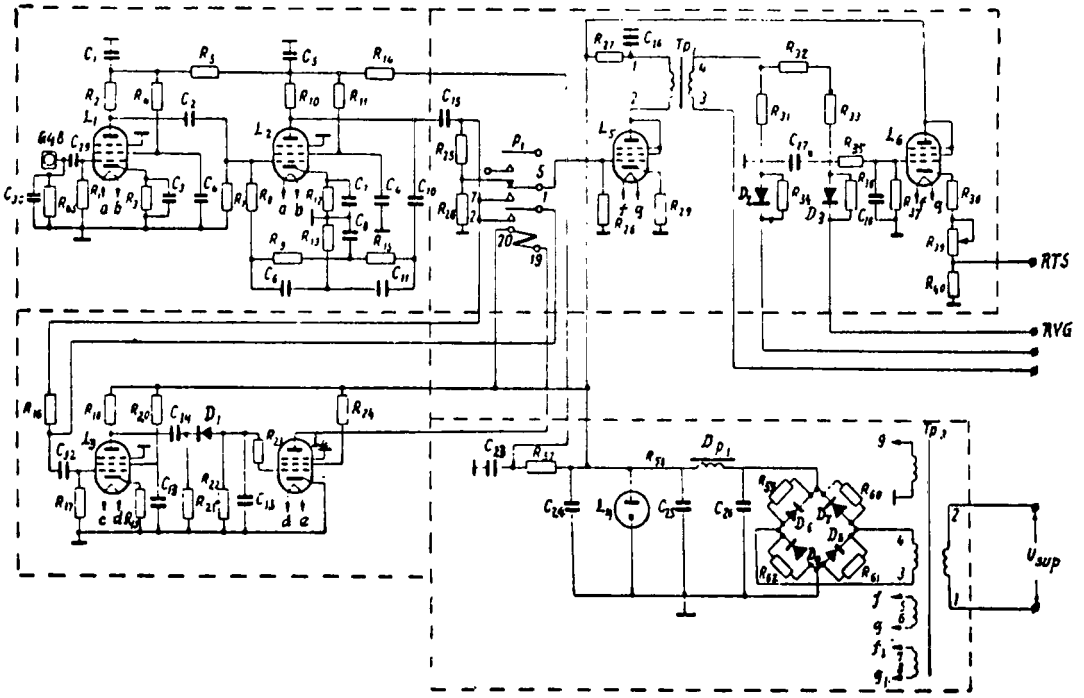

Fig.4.VIII Principal Wiring Diagram of One Channel of the Instrument for Measuring the Electrostatic Field Strength.

The maximum sensitivity of the instrument (before switching to the coarse range) is such that 0.1 v at its output corresponds to a measured field strength $\Delta E = 0.2$ v/cm. Switching to the coarse range (and back) occurs at a strength $E_1 = 6$ v/cm (without consideration of the noise current).

The synchronous detector is a bridge into whose two arms DGTs-8 diodes D_2 and D_3 are connected. The measured voltage is fed to the synchronous detector from the third stage of the amplifier (tube L_5). The reference voltage RV is generated by the reference voltage generator RVG.

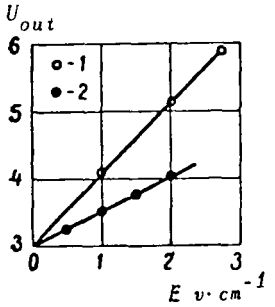

Fig.5.VIII Calibration Curves of the Instrument for Measuring the Electrostatic Field Strength.

The time constant of the instrument $\tau = 5 \times 10^{-5}$ sec (Bibl.3) is approximately by one order of magnitude greater than the calculated time of establishing the plate potential.

Calibration of the instrument was done in the conventional manner (Bibl.13) by using an auxiliary plate to which a known potential was applied from an auxiliary source. This plate was placed at a distance of 1 cm from the measuring plate. The calibration curves of this equipment are plotted in Fig.5.VIII. Curve 1 was obtained with a calibration plate and curve 2 in a flat capacitor. We note that in this case the correction factor, which usually takes the edge effects into account, is equal to 2.2.

Studies of this type of equipment (Bibl.3) showed that its sensitivity drift during flight does not exceed 15% and that its zero drift is not more than 0.2 v in 30 min. Since 0.2 v corresponds to an external field strength of 0.4 v/cm, the maximum error of the field measurements in the absence of noise is considered to be not more than 0.6 v/cm or approximately 20% if $E \geq 3$ v/cm. However, the presence of noise may substantially distort the results obtained (Bibl.12, 10).

Section 4. Magnetic Field in the Atmosphere and in Space /189

The geomagnetic field can be represented with great accuracy by a dipole field having a magnetic moment $M = 8.3 \times 10^{25}$ oe·cm^3, whose south pole is located close to the north pole N and whose axis is inclined to the axis of rotation of

the earth at an angle of about 12°. The intercepts of the axis of the equivalent dipole (Fig.6.VIII) with the surface of the earth are called the geomagnetic poles. The horizontal component of the field strength has a maximum value (about 0.4 oe) near the Equator and the vertical component, near the poles (about 0.7 oe).

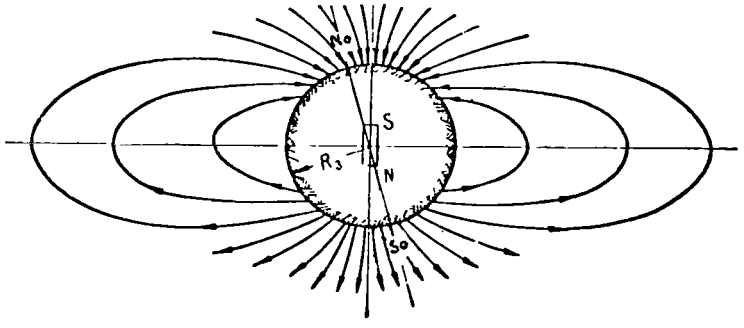

Fig.6.VIII Isolines of the Earth's Magnetic Field.

The remanent field obtained by subtracting the field of the homogeneously magnetized earth from the observed field mainly represents six world anomalies, whose strength differs by a magnitude up to 30% from the strength of a normal dipole field. These anomalies include the Eastern Siberian continental anomaly extending over the entire territory of the Soviet Union with a peak at the center of about 0.6 oe West of Yakutsk (Bibl.7), the African anomaly opposite to it in sign, the anomaly close to Antarctica, and others.

The numerous regional and local anomalies of the earth's magnetic field, which reflect the structure and composition of the outermost layers of the earth's crust, render any map of the magnetic field quite varied. A study of the distribution of these anomalies forms the basis of magnetic surveying methods.

The magnetic field of the earth is usually divided into constant and variable fields. The constant field also includes very slow, so-called secular field changes, while all other more rapid changes such as magnetic storms, fluctuations, diurnal variations, etc. belong to the variable field. The diurnal variations reach 40 gammas ($\gamma = 10^{-5}$ oe) and more. The amplitude of variation /190 in the horizontal and vertical components of the field strength during magnetic storms reaches hundreds and thousands of gammas. In such a case, abrupt changes of the field may occur within a short period, counted in seconds (up to 20,000 gammas/sec).

Numerous analyses of the constant field show that 99% of the field is produced by sources within the earth. Most of the variable field (about 70%) is due to extraterrestrial sources.

The magnetic field strength at a distance R from the earth decreases ap-

proximately by an exponential law [proportional to the ratio $\left(\frac{R_3}{R_3+R}\right)^3$ where R_3 is the earth's radius], dropping from 1500 γ at a height of about 18,000 km to approximately 100 γ at a distance of 50,000 km (Bibl.8).

Investigations of the field in the immediate vicinity of the earth, at distances R from 0.05 to 0.5 R_3, which are of greatest interest and were the most extensive of the studies made with the third satellite, make it possible to establish a correspondence between the measured and calculated values of the geomagnetic field with an accuracy to within 0.1 - 1.5%, which lies within the limits of accuracy of modern magnetic charts (Bibl.7). At greater distances R = = 2.5 - 4 R_3 substantial deviations of the measured values of the field from the calculated values occurred, both with respect to magnitude and character of the gradients. At distances greater than 8 R_3 the measured values of the total vector of the field strength were higher than the calculated values; at a distance of 13 R_3, this excess reached 100% although the overall variation of the field is characterized by its decrease with distance from the earth. At distances of 10 - 15 R_3, appreciable field fluctuations are observed with respect to magnitude and direction (by approximately 50%, at an absolute magnitude of strength of several tens of gammas). Sh.Sh.Dolginov and N.V.Pushkov (Bibl.7) suggest that this region is transitional between the geomagnetic field and the solar plasma.

Streams of solar ionized gas are able to transport magnetic fields with a magnitude up to 10^{-4} gauss to great distances from the sun. The velocity of these streams is comparable with the velocity of space vehicles, so that the duration of the effect of "frozen" fields on the magnetometric instruments may be sufficiently great.

Measurements of the magnetic field in interplanetary space, performed during flights of the Pioneer-V (1960) and of the Soviet interplanetary spacecraft launched toward Venus (1961) yielded field strength values during quiet days of 2 - 5 γ and during storms, of up to 50 γ (Bibl.7).

A direct study of the magnetic field of celestial bodies began with the flight of the second Soviet lunar probe. During these measurements, up to distances of 55 km from the lunar surface, no signs of a noticeable magnetic /191
field were noted, at a threshold sensitivity of the equipment of 20 - 30 γ (Bibl.5). The American spacecraft Mariner-2 (1962), at a distance of 32,000 km from the surface of Venus, also detected no noticeable magnetic field. These data indicate that the magnetic moment of the moon cannot be more than 10^{-4} and that of Venus 10^{-1} of the magnetic moment of the earth (Bibl.7).

Sunspots are accompanied by intense magnetic fields whose strength reaches 4×10^3 oe. Fields of this order were found also for certain stars. The presence of a general dipole field has not yet been reliably established for the sun. The most probable magnetic moment of the sun is considered to be $4 \times \times 10^{33}$ oe·cm^3. At this value of the moment, the field strength at the solar poles should be about 25 oe, whereas on earth the field strength of the sun is not more than 10^{-6} oe (Bibl.7).

The magnetic fields play a major role in processes taking place in outer space and in the upper atmosphere. These fields affect the movement of large particles in the atmosphere and of particles entering from without; influence the character of radiowave propagation; cause latitudinal effects in cosmic rays (see Chapt.V); are associated with the formation of the radiation belts, etc.

The characteristics of measuring magnetic fields in the upper atmosphere and in space require the measurement of rather small quantities in a large range and at a high rate of change of the field in time and space and also in the presence of appreciable magnetic disturbances caused by various measuring and auxiliary equipment that generate such fields on the space vehicle.

A main task of present-day investigations is to refine the available data and to accumulate data for various conditions and geophysical processes and also to perform magnetic surveys at great heights.

Section 5. Magnetometric Equipment

Measurements in the upper atmosphere and space are accomplished by magnetometers based on various principles: induction, magnetodynamic (ferroprobe), nuclear or atomic resonance, and optical pumping.

Instruments operating by all of these methods have found practical application, with the most widely used being ferroprobe three-component magnetometers (with saturated cores) by means of which the most important results of measurements were obtained, especially in the USSR (Bibl.7). In these magnetometers there are three completely identical independent channels, each of which /192 measures the magnitude of the projection of the field strength vector $\vec{T}$ onto the axis of the saturated core. The range of measured quantities is determined by the sensitivity. By installing the pickups along three mutually perpendicular directions, three field components T_x, T_y, T_z are obtained, from which the total vector is determined. For example, on the first Soviet spacecraft (Jan.2, 1959) a ferroprobe three-component magnetometer with independent channels was used. The measuring range with respect to each channel was $\pm 3000\ \gamma$ at a sensitivity of $600\ \gamma$ per volt on the telemetry scale (Bibl.4).

The first magnetic surveys in space were performed by means of a self-orienting ferroprobe magnetometer installed on the third satellite by Sh.Sh. Dolginov et al. (Bibl.9). Ferroprobe three-component magnetometers were installed on the interplanetary spacecraft launched in the USSR toward Venus and Mars (Bibl.4 - 8).

Magnetometers of this type were also used in the USA. In particular, they were installed on Explorer-X and Explorer-XII and on Mariner-II (Bibl.7).

The three-component magnetometer with ferroprobe pickups installed on the Explorer-XII (1961) had a range of $\pm 1000\ \gamma$ for each channel and an error of not more than $\pm 20\ \gamma$ (Bibl.7). The instrument installed on Mariner-II (1962) had a higher sensitivity: the entire range for each channel was only $\pm 60\ \gamma$ (Bibl.7).

Single-channel instruments with ferroprobe pickups were used as variometers [Venus and Mars probes (Bibl.6, 7), Explorer-X (Bibl.7)]. One-component magnetometers of the ordinary induction type were successfully used on the first American spacecraft, Pioneer-I, Pioneer-V, Explorer-VI (Bibl.7, 21).

To increase sensitivity, nuclear-induction, mainly proton [Vanguard-III and others (Bibl.7, 20)] and also rubidium-vapor [Explorer-X (Bibl.7, 22)] magnetometers have recently come into wider use in the USA in space research on the magnetic field.

Features of the proton magnetometers include their higher sensitivity and accuracy and the absoluteness of the measurements; magnetometers of this type are generally used as standards. However, Hepner et al. (Bibl.24) mentioned that magnetic surveys in space do not require measurement of the field with an accuracy of more than 0.1%, since the low accuracy of tying-in the data with respect to satellite orbit measurements places a limit on the required accuracy of the measurements. Thus, in measurements with the nuclear-induction magnetometer installed on Vanguard-III the total error of measurement at a height of /193
500 km was at least ±60 γ (±40 γ at a height of 1000 km) although the measurement error of the field by the instrument itself was appreciably less (Bibl.7, 24).

Optically-pumped magnetometers apparently have good prospects for future use in investigations of the magnetic field. Their virtues are a wide range of measurable quantities, appreciably lower power consumption than that of nuclear-induction magnetometers, rapid response, and absoluteness of the measurements. For example, the rubidium-vapor magnetometer installed on Explorer-X operated in a range from 3 to 10,000 γ. Its total weight was only 1.2 kg, and the power requirement was 5.5 w (Bibl.22). According to the data by K.Ruddock (Bibl.22), a sensitivity to 0.001 γ can be obtained for magnetometers of this type.

Section 6. Principles of the Nuclear-Induction Method

The nuclear induction method of measuring field strength utilizes the phenomenon of free precession of a nucleus in an external magnetic field.

The frequency of nuclear precession in a magnetic field, whose direction does not coincide with that of the magnetic moment of the nucleus, is determined by the relation

$$\omega = \Gamma (1 - \sigma) T, \qquad (8.VIII)$$

where Γ is the gyromagnetic ratio equal to the quotient from the division of the magnetic moment by the angular moment, σ is a small quantity taking into account the shielding of the nucleus by the electron shell (sometimes disregarded).

On the basis of eq.(8.VIII) the measured frequency of the free precession of the nucleus will yield the scalar quantity of the total field strength T. The gyromagnetic ratio of protons $\Gamma_p = (2.67528 \pm 0.00006)10^4$ cm^{-1} · oe^{-1} is known with extreme accuracy. Therefore, proton magnetometers operating on the principle of measuring the frequency of free precession of protons in the work-

ing medium of the sensor are in general use. The character of the precession of an atom depends on the magnitude of the external field: in weak fields ($T < 10^2$ oe) it precesses with the total magnetic moment as a whole; in strong fields the bond between the nuclear and electron moments is ruptured so that these vectors precess about the external field independently of one another.

To obtain free precession in the working medium of the sensor, a sufficiently strong magnetic field ($T > 10^2$ oe) must first be set up, causing nuclear magnetization, after which the frequency of nuclear precession can be measured. Thus, the measuring proceeds in discrete steps, consisting of excitation (polarization) of the sensor and measurement of the frequency ω. Nuclear magnetization of the sensor is brought about by the effect of the magnetic field of an exciting coil, encompassing the working body. The exciting field should be directed approximately perpendicular to the measured field $\vec{T}$. In this case, the macroscopic magnetization of the body M increases with time t by the exponential law /194

$$M(t) = \varkappa T_0 \left(1 - e^{-\frac{t}{t_r}}\right), \qquad (9.\text{VIII})$$

where $\varkappa$ is the magnetic susceptibility of the body of the sensor, T_0 is the strength of the exciting field, and t_r is relaxation time.

For substances whose magnetic susceptibility is small, the required magnetization M is achieved over a rather long time $t \geq t_r$ (for water, which is frequently used in the sensors of proton magnetometers, the quantity $t_r = 3$ sec). The possibility of increasing the magnetization M by increasing the field strength T_0 in the exciting coil is limited by the possible power consumption of the instrument and by the appearance of transients in the magnetizing circuit (in a field $T_0 > 200$ oe). After switching off the exciting field T_0, the macroscopic magnetic moment of the working body begins to precess freely about the measured field T, with a frequency ω. To find the latter, the frequency of the voltage ω induced in the same coil switched to the input of an amplifier is measured. The amplitude of the variable emf excited by the field decreases with time by an exponential law, in conformity with the decrease in the macroscopic magnetic moment of the working body. Consequently, the signal amplitude U arising in the coil is equal to

$$U = U_0 e^{-\frac{t}{t_p}}, \qquad (10.\text{VIII})$$

where $U_0 = k\varkappa T_0 T\Gamma \sin^2\theta$ is the initial signal amplitude, k is a constant depending upon the coil parameters, t is the time from the instant of cutoff of the exciting field, and θ is the angle between the field strengths T and T_0.

We see from eq.(8.VIII) that the accuracy of determining the field strength by this method is determined by the accuracy of measuring the precession frequency ω and by the reliability of knowing the gyromagnetic ratio Γ and the quantity σ. For example, for water the relative error of determining the quantity $\Gamma(1 - \sigma)$ is 7.5×10^{-6}. This permits measuring a field with a strength of $T = 10^4 - 10^5$ gammas with an error of not more than 0.1 - 1 gamma, if the relative error of measuring the precession frequency is of the same order, i.e.,

$\pm 10^{-4}$% (Bibl.15). The block diagram of the nuclear magnetometer (Fig.7.VIII) contains a sensor S, an exciting battery B furnishing the polarization current (up to several amperes), an amplifier A, and a transmitter Tr whose frequency is modulated by the sensor signals. /195

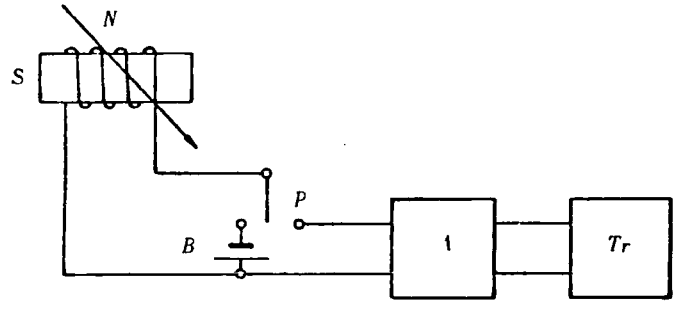

Fig.7.VIII Block Diagram of Nuclear Magnetometer.

Our own nuclear magnetometer AYaAM-6, designed along similar lines (Bibl.1), has the following basic technical characteristics: measuring limits 46,000 - 56,000 γ, measurement error ±1 γ at a measuring time of 1 sec and ±2 γ at a measuring time of 0.5 sec.

The method of measuring the magnetic field on the basis of nuclear induction has the following important features:

1. The results of the measurements are absolute.
2. The accuracy of measuring the field is high and is determined only by the accuracy of measuring the frequency.
3. The sensor and measuring channel are theoretically free from zero drift.

However, complications arise when using this method on space vehicles which hamper the measurements and increase the error. The causes of these complications are as follows:

1. The precession frequency does not depend on the orientation of the exciting coil with respect to the vector of the measured field strength $\vec{T}$, but the amplitude of the signal is proportional to $\sin^2 \theta$ and, at a small angle θ, is close to zero.

2. Upon rotation of the coil together with the carrier at a rate of $\frac{d\varphi}{dt}$ about an axis perpendicular to the coil axis, the field will be measured with an error

$$\Delta T = \pm 3.7 \frac{d\varphi}{dt}, \qquad (11.VIII)$$

where T is expressed in gammas and $\frac{d\varphi}{dt}$ is expressed in rad/sec (Bibl.15).

3. There is a strong dependence of the results on external noises, causing field gradients in the sensor.

4. The amplifier of the magnetometer should ensure a sufficiently high /196 signal-to-noise ratio in a broad frequency band.

5. There is large power consumption, and the measurements have a discrete character. The former drawback is caused by the endeavor to obtain a sufficiently high signal-to-noise ratio at the output of the sensor. Thus, for a signal-to-noise ratio equal to 12 in a proton magnetometer designed for measurements on board a satellite in the wide range of 15 - 55,000 gammas and having an amplifier passband of the order of 1600 cps, a polarization power of about 200 w is required (Bibl.15). The latter drawback can be eliminated by using methods of dynamic polarization.

Section 7. Optical Pumping Method

This method is based on measuring the resonance frequency of splitting energy levels of atoms in a magnetic field. This is done by optical pumping in an auxiliary magnetic field whose frequency is brought to resonance and measured.

It is known that, for atoms located in a magnetic field, splitting of the energy levels into several sublevels occurs (Zeeman effect); the atoms acquire an additional angular momentum determined by the magnetic quantum number m. The intensity of the process of splitting the atomic levels depends upon the field strength T, since the Zeeman frequency coincides with the Larmor frequency of precession of electrons determined by the formula $\nu = \frac{\omega_L}{2\pi} = \frac{eT}{2\pi mc} \approx 28$ cps/γ. To measure the resonance frequency, population of one of the energy sublevels by atoms and then their resonant transition to another sublevel are effected. The population of the sublevel in the vapors of alkali metals and of certain gases [for example, helium (Bibl.19)] can be accomplished by optical pumping. For this, a chamber is filled usually with the vapors of the most readily boiling alkali metal, rubidium (t_b = 15 °C at a pressure of p = 10^{-7} mm Hg) and is irradiated by circularly polarized radiation whose frequency coincides with the frequency of transition from one energy level to another.

The diagram of the energy levels of the atom Rb^{87}, at various magnetic field strengths T, is shown in Fig.8.VIII.

The quantity v, which is the relative excess of atoms at one level in comparison with the number, is called the pumping parameter. In a state of thermal equilibrium, the pumping parameter for a lower sublevel m of alkali metals is equal to v = 10^{-3} - 10^{-4} (Bibl.19).

If the vessel with the rubidium vapors is irradiated by a monochromatic beam of radiant energy with a wavelength corresponding to the absorption lines, circularly polarized (corresponding to $\Delta m = +1$) and directed along the magnetic field, the absorption of radiant energy causes transition of the atoms from /197 state $2_{s_{1/2}}$ to state $2_{p_{1/2}}$ and a corresponding increase by +1 of sublevel m.

Reverse transition of atoms is possible to any sublevel of the ground state since the selection rule in the first case has the normal $\Delta m = +1$, and in the second $\Delta m = 0$, $\Delta m = +1$, or $\Delta m = -1$.

The state $2_{p_{1/2}}$ does not contain the level m = +3, and therefore transitions from the state $2_{s_{1/2}}$ m = +2 to a higher sublevel are impossible. At this sublevel, continuous accumulation of atoms occurs under the effect of optical pumping. Experience has shown that in this manner it is possible to obtain a pumping parameter v equal to 0.99, i.e., to populate the sublevel m = +2 by 99% (Bibl.19). In this state, rubidium vapors - for all practical purposes - will no longer absorb radiant energy in the given spectral band. The rubidium chamber becomes transparent and a photoelectric cell installed behind it records maximum irradiance. If a weak variable magnetic field is excited with a frequency close to resonant (Larmor frequency) and is directed perpendicular to a constant field, then under the effect of the variable field the atoms will begin to pass from the level $2_{s_{1/2}}$, m = +2 to lower sublevels and the process of absorption of radiant energy will be restored. The most rapid transition of atoms from the sublevel m = +2 to the sublevel m = +1 will occur when the transition frequency coincides with the frequency of the variable field so that absorption will be most intense at this instant. Thus, from the minimum irradiance of the photoelectric cell we can determine the resonant frequency ν of the variable magnetic field, which depends upon the state of the atomic energy levels and thus on the constant field strength T. The decrease in the signal of the photoelectric cell may amount to 80% (Bibl.22).

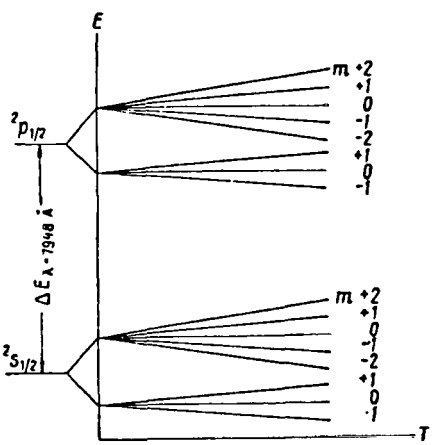

Fig.8.VIII Diagram of Energy Levels of the Rubidium Atom.

The presence of nuclear spin in atoms of alkali metals leads to a non- /198
linear dependence of the resonant frequency ν on the external field strength T, having the form

$$\nu = BT + CT^2, \qquad (12.VIII)$$

where B and C are constants equal to 28 cps/gamma and 1.3×10^{-4} cps/gamma for rubidium.

The block diagram of the simplest rubidium-vapor magnetometer (Fig.9.VIII) consists of a rubidium tube (1) radiating light under the effect of an electrodeless discharge, focusing lenses (2) and (9), an interference filter (3) which passes only radiation at the rubidium line λ = 7948 Å, a circular polarizer (4), chambers with rubidium vapors (5), feedback coils (6), a phase selection circuit (7), a phase inverter (8), and a photoelement (10) with an amplifier (11).

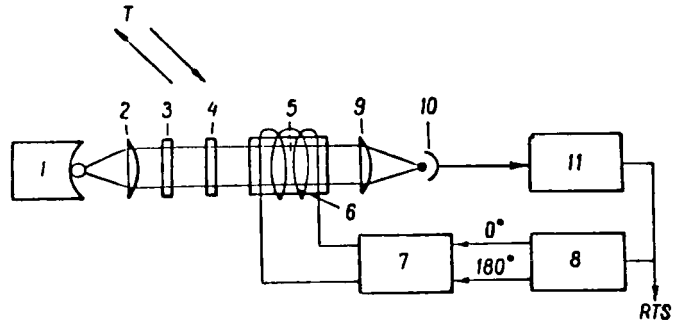

Fig.9.VIII Block Diagram of Rubidium-Vapor Magnetometer.

The radiant flux passing through the absorbing rubidium chamber strikes the low-inertia photoelectric cell. The signal of the photoelectric cell produces weak vibrations, with a frequency close to resonant (Larmor frequency). This is amplified with respect to voltage and fed to the phase-selection circuit which excites oscillations of the auxiliary magnetic field (with an amplitude of several hundreds of gammas) in the feedback coil. In turn, this causes fluctuations in the intensity of the radiant flux and in the signal of the photoelectric cell. The phase-selection circuit ensures adjusting the oscillations to the resonant frequency ν. The latter is a measurable quantity and is transmitted over the telemetry system. When the direction of the magnetic field is reversed, the possibility of changing the current phase in the feedback coil by means of an inverting circuit (8) is provided.

Studies of the instrument (Bibl.22) show that the optimum signal-to-noise ratio is obtained when the light beam is at an angle of 45° to the magnetic field vector. Therefore, instruments were later developed in which a double gas chamber with a crossed optical system was used. Equipment of this type, in- /199
stalled on the Explorer-X along with a ferroprobe magnetometer (Bibl.22), was able to measure the resonant frequency ν without switching phases in any direction of the magnetic field.

Section 8. Method of Ferroprobes or Magnetically Saturated Sensors

Magnetically saturated sensors convert the strength of the measured magnetic field into an electric quantity (voltage or current) by means of an aux-

iliary field. Here, use is made of the nonlinearity of the change in permeability of soft-metal alloys in a magnetizing field, which causes the total magnetic flux in the sensor to vary. Soft-magnetic alloys belong to the group of ferromagnetic materials, for which reason such sensors are called ferroprobes.

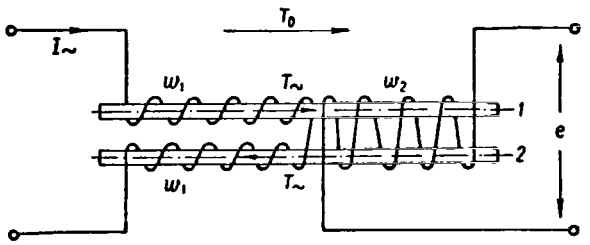

Fig.10.VIII Diagram of a Ferroprobe Sensor.

The most widely used ferroprobes are those with two cores (usually Permalloy), with excitation coils w_1 (Fig.10.VIII) supplied by an alternating current, and a common search coil w_2.

The current amplitude of the excitation coils is selected so that the core material is periodically brought to a state of saturation. The coils w_1 are so designed that the fields $T_\sim$ they excite in the cores are equal but in opposite directions. Therefore, in the absence of core magnetization by an external field, no emf is induced in the search coil.

In the presence of an external field, whose strength vector projection in axial direction of the cores 1 and 2 is equal to T_0, a magnetizing field is added to the alternating field. The strength acting on the cores 1 and 2 will be different, namely,

$$T_1 = T_\sim + T_0,$$
$$T_2 = T_\sim - T_0. \qquad (13.VIII)$$

As a result of the change in magnetic flux in the first core (sufficiently high load resistance), an emf arises in the search coil equal to /200

$$e_1 = -n\frac{d\Phi_1}{dt}\cdot 10^{-8} = -ns\cdot 10^{-8}\frac{dB_1}{dt} = -A\frac{dB_1}{dt}, \qquad (14.VIII)$$

where n is the number of loops in the measuring coil, s is the cross-sectional area of the core, Φ_1 and B_1 are the magnetic flux and magnetic induction in the first half-cell.

The induction B_1, which depends on the field strength T_1, can be expanded in a series, limiting the series to three terms for small magnitudes of the external field T_0

$$B_1(T_\sim + T_0) = B_1(T_\sim) + T_0\frac{dB_1}{dT_\sim} + \frac{T_0^2}{2}\frac{d^2B_1}{dT_\sim^2}. \qquad (15.VIII)$$

Substituting the obtained expression into eq.(14.VIII) will yield

$$e_1 = -A\frac{dB_1(T_\sim)}{dt} - AT_0\frac{d}{dt}\left(\frac{dB_1}{dT_\sim}\right) - \\ -A\frac{T_0^2}{2}\frac{d}{dt}\left(\frac{d^2B_1}{dT_\sim^2}\right). \qquad (16.VIII)$$

A similar expression can be obtained for the emf arising in the search coil w_2 as the result of the change in magnetic flux in the second half-cell

$$e_2 = -A\frac{dB_2(T_\sim)}{dt} + AT_0\frac{d}{dt}\left(\frac{dB_2}{dT_\sim}\right) - \\ -A\frac{T_0^2}{2}\frac{d}{dt}\left(\frac{d^2B_2}{dT_\sim^2}\right). \qquad (17.VIII)$$

As a consequence of the opposed connection of the excitation coils, the total emf will be equal to the difference $e_2 - e_1$

$$e = 2AT_0\frac{d}{dt}\left(\frac{dB_\sim}{dT_\sim}\right) = 2AT_0\frac{d\mu_d}{dt} = 2AT_0\frac{d\mu_d}{dT_\sim}\frac{dT_\sim}{dt}, \qquad (18.VIII)$$

where $B_\sim = B_1 = B_2$ is the induction in any of the half-cells when they are identical, and μ_d is the differential permeability. It follows from eq.(18.VIII) that the emf, whose magnitude is proportional to the external field strength, arises only when the curve of the magnetic reversal of the core is nonlinear $\left(\frac{d\mu_d}{dT_\sim} \neq 0\right)$. The sensitivity of the sensor depends on the cross-sectional area of the cores and on the number of loops in the search coil.

Since, at symmetric magnetic reversal of ferromagnetic materials, the /201 differential permeability μ_d changes at double frequency, the derivative $\frac{d\mu_d}{dt}$ also changes at double frequency. Consequently, the output emf e has a frequency twice as high as the exciting field $T_\sim$. This is illustrated for a sinusoidal exciting field by the curves in Fig.11.VIII. A consideration of all terms of the series (15.VIII) leads to the conclusion that the output voltage should include an entire spectrum consisting of even harmonics, where the amplitude of any even harmonic of the emf largely depends on the exciting field strength and the core parameters. The polarity of the emf generated by the sensor is determined by the direction of the field component being measured.

The average value of the output voltage at half-wave rectification, in conformity with Fig.11.VIII and eq.(18.VIII), will be

$$U_{av} = \frac{1}{P/2} \int_0^{P/2} K_U e \, dt = \frac{4K_U A T_0}{P} \int_{\mu_{d\,min}}^{\mu_{d\,max}} d\mu_d, \qquad (19.VIII)$$

where P is the period of the oscillation; K_U is the voltage amplification factor of the measuring circuit preceding the phase detector.

Taking into account that $\mu_{d\,min} \approx 0$ and $\mu_{d\,max} \approx m$ (the quantity m is called the mode permeability) and that the excitation period P is correlated with the frequency of the exciting field ω over the relation $\omega = \frac{2\pi}{P}$, we obtain

$$U_{av} = 2k_U A T_0 \frac{\omega}{\pi} m. \qquad (20.VIII)$$

It follows from this expression that the output voltage U_{av} is independent of the amplitude of the exciting field and the character of the curve of the magnetic reversal of the core.

With this method of connecting the coils w_1 and w_2, uneven harmonics theoretically should be completely compensated in the search coil, and the even harmonics should be added. Thus, the sensor is a converter of the measured magnetic field into the emf of even harmonics whose amplitudes are proportional to the field strength. An analysis (Bibl.2) shows that the ratio of these amplitudes depends upon the amplitude of the exciting field: with an increase in the latter, the higher even harmonics increase and the lower harmonics decrease. Therefore, during operation at any one of the even harmonics it is necessary to appropriately select and stabilize the amplitude of the exciting field.

Instruments operating on the second harmonic are widely used, since they permit an optimum signal-to-noise ratio (Bibl.7, 19). /202

In conformity with the above statements, the block diagram of a single-channel second-harmonic ferroprobe magnetometer (Fig.12.VIII) contains a sensor S, a generator G_ν supplying the exciting coil w_1 of the sensor, a selective amplifier $A_{2\nu}$ tuned to the double excitation frequency, and a phase-sensitive rectifier PSR whose output voltage is fed across the matching amplifier A to the telemetry system PTC. The selective element in the circuit ensures separation of the second harmonic and suppression of the noise. The latter is due mainly to nonideal balancing of the sensor, as a result of which the exciting fields in the cores are compensated incompletely and odd harmonics occur in the signal. The phase-sensitive elements serve to determine the phase of the second harmonic and, consequently, the direction of the vector of the measured field.

We note that the emf of the second harmonic of the sensor almost always contains odd harmonics which, owing to phase distortions, lead to null instability of the magnetometer.

R.I.Yanus et al. (Bibl.2) proposed using the sum of even harmonics of the emf output of the sensor in a magnetometer. However, the presence of odd harmonics in this case does not permit strong amplification of the signal (owing to

saturation of the amplifier), which is needed for measuring weak fields.

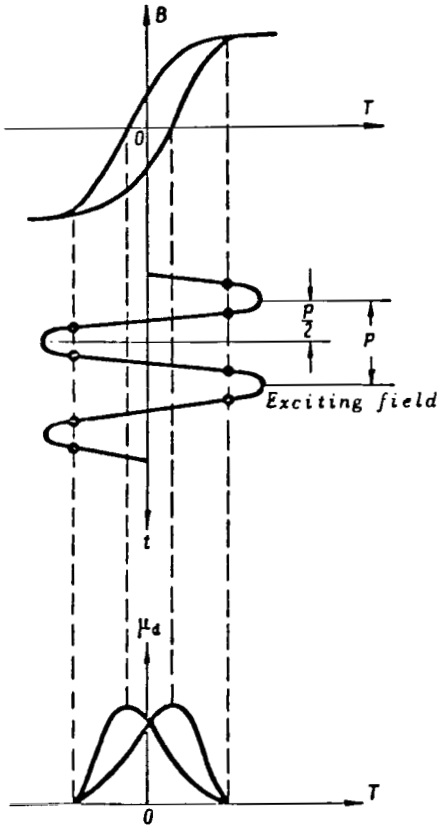

Fig.11.VIII Relation between Sinusoidal Exciting Field, Changes of Magnetic Induction B, and Differential Permeability μ_d of the Core.

When it is necessary to measure the magnetic field strength over a wide range at sufficiently high sensitivity and accuracy (up to 0.05 - 0.1%), /203 the null (compensation) method of measurement can be used. In that case, the sensor is equipped with an auxiliary coil w_3 wound on top of the search coil. At static balancing, the signal after rectification and additional amplification is fed to the coil w_3, producing a balancing field. The balanced current is the measured quantity. A reversing motor, shifting the slide-wire of a potentiometer which regulates the balanced current, is used in astatic balancing circuits.

To measure the total vector of the field strength T, magnetometers with three mutually perpendicular sensors are used. They can be of the self-orienting type. In this case, the sensors are attached to the surface of the orientation unit. The sensor installed perpendicular to the surface is the measuring sensor. The other two lying in the plane of the surface serve to place it per-

pendicular tc the total vector of the field. Equipment of this type (SG-45) was used on the third satellite (Bibl.9). Its shortcoming is the presence of a complex mechanical orienting system. Unoriented magnetometers, installed on oriented or unoriented capsules, measure the field components along three axes x, y, and z. The modulus of the total vector in this case is determined by a computer connected to the output of the instrument or is calculated from the formula

$$T = \sqrt{T_x^2 + T_y^2 + T_z^2}. \qquad (21.VIII)$$

The accuracy of measurement with an automated instrument, however, is low since the error of the squaring elements amounts to ±5% within a wide signal range (Bibl.8). Therefore, equipment with magnetically saturated sensors has the following important characteristics:

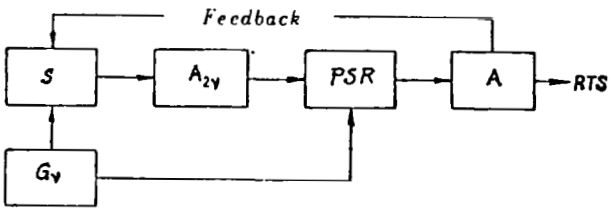

Fig.12.VIII Block Diagram of a Single-Channel Second-Harmonic Ferroprobe Magnetometer.

1. antinoise features when operating in a large complex of measuring and auxiliary onboard equipment;
2. possibility of continuous measurement of the total vector or of the magnetic field strength; /204
3. less power consumption, lower weight, and smaller size than nuclear magnetometers.

The basic shortcoming of equipment with magnetically saturated sensors is the relative character of the data and the zero drift.

Section 9. One-Component Ferroprobe Magnetometer

Let us next discuss the characteristics of constructing the electronic circuits of ferroprobe magnetometers on the example of the simplest one-component instrument whose principal wiring diagram is given in Fig.13.VIII.

The detector of the instrument D has cores made of Permalloy 80NKhS of 0.1 × 1.5 × 50 mm dimensions (permeability μ = 300,000, coercive force $H_c \approx$ ≈ 0.01 oe). The exciting coils w_1 each have 1000 loops of PEV 0.12 wire and the search coil w_2 has 2500 loops of PELShO 0.1 wire (Bibl.2). The measuring circuit of the instrument is assembled in accordance with the block diagram in Fig.12.VIII.

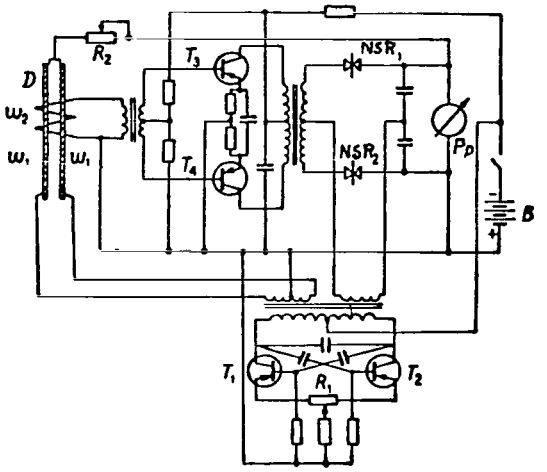

Fig.13.VIII Principal Wiring Diagram of Ferroprobe Magnetometer.

The excitation oscillator for the sensor and reference voltage of the phase detector is based on a push-pull circuit with capacitive feedback, on junction transistors T_1 and T_2. The resistance R_1 adjusts the phase relation when setting the oscillator to minimum content (of the order of 0.2%) of even harmonics. The frequency of the generated voltage is 2 kc.

The push-pull broadband amplifier of the signal of the even harmonics /205 produced by the detector is composed of junction transistors T_3 and T_4 in a circuit with a common emitter. The amplifier load is a transformer to whose output the phase detector is connected. The resistances connected into the emitter circuits of the transistors and shunted with respect to the variable component ensure thermal stabilization of the circuit.

The advantages of the amplifier push-pull circuit used in the instrument include: less possibility of appearance of spurious even harmonics in the amplifier itself, and decrease in nonlinear distortions at large power amplification of the signal. The amplified signal is fed to the bases of the transistors in opposition, so that the currents flowing in their collector circuits produce the total effects of magnetization of the transformer core. At the same time, the constant components of the collector currents produce mutually opposite effects of magnetization of the core. Thanks to this, saturation is not achieved and nonlinear distortions are eliminated.

The phase detector is composed of nonlinear semiconductor resistances (NSR) of a symmetric type whose conductivity depends on the magnitude of the applied voltage (Bibl.16).

We can show (Bibl.16, 17) that, if the sum of two variable voltages U_1 + + U_2 is fed to the NSR, the rectification effect of one of these appears. In this case, only voltages (harmonics) for which a certain frequency ratio ω_1 and ω_2 is satisfied, are rectified. For NSR (varistors) with a nonlinearity of the

third order, the necessary ratio will be $\frac{\omega_1}{\omega_2} = 2$ or 1/2. This property of NSR is used in the phase-sensitive detector of the magnetometer, for better discrimination of the signal from the noise background.

We note that the use of NSR is especially effective in circuits of second-harmonic magnetometers.

The circuit includes a negative feedback across the resistance R_2; changing the magnitude of this resistor permits regulation of the measuring range of the magnetometer.

According to the data by Yu.V.Afanas'yev (Bibl.2) an instrument constructed in this manner has a measurement error of not more than 10 γ in a ±1000 γ range.

Section 10. Measurement Procedure

To monitor the zero of ferroprobe magnetometers, standard (usually proton) magnetometers, which are periodically compared, are used.

Calibration of the magnetometers (with respect to each channel) is done by a system of Helmholtz coils which produce a homogeneous and previously known /206 magnetic field in the detector of the magnetometer. Each pair of the coils has two windings: the main winding for producing a field of a specified strength and a compensating winding which cancels the corresponding component of the external field strength (of the earth, etc.). The magnitude of the magnetic field strength at the center of a given pair of coils is determined by the formula

$$T_0 = \frac{Mwi}{r}, \qquad (22.VIII)$$

where w is the number of turns of the winding on the coil, i is the current strength measured by the instrument, r is the radius of the winding, and M is an experimentally determined constant.

The calibration curves of the channels of the ferroprobe magnetometers proved to be linear with a high accuracy.

The detectors of this equipment are installed on a special boom outside the capsule at a sufficient distance from noise sources. The bulk of the constant magnetic interference created by the permanent magnets on the instrument within the capsule can be compensated by installing special balancing temperature-compensated magnets attached near the base of the boom. The total magnetic interference (deviation) from the uncompensated fields of the container, under given working conditions, is determined experimentally for each detector. For example, for the ferroprobe instrument on the first spacecraft, the total deviation with respect to each of the detectors did not exceed 70 γ (Bibl.4) at a sensitivity of 600 γ per volt obtained with respect to the telemetry system.

The zero drift of the magnetometers amounts to several gammas an hour

[20 gammas in 24 hrs on the first spacecraft and maximum drift of seven gammas per hour on the second, where the equipment had an approximately four-fold sensitivity (Bibl.4, 8)]. In this connection, the stability of the null point of the magnetometers is controlled. The procedure of controlling the operation of magnetometers during flight on unstabilized objects (Bibl.5 - 9) is based on their rotation, since signals caused by magnetic deviation and zero drift of rigidly attached detectors are independent of orientation of the capsule and the projection of the external field onto the detectors changes with the frequency of rotation of the capsule.

The threshold sensitivity (and the absolute error) of equipment used under laboratory conditions can be reduced to several gammas. It proves to be less than 20 - 30 gammas under the operating conditions on capsules of spacecraft (Bibl.5, 7).

PART III

MEASUREMENTS IN THE OPTICAL RANGE

The optical range encompasses the X-ray, ultraviolet (UV), visible, and infrared (IR) regions of the radiant energy spectrum. The visible region is bounded by wavelengths from 0.38 to 0.76 μ. To its left lies the spectral region encompassing ultraviolet radiant energy (from 0.38 to 10^{-2} μ or from 3800 to 100 Å), X-rays (from 100 to 0.1 Å) and γ-rays (shorter than 0.1 Å); to its right, the infrared region, which extends from 0.76 to 350 μ (0.35 mm). /207

CHAPTER IX

MEASUREMENTS OF X-RAY AND ULTRAVIOLET RADIANT ENERGY

Section 1. Characteristics of Emissions Subject to Measurement

The ultraviolet region of the spectrum is usually divided into the near (3800 - 3000 Å), far (3000 - 2000 Å), and vacuum-ultraviolet (2000 - 100 Å) portions (Bibl.13). X-radiation is divided into hard ($0.1 < \lambda < 1$ Å), soft ($1 < \lambda < 10$ Å), and ultrasoft ($10 < \lambda < 100$ Å) (Bibl.1).

The principles and apparatus for measuring hard X-radiation and γ-radiation are the same in both cases. They have been described earlier (see Chapt.V) so that we will here discuss the methods of measuring radiant energy only in the region from 1 to 3800 Å.

The principal natural source of radiant energy is the sun whose structure markedly affects the character of the emission.

Let us recall that the solar atmosphere consists of three layers: a) the photosphere, several hundred kilometers in thickness which determines the visible disk of the sun; b) the chromosphere, surrounding the photosphere with a ring ~10,000 km in thickness, and c) the corona, the discharged and much more heated external atmosphere of the sun which extends over millions of kilometers. /208

The radiation of the abyssal strata of the sun migrates outward as a result of numerous acts of absorption and re-radiation; with its approach to the photosphere, its maximum spectral intensity gradually shifts into the region of longer wavelengths. The visible continuous spectrum of solar radiation emitted by the photosphere has a total intensity close to that of a black-body radiation spectrum at a temperature of ~6000°K. At shorter wavelengths ($\lambda < 4000$ Å), the intensity of solar radiation decreases more rapidly, as is implied by Planck's law.

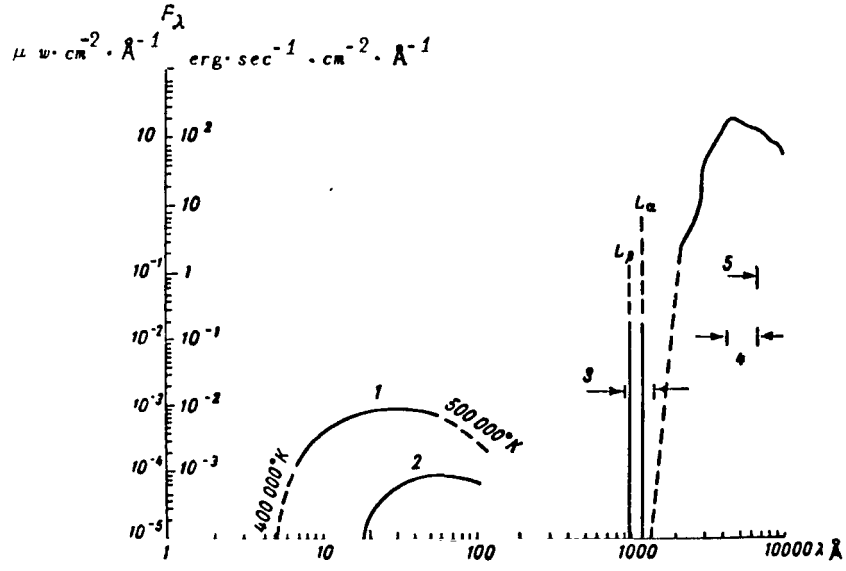

Fig.1.IX Solar Radiation in the Visible and Shortwave Spectrum Regions.
1 and 2 - Upper and lower limits of X-ray region;
3 - Region of ultraviolet line spectrum;
4 - Visible region; 5 - Beginning of infrared region.

The far and vacuum-ultraviolet radiation of the sun, emitted chiefly by the chromosphere and corona, is characterized by the presence of bright lines against the background of a comparatively weak continuous spectrum. A particularly marked decrease in intensity of the continuous spectrum and a transition to a line spectrum, more or less, are observed for wavelengths λ shorter /209 than ~1500 Å (Fig.1.IX). In the X-ray region, particularly for λ < 20 Å, a spectrally continuous radiation flux again begins to predominate; its intensity depends greatly on the state of the sun.

The presence of a continuous emission spectrum side by side with a line spectrum is attributable to the physics of the glow of high-temperature plasma. Let us consider the emission of hydrogen, an element which plays a highly important role in all processes occurring on the sun.

The emission spectrum of excited hydrogen atoms consists of a series of lines produced by the transitions of electrons to allowed energy levels. Electron transitions from upper levels to the level with the quantum number n = 2 form the so-called Balmer series. Many of the lines in this series are located in the visible region (H_α with λ = 4863 Å, and others).

Transition of electrons to the low level n = 1 results in the emission of Lyman-series lines.

In the process of transition of an electron from the orbit n_i to the orbit n, which is located closer to the nucleus, an energy of

$$\Delta E = R\left(\frac{1}{n^2} - \frac{1}{n_i^2}\right), \qquad (1.IX)$$

is released, where R is Rydberg's constant.

Equation (1.IX) implies that the wave numbers (cm^{-1}) of the Lyman series are determined by the formula

$$\frac{1}{\lambda} = 1.09 \cdot 10^5 \left(1 - \frac{1}{n_i^2}\right). \qquad (2.IX)$$

These lines, as can be seen from eq.(2.IX), are located in the ultraviolet region of the spectrum. The line α from the Lyman series L_α with λ = 1215.7 Å, which is the most intensively emitted by the sun, corresponds to the transition from the level n_i = 2 to the level n = 1. Photometric studies by Purcell and Tousey (Bibl.20) show that about 94% of the total radiation intensity in the spectral range from 1050 to 1350 Å is emitted in the line L_α. The spectral width of this line is of the order of 1 Å, as can be seen from Fig.2.IX. An absorption nucleus is clearly visible at the center of the line (decrease in density P of the spectrogram); this is due to the absorption of solar radiation by the hydrogen of outer space.

The presence in the solar spectrum of X- and γ-radiation is due to the deceleration of the high-energy electrons [with an energy of $E_e \approx 1$ Mev and higher (Bibl.17)] emitted by the internal region.

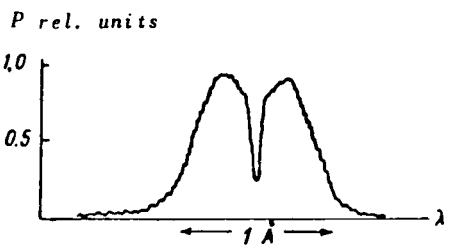

Fig.2.IX Profile of Lyman line.

The emission of a continuous spectrum is attributable (Bibl.20) to "free-free" and "free-bound" electron transitions, i.e., to deceleration and capture of electrons during their interaction with nuclei of various elements, chiefly with protons. In both cases, any amount of energy may be emitted; the /210 energy emitted in the latter case will be higher the lower the level at which the electron is captured. It is the combined emission of many particles that leads to a continuous spectrum. Capture of free electrons at the level n = 2 leads to the emission of - in addition to the Balmer series - a continuous spectrum termed the Balmer continuum. The Lyman continuum is of similar origin. As can be seen from the eq.(2.IX), this starts with the wave number 1.09 × $\times 10^5$ cm^{-1} ($\lambda \approx 920$ Å) and continues into the region of shorter wavelengths.

The electron temperature of the solar atmosphere varies widely with alti-

tude; from about 5000°K in the lower chromosphere to 1 - 2 × 10^6°K in the inner corona (Bibl.20). As a result, virtually all the atoms in the corona are ionized. The wavelengths of the radiation originating there are determined by the charge of the nuclei and the degree of their ionization. Hence, the short-wave spectrum of the sun, emitted by the chromosphere and the corona, contains a large number (more than 200) emission lines. For example, lines of Fe ions in various ionization states (up to Fe XVI) as well as of Ca ions, etc. have been identified in this spectrum. The brightest lines of the short-wave solar spectrum and their flux densities, as taken from the data of G.M.Nikol'skiy (Bibl.17), are presented in Table 1.IX. For comparison, note that the flux density of the continuous spectrum in the 900 - 1300 Å region is of the order of 10^{-3} erg·cm^{-2}·sec^{-1} Å^{-1}.

TABLE 1.IX

FLUX DENSITY F FOR THE BRIGHTEST LINES IN THE SHORT-WAVE EMISSION SPECTRUM OF THE SUN

λÅ	Ion	F·erg·cm^{-2}·sec^{-1}
2795.5and2802.7	Mg II	18
1817.4and1808.0	Si II	about 1
1215.7	H I (L_α)	3—6
303.8	He II	0.3—1.6

The integral energy density in the X-ray region outside the confines of the atmosphere is comparatively low (not more than 1 erg·cm^{-2}·sec^{-1}), whereas the energy of the entire region of the solar spectrum amounts to 1.3 × /211
× 10^3 erg·cm^{-2}·sec at the top of the atmosphere (Bibl.13). A large part of this energy is absorbed by the upper atmosphere and expended on various geophysical processes and, particularly, on the formation of the ionosphere.

The optical "window" of the earth's atmosphere extends roughly from 2900 to 140,000 Å. Therefore, solar radiation shorter than 2900 Å cannot be measured from the earth. Measuring apparatus must be lofted to altitudes which can be estimated with the aid of Fig.3.IX. This diagram shows the altitudes above the earth's surface at which the radiation flux of a given wavelength is attenuated e times compared with its value at the top of the atmosphere [when the sun is at the zenith (Bibl.20)]. At the same time, the graph plots the pattern of variation in the transparency of the atmosphere as a function of wavelength and indicates the principal absorbing components of the atmosphere. It can be seen from Fig.3.IX that the sharp boundary of the solar spectrum in the neighborhood of the earth's surface is due to absorption by the ozone layer (in the Hartley and Higgins bands). Although the thickness of the ozone layer in the atmosphere is only 2 mm when referred to pressure at sea level, the decimal attenuation factor of radiation, e.g. in the neighborhood of 2500 Å (Hartley band) reaches 140 (Bibl.13).

In part of the vacuum-ultraviolet region ($1000 \leq \lambda \leq 2000$ Å), absorption is dependent chiefly on molecular oxygen which, as a result, dissociates (bands 1102 - 1110, 1800 - 2000, ~1158, 1189 Å, etc.).

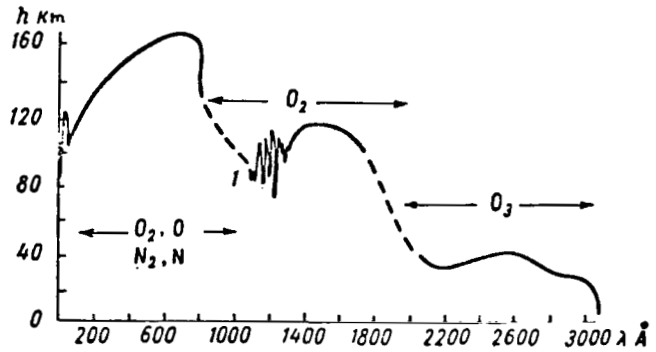

Fig.3.IX Penetration of Solar Radiation into the Atmosphere.
1 - Lyman lines and continuum.

It should be noted that, during the periods of high solar activity, the radiation intensity in the X-ray region sharply increases [by a factor of several tens in part of the 2 - 20 Å region (Bibl.17)]. In this case it reaches to even lower altitudes, as shown in Fig.3.IX. /212

The intensity of solar radiation rapidly decreases with decreasing the wavelength < 1300 Å. Thus, the flux density in the 3000 - 2000 Å spectral region (at the altitude of 30 - 40 km) is approximately 2×10^4 erg·cm^{-2}·sec^{-1}; in the 2000 - 1300 Å region (altitudes of 50 - 125 km), it is about 260 erg·cm^{-2}·sec^{-1}; in the 1300 - 8 Å region (altitudes of 70 - 140 km), of the order of 10 erg·cm^{-2}·sec^{-1}; and in the $\lambda < 10$ Å region, from 10^{-2} to 10^{-4} erg·cm^{-2}·sec^{-1} (Bibl.17).

The temperatures of an absolutely black body, emitting the above-specified energy fluxes in the short-wave region, are relatively low (< 5500°K for $\lambda <$ < 3000 Å). Thus, the spectral and energy temperatures in this region do not coincide.

Other natural sources of short-wave radiation are characterized by markedly smaller fluxes. Thus, the diffuse glow in the line L_α, characteristic of the entire night sky, has an intensity of 3×10^{-3} erg·cm^{-2}·sec^{-1} ster^{-1} (Bibl.10), while the flux in the ultraviolet region $1230 \leq \lambda \leq 1350$ Å, from the brightest nebula located in the neighborhood of the Constellation of Orion, is $2 \times$ $\times 10^{-5}$ erg·cm^{-2}·sec^{-1} at the top of the atmosphere. The measured radiation fluxes from the stars in the L_α line do not exceed this magnitude (Bibl.10, 20). Thus, depending on the spectral region and the investigated source, the sensitivity and measurement limits of the apparatus must differ markedly.

Measurements of radiant fluxes in the short-wave region are necessary to elucidating the basic properties and features of the upper atmosphere and outer space. For example, solar radiation in the so-called ionizing region of the

spectrum ($\lambda < 1000$ Å) in strong lines such as L_α and penetrating radiation ($\lambda <$ < 10 Å) considerably affect the state of the ionosphere and the operating conditions of ground-based and orbited means of radio communications. An extremely important factor, which must be taken into account in manned space flights, also to ensure the operating reliability of KA equipment, is the radiation produced by the emission of penetrating radiation from the sun (cf. Chapt.V, Sect.1).

Most valuable experimental data may be obtained with the aid of spectral instruments. However, difficulties in calibrating their energy sensors [for spectrographs, the errors reach ±150 - 200% (Bibl.17)] as well as their considerable weight, large dimensions, and high power requirement often discourage the use of these instruments.

In this connection, comparatively simple filter instruments, used for measurements of radiative fluxes in the most important and sufficiently narrow spectral intervals, are widely employed. These instruments, in turn, are classified according to the type of detector used (thermoluminescent phosphor, secondary-electron multiplier, ionization detector).

Section 2. Instruments with Thermoluminescent Phosphor /213

The operation of instruments in this group is based on the principle of thermoluminescence which consists in that certain substances - the phosphors of $CaSO_4(Mn)$, $CaCO_3$, MgO and others - are capable of storing up the energy of short-wave radiation when irradiated and releasing this energy in the visible region of the spectrum when heated.

Investigations (Bibl.1, 2) established that the "light sum", i.e. the number of the emitted light quanta, is proportional to the energy of the exciting short-wave emission acting on the surface of the phosphor during its exposure. This pattern, however, does not apply in the presence of extremely high intensities of the exciting flux and long durations of exposure.

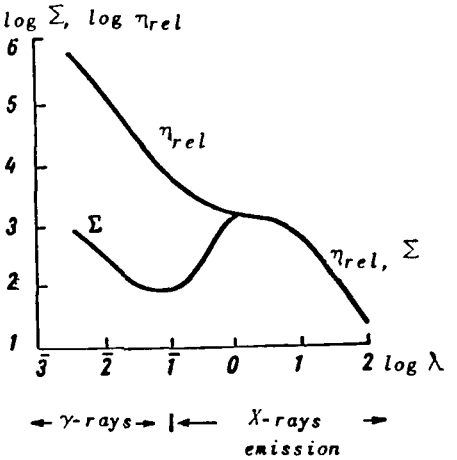

Fig.4.IX Light Sum Σ and Relative Quantum Yield η_{rel} of Thermoluminescent Phosphor.

It should be noted that the light sum does not reflect the spectral distribution of the exciting radiation but merely provides information on its total energy.

Thermoluminescent phosphor of CaS, activated by the manganese of $CaSO_4$(Mn), has found practical application in United States and Soviet instruments (Bibl.11). This compound displays a number of valuable qualities which permit its use for absolute measurements of short-wave radiant energy.

The magnitude of the relative quantum yield η_{rel} of the $CaSO_4$(Mn) phosphor, in percent with respect to one quantum of the exciting radiant energy of various wavelengths λ, as based on the data by V.A.Arkhangel'skaya and T.K.Razumova (Bibl.1), is presented in Fig.4.IX. The graph shows that the relative quantum yield continuously increases with decreasing wavelength. At the same time, the sensitivity of this phosphor crystal decreases with decreasing wavelength from 3 - 5 to 0.2 - 0.4 Å. This is attributable to the absorption of both the exciting radiation in this wavelength range and of the natural radiation of the active layer [which is approximately 0.6 mm in thickness (Bibl.1)].

An important feature of this phosphor crystal is its lack of sensitivity to radiant energy at wavelengths exceeding 1300 Å. The efficiency η of a phosphor crystal with a filter is illustrated in Fig.5a.IX (Bibl.2). As we can see, /214 the use of a LiF filter makes it possible to record almost exclusively energy in the region of the L_α-line (λ = 1215.7 Å) which, in the spectral range of 1050 to 1220 Å, accounts for approximately 95% of the energy of the solar spectrum (Bibl.20).

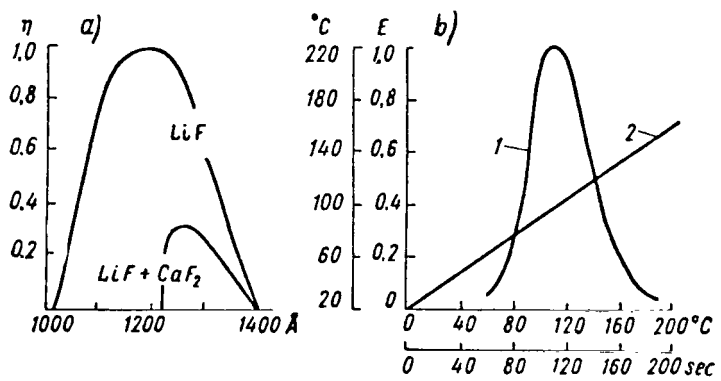

Fig.5.IX Efficiency of Sensor (in Relative Units) with Various Filters (a), and Temperature Dependence of Thermoluminescence in the Presence of Uniform Heating (b).
1 - Energy released (relative units); 2 - Temperature curve.

Investigations showed that, in measuring the intensity of exciting radiation over wide limits [example based on the series (Bibl.11) of $CaSO_4$(Mn)], no saturation was found.

The thermoluminescence spectrum of this phosphor has a sufficiently sharp

peak in the green portion of the spectrum [$\lambda \approx 0.5\ \mu$ (Bibl.1)], which is satisfactorily detected by a photomultiplier with Sb-Cs photocathodes.

The energy stored by the thermoluminescent phosphor, generally speaking, is continuously released, but at temperatures below about 60°C the energy release of $CaSO_4(Mn)$ is small. For example, Fig.5b.IX indicates that in this case virtually all of the stored energy is already released at a temperature of approximately 200°C.

Let us establish a correlation between the parameters of an instrument with a thermoluminescent detector and the density F of the exciting radiation. The magnitude of the latter is

$$F = \frac{F'}{\bar{\eta}} \tag{3.IX}$$

where F' is the density of the flux released by the phosphor, and $\bar{\eta}$ is the mean quantum yield.

The area underneath the curve of energy release Σ (light sum) is determined by the output voltage U_{out} of the instrument and by the time T of the energy release /215

$$\sum = \int_0^T U_{out}\, dT = k \int_0^T U\, dt, \tag{4.IX}$$

where k is the amplification factor of the measuring circuit.

If the current across the load R_ℓ of the photomultiplier is denoted by i and the mean quantum efficiency of the photocathode with respect to phosphor emission by $\bar{\varepsilon}$, then, given an ideal gathering of light, we have

$$U = \frac{i}{R_\ell} = \frac{F' \bar{\varepsilon} M s}{R_\ell}, \tag{5.IX}$$

where M is the current amplification factor due to the dynode photomultiplier system and s is the sensitive area of the phosphor (and photocathode).

From eqs.(3 - 5.IX), we obtain

$$\int_0^T F\, dT = \frac{R_\ell \sum}{k \bar{\varepsilon}\, \bar{\eta} M s}. \tag{6.IX}$$

If the intensity of the measured radiation is constant during the measurements and its spectral composition is homogeneous (mean frequency equal to $\bar{\nu}$), we derive the formula for determining the density F in energy units

$$F = \frac{R \sum h\bar{\nu}}{k \bar{\varepsilon}\, \bar{\eta} M T s}, \tag{7.IX}$$

where h is Planck's constant.

Inaccuracies in determining the parameters entering eq.(7.IX) cause errors in measuring short-wave radiation by the method considered here. It must be borne in mind that phosphors are also excited by γ-rays and high-energy particles, particularly by electrons. The presence of fluxes of such particles may also lead to errors in radiation measurements. Thus, it has been established (Bibl.12) that the sensitivity of $CaSO_4$(Mn) phosphor to electrons equals its sensitivity to X-ray quanta of the same energies.

In the United States instruments based on the use of $CaSO_4$(Mn) thermoluminescent phosphors have been used in sounding-rocket measurements of short-wave and X-radiation within limited spectral ranges, isolated with the aid of LiF and CaF_2 filters (Bibl.25).

/216

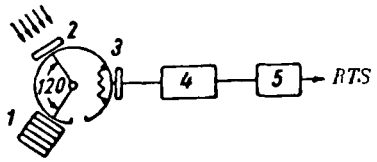

Fig.6.IX Block Diagram of Instrument with Thermoluminescent Detector.

Specimens of phosphors exposed at high altitudes were de-excited in the laboratory, following recovery of the rocket. The accuracy of measurements decreases, since the instrument capsule is heated during reentry causing some de-excitation (energy release) of the phosphors.

The block diagram of the automatic instrument (Fig.6.IX) contains a magazine with plates (1) successively advanced by means of a disk into the exposure position (2) (outside the entrance window) and into the de-excitation position (3) (in the neighborhood of the heating element), as well as a photomultiplier unit (4) and a cathode follower (5).

$CaSO_4$(Mn) phosphor was implanted in orifices drilled into brass plates; the overall sensitive surface area was 0.8 cm^2(Bibl.11). Both exposure time and excitation time were 22 sec each. After de-excitation, the plate was discarded and replaced with a new plate extracted by the disk from the magazine; this was repeated until the supply of plates was exhausted.

To verify the operating stability of the instrument in flight during the replacement of plates, the replacing mechanism mounted in front of the photomultiplier, a continuous-action luminous compound (Zn(Cu)) activated with the isotope C^{14}, with a luminescence peak in the spectral region at $\lambda \approx 5200$ Å, is used.

To isolate emission in the L_α region, the entrance window of the instrument is covered with a LiF filter. The range of flux densities measured in this region overlaps by one order of magnitudes, from 0.03 to 0.3 $erg \cdot cm^{-2} \cdot sec^{-1}$.

The angle of view of the instrument is close to 2π steradian.

The error in plotting the calibration curve of the instrument for the vacuum UV range is ±55% and for the X-ray range, ±30%. Errors in the analysis of telemetered data when determining the light sums do not exceed ±30%, and the other errors do not exceed ±10%.

The total error of flux measurement for the above instrument thus reaches ±100% (Bibl.11).

It should be noted that in flight the instrument was strongly influenced by the electrons of corpuscular fluxes with energies of the order of 1 - 10 Kev (Bibl.22).

Section 3. Apparatus with Ionization Sensors

Owing to its simplicity, high accuracy and reliability, instruments with ionization sensors are used widely in upper-atmosphere measurements, particularly in the USA (Bibl.10, 20). The sensors may be gas-discharge counters or ionization chambers. They are so designed as to meet the requirements for ion- /217
ization sensors and at the same time to ensure the required efficiency (sensitivity) in the spectral region concerned.

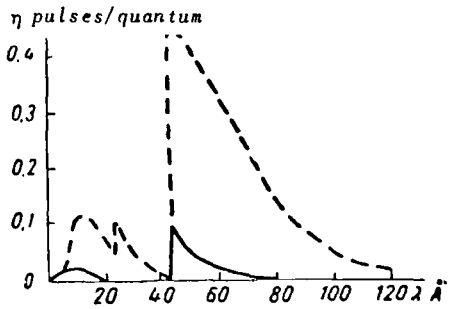

Fig.7.IX Quantum Yield of Photon Counters with Mylar Windows (Solid Line) and Glyptal Windows (Broken Line).

The most suitable filling gases for such sensors, from the viewpoint of a number of properties, are the inert gases He, Ne, Ar, Kr, and Xe, whose ionization thresholds correspond to 507, 577, 591, 890, and 1027 Å according to Friedman (Bibl.20). These gases may be used in combination with various quenching agents: hydrocarbons (vapors of alcohol or ether), halides (chlorine or bromine) or nitric oxide.

On exposure to short-wave radiation, photoelectrons leading to ionization of the gas may strike not only the gas but also the walls of the sensor. Either effect may predominate, depending on the spectrum region of the measured radiation, the composition and pressure of the filling gas mixture, and the design

of the sensor.

In the region of soft and ultrasoft X-rays (1 Å < λ < 100 Å), the main role is played by photoelectrons emitted by the filling gas, since the photoelectric yield of any material is low in this region. By selecting the filling gases in the sequence specified above and varying their pressure, sensors with different spectral sensitiveness are obtained.

The quantum yield of photon counters with Mylar filter ($C_{10}H_8O_4$) windows (0.73 mg/cm^2 film thickness) (solid line) and with glyptal filter window (0.18 mg/cm^2 film thickness) (Bibl.20), is shown in Fig.7.IX. The counters (diameter, 2 cm) were filled with He and ethyl formate at a pressure of p = = 750 mm Hg.

The values of the spectral sensitivity η of SBT-9 type counters (Bibl.16) with windows of beryllium foil and mica (along with aluminum shielding against UV radiation) are indicated in Fig.8.IX.

The former (with Be-foil windows), as we can see, operate in the range of approximately 5 to 80 - 120 Å, and the latter, of 1 - 2 to 10 - 12 Å.

The curves distinctly reveal the absorption bands of X-rays by carbon (~ 43 Å), oxygen (~ 22 Å) and aluminum (~ 8 Å). The absorption band for beryllium is distant from the region considered, so that the curve of the spectral sensitivity of a beryllium-window counter has a smooth slope. /218

For the UV region of 100 to 1000 Å, for which suitable materials do not exist, it is possible to employ windowless sensors with a continuously flowing gas which should be selected according to the ionization potential (Bibl.20).

In the region of longer wavelengths λ > 1027 Å, the spectral characteristics of the sensors begin to be determined by the external and internal photoeffects of the cathode material. The threshold of the internal photoeffect for the materials employed lies in the region of 1000 < λ ≤ 1500 Å (Bibl.20). The external photoeffect also manifests itself in a more distant region, where the flux of solar radiation rapidly increases.

The quantum effectiveness of the ionization sensors used in the /219
1500 - 3000 Å region is determined by the photoeffect at the cathode surface and is comparatively small (the quantum yield being 10^{-5} - 10^{-7} electrons per quantum).

Instruments with ionization sensors have found broad application. In particular, ionization chambers with LiF and CaF_2 filters for measuring solar emission in the L_α-line and others with a beryllium window for measurements of solar X-radiation have been used on the Vanguard-III and Explorer-VII artificial earth satellites (Bibl.10, 20).

Let us consider the apparatus widely used in measurements of the solar X-radiation on geophysical rockets and spacecraft by S.L.Mandel'shtam, B.N. Vasil'yev, and others (Bibl.16). They employed standard SBT-9 type counters with a mica or beryllium window. The sensor unit consisted of several (2 to 6)

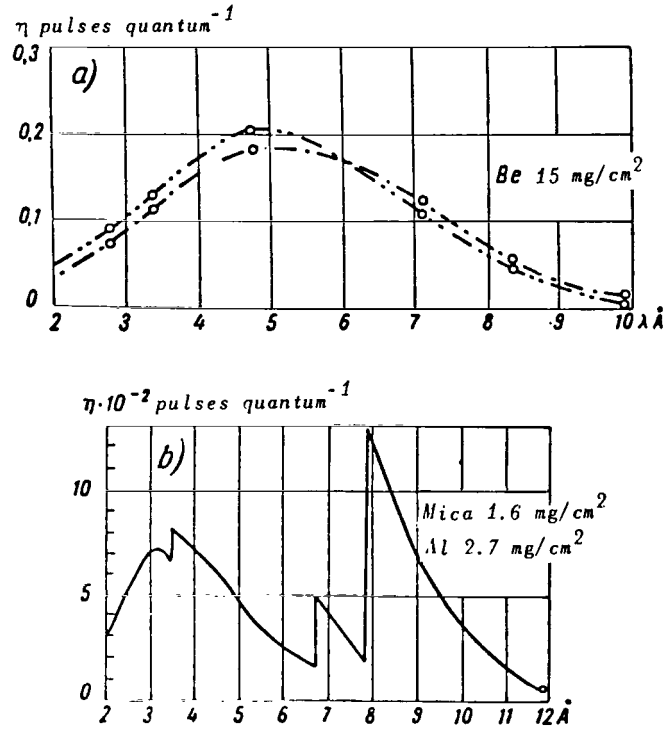

Fig.8.IX Spectral Sensitivity of Counters with Beryllium (a) and Mica (b) Windows.

identical counters required to ensure a sufficiently long observation of the sun (in the absence of an orientation system) and to record the background radiation acting on the counters whose field of view happens to exclude the sun. To reduce the background due to the particles of corpuscular fluxes, magnetic shielding was used in some cases (a variant of this shielding is illustrated in Fig.9.IX). When the field intensity in the gap between the constant magnets (1) is of the order of 1000 oersted, shielding of this kind is effective for electrons with energies of up to 20 Kev (Bibl.16). The windows of the measuring and background counters (2) in such a device have an angle of view of about 45° and are oriented in various directions. The side surfaces of the counters were protected by a lead shielding of approximately 2 mm thickness against brems- /220 strahlung arising in the casing of the sensor unit (Bibl.16).

The load characteristic of the counters used is shown in Fig.10.IX, indicating that this characteristic droops sharply at a counting rate of $N \approx \approx 10^3 - 10^4$ pulses/sec. This is attributable to the recombination of gaseous-mixture ions, which results in a decrease in the working volume of the counter in the presence of a high irradiation intensity. Over the range from 0.1 to 10^3 pulses/sec, as can be seen from Fig.10.IX, the counter performs almost perfectly.

The measuring channels of all the counters were based on the same circuits. A block diagram of one of these is shown in Fig.11.IX. The pulses generated by the recorded quanta in the photon counter PhC proceed to the pulse shaper PS

which standardizes them with respect to the amplitude and duration required for a reliable performance of the flip-flop scaling circuit which consists of K intermediate and n mean-frequency scanned flip-flops (FFI and FFM). The state of the mean-frequency flip-flop elements is recorded via separating stages S by a memory device MD with a diurnal memory volume which performs the scanning once every three minutes.

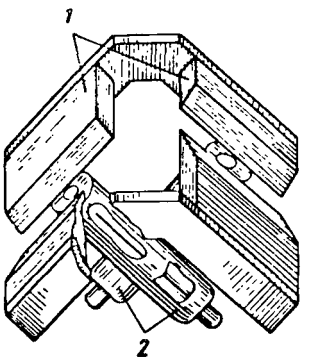

Fig.9.IX Magnetic Shielding of End-Window Photon Counters.

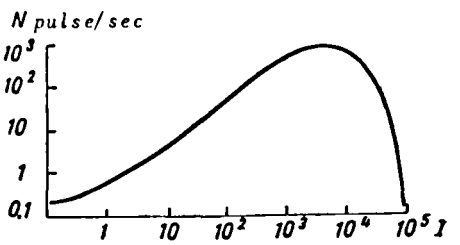

Fig.10.IX Counting Rate N as a Function of the Intensity I of Irradiation (Rel. Units) of a Gas-Discharge Counter.

The total capacity of the scaling circuit of the measuring channel of the device installed in, e.g., the second spacecraft was 2^{20} pulses. Recording in MD was carried out from 20 flip-flop elements. This made it possible, in the presence of a three-minute scanning cycle, to record the mean pulse counting rate from 0.1 to 5×10^3 pulses/sec (Bibl.16).

Provision was also made for the possibility of direct transmission of the pulse counting rates within the range from 0.5 to 2×10^4 pulses/sec. To this end, the outputs of five flip-flop elements (FFM_1 - FFM_5) were connected to the adder circuit AC.

The sensor unit was mounted outside and connected by a cable to the measuring circuit housed within an airtight capsule. /221

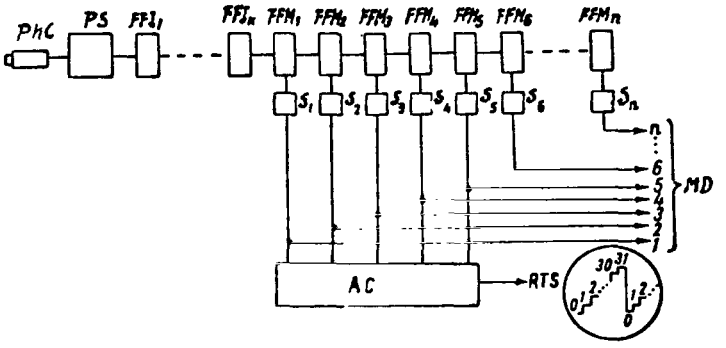

Fig.11.IX Block Diagram of Measuring Channel of Counter.

The principal components of the measuring channels (Fig.11.IX) are of the same transistorized type; the special features of the measurements required the development of specific circuits.

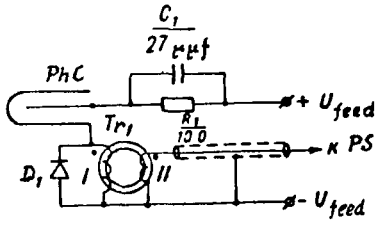

Fig.12.IX Circuit Diagram of Photon Counter.

The circuit diagram of the photon counter is shown in Fig.12.IX. The feed voltage (U_{feed}) is fed across current-limiting resistors R_1 which are shunted by the capacitor C_1 to enhance the amplitude of the received pulses. The output pulses (of negative polarity) are tapped from the secondary winding of the matching transformer Tr_1 connected to the cathode circuit of the counter. The transformer makes it possible to transmit the output signal over a cable of considerable length (as long as 10 m) and to utilize a shaping device with a low input resistance. To eliminate the oscillations arising during the passage of current pulses across the transformer (owing to the accumulation of energy by the core), the transformer primary is shunted with a D_1 diode (of the D101 type).

The amplitude and shape of the pulses taken off the photon counter are greatly influenced by the counter load, temperature, feed voltage, etc. The conversion of counter pulses to the standard form, having the amplitude and duration required to trigger the scaling element, was accomplished with the aid of a shaping device containing a biased blocking oscillator.

The resolving time of the flip-flop scaling elements is 40 - 50 μsec.

To eliminate any triggering of the flip-flop elements during scanning by the memory device, separating stages are mounted at the output of the scanned flip-flops; each of these stages is represented by a transistor operating in the on-off regime, with two diode limiters. The latter block the admission of pulses of any polarity to the flip-flop circuit.

The operation of this apparatus can be tested with the aid of radioactive isotopes in the same manner as when measuring cosmic radiation (cf. Chapt.V). The processing of the telemetered data is done in the same way: The difference in the number of pulses passed during three minutes, with an error of not more than ±10% in determining the counting rate, is determined for each channel.

Section 4. Filter Apparatus with Secondary-Electron Multipliers (SEM) /222

The operating principle of instruments with secondary-electron multipliers (SEM) is based on isolation of various spectral regions of short-wave radiation by means of a set of filters successively placed in front of one and the same receptor. The receptor used is an open-type secondary-electron multiplier, represented by a system of diodes fabricated from a material with a high coefficient of secondary-electron emission, which operates under the conditions of the natural vacuum of the upper atmosphere. The role of the radiant energy receiver is performed by the first diode of the SEM.

SEM-based apparatus displays a number of advantages compared with ionization receivers. The advantages are: a) possibility of using as filters a number of materials which do not meet the requirements of vacuum density, mechanical strength, etc. made on the materials to be used for windows of ionization counters; b) measurement of any spectral region by means of a single receiver whose sensitivity is checked during each measurement cycle; c) high stability of spectral characteristics of the receiver; and d) lower sensitivity of the SEM to the background of cosmic radiation.

This last advantage is particularly significant. It is mainly due to the sharp decrease in sensitivity of the SEM in the near-ultraviolet spectral region as well as to its low sensitivity to hard X-rays, γ-rays, and cosmic-ray particles.

Other investigations (Bibl.22) show that the optimum dynode materials from the standpoint of maximizing these advantages are Cu-Be alloys; owing to selective oxidation, photosensitive layers of beryllium oxide BeO will form on the surface of these alloys.

The spectral sensitivity η (efficiency) of the SEM with the widely used BeO photocathode, as based on studies by A.I.Yefremov et al. (Bibl.7, 22) for the regions of 1 - 100 and 1000 - 3800 Å is shown in Fig.13.IX (correct to within ±60%). Thus, it can be seen that these receivers can be effectively used in the soft X-ray and ultraviolet regions of the spectrum where the solar radiation flux is so small that the apparatus can be expected to count each individual photon.

Sufficiently high stability with respect to external effects (prolonged

stay in air, intense irradiation, temperature fluctuations, etc.) as well as satisfactory sensitivity are also exhibited by dynodes of strontium fluoride SrF_2 and nickel (Bibl.22).

The amplification factor with respect to the measuring-circuit voltage should not be too high, since the pulse amplitude of the SEM is sufficiently large /223

$$U = \frac{q}{C_s} = \frac{ke}{C_s}, \qquad (8.IX)$$

where q is the charge accumulated by the stray capacitance C_s of the circuit during a single pulse; k is the SEM amplification factor; and e is the electron charge.

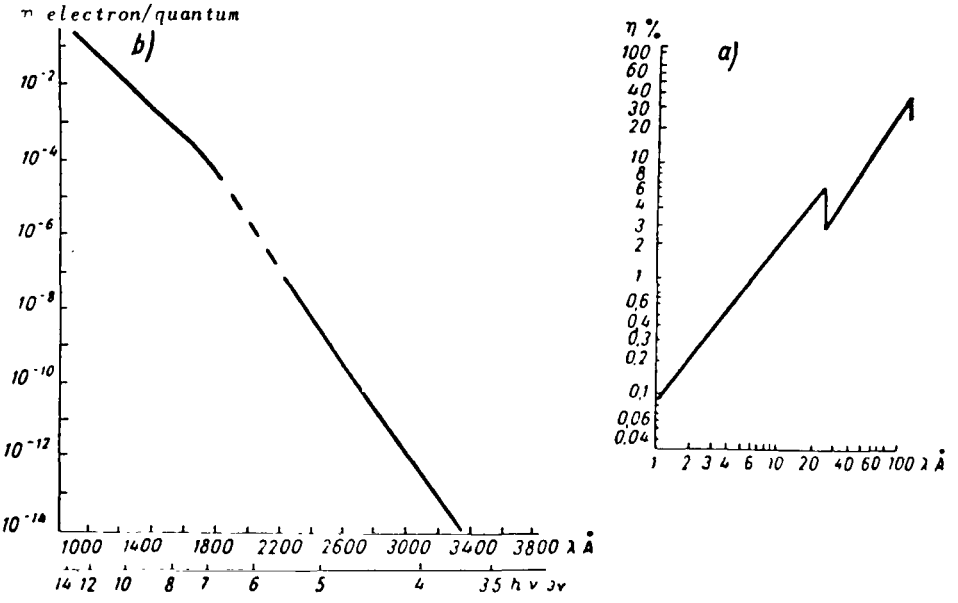

Fig.13.IX Spectral Sensitivity of SEM to 100 Å (a) and more than 1000 Å (b).

For an SEM with 14 BeO dynodes - if a 5000-v voltage is applied to it - we have $k \approx 10^7$ (Bibl.22). If $C_s = 10^2$ μμf, we have $U \approx 10^{-2}$ v.

The duration of pulses from each recorded quantum is short [only 10^{-8} to 10^{-9} sec (Bibl.7)].

The filter system installed in, e.g., the second spacecraft (Bibl.8) contained a disk with a set of nine filters. Once every second, the disk rotated through 1/12 revolution so that a new filter moved in front of the receptor intake. One-half of the 12 positions of the disk was occupied by filters for isolating the X-ray and far-ultraviolet regions of the spectrum. Of the remaining positions, three were occupied by quartz crystal filters for isolating the UV region of $\lambda > 1500$ Å where the solar emission is stable and the variation /224

in the output signal is due to the variation in sensitivity of the apparatus or to the variation in the angle between the optical axis of the SEM and the orientation toward the sun. In one position, a β-source (carbon isotope C^{14}), designed for autonomous verification and calibration of sensitivity, faced the SEM. The last two positions served to check the null point of the instrument. In this case, the SEM intake was covered with shutters, and standard signals were transmitted to the telemetry channel and utilized to determine the onset of the measurement cycle.

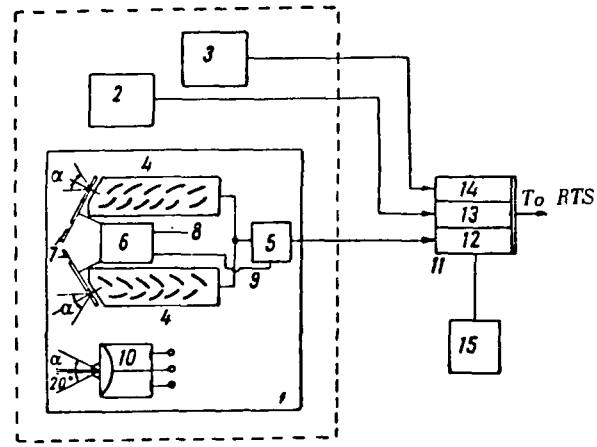

Fig.14.IX Block Diagram of Instrument with SEM.

The block diagram of the system is shown in Fig.14.IX. Each optical unit contains two SEM receivers (4), with filter disks (7) synchronously rotating in front of them. The SEM outputs are connected in parallel so as to enlarge the overall angle of view of the instrument.

The tetrahedral solid angle of view of each SEM subtends $50 \times 60^{\circ}$ while the angle between the optical axes of both receivers is 80°. This created a dead zone of 20° between the fields of view α of the receivers in a single unit (Fig.14.IX).

The optical units contained preamplifiers (5), step-up motors (6) for the disks (7) and autonomous-connection sensors (10). The control signal was /225 transmitted from the motor (6) across the line (9). The engine was powered from the unit (15) over the line (8). The recording circuit PT (11), mounted inside the capsule, contained rapid-acting normalizing flip-flop circuits T and counting-rate meters CRM (12, 13, 14). To enhance the accuracy of measurements, each channel is provided with three series-connected CRM, each operating in a different frequency range. The outputs of the CRM operating in the same frequency ranges, and making connection with the telemetry system RTS, were not separated.

The operating range of the CRM over the linear segment of the output characteristic could be adjusted by varying the proportioning capacitance C_{pr} (cf. Chapt.V).

The autonomous connection of power supply to this entire unit, at least one of which faces the sun, is assured by autonomous connection sensors (10).

Processing of the data necessitated corrections for the variation in the sensitivity and null point of the instrument; in accordance with the calibration curve for a given CRM, the magnitudes of U_{out} were then converted to counting rate N in pulses/sec for the spectral range concerned.

Section 5. Spectral Devices

A characteristic component of any spectral device is a dispersing system for the spatial separation of rays of different wavelengths.

Depending on the dispersing system used, spectral devices are classified into prism and diffraction types; depending on the method of spectrum recording, into spectrographs and spectrometers.

So far, spectral interference devices which permit obtaining hyperfine structures in a narrow spectrum range, have never been used on rockets and satellites.

The basic components of a spectrometer are: an optical focusing system with an entrance aperture usually of the slit type, a dispersing system, a spectral recording unit (exit slit with a detector and a scanning system), an amplifier unit, and a signal-shaping unit.

The focusing optics of spectral instruments employing prisms or plane diffraction gratings consists of two lenses: the collimating lens O_1 and the camera objective O_2 (Fig.15.IX). The collimating lens O_1 produces a parallel beam of rays traveling from the slit to the dispersing system D; the entrance slit s of the spectroscope lies in the focal plane of the lens O_1. Images of the entrance slit s are formed in the focal surface P of the camera objective O_2; each of /226 these images represents a spectral band (line) and their entity gives the spectrum. The focal plane of the objective O_2 lies at an angle ϵ to the optical axis of the camera.

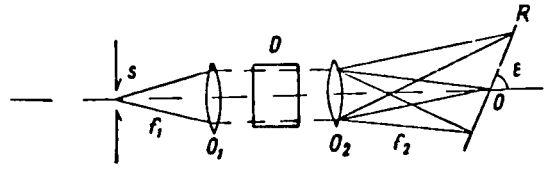

Fig.15.IX Principal Optical Diagram of the Spectral Instrument with Lens Optics.

In spectral devices, operating on an autocollimating circuit, when the ray passes through the dispersing system, one lens takes over the role of both collimating lens and camera objective.

In devices with concave diffraction gratings, focusing is accomplished by this same grating without additional optics. Such devices find the widest application in short-wave spectrum regions, while in the above-mentioned far-ultraviolet regions their use appears only potentially possible.

The dispersing system and focusing optics determine the basic characteristics of the spectral device. Let us briefly discuss these characteristics.

1. Dispersion. The spacing of the spectral lines, differing by $d\lambda$, is characterized by an angular dispersion $D_\varphi = \frac{d\varphi}{d\lambda}$ in terms of angular units $d\varphi$ and by an inverse linear dispersion $D = \frac{d\lambda}{d\ell}$ in terms of linear units $d\ell$, where the dispersion is expressed by the number of wavelengths (Å) per unit length of the spectrum (in mm). The inverse linear dispersion D, indicated in Fig.15.IX, is correlated with the angular dispersion D_φ by the simple relation

$$D = \frac{\sin \varepsilon}{f_2 D_\varphi}. \qquad (9.IX)$$

For prism-type spectroscopes (with the prism in a minimum-deviation position), the dispersion is determined by the refracting angle A and by the refractive index $n = f(\lambda)$ in accordance with the well-known formula

$$D_\varphi = \frac{2 \sin \frac{A}{2}}{\sqrt{1 - n^2 \sin^2 \frac{A}{2}}} \frac{dn}{d\lambda}. \qquad (10.IX)$$

The dispersion of a system with several prisms equals the sum of the dispersions of its components. However, the number of prisms in the system is limited by the allowable losses during the reflection and absorption of radiant energy. A decrease in the angle of incidence of the rays, compared with the angle of minimum deviation of the prism leads to an increase in the dispersion D_φ, which also involves an increase in losses and aberration, chiefly, astigmatism. /227

The angular dispersion of instruments with diffraction gratings is determined by the order K of the recordable spectrum, the lattice constant a and the diffraction angle φ, as shown by the formula

$$D_\varphi = \frac{K}{a \cos \varphi}. \qquad (11.IX)$$

The maximum order K_{max} of the diffraction spectrum is limited by the condition $\sin \varphi_{max} = 1$, which implies that

$$K_{max} = \frac{a}{\lambda_m}, \qquad (12.IX)$$

where λ_m is the smallest wavelength in the spectrum.

At $a = \lambda_m$, only first-order spectra can be obtained.

The gratings used in the short-wave region with a lattice constant of $a = 0.45\ \mu = 4500$ Å (1200 lines/mm) thus make it possible to obtain in the short-wave region spectra with an extremely large dispersion (up to 1 Å/mm for $K = 5$ and $f_2 = 10^2$ cm).

At normal incidence of rays on the grating ($\varphi \approx \psi \approx 0$), the dispersion D_φ is practically a constant ($D_\varphi \approx \frac{K}{a}$). The resultant spectrum is known as normal. For concave gratings, the inverse linear dispersion is

$$D = \frac{a \cos \varphi}{K\rho}. \qquad (13.IX)$$

At normal incidence of rays, the inverse dispersion D is constant and equal to $\frac{a}{K\rho}$. For example, at $a = 4500$ Å, $K = 1$ and $\rho = 1$ m, we have $D = 4.5$ Å/mm.

2. Resolution. The resolving power R with respect to the spectrum characterizes the least distance between two adjacent spectral lines detected separately. Here, R is determined quantitatively as the ratio of the wavelength λ of a given spectral line to the resolving power $\Delta\lambda$. In practice, the least distance $\Delta\lambda$ between two resolvable spectral lines depends on the sensitivity of the receiver or photographic material, on the diffraction in the effective aperture of the dispersing system, on the quality of the lens system, and on the width of the entrance slit. On the basis of Rayleigh's diffraction condition, i.e., assuming that a gap of approximately 20% in spectral intensity is recorded when using a device with an extremely thin entrance slit (Bibl.6), it is possible to relate the theoretical resolving power R of the dispersion element to its angular dispersion: /228

$$R = \frac{\lambda}{\Delta\lambda} = dD_\varphi, \qquad (14.IX)$$

where d is the effective aperture of the dispersing element.

The resolution of a system of b identical prisms, in a device with minimum deviation of the prism, is equal to

$$R = tb\frac{dn}{d\lambda}, \qquad (15.IX)$$

where t is the baseline of one prism.

The resolving power of the prisms thus changes with the wavelength; it increases in the short-wave region of the spectrum. Use of prisms of larger dimensions (longer base t and larger effective aperture d) increases the resolu-

tion of the instrument without changing the linear dispersion and thus augments the brightness of the spectrum. The resolving power of prism spectrographs is of the order of 10^3 - 10^4 (Bibl.6).

The theoretical resolving power of a diffraction grating for a spectrum of a given order K is a constant and equal to

$$R = KN. \tag{16.IX}$$

To increase the resolution R, attempts are being made to incorporate in the devices large-size gratings with a large number N of rulings per mm.

For both the ultraviolet and visible spectrum regions, gratings with 600 or 1200 rulings per mm and with a working (ruled) surface up to 100 mm in length are normally used (Bibl.10, 17). The theoretical resolving power of gratings of this kind reaches 6×10^4 and 1.2×10^5, respectively, already for the first-order spectrum, as can be seen from eq.(20.IX).

Reflection gratings of the echelon type, because of the variation in profile of the rulings, make it possible to concentrate nearly the entire reflected energy in a higher-order spectrum. The theoretical resolving power of gratings of this kind reaches approximately 10^6 in the wavelength region $\lambda \approx 2000$ Å /229 (Bibl.6).

3. Relative aperture. The aperture ratio of spectroscopes is characterized by the magnitude of the radiant flux Φ_λ for a narrow portion $\Delta\lambda$ of the spectrum. If the spectral brightness of the entrance slit of the spectroscope is B_λ then the radiant flux passing through the device within the spectral range $\Delta\lambda$ obviously will be

$$\Phi_\lambda = B_\lambda s l \omega P_\lambda \Delta\lambda, \tag{17.IX}$$

where s and l are the width and height of the entrance slit, ω is the solid angle at which the effective aperture of the dispersion system is visible from the center of the entrance slit, and P_λ is the transmittance of the entire optical system for the spectral range $\Delta\lambda$.

For the system shown in Fig.17.IX eq.(17.IX) can be rewritten in the form of

$$\Phi_\lambda = \frac{\pi B_\lambda l s P_\lambda}{4} \left(\frac{d}{f_1}\right)^2 \Delta\lambda, \tag{18.IX}$$

where d is the diameter of an equidimensional circle of the effective aperture of the dispersion system.

Equation (18.IX) applies to spectrometers where the dimensions s' and l' of the exit slit are such as to allow for the increase in s and l by the optical focusing system.

The height of the entrance-slit image on the spectrum will be

$$l' = l\frac{f_2}{f_1}. \qquad (19.IX)$$

The width s' of the exit slit must be taken with allowance for broadening due to ray scattering, i.e.,

$$s' = s\frac{f_2}{f_1} + \Delta\lambda\frac{dl}{d\lambda}, \qquad (20.IX)$$

where $\frac{d\ell}{d\lambda}$ is the linear dispersion of the instrument.

If the sensitive surface area of the receiver is small (smaller than $s' \times \ell'$), it may be necessary to install a converging lens beyond the exit slit of the spectrometer.

Equation (18.IX) shows that an increase in the aperture ratio of spectrometers may be accomplished by enlarging the angular dimensions of the entrance slit $\frac{\ell}{f_1}$ and partly also $\frac{s}{f_1}$ as well as of the effective aperture d of the dispersion system. However, the possibilities for enlarging the entrance-slit width s and hence also the spectral lines in $\Delta\lambda$ are limited, since this leads to a deterioration of the other characteristics of the spectral instrument. This enlarging may be done only when measuring widely spaced spectral lines.

The aperture ratio of spectrographs is usually characterized by monochromatic illumination E_λ in the spectral plane, since the effect of radiation on the photographic material is determined by the magnitude of E_λ. With the aid of the formulas derived previously, this can be written as /230

$$E_\lambda = \frac{F_\lambda}{l's'} = \frac{\pi B_\lambda P_\lambda}{4}\left(\frac{d}{f_2}\right)^2 \frac{s\,\Delta\lambda}{s + \Delta\lambda\frac{f_1}{f_2}\frac{dl}{d\lambda}}. \qquad (21.IX)$$

For fine monochromatic lines ($s \gg \Delta\lambda$), as can be seen from eq.(21.IX), the aperture ratio of the spectrograph is independent of the entrance-slit width s and is equal to

$$E_\lambda = \frac{\pi B_\lambda P_\lambda}{4}\left(\frac{d}{f_2}\right)^2 \Delta\lambda. \qquad (22.IX)$$

Equations (21.IX) or (22.IX) indicate that the aperture ratio of spectrographs is independent of the size of the entrance slit of the instrument and chiefly increases as a function of the relative aperture d/f_2 of the camera.

Spectra of extremely feeble sources (nightsky glow, etc.) are taken with the aid of spectrographs having an aperture ratio up to $\frac{d}{f_2} = 1 - 0.5$.

For reflecting types of diffraction gratings, the solid angle between the entrance slit and the grating is

$$\omega = \frac{Q \cos \psi}{r_1^2}, \qquad (23.IX)$$

where Q is the operating surface area of the grating, r_1 is the distance between entrance slit and grating.

The radiant flux across the exit slit can be written as

$$\Phi_\lambda = \gamma B_\lambda s l \frac{Q \cos \psi}{r_1^2} \Delta\lambda \qquad (24.IX)$$

where γ is grating efficiency for a given angle of incidence ψ and a diffraction angle φ.

Then, the dimensions of the exit slit must be

$$l' = l \frac{r_2}{r_1} \quad \text{and} \quad s' = \frac{s}{\cos \varphi} \qquad (25.IX)$$

where r_2 is distance between grating and exit slit.

Note that in the direction at right angles to the diffracted beam the widths of the entrance and exit slits will be the same. This markedly differentiates devices with concave gratings from systems with focusing optics. /231

Hence, the illumination of the photographic film of a concave-grating spectrograph in the central portion of the spectrum will be

$$E_\lambda = \gamma B_\lambda Q \frac{\cos \varphi \cos \psi}{r_1 r_2} \Delta\lambda = \gamma B_\lambda \Delta\lambda \frac{Q}{\rho^2}, \qquad (26.IX)$$

where ρ is the radius of curvature of the grating and $\frac{\sqrt{Q}}{\rho}$ is a quantity representing the relative aperture of the grating.

The illumination E_λ is a function of the angles φ and ψ, as expressed by the efficiency γ, so that the aperture ratio of grating spectrographs varies with the length of the spectrum.

The efficiency of echelon gratings (Bibl.19) may exceed 60% in the region of about 2000 Å. This means that the intensity of the emergent monochromatic flux Φ_λ accounts for more than 60% of the intensity of the integral incident flux.

In the X-ray region ($\lambda < 30$ Å) gold-coated gratings are the most effective

(Bibl.14), particularly for low angles of incidence. In the UV region ($\lambda >$ > 500 Å) aluminum-coated gratings exhibit high efficiency (up to $\gamma \approx 75\%$).

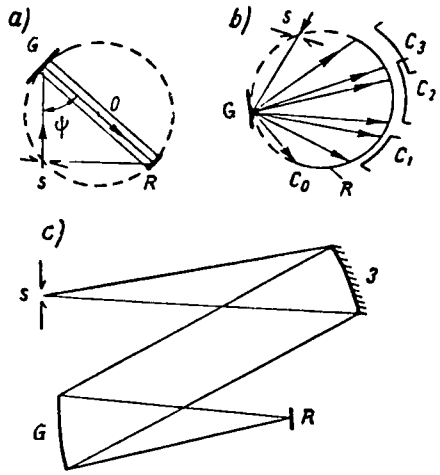

Fig.16.IX Mounting of Concave Gratings according to the Systems of: Rowland (a), Paschen (b) and Wadsworth (c).

The methods of installing concave diffraction gratings in the instruments may differ. We will describe the most often used methods of this kind.

The Rowland method (Fig.16a.IX), which is most often used in these devices (Bibl.6, 10, 17, 20) provides for aligning the working surface of the grating G, the entrance slit s, and the spectrum receiver R over the perimeter of a circle whose diameter equals the radius of curvature ρ of the grating. The elements G and R are so mounted on a rigid base O that they can be displaced in two mutually perpendicular directions, with the entrance slit s being located at their point of intersection. By moving the base O along guide rails, the angle /232 of incidence ψ of the beam on the grating can be altered and various portions of the spectrum can be focused on the receiver.

The Paschen system (Fig.16b.IX) differs from the Rowland system in that the surface of the receiver itself is curved along an arc of the Rowland circle. In this case, the concave grating G, the slit s, and the sensitive surface R are along the Rowland circle. Such a method ensures the simultaneous measurement of first-, second- and third-order spectra, C_1, C_2, and C_3, as well as obtainment of the central image C_0.

Mounting the grating so that the beams will be parallel (Wadsworth system, Fig.16c.IX) is accomplished with the aid of a spherical concave mirror M at whose focus the entrance slit s is located. In this system, the spectrum is formed at the cylindrical surface R.

To obtain smaller dimensions of the spectral device and enhance its optical

qualities in the vacuum UV region, use is made of a normal-incidence system with a small angle of incidence of the beams on the grating ($\psi < 10^\circ$). In this case, the grating is mounted in a slanted position, such that the spectrum is obtained beneath the entrance slit. The normal-incidence system has the advantage of minimizing astigmatism and ensuring a virtually constant dispersion with respect to the spectrum (Bibl.6, 17).

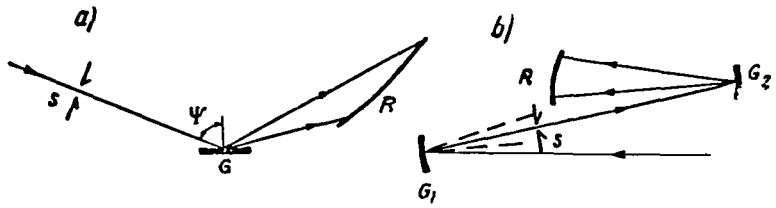

Fig.17.IX Mounting of Concave Gratings in Oblique-Incidence (a) and Normal-Incidence (b) Systems.

With respect to the X-ray ($\lambda < 100$ Å) and far-UV ($\lambda < 500$ Å) regions of the spectrum, the reflection factor (efficiency) of the grating and the dispersion can be increased by a Rowland-circle alignment based on an oblique-incidence ($\psi \sim 90^\circ$) system (Fig.17a.IX). However, the dispersion then varies considerably with the length of the spectrum and the astigmatism is substantial (Bibl.6, 17). Short-wave boundaries of spectra obtained with one and the same grating at angles of incidence of 0° and 85° were approximately 320 and 53 Å, respectively (Bibl.6). In the normal-incidence system, an additional predispersion grating (Fig.17b.IX) is often employed along with the main grating in order to reduce the scattered-light background and increase the dispersion.

Spectrographs find wide application in the United States, where extra- /233
atmospheric studies of short-wave radiation have been conducted since 1946 with the aid of V-2, Aerobee, Viking, and other rockets (Bibl.20). Most of the spectrographs used are compact diffraction spectrographs with reflection gratings mounted in a normal- or oblique-incidence system depending on the spectral region measured.

During the initial rocket-borne studies of this kind, performed over limited periods of time, it was expedient to use diffraction devices with a sufficient aperture ratio and limited resolution ($R \approx 10^4$) as well as with dispersion ($D \sim 10$ Å/mm) in the first-order spectrum. In later devices, these characteristics were improved by one order and more (Bibl.10).

With the object of prolonging the observation period and obtaining sufficiently long exposures, the original rocket-borne spectrographs incorporated wide-angle optical slit-illuminating systems. The principal shortcoming of the wide variety of these systems (Bibl.10, 20) was the randomness of the selection of instants suitable for triggering the instrument, as well as the displacement of the slit with respect to the spectrum during exposure, owing to the change in the position of the sun relative to the rocket. This caused blurring of the spectra. In view of the inconvenience of wide-angle systems for slit illumination, at present only instruments with a small angle of view as well as with a

system of automatic sun tracking are employed. This ensured the necessary exposure time [up to tens of seconds and longer (Bibl.10, 17)].

The sensitive materials used were sensitized fine-grain positive films and - in the vacuum region of the spectrum - gelatin-free films and plates (of the Schuman type).

For absolute intensity measurements of spectral emission, the film must be calibrated with respect to a standard source. In view of the difficulties of such calibration [the errors in wavelength regions shorter than 2000 Å reach 100% (Bibl.17)], supplementary measurements are occasionally made of the intensity in the spectral region emitted by the sun or in the spectral line L_α, which were used as a criterion for estimating the intensity of the other spectral regions or lines (Bibl.10).

To reduce scattered light in the instruments, the entrance slits are made sufficiently narrow (to 6 μ) and the gratings sometimes are deposited on materials whose reflecting properties decrease in the spectral region with longer wavelengths, where the intensity of the sunlight is considerable [quartz crystal, certain resins, red glass, etc. (Bibl.10)]. For the same reason, the internal components of the spectrograph are coated with an absorbent dye.

The improvements in the properties of diffraction gratings in certain American spectrographs (Bibl.10) are due to the use of a toroidal slit-illuminating mirror whose astigmatism offsets the astigmatism of the grating. /234

The use of pre-dispersion systems with echelon gratings enabled Purcell and Tousey (Bibl.10, 20) to obtain a dispersion of ~ 0.5 Å/mm and a resolution of about 10^5 and to investigate the contour of the L_α line (cf. Fig.2.IX). A spectrograph widely utilized by Tousey et al. (Bibl.10, 17) incorporated a concave diffraction grating with a radius of curvature ρ = 40 cm and with 600 lines per mm, to obtain spectra in the region from 500 to 2500 Å at a resolution of 1 Å. The grating was mounted in a normal-incidence system ($\psi = 2.3^\circ$), and the first-order spectrum was recorded on film. The spectrograph casing was mounted on a twin-axis tracking drive which kept the slit oriented toward the sun. To eliminate the effect of the rocket tumbling, the entire nose cone, including the spectrographs, was able to rotate about its axis. A tracking system ensured orientation toward the sun, with an accuracy to ±5 seconds of arc.

The oblique-incidence ($\psi = 85^\circ$) system used in various rocket-borne experiments by Violet and Rense (Bibl.10, 17), has made it possible to record spectra to λ = 84 Å. This spectrograph is equipped with gratings of various size with 600 lines to the millimeter, a radius ρ = 50 cm, and dispersion of from 12.6 Å/mm for λ = 1200 Å to 6.6 Å/mm for λ = 300 Å. The resolving power of this instrument was 0.4 Å in the region of L_α.

The automatic diffraction spectrograph with a concave grating, designed to obtain the solar spectra in the 1000 - 3000 Å range on board geophysical rockets, which was developed by A.V.Yakovleva et al. (Bibl.23) has found wide application. The optical system of this spectrograph (Fig.18.IX) contains a mirror (1) of the sun-tracking system, an entrance slit (2) of fixed size 2 × × 0.02 mm, and a concave diffraction grating (3) mounted in a normal-incidence

system on the Rowland circle. The diffraction grating of this instrument has 600 rulings to the millimeter and ensures a linear dispersion of 16.7 Å/mm. Photographic film (4) is placed below the entrance slit of the instrument, with the grating inclined in the vertical plane. Mounted in the lower part of the optical system are two mirrors (5) and (7), a lens (6) and illuminating lamps (9) designed to obtain an image of the face of the clock dial (8) at the beginning and end of exposure of the spectrum on the same film.

The optical system of this spectrograph is assembled inside a tube designed for attachment in lieu of the rocket nose cone. The upper part of the spectrograph (the head) can revolve through 360° about the rocket axis to ensure steady orientation toward the sun. The sun-tracking system is controlled by photoresistors installed in the windows of the head. Mounted outside an opening in the casing is the mirror (1) of the sun-tracking system, which can deflect /235 20° toward either side from its central position. This ensures operation of the sun-tracking system in two planes: azimuthal and vertical.

The automatic device of the spectrograph operates so that the window of the instrument head opens one minute after launching of the rocket and after triggering the sun-tracking system. After the instrument is oriented toward the sun, automatic multiple photographing of the spectrum at a fixed (prior to launching) exposure time is started. After the photographing is completed, the window of the tracking head closes and the film is rewound into the magazine. Time marks are printed on the film at the beginning and end of every photographing cycle.

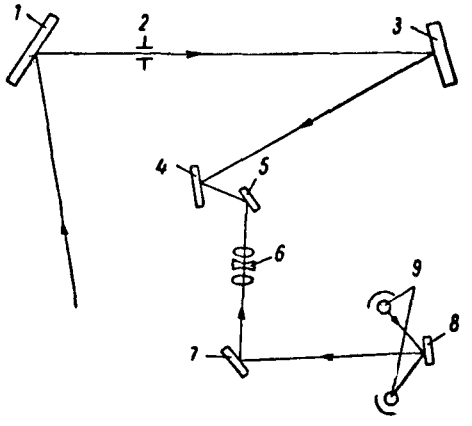

Fig.18.IX Optical System of Rocket-Borne Spectrograph.

Various sun-tracking systems for orienting the instrument toward the sun either directly or by shifting the intake mirror have been developed.

The operation of these systems which, as a rule, have two stages of guiding (rough and precise) is based on the use of FSK-type photoresistors whose maximum spectral sensitivity is close to $\lambda \approx 5000$ Å and which have a high dark resistance. The sensor of the tracking system includes two photoresistors mounted

at a mutual angle such that one half of the working surface of each is shaded by a forward-projecting disk when it is oriented toward the sun. When the sun deviates from the sensor axis a mismatch signal produced by motors is generated in the bridge circuit to which the photoresistors are connected. One of the /236 mirror-type sun-tracking systems, e.g., based on FSK-0 photoresistors (Bibl.5) provides for orientation of the disk center with respect to the sun, with an accuracy to within at least five minutes of arc.

Soviet-built rocket-borne spectrographs of various design (fluorite-type with a 360° illuminating lamp and a sun-tracking system) have been used in rocket studies of atmospheric ozone (Bibl.23).

For spectral analysis, characteristic film curves were recorded in advance. These curves were plotted every 50 Å in the spectral region from 2500 to 3100 Å by means of hydrogen-lamp blackening marks. The characteristic operating curve for this spectrum region was obtained by averaging all curves plotted. The spectra photographed at various altitudes were analyzed with an MF-4 type recording microphotometer, and the blackening marks were recalculated in terms of relative intensities by means of the averaged characteristic curve.

So far, spectrometers have been used much less frequently for studies of the short-wave spectrum region than spectrographs. As pointed out previously, this can be attributed to the lower reliability of telespectrometers and the lack of proper receivers, particularly in the UV region of $1000 < \lambda < 3500$ Å.

The most suitable receivers for UV spectrometers are secondary-electron multipliers (SEM) of the open type, whose properties were described previously (cf. Sect.5 of this Chapter). The spectral range of SEM-containing instruments is limited by their sensitivity range; for BeO this is approximately 1 to 1000 Å (cf. Fig.13.IX). United States telespectrometers incorporate SEM-type detectors with tungsten dynodes whose sensitivity reaches to the vacuum UV region, up to 1800 Å (Bibl.24).

The existing (Bibl.3, 24) devices can measure spectra in the far-UV region and use concave diffraction gratings mounted in an oblique-coincidence system. Scanning of the spectrum is accomplished by mechanical systems.

The parameters and operating features of spectrometers will be described on the example of the photoelectric diffraction device installed in the third satellite (Bibl.3). This spectrometer was developed to ensure reliable performance of the measuring circuit in the presence of extremely weak and extremely strong radiant fluxes of as high as 10 $erg \cdot cm^{-2} \cdot sec^{-1}$.

The variant of the device (Bibl.4) described here was designed for measurements in the region of the resonance line of ionized helium He II with $\lambda = 304$ Å, emitted by the sun. It can be adjusted to studies of other lines, in particular, of L_α or He II with $\lambda = 584$ Å.

The device consists of four main components: 1) spectrometer with a sun-tracking system; 2) electric sun-tracking system unit (ESU); 3) electronic /237 measuring and recording system unit (ERU); and 4) power pack which consists of a battery of chemical cells.

The optical system of the device (Fig.19.IX) contains an entrance slit S (dimensions, 0.2 × 7 mm), a diffraction-grating replica G [with 1200 rulings to the millimeter, radius of curvature 500 mm, dispersion (16 Å/mm)], miniature quartz prism Pr, a trap Tr, an outlet diaphragm O, an exit slit S' (dimensions 0.1 × 0.15 mm), and a SEM detector with BeO dynodes.

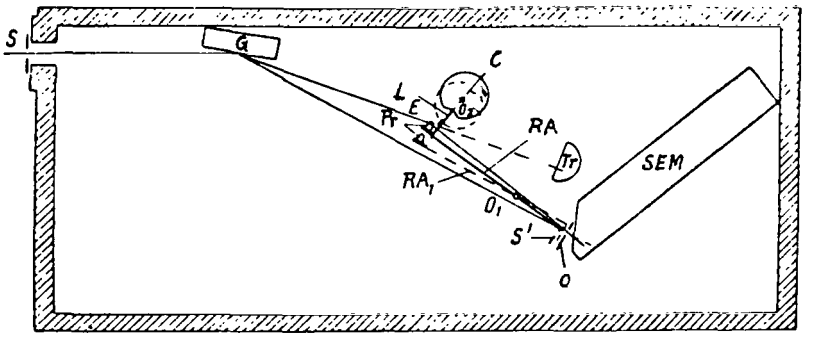

Fig.19.IX Optico-Kinematic Diagram of the Telespectrometer.

The prism Pr and the scanning slit S' are mounted on the ends of a rocking arm RA swinging about the point O_1. The swinging of the rocking arm is accomplished by a pulsed cadence motor which turns the cam C with a double cardioid on which rests the lug L of the rocking arm. The rocking arm swings back and forth between the positions RA and RA'; while it is in the position RA, the prism enters the focus of the zeroth-order spectrum and directs it toward the receiver. This unresolved portion of the spectrum (from 2000 to 1700 Å) is emitted with extreme stability by the sun and serves to verify the sensitivity of the measuring circuit at the end of each spectral scanning cycle. As the slit shifts from its extreme left-hand position, the zeroth-order spectrum is absorbed by the trap Tr. When in the position RA', the rocking arm closes the contact energizing the operation of the scanning system (off-null).

The total duration of the spectral scanning cycle, which is 30 Å wide in both directions from the center of the line being recorded, is 170 sec. The displacement rate of the slit is 0.05 mm/sec and its optical width is 1.5 Å.

The device is triggered by a relay on command, during the 20th minute after the probe is injected into orbit. This is done to protect the SEM from inter-dynode discharges that might occur in the presence of insufficient vacuum. /238 After this, the sun-tracking system and the scanning device controlling the clock-pulse generator CPG begin to operate (Fig.20.IX). The SEM is supplied with a voltage of 5.5 kv from the converter Co. SEM pulses, whose repetition rate is proportional to the illumination of the receiver, are amplified by a preamplifier PA and are fed from here, across a coaxial cable, to the ESU unit where they are additionally amplified. The amplified SEM pulses trigger the flip-flop T which has the role of a rapid-acting standardizing device; after amplification by amplifier A, the pulses travel simultaneously to the output counting rate meters CRM_1, CRM_2, and CRM_3. The counting rate meter CRM_1 has a logarithmic scale and operates in the frequency range from 1 to 10^5 cps, while

the CRM_2 and CRM_3 operate successively in two subranges connected by the analyzer (3) over the switches (1) and (2).

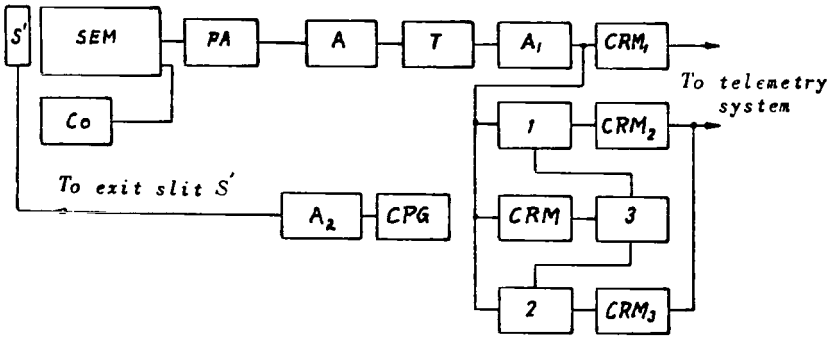

Fig.20.IX Block Diagram of Telespectrometer.

Processing of the data involves a determination of the counting rate and relative intensity in a given spectrum region $J = \frac{A_1}{A_0}$, where A_1 is the recording amplitude, and A_0 is the amplitude of the zeroth-order spectrum.

The absolute intensity of the investigated spectral line may be calculated with an error of the order of ±100%, according to the known parameters of the spectrometer and the radiation receiver (Bibl.4).

CHAPTER X

MEASUREMENTS OF RADIANT ENERGY IN THE VISIBLE AND INFRARED SPECTRUM REGION

Section 1. Basic Problems of Measurement and Instrumentation

The visible region of the spectrum encompasses a comparatively narrow /239 wavelength range from 0.38 to 0.76 μ, whereas the infrared region extends from 0.76 to 350 μ. Hence, the latter is additionally divided into the near-infrared (up to 2.5 μ or more than 4000 cm^{-1}), the middle (from 2.5 to 50 μ or from 4000 to 2000 cm^{-1}), and the far-infrared (more than 50 μ or less than 2000 cm^{-1}).

The sun is the most important source of the radiant energy received by the earth in the visible and near-infrared region. The integral flux of solar radiation incident on an area of one square centimeter at right angles to its rays outside the atmosphere, for the mean distance between earth and sun, known as the solar constant, is $F_0 = 1.97 \pm 0.01$ cal/cm^2 · min (or 0.137 w/cm^2) (Bibl.2).

The spectrum of the visible and infrared radiation of the sun has a continuous character. It is due to recombinations of various atoms in the photo-

sphere. The maximum solar energy is emitted in the visible spectrum region (about 0.5 μ). The temperature of an absolutely black emitter (the effective temperature of the sun) which has a similar spectrum and emits an integral flux of the same density F_o is $T_e = \left(\frac{F_o}{\sigma}\right)^{1/4} = 5785^\circ K$, where $\sigma = 5.672 \times 10^{-12}$ w • • cm^{-2} • deg^{-4} is the emission constant.

The mean luminance or radiant intensity of the solar disk is $J = 2.02 \times \times 10^3$ w • cm^{-2} • $ster^{-1}$ and the mean luminosity of its surface outside the bounds of the atmosphere is $B = 2 \times 10^5$ stilb. The illumination E amounts to 13.6 phots for the mean distance between earth and sun (Bibl.2).

The spectral course of the radiant-energy intensity of the sun, J_λ in cal/cm^2•min•ster•μ at the top of the atmosphere, according to M.S.Malkevich (Bibl.4) is presented in Fig.1a.X (Curve 1). The solar energy (Bibl.2) is basically (~99.9%) enclosed within the spectral interval from 0.2 to 4 μ.

The passage of radiant energy through the atmosphere is accompanied by its selective absorption by gas molecules and scattering by molecules and particles of aerosols. As a result, the radiant energy of the sun is attenuated before it arrives at the earth's surface (Curve 2 in Fig.1a.X) and its spectrum contains gaps due chiefly to absorption by water vapor. The main intensity of the radiant energy of the sun, reflected back from the earth in the visible and near-infrared regions, is illustrated by Curve 3 in Fig.1a.X.

Note that more distant bands - compared with those shown in Fig.1a.X - /24 of absorption by atmospheric gases, according to K.Ya.Kondrat'yev and K.Ye. Yakushevskaya (Bibl.4), are located in the neighborhood of 1.87 μ (H_2O), 2.7 μ (H_2O), 6.3 μ (H_2O from 4.88 to 8.70 μ), 9.6 μ (O_3 from 9.01 to 10.29), 15 μ (CO_2 from 12 to 18 μ), 30 μ (H_2O from 18 to 40 μ), and 80 μ (H_2O from 40 to 120 μ). The sectors with the highest transmissivity are: 3.6 to 4.1 μ, 8.70 to 9.01 μ and 10.29 to 12.00 μ. The latter two usually combine into a single "transparency window" in the atmosphere within the range from 8 to 12 μ.

It is this 8 - 12 μ spectral range that exactly accounts for the maximum in the emission spectrum of bodies with temperatures of 200 - 300°K, i.e., in the natural radiative flux of the earth-atmosphere system.

The spectral density of the natural radiative flux of bodies at the above temperatures, according to Planck's law, is of the order of 10^{-4} to 10^{-3} w/cm^2μ in the neighborhood of the maximum, while about 99.9% of the energy of this radiation lies within the spectral region of roughly from 4 to 40 μ.

In meteorology, radiant energy of wavelengths shorter than 3 - 4 μ is sometimes termed short-wave as distinct from the long-wave or thermal natural radiation of the earth, clouds, and the atmosphere located beyond this spectral boundary.

Solar radiation reflected from the surfaces of the planets and scattered in their atmospheres in an outward direction from the planet's surface, escapes into outer space along with the natural emission of the planet-atmosphere system

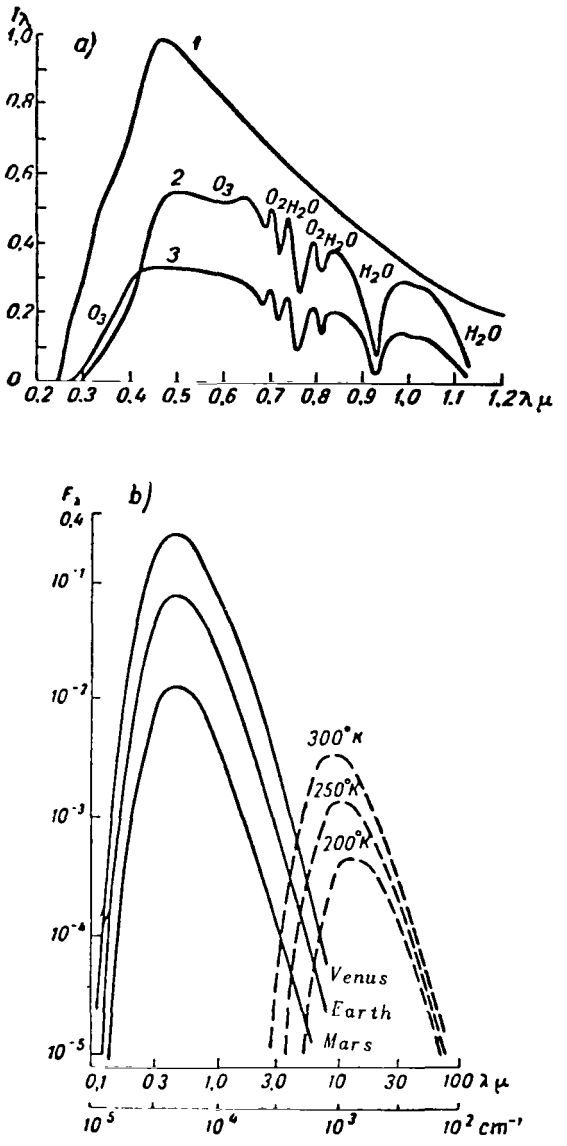

Fig.1.X Spectral Course of the Intensity of the Radiant Solar Energy (a) and Spectral Density of the Flux of Outgoing Radiation from the Planets (b).

(outgoing radiation). At wavelengths exceeding 5 - 6 μ, the spectral density F_λ (in w/cm^2 • μ) (Fig.1b.X) of the natural radiation flux of the earth and other planets (broken curves) already begins to exceed the mean spectral density of the solar radiation flux reflected from them (solid curves). In plotting these curves, the authors (Bibl.9) assumed that reflection from the planets is diffuse and that solar radiation corresponds to a black body with a temperature of 5783°K and that the radiation constant of the planets is ε = 1. The mean planetary albedo was taken as 0.7 for Venus, 0.15 for Mars, and 0.4 for Earth. In reality, it appears that the natural radiation of the planets begins to pre-

dominate (on the illuminated side) even at shorter wavelengths, since the calculations did not allow for the absorption of solar energy by atmospheric gases.

A most important purpose of measuring electromagnetic radiation in the visible spectrum region, performed by space probes and rockets, is a determination of the optical characteristics of the atmosphere and surfaces of the planets. An additional task at present is that of observing the surfaces of the moon and planets with the aid of space probes. Of not less importance is a determination of the analogous characteristics which determine the conditions /242 for using instruments operating in the IR portion of the spectrum, considering that IR rays undergo smaller attenuation while propagating through the regions of atmospheric transparency.

Measurements of the spectral character and absolute quantities of the radiative fluxes reflected from and emitted by the earth and planets make it possible to obtain various important geographical and meteorological data on the planets and their atmospheres. Spectral analyses of short-wave ($\lambda < 4\ \mu$) radiation reflected from a planet make it possible to determine the nature of the reflecting and scattering layers (solid surface, water, or clouds), as well as the impurity content of the atmosphere. In the latter case, measurements must be made at various altitudes in the atmosphere or the ratios of the fluxes of scattered radiant energy in various spectral intervals must be determined. K.S.Shifrin et al. (Bibl.4) developed a simple method for calculating the fluxes of short-wave radiation by using a device with a narrow field of view, installed on an artificial earth satellite, provided that its orientation is known.

Measurements of outgoing long-wave radiation ($\lambda > 4\ \mu$) in the bands of strong absorption (and emission) of water vapor and carbon dioxide (present in the atmosphere of every planet in the terrestrial group) are a means of determining the temperature at various altitudes in the atmosphere. Thus, the earth's emission in the H_2O band, with a center at about 6.3 μ, originates in the uppermost boundary of the distribution of water vapor in the atmosphere, i.e., at a level close to the tropopause. Hence, the radiation flux in this band is quantitatively limited and is determined by the temperature near the tropopause ($\sim 220\ ^\circ K$). On the other hand, measurements of radiant energy in the atmospheric transparency windows where radiation almost freely escapes into outer space, make it possible to determine the temperature of the earth's surface at the measuring site or the temperature of the upper boundary of the cloud blanketing this surface.

An analysis of possibilities for measuring the radiation temperature from a meteorological satellite, performed by V.L.Gayevskiy and Yu.I.Rabinovich (Bibl.4) shows that the effect of the attenuation of radiant energy by aerosols in the 8 - 12 μ transparency window is smaller by one order of magnitude than the effect of the absorption and emission of water vapor in this spectrum region. To enhance the accuracy of measurements, a correction for the moisture content and stratification of the atmosphere has been proposed. The extent of this correction, according to Gayevskiy and Rabinovich (Bibl.4), may reach $10^\circ C$ and more. If this correction is taken into account, the measurements can be correct to within as little as 4 - $5^\circ C$, but this requires concomitant measurement of the moisture content of the atmosphere. The correction for absorption by ozone (in the 9.6 μ band) does not exceed 5° (Bibl.4) and can be dispensed with by using

apparatus operating in a more narrow spectral range (e.g., 10 - 12 μ).

Certain investigators, in particular V.L.Gayevskiy et al. (Bibl.4) have /243 shown that on the basis of the satellite measurements of radiation temperature or radiative flux and the vertical temperature gradient, or on the basis of measurements in the absorption band of oxygen (in the neighborhood of 0.762 μ), whose distribution in the atmosphere is known, it is also possible to determine the altitude of the upper cloud boundary correct to within as little as 0.5 - 1 km.

According to L.R.Rakipova (Bibl.4), the required accuracy of measurements of radiative fluxes in the IR region by an artificial earth satellite should be at least 4 - 5% before these measurements can be utilized to calculate the fields of meteorological elements.

The apparatus used for the solution of these problems must perform absolute measurements of radiative fluxes from a sufficiently small area and must be of the scanning type, i.e. it must successively survey various portions of the planet's surface during the flight of the rocket or space probe. The instantaneous viewing angle depends on the required degree of detail of the picture and on the sensitiveness of the instrument.

The flux density of the radiation of a black surface into a half-sphere with a temperature of 200°K in the spectral interval of 10 - 12 μ is approximately 4×10^{-4} w/cm^2, as can be seen from Fig.1b.X. The measurable fluxes are substantially attenuated by the atmosphere and the instrument's optics, and moreover they are limited by the viewing angle of the receptor.

Measurements of outgoing radiation in various absorption bands are a means of the thermal sounding of the atmosphere, because the predominant part of the radiation flux forms at various atmospheric levels, depending on the amount of the radiating gas in the atmosphere and on the band intensity (Bibl.4, 20). Thermal sounding may also be accomplished through spectral measurements of outgoing radiation in a strong band of a gas whose altitude distribution is known [Kaplan's method (Bibl.10)]. The nature of the transmission spectrum of an atmosphere can clearly serve as a criterion for quantitative spectral analysis of its content of various absorbing components (total moisture content, carbon dioxide content, ozone content, etc.). This task may be accomplished not only by means of spectral apparatus but also by means of filter apparatus which can isolate the near regions of transmission and absorption for the investigated component. In this case, relative measurements of fluxes in selected spectral intervals may suffice to solve the problem.

Note that this last circumstance is highly significant, since absolute measurements of radiation fluxes require a reference source with a corresponding emission spectrum which is compared with the results of the measurements, and the control of the sensitiveness or zero level of the apparatus requires its periodic calibration with respect to an independent reference source.

Integral measurements of the influx (or loss) of energy to and by a planet or its individual regions make it possible to determine the radiation balance/244

$$B = \Phi_s - \Phi_s A - \Phi_\ell = \Phi_s (1 - A) - \Phi_\ell, \qquad (1.X)$$

where Φ_s and Φ_ℓ are the fluxes of shortwave and longwave radiant energy, respectively, incident on a horizontal surface located at the measurement point from the upper or lower half-sphere of space, and A is the mean albedo of the region present in the field of view of the measuring device.

Note that the location of cloud over the earth's surface and the anisotropy of the radiant energy field due to other causes (nonuniformity of underlying surface and atmosphere) cause the angular distribution of the outgoing radiation as well as the radiation balance to be highly dependent on concrete conditions at the moment of observations.

The calculated density of the integral flux of outgoing heat radiation at the top of the atmosphere, as determined for mean cloud conditions correct to $< \pm 6\%$ (Bibl.10) varies from 0.20 cal/cm^2 · min in the polar regions to 0.36 cal/cm^2 · min in the subtropics. The limits of the density of the outgoing radiative flux vary from 0.14 to 0.394 cal/cm^2 · min. The mean density of this flux in the spectral interval of 2.5 - 40 μ is 0.28 cal/cm^2 · min (1.4×10^{-2} w/cm^2) according to measurements by geophysical rockets at altitudes of 100 - 500 km (Bibl.12).

Important studies of optical characteristics of the atmosphere in the visible and infrared portions of the spectrum as well as measurements of absolute values of radiative fluxes and radiation balance at altitudes of up to 500 km were carried out with the aid of the VOS-type upper-air geophysical probes launched by the Soviet Union [cf. Sect.2, Chapt.I (Bibl.1, 8, 12, 14)]. The United States is performing prolonged and extensive measurements with the aid of Tiros type weather satellites. Certain measurements have been carried out by using this apparatus, as well as the IR apparatus of the American exploratory satellites, in rockets and satellites of the Vanguard, Explorer, and other series (cf. Sect.4, Chapt.I). Considerable experience in operating this apparatus has been obtained in the work with space-probe orientation systems which operate in both the visible and the infrared regions of the spectrum (Bibl.20).

Varied telemetering apparatus used to measure radiative fluxes in the wavelength range considered above, owing to methodological considerations, are divided into photometers, radiometers, spectrophotometers, and actinometric instruments. This division is largely conditional, however.

Various parameters are used to characterize optical apparatus, and chiefly:

threshold sensitivity, characterized by the least detectable or measurable radiative flux Φ_f, w; /245
instrument sensitivity S, v/watt;
time constant (inertia) τ of instrument, in sec;
limits of measurement of radiative fluxes $\Phi_{max} - \Phi_{min}$;
spectral range of instrument $\lambda_2 - \lambda_1$, in μ;
dispersion D and spectrum resolution R (for spectral instruments);
viewing angle ω, in ster, or δx deg;
precision of measurements.

The most important parameters of an instrument are determined by its radiant energy receptor.

In the visible and neighboring portions of the spectrum, optimal instrument parameters are assured by using various types of electronic photomultipliers as depending on their spectral characteristics (cf. Fig.5.V).

In the infrared portion of the spectrum, the highest instrument parameters (τ, Φ_f, etc.) can be achieved by using cooled receptors (photoresistors and superconducting bolometers). The technical difficulties involved in the development of long-term coolant devices for the maintenance of the required low temperatures, as well as the marked increase in the dimensions and energy requirement of the apparatus incorporating such devices, have at present led to the broad use of non-cooled receptors of the bolometric type. In the near-IR region photoresistors are used, while instruments admitting comparatively large inertia contain thermoelements (Bibl.4, 8, 9, 10, 19, 20).

The basic criterion for selecting the optical material used in the apparatus is its spectral transmittivity P_λ, which is determined by the equation

$$P_\lambda = \frac{1}{l} \ln \frac{\Phi_{2\lambda}}{\Phi_{1\lambda}}, \qquad (2.X)$$

where l is thickness of the layer of substance and $\Phi_{1\lambda}$ and $\Phi_{2\lambda}$ are the spectral flux densities before and after the passage of radiant energy through this layer.

The spectral transmission characteristics of certain widely used materials according to Hackford (Bibl.24), Yu.A.Ivanov and B.V.Tyapkin (Bibl.6) are presented in Fig.2.X.

For the visible spectral region and the adjoining regions, conventional glass optics (approximately 0.3 - 3.0 μ) is used and special glasses may be used in the region reaching 12 - 13 μ (Bibl.24). In cases where the ultraviolet region must also be included (roughly as far as 0.1 μ), quartz optics is employed, and in cases where the ultraviolet region to be included must extend as far as 0.17 μ, and where the near infrared region must also be included (as far as 5 - 6 μ), sapphire optics is used. In the infrared region, the most /246
widely used materials are germanium (1.8 to 15 - 20 μ or higher (Bibl.21), thallium iodobromide (KRS-5) and thallium chlorobromide (KRS-6). The transmission range of the latter two materials extends from 0.6 to 45 μ and from 0.4 to 30 μ, respectively (Bibl.24).

The optical materials for the lenses in the spectral sensitivity region usually are selected in accordance with the spectral interval that must be isolated. If additional correction of the spectral range is required, interference or absorption filters made of materials of various thickness are used. In this case the optical system of the instrument is so designed that the filters, particularly those of the interference type, are positioned in parallel beams (half-width $\Delta\lambda$ and the location of the transmission maximum λ_{max} of the interference filter essentially depends on the angle of incidence of the rays). Reflection

filters also are widely used.

A high reflecting power in the IR region of the spectrum is displayed by silver, gold and aluminum [as much as 92 - 99% (Bibl.6)], with the last-named element displaying a sufficiently high reflection factor throughout the optical range.

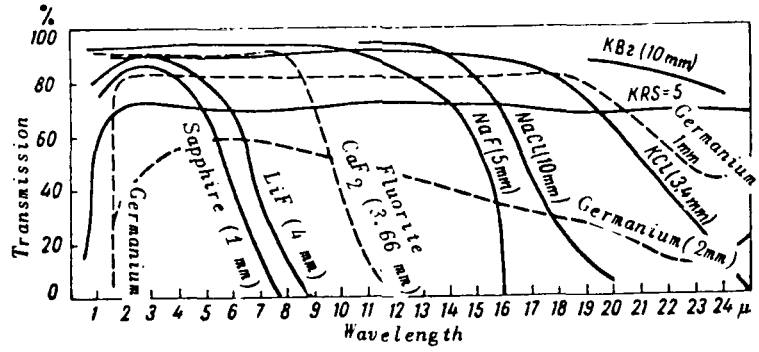

Fig.2.X Transmission of Certain Materials in the Infrared Region.

Section 2. Photometers

The design of photometric instruments is based on the comparison of two radiative fluxes. In principle, two types of photometer schemes are possible: a) the luminous characteristic of the receptor (current-radiative flux) is used as the photometric characteristic and b) the receptor merely fulfills the role of an indicator showing which one of the compared fluxes is greater. In this last case the differential-zero method is usually employed: the receptor /247 triggers a light-attenuating device (diaphragm, wedge, etc.) which operates until both fluxes become equalized.

Photometers of both types may be based on the single or double beam optical design. In the latter case, instead of two receptors, a single receptor alternately illuminated by each of the two compared sources may be employed. In single-beam photometers (Fig.3a.X) the photoelectric receptor R is illuminated via lens L and filter f (in spectrum analyzers the filters are periodically replaced). The diaphragm D serves to restrict the viewing angle of the instrument. The modulator M, whose rotation is triggered by an electric motor, is designed to interrupt the radiative flux. This is done with the object of utilizing the AC amplifier A~ which is distinguished by the stability of its zero level in the presence of fluctuations in supply voltage, temperature, etc. In addition, the use of a narrowband amplifier tuned to the modulation frequency makes it possible to reduce the noise level and the threshold flux Φ_f of the instrument. The output device O serves to convert the signals to a form convenient for telemetering to the ground.

The output voltage of the instrument (Fig.3a.X) is, as can be readily seen,

$$U_{out} = s_D K R_\ell \int_{\lambda_1}^{\lambda_2} F_\lambda P_{\ell\lambda} P_{f\lambda} \gamma_\lambda d\lambda, \qquad (3.X)$$

where s_D is the diaphragm aperture; F_λ is the spectral illumination density /248 at the input of the instrument ($w \cdot cm^{-2} \cdot \mu^{-1}$); K is a coefficient which takes into account the amplification and conversion of the signal in the circuit (transfer function); $P_{\ell\lambda}$ and $P_{f\lambda}$ are the spectral transmissivities of the lens and filter; γ_λ is the spectral sensitivity coefficient of the receptor with respect to current; R_ℓ is the load resistance of the receptor; and $\lambda_1 - \lambda_2$ is the spectral range of the instrument.

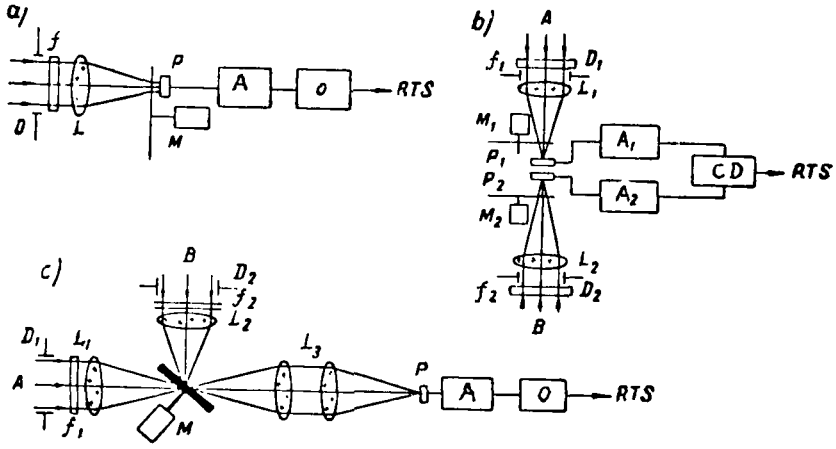

Fig.3.X Block Diagram of Single-Beam (a), Double-Beam (b) and Double-Beam Single-Receptor (c) Photometers.

Variation in any one of these quantities during the instrument's operation causes measurement errors. Therefore, a provision has been made in the circuits for periodic control of their stability. As a rule, the sensitivity of the instrument is checked by mounting a standard radiator (a luminous compound with constant action) at the input, while the stability of the zero signal is checked by covering the inlet with a screen (the spectral range does not extend to its heat emission).

Note that elements altering the instrument's sensitivity may be introduced into the circuit in order to expand the measurement range (Fig.3a.X).

In a double-beam telephotometer with two receptors P_1 and P_2 (Fig.3b.X) the measuring circuit is so designed that the comparison device CD would measure the difference in radiative fluxes entering in the directions A and B. Such an optical scheme is best for the case where one of the compared sources gives a flux whose magnitude is known in advance. A shortcoming of this scheme lies in that the measurements are affected by all the quantities entering into equations of the (3.X) type for each channel. This shortcoming can be largely offset if

the operation of the device is based on the differential-zero circuit (or a circuit maintaining a constant ratio between the signals in the channels), with

$$U_{1\,out} - U_{2\,out} = 0. \qquad (4.X)$$

Equation (4.X) may be written in simplified form on using means of the quantities entering into it (mean with respect to the spectrum):

$$s_{D\,1} J_1 \omega_1 P_{o\,1} K_1 R_{\ell\,1} P_{f\,1} \gamma_1 = s_{D\,2} J_2 \omega_2 P_{o\,2} K_2 P_{f\,2} R_{\ell\,2} \gamma_2, \qquad (5.X)$$

where J_1 and J_2 are the intensities of radiation at the input of channels A and B, ω_1 and ω_2 are the solid viewing angles of the channels.

From eq.(5.X) it can be seen that in this case identical changes in the corresponding quantities in both channels (P_{o1} and P_{o2}, $R_{\ell 1}$ and $R_{\ell 2}$, etc.) do not affect the results of the measurements. These results are usually expressed in changes in one of the parameters of the controlled channel (s_D, K, etc.).

The difficulties in the regulation of parameters in the presence of variation in the radiative flux complicate the practical realization of the differential-zero circuits of telephotometers. Single-receptor circuits display a major advantage. The technical variants of double-beam single-receptor schemes are numerous. One of them is illustrated in Fig.3c.X, where modulator M, owing to its specular lobes, commutates the channels at the inlet of receptor P. The measuring circuit of the device in this case fixes only one variable component of the signal, whose amplitude is proportional to the difference in the fluxes of radiant energy arriving at the receptor in directions A and B (clearly, this variable component is zero when the fluxes are equal). /249

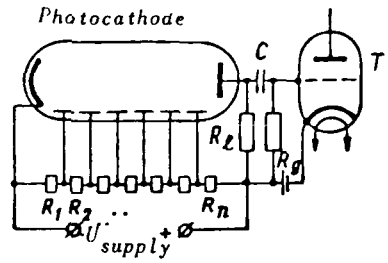

Fig.4.X Circuit Diagram of the Photometer Receptor.

Such a scheme has the advantages of the double-beam scheme, yet at the same time it makes it possible to preclude the influencing of the measurements by the parameters of the part of the instrument through which both signals pass in succession. The advantages of the double-beam single-receptor scheme are particularly important as regards measurements in the longwave region of the spectrum, where, insofar as possible, the effect of the natural radiation of the optical parts of the scheme on the measurements must be eliminated (cf. Sect.3 of this Chapter).

In instruments with a scanning system, devices assuring the displacement of the optical axis according to a specified law are incorporated.

In every scheme, the modulation frequency ν_m (frequency of interruption of the radiative flux) must be matched to the inertia τ of the receptor in its circuit diagram. Thus the signal amplitude may reach a practically full value (95 - 98%), the modulation period must be 3 - 4 times as long as τ, i.e.

$$(3 \text{ to } 4\times)\tau\nu_m \leq 1. \qquad (6.X)$$

A typical circuit diagram of the photometer receptor (photomultiplier or photocell) is shown in Fig.4.X (with flux modulation), where R_1, R_2, ..., R_n denote the resistances of the supply-voltage divider of the photomultiplier dynodes, while R_ℓ and R_g denote the load resistances of the photomultiplier and the grid leakage of the tube T_1 of the first stage of the AC amplifier.

We will determine the factors affecting the integral threshold flux Φ_f detectable or measurable by an instrument with such a circuit diagram. Note here that the method of calculating Φ_f can be also applied for other photoelectric receptors or for a limited spectral interval.

Threshold flux Φ_f is given with some above-unity signal/noise ratio which is determined by the assurance factor /250

$$c = \frac{U_s}{\sqrt{\overline{U_\Sigma^2}}} = \frac{\Phi_f \gamma R_\ell}{\sqrt{\overline{U_\Sigma^2}}}, \qquad (7.X)$$

where U_s is the minimum receptor-signal voltage that can be recorded by the measuring circuit; $\sqrt{\overline{U_\Sigma^2}}$ is the mean square voltage of total noise at the input of the receptor circuit; γ is the integral current sensitivity of the receptor; and R_ℓ is the load resistance.

The extent of the factor of assurance c is determined by the purpose of the measurements. To detect the flux Φ_f we take c = 3 - 5 depending on the required reliability of detection, while for flux measurements within a specified degree of accuracy c must be correspondingly increased. For example, to measure flux correctly to 1% we must have $c \geq 100$ (Bibl.18).

The mean square of the total-noise voltage for the circuit in Fig.4.X will consist chiefly of the mean square voltage of the shot noise of shadow current i_s due to the photomultiplier cathode, amplified by the dynode system to $\overline{U_{sh.ph}^2}$, the thermal noise $\overline{U_{th}^2}$, the resistance R_ℓ (if $R_\ell \gg R_g$), the shot noise of the plate $\overline{U_{sh.p.}^2}$ and of the grid $\overline{U_{sh.g.}^2}$, and of the currents of the tube T_1, i.e.

$$\overline{U_\Sigma^2} = \overline{U_{sh.ph.}^2} + \overline{U_{th}^2} + \overline{U_{sh.p.}^2} + \overline{U_{sh.g.}^2} \qquad (8.X)$$

The mean square of the fluctuation current of the shot noise according to the Schottky formula (Bibl.25) is

$$\overline{i_{sh}^2} = 2ei_s\Delta\nu, \qquad (9.X)$$

where i_s is the mean shadow current of the receptor photocathode, e is the electron charge ($e \approx 1.6 \times 10^{-19}$ k), and $\Delta\nu$ is the frequency band passed by the amplifier.

The analogous formula for photomultipliers, taking into account the amplification of shot noise by the dynode system, as shown in (Bibl.25), is more complicated:

$$\overline{i^2_{sh.ph.}} = 2ei_s(1+B)M^2\Delta\nu = 2eI_s(1+B)M\Delta\nu, \qquad (10.X)$$

where I_s is the shadow current of the photomultiplier, B is an empirical coefficient that takes into account the additional noise arising at the dynodes, and M is the amplification factor of the photomultiplier.

For photomultipliers with electrostatic focusing it may be assumed /251
fairly accurately (Bibl.25) that B = 1.5. In view of this, we shall write as follows the formula for the mean square voltage of the shot noise of the load resistor R_ℓ of the photomultiplier

$$\overline{U^2_{sh.ph.}} = 5eI_sR_\ell^2M\Delta\nu. \qquad (11.X)$$

In the case that the tube T_1 does not operate in a saturation regime, and the more so in the case where it operates in the electrometric regime and in the presence of a good insulation of the grid electrode, the total shot noise $\overline{U^2_{sh.p.}} + \overline{U^2_{sh.g.}}$ of the tube does not exceed the shot noise of the photomultiplier (Bibl.25). To simplify the calculations we will assume that the tube noise need not be taken into account.

The mean square of the fluctuation e.m.f. of thermal noise according to the Nyquist formula (Bibl.25) is written as

$$\overline{U^2_{th}} = 4kTR_\ell\Delta\nu, \qquad (12.X)$$

where k is Boltzmann's constant ($k = 1.38 \times 10^{-16}$ erg/deg) and T is the temperature of the resistor R_ℓ.

For a temperature T = 300°K, $\Delta\nu$ = 1 cps and $R_\ell = 10^6$ ohm we have $\overline{U}_{th} \simeq 1.3 \times 10^{-7}$ v/cps. For the same circuit parameters $M = 10^6$ and $I_s = 10^{-8}$ and from eq.(11.X), we have $\overline{U}_{sh.ph.} \simeq 9 \times 10^{-4}$ v, i.e., for the customary parameters of the circuit $\overline{U}_{sh.ph.} \gg \overline{U}_{th}$ and the second term of eq.(8.X) also may be disregarded. Hence, for the standard circuit diagram and for a low noise level of the first amplifier stage, the working formula will be, on the basis of the above reasoning,

$$\Phi_f \approx \frac{C}{\gamma}\sqrt{5eI_sM\Delta\nu}, \qquad (13.X)$$

The bandwidth $\Delta\nu_a$ of the amplifier frequencies is - unless special steps

are taken to change the transmission band in the amplifier circuit - determined by the time constant τ_1 in the circuit diagram of the receptor. For the above case of the low-inertia receptor, we have $\tau_1 = R_\ell C_s$ and

$$\Delta\nu = \frac{1}{2R_\ell C_s}, \qquad (14.X)$$

where C_s is the stray capacitance of the photomultiplier circuit diagram.

For $R_\ell = 10^6$ ohm and $C_s = 10$ pf, we have $\tau_1 = 10^{-5}$ sec and $\Delta\nu = 50$ cps. The allowable modulation frequency is $\nu_m = 25$ cps, as follows from eq.(6.X).

It must be borne in mind that for a low modulation frequency ($\nu_m < 1$ cps) in emission receptors, allowance must be made for the flicker noise of the photocathode, $\overline{U_{fl}^2} = 2eiR_\ell^2\left(1 + \frac{iB}{A\nu_m}\right)$, where B is a constant which depends on the properties of the photocathode with the area A. /252

If the receptor used is a photomultiplier with a multiple-slit photocathode, which displays the optimal parameters ($I_s = 10^{-16}$ a, $M = 10^7$, $\tau \approx$ $\approx 10^{-9}$ sec, and $\gamma = 10^2$ a/lu)(Bibl.18), then [as is implied by eq.(13.X)] it is possible to measure the minimal flux of the order of $\Phi_f' \approx 10^{-12}$ lu or 10^{-15} w correct to 1%.

Instruments incorporating photomultipliers with Sb-Cs photocathodes make it possible to measure luminous fluxes of $\geq 10^{-14}$ w within the same degree of accuracy, but then $R_\ell \simeq 10$ gm-ohm, which markedly enhances the instrument inertia ($\tau_1 \sim 10^{-1}$ sec) and reduces the allowable modulation frequency ($\nu_m \sim$ ~ 10 cps). This clearly restricts the possible speed of measurements and scanning for the instruments of this kind, and it also increases the flicker noise.

The threshold flux Φ_f arriving at the photometer receptor, on the other hand, is determined by its optical system. The latter should be so designed that even under the pessimal conditions of observation the radiative flux Φ_{min} arriving at the detector would not be smaller than Φ_f. The method of selecting the parameters of the optical scheme may be illustrated by the following example (where we will assume that the aberrations of the optical system are small).

Suppose a photometer is located at the altitude h (Fig.5.X) and measures a radiative flux diffusely reflected by an area a whose spectral reflection coefficient in the direction of the instrument is ρ_λ. If the minimal, for the particular conditions of these measurements, intensity of the radiative flux illuminating area a uniformly from the entire upper half-space is $J_{\lambda min}$ w·ster^{-1}·μ^{-1} at the surface of this area, then the minimal flux Φ_{min} subject to measurement by receptor R will be

$$\Phi_{min} = \omega_1 a \int_{\lambda_1}^{\lambda_2} \rho_\lambda \frac{J_{\lambda min}}{\pi} P_{\lambda a} P_{\lambda o}\, d\lambda =$$

$$= \frac{\omega a_0}{\pi} \int_{\lambda_1}^{\lambda_2} \rho_\lambda J_{\lambda \min} P_{\lambda a} P_{\lambda o} d\lambda, \qquad (15.X)$$

where $\omega_i = \frac{a_o}{h^2}$ is the solid angle at which the entrance aperture D with the area a_o is visible from the center of the observed area a; $\omega = \frac{a}{h^2}$ is the solid angle of the instrument's field of view; $P_{\lambda a}$ and $P_{\lambda o}$ are the spectral transmissivities of the atmosphere and of the instrument's optics, respectively. /253

The requirement that the threshold flux Φ_f, measurable by the circuit, should agree with the minimal flux Φ_{min} subject to measurement by the instrument concerned ($\Phi_f = \Phi_{min}$) can be used to determine the minimal possible area a_o of the entrance aperture of the instrument or the minimal permissible viewing angle ω of the instrument.

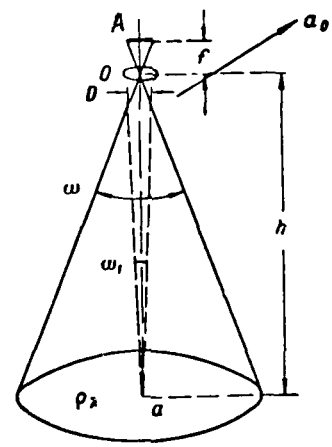

Fig.5.X. Diagram for Determining the Radiative Flux Incident on the Photometer.

As can be seen from Fig.5.X, the instrument's field of view is related to the working area A of the receptor and the distance f from the plane of the entrance blende to the image plane (if the distance to the observed object is so large that the image is obtained in the focal plane of the lens) by the ratio

$$\omega = \frac{A}{f^2} \quad \text{or} \quad \delta_x \approx \frac{3.4 \cdot 10^3 d}{f}, \qquad (16.X)$$

where d is the diameter of the working area A of the receptor and δ_x is the viewing angle in minutes of angle.

Thus, for given dimensions of the receptor or of the surveyed area a, only the size of the entrance aperture a_o need be varied in order to match Φ_f with

Φ_{min}.

As an example, consider certain models of photometers incorporated in the upper-air geophysical probes (Bibl.8, 14).

The TF9 photometer is designed to measure the angular distribution of luminance along the scanned surface. The spectral range of the instrument is determined by the type of the replaceable filter mounted in the rotating disk located in the path of the radiative flux toward the receptor (one type of photomultiplier or another). The spectral regions isolated by certain glass filters, the approximate range of spectral sensitivity of the photomultiplier with Sb-Cs photocathode (Bibl.2, 25) and the energy distribution in the solar spectrum at altitudes of 80 - 100 km (Curve 1) are presented in Fig.6.X.

The TF9 photometer (Fig.7.X) is based on the single-beam scheme. To maintain instrument stability, a stable source with a known luminance (a luminous compound with constant action) is mounted in the disk with light filters 12. The instrument is provided with a rotary scanning head containing mirror 1 and collimator 3. The latter is represented by a bundle of thin-walled tubules with blackened inner surface. Their length is so selected that the instantaneous /255 viewing angle of the receptor is 2°. To assure airtightness of the container, the part of scanning head projecting from the container is covered with transparent dome 2.

Scanning is accomplished during rotation of the head through 360° about its optical axis at the rate of one revolution per minute. Thus, when the upper-air probe is in a position above the Equator, a picture of the distribution of measurable radiant energy is obtained over the planet's disk from one horizon through the nadir to another in a zone 2° wide.

The filters are mounted in disk 12 which is rotated by means of the Maltese mechanism 11. The contacts 9 and 10 serve to transmit information on the position of the disk with filters.

Interruption of the luminous flux is accomplished by means of modulator 5. Mounted on the modulator shaft is the rotor of the generator 6 of reference pulses supplied to the synchronous output detector. All the mobile parts of the instrument are driven by electric motor 4. Photomultiplier 7 is powered across divider 8 on resistors.

The AC amplifier and the synchronous output detector are mounted in the electronic unit. The dependence of output voltage on the measured radiation flux is usually of a semilogarithmic character (Bibl.8).

Spectrum analyzer SAZ (or photoelectric radiation meter FIR)(Bibl.8) is designed to record the luminance of the sky at high altitudes in various spectral intervals isolated by means of a set of filters. The overall spectral range of the instrument encompasses the near-UV and IR regions, if replaceable photomultipliers of various types are used (Bibl.14). The instrument whose diagram is shown in Fig.8.X represents a photometer based on the single-beam design. Its spectral characteristics are determined by the filters used (of the

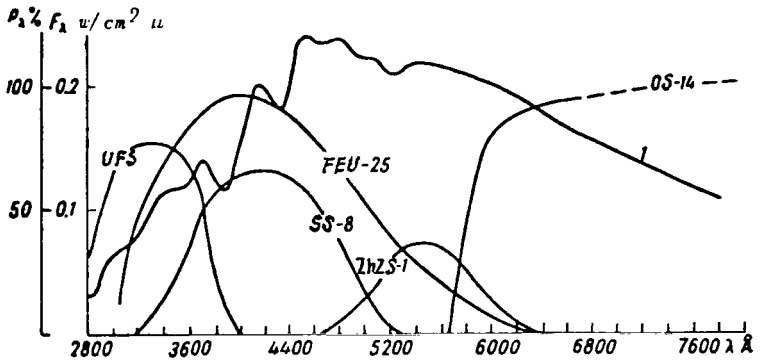

Fig.6.X Spectral Characteristics of Photometer.

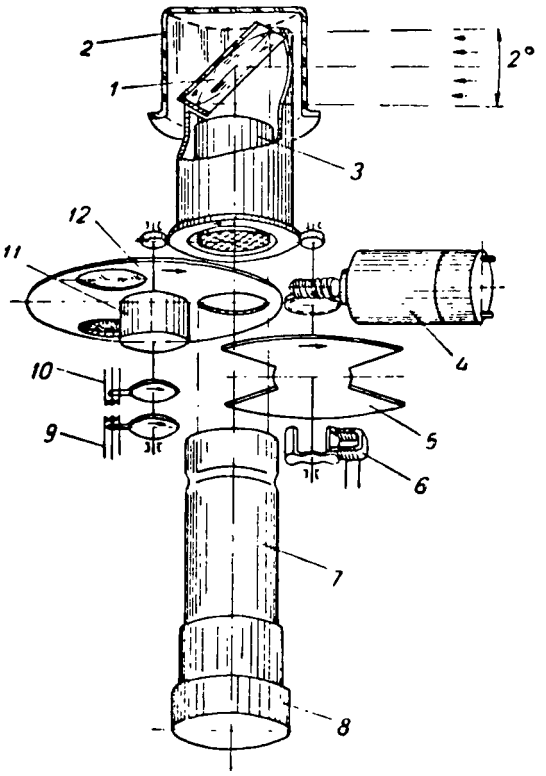

Fig.7.X Optical-Kinematic Diagram of the TF9 Telephotometer.

UFS, ZhZS and other types) (see Fig.6.X). The optical diagram of the instrument includes inlet shade 3, quartz lens 4, light filters f_1 - f_5 mounted in the rotating disk 6, wedges mounted in disk 7, concave spherical mirror 13 and receptor 14 (photomultiplier). Mounted in disk 6 containing a set of filters is a fixed-action luminous compound with a luminance of the order of 10^{-8} stilb (Bibl.14). Disk 7 contains a free aperture, reducers with transmission of 1

and 10%, and a shutter for zero reading. The use of three degrees of reduction by means of optical wedges makes it possible to obtain a dynamic range of 10^3. The duration of each measurement with a light filter is 0.2 sec, and the total cycle of measurements (24 individual measurements) lasts 6 sec (Bibl.14). Photoresistor 2, which triggers the shutter relay 1, serves to protect the receptor against excessive illumination.

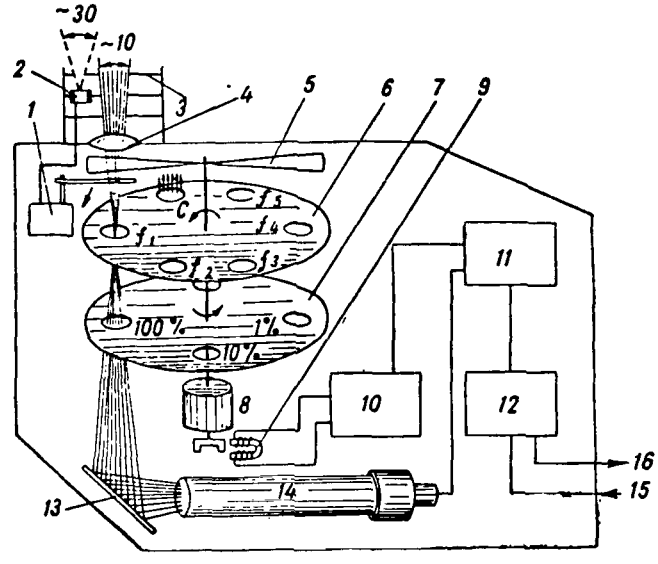

Fig.8.X Diagram of the SAZ Spectrum Analyzer (FIR, Photoelectric Radiation Meter).

The receptor signal proceeds to the selective amplifier 11 and thence to the synchronous detector 10 which is supplied with reference voltage from /256 the generator 9, actuated by motor 8 synchronously with the modulator 5. The rectified signal proceeds to the output device 12 and to the telemetering system 16. The instrument is powered from the power system 15 of the instrument container (to broaden the range, on any increase in signal, the power supply to the photomultiplier automatically decreases).

According to A.Ye.Mikirov (Bibl.14), the sensitivity of the spectrum analyzer described above is 9×10^{-9} stilb for integral light and 1.5×10^{-10} w · · cm^{-2} · $ster^{-1}\mu^{-1}$ for individual wavelengths. The range of luminances measured is from 5×10^{-9} to 5×10^{-6} stilb.

Instruments of this type require prior calibration. This may be accomplished with the aid of a device of the photometric bench type with a calibrated source and with reducers in the form of neutral filters (NS). A filter of the S type (GOST, All-Union State Standard 7721-55) is used to adjust the source's spectrum to the solar spectrum, and opal glass assuring uniform illumination of the sensitive area is mounted in front of the inlet window of the instrument.

The luminance B of the opal glass without reduction by light filters satisfies Lambert's law

$$B = \frac{E}{\pi} = \frac{\Phi}{\pi s} = \frac{J \cos \alpha}{\pi r^2}, \qquad (17.X)$$

where E is the integral illumination of the glass, Φ is the integral luminous flux in the solid viewing angle of the receptor $\omega = \frac{s}{r^2}$; J is the glow intensity of the source; s is the illuminated area of the opal glass; r is the distance between glass and receptor; α is the angle of incidence of the parallel beam on the glass. /257

In the presence of light-reducing filters, we have the following working formula for calibrating the telephotometer:

$$B = \frac{J \cos \alpha}{\pi r^2} R_{o.g.} R_S R_{NS}, \qquad (18.X)$$

where $R_{o.g.}$, R_S, R_{NS} are the transmissivities of the opal glass, the S type filter and the NS neutral light filter, respectively.

The signal at the instrument output may be calculated according to the known spectral transmission of the filter in the instrument and the sensitivity of the receptor.

Section 3. Radiometers

The design principles of radiometers and photometers are similar, but radiometers display a number of special features associated with operation in a more distant region of the IR spectrum. These features are due to the need to exclude from the results of measurements the natural radiation of elements of the optical system of the instrument (lenses, filters, mirrors, modulator, etc.). The optimal instrument parameters, particularly as regards rapidity of action, are assured by using bolometers as non-cooled receptors. The thermoelements still display considerable inertia while, on the other hand, the use of optico-acoustic receptors involves difficulties owing to the need to control the microphone effect (Bibl.1, 20).

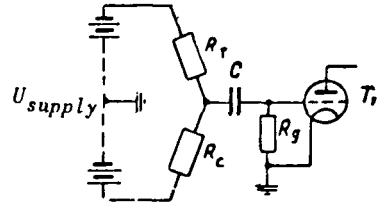

Fig.9.X Circuit Diagram of the Bolometer.

Present-day bolometers (Bibl.15, 19, 24) display a good quality of the blackening of the sensitive surface, but are virtually nonselective in the spectral range of 1 - 40 μ. Semiconductor (thermistor) bolometers with a comparatively high sensitivity and resistance are most widely used in radiometers. Thus, American-made bolometers have a resistance of 1 - 10 megohm, a time constant of several milliseconds and the threshold flux $\Phi_f \approx 10^{-8}$ w (Bibl.24). Bolometers are included in pairs in the measuring circuit so that one of them (compensation bolometer) would, insofar as possible, offset the effect of the fluctuations in ambient temperature and, occasionally, in the supply voltage as well, on the performance of the other (measuring) bolometer.

Figure 9.X shows the elementary bolometer circuit diagram, which is /258 widely used in radiometers (Bibl.19, 24). In this diagram the compensation element fulfills the role of the load resistor for the measuring bolometer. The bolometer is powered by a constant-voltage source U_{supply}. The luminous flux incident on the measuring bolometer R_T is modulated with the frequency ν_m.

The amplitude ΔU_s of the variable signal voltage arriving at the input of the AC amplifier (tube T_1) equals the voltage difference at the resistor of the compensation bolometer R_c with respect to the presence and absence of illumination of the measuring bolometer whose resistance R_T then changes by ΔR_T, i.e.,

$$\Delta U_s = U_{illum.} - U_{th} = U_{supply}\left[\frac{R_c}{R_c + (R_T - \Delta R_T)} - \frac{R_c}{R_c + R_T}\right] \approx$$
$$\approx U_{supply}\frac{R_c \Delta R_T}{(R_c + R_T)^2} \approx U_{supply}\frac{\Delta R_T}{4R_T} \qquad (19.X)$$

for $R_c \approx R_T$.

The magnitude of ΔR_T is proportional to the change in the temperature ΔT of the measuring bolometer and the heat balance due to the absorption of radiant energy. Hence, for a semiconductor (thermistor) bolometer we may write

$$\Delta R_T = -\frac{B}{T^2} R_T \Delta T = -\frac{B R_T \alpha \Delta \Phi}{T^2}, \qquad (20.X)$$

where $\frac{B}{T^2}$ is the temperature coefficient of resistance, B is a constant which depends on the material of the bolometer concerned, $\Delta\Phi$ is the change in the mean power of the modulated luminous flux, and α is the conversion (sensitivity) factor of the bolometer.

Equations (19.X) and (20.X) imply that the receptor sensitivity S in v/w in such a circuit diagram will depend on the temperature, supply voltage and the parameters of the bolometer itself.

$$S = \left|\frac{\Delta U_s}{\Delta \Phi}\right| = \frac{\alpha B U_{supply}}{4T^2}. \qquad (21.X)$$

It must be noted that the possibility of enhancing sensitivity by increasing the supply voltage is limited by the maximally permissible dissipated power W_{perm} (or permissible bolometer current i_{perm}) under operating conditions

$$W_{perm} = U_{supply} i_{perm} \qquad (22.X)$$

There will be no temperature (T) dependence of the receptor if the temperature coefficient of the receptor resistance is constant. This may be accom- /259
plished by means of a bridge circuit. The value of α depends on the modulation frequency ν_m of the radiative (luminous) flux and on the inertia (time constant) τ of the bolometer, since the mean power of the flux sensed by the bolometer decreases with increasing modulation frequency. Experimental (Bibl.15) and theoretical [for semiconductors with an elementary mechanism of carrier recombination and with sinusoidal modulation (Bibl.17)] findings point to a dependence of the form of

$$S_\nu = S_0 \frac{1}{\sqrt{1 + 4\pi^2\nu^2\tau^2}}, \qquad (23.X)$$

where S_ν and S_0 are the sensitivities of the bolometer in the presence of the modulation frequency ν_m and in the absence of modulation $\nu_m = 0$ (correspondingly, α and α_0).

The time constant of the present-day non-cooled semiconductor bolometers is still undesirably large [τ = approximately several milliseconds (Bibl.24)]. This complicates using them in the instruments and leads to a substantial decrease in sensitivity S_ν during the modulation of the radiative flux.

The principal types of noise in semiconductor bolometers, which affect the threshold flux Φ_f, are thermal and current noise (Bibl.15). Current noise arises during passage of the current across the bolometer and is due to defects in the contacts between the bolometric film and the current-conducting electrodes, contacts between individual grains of the film itself, fluctuations in the number of free electrons in the semiconductor film, and other effects. The magnitude of the current noise depends on the modulation frequency ν_m, namely, $\overline{U_i^2} = A_t \nu_m^{-1} i^2 R_\ell^2 \Delta\nu$, where A_t is a constant which depends on the production technology of the bolometer. We will assume that the magnitude of this noise is smaller than that of the thermal noise.

At the low modulation frequencies permitted by the inertia of the bolometer (of the order of tens of cps and less), the noise of the amplifier tube stage (Fig.9.X) is determined not by shot effects but chiefly by the cathode flicker effect. For high-voltage bolometers ($R_T \geq 10^5$ ohm) this noise may be disregarded in comparison with the thermal noise of the circuit (Bibl.15). In this case the threshold flux Φ_f for this circuit diagram (Fig.9.X) will be determined from the following relation, which is similar to that considered earlier (cf. Sect.2):

$$S\Phi_f = F_f AS = c\sqrt{\overline{U_\Sigma^2}} = c\sqrt{4kTR\Delta\nu}, \qquad (24.X)$$

where F_f is the density of the threshold flux incident on a receptor with area A

and sensitivity S (with respect to voltage).

For c = 1 and $\Delta\nu$ = 1 cps, the working formula is written as /260

$$F_f = \frac{1{,}3 \cdot 10^{-10}}{AS} \sqrt{R}. \qquad (25.X)$$

The circuit of the instrument with resistances $R = R_c = R_T = 2 \times 10^6$ ohm and S_0 = 500 v/w can detect the flux $\Phi_f = F_f A = 5 \times 10^{-10}$ w (in the absence of modulation). If the time constant τ of the bolometer is 5 msec and the modulation frequency ν_m = 50 cps, then, as eq.(23.X) implies, the bolometer sensitivity decreases to S_ν = 270 v/w and the threshold flux detectable by the bolometer increases to $\Phi_f = 9 \times 10^{-10}$ w. For bolometers with a high inertia or with a high modulation frequency, these effects manifest themselves even more distinctly.

Note that the use of highly sensitive receptors may require taking into account the quantum noise of the detected flux. The formula for calculating the minimal flux Φ_{min} focused by the optical system on the receptor is, by analogy with eq.(15.X), written as

$$\Phi_{min} = \frac{\omega a_0}{\pi} \int_{\lambda_1}^{\lambda_2} (\rho_\lambda I_\lambda + \varepsilon_{e_a \lambda} r_{\lambda\, \tau_{e_a}} + r_{\lambda\, a})\, P_{a.\lambda} P_{o.\lambda} d\lambda, \qquad (26.X)$$

where $\varepsilon_{earth\,\lambda}$ is the spectral emissivity of the underlying surface of the planet or cloud; $r_{\lambda\, T_{earth}}$ is the spectral density of the radiation intensity of an absolutely black body, calculated from Planck's formula for the minimal temperature T_{earth} of the underlying surface; $r_{\lambda\, a}$ is the spectral density of the radiation intensity of the atmosphere.

Note that on the dark side of the planet or for $\lambda > 3 - 5\ \mu$, the first term of eq.(26.X) will be absent. The viewing angle for a receptor with specified dimensions is determined from eq.(16.X) or eq.(17.X). It is analogously possible to find from the requirement for the matching of fluxes $\Phi_f = \Phi_{min}$, determinable from eqs.(25.X) and (26.X), the required area of the entrance aperture of the teleradiometer optics.

We will now consider how these general postulates can be translated into reality in specific varieties of instruments.

The five-channel radiometer of the satellites of the Tiros and Nimbus series is designed to measure radiative fluxes in five spectral intervals, isolated by means of filters. The instrument is part of the complex total of instrumentation used in the weather satellites and hence its operating spectral intervals are so selected as to obtain information on the state of the atmosphere (including its lower layers) and on the temperature of emitting surfaces as well.

The principal features of the five-channel radiometers installed in various satellites of this series have remained virtually unchanged (Bibl.19). We /261 will examine them on the basis of description by R.Estrkheymer et al. (Bibl.27).

The spectral ranges of the radiometer channels and the methods of their

isolation (materials of the lenses L_1 and L_2 and of the filter) are specified in Table 1.X. The spectral characteristics of the channels are given in Fig.10.X.

TABLE 1.X

SPECTRAL RANGES AND OPTICAL MATERIALS OF RADIOMETER CHANNELS

Channel No.	Spectral Range, μ	Lens	Filter
1	5.7 - 6.9	Germanium (L_1 and L_2)	Interference band filter
2	7.5 - 14	Germanium (L_1 and L_2)	Indium antimonide (InSb) and arsenic trisulfide (As_2S_3)
3	0.2 - 5.5	Sapphire (L_1), barium fluoride (L_2)	No filter
4	7.5 - 30(50)	KRS-5 (L_1)	InSb
5	0.55 - 0.75	Sapphire (L_1), Quartz (L_2)	Interference band filter

The characteristics presented above show that channel 1 performs measurements of radiation in the basic water - vapor absorption band with a center at ~ 6.3 μ; channel 2, radiation in the atmospheric transparency window; channel 3, the solar radiation reflected by the earth and its atmosphere; channel 4, the outgoing radiation of the earth-atmosphere system; and channel 5, the reflected luminous energy in the sensitivity range of vidicon and photographic films. Each of the five channels of the radiometer is designed to operate autonomously, and all are of the same design. The greatest sensitivity is displayed by channel 1, since the radiation it measures is formed by the upper layers of the atmosphere, which have a low temperature.

A diagram of the optics and the block diagram of a channel of the radiometer are shown in Fig.11.X. The radiation arriving from two mutually perpendicular directions A and B is reflected by aluminized sides of prism 4 and directed toward the disk of the reflector interruptor 5. One half of disk 5 is blackened and the other half is an aluminized mirror. The radiant energy reflected from both halves of disk 5 passes through the optical filter 3 and is focused by lens 2 on the receptor 1. The receptors used in all channels are semiconductor (thermistor) bolometers. Viewing angle: $5 \times 5^{\circ}$.

During rotation of the modulator, its mirror part transmits to the re- /263
ceptor alternately the radiation arriving from direction A and from direction B. If the radiation arriving at the receptor from one of these directions originates from the earth, then the radiation arriving from the other direction origi-

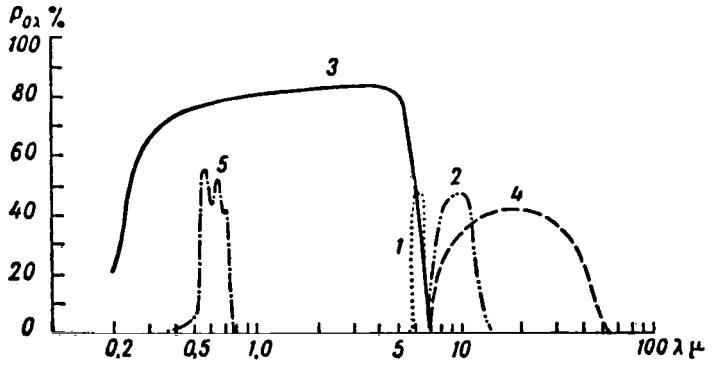

Fig.10.X Transmission ($P_{0\lambda}$) Curves of the Optical Channels of the Radiometer. The numbers (1 - 5) of the curves correspond to the numbers of the channels.

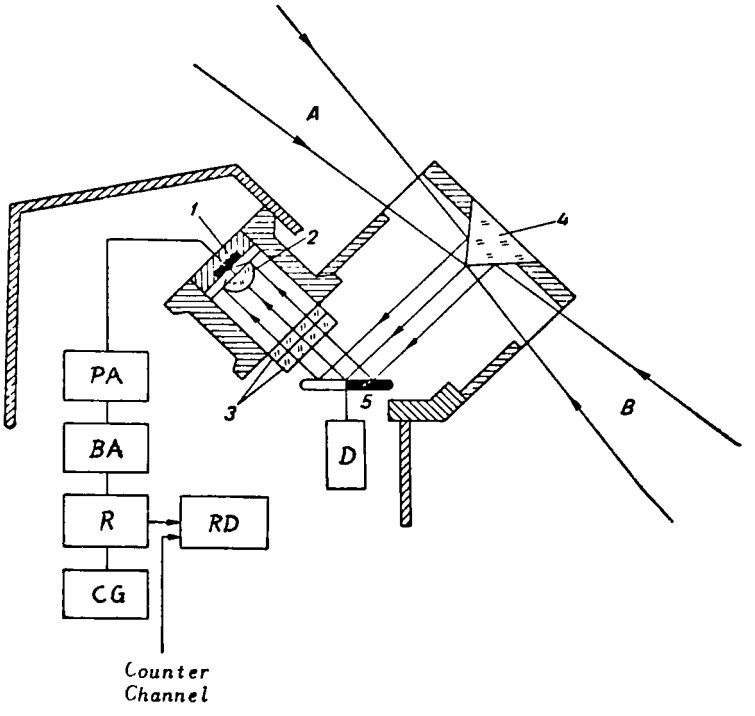

Fig.11.X Optical-Kinematic Diagram of a Radiometer Channel.

nates from outer space. Thus, the channels operate on the basis of the double-beam single-receptor scheme, and the assumption is that the radiation (light emission) from outer space is virtually zero and may be used as a reference criterion.

The reflectors/modulators of every channel of the radiometer are rotated by the same synchronous motor D. The modulation frequency is 44 cps.

Note that owing to the symmetry of the optical paths A and B the results of the measurements do not depend on which one of these paths faces the earth.

The natural radiation of the interruptor is virtually not modulated, so that both of its halves always lie in the field of view of the detector. The radiation of the optical elements (lenses and filter) located beyond the interruptor also is not modulated. The reflecting sides of the fairly massive glass prism 4 must have virtually identical temperatures and hence also their contribution to the measured fluxes will be virtually identical and will be eliminated through the AC amplification of the signal, since then it will prove to be non-modulated.

These features of the optical system of the instrument make it possible to markedly reduce the effect of the natural radiation of the elements of this system and hence also the effect of the instrument temperature on the measurements.

A special feature of the optical system of channel 1 is the mounting of a concentric germanium immersion lens 2 directly ahead of the receptor (Fig.11.X). This lens enhances S owing to the normal incidence of flux on the receptor. The block diagram of the amplifier of channel 1 contains, moreover, preamplifier PA, assembled on an SK6419 type electron tube connected by a triode. In the other channels, this stage is absent and only the basic amplifier BA is present.

The basic six-stage amplifier (Fig.12.X) is assembled from transistors T_1 - T_6 (the first two are of the 2N1027 type and the others, of the 2N543 type). The first stage is based on a common-collector circuit; the second, on a common-base circuit; and the third, on a common-emitter circuit.

To assure a high signal/noise ratio, a narrowband AC amplifier tuned to the modulation frequency (~44 cps) is employed. Selectivity of the amplifier is assured by incorporating a negative feedback in the circuit (between the fourth and second stages) with respect to the double T-bridge tuned to the modulation frequency. The bridge is assembled from resistances R_2, R_3, R_4 and capacitances C_1, C_2, C_3. For better tuning of the bridge, the resistance R_1 is additionally included (Bibl.3). The presence of a strong negative DC feedback stabilizes the performance of the transistor T_2. The last two stages of the amplifier, assembled from transistors T_5 and T_6, also are encompassed by the negative feedback circuit. The feedback coefficient may be varied by varying one arm of the divider connected to this circuit, by means of the potentiometer R_5. Thus, the amplification factor changes with the tuning of the circuit. /265

The presence of feedback between the stages broadens the range of measurements and stabilizes the amplification, while at the same time it reduces the

output impedance of the amplifier. The voltage amplification factor for the first four stages (transistors T_1 - T_4) is 1.5×10^3 and the maximum amplification factor of the entire amplifier reaches 3×10^5 at a frequency of ~44 cps (Bibl.30). After the amplification, the signal is conveyed to the full-wave

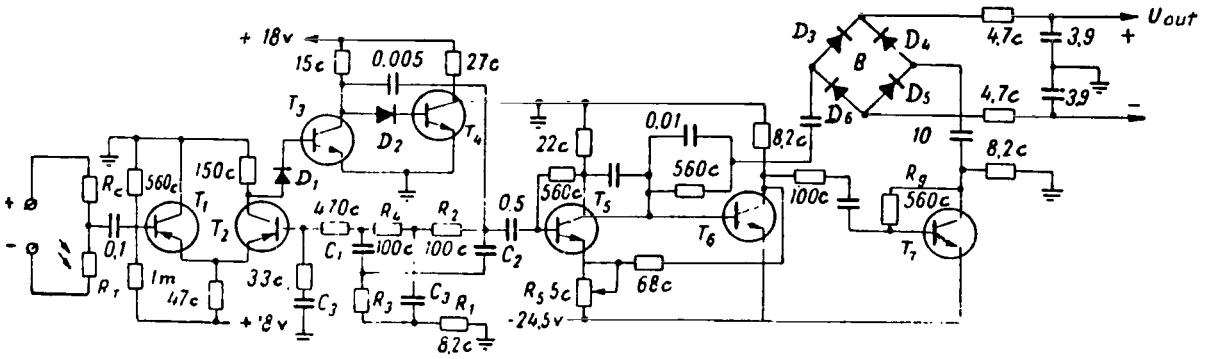

Fig.12.X Measuring Circuit of a Radiometer Channel.

rectifier R assembled from the germanium diodes D_2 - D_5 (of the 1N68A type), which at the same time is supplied with the voltage passing across the phase-inversion stage based on the transistor T_7 (2N543 type) (common-emitter amplifier circuit). Owing to intra-stage feedback, its amplification factor is roughly unity. This assures the doubling of the rectified voltage of the signal which is taken off the smoothing RC filter with a grounded central point. The latter serves to minimize noise and to reduce the variable component with frequencies of more than 5 - 8 cps which may adversely affect the recording of the data on magnetic tape.

The levels and amplification of the signals are such that accuracy is limited not by the noise but by the possibilities of the telemetering system and the drift due to temperature fluctuations. The signal equivalent to noise for channel 1 is obtained in the presence of a flux with the density 1.5×10^{-9} w/cm^2; and for the other channels, in the presence of a flux with the density $4.5 \times$ $\times 10^{-9}$ w/cm^2 (Bibl.27).

The incomplete compensation of the effect of temperature on the bolometer, the differences in the temperatures of various sides of the prism as well as in the temperature along the surface of the interruptor-reflector, and other effects, cause the instrument readings to be temperature-dependent. In the range of working temperatures of from 0 - 45°C this leads to an error reaching ±10%. To make allowance for this effect, the temperature of the instrument housing was measured and telemetered along with the output signal.

A constant output voltage U_{out} is supplied to the controlled generator CG. Signals from all of the channels are added together in the recording device RD and recorded on magnetic tape. The recording of the radiometer signals was performed over the frequency range of from 100 to 410 cps at the rate of 10 mm/sec,

and their reproduction at the rate of 300 mm/sec (Bibl.19). The voltage-controlled generator of channel 1 operates in the 100 - 150 cps frequency range; /266 the generator of channel 2 in the 165 - 215 cps frequency range, and so on, with the frequency range for each successive channel shifting upward by 50 cps with intervals of 15 cps between the channels.

The overall dimensions of the five-channel radiometer are 150 × 115 × × 115 mm, its weight is about 2 kg and its power requirement is about 1 w (Bibl.27).

The circuit diagrams of the measuring R_T and the compensation R_c bolometers are the same for each channel (Fig.12.X). The output signal U_{out} of the radiometer channel is proportional to the variable component $\Delta\Phi$ of the radiative flux arriving at the measuring bolometer of the channel,

$$U_{out} = KS\Delta\Phi, \tag{27.X}$$

where K is the circuit transfer coefficient and S is the volt sensitivity of the bolometer.

The variable component $\Delta\Phi$ equals the difference between the radiative fluxes arriving at the receptor in the presence of two opposite positions of the reflector. The magnitude of the flux $(\Phi_A + \Phi_B)_1$ arriving at the bolometer in the first position of the modulator (shown in Fig.11.X), taking into account the radiative contribution of all the elements of the optical system, is as follows:

$$\begin{aligned}(\Phi_A + \Phi_B)_1 = \int_{\lambda_1}^{\lambda_2} [&\Phi_{A\lambda}\rho_{p.\lambda}\rho_{m.\lambda}P_\lambda + \\ &+ \Phi_{B\lambda}\rho_{p.\lambda}\rho_{b.\lambda}P_\lambda + \varepsilon_{p.\lambda}r_{\lambda\tau_p}(\rho_{m.\lambda} + \rho_{b.\lambda})P_\lambda + \\ &+ (\varepsilon_{b.\lambda} + \varepsilon_{m.\lambda})\, r_{\lambda\tau_m}P_\lambda + \varepsilon_{o.\lambda}r_{\lambda\tau_0}]\, d\lambda,\end{aligned} \tag{28.X}$$

where $\varepsilon_{p\lambda}$, $\varepsilon_{b\lambda}$, $\varepsilon_{m\lambda}$, and $\varepsilon_{o\lambda}$ are the spectral emissivities of the sides of the prism, parts of the modulator (black and specular), and the optical system, respectively, $\Phi_{A\lambda}$ and $\Phi_{B\lambda}$ are the spectral densities of the radiative fluxes at the input in directions A and B, respectively, $\lambda_1 - \lambda_2$ is the spectral range of the concerned filter channel, $\rho_{p\lambda}$, $\rho_{b\lambda}$, $\rho_{m\lambda}$ are the spectral reflection coefficients of the sides of the prism and of the blackened and mirror halves of the modulator-reflector, ρ_λ is the spectral transmissivity of the optical system, λ_T is Planck's function giving the spectral intensity of radiation in relation to the temperature of prism T_p, the temperature of the modulator T_m and the temperature of the optical system T_o.

Similarly, for a single counter-directed position of the modulator-reflector we have

$$\begin{aligned}(\Phi_A + \Phi_B)_2 = \int_{\lambda_1}^{\lambda_2} [&\Phi_{A\lambda}\rho_{p.\lambda}\rho_{b.\lambda}P_\lambda + \Phi_{B\lambda}\rho_{p\lambda}\rho_{m.\lambda}P_\lambda + \\ &+ \varepsilon_{p.\lambda}r_{\lambda\tau_p}(\rho_{b.\lambda} + \rho_{m.\lambda})\, P_\lambda + (\varepsilon_{b.\lambda} + \varepsilon_{m.\lambda}) \times r_{\lambda\tau_m}P_\lambda + \varepsilon_{o.\lambda}r_{\lambda\tau_0}]\, d\lambda.\end{aligned} \tag{29.X}$$

The formula for the variable component $\Delta\Phi$ of the flux arriving at the bolometer, assuming that the sides of the prism have identical optical properties and the temperature of all the elements of the optics is the same throughout the cycle of measurements, is as follows: /267

$$\Delta\Phi = (\Phi_A + \Phi_B)_1 - (\Phi_A + \Phi_B)_2 =$$

$$= \int_{\lambda_1}^{\lambda_2} (\Phi_{A\lambda} - \Phi_{B\lambda})(\rho_{m.\lambda} - \rho_{b.\lambda})\,\rho_{p.\lambda} P_\lambda d\lambda. \qquad (30.X)$$

For fixed parameters of the optics (ϵ, ρ and P), the channel output voltage is determined by the difference between the radiative fluxes, incident on the instrument in directions A and B,

$$U_{out} = KS \int_{\lambda_1}^{\lambda_2} \varphi(\lambda)(\Phi_{A\lambda} - \Phi_{B\lambda})\, d\lambda, \qquad (31.X)$$

where $\varphi(\lambda)$ is a quantity characterizing the spectral sensitivity of the optics of the concerned channel.

The thermal channels of the radiometer (1, 2, and 4) were calibrated with the aid of two blackbodies (Bibl.19). One of these, simulating the radiation of outer space, was maintained at the temperature of liquid nitrogen T_1. The temperature T_2 of the other blackbody, simulating the radiation of the earth-atmosphere system, was varied. To eliminate the errors due to water-vapor condensation and to radiant energy absorption, the calibration was performed in a dry nitrogen atmosphere.

The signal at the output of a given channel is determined by the blackbody temperature T_2 in accordance with eq.(31.X), where the quantities $\Phi_{A\lambda}$ and $\Phi_{B\lambda}$ are substituted by the spectral radiation intensities $r_{\lambda T_1}$ and $r_{\lambda T_2}$ of an absolutely black body. The thermal channels 3 and 5, which encompass the visible portion of the spectrum, were calibrated by the standard method (cf. Sect.2). The standard source used was a tungsten filament lamp (laminated type).

In addition, all the thermal channels of the radiometer were calibrated in the presence of different ambient temperatures T_a and a fixed magnitude of radiative fluxes at the input. This made it possible to plot curves of the type $U_{out} = f(T_a)$, which were used to introduce corrections for the temperature of the radiometer housing. The calibration procedure for channel 4, measuring the integral longwave radiation, is shown in Fig.13.X where 1 and 2 are calibration curves at the housing temperature of 25°C, with a blackbody of variable temperature mounted in front of the inlets A and B; 3 is the calibration curve as in case 1 but for a housing having a temperature of -45°C.

Tiros-series satellites have a spatially stabilized spin axis and are lobbed into near-circular orbits 3 (Fig.14.X). A five-channel radiometer is installed in the lower base of the satellite near one of the sides in such a manner that in one position the earth's surface is viewed through the window in the bottom and in the opposite position, through the window in the side. As the satellite spins (at the rate of about 10 rpm), the optical axis of the radio- /268

meter describes a cone about the axis of rotation of the satellite, with a 90° angle of taper. This is accompanied by scanning over the curve 2 or 2' on the earth's surface. The mean error in determining the effective temperature,

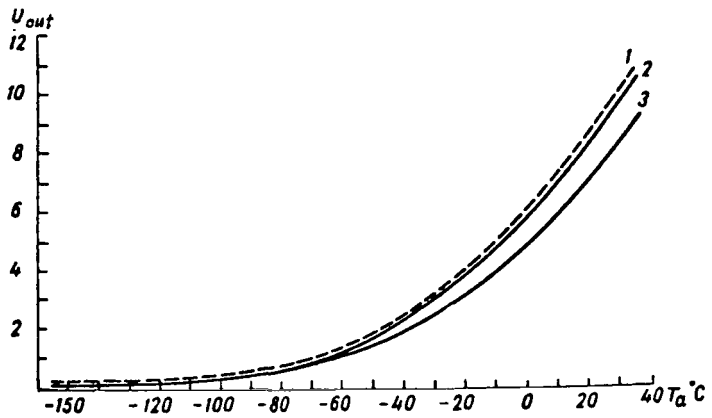

Fig.13.X Calibration Graphs of the Radiometer Channels.

according to the data of channels 1 and 2, has been estimated by the authors (Bibl.23) at not more or less than ±2%, and the maximum error in determining the absolute values, at not more or less than ±5%.

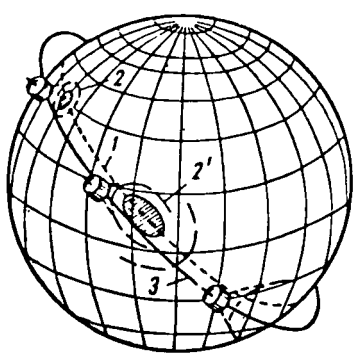

Fig.14.X Scanning Bands of the Radiometers Mounted in the Tiros Satellite.

An improvement on this instrument is the two-channel radiometer installed in the Mariner II space station, with the object of measuring the temperature of the cloud cover of Venus as well as the temperature of its surface in the presence of windows in the clouds (Bibl.31). In this device, the radiation from the planet and from outer space OS is alternately focused by the lenses L_1 and L_2 (Fig.15.X) onto channels A (8.5 μ) and B (10.4 μ), interrupted by means of /269 the mirror modulator M with a frequency of 20 cps. The plane mirror M_1 and the

dichroic mirror M_2 serve to alter the direction of the fluxes. The viewing angle of the channels is approximately $1.2 \times 1.2^{\circ}$ (Bibl.32). The detectors of the radiative fluxes in both spectral ranges, isolated by means of filters f_1 and f_2, are thermistor bolometers of the immersion type. The field of view of the lenses is such that the surface of Venus will occupy it during transit of the Mariner at a distance of 34,000 km from this planet.

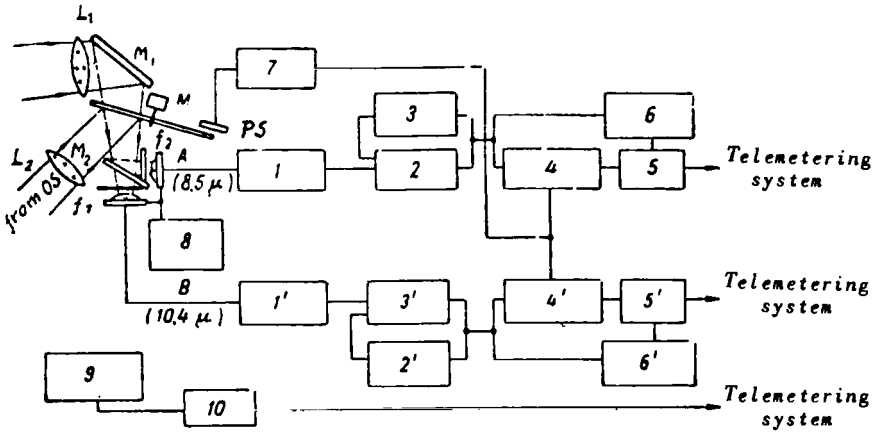

Fig.15.X Diagram of Two-Channel Radiometer. 1 and 1' - Preamplifiers of channels A and B; 2 and 2' - Logarithmic generators; 3 and 3' - Logarithmic amplifiers; 4 and 4' - Synchronous detectors; 5 and 5' - Output devices; 6 and 6' - Calibration circuits; 7 - Amplifier of the reference voltage; 8 - Receptor power pack; 9 - Temperature pickup; 10 - Amplifier of the bridge unbalance.

The electrical circuits of both channels are identical. They include a transistorized preamplifier of the same design as that of the five-channel radiometer (transmission band 1.7 cps, voltage amplification factor 7.2×10^3), a logarithmic amplifier for reducing the dynamic range (to 200 - 600°K), a synchronous detector with a filter and an output matching the amplifier.

The reference voltage supplied to the synchronous detector, which is used to attain a high signal-to-noise ratio, is produced by the photosensor PS and amplified by a special amplifier. A special calibration circuit serves to check the performance of the synchronous detector. The sensitivity of the radiometer is ~2° for a time constant of 3 sec (Bibl.32).

The calibration of the radiometer is verified by periodically covering its field of view with a calibration plate. The temperature of this plate, as /270 well as the temperature of the instrument housing is measured with the aid of pickups whose readings are, after amplification, transmitted to the telemetering system (Fig.15.X).

The total weight of the instrument is 1.3 kg; the dimensions are 13 × 14 ×

× 10 cm, the power requirement is 2.4 w (Bibl.32). For both radiometer types considered above, the same methods of calibration and data processing are used. In the latter experiment it was feasible to determine the CO_2 content of the planet's atmosphere (by comparing the radiation in the ~10.4 μ CO_2 band and in the 8.4 μ window).

Section 4. Actinometric Instruments

The most suitable devices for actinometric measurements, in which the integral fluxes of the radiant energy must be determined chiefly in the 0.2 - 40 μ spectral range, are nonselective heat receptors.

In instruments in which considerable inertia is permissible (up to several tens of milliseconds), the receptors employed are radiation thermoelements displaying a sensitivity nearly one order of magnitude greater than that of the modern bolometers (Bibl.16). The inertia of the receptor leads, however, results in averaging the measured fluxes.

To estimate the threshold flux recorded by the thermoelement, we will assume that there exists only the influx of heat via the electrodes forming the thermocouple and that the resistance of the leads is small. In this case, the change ΔU_s in the receptor signal due to the change $\Delta T^{\circ}C$ in the temperature of the working junction owing to the absorption of radiative flux $\Delta\Phi$, will be

$$\Delta U_c = S\Delta T = \frac{\alpha S \Delta \Phi}{\varkappa}, \tag{32.X}$$

where S is thermo-e.m.f.; α is the coefficient of the absorption of radiant energy by the black coating of the junction or of the foil to which the junction is attached; $\varkappa$ is a coefficient which takes into account the energy losses due to the heat conduction of the thermocouple and the radiative heat transfer.

The thermocouple noise, assuming that the amplifier noise and the induction noise are negligibly small, is virtually determined by the thermal noise of the ohmic resistance R_{th} of the thermocouple, but the determination of the latter must take into account the Peltier effect. This effect causes cooling of the heated thermocouple junction and the occurrence of a counter-directed e.m.f. To take into account the Peltier effect, the dynamic resistance R_d, whose magnitude, according to Moss (Bibl.16), is

$$R_d = \frac{S^2 T}{\varkappa} \approx 0.1 R_{th}. \tag{33.X}$$

is added to the thermocouple resistance R_{th}.

Thus, the mean square of the voltage of the thermal noise of the thermo- /271
couple, as determined from Nyquist's equation, will be

$$\overline{\Delta U_T^2} = 4kT\,(R_{th} + R_d)\,\Delta v. \tag{34.X}$$

The threshold flux with the factor of assurance c will be

$$\Phi_A = \frac{2\varkappa}{\alpha S} c \sqrt{kT (R_{th} + R_d) \Delta\nu}. \qquad (35.X)$$

Note that for an ideally designed thermoelement, in which there is no heat flow through the electrodes, we have $\varkappa = 4A\sigma\bar{T}^3$ (where A is the area of the sensitive surface of the thermoelement). In this case, for $\bar{T} = 290^\circ$K, A = 2 × × 0.2 mm^2 and $\Delta\nu$ = 1 cps, c = 1, α = 1, S = 5 × 10^{-4} v/deg and $R_{th} + R_d$ = = 200 ohm, we have $\Phi_f \approx 2 \times 10^{-11}$ watt.

B.P.Kozyrev (Bibl.4) has developed multiple-junction thermopiles designed to measure powerful fluxes of natural radiation of the earth or direct radiation of the sun (from 0.07 w/cm^2 to 0.14 w/cm^2) over a wide solid angle (~2π).

The 0.3 - 2.5 and 2.5 - 40 μ spectral sensitivity ranges of these thermopiles are isolated by means of a set of coatings of the sensitive surfaces and filters in the form of a semispherical inlet window. Within these spectral ranges, the thermopiles are virtually nonselective. The time constant of the 16-junction receptors is ~ 2.5 sec and the area of the sensitive surface is 2 × × 3 mm.

The receptor-calibration error (with respect to a spherical blackbody and an incandescent lamp with a sapphire window) is estimated at not more or less than ±3%.

In view of the considerable magnitude of the measured fluxes (cf. Sect.1 of this Chapter), the actinometric instrument is based on thermal methods of radiant-energy measurement, with the temperature of the sensitive surfaces serving as the measured quantity. To separate the fluxes of solar and longwave radiation, the sensors usually are coated with a black or white dye. The black coating absorbs and emits radiative fluxes almost equally well over the spectral range considered, while the white coating virtually does not absorb shortwave radiant energy (approximately from 0.2 to 4 μ), but behaves in the longwave region in roughly the same manner as the black coating.

To determine the radiative fluxes composing the radiation balance, or to directly determine the radiation balance, the equation of the heat balance of the receptor is solved. The terms of this equation are, in the general case:

a) The heat influx due to absorption of shortwave and longwave radiant /272 energy, whose densities in the neighborhood of the receptor will be denoted by F_s and F_ℓ, respectively, while the areas of the receptor sensitive to each type of radiant energy will be denoted correspondingly by a_1 and a_2:

b) to the heat influx due to radiative heat exchange between the concerned receptor area a_3 with temperature T and the container surface "visible" to it and having the temperature T_4 as well as the same emissivity ϵ;

c) to the heat influx from internal sources, and in particular owing to the heating of the electron thermometer by current i which flows across it in the measuring circuit;

d) to the heat influx from the receptor-fastening system, which is taken into account by introducing the equivalent coefficient of heat conduction $\varkappa$ and cross sectional area a of this system;

e) to the heat losses due to natural radiation from the effective surface a_4 of the receptor in the presence of the emission coefficient ε.

If, owing to the action of these heat fluxes, over the time Δt, the temperature of the receptor changes by ΔT, the change in its enthalpy (cf. Sect.1, Chapt.III) will be

$$mc\Delta T = [\alpha F_s a_1 + \varepsilon F_\ell a_2 + 4\varepsilon\sigma\bar{T}^3 (T_1 - T) a_3 + \\ + 0.24i^2R + \varkappa a (T_1 - T) - \varepsilon a_4\sigma T^4]\Delta t, \qquad (36.X)$$

where m is the mass of the receptor; c is its specific heat; α and ε are the absorption and emission coefficients; T is the mean temperature determined from the condition $T_1^4 - T^4 = 4\bar{T}^3(T_1 - T)$; and R is the resistance of the receptor.

The equation of the heat balance obtained above [eq.(36.X)] is rewritten as follows in the event that the design is modified to assure the equality of all of the effective areas $a_1 = a_2 = a_3 = a_4$:

$$\alpha F_s + \varepsilon F_\ell - \varepsilon\sigma T^4 + 4\varepsilon\sigma\bar{T}^3 (T_1 - T) + \\ + H_1 i^2 + H_2 (T_1 - T) - \eta \frac{\Delta T}{\Delta t} = 0, \qquad (37.X)$$

where H_1 and H_2 are coefficients determining the heat influx due to the passage of current across the receptor and the heat conduction of the receptor's fastening system; η is the coefficient characterizing the receptor's thermal inertia (cf. Sect.1, Chapt.III).

The equation (36.X) of the heat balance of the receptor implies that it is fundamentally possible to employ both static (on condition that $\Delta t \approx 0$) and dynamic thermal methods for measuring the integral fluxes of the radiant energy. In the latter case, however, it would be necessary to record the nature of the rate of variation in the receptor temperature $\Delta T/\Delta t$, which involves considerable technical difficulties. /273

In static measurements it is possible to employ either the thermometric or the compensation method. In the latter case, the absorption of radiant energy by the receptor is compensated by the passage of current i_c. Even this method, however, is technically difficult to apply to telemetric measurements, although it has the advantages of the differential-zero measurement principle (cf. Sect.2 of this Chapter).

When employing the thermometric measurement method, the receptor design must be such that all of the heat fluxes other than the influx due to the absorption of radiant energy would be of a minimal magnitude.

To determine the flux Φ_ℓ of longwave radiant energy on the planet's dark

side, it is sufficient to measure the temperature of any (black or white) receptor, since in this case the terms of the balance containing shortwave Φ_s are absent. To determine the fluxes Φ_ℓ and Φ_s on the illuminated side of the planet, it is necessary to measure the temperatures of the black and white receptors and to solve jointly the obtained equations of the balance (the values of all of the parameters entering into these equations must be determined during laboratory tests of the instrument).

The parameters of the instrument's optical system may be estimated from equations derived earlier (cf. Sect.3 of this Chapter), considering that the integral radiation flux of a body with the temperature T_{earth} into the half-sphere is

$$\int_0^\infty \varepsilon_\lambda r_\lambda T_{ea} \, d\lambda = \varepsilon \sigma T_{ea}^4 \qquad (38.X)$$

where σ is the radiation constant.

Calculations show that a 0.01 w variation of the flux at the angle π radian causes a variation of $\sim 1^\circ$C in temperature (exclusive of the optical system). Various actinometric devices are used on a fairly broad scale in meteorological studies performed with the aid of rockets and satellites in the USSR (Bibl.4, 8, 12) as well as in the United States (Bibl.10. 13, 19, 20).

One of the first of these devices was the thermometric-type instrument designed to measure the radiation balance from the Explorer VII satellite (13 Oct, 1959) by means of wide-angle receptors designed in the form of half-spheres with various coatings and attached on insulating supports in the neighborhood of mirrors reducing the effect produced by the radiation from the surface of the instrument housing. The temperature of the half-spheres and mirrors was measured by thermistors (Bibl.13, 19).

Actinometric measurements by means of Soviet upper-air optical probes /274
have been carried out by means of net radiometers or total radiation pickups (TRP). In these instruments, film-type thermoelements with black-and-white coatings were attached in the shear plane of a massive copper cup with a blackened inner surface. The cup temperature and its difference from the junction temperatures were measured (Bibl.8).

The Tiros-series satellites employ a two-channel wide-angle radiometer to determine the components of the radiation balance of the earth-atmosphere system.

The receptors of radiative fluxes in this instrument (Fig.16.X) are thermistors with black 1 and white 2 coatings attached to the tops of cone-shaped aluminized reflectors 4 which assure a roughly fivefold optical amplification (Bibl.27). To reduce the flow of heat through the thermometer fastening system, the cones are constructed of thin insulating (Mylar) film and the receptor is attached by means of a fine synthetic filament. The reverse side of the receptor is coated with gold, having a radiation factor such that the losses due to heat conduction and radiative heat exchange with lid 7 are roughly compensated. The angle of taper of the cones is $\sim 50^\circ$. The thermoreceptors have a diameter of 5 mm and a thickness of 0.01 mm (Bibl.27). To compensate for the

effect of ambient temperature on the thermistor readings, the resistors 5 with a positive temperature coefficient of resistance are connected to the circuit parallel to the thermistors.

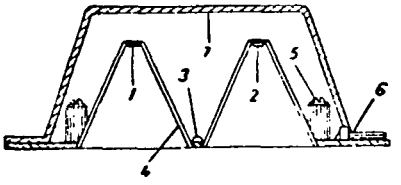

Fig.16.X Diagram of the Sensitive Part of a Wide-Angle Radiometer.

Considering that this instrument does not ideally eliminate the effect of the heat fluxes to distort the measurements, the temperature of the instrument housing is measured by the thermistor 3 attached between the bases of the

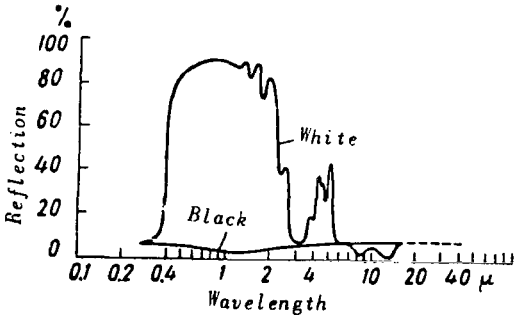

Fig.17.X Spectral Characteristics of Receptor Coatings.

housing 4. The output impedance of the receptors within the range of the measured radiative fluxes varies from 300 to 1500 ohm (Bibl.27). The voltage drop on the receptors is conveyed via a commutator to a controlled generator /275 whose frequency then varies within the limits of 425-485cps (Bibl.19). The signal produced by the generator arrives at the recording system. Note that the same system with a commutator is used for measuring the temperature of other elements of the satellite and particularly of the housing of the five-channel radiometer, and also for transmitting the voltage-calibration signals (Bibl.19).

The spectral characteristics (Fig.17.X) of the white and black coatings (and particularly of the white coating in the region of ~4 μ) differ markedly from the ideal. In this connection, the thermistor temperature is not equal to the true temperature of the earth. The presence of distorting fluxes disturbs the radiative equilibrium between the receptor and the sector of the emitting surface present in the field of view of the optical system. To determine the density of the radiative fluxes sensed by the thermistors, it is necessary to employ an equation of heat balance of the eq.(36.X) type.

The primary processing of the results of the measurements involves the solution of a simplified equation which, for night measurements, is written as

$$I_s \alpha\omega = \varepsilon\sigma T^4 + H_2(T_1 - T) + \eta\frac{dT}{dt}, \qquad (39.X)$$

where I_s is the intensity of the measured longwave radiation and ω is the fixed viewing angle of the instrument.

ω is determined according to the angular characteristics of the instrument's field of view (Fig.18.X). Taking into account the half-intensity signal, the viewing angle roughly corresponds to the angle of taper of the cone-shaped reflectors (50°).

The calibration of the radiometer was conducted in a vacuum ($\sim 10^{-5}$ mm Hg); it was then attached to a metal frame simulating the satellite (Bibl.19). The frame temperature was varied in stages from -10 to +60°C. The temperature of the blackbody simulating the earth's radiation was varied within limits of from -130 to +60°C. A quartz-window incandescent lamp was used to simulate solar radiation.

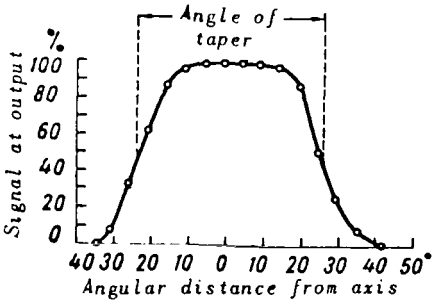

Fig.18.X Angular Characteristics of the Field of View of a Wide-Angle Radiometer.

Calibration curves of the blackened thermistor for various temperatures of the housing are shown in Fig.19.X, where equivalent earth temperatures are specified in lieu of blackbody temperatures. The broken line traces the ideal curve that would have been obtained as a result of calibration for any temperature of the housing, if the heat insulation had been perfect and the emissivities of the thermometer and of the earth had been equal to unity. The graph in Fig.19.X is used for the primary processing of observational findings.

The two-channel radiometer is mounted in the central part of the satellite bottom in such a manner that the optical axes of both channels are virtually /276 parallel to the axis of spin (cf. Fig.14.X).

On upper-air automatic geophysical probes, outgoing radiation within the 0.5 - 40 μ spectral range was measured by means of scanning teleradiometers with a bolometric receptor (Bibl.1). These instruments are based on the double-beam scheme (Fig.20.X). The thermal radiation of the earth is sensed through one

channel (scanning optical head 1), while the reference radiation of outer space is sensed through the other channel (fixed head 2). Both receptors have the

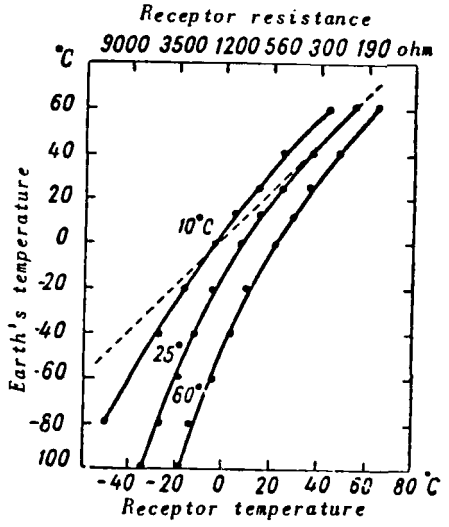

Fig.19.X Calibration Curves of the Blackened Thermistor for Various Housing Temperatures.

same mirror lenses with the relative aperture 1:4. In order to employ the variable-voltage amplifier 5, the fluxes are modulated with a frequency of 80 cps. In order to exclude the natural radiation of the modulator, the circuit

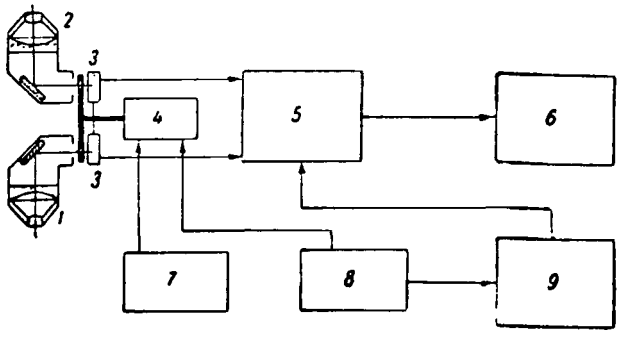

Fig.20.X Block Diagram of the Instrument for Measuring Thermal Radiation:
1 - Optical scanning head; 2 - Optical zero-signal head; 3 - Bolometers; 4 - Scanning mechanism; 5 - Amplifier; 6 - Telemetering system; 7 - Motor supply source; 8 - Satellite command system; 9 - Power pack.

of the bolometers 3 is of the differential type. As a result, the instrument produces the signal U_{out} proportional to the difference in the intensities I_{earth}

and $I_{o.s.}$ of the radiative fluxes incident on the instrument from the earth and from outer space:

$$U_{out} = K(I_{e.s} - I_{o.s}) = KI_{e.s}, \qquad (40.X)$$

where K is a coefficient which depends on the reflection of the mirrors, on the properties of the bolometers, and on the amplification of the signal within the circuit.

The optical axis of lens 1 is actuated by being driven from the motor of the modulator 4. It alters its direction within the limits of the scanning angle (180°). The scanning rate is 6° per sec. The extreme positions of the scanning lens are recorded by sending pulses to the telemetering system. /277

The sensitive area of the bolometers measures 3 mm^2, their sensitivity S in the bridge circuit diagram is 15 v/w, and the time constant τ is 5 msec. Their spectral sensitivity is uniform throughout the 1 - 40 μ range (Bibl.1). At a frequency of ν_m = 80 cps, the sensitivity threshold Φ_t of the instrument is 10^{-9} w/cps for a viewing angle of ~1°.

Note that in certain variants of this instrument the solar radiation ($\lambda < 2.5\ \mu$) was cut off by means of filters (Bibl.12).

The total voltage amplification factor of the selective five-stage amplifier 5 was ~10^6 and the equivalent noise width of the frequency passband $\Delta\nu$ = = 40 cps. The amplified signal was detected and averaged by an RC filter. The time constant of this filter, which determines the total inertia of the instrument, was 0.4 - 0.5 sec for the variant considered here (Bibl.1). Sensitivity of the instrument was checked during its operation by means of a periodically energized incandescent lamp incorporated in its design. This lamp was powered from a separate source.

The total calibration error for the obtained calibration by means of two blackbodies was estimated by the authors (Bibl.1) as 2 - 3%, and the total measurement error, due to the presence of electromagnetic induction at the instrument output, reached ±15% and ±20%.

Section 5. Spectral Instruments /278

In spectral instruments designed to operate in the visible and infrared regions of the spectrum, both prisms and diffraction gratings are used as dispersion elements. The gratings display a higher resolving power and hence they are used more often. In the far-IR region, reflection gratings and monochromators of the lensless type are employed, but, as was pointed out earlier (cf. Sect.5, Chapt.IX), then steps must be taken to reduce astigmatism. The grating as well as the entrance slit and receptor are mounted on a Rowland circle (Bibl.24) in accordance with the schemes described earlier. Photomultipliers represent highly effective receptors for telespectrometers in the visible and near-IR regions, while photoresistors are highly effective in the central-IR region.

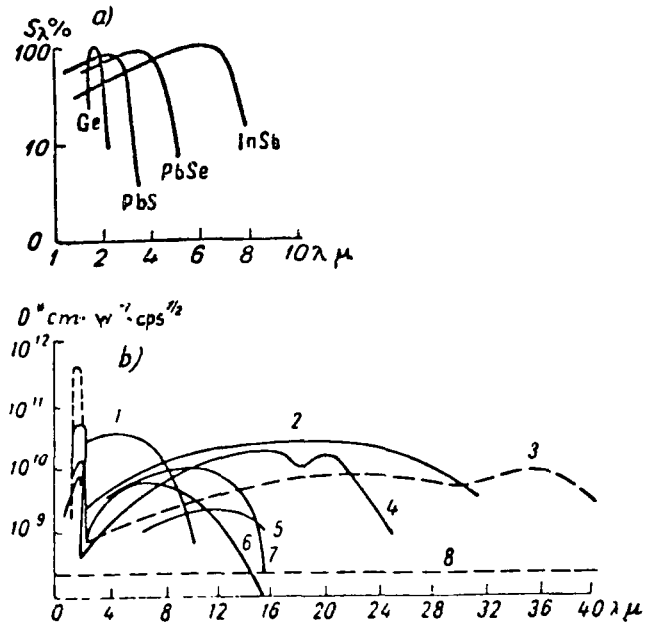

Fig.21.X Spectral Sensitivity of Certain Photoresistors at Room Temperature (a) and on Cooling (b).
1 - Ge:Au at 65°K; 2 - Ge:Cu at 4.2°K; 3 - Ge:Zn at 4.2°K; 4 - Ge:Cd at 4.2°K; 5 - Ge:Zn, Sb at 50°K, Ge-Si:Au at 50°K; 6 - Ge-Si:Au at 3.50°K; 7 - Ge-Si:Zn, Sb at 50°K; 8 - Thermistor bolometer at 293°K.

The circuit diagram of photoresistors with a load resistance equal to the shadow resistance of the receptor is analogous to the circuit diagram of /279 bolometers described earlier (cf. Sect.3 of this chapter).

The principal types of photoresistor noise are thermal noise and current noise [generation-recombination and contact noise (Bibl.19, 21)].

The spectral sensitivity S_λ of photoresistors at room temperature is limited to wavelengths of 2 - 8 μ (Fig.21a.X). On cooling the curve of spectral sensitivity gets displaced in the direction of longer wavelengths. By cooling photoresistors made of germanium doped with various additions (or of a germanium-silicon alloy) it is possible to obtain receptors displaying high qualities also in the central-IR region (Fig.21b.X).

As a criterion for various receptors in which the ratio of threshold sensitivity Φ_f to the area A of the receptor is independent of the dimensions of the latter, it is convenient to employ detectability D^*, determinable from the equation

$$D^* = \frac{S\sqrt{A\Delta\nu}}{\sqrt{U_\Sigma^2}}, \qquad (41.X)$$

where S is the volt sensitivity and $\Delta\nu$ is the frequency band at which the total noise U_{Σ} is determined.

The values of D^* for doped germanium resistors and for a thermistor bolometer according to (Bibl.17 and 24) are specified above (Fig.21b.X). For a PbS photoresistor at room temperature, doped germanium $(D^*) = 10^{12}$ cm-cps$^{1/2}$ w^{-1}, while at -196°C it reaches 1.5×10^{13} cm-cps$^{1/2}$ w^{-1} (Bibl.24). For the other types of photoresistors indicated in Fig.21a.X, D^* is of the order of 10^9 cm · cps$^{1/2}$ w^{-1}.

The time constants of photoresistors are comparatively small. They are measured in microseconds, particularly in the cooled state. The lowest time constant, according to Hackford (Bibl.24), is displayed by germanium doped with gold (10^{-8} sec). This makes it possible to effectively employ photoresistors in instruments with high scanning speeds.

The spectral instrument in the range considered here finds its greatest practical applications in the determination of the gaseous components of planetary atmospheres. Thus, as far back as in 1957, Singer and Wentworth suggested a method of calculating the ozone content of the atmosphere based on measurements of scattered solar radiation in the Hartley band (1800 - 3400 Å) by means of a spectrophotometer mounted in an artificial earth satellite (Bibl.5). Later, this method was further developed by G.P.Gushchin (Bibl.5) and proposed for use on weather satellites. It is based on periodic orbital measurements of the /280 monochromatic solar radiation with the wavelength λ = 6020 Å (maximum of the Shapuis absorption band 4400 - 7500 Å).

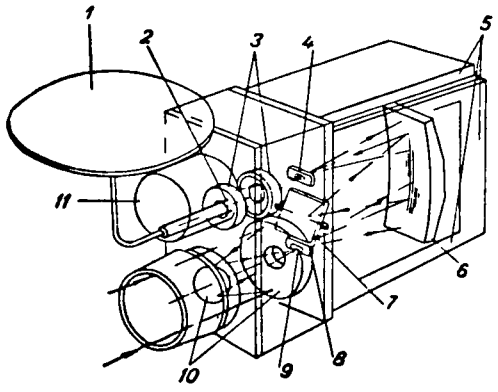

Fig.22.X Infrared Telespectrophotometer for Investigating the Atmospheres of Planets.

The spectrophotometer designed for the investigation of Mars and Venus from space probes of the Mariner series, with the object of resolving the question of the existence of life on the planets [according to the presence or absence of CH-group absorption in ~3.5 μ (Bibl.20)], makes it possible to obtain spectrograms in the IR region (roughly from 3 to 4 μ) with a high resolution [0.1 - 0.2 μ (Bibl.20)].

The instrument (Fig.22.X) has a Cassegrain-system mirror lens 10 and a mirror monochromator with swinging diffraction grating 7. The radiant energy, dissociated into its spectrum, passes through exit slit 4 and is focused by the mirror condenser 3 on a sulfur-lead photoresistor 2. Owing to the tilted position of the grating, spectral scanning takes place. The receptor is cooled to a temperature of approximately -78° C (Bibl.20) by means of the radiating disk 1.

The lobe-type modulator 9, located in front of the entrance slit of the monochromator 8, serves to interrupt the radiative flux (frequency 300 cps). The electronic blocks 5 are positioned beyond the concave mirror 6 of the monochromator.

The mirror lens of the instrument has a diameter of 102 mm and a viewing angle of $0.25 \times 2.5^{\circ}$. The latter is so selected that scanning of overlapping sectors of the planet's surface, measuring 64 × 640 km in area each, would be performed at a distance of 15,000 km from the planet.

To accomplish the temperature sounding of the atmosphere from a satellite by the Kaplan method (Bibl.10, 20), the United States has developed an infra- /281
red telespectrophotometer measuring radiative fluxes in five narrow spectral intervals in the region of CO_2 absorption in the neighborhood of 15 μ (698.8; 694.5; 688.5; 677.5, and 667.5 cm^{-1}), approximately 5 cm^{-1} wide (Bibl.28).

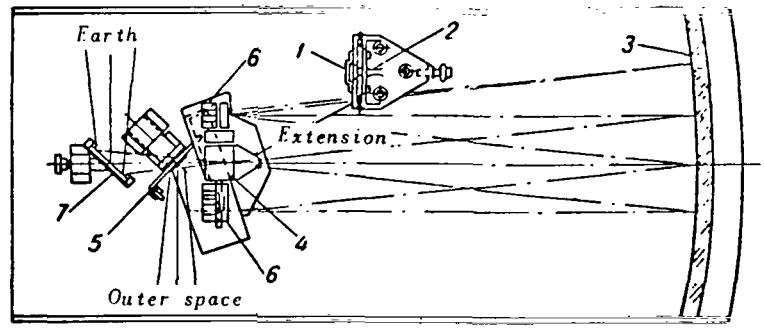

Fig.23.X Diagram of the Spectrometer for Temperature Sounding.

The instrument monochromator (Fig.23.X) has a reflecting diffraction grating 4 with an area of ~30 cm^2, ruled with 49 lines to the millimeter, as well as spherical mirror 3 with a diameter of ~41 cm.

The telespectrophotometer operates on the principle of the double-beam single-receptor system. The radiation of the earth-atmosphere system is directed toward the monochromator following its reflection from the plane mirror 7, while the radiation of outer space is directed following its reflection from the mirror sides of the two-sector modulator 5 positioned at the angle of 45° to the optical axis of the monochromator. The modulation frequency of the radiative flux is 15 cps.

The radiation passing through the entrance slit 2 with the filter 1 is gathered by the mirror 3 and directed onto the diffraction grating 4 positioned

above the entrance slit. The spectrum reflected by the grating again falls onto the mirror 3 which focuses nearly monochromatic radiative fluxes onto the five exit slits 6 of the monochromator which are positioned above the grating.

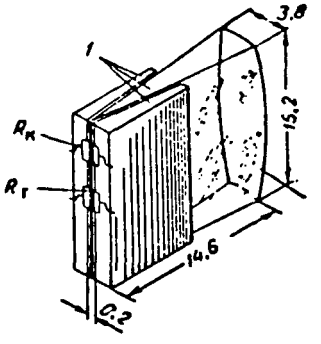

Fig.24.X Immersion-Type Thermistor-Bolometer Receptor.

To verify the sensitivity, a provision has been made for periodic rotation of the inlet-plane mirror 7 directing toward the instrument the radiation of an absolutely black body with a temperature equal to the temperature of the telespectrophotometer housing (from 0 to 60°C), which is measured. /282

The spectrum detectors employed are thermistor (selenium) bolometers mounted beyond the exit slits of the monochromator. The germanium immersion lenses 1 (Fig.24.X), combined into a system with reflecting sides, are used to focus the radiative flux onto the bolometers, with the compensating R_c and the operating $R_т$ thermistor receptors being attached to these lenses.

Under laboratory conditions, the above telespectrophotometer made it possible to record at room temperature a temperature fluctuation of 0.2°C. A goal of its development was the measurement of a temperature of 0.5°C against the background of -70°C. The measured spectral intensities range from 25 to 180 $erg \cdot cm^{-2} \cdot sec^{-1} \cdot cm^{-1} \cdot ster^{-1}$ (Bibl.20).

PART IV

/283

OBTAINING THE IMAGES OF THE PLANETS AND OF THE CLOUD COVER

Planet images from rockets and space vehicles may be obtained with the aid of photographic, phototelevision or scanning instruments. Each type of apparatus may operate in various portions of the optical range of the spectrum.

The use of photographic methods for obtaining images in outer space involves difficulties in developing the photographs and transmitting the information to earth. Hence, they are less widely used than television methods, which are based on obtaining electric signals and transmitting these via communication channels. Television methods, however, are as yet difficult to employ under conditions of low illumination of the transmitted image. Accordingly, in order to obtain images of the night-cloud cover, infrared scanning instruments, which essentially represents a variety of television apparatus with certain specific features of their own, began to be employed in the weather satellites of the Nimbus series.

CHAPTER XI

SCANNING INSTRUMENTATION

Section 1. Optical-Kinematic Diagram

The operating principle of a scanning apparatus lies in that the radiative flux from elements of the scanned surface is successively converted into electrical signals which are transmitted to the receiving side, where they are reconverted in the same sequence to mean brightness of the image elements. The operating principle of a scanning instrument thus resembles the operating principle of every currently used apparatus for the transmission of images via communi- /284
cations channels, and particularly that of a television apparatus. The principal difference between an optical scanning apparatus and a television apparatus lies in that scanning apparatus usually employs a single receptor which successively receives the radiative flux from elements of the scanned surface. The successive survey of elements (scanning) is then, as a rule, accomplished by means of optico-mechanical systems of various designs. The dimensions of the scan elements, the operating spectral range and other parameters of the apparatus depend on the particular purpose for which it is designed.

Scanning instruments are used for measurements of every portion of the electromagnetic energy spectrum.

In the optical range, scanning instruments are used for measurements of the angular distribution of the radiation of the earth, clouds and the atmosphere,

i.e., of parameters measurable by optical methods (cf. Chapt.IX and X). They can be used, in particular, for satellite measurements of the temperature and humidity fields, of the ozone distribution, of the carbon dioxide distribution, etc.

In observations of the cloudiness, the principal advantage of an infrared scanning instrument compared with television apparatus lies in that it detects the natural radiation of objects and hence can operate on a 24-hour basis and not just during solar illumination. Considering that the attainment of a high resolving power R of infrared scanning instruments involves various technical difficulties, the American satellites of the Nimbus series employ a combination of television and infrared-scanning instruments (the former for daylight operation and the latter for night operation) (Bibl.5).

Optico-electromechanical devices, designed to determine the coordinates of various targets according to their own natural thermal emission, are termed heat radar. Both scanning and scanning-tracking systems of this kind are used for military purposes. The former serve to detect heat-emitting targets during heat reconnaissance of terrain and the latter, to home-in weapons (Bibl.1).

In infrared scanning instruments, images are most often obtained by surveying the investigated area with a narrow (needle-like) beam with a rectilinear line scanning. The scanning is performed for instance in the instrument used in the United States (Bibl.4) by means of the rotation of a prismatic mirror drum 1 (Fig.1.XI) with n sides. Following reflection from one of the sides, /285 the bundle of rays reflected from or emitted by the scanned surface is focused by the parabolic mirror M_1 onto the receptor R. The plane mirror M_2 serves to vary the direction of this bundle for a given layout of the instrument. Every time a drum side passes through the field of view of the mirror M_1, a different line of terrain is scanned.

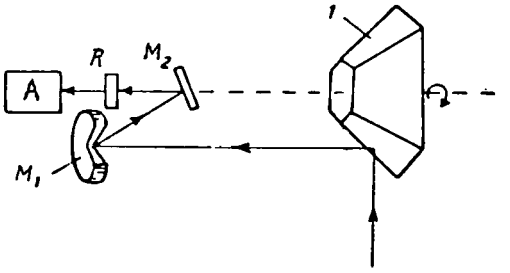

Fig.1.XI Diagram of an Optico-Mechanical Scanning System.

The signal produced by the receptor is conveyed to the amplifier A and thence to the electronic circuit where it usually combines with the timing pulses determining the beginning and end of every scanning line according to the signals of the pickups connected to drum 1.

Scanning in the form of parallel lines, as obtained in the above case, is termed rectilinear. The techniques of such scanning may vary. In particular,

drum 1 may be replaced by a single swinging or nonuniformly revolving tilted mirror.

Scanning devices of the survey-and-search type are also based on other forms of scanning. Thus spiral, or zigzag-like, scanning is more effective in heat radar devices (e.g., in infrared homing instruments) (Bibl.1).

Devices for measuring the radiation balance, as well as photometers and radiometers (cf. Chapt.IX and X) employ an elementary scanning system based on the uniform rotation of a sensitive head equipped with a tilted mirror.

The selection of the form of scanning and the design of the optical-kinematic system are thus a function of the purpose for which the scanning instrument happens to be designed and of the information which it provides. All kinds of such instruments, however, have in common certain features stemming from their operating principle. We will examine these features as exemplified by the rectilinear optical-mechanical scanning system employed in the instrumentation of the Nimbus-series satellites.

Section 2. Dimensions of the Scan Element and Form of the Scan Line

/286

The dimensions Δx and Δy of the terrain-scan element (Fig.2.XI) are determined by the instrument altitude H, the fixed angle of the field of view (characterized by the angular dimensions δx and δy), and the scanning angle γ (deviation of the line of sight from the vertical). It follows from Fig.2.XI, that for a tetrahedral instantaneous viewing angle of the instrument, required for the compact coordination of the scan elements, the line width will be

$$\Delta y = 2D \tan\frac{\delta y}{2} = \frac{2H \tan\frac{\delta y}{2}}{\cos\gamma}. \qquad (1.XI)$$

The dimension of an arbitrary scan element along the line will be

$$\Delta x = \frac{2H \tan\frac{\delta x}{2}}{\cos^2\gamma + \cos\gamma \sin\gamma \tan\frac{\delta x}{2}}. \qquad (2.XI)$$

For a needle-shaped scanning beam ($\delta x \approx \delta y \approx 0$) eqs.(1.XI) and (2.XI) may be simplified and written as

$$\Delta y \approx \frac{2.9 \cdot 10^{-4} H \delta y}{\cos\gamma} \text{ and } \Delta x \approx \frac{2.9 \cdot 10^{-4} H \delta x}{\cos^2\gamma}, \qquad (3.XI)$$

where 2.9×10^{-4} is the conversion factor for converting the angle minutes into radians.

If the line length L for the terrain or for the maximum scanning angle γ_{max} is large (L > 400 - 500 km), the dimensions of the scan elements at the line

edges must be determined, taking into account the curvature of the earth surface, since obviously the errors in the calculations from the equations for scanning a plane surface [eqs.(1.XI) and (2.XI)] would otherwise be substantial (several tens of percent or even higher).

Equations taking into account the curvature of the planet surface to a first approximation (assuming that the planet has the shape of a sphere with the radius R_{earth} and disregarding the curvature of the scan element itself, and further assuming that all the rays running from the instrument to the scan element encounter it at the same angle θ) may be derived with the aid of Fig.3.XI. It follows from this figure that the dimension of the scan element over the line length will be, on taking curvature into account,

$$\Delta x_c = MC = \frac{MP}{\sin\theta} = \frac{2D\tan\frac{\delta x}{2}}{\cos\gamma\cos\left(\gamma+\frac{\psi}{2}\right)} \approx \approx \frac{2.9\cdot 10^{-4} D\delta x}{\cos\gamma\cos\left(\gamma+\frac{\psi}{2}\right)}, \qquad (4.XI)$$

where $D = \frac{H + R_{earth}\left(1 - \cos\frac{\psi}{2}\right)}{\cos\gamma}$ is the inclined distance to the scan element, ψ is the angular dimension of the scan zone from the center of the earth and R_{earth} is the radius of the earth (or of a planet). /287

Proceeding from the same reasoning, the dimension of the scan element over the line width, taking into account the curvature as well as the smallness of the viewing angle ($\tan\delta y \approx 2.9 \times 10^{-4}\ \delta y$) will be

$$\Delta y_c \approx 2.9\cdot 10^{-4} D\delta y. \qquad (5.XI)$$

These equations show clearly that on the curve of the planet's surface the dimensions of the scan elements at the line edges, and especially the dimension over the line length Δx_c, are greater than on a plane surface. As the orbiting altitude H increases, for a fixed viewing-angle δx and δy the dimensions Δx_c and Δy_c increase, particularly when the line of sight D approaches the tangential position (Fig.3.XI). This is illustrated by the curves of the ratio between the dimensions Δx_c and Δy_c and the minimal Δx_0 and Δy_0 (when $\gamma = 0$), as is shown in Fig.4.XI. It can be seen from these curves that, depending on the altitude H of the satellite, a limiting scanning angle γ_{max} exists beyond which the dimensions Δx_c and Δy_c begin to increase sharply.

Hence, the dimensions of the scan elements, in the scanning of both plane and particularly in curved surfaces, increase with the approach to the line edges (with increasing scanning angle γ) and the lines broaden, as is schematically shown in Fig.2.XI.

We will construe the resolving power of the scanning instrument as the quantity R inversely proportional to the area ΔA of the terrain scan element. Then, on using equations (1.XI) and (2.XI) for a plane surface, we have

$$R = \frac{1}{\Delta A} = \frac{1}{\Delta x \Delta y} \approx R_0 \cos^3 \gamma, \qquad (6.XI)$$

where $R_0 = \frac{1}{8.4 \times 10^{-8} H^2 \delta x \delta y}$ is the resolution at the center of the line (at the nadir).

/288

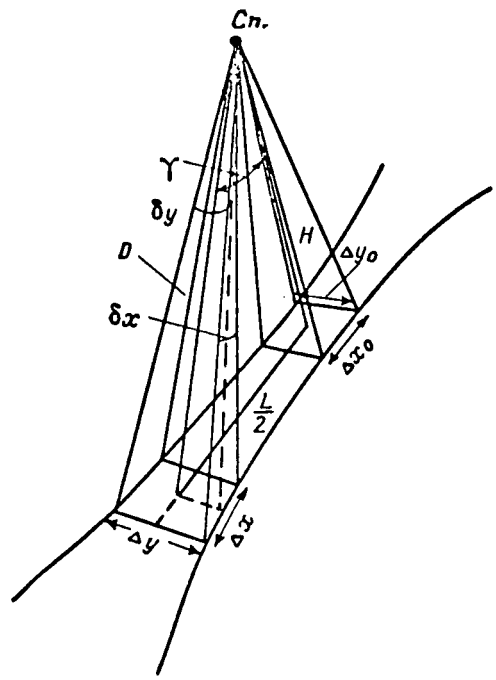

Fig.2.XI Variation of a Scan Element along a Line.

For a spherical surface, to a first approximation, we have

$$R_c \approx R_0 \cos^3 \gamma \cos\left(\gamma + \frac{\psi}{2}\right). \qquad (7.XI)$$

These equations show that the resolving power of the instrument with an optical-mechanical scanning system decreases with an increasing scanning angle /289 in a roughly direct proportion to $\cos^3 \gamma$ or $\cos^3 \gamma \cos\left(\gamma + \frac{\psi}{2}\right)$, if the line length is considerable and allowance for the planet's curvature is required.

The decrease in resolving power at the edges of the scan line may be estimated with the aid of the graphs shown in Fig.4.XI. Thus, e.g., for a Nimbus type satellite which scans the earth's surface from an altitude of 1000 km at a viewing angle $\alpha = 2\gamma_{max} = 105^\circ$ on using television cameras during the daylight hours, in such a manner that the entire space between any two orbits around the earth ($L \approx 3000$ km) would be scanned without leaving out any gaps (Bibl.5), the

deterioration in the resolution at the line edges is

$$\frac{R_0}{R_c} \approx \frac{\Delta x_c}{\Delta x_0} \frac{\Delta y_c}{\Delta y_0} \approx 3.4 \cdot 2.1 \approx 7,$$

and, since the viewing angle increases furthermore, the rate of the loss of resolution increases even more rapidly.

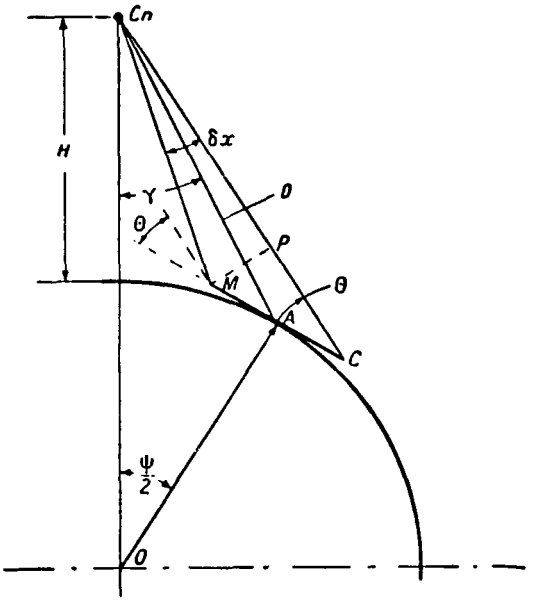

Fig.3.XI Position of a Scan Element on a Spherical Surface.

Line broadening at the edges leads at the same time to the overlapping of lines. The extent of the overlap of neighboring lines clearly contributes /290 to the deterioration of resolving power if the lines adjoin each other closely in their central parts.

Thorough scanning without any gaps thus requires the matching of the dimension of the scan element over the line width at the line center Δy_0 (for $\gamma = 0$) with the scanning time t_s and the rate of motion of the instrument's projection over the planet surface v_{pr}. Figure 2.XI shows that for line contact the relation

$$t_s = \frac{\Delta y_0}{v_{pr}} \approx 2.9 \cdot 10^{-4} \frac{H \delta y}{v_{pr}} \qquad (8.XI)$$

must be satisfied.

The pulse time or the scanning time t_e per scan element decreases in proportion with the number of elements present along a line, namely:

$$t_e = t_s \frac{\delta x}{\alpha} \approx 2.9 \cdot 10^{-4} H \frac{\delta y \delta x}{\alpha v_{pr}}. \qquad (9.XI)$$

Equation (9.XI) makes it possible to infer the required modulation frequency ν_m and the frequency band $\Delta\nu$ at the amplifier input, as well as to determine the requirements as to the inertia τ of the receptor.

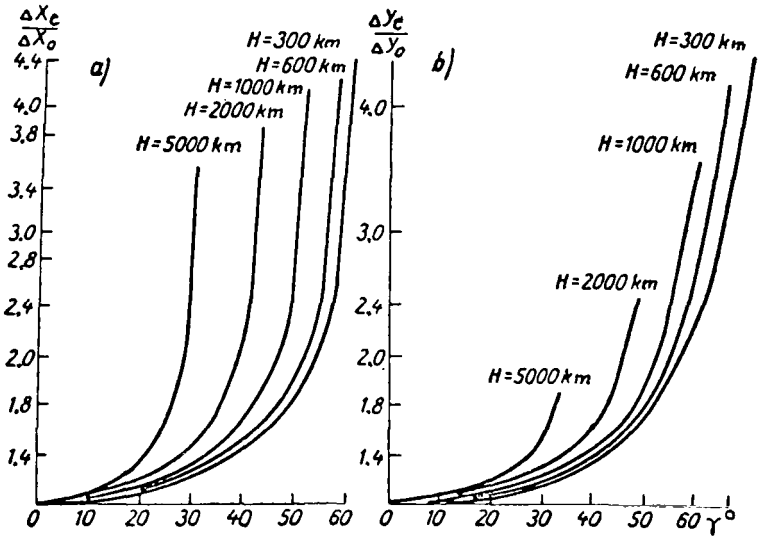

Fig.4.XI Variation in Relative Dimensions of Scan Elements along (a) and across (b) a Line during Scanning.

If there is no modulation of the radiative flux, the inertia τ of the receptor should be small enough to cause, over the time t_e, the signal amplitude in its circuit diagram to reach nearly 100% of its steady-state value (compared with the preceding element). If $\tau = \frac{1}{2} t_e$, the signal amplitude will reach ~95% of its steady-state value, and if $\tau = \frac{1}{4}$, t_e = ~98%.

Thus, the inertia (time constant) of the detector must satisfy the relation

$$\tau \leqslant \left(\frac{1}{2} \div \frac{1}{4}\right) t_e \approx \left(\frac{1}{2} \div \frac{1}{4}\right) \frac{2.9 \cdot 10^{-4} H \delta x \delta y}{\alpha v_{pr}}. \qquad (10.XI)$$

It follows from eq.(10.XI) that a sufficiently high resolution of the instrument with an optical-mechanical scanning system may be achieved only on using a low-inertia receptor. For example, in the Tiros type weather satellite [H = 700 km, orbital velocity v = 7.65 km/sec, v_{pr} = 6.8 km/sec (Bibl.2)] a non-cooled bolometer with the inertia $\tau = 5 \times 10^{-3}$ sec, for the viewing angle α = = 43°50' (L = 1500 km), assures a resolution of not more than $R_o \approx 0.014$ km^{-2} at the nadir (then $\delta x = \delta y \approx 42'$ and $\Delta x_o \Delta y_o \approx 8.5 \times 8.5$ km^2). To assure a resolu-

tion of $R_o = 1\ km^{-2}$ ($\Delta x_o = \Delta y_o = 1$ km, $\delta x = \delta y = 6'$) at the nadir, a receptor with the inertia $\tau \leq 0.1$ msec is required, as implied by eq.(10.XI).

The upper frequency ν_u of the signal, as implied by A.V.Kotel'nikov's theorem (Bibl.3) and eq.(9.XI) will be /291

$$\nu_u = \frac{1}{2t_e} \approx \frac{\alpha v_{pr}}{5.8 \cdot 10^{-4} H \delta x \delta y}. \qquad (11.XI)$$

The lower frequency, corresponding to the transmission of a monotone image, will correspond to the line frequency, i.e., will be low. Thus, the signal frequency band at the amplifier input will be $\Delta\nu \approx \nu_u$.

DC amplifiers are rarely used in scanning instruments. This is due to their zero drift and unstable amplification factor. To employ AC amplifiers, the signal is modulated with the aid of a mechanical flux interruptor-modulator (Bibl.1, 2).

The modulation frequency ν_m must be taken at one order of magnitude greater (Bibl.3) than the upper signal frequency ν_u, so as to reproduce the signal shape more accurately, i.e., it must satisfy the relation

$$\nu_m \approx 10\nu_u \approx \frac{10^5 \alpha v_{pr}}{5.8 H \delta x \delta y}. \qquad (12.XI)$$

The frequency band in the instrument with modulation is broadened by roughly one order of magnitude, as we can see, and the requirements for the receptor's inertia correspondingly increase. This means that a receptor with the time constant $\tau \approx 10^{-5}$ sec is required in order to obtain the resolution $R_o = 1\ km^{-2}$.

The sensitivity of the scanning instrument in the event that the absolute magnitude of radiative fluxes from the scan elements is measured, is determined, as usual, by a specified signal/noise ratio at the pre-amplifier input (cf. Chapt.IX and X). The sensitivity of the scanning instrument designed to obtain only the image of some surface is characterized by its energy resolution.

Section 3. Energy Resolution

The energy resolution of the scanning instrument designed to obtain images is defined as the minimal difference between signals corresponding to the arrival of radiation fluxes at the receptor from two adjacent scan elements, one of which is taken as the reference reckoning level (background). As was pointed out earlier (Chapt.X), the illumination of the receptor of an IR instrument is due to the combination of the fluxes of natural and reflected radiation of the observed object or background, the fluxes of the natural and scattered radiation of the atmosphere, and the natural radiation fluxes of the parts of the instrument (in the IR region). As a result, the energy resolution of the IR scanning instrument depends on many factors: /292

on the state and physical nature and temperature of the object and

background;
on the properties of the receptor;
on the parameters and design of the optical system;
on the conditions of observation and the state of the atmosphere.

The basic condition for the energy resolution of an object against its background under given observation conditions is, in accordance with this definition, written as

$$U_{ob} - U_b = cU_n, \tag{13.XI}$$

where U_{ob} and U_b are the object and the background signal voltages, respectively; U_n is the mean square noise in the receptor's circuit diagram for a given transmission band Δf; and c is the factor of assurance, whose magnitude depends on the nature of the problem (cf. Chapt.IX).

The receptor signal within the spectral sensitivity range $\lambda_1 - \lambda_2$ of the instrument is determined by its spectral sensitivity S_λ and calculated from the equation

$$U_{ob.b.} = \int_{\lambda_1}^{\lambda_2} S_\lambda \Phi_\lambda d\lambda, \tag{14.XI}$$

where Φ_λ is the spectral density of the radiative flux incident on the receptor.

For plane objects obeying Lambert's law and occupying the entire field of view of the instrument's optics, the monochromatic radiative flux incident on the receptor is

$$\Phi_\lambda d\lambda = \frac{\omega \Delta a}{\pi} \cos\alpha \cos\beta P_{\lambda o} \times \\ \times P_{\lambda a} r_\lambda d\lambda, \tag{15.XI}$$

where $\omega = \frac{\Delta A}{H^2}$ is the solid viewing angle of the instrument; α and β are the angles between the scanning beam and the normal to the radiating surface ΔA, $P_{\lambda o}$ and $P_{\lambda a}$ are the spectral transmittivities of the instrument's optics and of the atmosphere, respectively; r_λ is the spectral density of the radiant emittance of the scan element ΔA; and Δa is the area of the entrance pupil of the optical-system eyepiece.

Note that in passive IR instruments, which are of the greatest interest to the study of the planets, r_λ is determined from Planck's equation in accordance with the temperature T of the radiating surface and its emissivity ε.

From eqs.(13.XI) - (15.XI) we find that the energy resolution of the scanning instrument is determined by the relation

/293

$$\frac{\Delta a \Delta A \cos\alpha \cos\beta}{\pi H^2} \int_{\lambda_1}^{\lambda_2} P_{o\lambda} P_{a\lambda} S_\lambda (r_{\lambda ob} - r_{\lambda b})\, d\lambda = kU_n. \tag{16.XI}$$

For given parameters of the instrument (S_λ, ΔA, U_n, etc.), on using eq.(16.XI), it is possible to find the required area Δa of the entrance pupil of the eyepiece (area of the sensitive mirror). The focal length f of the lens is determined by its speed $\frac{d}{f}$ on taking into account the required geometric resolution. The optical scheme of the scanning instrument implies that (for $f \ll H$)

$$f = \frac{a}{2\tan\frac{\delta x}{2}} = \frac{b}{2\tan\frac{\delta y}{2}}, \qquad (17.XI)$$

where a and b are the dimensions of a tetragonal receptor.

It must be borne in mind that the illumination of a receptor with a nonlinear luminous characteristic alters its sensitivity. Changes in the illumination of a receptor of this kind result in changes in the energy resolution of the instrument, although the energy contrast between the object and the background ($r_{\lambda ob} - r_{\lambda mean}$) remains the same. With increasing illumination of the receptor the instrument's sensitivity decreases. For this reason, instruments operating in the visible or near-IR region sometimes are provided with a photorelay which reduces daytime illumination by means of an optical wedge (Bibl.1).

To increase resolving power with respect to area and energy, it is clearly necessary to use receptors with a small area, a minimum inertia and a maximum sensitivity. In a single-receptor scanning system the requirements for the receptor with respect to these parameters are thus extremely high. Moreover, terrain surveying with a needle ray requires an intricate kinematic diagram of the scanning system. A way out of this situation was found by resorting to a mosaic-type receptor, consisting of a sufficiently large number N of small sensitive elements (Bibl.1). Each element of the mosaic surveys a corresponding element of terrain, and scanning in this case is accomplished electronically with the aid of a commutator mounted at the receptor output (in front of or beyond the preamplifiers) or in the receptor power supply circuit. In the former case it is possible to enhance sensitivity owing to the accumulation of energy in the receptor tank circuit which is tuned to the modulation frequency of the radiative flux (Bibl.1).

The requirements for the inertia τ_m of the mosaic elements will clearly /294 be N times smaller than the requirements for a single receptor, i.e.,

$$\tau_m \leqslant \left(\frac{1}{2} \div \frac{1}{4}\right) \frac{2.9 \cdot 10^{-4} H \delta x \delta y}{\alpha N v_{pr}}. \qquad (18.XI)$$

The conversion to mosaic receptors, however, involves the need to solve various additional problems. The principal difficulties pertain to the construction of receptors and the design of the optical systems and commutators for a large number of elements (Bibl.1). Television tubes represent a new advance in the development of mosaic receptors with electronic commutation. Thus, in the long run the development of scanning devices will hinge on the development

of television engineering.

Section 4. Narrow-Angle Scanning Radiometer

The block diagram of the scanning radiometer used in the Nimbus-series satellites to obtain information on global-scale cloud conditions is shown in Fig.5.XI. Scanning in this case is assured by the swinging of the plane mirror 1 linked to the scanning-system drive SSD and positioned at the angle of 45° to the optical axis. The direction of scanning is at right angles to the flight direction of the satellite. The swinging rate of the mirror corresponds to 0.67 rev/sec (Bibl.5). The radiative flux reflected by the scanning mirror 1 is focused on the receptor R by a Cassegrain-system mirror lens consisting of the mirrors 6 and 7. The filter 4 is used to isolate the operating spectral range [in this case the atmospheric window of from 3.5 to 4.2 μ (Bibl.5)]. The modulation of the radiative flux [with a frequency of ~260 cps (Bibl.6)] is accomplished by the interruptor 3.

The receptor of the radiative flux is represented by a low-inertia PbSe receptor, cooled by the element 5 [the PbSe photoresistor operates at a temperature of approximately -80°C (Bibl.25)]. The signal from the receptor R is amplified by the multi-stage amplifier A (at 260 cps) and thereupon rectified by the circuit Rect. After this, a constant voltage is supplied to the controlled generator CG and recorded on the magnetic tape of the recording device RD. The frequency deviation of CG is 2.5 cps, and the zero level (signal from outer space) in this instrument corresponds to the recording of a 10 cps frequency while the maximum temperature $T_{e.max}$ of the emitting surface (earth) corresponds to the 7.5 cps frequency (Bibl.6).

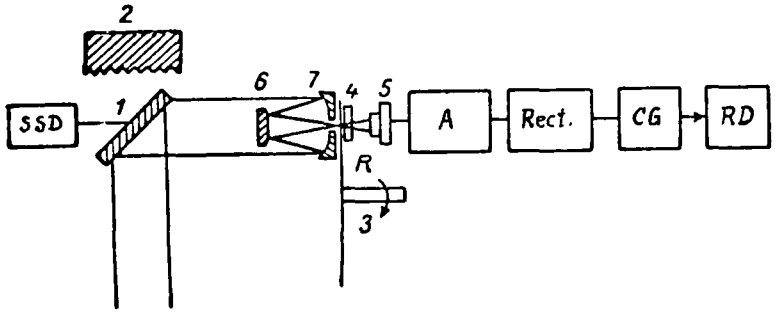

Fig.5.XI Block Diagram of the IR Scanner of the Nimbus Satellite.

The sensitivity of the measuring circuit is checked with the aid of signals from the blackbody 2, supplied periodically during rotation of the scanning mirror 1.

Thus, in this case the scanning device is a radiometer which measures the angular distribution of the absolute values of outgoing radiation in the region of the atmospheric transparency window (in the neighborhood of 4 μ). The /295

results of such measurements clearly can be utilized not only to determine the picture of the cloud distribution, but also to obtain various other information supplied by radiometers and, in particular, the temperature of radiating surfaces. The estimated measurement error for the effective temperature in this case is ~2.5°C (Bibl.2).

The viewing angle of the instrument mounted on the Nimbus satellite (Bibl.2) was $w = 8.4 \times 10^{-3}$ ster or 30 × 30 sec, which, at an orbit altitude of ~1000 km, assures a linear resolving power of ~10 km at the line center. The resolving power at the line edges for a viewing angle of ~110° deteriorates by roughly one order of magnitude, as is shown in Fig.4.XI.

CHAPTER XII

PHOTOGRAPHIC INSTRUMENTATION

Section 1. General Information on Aerial Photographic Instruments

The cameras mounted in various flight vehicles are termed aerial cameras. They are distinguished by their automated design and by the high quality of the photographs they obtain.

There is a large number of various designs of aerial cameras in existence (Bibl.1, 4, 15), but they all have the same principal components and elements in common.

The typical diagram of an aerial camera (Bibl.4) includes the housing 1 (Fig.1a.XII), the aerial photographic lens 2, the shutter 3, the magazine 9, the distributing mechanism 4, the mount 5, to which it is attached via shock ab- /296
sorbers, the control device 8 and the motor 6, linked by the cables 7.

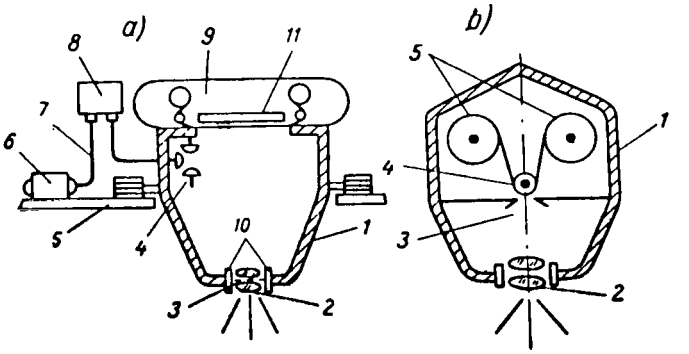

Fig.1.XII Diagrams of Conventional (a) and Slit-Type (b) Aerial Cameras.

The camera housing 1 is a round or rectangular duraluminum casting. Located in the upper part of the housing is the leveling glass 11. The magazine 9

contains a store of film as well as devices for moving, proportioning and leveling of the film during exposure.

The distributing mechanism 4 of the camera transmits the motion of the motor 6 to the magazine and the shutter elements. The currently existing cameras contain mechanisms of the mechanical or electrical type (Bibl.1, 4).

The control device 8 automatically triggers the operation of the camera at fixed time intervals and it also controls the performance of every mechanism of the camera. It can be preset to regulate the required exposure time t_e according to the conditions during picture taking. The time interval t between exposures is fixed according to the specified length of the photograph l_x along the flight line and the overlap q_x between the photographs (Bibl.4).

In the event that the picture taking must be performed at high flight speeds, slit-type cameras are employed (Bibl.10). The slit 3 (Fig.1b.XII), located in the focal plane of the slit-type camera, serves to project the image onto a film continuously moving across the spool 4. To obtain a sharp image (to eliminate crabbing) the movement of film and camera must be rigorously coordinated, namely, the displacement rate v_i of the image in the focal plane of the lens 2 must equal the rate of motion v_f of the film ($v_i = v_f$).

The exposure time is determined by the time of movement of the film across a slit of width b, i.e., $t_e = \frac{b}{v_f}$. Hence, the exposure time may be changed /297 by changing the slit width b.

The aerial photograph obtained by the slit-type camera thus represents a continuous tape onto which all objects are projected at virtually the same angles. Displacing the slit in the focal plane makes it possible to take pictures from various angles. The film in the slit-type camera is stored on spools 5 placed in the housing 1. In order to photograph simultaneously large areas of ground, multiple-lens cameras of both types have been developed (Bibl.10).

Figure 2.XII illustrates the course of the projective lines for certain points O, N, P and their corresponding points o, n, p during aerial photographing from the altitude H. Point S represents the combined anterior and posterior nodal points of lens 1.

Distance f from the posterior nodal point of the lens to the focal plane op represents the camera constant (focal length). Point O, representing the base of a plumb line running from the anterior nodal point of the lens to the plane op of the photograph, is termed the principal point of the photograph. The angle β, formed by the principal line oS and the nadir line Sn, is the angle of inclination of the photograph.

Photography performed at angles of inclination amounting to not more than 5° is termed plane photography, and that performed at $\beta > 5^\circ$, is termed perspective photography (Bibl.1, 7).

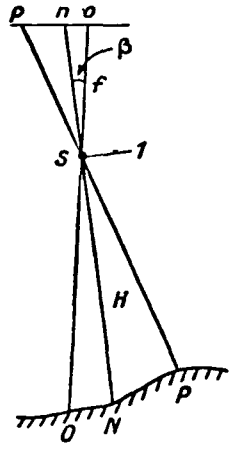

Fig.2.XII Course of the Projective Line.

The scale m of the photograph is the ratio of the length of a segment δ on a photograph to its actual length Δ on the terrain. For vertical photography ($\beta = 0$) of a flat surface from a considerable height ($H \gg f$), as Fig.2.XII shows, we have

$$m = \frac{\delta}{\Delta} \approx \frac{f}{H}. \qquad (1.XII)$$

For dissected terrain or if the camera axis is inclined during the photography, scale distortions are present on the photograph; allowance for these distortions can be made by photogrammetric techniques (Bibl.4, 7).

As pointed out by A.Katz (Bibl.16), using wide-angle aerial cameras placed in a high orbit makes it possible to encompass large expanses of area during the cloud observations needed for the analysis of meteorological processes.

To retain a fixed scale and field of the image, proposals have been made for using aerial photographic equipment installed in satellites with a circular orbit. In this case, the camera together with the standard cartographic /298 lens used in the United States (camera constant f = 130 mm, viewing angle ~60°), when at an altitude of 5200 km (orbital period of the satellite ~4 hr) can encompass an area of 8200 × 8200 km on the planet's surface for a vertical scale of m = 1:40,000,000 [format of photograph 22.5 × 22.5 cm (Bibl.16)]. The photograph thus obtained would encompass a part of the terrestrial globe roughly equal in area to that of the standard synoptic chart.

The equatorial spacing of the successive orbits of this satellite would be approximately 5400 km, while at the latitude of 45° this spacing would be approximately 4000 km. Hence, global photographing with some overlapping of photographs for the exposure interval t = 10 - 15 min can be readily accomplished. This makes possible the on-satellite processing of photographs and their transmission via a radio channel.

When the resolving power of the aerial camera is 50 lines per mm, the

resolving power with respect to the photographed area is ~800 m.

Section 2. Basic Parameters and Characteristics of Photographic Instruments

The basic parameters of aerial cameras rendering them suitable for the conduct of various investigations are: the camera constant f, the angle of view ω_{ster} or α° (or, sometimes, the coverage angle of the lens, characterizing an image with minimal lens aberrations), the resolving power $N_{\ell,ph.}$ at the center and on the edge of the field of view, the lens speed, and the format of the photos.

As we can see, the principal parameters of the camera are determined by a combination of the properties and characteristics of the lens and of the photographic material used.

The lenses used in aerial cameras are the most important part of these cameras and are characterized by: the camera constant f, the relative aperture d/f, the field of view α, the lens speed, and the lens resolving power N_ℓ.

The lenses are divided into wide-angle ($\alpha > 70^\circ$, $f \leq 135$ mm), medium-angle ($70^\circ \geq \alpha \geq 50^\circ$) and narrow-angle ($\alpha < 50^\circ$, $f > 300$ mm) lenses, depending on the width of the angle α (Bibl.44).

Another important indicator of the lens quality is the aberrations. They usually are corrected (chiefly in the central part of the field of view) by selecting various types of glass with various radii of the surface curvature (Bibl.12). The aberrations are characterized by the diameter of the circle of confusion in the image of a point source. The magnitude of the circle of confusion decreases with irising of the lens owing to the decrease in broad-beam aberrations(spherical, coma and astigmatism). Coating the optics makes it possible to greatly enhance the transmissivity P_ℓ of the lens [to 0.7 and higher (Bibl.12)].

In scientific photography, an important characteristic of the lens is its distortion as manifested in violation of the geometric similarity between the contour of an object and its image. /299

The ability of the lens to produce sufficient image illumination is termed the lens speed. The illumination in the central part of the field of the image of a distant ($H \gg f$), ideally diffusing, surface is

$$E_i = B\omega P_o P_a \cos z = \bar{\rho}\frac{E}{\pi}\omega P_o P_a \cos z = \\ = \bar{\rho}\frac{E}{4}\left(\frac{d}{f}\right)^2 P_o P_a \cos z, \qquad (2.XII)$$

where $\bar{\rho}$ is the mean reflection factor of the surface of the observed object; B and E are the brightness and illumination of the observed surface (normal to the solar rays); z is the zenith angle of the sun; $\omega = \frac{\pi}{4}\left(\frac{d}{f}\right)^2$ is the solid angle

of view of the lens (for $H \gg f$); P_o and P_a are the transmissivities of the optics and the atmosphere.

Note that the illumination decreases in the direction toward the image edge owing to the inclination of rays to the lens plane by the angle γ [roughly proportional to $\cos^4 \gamma$ (Bibl.11)].

In accordance with eq.(2.XII), the lens speed is characterized by the square of the relative lens aperture $Ö = \left(\frac{d}{f}\right)^2$. Such a lens speed (taken without making any allowance for the attenuation of the radiant energy) is termed geometric. Lenses with a high geometric speed $\left(\frac{d}{f} \geq 1{:}2.5\right)$ are termed fast lenses. The lens speed can increase only within narrow limits. In fact, if $\bar{\rho} = 1$, $z = 0^\circ$, $P_o = P_a = 1$ and $\frac{d}{f} = 1{:}0.5$, then the image illumination will equal the surface illumination (or the luminous emittance) $E_i = E$.

Owing to thermodynamic considerations, any further increase in lens speed is not feasible. In practice lenses with a relative aperture of only $Ö = 1{:}0.6$ can be made, but their angle of view is extremely small and their aberrations are considerable (Bibl.11). In the best lenses, the relationship between relative aperture and maximum angle of view is as follows: for $Ö = 1{:}0.8$, $\alpha \leq 15^\circ$; for $Ö = 1{:}1.5$, $\alpha \leq 30^\circ$; and for $Ö = 1{:}8$, $\alpha \leq 120^\circ$ (Bibl.11). Using extremely /300 fast lenses is often inconvenient, because, owing to the large number of lenses involved, transmissivity P_o is limited.

To alter the image illumination, the aperture diaphragm in the lenses of photographic and television pickup cameras is of the variable kind.

The resolving power N_ℓ of a lens characterizes its ability to separately depict minor details δ of the object. It is determined by the number of lines or strokes N_ℓ separately depicted at a distance of 1 mm in the image plane (taking into account the lines and the light intervals between them). The resolving power is limited by the aberrations (circle of confusion δ') and diffraction of a lens. In an ideal (aberration-free) lens, the resolving power $N'_\ell = \frac{1}{\delta'}$, determined according to Rayleigh's diffraction condition (Bibl.11) is

$$N'_\ell = \frac{0.95}{\lambda}\left(\frac{d}{f}\right), \qquad (3.XII)$$

where λ is the wavelength of the monochromatic light.

The resolving power, conditioned by aberrations, decreases with increasing relative aperture d/f, since then the aberrations increase (the spherical aberration is proportional to $\left(\frac{d}{f}\right)^3$; the coma, to $\left(\frac{d}{f}\right)^2$; and the astigmatism, to

$\left(\frac{d}{f}\right)$. This accounts for the low resolving power of fast lenses (Bibl.11, 12).

The diffraction equation (3.XII) applies completely only when Ö = 1:18 to 1:20 (Bibl.4).

In practice, the resolving power of a lens is determined with the aid of various tests such as the determination of the distance δ between the centers of the still discernible adjacent dark lines separated by bright intervals of the same width. The resolving power is the reciprocal of this quantity $N_\ell = 1/\delta$.

The real resolving power N_ℓ at the center of the field of the image is lower than the theoretical N'_ℓ for relative apertures Ö > 1:18. Thus, for Ö = = 1:4.5 and λ = 0.555 μ, from eq.(3.XII) we have N'_ℓ = 400 lines/mm, whereas the actually determined resolution N_ℓ for such a lens is ~300 lines/mm (Bibl.11). The resolving power of the lenses of ordinary cameras does not exceed 45 lines/mm at the center of the field of image and 33 lines/mm at the edges /301 (Bibl.15). The resolving power of the unaided eye varies from 5 to 10 lines/mm depending on the manner of its determination (Bibl.1, 11).

Of major significance to photographic and television lenses is the depth of definition, i.e., their ability to produce a sufficiently sharp image of objects located at various distances from the lens. It is expressed by the length (in meters) of a sufficiently sharp image of the terrain space DD on both sides of the focusing plane. The depth of the definition DD depends on the relative aperture of the lens, the distance to the object of focusing, and the degree of irising of the lens (Bibl.7, 15). In order to increase the depth of definition, the diaphragm must be reduced.

Photographic films of various width are used as the negative materials. They may consist of nitrocellulose or triacetate as the base, a bonding layer of sodium silicide, and an aqueous solution of gelatin containing a silver halide in the suspended state. Such a (non-sensitized) emulsion is sensitive to radiant energy within the range of roughly 0.28 to 0.5 μ, with a maximum at ~0.36 μ (a glass lens does not transmit rays below ~0.33 μ (Bibl.1). Sensitivity to longer wavelengths is enhanced by adding organic dyes which sensitize the film to the rays being absorbed by such sensitizers. Thus, panchromatic (all-color) films are obtained. The sensitivity of these films is virtually constant over the spectral range of 0.28 to 0.7 μ. The greatest infrared limit of spectral sensitivity (up to 0.85 μ and more) is displayed by infrachromatic films (Bibl.15).

The basic characteristics of the photographic material (contrast factor, sensitivity, range of density, inherent fog) are determined from the characteristic darkening curve as a function of the illumination (Bibl.8).

The sensitivity of the film is the reciprocal of the amount of illumination, creating a specified photographic effect on the photographic material (after development). Usually (Bibl.8, 15), the criterion applied is the point on the characteristic curve at which the fog level (darkening of the photographic layer in areas not exposed to the action of light) is exceeded by 0.85. In such a system, the adopted unit of sensitivity is the sensitivity of a material which, on the exposure of $E_1 t_0$ = 10 lux·sec, yields the optical density D equal to

$$D = D_0 + 0.85, \qquad (4.XII)$$

where D_0 is the fog density.

The sensitivity $S_{d_{0.85}}$ of any layer is expressed in degrees according to /302 the equation

$$S_{d_{0.85}} = \frac{10}{E_i t_e}. \qquad (5.XII)$$

The sensitivity of ordinary aerial photographic materials ranges from hundreds to thousands of degrees (Bibl.8).

The exposure required for photographing with a film of known sensitivity $S_{d_{0.85}}$ is according to eq.(2.XII) determined by the relation

$$t_e = \frac{10}{E_i S_{d_{0.85}}} = \frac{40f^2}{\bar{\rho} E d^2 k S_{d_{0.85}}}, \qquad (6.XII)$$

where k is a coefficient which takes into account the effect on exposure of the attenuation of light by the atmosphere and camera optics, as well as the shutter efficiency, the reduction by filter, and the diffusion of light by parts of the aerial camera which results in an additional illumination of the film.

For example, for the illumination E = 5000 lux for an aerial camera with k = 0.50 (without a filter), $\bar{\rho} = 0.15$ and $\frac{f}{d} = 4.5$ (Bibl.8). The required normal exposure t_e is 0.01 sec for photographing on a film with the sensitivity $S_{d_{0.85}} = 200^{\circ}$.

The resolving power N_{ph} of the photographic film, in lines/mm, is of special significance in large-scale photography which employs projective printing with magnification. The extent of N_{ph} is closely related to the film sensitivity, the grain of the layer, and the photographing conditions. Considerable resolving power (100 lines/mm and higher) is displayed by low-sensitivity positive materials. With the increase in exposure time or in developing time, and hence also in the density of the obtained image, the resolution of the film increases up to a specified maximum.

In conventional aerial photography, films with the resolution $N_{ph} = 35 - 50$ lines/mm or $\delta = 0.02 - 0.03$ mm between the lines are used (Bibl.15).

The resolving power $N_{\ell ph.}$ of the lens-photographic material system is always substantially smaller than the resolving power of the components N_ℓ and N_{ph}. Between these an approximate relationship exists, expressed by

$$\frac{1}{N_{\ell.ph.}} = \frac{1}{N_\ell} + \frac{1}{N_{ph.}} \qquad (7.XII)$$

It follows from eq.(7.XII) that, given equal resolution of each component,

$N_\ell = N_{ph} = N$, the resolution of the system is half as high, $N_{\ell.ph.} = \frac{1}{2} N$. /303

Moreover, the high resolving power of one component of the system may not be actually attained if the other component has a low resolving power. For example, for N_ℓ = 300 lines/mm and N_{ph} = 50 lines/mm, we have $N_{\ell.ph.}$ = 43 lines/mm.

The terrain-resolving power $N_{\ell.ph.}$ of the system, characterized by the least dimension Δ of the discernible detail, is expressed by the relation

$$\Delta = \frac{1}{mN_{\ell.ph.}} = \frac{H}{fN_{\ell.ph.}}, \qquad (8.XII)$$

where m is the scale of the photo and H is the photographic altitude.

Using eq.(8.XII) with respect to the American camera with the camera constant f = 130 mm mounted in a circular-orbit satellite with H = 5200 km (m = $= 1{:}4 \times 10^7$), we obtain a terrain resolution Δ = 800 m for $N_{\ell.ph.}$ = 50 lines/mm, as was pointed out earlier (cf. Sect.1 of this chapter).

It must be noted, however, that some margin is necessary, since the real resolution of a photograph depends on the displacement of the image during exposure, owing to the motion of the carrier, degree of leveling of the film, and other factors (Bibl.7).

Of major significance also are the operations involved in the photographic processing of the material in flight or following its reception on earth.

The effect of meteorological conditions is expressed in the dependence of illumination E on the position of the sun, the cloud conditions, the degree of haze, and the quantity P_a entering into eqs.(2.XII) and (6.XII). The brightness B_h of the aerial haze leads to the loss of image contrast.

This effect of haze is offset by using color filters which cut off the shortwave portion of the spectrum conditioned by the molecular scattering (Bibl.1). Thus, image illumination does not decrease markedly if the sun is sufficiently high above the horizon (when the sun is 30° above the horizon, illumination by scattered light does not exceed 25% of the direct solar illumination)(Bibl.1, 12). Films insensitive to the shortwave portion of the visible region of the spectrum may also be used for this purpose.

Section 3. Requirements for the Image Sharpness and the Camera Resolving Power

The possibility of discerning minor objects or details of objects on a photograph is determined by the sharpness with which the boundaries of objects are imprinted (detail of photographs). Image sharpness is determined by the following basic factors:

by the resolving power $N_{\ell.ph.}$ of the system; /304
by the contrast K' between the detectable details and their background on the film;

by the displacement of the object of the photograph during exposure, causing the blurring of boundaries on the image (crabbing);
by the properties and shape of the photographed object.

The discernment of various objects by the eye is determined by their relative contrast K in brightness with the background. In observations over considerable distances or in the presence of a turbid atmosphere, the visible contrast K' decreases owing to the superposition of the brightness of haze B_h on the apparent brightness B_{ob} of the object and the apparent brightness B_b of the background. For a bright object ($B_{ob} > B_b$) we have, in accordance with the known equation (Bibl.12)

$$K' = \frac{(B_{ob}P_a + B_h) - (B_bP_a + B_h)}{B_{ob}P_a + B_h} = \frac{(B_{ob} - B_b)P_a}{B_{ob}P_a + B_h} < K. \qquad (9.XII)$$

The threshold contrast for the eye is approximately 0.02 or 2%, at observations under daylight conditions. At night and in twilight this contrast increases (Bibl.12).

From eq.(9.XII) it can be seen that in the presence of haze or fog on the image, the visible contrast K' between detail and the background, or between an object and the background, will decrease and this will lead to a corresponding decrease in image sharpness and in the discernibility of details of the image. This is reflected in a decrease in the real resolving power $N_{l.ph.}$ of the system, as compared with its rated $N_{l.ph.r.}$ which is determined in laboratory conditions for the contrast K = 1 (at $B_h = 0$) on the basis of a stationary test. It is for this reason that photography under real conditions requires a certain margin of resolution.

The informational value of photographs of moving objects is markedly reduced by blurring during exposure, due to the displacement of projective lines.

During photographing from a non-stabilized object in motion, six displacements are possible, corresponding to six degrees of freedom of the camera: linear displacements as well as revolution about three axes pertaining to the center of gravity of the camera. However, all these displacements, except the displacement pertaining to the linear movement along the trajectory, may be reduced to a minimum by stabilizing the carrier.

For a camera moving in the flight plane at the rate v', the points of terrain projected onto the sensitive layer get displaced with respect to this layer at the rate v_i equal to

$$v_i = mv', \qquad (10.XII)$$

where m is the scale of the photos taken.

Hence, during the exposure t_e, the projective lines will be displaced, /305
e.g., from point O_1 (Fig.3.XII) to point O_1' (in the direction of travel of the carrier). The unsharpness of the resulting image, as conditioned by this dis-

placement, will be, as Fig.3.XII or eq.(10.XII) show,

$$\delta = O_2O_1' = \frac{fv't_e}{H} = mv't_e \cdot \qquad (11.XII)$$

The terrain displacement will be

$$\Delta = S_1S_2 = v't_e = \frac{\delta}{m}. \qquad (12.XII)$$

Thus, the displacement due to the linear movement of the camera in the flight plane is determined by the rate of motion of the carrier with respect to the photographed object and by the exposure time. It is identical for all of the image points. For example, if $t_e = 10^{-2}$ sec and $v' = 3000$ km/hr = 830 m/sec, the terrain displacement will be $\Delta = 8$ m and the image unsharpness $\delta = 0.8$ mm for m = 1:10,000. The actual image unsharpness will, however, be somewhat smaller than its geometric value specified above, because the rate of photographic imprinting at the commencement of exposure is faster than at its end (Bibl.5, 6).

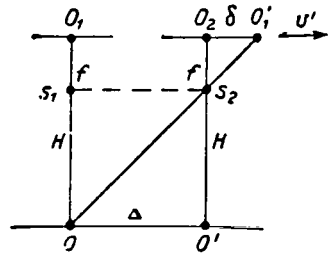

Fig.3.XII Displacement (Crabbing) of the Image due to Rectilinear Movement of the Camera during the Exposure.

The permissible unsharpness (crabbing) δ' obviously varies depending on the purpose of the photography and the dimensions of the terrain details Δ' subject to identification and related to the scale of the photography by eq.(12.XII). Thus, e.g., if the object of photography is altocumulus clouds whose characteristic details are of the dimension $\Delta_1' = 5$ m, then, for the scale of photography m = 1:100,000 = 10^{-5}, the permissible unsharpness of boundaries on the photographs should be not more than $\delta_1' = 0.05$ mm, and for m = 10^{-3} not more than 5 mm.

The resolving power $N_{\ell.ph.}$ of the system must correspond to the required detail of the photograph. To assure the discrimination of linear elements of the dimension δ', and as implied by the foregoing (cf. Sect.2), this resolving power must be

$$N_{\ell.ph.} \geqslant \frac{1}{\delta'} = \frac{H}{f\Delta'} = \frac{1}{m\Delta'}. \qquad (13.XII)$$

From eq.(13.XII) it can be seen that the assurance of a high detail of photographs requires the use of long-focus cameras with a narrow angle of view. Thus, to obtain the line resolution of the terrain with $\Delta' = 5$ m from the /306

altitude H = 200 km by means of a system with the resolution $N_{l.ph.}$ = 20 lines/mm (without taking into account the atmospheric influences), a camera with the camera constant f ≥ 2000 mm is required. The dimensions of and weight of such lenses are very considerable (even if telephoto lenses are used). Thus, for Ö = 1:4 the lens diameter in the example considered above must be 500 mm and the weight of the lens must be about 100 kg.

Section 4. Photographing from Objects in Outer Space

An outstanding achievement of Soviet scientists was the photographing of the far side of the moon, accomplished with the aid of instrument installed in the third cosmic rocket (4 Oct, 1959). This experiment opened up a new domain of astronomical observations of the planets from spacecraft. The obtained image was developed in the instrument container and transmitted to earth by a television-type system. Thus, this instrument is of the phototelevision type.

The moon was photographed with the aid of a camera with two lenses [f_1 = = 200 mm and f_2 = 500 mm (Bibl.13)] with relative apertures 1:5.6 and 1:9.5.

At the photographing distance (from 65,200 km at the beginning of its operation to 68,400 km at the end)(Bibl.3), the first lens provided an image of the lunar disk completely encompassed within the frame, while the second assured obtaining large-scale images of part of the lunar surface.

The orientation of the camera toward the moon was accomplished by an orientation system which rotated the entire spacecraft. Medium-sensitivity 35 mm photographic film, distinguished by its high resolving power and heat resistance, was used (Bibl.2).

Considering that one of the main aims of this project was to obtain details of the photographed object, special attention was devoted to assuring a sufficiently high resultant contrast factor γ_r, which in this case equals

$$\gamma_r = \gamma_{s.n}\,\gamma_{s.i.}\,\gamma_{e.i.}\,\gamma_{e.n.}\,\gamma_{pos}, \qquad (14.XII)$$

where $\gamma_{s.n.}$, $\gamma_{s.i.}$, $\gamma_{e.i.}$, $\gamma_{e.n.}$, and $\gamma_{pos.}$ denote, respectively, the contrast factors of the negative in the spacecraft, the image transmitted from the spacecraft, the image received on earth, the ground negative, and the positive copy subject to scientific analysis.

The required $\gamma_{e.n.}$ was found to be of the order of 0.7 (Bibl.2). Calculations of the fog due to cosmic radiation in the presence of a quiet sun showed that in this case the noise is insignificant, whereas a solar flare may lead to a sharp increase in the fog on the film (Bibl.2).

The photographing was performed on varying the frame exposure time so as /307 to obtain negatives with optimal densities and it lasted for about 40 min, during which time the moon was repeatedly photographed (Bibl.13).

After photographing, the film entered an automatic developing device operating under conditions of weightlessness and over a broad range of temperatures,

with a fixed film-processing time.

A schematic diagram of a model of the compact (~10 cm tall) (Bibl.2) developing device carried by the spacecraft is shown in Fig.4.XII. The exposed

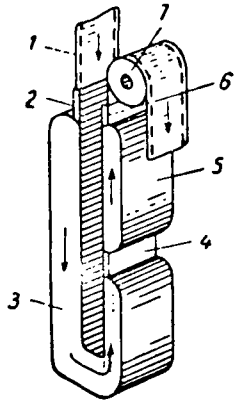

Fig.4.XII Diagram of the Spacecraft-Borne Device for Processing a Heat-Resistant Film.

film 1 entering the developing device via the elastic sponges 2 proceeds to the tank 3, where it is simultaneously developed and fixed. After passage through

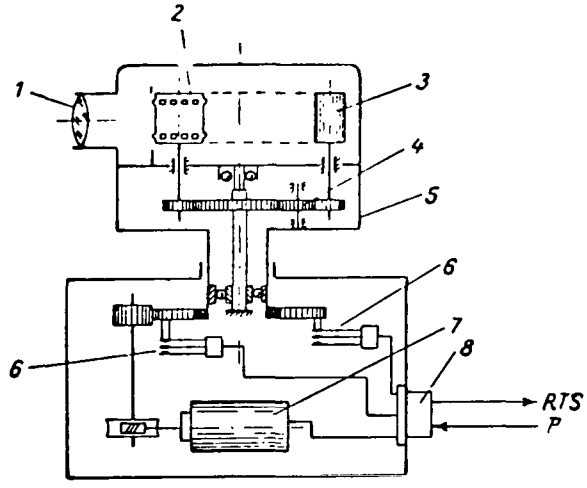

Fig.5.XII Diagram of the Rocket-Borne Panoramic Camera (FAKO).

the squeegee element 4, it is rinsed in the tank 5, again squeegeed in the element 6 and passed via elastic sponges to the hot drum 7, which it leaves completely dried. Heating elements maintaining a fixed temperature during the processing of the film are placed in the space between the tanks 3 and 5. The

processed and dried film proceeds to a magazine whence it proceeds to an image-transmitting device.

Transmission of the images was carried out on instructions from earth over distances exceeding several hundreds of thousands of kilometers [as much as 470,000 km (Bibl.13)]. The conversion of the negative image on the photographic film to the electric signals was accomplished in the same manner as that in which a motion picture is transmitted by television. The slowly moving film was illuminated with a bright beam projected onto it by an optical system. The beam, produced by a compact cathode-ray tube, traveled from one edge of the film to another, thus causing line scanning. The beam passing through the film was directed toward a photomultiplier which converted light signals to the electric signals. The amplification and shaping of the image signals were accomplished by means of a special narrow-band stabilized amplifier. /308

The scheme included the automatic regulation of the amplification and brightness of the exploring beam as well as the provision of timing signals (Bibl.13). The number of lines per frame varied, depending on the selected regime of transmission. At its maximum it reached 1000 lines per frame.

The images from the spacecraft were transmitted by a radio communications line which at the same time served to measure the parameters of the movement of the spacecraft itself (Bibl.3, 13).

Upper-air optical stations (VOS), launched with the aid of geophysical rockets (cf. Chapt.I), use special slit-type panoramic FAKO cameras for the control observations of the form and nature of the earth's disk observed by the scanning instruments (Bibl.9).

The FAKO camera (Fig.5.XII) has a mobile lens 1 with a slit positioned at right angles to the direction of spin. Its anastigmatic lens has the focal length f = 1.25 cm and the relative aperture 1:1.9. The 16 mm photographic film is reeled around the drum 2 whence it proceeds to receiving spool 3. Rotating the optical head 5 is actuated by means of the motor 7 and the reducing gear 4. The rotation of the lens is controlled by the contact mechanism 6. The power P is supplied to the plug-type connector 8 of the instrument, and the information on the position of the lens is transmitted by the telemetering system.

When in operation, the FAKO camera continuously photographs a 360° panorama with a 1-sec period.

CHAPTER XIII

TELEVISION EQUIPMENT

Section 1. Basic Principles of Television

Modern television is one of the most interesting and rapidly developing fields of sciences and engineering. Television systems, which greatly expand the possibilities for the observation of various processes, find broad and /309

varied application. By now they are playing an important role also in the exploration of space. Television has found practical application in observations of manned spaceflights (which are accessible to millions of TV viewers) as well as in observations of the cloud, ice and snow cover of the earth's surface which are systematically conducted in the United States with the aid of the Tiros weather satellites. As was pointed out above (cf. Sect.4, Chapt.XII), the phototelevision method was employed to transmit images of the far side of the moon from the Third Space Rocket.

Clearly, even more interesting results will be obtained from television observations of the surfaces of the moon and the planets and primarily of Mars and Venus (Bibl.3). Television systems may be used to orient optical instruments (Bibl.22), to monitor the performance of various equipment, etc.

The final element receiving the image reproduced by television instruments is the eye of the observer. Hence, the basic characteristics of this instrument are selected to take into account the features of human vision: a limited resolving power and inertia of the visual perception.

The resolving power of the average eye in the presence of satisfactory illumination (20 - 40 nit) and maximum contrast (K = 1) averages 5 - 10 lines/mm, as was pointed out in Section 2 of Chapter XII.

The inertia of vision, due to the finite speed of photochemical reactions in the optic-nerve endings, is characterized by the time constant $\tau \approx 0.1$ sec (Bibl.7, 9). Hence, given the pulsed character of the bursts of an inertia-free source with the pulse time $4\tau \approx 0.4$ sec, the visual perception of the brightness B_a can be depicted by the convoluted curve 1 in Fig.1.XIII. This curve of the apparent brightness B_a contains, as is shown, in addition to the constant component $\overline{B}_a$ existing at the level of the mean true brightness B, which is also a variable component. This variable component causes the unpleasant sensation of flicker and fatigues the observer.

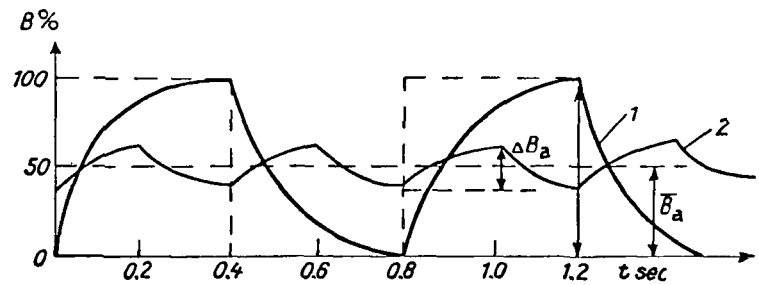

Fig.1.XIII Response of the Eye to Pulsed Visual Stimulation.

As the frequency of light pulses of the same amplitude is increased, e.g., doubled (curve 2), the mean B_a persists at the level of the constant component, but the amplitude of the variable component ΔB_a markedly decreases owing to the inertia of the sensor. Given a certain critical (with respect to a given average background brightness) pulse frequency, the flicker will be unnoticeable. Experimental findings (Fig.2.XIII) show that for a mean brightness of 30 nit

(average brightness of the ordinary television screen), the critical flicker frequency n is approximately 30 cps, whereas for a mean brightness of several /310 hundred nit the flicker becomes unnoticeable only at frequencies of ~50 cps and higher (Bibl.20).

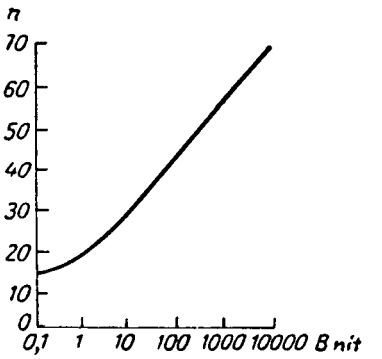

Fig.2.XIII Critical Flicker Frequency n as a Function of the Brightness B of the Picture-Tube Screen.

Transmission of images by television is accomplished by a system whose simplified block diagram is shown in Fig.3.XIII. The image of the transmitted object, projected by a lens onto the pickup tube, is scanned by the latter and converted to a sequence of signals. The scanning process consists in that the image plane x, y (Fig.4.XIII) is scanned in a definite sequence by a commutating electron beam deflected by the electrical or magnetic field of the scanning system of the pickup tube. Owing to scanning, the sequence of mean picture brightness elements on the transmitting side B (x, y, t) is converted to a time sequence of electric signals U(t) termed video signals.

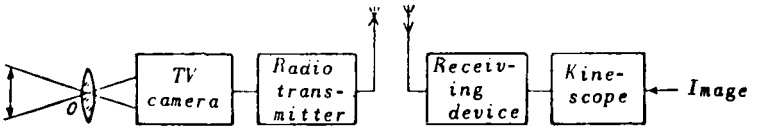

Fig.3.XIII Block Diagram of the Television System.

The differences in the brightness of image scan elements correspond to differences in the amplitude of the video signals, which is limited by the levels of the black (the darkest) and white (the brightest) elements.

The video signal has a constant component (the mean), whose level $\overline{U}$ depends on the illumination of the object (Fig.5.XIII) and a variable component which is determined by the configuration and detail of the transmitted image.

The shape of the video signal, received during the transmission of the /311

image of a given object, does not change with variation in the mean illumination within the limits of the tube sensitivity. Hence, the basic information on the transmitted image is carried by the variable component U(t) of the video signal, which must be transmitted to the receiving side with a minimum of distortions.

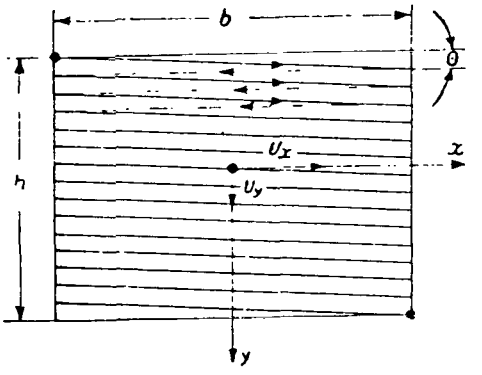

Fig.4.XIII Raster Formation during Progressive Scanning.

Following its amplification, the video signal proceeds to the radio transmitter modulator, from where it is radiated by an antenna in the form of high-frequency oscillations.

The received high-frequency oscillations enter a radio receiver, where they are amplified and detected. After this they are (in the same sequence as on the transmitting side) supplied to the cathode-ray picture tube.

The sequence of image scanning by the scanning beam may be changed as desired. An elementary type of television scanning is the progressive scanning, where the analyzing spot uniformly moves from left to right at the rate v_x (cf. Fig.4.XIII), while it at the same time uniformly moves vertically at the rate v_y (then $v_x \gg v_y$).

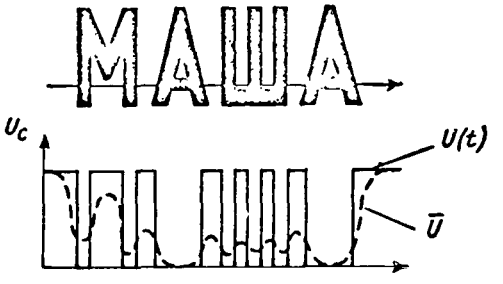

Fig.5.XIII Diagram of the Formation of a Video Signal.

The trajectory of movement of the spot from the left-hand edge of the image to the right-hand edge is a scan line. The inclination θ of the lines with

respect to the horizontal is clearly determined by the ratio between the rates v_y and v_x. The complex whole of the lines covering a single image (frame) is termed raster.

The trajectory of the rapid return travel (retrace) of the spot from the end of one line to the beginning of the next line is termed the line retrace, and from the edge of the image to the commencement of scanning is called the frame retrace.

The time required to scan the entire image and to return the beam to its /312
original position is termed the frame period T_f and its reciprocal, the frame frequency $\nu_f = \frac{1}{T_f}$.

The number of lines transmitted during one second (taking retraces into account) is termed the line frequency $\nu_z = \frac{1}{T_z}$.

The ratio of frame period to line period determines the total number of scan lines

$$z = \frac{T_f}{T_z} = \frac{\nu_z}{\nu_f}. \qquad (1.XIII)$$

The frame frequency ν_f and the number z of scan lines are the principal parameters of television scanning. Note that in reality the image is scanned only while the exploring element sweeps forward along the line $(1 - \alpha)T_z$, while the time αT_z must be expended on retracing the line. This applies equally to the frame scanning, where the retrace time is βT_f. Hence, the number of usefully scanned lines, termed active lines, is $z_a = (1 - \beta)z$, and the βz lines do not participate in the frame scanning.

The standards adopted by the television broadcasting systems in the USSR and in the United States (Bibl.18, 20) fix the number z of scan lines at $z = 625$; the frame frequency $\nu_f = 25$ cps; $\alpha = 18$ and $\beta = 0.08$. Accordingly, the other parameters of standard scanning are: the line frequency $\nu_z = z\nu_f = 15\,625$ cps; the line period $T_z = \frac{1}{\nu_z} = 64$ μsec, and the frame period $T_f = \frac{1}{\nu_f} = 40$ msec.

The frame repetition frequency $\nu_f = 25$ cps causes, however, flicker of the television image at the receiving end, especially in the image highlights /313
where the brightness may reach hundreds of nit. To eliminate this effect, which is fatiguing to the viewer, interlaced scanning is employed. In this case, the flicker frequency of the screen is doubled in comparison with progressive (parallel line) scanning, but the frame repetition frequency ν_f remains the same. In interlaced scanning, each frame is transmitted twice (in half-frames): the first half-frame contains all of the even-numbered lines of the raster and the second has all of the odd-numbered lines, as is shown in Fig.6.XIII. The retrace paths are indicated by broken lines. The time diagrams of a raster with a sawtooth scanning pattern are shown in the upper part of the illustration.

The transmitted image is normally of a rectangular shape. We will denote its width by b and its height by h. The ratio $\frac{b}{h} = k$ is termed the image format.

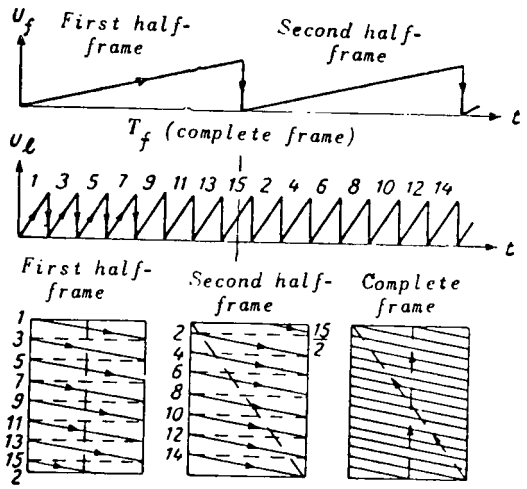

Fig.6.XIII Formation of a Raster during Interlaced Scanning.

The possibility of transmitting minute details of an image is limited by the cross-sectional area δ of the electron beam scanning the image being transmitted. The quantity δ, which determines the dimension of the scan element, is related to the frame parameters

$$\delta = \frac{h}{z}. \qquad (2.XIII)$$

The total number of elements of a frame of the format k is

$$n = zkz = kz^2. \qquad (3.XIII)$$

The transmission time T_e per element is determined by the equation /314

$$T_e = \frac{T_f}{n} = \frac{1}{kz^2 \nu_f}. \qquad (4.XIII)$$

For the standard scanning parameters specified above, $T_e = 7.8 \times 10^{-8}$ sec.

For undistorted image transmission and assurance of the same resolving power over the height and the width of the frame, the electrical tract of the television apparatus must pass a definite frequency band.

On transmission of a monotonic image the video signal will be periodic, with the period a equal to the frame repetition period T_f. Hence, the lower limit ν_{min} of the frequency band equals the frame repetition frequency $\nu_{min} = \nu_f$.

To determine the upper limit ν_{max} of the band, assume that a checkerboard-like image with the maximum number of discernible parts of the dimension δ is

being transmitted. The repetition period of the video signal along a line in this case will be equal to the time $2T_e$ of the transmission of two image elements (one black and one white), and the maximum frequency will be according to eq.(4.XIII)

$$\nu_{max} = \frac{1}{2T_e} = \frac{1}{2} kz^2 \nu_f . \qquad (5.XIII)$$

For standard scanning $k = 4/3$, and hence the video-signal frequency band subject to transmission will be $\Delta\nu = \nu_{max} - \nu_{min} = 6.5$ mega-cps. Then the spectrum of the video signals will contain low frequencies of the order of tens of cps.

In view of the considerable technical difficulties involved in transmitting a wide frequency band through a communications channel, the television standard has, as was pointed out above, adopted interlaced scanning (instead of increasing the frame frequency ν_f) in order to increase the frame flicker frequency.

During transmission of relatively stationary images, the frame scanning period may be increased, which makes it possible to markedly reduce the frequency band subject to the transmission.

It follows from the foregoing that the resolving power with respect to the frame height is determined by the number of scan lines and with respect to the frame width (along the line) by the upper frequency limit of the range of the video signals. In this connection, the passband of the television set must be matched to the required resolving power, usually expressed by the number of scan lines.

Section 2. Television Pickup Tubes

The principal characteristics of a television system (resolving power, spectral sensitivity, etc.) are determined by the pickup tube.

The operating principle of modern pickup tubes is based on the photo- /315
electric effect combined with the charge storage. The latter makes it possible to utilize the prolonged action of light on the photoelectric converter (of a duration determined by the frame period) instead of instantaneous action. As a result, the sensitivity of the converter is enhanced. The storage device, which is termed "target", consists of a large number of storage elements corresponding to the scan elements, with each element storing up the charge during the frame period (during exposure) and releasing it at the moment in which the signal is removed from a given scan element (on charge interchange).

In accordance with the division of the photoeffect into extrinsic and intrinsic photoeffects, various tubes employ either photoemissive or photoconductive converters.

Photoemissive converters usually are designed in the form of a mosaic of a large number of photosensitive grains (several millions) coating the surface of a dielectric.

Photoconductive converters with a sufficiently high resistance (of the order of 10^{11} ohm • cm (Bibl.10) are constructed in the form of continuous thin films. They can at the same time fulfill the role of a storage device. The scan elements in this case are determined by the area s of the spot of the scanning (charge-interchange) beam on the target.

After scanning, the elements are returned to their initial state, required for transmission of the next frame. This is accomplished by erasing the electrical image on the target. Frequently the scanning and erasing processes are combined (the vidicon, the image orthicon, etc.).

Usually a distinction is made between pickup tubes depending on whether the interchange of the charge occurs on one side of the target or on both sides of it (Bibl.15). In the former case, the processes of charge and discharge (storage and scanning) both occur on one side of the target (the orthicon, the vidicon, etc.). In the latter, the target and the photoconverter are separated and the charge and discharge occur each on a different side of the target (the image orthicon, the ebicon). Owing to the increase in the storage effect on the target, the sensitivity of these tubes is the highest.

From the standpoint of the type of electron-beam scanning, the tubes are divided into tubes with scanning by a high-velocity beam (the iconoscope, the image iconoscope) and those with scanning by a low-velocity beam (the orthicon, the image orthicon, the vidicon). In the former, the secondary emission ratio of the beam exceeds unity, whereas in the latter it is low and hence the scanning beam reduces the illuminated surface to the cathode potential of the electron gun.

In addition to the photoconverter, the target and the electron gun, present-day pickup tubes may also be equipped with secondary-electron multipliers to amplify the video signal (the image orthicon), the electron-optical intensifiers of image brightness or optical transformers of the spectral range which make /316 it possible to operate in the ultraviolet or infrared portions of the spectrum.

An invariable component of any pickup tube is the focusing and deflecting system (FDS).

The chief parameters of the television tubes, which determine the possibility of using them in spacecraft are the limiting sensitivity and resolving power (given a sufficient reliability). At present, the greatest sensitivity is displayed by tubes of the image orthicon type. Special models of image orthicons may operate even in a dark night (illumination $\sim 10^{-4}$ lu), since the limiting illumination of the photocathode with the definition z = 200 lines reaches 10^{-7} lu (Bibl.27). Nevertheless, the vidicon-type tubes, which display a comparatively lower sensitivity but much higher operational qualities (reliability, simplicity of power supply, low power requirement, low weight and dimensions), have found greater applications in space research (on weather satellites, Bibl.23, 26, 32, 33, 40), orbiting laboratories (Bibl.14, 29), Ranger satellites (Bibl.11, 34), etc.). The outlook for the future is that tubes of the image orthicon type but with an increased reliability will be used (Bibl.21, 22, 35), and so will be stereoscopic and color television (Bibl.38).

The resolving power of the present-day types of tubes is roughly the same for all types. In the best models it reaches 800 - 1000 lines at the center of the image field (Bibl.21, 31, 35).

The Vidicon. The tube with a photoconductive target has been termed vidicon (its other, less frequently used apellations are: staticon or resisticon).

The credit for the idea of developing this tube belongs to A.A.Chernyshev and his idea dates back to 1924, but for technical reasons the first operational models of the vidicons appeared as late as 1950 (Bibl.10) and they continue to be perfected to this very day.

Various models of vidicons exist, differing in both their photoconductive films and design features, including weight and dimensions. The latter are smaller for the vidicons than for all of the other known types of pickup tubes. Thus, the Soviet-made LI-407 miniature vidicon has a diameter of 13.5 mm, length of 115 mm and weight of 15 gm, with the working area of the target measuring 4.5 × 6 mm (Bibl.4).

The broadest applications for vidicons are found in special television systems, such as industrial television, since these systems are the most inexpensive, operationally simple, reliable and compact (Bibl.16). The principal tubes manufactured in the USSR for these purposes are vidicons of the LI-23 type and in the United States their similar counterpart is the RCA-6198 (Bibl.16, 18).

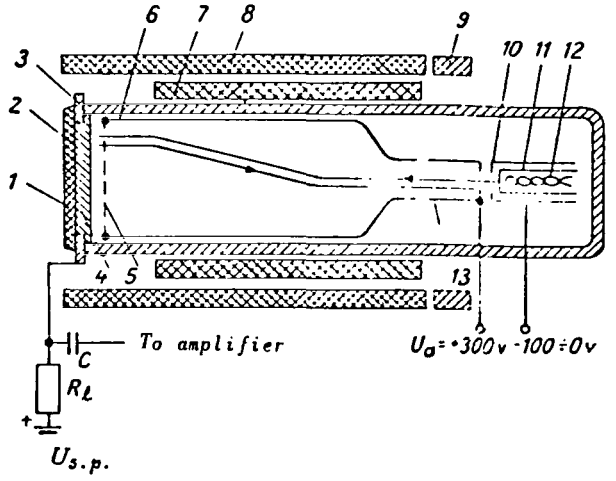

Fig.7.XIII Diagram of the Vidicon Pickup Tube.

The basic element of the vidicon is the photoconductive target 4 /317 (Fig.7.XIII), deposited on the sufficiently transparent signal plate 2 formed by spraying gold or tin oxide onto the plane-parallel glass end window of the tube 1. The resistance of the signal-plate layer must not exceed 1 k-ohm, since otherwise an appreciable potential difference may arise in it (Bibl.5). The signal plate contacts its voltage source $U_{s.p.}$ via metal ring 3.

The most widely used vidicons contain targets of selenium and stibnite (Sb_2S_3), operating in the visible region of the spectrum (Fig.8.XIII). The possibilities for expanding the spectral sensitivity range of the vidicons by using other materials (lead sulfide, germanium, or silicon with alloy elements, etc.) are being experimentally investigated. Vidicons with a spectral sensitivity range extending to wavelengths of 1 μ and higher have already been developed (Bibl.2).

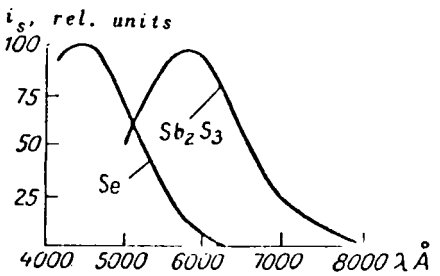

Fig.8.XIII Spectral Characteristics of the Vidicons with Various Targets.

The rear surface of the photoconductive layer 4 (cf. Fig.7.XIII) is illuminated by a beam of electrons formed by a triode-type electron gun. The latter consists of the thermionic cathode 11 with the filament 12, the control electrode 10 with an aperture through which the electron beam emerges, and the anode 13 connected to the internal conducting coating of the cylinder 6.

The magnetic coils 7 and 8, located outside the cylinder, serve to focus and deflect the beam. The small correcting coil 9 is normally used to correct the assembling defects of the electron gun (centering of the beam). To /318 assure a maximally normal impingement of the electron beam onto the target surface, the mesh 5 is mounted 5 - 10 mm in front of that surface. This mesh 5 produces a uniform decelerating field similar to that of a flat capacitor. The normal impingement of the beam onto all of the target elements makes it possible to preserve a nearly constant resolving power of the tube with respect to the entire frame, as well as a uniform image field.

The conductive layer 6 and the mesh 5 have an anode potential U_a = 300 v with respect to the cathode). A signal-plate voltage of several tens of volts, e.g., $U_{sp} \approx +20$ v, is supplied to the signal electrode.

The potential U_t of the target surface facing the electron gun will be close to U_{sp} and hence the velocity v of the electrons of the beam passing through the mesh will diminish to

$$v = \sqrt{2\frac{e}{m}U_t}, \qquad (6.XIII)$$

where e and m are the charge and the mass of the electron.

On illumination of the light-sensitive target by a low-velocity electron

beam, the number of arriving electrons exceeds the number of the secondary electrons leaving the target. These secondary electrons are collected by the mesh and the conductive coating of the cylinder. As a result, the potential of the target elements illuminated by the electron beam will equal the cathode potential, and then the beam electrons get repelled at the target surface in the direction of the anode.

Suppose the optical image of an object is projected onto the front surface of the target and the frontal glass via the transparent signal-plate layer. Then the resistance R of individual parts of the photoconductive target will differ, varying within the limits of from R_d (resistance of the dark elements) to R_ℓ (resistance of the light elements).

In the ideal case every target element may be represented as a fixed capacitor C shunted by the variable resistor R of the photolayer (Fig.9.XIII). The extent of resistance R depends on the thickness d and conductance σ of the target, namely,

$$R = \frac{1}{\sigma}\frac{d}{s} = \frac{4d}{\pi\delta^2(\sigma_d + aE_t^b)}, \qquad (7.XIII)$$

where s is the area of the scan element (spot) with the diameter δ on the target; σ_d is the dark conductance of the target in the transverse direction; E_t is the illumination of the target; a and b are constant coefficients. /319

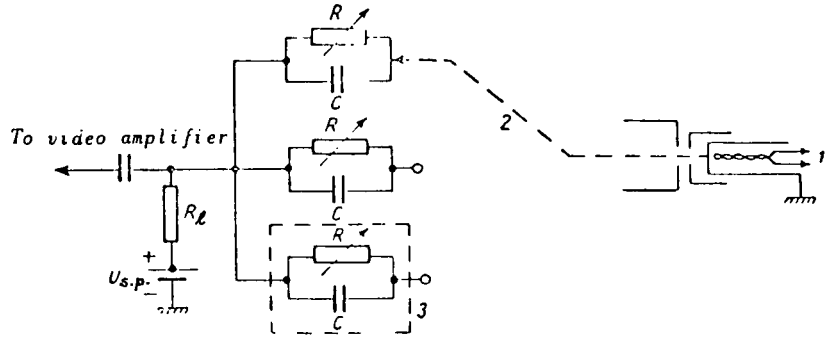

Fig.9.XIII Equivalent Circuit of the Elements of a Photoconductive Target.
1 - Electron-gun cathode; 2 - Low-velocity electron beam; 3 - Target element.

The capacitance of an element is defined as the capacitance of a capacitor whose dielectric is the photolayer, with the aid of the known equation

$$C = \frac{\varepsilon s}{4\pi d} = \frac{\varepsilon\delta^2}{16d}, \qquad (8.XIII)$$

where ε is the dielectric constant.

The time constant τ of the target elements thus will be determined by the properties of the target material and the illumination of a given sector in accordance with the relation

$$\tau = RC = \frac{\varepsilon}{4\pi(\sigma_d + aE_t^b)}. \qquad (9.XIII)$$

As we can see, the best-illuminated elements will have the lowest time constant τ.

Hence, when the target is not illuminated ($E_t = 0$), the potential of its rear surface is close to the potential $U_{s.p.}$ of the signal plate (Fig.10.XIII). On illumination of the target with a low-velocity beam, the potential of each element is reduced to the cathode potential (to zero). The capacitor C proves to be charged, and the potential difference on its plates equals $U_{s.p.}$. After the beam sweeps past the concerned element, the capacitor C gets discharged across the resistor R with a time constant τ, dependent on the illumination of the element. The potential U of the target surface facing the electron gun again begins to increase and tends to reach the potential $U_{s.p.}$ until the electron beam again sweeps over this surface element (following the frame period T_f). /320

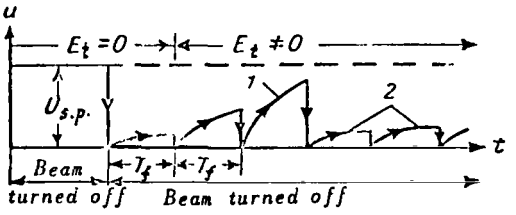

Fig.10.XIII Potential Relief on the Target.
1 - Change in potential of the white element with time;
2 - The same, for the black element.

The change in the potential U with the time t in the ideal case is described by the function

$$U(t) = U_{s.p.}(1 - e^{-\frac{t}{RC}}) \quad (0 \leqslant t \leqslant T_f) \qquad (10.XIII)$$

At the time instant t = 0, when U(t) = 0, a new working cycle commences. At the end of the cycle ($t = T_f$), the more illuminated elements will have a higher scanned-surface potential than the darker elements (Fig.10.XIII). Thus, a charge image corresponding to the illumination of the elements into which the image gets dissociated, forms on the photoconductive target.

The depth of the charge image on the target equals the difference between the light U_l and the dark U_d surface-element potentials and, prior to the new scanning cycle, it is

$$\Delta U = U_l - U_d = U_{s.p.}(e^{-\frac{T_f}{R_l C}} - e^{-\frac{T_f}{R_d C}}). \qquad (11.XIII)$$

From eq.(11.XIII) it can be seen that the depth of the charge image is greatly affected by the signal-plate potential $U_{s.p.}$.

In the course of the charge interchange, the electron beam erases the charge image of the target and charges the storage elements, so that their potential difference roughly equals that of $U_{s.p.}$. This charging current, flowing across the load resistor R_l incorporated in the charging circuit (cf. Figs.8 and 9.XIII), generates pulses of the video signal voltage U_s. The duration of these pulses is a function of the time T_e of the scanning or transmission of one element.

The amplitude of video signal current i_s may be defined as the difference in mean currents during the charge-interchange period T_e. This refers to the /321 mean currents required to reduce the potentials of the light and the dark elements to the cathode potential, i.e.,

$$i_s = \frac{C(U_l - U_d)}{T_e}. \qquad (12.XIII)$$

With the aid of eq.(12.XIII), we will estimate the beam current i_b required for the complete scanning and hence also the erasure of the charge image. To this end, the beam must, within the charge-interchange period T_e, reduce to the cathode potential even the surface of the elements whose potential reaches its upper limit, i.e., equals $U_{s.p.}$. Assuming in eq.(12.XIII), that $U_l - U_d = U_{s.p.} = 20$ v, $C = 1.3 \times 10^{-4}$ farad, $T_e = 7.8 \times 10^{-8}$ sec, and considering that the mean effectiveness of the action of the beam electrons is 0.3 (i.e., that $i_s = 0.3\, i_b$), we find that the beam current $i_b = 10$ μa. In reality, focusing conditions make it impossible to obtain such a large beam current in the presence of an adequately small scan element. The present-day vidicon designs yield a beam current that is roughly one order of magnitude smaller than that required for the complete erasure of the charge image. Therefore, in reality, the lower limiting potential, which is equal to the cathode potential, is not reached at the rear surface of the target and so the charge image is not completely erased when the charge interchange takes place. The residual charge image is superposed on the charge image of the next frame, and this manifests itself in the increase in the inertia of the tube (blurring of the images of moving objects) and in the decrease in its contrast range, owing to the decrease in the signal.

The inertia caused by the charge-interchange beam whenever its current is not sufficiently large to completely erase the charge image is termed charge-interchange inertia. For vidicons, the extent of this inertia depends on the potential $U_{s.p.}$ of the signal plate, which determines the depth of the charge image on the target. Therefore, $U_{s.p.}$ must be so fixed as to make allowance for the desired compromise between the sensitivity and inertia of the tube.

Note that an appreciable increase in $U_{s.p.}$ leads to a sharp increase in the shadow current of the photoconductive target, and this also restricts the possibilities for enhancing the tube sensitivity by increasing $U_{s.p.}$.

The photoelectric component of inertia, due to the physical nature of the intrinsic photoeffect, predominates when the illumination is small, while the charge-interchange component predominates when the illumination is considerable.

The total inertia of vidicons, however, increases with decreasing illumination.

The tube inertia is normally estimated according to the decrease in the resolving power N on the transmission of the mobile test pattern 0249 whose image moves over the target at the rate of 3 mm/sec. For vidicons of the LI-23 type, the resolving power on transmission of a stationary test pattern 0249 amounts to 550 lines at the frame center and 350 lines at the frame corners, and on transmission of a mobile test pattern it is 300 lines at the center (Bibl.10). /322

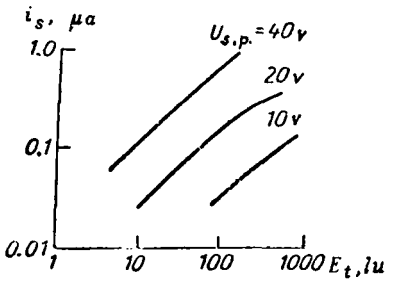

Fig.11.XIII Luminous Characteristics of the LI-23 Vidicon.

The dependence of the signal current on the photocathode illumination as a function of various signal-plate potentials is described by means of the luminous characteristics. The luminous characteristics of the LI-23 vidicon (Bibl.15) are shown in Fig.11.XIII which indicates that the real sensitivity of this vidicon for the potential $U_{s.p.} \approx 20$ v is characterized by the photolayer illumination $E_t \approx 10$ lu for the signal current $i_s \approx 5 \times 10^{-8}$ a.

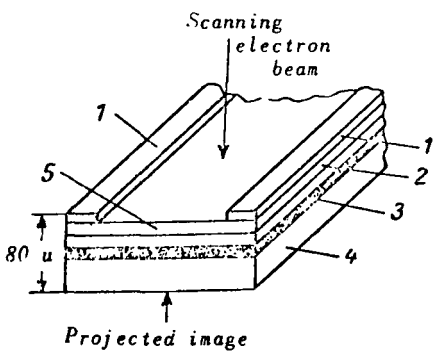

Fig.12.XIII Tape for Electrostatic Recording of Images.

The noise in the vidicon TV systems is determined by the noise due to the charge-interchange beam and to the preamplifier (cf. Sect.4 of this chapter). The energy sensitivity of the vidicons used in the United States rockets and satellites is 40 - 50 ma/w.

Investigations (Bibl.10) show that in the presence of a stable power-supply regime for all of the electrodes of the vidicon and a sufficient beam-current intensity it is possible to preserve a high quality of images with a variation in the illumination within sufficiently broad limits, by adjusting only the signal-plate potential. This special feature of the vidicon is utilized in the construction of circuits for the automatic regulation of their illumination, operating over a range of illuminations E of from several to hundreds lux. The changes in $U_{s.p.}$, taking into account the requirement of assuring a low inertia, usually range within the limits of from 10 to 60 v (Bibl.5).

There are some vidicon varieties operating in high-velocity electron-beam regimes such as the LI-401 and others (Bibl.10). In addition to the differences in the power supply regime of their signal plates, they also differ /323 somewhat in their design, and in particular that no mesh is mounted in the neighborhood of the target.

The resolving power of the vidicons, operating in the high-velocity beam regime, is somewhat higher than that of the conventional vidicons, whose other parameters are similar and their inertia is smaller. Their chief shortcoming is the shorter service life of 120 and 500 hr, respectively, for the LI-401 and for the LI-23 (Bibl.10).

Further development of the vidicons is being carried out particularly in the direction of enhancing their sensitivity. To this end, e.g., the induced conductance effect may be utilized very effectively (Bibl.5). This effect consists in the decrease in the resistance of a dielectric or semiconductor on illumination with electrons of sufficiently high energies.

The induced conductance effect is utilized in the recently developed ebicon tube. This tube contains a section for the transfer of the electron image from a semitransparent antimony-cesium photocathode to a two-sided target with charge-interchange on the back side being carried out by a low-velocity electron beam (Bibl.15). A semiconductor layer with a sharply expressed induced conductance effect is deposited on the target surface facing the electron gun. The photoelectrons emitted by the photocathode become accelerated to an energy of ~20,000 ev. They excite induced conductance in the semiconductor layer and, as a result, the target storage elements become discharged. In this respect the operation of the ebicon resembles that of the vidicon, although the sensitivity of the former is much higher. Thus, plans exist to equip orbiting astronomical observatories with an ebicon operating with a target illumination of up to $E = 5 \times 10^{-5}$ lu (Bibl.14, 15).

Of great promise to space research is the use of tubes analogous to the vidicons with a moving electrostatic target on which the charge image may be preserved (Bibl.3, 15, 32). In this case, the conversion of the optical image to the charge image is carried out on a special tape consisting of four transparent layers: the polystyrene substrate 4 (Fig.12.XIII), the signal electrode in the form of a thin (0.01 μ) layer of gold 3, the photoconverter layer 2 resembling the vidicon target, and an additional layer of the dielectric 5 (polystyrene 0.6 μ). This tape fulfills the role of the vidicon target and is connected to the amplifier circuit by the metal strips 1. The tube through which this tape is drawn has an electron gun and a focusing and deflection system.

Prior to its actuation, the tape is sensitized by creating a constant potential difference in the dielectric layer. For this purpose, the latter is illuminated with a broad electron beam of an energy of approximately 200 ev. As a result, a potential difference of approximately 200 v is created between /324 the surfaces of the dielectric. To produce a charge image on the dielectric layer, the optical image of an object is projected onto the tape, while simultaneously the dielectric surface is swept by a slow-velocity electron beam. At points where the illumination is greater, the conductivity of the photolayer is considerable and the potential considerably reduced. Thus, the optical image is converted to the charge image. The tape with the charge image is wound into a coil and may be stored for a prolonged period of time.

Reconversion of the charge image to the video signal is accomplished in the same tube by means of a well-focused high-velocity electron beam. Thus each element is reduced to the potential U_a and the video signal arises as the load resistor.

The light sensitivity of present-day electrostatic tapes is comparable to the sensitivity of photographic films, and their resolution reaches 330 television (black and white) lines per millimeter (Bibl.15). The electrostatic tape may be stored for several months and repeatedly re-used.

The Image Orthicon. The tube with a two-sided semiconductor target, termed the image orthicon, was suggested by a Soviet scientist, G.V.Braude, in 1938. The first models of this tube appeared in 1946 (Bibl.10) and found broad application in various high-sensitivity applied television systems as well as in television broadcasting. The use of these tubes in space research is, as has been pointed out above, highly promising.

The electron image is created and transferred in the front part of the tube, onto which the lens 2 projects the image 1 (Fig.13.XIII) of an object. The tube diameter in this part is the largest, namely, 77 mm in the Soviet-produced LI-13, LI-17, LI-201 image orthicons (Bibl.10). The middle part of the tube represents the scanning section, while its rear part contains a secondary-electron multiplier serving to amplify the video signal. The overall length of an LI-201 tube is 390 mm. It is placed in a set of the focusing and deflecting coils 9 and 10. The coil 11 serves to correct the electron-gun beam.

The semitransparent photocathode 3 is deposited on the internal surface of the front glass and has a potential of 300 v. Most Soviet-made image orthicons include a bismuth-silver-cesium photocathode, except the LI-13 which has an oxygen-silver-cesium photocathode sensitive to near-IR radiation (Bibl.10).

Mounted not far from the photocathode 3 is the accelerating electrode 4 which generates the field of the transfer of electrons onto the target. The electrons emitted by the photocathode retain their cross-sectional density /325 distribution in the focusing plane while traveling toward the target. On striking the target 6, the electrons cause secondary emission and the formation on the target of a charge image corresponding to the distribution of illumination on the photocathode. The secondary electrons are collected by a very fine wire-mesh screen 5 with a voltage of 1 - 2 v (with respect to the thermionic cathode), located at a distance of several tens of microns from the target. The target

is a thin (3 - 5 μ) film of special semiconducting glass or of some other material, mounted on a ring together with the mesh screen 5.

The process of the formation of charge image reduces to the charging of the storage elements between the mesh and the target during the secondary emission from the target. Clearly, a higher potential is created on the sectors corresponding to the brighter elements of the image. The depth of the charge image on the target is determined by the magnitude of the accumulated charge and

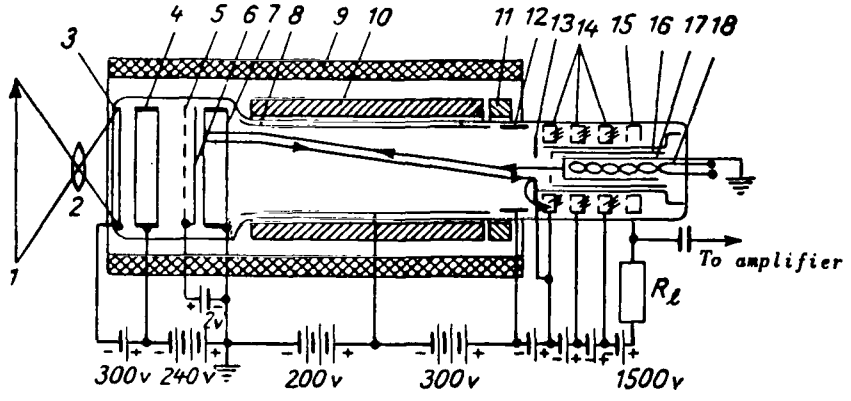

Fig.13.XIII Diagram of Image-Orthicon Type Tube.

depends on the potential applied to the mesh as well as to the mesh-target capacitance. This capacitance itself depends on the distance between the mesh and the target. As this distance increases, the tube sensitivity increases, since a low capacitance means that a lower photocurrent and a lower illumination of the photocathode are required to attain the same potential difference. However, the video signal then decreases in magnitude. Therefore, in the image orthicons the mesh-to-target spacing must be selected and maintained very rigorously. The depth and the charge-image definition depend also on the target temperature, since the temperature alters the properties of the target and primarily of the conductivity.

The image charge is, owing to electrostatic induction, virtually transmitted completely to the reverse side of the target, which is scanned by a low-velocity beam. /326

The electron gun of the tube consists of the thermionic cathode 17 with the filament 18, the control electrode 16 and of the anode 13 with a small beam-exit aperture. The annular decelerating electrode 7 with a small positive potential serves to reduce the velocity of the electrons during their approach to the target. The internal positive-potential electrode 8 serves to focus the beam and to protect it against external electrical fields.

If a charge image is present on the target, part of the electrons from the scanning beam will be expended on erasing the image. The number of electrons bouncing off the target and returning to the electron gun, where they are

collected into a beam by the same field which had decelerated and focused them during their travel toward the target, is inversely proportional to the depth of the positive charge image on the target. The returning electrons strike the forward part of the annular anode 13, which is the first stage of the secondary-electron multiplier. The secondary-electron multiplier consists of several louver-type dynodes 14. The anode cylinder 12 contributes to an improved selection of secondary electrons from the first dynode 13. The amplified ($\sim 10^3$ ×) electron flux is collected by the collector 15 of the multiplier. Connected to the collector circuit is load resistor R_ℓ, from which the video signal $U_{v.s.}$ is taken, which is additionally amplified by the electron amplifier (for R_ℓ = = 10 - 25 k-ohm, $U_{v.s.}$ amounts to several hundred millivolts).

In tubes of the image orthicon type there is virtually no inertia when the test pattern is moved at the rate of 3 mm/sec (Bibl.10).

The resolving power of the serially manufactured tubes LI-17 at the center of the image field is characterized by the line number z = 625 for the photocathode illumination E_t = 0.5 lu, and z = 550 for E_t = 0.1 lu (Bibl.10).

The maximum permissible photocathode illumination $E_{t.max}$ = 5 lu for the illumination time of 5 min. The permissible temperature fluctuations during normal operation are from 35 to 60° C, with a temperature drop Δt along the cylinder of not more than 5° C. This requires the maintenance of a sufficiently stable temperature regime during the operation of the serially manufactured image orthicons, as well as preheating for 30 - 60 min following the start of operation. Their service life is approximately 200 hr (Bibl.10). A major shortcoming of the image orthicons is the presence of image defects, i.e., "snowflakes" due to noise, blurring of the black boundaries, halo, etc. (Bibl.10, 15).

Improvements of the image orthicons are being carried out in the direction of selecting optimal material and a design of the principal electrodes (target, mesh) as well as increasing their reliability. The most sensitive are the /327 American-developed (Bibl.21, 27) image orthicons with an oxide-magnesium target: their sensitivity (reaching 10^{-7} lu) greatly exceeds the sensitivity of human vision.

Any further increase in the sensitivity of the image orthicons, as well as of other types of pickup tubes, may be attained by intensifying the incident luminous flux. This is accomplished chiefly with the aid of amplifiers of the brightness of the optical image (electron-optical image intensifiers) incorporated into the design of the pickup tube (Bibl.15). A particularly high degree of intensification may be obtained by the intensifiers in which the intercascade coupling is based on the fiber optics (Bibl.30).

Another significant trend in the development of pickup tubes is the use of electron-optical spectrum transformers, which make it possible to displace the spectral operating characteristic of the system into the ultraviolet or infrared region of the spectrum (Bibl.14).

Plans exist for installing television apparatus with high-sensitivity image orthicons assuring round-the-clock operation in various spacecraft and primarily in those designed to investigate the lunar surface (Prospector, Surveyor).

Section 3. Principal Elements of Electrical Circuitry

The electrical circuitry of a television system includes units (Fig.14.XIII) which assure the amplification of video signals, synchronous operation of the transmitter and receiver, as well as transmission and reception of signals over a radio channel. The electrical tract transmits the video signal from the output of the pickup tube to the control electrode of the cathode-ray picture tube.

The most important element of the electrical tract is the broadband amplifiers, $\Delta\nu$ from tens of cps to several mega-cps in broadcasting systems (Bibl.15), termed video amplifiers, which assure undistorted transmission of the video signal.

The first stages of the amplifier (the preamplifier) are installed in the neighborhood of the pickup tube and their design is such that the noise they contribute is minimal. To this end, special measures (anti-noise correction) usually are taken in the video amplifiers of the transmitting side.

The sawtooth line and frame scan pulses which drive the deflection coils (FDS) are shaped by the sweep unit. The control pulses energizing the sweep /328 generators are produced in the synchronizing generator. The latter also produces blanking pulses which, after appropriate amplification, are conveyed to the control electrode of the pickup tube electron gun. To assure smooth image edges, the duration of the line blanking pulses is made somewhat shorter than the retrace time of the beam.

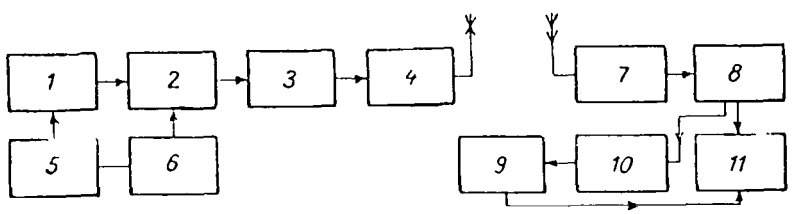

Fig.14.XIII Block Diagram of the Electrical Tract of a Television System.
1 - Pickup camera; 2 - Video amplifier; 3 - Modulator; 4 - Ultrashort-wave radio transmitter; 5 - Sweep unit; 6 - Synchronizing generator; 7 - Ultrashort-wave radio receiver; 8 - Video amplifier; 9 - Sweep unit; 10 - Synchronizing unit; 11 - Visual-display tube.

The synchronizing pulses are, moreover, conveyed to the video amplifier where they are mixed with the video signal. Thus, the transmitted (complete) television signal includes the video signal plus the blanking and synchronizing pulses.

In order to facilitate the separation of synchronizing pulses and image pulses on the receiving side, the former are transmitted in the "blacker than black" region. In television broadcasting, the apex level of the synchronizing

pulses is taken at 100%. The black level then is 75% and the white level, from 10 to 15% (Bibl.18). The ratio between signal levels in special systems is not standardized.

The relationship between the video signal, the line retrace and the synchronizing and blanking pulses is shown in Fig.15.XIII.

The frame synchronizing and blanking pulses differ in duration. In simplified television systems which transmit individual frames, the synchronization may be accomplished with the aid of only the line-synchronizing pulses, provided that the initial instant of the frame transmission is preset.

Note that in cases where it is necessary to transmit information about the mean illumination level of the transmitted scene, i.e., about the constant component of the video signal, the height of the blanking pulses usually is varied in proportion to this constant component, so that their upper part would persist at the black level (Fig.15.XIII).

In television transmitting devices of an applied nature, special attention is devoted to assuring the reliability of their performance. Various steps are taken to enhance this reliability, including the duplication of the least reliable elements. Elementary electrical circuits with a minimum number of radio tubes are employed, because of these tubes break down roughly five times as often as the other circuit elements (Bibl.16). In certain television systems in use, pulses arising in the deflection coils during the retrace are utilized instead of radio tube circuits to blank the beam. The pickup cameras are enclosed in a special housing within which normal operating conditions are assured (Bibl.16). /329

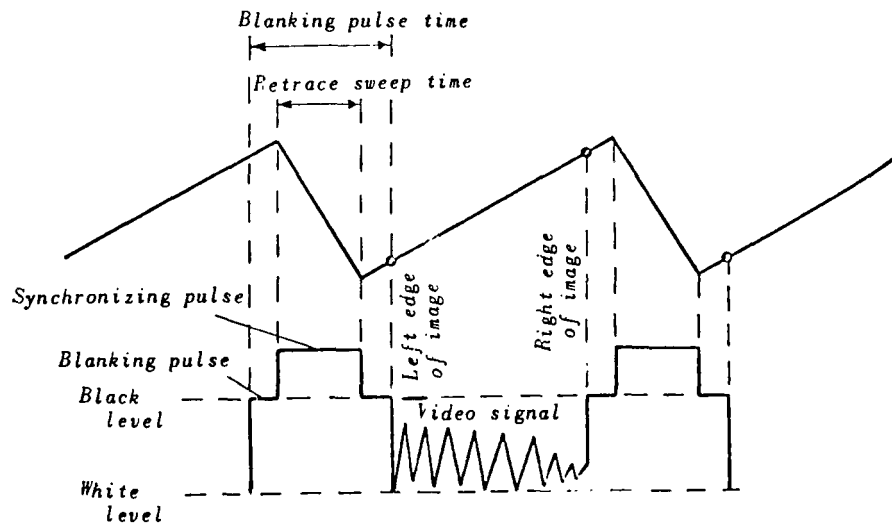

Fig.15.XIII Relationship between Sweep Retrace Time and the Synchronizing and Blanking Pulses.

The television cameras designed for installation in spacecraft must, moreover, be equipped with devices assuring automatic operation over a prolonged

period of time. They also must satisfy various common requirements for the measuring equipment operating in outer space.

In this case the weight, dimensions and power requirement of the instruments acquire special significance. The power requirement must be such as to assure sufficient power to transmit the television signal to the earth. To reduce the dimensions and the power of the spacecraft-borne transmitter, the current American space television systems (Bibl.11, 14, 37, 39) employ a slow vertical sweep which assures narrowing the frequency band to several tens of kilo-cps and less. For example, in the Tiros-series satellites (Bibl.32, 40) /330 the frame period was increased to 2 sec, which leads to a 60 × reduction in the frequency band and a corresponding reduction in the transmitter power required to transmit a frame as compared with the United States commercial television

where the frame period $T_f = \frac{1}{30}$ sec. The reduction in the scanning rate makes it possible, moreover, to reduce the beam current of the vidicon and to increase its resolving power, [by ~30% in the above example (Bibl.37)] compared with the normal. Clearly, the shadow current of the target must in this case be reduced to a minimum.

To eliminate blurring of the image in the presence of a long T_f, it is necessary to employ compensation methods for the displacement or for the shutter by utilizing the memory effect of the vidicon target. Investigations (Bibl.32, 37) have shown that for the slow-sweep vidicons used in the United States an exposure time of 1 - 2 μsec is sufficient, if the earth's illumination is sufficiently bright.

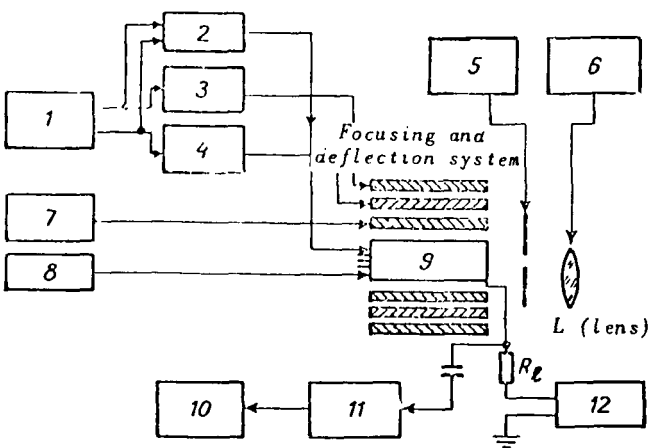

Fig.16.XIII Block Diagram of a Spacecraft-Borne Television Transmitting Apparatus:
1 - Timer; 2 - Blanking-pulse generator; 3 and 4 - Horizontal and vertical-sweep generators; 5 - Shutter control circuits; 6 - Focus control circuit; 7 - Regulator of power supply to focusing system; 8 - Power pack; 9 - Vidicon; 10 - Memory unit; 11 - Video amplifier; 12 - Control circuit of voltage $U_{s.p.}$.

The operational control of the tube 9 as well as the focusing of the optical image and of the irising of lens L may be accomplished with the aid of the special systems 5 and 6, as illustrated by the block diagram of a typical space television transmitting apparatus (Fig.16.XIII) developed in the United States /331 (Bibl.37). Simplified forms of instruments of this kind are also used in weather satellites (Bibl.26, 32). In this case, reliability is assured by using a vidicon-type pickup tube, printed and transistorized circuits, filling of panels with a compound, temperature stabilization, etc.

The vidicon used in typical instruments of this kind (diam. 12.7 mm) has a square-shaped raster measuring 6.5 × 6.5 mm and a definition of 500 lines. For a line frequency of 250 cps and a frame period of 2 sec, the frequency band of the video signal recorded on the magnetic tape is 62.5 kilo-cps. The weight of the camera is 2.7 kg and the required power does not exceed 10 w (Bibl.37).

The set of the satellite-borne TV equipment includes in addition a command receiver, a timer, and a controller which direct the camera operations on command from the earth or from the spacecraft-borne programming mechanism, and in addition a memory device and an image signal transmitter.

Certain vidicon-employing transmitters include the regulation of the voltage supplied to the signal plate, which is carried out by means of a special photoresistor or by the photocurrent of the tube itself (Bibl.16). The more intricate systems also employ regulation of the beam current. This broadens the operational illumination range of the transmitting device and enhances the clarity of the transmission.

The television receivers, which are a most important part of the ground-based measuring equipment, are distinguished by their considerable variety: they may operate in the meter range, or in decimeter and centimeter waves; they may be based on the superheterodyne circuit or on the direct-gain circuit; they may be designed for observation from the visual-display tube or from a projection screen; and they may handle the insertion of the received information into a computer for subsequent processing or its re-transmission along a radio delay line, etc. (Bibl.3).

The basic elements of the electric tract on the receiving side (cf. Fig.14.XIII) in addition to the high-frequency part of the receiver and the visual-display tube with a focusing and deflection system, are: a) the detector assuring the isolation of the video signal; b) the video amplifier amplifying the signal to the extent required to control the operation of the visual-display tube (20 - 40 v); c) the synchronizing unit, which isolates the synchronizing pulses from the overall television signal (by methods of amplitude and time selection); and d) the sweep unit, generating the sweep pulses.

Radiotelevision communications over large distances in outer space are greatly complicated by the decrease in the strength of the arriving signal. Thus, f.e., during a nondirectional transmission, the energy of the radiowaves from the spaceship located in the neighborhood of Mars (at a distance of /332 60 million km) will be 10^4 × smaller than when photographs of the far side of the Moon are transmitted from outer space (0.5 million km) (Bibl.3). Hence, space communications lines use transmitting and receiving antennas with a high

directive gain. In this case, the planned antenna mirrors reach a size of 250 - 300 m (Bibl.3). To enhance the sensitivity of the receiving devices, molecular and parametric amplifiers with a low noise level are employed.

The use of lasers and optical-range amplifiers is of particularly great promise to assuring radiotelevision communications over distances of many millions of kilometers. In this case, the communication channel displays a very sharp directivity and a high noiseproof feature, while at the same time transmitting an extraordinarily large amount of information [as many as 10,000 television programs via a single channel (Bibl.3).

Section 4. Basic Parameters of a Television Apparatus

The special features of the television method of image transmission and the distortions caused by the electrical tract during transmission of the video signal cause the picture received on the screen of the visual display tube to differ to a certain extent from the reproduced object. These differences are associated with the loss of minor detail owing to the limited resolving power of a system with a limited number of transmissible gradations in brightness and with a limited tube sensitivity (appearance of image noise in the form of "snowflakes"); with blurring of the black-and-white image boundaries owing to finite dimensions of scan elements, and with various other causes. In the presence of low illumination, the distorting effect of these factors may prove so pronounced that the image will be of an unsatisfactory quality. The minimal illumination at which the system may transmit an image of a satisfactory quality is chiefly determined by the sensitivity of the pickup tube.

The development of general criterion for the quality of television systems is encountering considerable difficulties (Bibl.13).

Fundamentally, parameters such as the resolving power, the image contrast range and the transmission of gradations in brightness serve to partially characterize the quality of the transmitted images (Bibl.1). These parameters are of decisive importance in the selection and evaluation of the pickup tube and the entire space-borne television system. In the latter case, the range and zone of observation also are of essential importance.

Sensitivity. The sensitivity of a television system is characterized by the minimum working illumination E_t of the tube. It clearly is a function /333 of the time of the charge accumulation (exposure) and of the sensitivity of the tube in its circuitry.

The sensitivity of the pickup tubes is characterized by the ratio of maximum magnitude U of the video signal to the mean square noise voltage at the output of the first amplifier stage

$$\psi = \frac{U}{\sqrt{\overline{U_\Sigma^2}}}. \qquad (13.XIII)$$

It may be generally assumed that the image begins to be visible against the

noise background when $\psi = 1$ and acquires a satisfactory quality when $\psi = 30$ (Bibl.15).

The fluctuation noise is due to a chaotic change of the resistor voltages and to fluctuations of the electron fluxes both in the pickup tube itself, and in the preamplifier tube, with the shot noise accounting for the greater part of this noise.

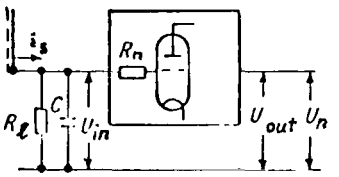

Fig.17.XIII Circuit Diagram of Pickup Tube.

A simplified diagram of the preamplification of the video signal of a vidicon-type tube is shown in Fig.17.XIII. The load impedance represented by the parallel-connected load resistor R_ℓ and the capacitor C is according to the known equation

$$z(\nu) = \frac{R_\ell}{\sqrt{1 + (\omega R_\ell C)^2}}, \qquad (14.XIII)$$

where ω is the cyclic frequency.

From eq.(14.XIII) it can be seen that as the frequency increases the signal taken off the load resistor decreases. This causes frequency distortions which must be compensated by correcting the video amplifier. The amplitude-frequency characteristic of the amplifier in the presence of the correction is

$$K(\nu) = K_0 \sqrt{1 + (2\pi\nu R_\ell C)^2}, \qquad (15.XIII)$$

where K_0 is a constant equal to the gain at low frequencies.

Thus, the video signal voltage at the preamplifier output will be, throughout the frequency range ν,

$$U = i_s K(\nu) z(\nu) = K_0 R_\ell i_s, \qquad (16.XIII)$$

where i_s is the signal current of the pickup tube.

In the circuit considered, the principal noise is due to the shot fluctuation noise $U_{s.t.}$ of the signal at the tube output, the thermal fluctuations in the load resistor ($U_{th.}$) and of the shot fluctuation noise ($U_{s.a.t.}$) at the output of the first amplifier tube. The fluctuations $U_{s.t.}$ of the vidicon signal, in their turn, contain two components due to the shot fluctuations of the beam current and the shot fluctuations of the secondary emission current of the target. /334

The relation for the mean square output voltage of the shot fluctuations of signal current i_s according to the Schottky equation, taking into account the

relation (16.XIII), is written as

$$\bar{U}^2_{s.t} = 2i_s K_0^2 e R_\ell^2 \alpha' \Delta\nu, \qquad (17.XIII)$$

where α' is a coefficient which takes into account the increase in fluctuations due to secondary emission during the charge interchange, and e is the electron charge.

The mean square voltage of the thermal noise due to the load resistance will be as follows at the amplifier output (according to the Nyquist's equation)

$$\bar{U}^2_{th} = 4kTK_0^2 R_\ell \Delta\nu. \qquad (18.XIII)$$

The mean square voltage of the shot noise of the preamplifier tube at the output, as determined from the analogous equation, will in this case be

$$\bar{U}^2_{s.a.t.} = 4kTR_n K^2(\nu)\Delta\nu, \qquad (19.XIII)$$

where R_n is the equivalent noise resistance of the first-stage preamplifier tube.

Note that the last noise component is not uniformly distributed over the frequency band $\Delta\nu$ but increases with increase in the frequency ν of the video signal, commensurately with the increase in the frequency-dependent stage gain.

The mean square resultant fluctuations will be, in accordance with the rule for the addition of noises from independent sources,

$$\bar{U}^2_{\Sigma} = \Delta\nu K_0^2 R_\ell^2 \left(2\alpha' e i_s + 4kT \frac{R_\ell + R_n}{R_\ell^2} + 16\pi^2 kTC^2 R_n \nu^2\right). \qquad (20.XIII)$$

Taking eqs.(16.XIII) and (13.XIII) into account, we have

$$\psi = \frac{i_s}{\sqrt{\left(2\alpha' e i_s + 4kT \frac{R_\ell + R_n}{R_\ell^2} + 16\pi^2 kTC^2 R_n \nu^2\right)\Delta\nu}}. \qquad (21.XIII)$$

The above relation shows that the thermal noise, which normally contri- /335
butes most to the overall noise, may be reduced by increasing the load resistance R_ℓ, although this requires a gain correction at high frequencies in accordance with eq.(15.XIII). The video signal i_s, generated by the vidicon in the presence of integral solar illumination E_t on the tube, may be expressed by the conventional equation

$$i_s = \gamma E_t s, \qquad (22.XIII)$$

where γ is the current sensitivity of the target, averaged over the region of its spectral sensitivity, and s is the area of the photosensitive surface of the target.

The relation of the illumination E_t on the tube to the illumination E of the object is determined by eq.(2.XII). Considering this, from eqs.(21.XIII) and (22.XIII) we find the illumination E required for a satisfactory performance of the vidicon-type television system (when $\psi = 30$):

$$E = \frac{120\sqrt{(2\alpha' e i_s + 4kT\frac{R_\ell + R_n}{R_\ell^2} + 16\pi^2 kTC^2 R_n \nu^2)\Delta\nu}}{\gamma s \rho P \ddot{O}^2 \cos z}, \qquad (23.XIII)$$

where ρ is the mean reflectivity of the object, P is the transmissivity of the lens and of the layer of the atmosphere, Ö is the relative lens aperture, z is the zenith angle of the sun at the moment of observations.

From eq.(23.XIII) it follows that the sensitivity of the vidicon-type pickup camera depends on a large number of parameters of the television system, as well as on the properties of its optics and atmospheric transparency.

For tubes of the image-orthicon type, which employ a secondary-emission multiplier, the amplification of the video signal is so considerable that the voltage fluctuations at the load resistor need not be taken into account. In this case, current fluctuations in the pickup tube itself are decisive. As a result, the illumination E of the object, required for operation of the tube, is markedly smaller; however, the ψ ratio in this case is low only for low i_s (Bibl.15).

In applied television systems of the type PTU-OM (closed-circuit industrial television), e.g., with serially manufactured vidicons, a satisfactory image quality is achieved when E = 50 lu, and in those incorporating an image orthicon, when E = several lux, given a definition of ~500 lines in the vertical and horizontal (Bibl.16). In special systems, as was previously pointed out (cf. Sect.2 of this chapter) pickup tubes with a much higher sensitivity may be employed.

Image contrast range and image distance. Image contrast range K_1 is the /336 term applied to the ratio of the greater brightness B_1 in the image field to the lesser brightness B_2, i.e.,

$$K_1 = \frac{B_1}{B_2} \geqslant 1. \qquad (24.XIII)$$

The maximum image contrast range $K_{1max} = \frac{B_{max}}{B_{min}}$ is termed the brightness range.

The contrast K is related to the image contrast range by the obvious equation

$$K = \frac{B_1 - B_2}{B_1} = \frac{K_1 - 1}{K_1} \leqslant 1. \qquad (25.XIII)$$

The image contrast range and the contrast are determined not only by the characteristics of the television system, but also by the contrast of the transmitted image on the pickup tube and the conditions under which the image is viewed. The external illumination due to atmospheric optics or to the increase

in the level of illumination of the visual-display tube screen reduce the magnitude of K and K_1.

If an object having a natural contrast K with its background is observed through a layer of atmosphere having the transmissivity P_a and the haze brightness B_h, the image-contrast range at the inlet of the optical system will be, as was pointed out previously (cf. Sect.3, Chapt.XII),

$$K' = \frac{(B_{ob} - B_b)P_a}{B_{ob}P_a + B_h} < K, \qquad (26.XIII)$$

where B_{ob} and B_b is the natural brightness of the object and of the background, respectively, when observed from a close distance ($B_h = 0$).

Thus, the influence of the atmosphere manifests itself not only in reducing the illumination of the image owing to the attenuation of radiant energy fluxes but also in the reduction of the image contrast range owing to the additional haze brightness.

The external illumination of the kinescope screen reduces the apparent image contrast range for the same physical reasons.

The natural contrast of the meteorological objects subject to detection with the aid of television systems is sufficiently large. Thus, e.g., in observations of stratus clouds with the reflectivity $\rho_{ob} = 30\%$ against the background of land ($\bar{\rho}_m = 15\%$) we have K = 50%. For the middle tier of thunderstorm clouds or for an overcast, K increases to 70 - 90% above land and sea. The contrast of icebergs ($\bar{\rho}_{ob} = 40\%$) against the background of water ($\bar{\rho}_m = 8\%$) reaches 80%.

The reduction in K of ground objects owing to atmospheric influences is largely a function of weather conditions. This effect exerts relatively little influence on the detection of clouds, since the most turbid layers of the atmosphere are located near the earth surface. /337

The range of the television observation from the altitude H is clearly determined by geodetic and meteorological factors. For a sufficiently high H or for observations in a direction close to the nadir, the decisive factors are meteorological, chiefly the haze brightness B_h.

The performance of a television system is not, of course, determined by the image contrast range at the pickup-tube photocathode. Instead it is determined by the image reception contrast, i.e., by the contrast range of the signal U_1 at the tube output. On observation of an object against its background, the signal contrast range will be

$$U_1 = \frac{U_{ob} + U_h}{U_b + U_h}, \qquad (27.XIII)$$

where U_{ob}, U_b and U_h are the tube output signals in the presence of a photocathode affected by radiative fluxes from the object, the background and the haze, respectively.

The values of the signals entering into eq.(27.XIII) will be written as before (cf. Chapt.X) for ideally diffusing surfaces of large objects (filling the entire field of view of the lens) and observed at the nadir

$$\left.\begin{aligned} U_{ob} &= \frac{a_0 \omega R_\ell}{\pi} \int_{\lambda_1}^{\lambda_2} E_\lambda \rho_{ob.\lambda} P_\lambda \gamma_\lambda \, d\lambda \\ U_b &= \frac{a_0 \omega R_\ell}{\pi} \int_{\lambda_1}^{\lambda_2} E_\lambda \rho_{b.\lambda} P_\lambda \gamma_\lambda \, d\lambda \\ U_h &= \frac{a_0 \omega R_\ell}{\pi} \int_{\lambda_1}^{\lambda_2} \varkappa_\lambda E_\lambda P_\lambda \gamma_\lambda \, d\lambda \end{aligned}\right\}, \qquad (28.XIII)$$

where a is the area of the entrance pupil (aperture) of the lens; ω is the solid angle of view; R_ℓ is the load resistance of the tube; E_λ is the spectral energy density of the illumination, $\varkappa_\lambda$ is the spectral coefficient of the presence of haze in the atmosphere; $\rho_{ob\lambda}$ and $\rho_{b\lambda}$ are the reflection factors of the object and the background, respectively; $P_\lambda = P_{a\lambda} P_{o\lambda}$ is the spectral transmissivity, taking into account the transmissivity of the atmosphere $P_{a\lambda}$ and of the optics $P_{o\lambda}$; γ_λ is the current sensitivity of the tube with respect to the spectrum; /338
$\lambda_1 - \lambda_2$ is the spectral sensitivity range of the system.

The quantities $\varkappa_\lambda$ and P_λ, entering into eqs.(28.XIII), depend on the distance of observation for a given state of the atmosphere and the position of the sun relative to the line of sight (on illumination by direct solar radiation, television visibility may be completely absent).

Hence, U_1 will decrease with the increasing distance to the object as a function of the increase in turbidity (opacity) of the atmosphere, chiefly owing to the increase in the haze coefficient $\varkappa_\lambda$ in the spectral sensitivity range of the optics-pickup tube system. The optical distance of the television observation will be the maximum distance L_{max} at which, under given conditions, the contrast range of the signals U_1 at the tube output will be equal to the threshold value for a particular television system $U_{1\,threshold}$.

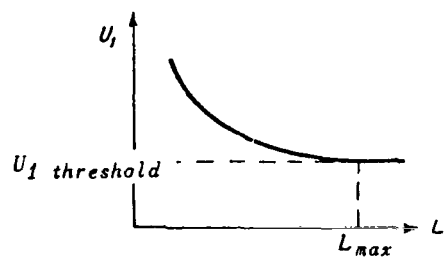

Fig.18.XIII Signal Contrast Range as a Function of Distance to Object.

The threshold contrast range $U_{1\,threshold}$ is one of the most important parameters of a television apparatus. Its magnitude depends on the tube sensitivity and varies within limits between 1.02 and 1.1 (Bibl.15).

Thus, the determination of the distance L_{max} of television observation is reduced to finding the signal contrast range for a given tube under given conditions of observation as a function of the distance to the object and its background $U_1 = f(L)$, and comparing the obtained quantity with the threshold contrast range $U_{1\,threshold}$ of the apparatus. The maximum distance L_{max} at which the equality $U_1 = U_{1\,threshold}$ is satisfied, represents the optical distance of television observation under given conditions (Fig.18.XIII).

The distance of television observation may be estimated with the aid of approximate equations (Bibl.15) derived on the basis of the following simplifications:

$$\left.\begin{aligned} U_{ob} &\approx \bar{E}\bar{\rho}_{ob}I \\ U_b &\approx \bar{E}\bar{\rho}_b I \\ U_h &\approx \bar{E}\bar{\varkappa}I \end{aligned}\right\} \quad \text{at} \quad I = \frac{a_0\omega R\ell}{\pi}\int_{\lambda_1}^{\lambda_2} P_\lambda \gamma_\lambda d\lambda, \qquad (29.XIII)$$

where $\bar{E}$, $\bar{\rho}$, and $\bar{\varkappa}$ are means with respect to the spectral sensitivity range $\lambda_2 - \lambda_1$.

Then it follows from eqs.(27.XIII) and (29.XIII) that /339

$$U_1 \approx 1 + \frac{\bar{\rho}_{ob} - \bar{\rho}_b}{\bar{\rho}_b + \bar{\varkappa}}. \qquad (30.XIII)$$

Hence, the operation of a television apparatus requires a sufficiently large contrast between the reflectivities of the object and the background, and the illumination of the necessary image details on the photocathode must exceed the limiting sensitivity E_t' of the apparatus.

Number of reproducible gradations of brightness. The number of gradations of brightness, i.e., of levels of variation in brightness discernible to the human eye, is determined by the threshold of the contrast sensitivity $K_{threshold}$ of the eye.

Suppose $K_{threshold}$ is known. Then the first discernible gradation B_1 in brightness is, in accordance with eq.(28.XIII), determined by the relation

$$B_1 = B_{min} + K_{thr.}B_1 = (1 - K_{thr.})^{-1}B_{min} \qquad (31.XIII)$$

and the second gradation

$$B_2 = B_1 + K_{thr.}B_2 = (1 - K_{thr.})^{-2}B_{min}. \qquad (32.XIII)$$

The last discernible gradation by analogy with eq.(32.XIII), is written as

$$B_{max} = (1 - K_{thr.})^{-n} B_{min} . \qquad (33.XIII)$$

From eq.(33.XIII) we obtain the number of discernible brightness gradations

$$n = -\frac{\ln K_{1\,max}}{\ln (1 - K_{thr.})} \approx \frac{2.3}{K_{thr.}} \log K_1 . \qquad (34.XIII)$$

It follows from eq.(34.XIII), that the maximum number of gradations of a good television image ($K_{1\,max} \approx 50$, $K_{threshold} = 0.2$ under conditions of observation of the cinescope screen) must be $n \approx 20$.

The process of the electron-optical conversion and transmission of the video signal is virtually nonlinear (Bibl.20) and may be expressed by a power function of the form

$$B_t = K_{1,0} B_0^{\gamma_0}, \qquad (35.XIII)$$

where B_t and B_0 are the brightnesses of elements at the input and output of the system; $K_{1,0}$ is the ratio between the mean brightnesses of the image and the object; γ_0 is the contrast factor which takes into account the distortions enroute from the transmitting to the receiving side.

The eq.(35.XIII) shows that $\gamma_0 > 1$ corresponds to a greater image-contrast range than the contrast range of the object, while $\gamma_0 < 1$ corresponds to a smaller image contrast range.

Thus, in television it is possible to vary the contrast range of the /340 dark or light image areas and thereby also to vary the number of the brightness gradations discernible in these areas. The special devices introduced for this purpose into the electrical tract are termed nonlinearity correctors or gamma-correctors.

The number of discernible brightness gradations in television systems is normally small. Thus, in industrial TV installations it is of the order of several unities, [usually n = 6 (Bibl.16)].

Resolving power and viewing range. The resolving power of a television system, which characterizes its ability to reproduce minor details of an image, determines the definition of the observed picture. As was previously pointed out (cf. Sect.1), it is estimated according to the number of resolvable lines z_a or optical lines N. The actual resolving power of a television system is determined with the aid of test patterns which contain a number of white and black lines of strips width, with gradations in hundreds of resolvable line numbers (300, 400, 500, etc. , with the width of strips and gradation intervals 300 being twice as large as at gradation 600). This may be exemplified by the well-known test pattern 0249, which is transmitted in television broadcasting.

Considering that the analyzing spot moves along rigorously definite trajectories, the actual resolving power of the system is smaller than the number of active scan lines z_a. In fact, suppose the number of the horizontal black and white lines of a test pattern is z_a and the diameter δ of the analyzing spot is determined by eq.(2.XIII). Then, the black and white strips of width δ will

be, on transmission, reproduced separately only when the center of the analyzing spot strikes exactly the center of the strip (Fig.19.XIII). If, on the other hand, the width of the test strips is doubled, then they will be reproduced separately regardless of their position with respect to the lines of the transmitting-side raster. Hence, the active number z_a of lines assures a resolving power of at least 0.5 z_a lines in the vertical direction. It is normally assumed that mean resolving power in the vertical direction is 0.75 z_a (Bibl.9). Hence, for z = 625 and α = 0.18 (cf. Sect.1 of this chapter), when z_a = 512 lines, the real mean resolving power in the vertical direction is 384 lines (television lines).

Real resolving power in the horizontal direction, as is known (cf. Sect.1 of this chapter), depends on the dimensions of the scanning spot and on the passband of the electrical tract. Given a passband whose upper frequency is taken in accordance with eq.(5.XIII), the real horizontal resolving power /341 will equal kz, i.e., it will exceed the real definition in the vertical even for a square frame (k = 1). So that the real vertical and horizontal resolutions could be the same, the upper frequency passed by the system may be reduced at least to

$$\nu_{max} = 0.75\frac{kz_a^2\nu_c}{2} = 0.375kz_a^2\nu_c. \qquad (36.XIII)$$

In a real system, moreover, the analyzing and synthesizing spots have finite dimensions and move continuously rather than in jumps. This results in limiting the horizontal resolving power of the system even when the frequency

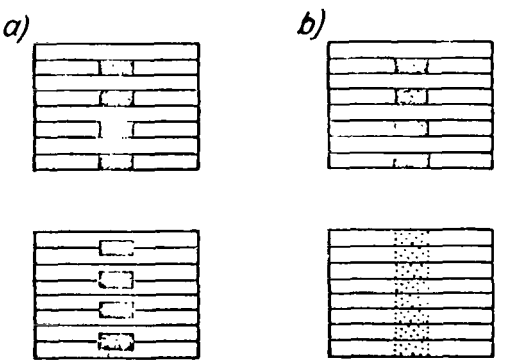

Fig.19.XIII Vertical Resolution as a Function of Raster Position.
a - Transmitted images; b - Received images.

passband of the television tract is unrestricted. The point is, that during the transmission of vertical black-and-white lines the video signal will be of a roughly rectangular shape only when the dimensions of the spot are small compared with the width of these strips. As the dimensions δ of the spot approach the width of the vertical strips, the video signal acquires a sine-wave shape and its amplitude (depth of modulation) decreases (Fig.20.XIII). In the event that strip width is smaller than δ, the variable component of the video signal

tends to zero. This effect is intensified by the analogous processes of a loss in depth of the modulation on the receiving side during reproduction of details of the object. This effect is termed aperture distortion. Owing to these /342 aperture distortions, the details of the image lose contrast with the decrease in size, until finally they cease to be resolvable and merge with the general gray background. The black-and-white boundaries get blurred to an extent which is roughly equal to the dimension of the greatest scan element (usually on the receiving side).

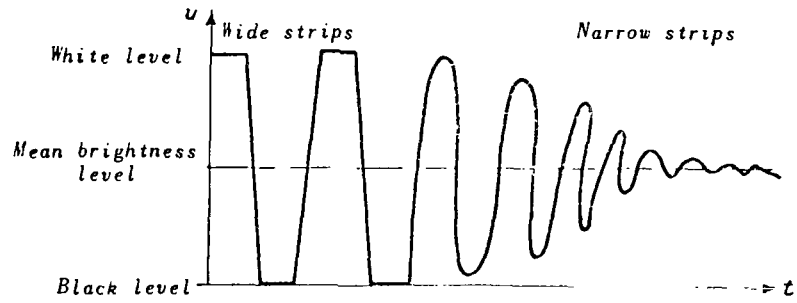

Fig.20.XIII Effect of Finite Dimensions of Scan Elements on the Video Signal Shape.

Sometimes the image definition can be increased by methods of aperture correction based on increasing the front steepness of the video signal in the electrical tract (Bibl.15).

The total resolving power of a television system is determined by the resolving power of its elements (lens, tube, electrical tract), each of which makes its own contribution to the obtained image. As in a photographic system (cf. Chapt.XII), the total resolving power is smaller than the resolving power of the individual elements. Assuming that the system consists of two basic elements: namely, of the lens and of the pickup tube with its electrical tract, then the resolving power N of the system may be estimated with the aid of eq.(4.XII). For example, for N_0 = 100 optical lines/mm = 200 scan lines/mm and the resolving power of the pickup tube N_t = 50 lines/mm (which corresponds to a vidicon with z_a = 500 lines and h = 10 mm), we have N = 40 lines/mm (at the center of the transmitted frame).

When evaluating the possibilities of a television device used to investigate a planet surface (Bibl.42), a vital factor to be considered is the terrain resolution, which depends on the altitude H of the system above the surface as well as on its angle of the field of view α (Fig.21.XIII). For a system resolving power equal to z_a active lines, the linear dimension Δl of the resolvable element on terrain surface will be, without taking its curvature into account, determined from the equation

$$\Delta l = \Delta l' \sec\gamma = \frac{\alpha}{z_a} D \sec\gamma = \frac{\alpha}{z_a} H \sec^2\gamma, \qquad (37.XIII)$$

where $\frac{\alpha}{z_a}$ is the angle at which the given resolvable terrain element Δl, /343

located at the angle γ to the vertical (in radians), can be seen, and D is the inclined distance to the element Δl.

From eq.(37.XIII), it follows, e.g., that from the altitude H = 700 km of the Tiros weather satellite a system with the fixed resolving power z_a = 500 television lines at h = 8 mm (Bibl.8) (N = 40 lines/mm), with respect to the entire field of view $\alpha = 104^\circ = 1.75$ rad, makes it possible to discriminate the elements $\Delta l_1 \approx 0.7$ km at the center of the field of view ($\gamma = 0$) and $\Delta l_2 \approx 2$ km at its edge. Allowing for aperture distortions and the deterioration in resolution at the edge of frame, it may be assumed that the resolution of the television devices installed in the first few Tiros satellites was 1 - 1.5 km at the center and 3 - 4 km at the edge of the field of view (Bibl.28).

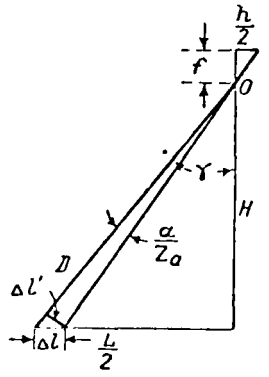

Fig.21.XIII Relation of Resolving Power z_a of the System to Terrain Resolution Δl.

Note that the terrain resolution at the center of the field of view (with respect to the nadir) may be estimated with the aid of the scale coefficient $m = \frac{f}{H}$ in the same manner as in the case of photographic systems (cf. Chapt.XII). Then we find that

$$\Delta l = \frac{h}{z_a}\frac{1}{m} = \frac{hH}{fz_a}, \qquad (38.XIII)$$

where h is the vertical dimension of the frame, on condition that the resolving power along and across the lines is the same; f is the focal length of the lens, in the focal plane of which the light-sensitive surface of the pickup tube is located.

The eq.(38.XIII) obviously is a particular case of being related with eq.(37.XIII).

These relations show, that the terrain resolving power of a television system is largely a function of the angle α of the field of view of the lens and of the altitude H. These parameters also determine the terrain viewing range (width of the viewing zone). A satellite traveling in a circular orbit retains

a fixed terrain resolving power and viewing range.

Disregarding the curvature of the viewed surface (cf. Chapt.XI) the width of viewing zone

$$L = 2H \tan\gamma_{max}. \qquad (39.XIII)$$

From eq.(39.XIII) we find that a zone having the approximate width L ≈ /344 ≈ 1100 km can be viewed from the altitude H = 700 km when the viewing angle is $\alpha = 2\gamma_{max} = 82^\circ$, whereas the broader zone L = 1850 km may be encompassed when $\alpha = 104^\circ$. Thus, the wide-angle optics of the camera of the Tiros satellite assures a terrain frame format of 1850 × 1850 km (Bibl.8).

The focal length of the lens, determinable from the requirement of the coincidence between dimensions of the image and the light-sensitive surface of the tube, shown in Fig.21.XIII, will be

$$f = \frac{h}{2} \cot\gamma_{max} \quad (\text{for } f \ll H), \qquad (40.XIII)$$

where h is the linear dimension of the light-sensitive surface.

For $\gamma_{max} = 52^\circ$ and h = 8 mm, as we can see, a short-focus length with f = = 4 × 0.78 = 3.12 mm is required.

The eq.(38.XIII) implies that the increase in focal length f (decrease in the angle α) leads to an increase in the terrain resolution. For satellite-borne television systems, such a method of increasing resolution, however, has a limited applicability, because it entails an increase in the weight and dimensions of the optics as well as in the need to incorporate devices compensating the temperature-induced variations in the focal length of the lens and to reduce the terrain-viewing range.

To assure the required illumination of the photosensitive tube surface, a sufficiently large relative lens aperture $\ddot{O} = \frac{d}{f}$ must be ensured (see eq.(5.XII). The optical systems used in American television cameras (Bibl.42) normally assure a relative aperture of f/1, i.e., $\ddot{O} = 1{:}1$ for the viewing angle $\alpha = 20 - 30^\circ$, and f/2.5 to f/4.5 for the viewing angle $\alpha = 60 - 90^\circ$.

The attempt to increase the terrain resolution leads to limitations on the possible observation time during the natural illumination. Thus, for the aperture f/50 (at the focus f = 6250 mm and an entrance pupil d = 125 mm), the image formed on the tube has an illumination not higher than 0.0001 of the terrain illumination E (Bibl.42). As the illumination approaches the limiting value of the tube sensitivity, the resolving power of the tube begins to decrease owing to image noise.

When evaluating the resolving power of television systems, it must, moreover, be considered that the terrain resolution of the area measuring $\Delta\ell\Delta\ell$ km^2 is not sufficient to allow the detecting of objects of the dimension $\Delta\ell$, since

the detection and recognition of an object depends on its dimensions and its configuration (given a sufficient contrast). Investigations (Bibl.42) show that the detection of an object requires its overlapping by 3 - 5 scan lines and its recognition is possible on overlapping by 10 - 20 lines. Thus, the terrain /345 reolution $\Delta\ell$ km means that it is possible to detect and recognize an object measuring approximately 10 $\Delta\ell$ or more.

For weather observations from a satellite, it is necessary to have a comparatively low terrain resolution of not more than 2 - 5 km (seats of thunderstorms, etc.). However, the determination of types of clouds according to their structural features requires a resolving power of the order of 150 m (Bibl.42).

Section 5. Television Equipment of Weather Satellites

The television equipment of weather satellites is designed for operative transmission of information about the distribution of clouds over the terrestrial globe. The orbits of these satellites are about 700 - 900 km high and are near-circular (Bibl.8, 33). The first few satellites in the Tiros series were equipped with two cameras, one wide-angle and one narrow-angle, which differed only in the focal length of their lenses and operated independently of one another. Certain satellites were equipped only with wide-angle cameras which provided the principal information, such as the Tiros III (Bibl.8).

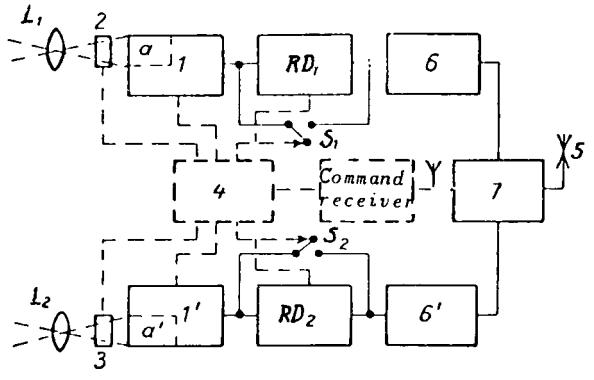

Fig.22.XIII Block Diagram of Television System of the Tiros I Satellite.

A block diagram of the TV equipment of the Tiros I satellite (Bibl.28) is shown in Fig.22.XIII. Pickup cameras 1 and 1' have vidicons a and a' of a special design (increased ability to withstand overloads, target shadow current reduced to a minimum) with the diameter of 12.5 mm and line number z = 500. Frame frequency ν_f = 0.5 cps makes it possible to narrow the video signal frequency band to 62.5 kilo-cps. The video signal amplifiers, located in cameras 1 and 1' are, except for the first stages (preamplifiers), assembled from semiconductor elements.

After amplification the video signal may be either directly transmitted /346

or recorded on magnetic tape in the recording devices RD_1 and RD_2 depending on the position of switches S_1 and S_2.

The television transmitters 6 and 6' of both cameras operate on antenna 5 across the separating filter 7. During the period while the satellite is within the range of communication with the receiving stations (6 - 12 min), 3.5 min are set aside for the transmission of the recorded signal, with a direct image transmission being carried out during the remainder of this period.

The ferromagnetic tape on which the images were recorded had a capacity of 32 frames (length 120 m).

The programmer 4, whose circuits are indicated by the broken line, contains the spacecraft timer. This timer determines the sequence of instructions and controls the operation of the cameras, their synchronizing generators, the shutters 2 and 3, and the recording devices. The programmer may be reset on instruction from the ground via the command radio link.

The shutters 2 and 3, located in the focal planes of the lenses L_1 and L_2, assured an exposure time of 0.0015 sec. The time interval between exposures was 10 sec.

The angle of the field of view of the camera 1 was 104° at a lens speed f/1.5, and that of the camera 2 was 12.7° at f/1.8. The dynamic operating range of the cameras varied within limits of from 0.7 to 66 lu (illumination on the photocathode).

The frame area (with respect to the nadir) of the first camera was 1200 × × 1200 km for the average orbiting altitude above the terrain, with a resolving power of 1.6 - 3.0 km. That of the second camera was 120 × 120 km and 0.3 - - 0.8 km, respectively.

The power required from the common source (solar batteries with a capacity of 30 watt and dry storage batteries) was 9 watt (Bibl.28). In the latest Tiros-series satellites, the angle of the field of view of the narrow-angle camera was increased to 75°, with the object of reducing the volume of the information subject to storage and transmission (Bibl.35).

The television apparatus installed in the Tiros VIII satellite has parameters similar to those of the equipment planned for the Nimbus satellites (Bibl.23, 26). It includes a vidicon with the diameter of 25 mm and the line number z = 800. The total weight of this instrument (pickup camera, timer, power converters and transmitter) is 9.6 kg.

The television cameras of the vidicon type used in the instrumentation of the Nimbus satellites were perfected by increasing their resolving power (roughly 2 ×), improving the linearity of the luminous characteristics of the pickup cameras and expanding their dynamic range (Bibl.33).

The principal television equipment of the satellite (AVCS) is designed /347 for daytime operation and consists of three pickup cameras, 1, 2, and 3 (Fig.23.XIII) with a common synchronization and control unit 9.

The pickup tubes are so aligned as to assure a broad terrain viewing range; the central camera (angle of field of view 37°) is directed with respect to the nadir, while the optical axes of the two side cameras are directed at the angle of 35° to the central. The overlap of the field of view of the cameras across the orbit thus is 2°. The entire system of cameras assures the scanning of a sector measuring 770 × 2900 km from the altitude of 900 km, with a photocathode illumination of at least 0.7 lu (Bibl.42).

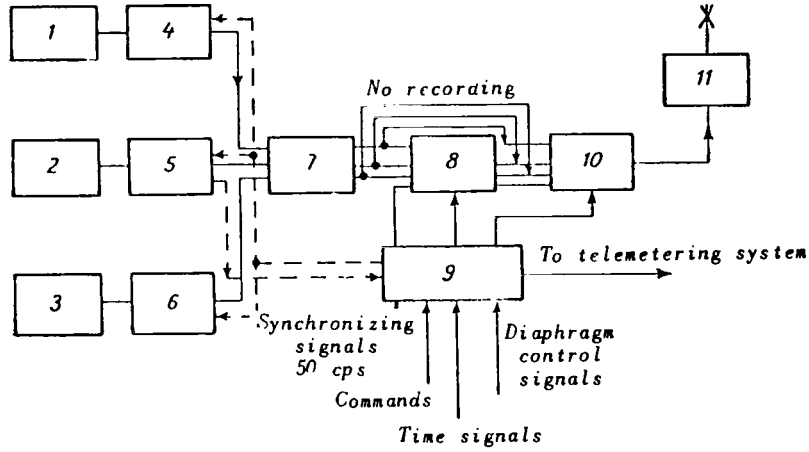

Fig.23.XIII Block Diagram of Television Equipment of the Nimbus Satellite.
1, 2, 3 - Pickup cameras; 4, 5, 6 - Video amplifiers; 7 - Frequency modulators; 8 - Storage device; 9 - Synchronization and control unit; 10 - Simultaneous transmission unit; 11 - Radio transmitter.

The intervals between exposures are 91 sec, which assures frame overlap by approximately 5% along the orbit. During a single orbit, each camera performs 32 exposures.

The terrain resolving power varies from 0.5 to 2.1 km over the frame. The frame-scanning period T_f = 5.3 sec; the frequency band ~60 kilo-cps.

Note that vidicons with similar parameters, installed in the Ranger VI spacecraft, enabled the operation of the television system in the presence of a landscape brightness reaching 10^{-4} stilb, and their dynamic range was 0.5 - - 5.4 lu-sec for the exposure time of 5 msec (Bibl.11).

The camera lenses (f = 17 mm) were equipped with diaphragms regulated /348 by means of a mechanism linked to the position of the solar-battery panels with respect to the sun. The relative apertures of the diaphragms varied within limits of from 1:4 to 1:16 for the fixed exposure time of 40 msec, which reduces blurring to not more than one-half of the width of a television line (Bibl.42).

To assure an adequate contrast range for cloud images, each camera contains

a brightness level calibrator (16 levels) in the shape of an optical wedge projected onto a tube, once the stable xenon lamp begins to glow.

The output video signals of all three cameras, which are mixed with synchronizing signals at the frequency of 50 kilo-cps, are frequency-modulated by subcarriers in the modulator unit 7 (Fig.23.XIII). The modulated subcarriers in the frequency band of 70 - 120 kilo-cps are admitted either to the direct transmission or to the storage device 8 with the capacity of 64 frames (per camera). The readout of the image signal with the simultaneous erasure of the recording is carried out on command given by radio from the earth.

In addition, the Nimbus satellite is equipped with a wide-angle (108°) operative television system (APT) containing an electrostatic-target vidicon. The increase in the frame scanning time (T_f = 200 sec) in this system makes it possible to reproduce the received image with the aid of a facsimile-telegraphy equipment. The resolving power with respect to a frame encompassing 2900 × 2900 km ranges from 1.7 to 8.5 km (z = 800).

At the receiving stations, the signals received from the weather satellites are recorded on magnetic tape and simultaneously pictured on the screen of the video receiver (at intervals of 8 sec), then photographed (not more than 32 frames per orbit).

During decoding of the received images, allowance is made for the distortions due to the optical system.

A most important element in the processing of television information is the reliable geographic identification of the received images. For this purpose, the identification is accomplished by graph-analytic methods correct to $\pm 2^{\circ}$ of the geographic latitude or, on utilizing the outlines of visible sectors of land on the image, to $\sim \pm 1^{\circ}$ (Bibl.17). Following this geographic identification, the frame is superposed on a synoptic chart in order to trace the cloud fields.

BIBLIOGRAPHY /349

CHAPTER I

1. Aleksandrov, S.G. and Fedorov, R.Ye.: Soviet Artificial Earth Satellites and Space Vehicles (Sovetskiye sputniki i kosmicheskiye korabli). Izd. Akad. Nauk SSSR, Moscow, 1961.
2. Alekseyev, P.P., et.al.: Rocket Studies of the Atmosphere (Raketnyye issledovaniya atmosfery). Meteorol. i Gidrol., No.8, 1957.
3. Vasil'yev, V.: American Lunar Spacecraft (Kosmicheskiye apparaty SShA dlya poletov na Lunu). Priroda, No.4, 1962.
4. Second Attempt to Study Venus in 1962 with the Aid of the "Mariner" Unmanned Spaceship (Vtorichnaya popytka issledovaniya Venery v 1962 g. s pomoshch'yu bespilotnogo kosmicheskogo korablya "Mariner"). Elektronika, Vol.35, No.30, 1962.
5. Kasatkin, A.M.: Upper-Atmosphere Optical Station for Studies of the Atmosphere (Vysotnaya opticheskaya stantsiya dlya issledovaniya atmosfery). Iskusstv. Sputniki Zemli, No.15, 1963.
6. King-Khili, D.: Artificial Satellites and Scientific Research (Iskusstvennyye Sputniki i nauchnyye issledovaniya). Izd. Inostr. Lit., Moscow, 1963.
7. Kondrat'yev, K.Ya.: Meteorological Satellites (Meteorologicheskiye sputniki). Gidrometeoizdat, Leningrad, 1963.
8. Kondrat'yev, K.Ya.: Meteorological Studies with the Aid of Rockets and Satellites (Meteorologicheskiye issledovaniya s pomoshch'yu raket i sputnikov). Gidrometeoizdat, Leningrad, 1962.
9. Kroshkin, M.G. and Samarin, V.G.: Five Years of Soviet Space Research (Pyat' let sovetskikh kosmicheskikh issledovaniy). Geofiz. Byul., No.13, 1963.
10. Kroshkin, M.G.: Geophysical Studies Conducted with the Aid of Rockets and Artificial Earth Satellites in the United States under the International Geophysical Year Program (Geofizicheskiye issledovaniya, provodimyye pri pomoshchi raket i iskusstvennykh sputnikov Zemli v SShA po programme Mezhdunarodnogo geofizicheskogo goda). Inform Bul., No.7, 1959.
11. - Space Weapon (Kosmicheskoye oruzhiye). Voyenizdat, Moscow, 1964.
12. - Electron Space System (Kosmicheskaya sistema "Elektron"). Kosmich. Issled., No.3, 1964.
13. - TASS Communique. Mars I in Flight (Soobshcheniye TASS. "Mars-I" v polete). Pravda, 28 January, 1963.
14. - Interplanetary Spacecraft Surveyor and Greencheese and Lunar Excursion Modules (Mezhplanetnyye letatel'nyye apparaty "Serveyyer" i "Grinchiz" i samokhodnyye ustanovki dlya issledovaniya Luny). Vopr. Raketnoy Tekhn., No.9, 1963.
15. Mezon, I.: Long Range Plan of Space Research (Perspektivnyy plan issledovaniya kosmosa). Elektronika, No.8, 1963.
16. Mikhnevich V.V.: Certain Results of Studies of the Upper Atmosphere and Outer Space Conducted with the Aid of Rockets and Satellites during hhe International Geophysical Year in the Soviet Union (Nekotoryye itogi

issledovaniya verkhney atmosfery i kosmicheskogo prostranstva pri pomoshchi raket i sputnikov v techeniye Mezhdunarodnogo geofizicheskogo goda v Sovetskom Soyuze). Geofiz. Bul., No.11, 1962.
17. - Equipment of the Pioneer Spacecraft (Oborudovaniye kosmicheskogo apparata "Pioner"). Elektronika, No.12, 1964.
18. - First Flight toward Mars (Pervyy polet k planete Mars). Pravda, December 15, 1962.
19. - Development of Rocket Engineering in the USSR (Razvitiye raketnoy tekhniki v SSSR). Izd. Akad. Nauk SSSR, Moscow, 1961.
20. - Rocket Studies of the Upper Atmosphere (Raketnyye issledovaniya verkhney atmosfery). Vopr. Raketnoy Tekhniki, No.5, 1956.
21. - Rockets and Satellites (Rakety i sputniki). Annaly MGG, Vol.VI, 1958.
22. - Rocket Studies of the Upper Atmosphere. Edited by R.L.Boyd and M.S.Seaton (Raketnyye issledovaniya verkhney atmosfery, pod red. R.L.Boyda i M.Dzh.Sitona). Izd. Inostr. Lit., Moscow, 1957. /350
23. Strasser, I.: Studies of the Moon's Surface with the Aid of Television Cameras (Issledovaniya poverkhnosti Luny s pomoshch'yu televizionnykh kamer). Elektronika, No.4, 1964.
24. Shvidkovskiy, Ye.G.: Rocket Meteorological Measurements (Raketnyye meteorologicheskiye izmereniya). Tr. Tsentr. Aerolog. Observ., No.29, 1960.
25. - Discoverer Success Speeds AF Plans. Missiles and Rockets, Vol.7, No.8, 1960.
26. - Explorer VII Continues Sending. Aviat. Week and Space Techn., Vol.73, No.17, 1960.
27. - Explorer VIII Mapping the Ionosphere. Aviat. Week and Space Techn., Vol.73, No.19, 1960.
28. Jones, L.: Upper Air Structure Measurements with Small Rockets. Space Research, Proc. II Symp., 1961.
29. Levis, C.: Juno II Fails to Put Satellite in Orbit. Aviat. Week and Space Techn., Vol.72, No.13, 1960.
30. - Satellite Sends Earth Image. Electron Eng., Vol.79, No.2, 1960.
31. - Space Research. Proc. I, II and III Symposium, North-Holland Publ. Co., 1960-1963.

CHAPTER II

1. Al'pert, Ya.L., Gurevich, A.V., and Pitayevskiy, L.P.: Artificial Satellites in Rarefied Plasma (Iskusstvennyye sputniki v razrezhennoy plazme). Izd. Nauka, Moscow, 1964.
2. Gdalevich, G.L.: Measurements of Electrostatic Field Intensity at the Surface of a Rocket during its Flight in the Ionosphere (Izmereniye napryazhennosti elektrostaticheskogo polya u poverkhnosti rakety vo vremya yeye poleta v ionosfere). Iskusstv. Sputniki Zemli, No.17, 1963.
3. Gringauz, K.I., Bezrukikh, V.V., Ozerov, V.D., and Rybchinskiy, R.Ye.: Studies of Interplanetary Ionized Gas, High-Energy Electrons and Corpuscular Radiation of the Sun with the Aid of Triple-Electrode Charged Particle Traps Borne by the Second Soviet Spaceship (Izucheniye mezhplanetnogo ionizovannogo gaza, energichnykh elektronov i korpuskulyarnogo izlucheniya Solntsa pri pomoshchi trekhelektrodnykh lovushek zaryazhennykh

chastits na vtoroy sovetskoy kosmicheskoy rakete). Iskusstv. Sputniki Zemli, No.6, 1961.
4. Gurevich, A.V.: Disturbances in the Ionosphere due to a Moving Body (O vozmushcheniyakh v ionosfere, vyzyvayemykh dvizhushchimsya telom). Iskusstv. Sputniki Zemli, No.7, 1961.
5. Kompaneyets, A.S.: Theoretical Physics (Teoreticheskaya fizika). Gostekhizdat, Moscow, 1957.
6. Kurt, V.G. and Moroz, V.I.: Potential of a Metallic Sphere in Interplanetary Space (Potentsial metallicheskogo shara v mezhplanetnom prostranstve). Iskusstv. Sputniki Zemli, No.7, 1961.
7. Mirtov, B.A.: Perturbances of a Gaseous Medium Caused by the Flight of a Satellite (Vozmushcheniya gazovoy spedy, vyzvannyye poletnom sputnika). Iskusstv. Sputniki Zemli, No.2, 1958.
8. Mirtov, B.A.: Gaseous Composition of the Earth's Atmosphere and Methods of its Analysis (Gazovyy sostav atmosfery Zemli i metody yego analiza). Izd. Akad. Nauk SSSR, Moscow, 1961.

CHAPTER III

1. Aleksandrov S.G. and Fedorov, R.Ye.: Soviet Satellites and Space Rockets (Sovetskiye sputniki i kosmicheskaya raketa). Izd. Akad. Nauk SSSR, Moscow, 1959.
2. Alekseyev, I.P., et al.: Rocket Studies of the Atmosphere (Raketnyye issledovaniya atmosfery). Meteorol. i Gidrol., No.8, 1957.
3. Al'pert, Ya.L., Gurevich, A.V., and Pitayevskiy, L.P.: Artificial Satellites in Rarefied Plasma (Iskusstvennyye sputniki v razrezhennoy plazme). Izd. Nauk, Moscow, 1964.
4. Baum, F.A., Kaplan, S.A., and Stanyukovich, K.P.: Introduction to Cosmical Gas Dynamics (Vvedeniye v kosmicheskuyu gazodinamiku). Fizmatgiz, Moscow, 1958.
5. Boyd, R.L. and Seaton (Siton), M.: Rocket Studies of the Upper Atmosphere (Raketnyye issledovaniya verkhney atmosfery). Izd. Inostr. Lit., Moscow, 1957.
6. Bulyga, A.V.: Analysis of the Circuits and Operating Regimes of Pirani-Type Vacuum-Gage Pressure Pickups (Analiz skhem i rezhimov raboty datchikov davleniya vakuummetrov tipa Pirani). Inzh.-Fiz. Zh., Vol.V, No.3, 1962.
7. Burgess, E.: Toward the Frontiers of Space (K granitsam prostranstva). Izd. Inostr. Lit., Moscow, 1957.
8. Grigor'yev, A.M.: Manometers for Measuring High Vacuum (Manometry dlya izmereniya vysokogo vakuuma). Pribory i Tekhn. Eskperim., No.6, 1959.
9. Grigor'yev, A.M. and Volkov, G.I.: Expansion of the Range of Pressures Measurable by Magnetic Electrical-Discharge Manometers (Rasshireniye diapazona davleniy, izmeryayemykh magnitnymi elektrorazryadnymi manometrami). Elektronika, Nauchn.-Tekhn. Sb., No.12, 1958. /351
10. Danilin, B.S., et al.: Problems of Measuring Pressure with the Aid of an Artificial Earth Satellite (Zadacha izmereniya davleniya a pomoshch'yu iskusstvennogo sputnika Zemli). Usp. Fiz. Nauk, Vol.63, No.1b, 1957.
11. Deshman, S.: Scientific Principles of Vacuum Engineering (Nauchnyye osnovy vakuumnoy tekhniki). Izd. Inostr. Lit., Moscow, 1950.

12. Ivanovskiy, A.I.: Certain Problems of the Interaction between the Measuring Cavity and the Flow of Rarefied Gas (Nekotoryye voprosy vzaimodeystviya izmeritel'noy polosti s potokom razrezhennogo gaza). Tr. Tsentr. Aerolog. Observ., No.56, 1964.
13. Kedrolivanskiy, V.N. and Sternzat, M.S.: Meteorological Instruments (Meteorologicheskiye pribory). Gidrometeoizdat, Leningrad, 1959.
14. Kondrat'yev, K.Ya. and Filipovich, O.P.: Thermal Regime of Upper Layers of the Atmosphere (Teplovoy rezhim verkhnikh sloyev atmosfery). Gidrometeoizdat, Leningrad, 1960.
15. Mikhnevich, V.V., et al.: Certain Findings on the Structural Parameters of the Atmosphere, Obtained with the Aid of the Third Artificial Earth Satellite (Nekotoryye rezul'taty opredeleniya strukturnykh parametrov atmosfery s pomoshch'yu tret'yego iskusstvennogo sputnika Zemli). Iskusstv. Sputniki Zemli, No.3, 1959.
16. Mikhnevich, V.V.: Preliminary Findings on Density of the Atmosphere above 100 km (Predvaritel'nyye rezul'taty opredeleniya plotnosti atmosfery vyshe 100 km). Iskusstv. Sputniki Zemli, No.2, 1958.
17. Mikhnevich, V.V. and Khvostikov, I.A.: Studies of Upper Layers of the Atmosphere (Izucheniye vysokikh sloyev atmosfery). Izv. Akad.Nauk SSSR, Ser. Geofiz., No.11, 1957.
18. Mikhnevich, V.V.: Measurements of Pressure in the Upper Atmosphere (Izmereniye davleniya v verkhney atmosfere). Usp. Fiz. Nauk, Vol.63, No.1b, 1957.
19. Mirta, S.K.: The Upper Atmosphere (Verkhnyaya atmosfera). Izd. Inostr. Lit., Moscow, 1955.
20. Morgulis, N.D.: Theory of the Ionization Manometer (Teoriya ionizatsionnogo manometra). Zh. Tekhn. Fiz., Vol.I, No.1, 1931.
21. Morgulis, N.D.: On the Theory of the Ionization Manometer (K teorii ionizatsionnogo manometra). Zh. Tekhn. Fiz., No.8, 1933.
22. Paty L.: Measuring the Superhigh Vacuum (Izmereniye sverkhvysokogo vakuuma). Pribory i Tekhn. Eksperim., No.6, 1959.
23. Penchko, Ye.A. and Khavkin, L.P.: Tetrode-Type Ionization Manometer (Tetrodnyy ionizatsionnyy manometr). Pribory i Tekhn. Eksperim., No.1, 1958.
24. - Rocket Studies of the Upper Atmosphere (Raketnyye issledovaniya verkhney atmosfery). Vopr. Raketnoy Tekhn., No.5, 1956.
25. Repnev, A.I.: Properties of the Upper Atmosphere and Articicial Earth Satellites (Svoystva verkhney atmosfery i iskusstvennyye sputniki Zemli). Tr. Tsentr. Aerolog. Observ., No.25, 1959.
26. Spitzer, L.: Physics of Completely Ionized Gas (Fizika polnost'yu ionizirovannogo gaza). Izd. Inostr. Lit., Moscow, 1957.
27. Tzyan, Kh.Sh.: Aerodynamics of Rarefied Gases (Aerodinamika razrezhennykh gazov). Sb. "Gazovaya dinamika", Izd. Inostr. Lit., Moscow, 1950.
28. Fedorov, Ye.K. and Skuridin, G.A.: Rockets and Artificial Earth Satellites in Studies of the Upper Atmosphere (Rakety i iskusstvennyye sputniki Zemli v issledovaniyakh verkhney atmosfery). Vestn. Akad. Nauk SSSR, No.8, 1957.
29. Khvostikov, I.A.: Upper Layers of the Atmosphere (Vysokiye sloi atmosfery). Gidrometeoizdat, Leningrad, 1964.
30. Shvidkovskiy, Ye.G.: Meteorological Rocket Measurements (Raketnyye meteorologicheskiye izmereniya). Tr. Tsentr. Aerolog. Observ., No.29, 1960.

31. Shklovskiy, I.S. and Kurt, V.G.: Determining the Density of the Atmosphere at the Altitude of 430 km by the Sodium Vapor Diffusion Method (Opredeleniye plotnosti atmosfery na vysote 430 km metodom diffuzii parov natriya). Iskusstv. Sputniki Zemli, No.3, 1959.
32. Shpitser, A.: The Earth's Atmosphere at Altitudes above 300 km (Zemnaya atmosfera na vysote svyshe 300 km). Sb. "Atmosfery Zemli i planet", Edited by D.Koyper, Izd. Inostr. Lit., Moscow, 1951.
33. Blamont, I.E., Donahue, T.M., and Lory, M.L.: Measurement of the Temperature in the Upper Atmosphere to 150 km in a Rocket Experiment. Phys. Rev. Letters, Vol.6, No.8, 1961.
34. Bartman, F.L. et al.: Upper-Air Density and Temperature by the Falling-Sphere Method. J. Appl. Phys., Vol.27, No.7, 1956.
35. Byram, E.T., Chubb, T.A., and Fridman, H.: The Solar X-Ray Spectrum and Density of the Upper Atmosphere. J. Geophys. Res., Vol.61, No.2, 1956.
36. Chubb, T.A.: The Use of Radiation Absorption and Luminescence in Upper Air Density Measurements. Ann. Geophys., Vol.14, No.1, 1958.
37. La Gow, H.E. and Ainsworth, I.: Arctic Upper-Atmosphere Pressure and Density Measurements with Rockets. J. Geophys. Res., Vol.61, No.1, 1956.
38. Jones, L.M.: Transit-Time Accelerometer. Rev. Sci. Instr., Vol.27, No.6, 1956.
39. Masterson, I.E., Hubert, W.E., and Thomas, R.: Wind and Temperature Measurements in the Mesophere by Meteorological Rockets. J. Geophys. Res., /352 Vol.66, No.7, 1961.
40. Nordberg, W. and Stroud, W.G.: Results of I.G.I. Rocket-Grenade Experiments to Measure Temperatures and Winds above the Island of Guam. J. Geophys. Res., Vol.66, No.2, 1961.
41. Sicinski, H.S., Spencer, N.W., and Dow, W.G.: Rocket Measurements of Upper Atmosphere Ambient Temperature and Pressure in the 30 to 75 Kilometer Region. J. Appl. Phys., Vol.25, No.2, 1954.
42. Spencer, N.W., Schulte, H.F., and Sicinski, H.S.: Rocket Instrumentation for Reliable Upper Atmosphere Temperature Determination. Proc. I.R.E. (Inst. Radio Engrs.), Vol.42, No.7, 1954.
43. Newell, H.E.: Sounding Rockets. New York-Toronto-London, 1959.
44. Massey, H.S.W.: Rocket Research in the Upper Atmosphere. Pergamon Press, 1954.

CHAPTER IV

1. Al'pert, Ya.L., Gurevich, A.V., and Pitayevskiy, A.P.: Artificial Satellites in Rarefied Plasma (Iskusstvennyye sputniki v razrezhennoy plazme). Izd. "Nauka", Moscow, 1964.
2. Bernard, D.: Modern Mass Spectrometry (Sovremennaya mass-spektrometriya). Izd. Inostr. Lit., Moscow, 1957.
3. Bochkova, O.V. and Shreyder, Ye.Ya.: Spectral Analysis of Gaseous Mixtures (Spektral'nyy analiz gazovykh smesey). Gostekhizdat, Moscow, 1955.
4. Vorsin, A.N., et al.: Radio-Frequency Mass Spectrometer (Radiochastotnyy mass-spektrometr). Izd. Akad. Nauk SSSR, Moscow, 1959.
5. Izakov, M.N.: Measurements of Temperature of the Atmosphere by Satellite-Borne Instruments (Ob izmerenii temperatury atmosfery pri pomoshchi priborov, ustanovlennykh na sputnike). Kosmich. Issled., Vol.I,

No.1, 1963.
6. Istomin, V.G.: Change in the Concentration of Positive Ions with Altitude according to the Data of Mass-Spectrometric Measurements Conducted with the Aid of the Third Satellite (Izmeneniye kontsentratsii polozhitel'nykh ionov s vysotoy po dannym mass-spektrometricheskikh izmereniy na tret'yem sputnike). Iskusstv. Sputniki Zemli, No.6, 1960.
7. Istomin, V.G.: Certain Results of Measurements of the Mass Spectrum of Positive Ions, Conducted with the Aid of the Third Soviet Artificial Earth Satellite (Nekotoryye rezul'taty izmereniya spektra mass polozhitel'nykh ionov na tret'yem sovetskom iskusstvennom sputnike Zemli). Iskusstv. Sputniki Zemli, No.4, 1960.
8. Istomin, V.G.: Geophysical Rocket Studies of the Ion Composition of the Earth's Atmosphere during the Years 1957-1959 (Issledovaniya ionnogo sostava atmosfery Zemli na geofizicheskikh raketakh v 1957-1959 gg.). Iskusstv. Sputniki Zemli, No.7, 1961.
9. Istomin, V.G.: Nitrogen Ions in the Earth's Upper Atmosphere and Night-Time Ionization in the E Region (Iony azota v verkhney atmosfere Zemli i nochnaya ionizatsiya v oblasti E). Dokl. Akad. Nauk SSSR, Vol.137, No.5, 1961.
10. Kostko, O.K. and Fedinskiy, A.V.: A Pumping System for Mass-Spectrometric Analysis of the Atmosphere (Sistema otkachki dlya mass-spektrometricheskogo analiza atmosfery). Tr. Tsentr. Aerolog. Observ., No.42, 1962.
11. Leont'yev, N.I. and Udovichenko, Yu.K.: The Omegatron (Omegatron). Pribory i Tekhn. Eksperim., No.1, 1959.
12. Martynkevich, G.M.: Reducing the Length of the Drift Space of a Direct-Flying Mass Spectrometer (O sokrashchenii dliny prostranstva dreyfa pryamoproletnogo mass-spektrometra). Tr. Tsentr. Aerolog. Observ., No.46, 1963.
13. Martynkevich, G.M.: In-Flight Mass Spectrometers (O poletnykh mass-spektrometrakh). Tr. Tsentr. Aerolog. Observ., No.42, 1962.
14. Matveyev, L.T.: Principles of General Meteorology (Osnovy obshchey meteorologii). Gidrometeoizdat, Leningrad, 1965.
15. Messi, G. and Barkhon, Ye.: Electron and Ion Collisions (Elektronnyye i ionnyye stolknoveniya). Izd. Inostr. Lit., Moscow, 1958.
16. Mirtov, B.A.: Gaseous Composition of the Earth's Atmosphere and Methods of its Analysis (Gazovyy sostav atmosfery Zemli i metody yego analiza). Izd. Akad. Nauk SSSR, Moscow, 1961.
17. Mitra, S.K.: The Upper Atmosphere (Verkhnyaya atmosfera). Izd. Inostr. Lit., Moscow, 1955.
18. Pavlenko, V.A., et al.: Radio-Frequency Mass Spectrometer for Analysis of the Ionic and Molecular Composition of Upper Layers of the Atmosphere (Radiochastotnyy mass-spektrometr dlya analiza ionnogo i molekulyarnogo sostava verkhnikh sloyev atmosfery). Pribory i Tekhn. Eksperim., No.6, 1960.
19. Pavlenko, V.A., Rafal'son, A.E., and Shutov, M.D.: A Series of Compact Mass Spectrometers for Investigating the Composition of Neutral and Ionized Gases of the Upper Layers of the Atmosphere (Seriya malogabaritnykh mass-spektrometrov dlya issledovaniya sostava neytral'nykh i ionizirovannykh gazov verkhnikh sloyev atmosfery). Kosmich. Issled., Vol.I, No.2, 1963.
20. Parshin, A.V., et al.: Methods of Reducing the Time Constant of the /353
Input Circuit of Electrometric Amplifiers (Metody umen'sheniya postoyannoy

vremeni vkhodnoy tsepi elektrometricheskikh usiliteley). Pribory i Tekhn. Eksperim., No.3, 1964.
21. Parshin, A.V. and Ustinova, L.B.: Electrometric Amplifiers on Subminiature Tubes (Elektrometricheskiye usiliteli na subminiatyurnykh lampakh). Pribory i Tekhn. Eksperim., No.3, 1964.
22. Pokhunkov, A.A.: Variation in the Mean Molecular Weight of Air in the Night Atmosphere at Altitudes of from 100 to 210 km according to Mass-Spectrometric Measurements (Ob izmenenii srednego molekulyarnogo vesa vozdukha v nochnoy atmosfere na vysotakh ot 100 do 210 km po mass-spektrometricheskim izmereniyam). Iskusstv. Sputniki Zemli, No.12, 1962.
23. Pokhunkov, A.A.: Distribution of Helium, Nitrogen and Argon in the Earth's Atmosphere up to Altitudes of 430 km (O raspredelenii geliya, azota i argona v zemnoy atmosfere do vysoty 430 km). Kosmich. Issled., Vol.I, No.1, 1963.
24. Pokhunkov, A.A.: Mass-Spectrometric Measurements of the Ion Distribution in the Earth's Atmosphere up to an Altitude of 430 km (Mass-spektrometricheskiye izmereniya raspredeleniya ionov v zemnoy atmosfere do vysoty 430 km). Kosmich. Issled., Vol.I, No.2, 1963.
25. Pokhunkov, A.A.: Gravitational Distribution, Composition and Structural Parameters of the Night-Time Atmosphere at Altitudes of 100 to 210 km (Gravitatsionnoye razdeleniye, sostav i strukturnyye parametry nochnoy atmosfery na vysotakh ot 100 do 210 km). Iskusstv. Sputniki Zemli, No.13, 1962.
26. Pokhunkov, A.A.: Possibilities for Using the Radio-Frequency Mass Spectrometer to Measure the Absolute Concentrations of Atomic Gases in the Upper Atmosphere (O vozmozhnosti izmereniya radiochastotnym mass-spektrometrom absolyutnykh kontsentratsiy atomarnykh gazov v verkhney atmosfere). Geomagnetizm i Aeronomiya, Vol.III, No.2, 1963.
27. Repnev, A.I.: Mass Selection in Tubes Moving in a Rarefied Gas (Massovaya selektsiya v trubkakh, dvizhushchikhsya v razrezhennom gaze). Tr. Tsentr. Aerolog. Observ., No.29, 1960.
28. Repnev, A.I. and Chizhov, A.F.: Certain Processes Occurring in the Mass Spectrometer (O nekotorykh protsessakh, protekayushchikh v mass-spektrometre). Tr. Tsentr. Aerolog. Observ., No.42, 1962.
29. Repnev, A.I.: Effect of the Recombination of Atoms in the Instrument on the Measurements of the Composition and Density of Upper Layers of the Up-Atmosphere (O vliyanii rekombinatsii atomov v pribore na izmereniya sostava i plotnosti vysokikh sloyev atmosfery). Tr. Tsentr. Aerolog. Observ., No.40, 1962.
30. Slutskiy, M.Ye., Zarkhin, B.I., and Pushkina, M.A.: Miniature Wideband Electrometric Amplifier (Malogabaritnyy shirokopolosnyy elektrometricheskiy usilitel'). Kosmich. Issled., Vol.I, No.2, 1963.
31. Fedynskiy, A.V.: Certain Findings on the Composition of Upper Layers of the Atmosphere (Nekotoryye dannyye o sostave verkhnikh sloyev atmosfery). Tr. Tsentr. Aerolog. Observ., No.42, 1962.
32. Fedynskiy, A.V.: Using the Electronic System of the FEU-34 Photomultiplier as an Amplifier of Weak Ion Currents (Primeneniye elektronnoy sistemy fotoumnozhitelya FEU-34 v kachestve usilitelya slabykh ionnykh tokov). Tr. Tsentr. Aerolog. Observ., No.42, 1962.
33. Khvostikov, I.A.: Upper Layers of the Atmosphere (Vysokiye sloi atmosfery). Gidrometeoizdat, Leningrad, 1964.
34. Chizhov, A.F.: The Omegatron Mass Spectrometer (Mass-spektrometr omegatron).

Tr. Tsentr. Aerolog. Observ., No.42, 1962.
35. Istomin V. and Pochunkov, A.: Mass-Spectrometer Measurements of Atmospheric Composition in the USSR. Space Research, Proc. III Space Symposium, North-Holland Publ. Co., Amsterdam, 1963.
36. Meadows, E.B. and Townsend, I.W.: Neutral Gas Composition of the Upper Atmosphere by a Rocket-Borne Mass Spectrometer. J. Geophys. Res., Vol.61, No.3, 1956.
37. Townsend, I.W., Meadows, E.B., and Pressly, E.C.: Rocket Exploration of the Upper Atmosphere. Edited by R.L.F.Boyd and M.S.Seaton, New York, 1954.
38. Wager, I.H.: Electronic Equipment for In-Flight Processing of Rocket-Borne Mass Spectrometer Data. J. Electron. Control, Vol.8, No.3, 1960.

CHAPTER V

1. Antonova, L.A. and Ivanov-Kholodnyy, G.S.: Experience in Measuring Corpuscular Radiation in the Upper Atmosphere (Opyt izmereniya korpuskulyarnogo izlucheniya v verkhney atmosfere). Izv. Akad. Nauk SSSR, Ser. Geofiz., No.5, 1960.
2. Aglintsev, K.K. et al.: Applied Dosimetry (Prikladnaya dozimetriya). Gosatomizdat, Moscow, 1962.
3. Blanter, S.G.: Industrial Electronics (Promyshlennaya elektronika), Moscow, 1963.
4. Bonch-Bruyevich, A.M.: Uses of Electron Tubes in Experimental Physics (Primeneniye elektronnykh lamp v eksperimental'noy fizike). Izd. 4-e (Sect.4e), Gostekhizdat, Moscow, 1956.
5. Brykina, L.S. et al.: Effect of High-Energy Protons on Semiconductor Detectors of Nuclear Radiation (Deystviye protonov vysokoy energii na poluprovodnikovyye detektory yadernykh izlucheniy). Kosmich. Issled., Vol.II, No.4, 1964.
6. Vernov, S.N. et al.: Measurements of Cosmic Radiation by means of an Artificial Earth Satellite (Izmereniye kosmicheskogo izlucheniya na iskusstvennom sputnike Zemli). Iskusstv. Sputniki Zemli, No.1, 1958. /354
7. Vernov, S.N. and Chudakov, A.Ye.: Studies of Cosmic Radiation and Corpuscular Fluxes by means of Rockets and Satellites (Issledovaniya kosmicheskoy radiatsii i korpuskulyarnykh potokov s pomoshch'yu raket i sputnikov). Usp. Fiz. Nauk, Vol.3, 1960.
8. Vernov, S.N. et al.: Studies of the Soft Component of Cosmic Rays beyond the Boundaries of the Atmosphere (Izucheniya myagkoy komponenty kosmicheskikh luchey za predelami atmosfery). Iskusstv. Sputniki Zemli, No.2, 1958.
9. Vernov, S.N.: Cosmic Rays and Outer Space (Kosmicheskiye luchi i kosmicheskoye prostranstvo). Vestn. Akad. Nauk SSSR, No.8, 1960.
10. Vernov, S.N. et al.: Study of Variations in Cosmic Radiation (Issledovaniye variatsii kosmicheskogo izlucheniya). Usp. Fiz. Nauk, Vol.63, No.1a, 1957.
11. Vernov, S.N. et al.: Measurements of Cosmic Radiation by means of an Artificial Earth Satellite (Izmereniye kosmicheskogo izlucheniya na iskusstvennom sputnike Zemli). Dokl. Akad. Nauk SSSR, Vol.120, No.6, 1958.
12. Vernov, S.N. and Chudakov, A.Ye.: Study of Cosmic Rays and Terrestrial

Corpuscular Radiation during Flights of Rockets and Satellites (Issledovaniye kosmicheskikh luchey i zemnogo korpuskulyarnogo izlucheniya pri poletakh raket i sputnikov). Usp. Fiz. Nauk, Vol.70, No.4, 1960.

13. Vernov, S.N. et al.: Radiation Studies during the Flights of the Interplanetary Mars 1 and Luna 4 Automatic Space Probes (Issledovaniya izlucheniy pri polete mezhplanetnykh avtomaticheskikh stantsiy "Mars-1" i "Luna-4"). Kosmich. Issled., Vol.II, No.4, 1964.
14. Vernov, S.N. et al.: Certain Results of Radiometric Measurements at the Altitudes 200 - 400 km during 1960-1963 (Nekotoryye rezul'taty radiometricheskikh izmereniy na vysote 200 - 400 km v techeniye 1960-1963 gg.). Kosmich. Issled., Vol.II, No.1, 1964.
15. Vakulov, P.V. et al.: Recording of Radiation during the Flights of Soviet Artificial Satellites and Space Rockets (Registratsiya izlucheniy pri poletakh sovetskikh iskusstvennykh sputnikov i kosmicheskikh raket). Geomagnetizm i Aeronomiya, Vol.I, No.6, 1961.
16. Vernov, S.N. et al.: Measurements of Radiation during the Flight of the Second Space Rocket (Izmereniya radiatsii pri polete vtoroy kosmicheskoy rakety). Iskuss Sputniki Zemli, Izd. Akad. Nauk SSSR, No.5, 1960.
17. - Problems of Dosimetry and Radiation Shielding (Voprosy dozimetrii i zashchity ot izlucheniy, No.2, Sb. pod red. V.I.Ivanova). Gosatomizdat, Moscow, 1963.
18. Vyazemskiy, V.O.: The Scintillation Method in Dosimetry (Stsintillyatsionnyy metod v radiometrii). Gosatomizdat, Moscow, 1962.
19. Gal'perin, Yu.I. and Krasovskiy, V.I.: Studies of the Upper Atmosphere with the Aid of the Cosmos 3 and Cosmos 5 Satellites (Issledovaniye verkhney atmosfery pri pomoshchi sputnikov "Kosmos-3" i "Kosmos-5"). Kosmich. Issled., Vol.I, No.1, 1963.
20. Grigor'yev, N.L., Kondrat'yeva, M.A., and Rapoport, I.D.: Cosmic Rays (Kosmicheskiye luchi). Fizmatgiz, Moscow, 1962.
21. Gringauz, K.I. et al.: Ionized Gas and Fast Electrons in the Neighborhood of Earth and in Interplanetary Space (Ionizovannyy gaz i bystryye elektrony v okrestnosti Zemli i v mezhplanetnom prostranstve). Iskusstv. Sputniki Zemli, No.6, 1960.
22. Dzhelli, D.: Cherenkov Radiation (Cherenkovskoye izlucheniye). Izd. Inostr. Lit., Moscow, 1960.
23. Dolgirev, Ye.I., Maleyev, P.I., and Sidorenko, V.V.: Detectors of Nuclear Radiation (Detektory yadernykh izlucheniy). Sudpromgiz, Leningrad, 1961.
24. Dobrotin, N.A.: Cosmic Rays (Kosmicheskiye luchi). Gostekhizdat, Moscow, 1954.
25. Dragun, G.S. et al.: Apparatus for Investigating the Nuclear Component of Cosmic Rays (Apparatura dlya issledovaniya yadernoy komponenty kosmicheskikh luchey). Iskusstv. Sputniki Zemli, No.9, Moscow, 1961.
26. Dorman, L.I.: Cosmic Rays and Geomagnetism (Kosmicheskiye luchi i geomagnetizm). Geomagnetizm i Aeronomiya, Vol.I, No.3, 1961.
27. Dorman, L.I.: Cosmic Ray Variations and Space Research (Variatsii kosmicheskikh luchey i issledovaniye kosmosa). Izd. Akad. Nauk SSSR, Moscow, 1963.
28. Key, Dzh. and Lebi, G.: Table of Physical and Chemical Constants (Tablitsa fizicheskikh i khimicheskikh postoyannykh). Fizmatgiz, Moscow, 1962.
29. Yeger, R.: Dosimetry and Protection against Radiation (Dozimetriya i zashchita ot izlucheniy). Gosatomizdat, Moscow, 1961.

30. Ivanov, V.I., Kenrim-Markus, I.B., and Kovalev, Ye.A.: Doses of Cosmic Radiation (Dozy kosmicheskoy radiatsii). Iskusstv. Sputniki Zemli, No.12, 1962.
31. - Studies of the Upper Atmosphere with the Aid of Rockets and Satellites (Issledovaniya verkhney atmosfery s pomoshch'yu raket i sputnikov, edited by G.S.Ivanova-Kholodnyy). Izd. Inostr. Lit., Moscow, 1961.
32. Krasovskiy, V.I. et al.: Detection of Corpuscles with the Aid of the Third Artificial Earth Satellite (Obnaruzheniye korpuskul pri pomoshchi tret'yego iskusstvennogo sputnika Zemli). Iskusstv. Sputniki Zemli, No.2, 1958.
33. Krasovskiy, V.I. et al.: Certain Features of Geoactive Corpuscles (Nekotoryye osobennosti geoaktivnykh korpuskul). Geomagnetizm i Aeronomiya, Vol.III, No.3, 1963. /355
34. Krasovskiy, V.I. et al.: Detection in the Upper Atmosphere of Electrons with Energies of about 10 kev (Obnaruzheniye v verkhney atmosfere elektronov s energiyey okolo 10 kev). Iskusstv. Sputniki Zemli, No.6, 1961.
35. Krasovskiy, V.I. et al.: Soft Corpuscles (Myagkiye korpuskuly). Kosmich. Issled., Vol.I, No.1, 1963.
36. Krasovskiy, V.I. et al.: Certain New Geophysical Research Findings Provided by the Satellites Cosmos 3 and Cosmos 5 (Nekotoryye novyye rezul'taty geofizicheskikh issledovaniy pri pomoshchi sputnikov "Kosmos-3" i "Kosmos-5"). Geomagnetizm i Aeronomiya, Vol.III, No.3, 1963.
37. - Silicon Counters for Spectrometry of Nuclear Particles (Kremniyevyye schetchiki dlya spektrometrii yadernykh chastits). Izd. Akad. Nauk SSSR, VDNKh, Moscow, 1961.
38. Kurnosova, L.V., Razorenov, L.A., and Fradkin, M.I.: Short-Time Increases in the Intensity of the Nuclear Component of Cosmic Rays, due to Solar Activity (Kratkovremennyye vozrastaniya intensivnosti yadernoy komponenty kosmicheskikh luchey, svyazannyye s deyatel'nost'yu Solntsa). Iskusstv. Sputniki Zemli, No.6, 1961.
39. Kurnosova, L.V., Razorenov, L.A., and Fradkin, M.I.: Studies of the Nuclear Component of Cosmic Rays with the Aid of the Third Space Rocket (Issledovaniye yadernoy komponenty kosmicheskikh luchey na tret'yey kosmicheskoy rakete). Iskusstv. Sputniki Zemli, No.8, 1961.
40. Kurnosova, L.V. et al.: Energy Spectra of Various Groups of Cosmic-Ray Nuclei according to Cherenkov-Counter Measurements by means of Spaceships-Satellites (Energeticheskiye spektry razlichnykh grupp yader kosmicheskikh luchey po izmereniyam cherenkovskimi schetchikami na korablyakh-sputnikakh). Iskusstv. Sputniki Zemli, No.12, 1962.
41. Kurnosova, L.V. et al.: Certain Results of Cosmic Ray Studies Conducted with the Aid of the Soviet Satellites and Space Rockets (Nekotoryye rezul'taty issledovaniy kosmicheskikh luchey, provedennykh na sovetskikh sputnikakh i kosmicheskikh raketakh). Tr. Fiz. Inst. Akad. Nauk SSSR, Vol.26, 1964.
42. Kurnosova, L.V. et al.: Investigation of Cosmic Rays during the Flight of the Second Space Rocket toward the Moon (Issledovaniye kosmicheskikh luchey pri polete vtoroy kosmicheskoy rakety na Lunu). Iskusstv. Sputniki Zemli, No.5, 1960.
43. Kurnosova, L.V., Razorenov, L.A., and Fradkin, M.I.: Heavy Nuclei in Primary Cosmic Radiation (Tyazhelyye yadra v pervichnom kosmicheskom izluchenii). Iskusstv. Sputniki Zemli, No.2, 1958.

44. Logachev, Yu.I.: Determination of the Electron Spectrum of the Outer Radiation Belt during the Flight of the Second Space Rocket (September 12, 1959) [Opredeleniye spektra elektronov vneshnego radiatsionnogo poyasa pri polete vtoroy kosmicheskoy rakety (12 sentyabrya 1959 g.)]. Geomagnetizm i Aeronomiya, Vol.I, No.1, 1961.
45. Science and Outer Space (Nauka v kosmose). Izd. Inostr. Lit., Moscow, 1964.
46. O'Brian, B. et al.: Absolute Intensities of the Fluxes of Electrons from the Core of the Earth's Outer Radiation Belt (Absolyutnyye intensivnosti istokov elektronov v serdtsevine vneshnego radiatsionnogo poyasa Zemli). Radiats. Poyasa Zemli, Izd. Inostr. Lit., Moscow, 1962.
47. The Mariner Studies the Cosmic Rays ("Mariner" issleduyet kosmicheskiye luchi). Elektronika, No.37, 1963.
48. Mel'nikov, V.V., Savenko, I.A., and Sazin, B.I.: Using Electrostatic Analyzers to Investigate the Soft Charged Component of Cosmic Radiation (O primenenii elektrostaticheskikh analizatorov dlya izlucheniya myagkoy zaryazhennoy komponenty kosmicheskogo izlucheniya). Geomagnetizm i Aeronomiya, Vol.I, No.6, 1961.
49. Matveyev, V.V. and Sokolov, A.D.: Photomultipliers in Scintillation Counters (Fotoumnozhiteli v stsintillyatsionnykh schetchikakh). Gosatomizdat, Moscow, 1962.
50. The Principles of Television, edited by Katayeva, S.I. (Osnovy televideniya. Pod red. Katayeva, S.I.). Svyaz'izdat, Moscow, 1940.
51. Pankov, S.F. et al.: Radiometric Instruments on the Second Soviet Spaceship-Satellite (Radiometricheskaya apparatura na vtorom sovetskom kosmicheskom korable-sputnike). Iskusstv. Sputniki Zemli, No.9, 1961.
52. Pavlov, V.V.: Semiconductor Measuring and Control Devices for Nuclear Energetics (Poluprovodnikovyye izmeritel'nyye i upravlyayushchiye ustroystva dlya yadernoy energetiki). Gosatomizdat, Moscow, 1962.
53. Semiconductor Triodes and Diodes, Chief Editor Nikolayevski, I.F. (Poluprovodnikovyye triody i diody. Sprav. pod red. I.F.Nikolayevskogo). Moscow, 1961.
54. Semiconductor-Type Radiation Counters (Poluprovodnikovyye schetchiki izlucheniy). Sb. Statei, Gosatomizdat, 1962.
55. Principles and Methods of the Registration of Elementary Particles (Printsipy i metody registratsii elementarnykh chastits). Edited by L.A.Artsimovich, Izd. Inostr. Lit., Moscow, 1963.
56. Rayder, D.: Engineering Electronics (Tekhnicheskaya elektronika). Sudpromgiz, Leningrad, 1961.
57. The Radiation Belts of the Earth (Raditsionnyye poyasa Zemli). Sb. Statei, Izd. Inostr. Lit., Moscow, 1962.
58. The Radiation Danger in Spaceflights, edited by V.E.Nesterova (Radiatsionnaya opasnost' pri kosmicheskikh poletakh, Pod red. V.Ye.Nesterova). Izd. "Mir", 1964.
59. Savenko, I.A., Pisarenko, N.F., and Shavrin, P.I.: Dosimetric Measurements on the Second Soviet Spaceship-Satellite (Dozimetricheskiye izmereniya na vtorom sovetskom kosmicheskom korable-sputnike). Iskusstv. Sputniki Zemli, No.9, 1961. /356
60. Savenko, I.A., Shavrin, N.P., and Pisarenko, N.F.: Soft Corpuscular Radiation at the Altitude of 320 km in the Near-Equatorial Latitudes (Myagkoye korpuskulyarnoye izlucheniye na vysote 320 km v priekvatorial'nykh shirotakh). Iskusstv. Sputniki Zemli, No.13, 1962.
61. Savenko, I.A., Pisarenko, N.F., and Shavrin, P.I.: Spaceflights and Radia-

tion Danger (Kosmicheskiye polety i radiatsionnaya opasnost'). Priroda, No.2, 1962.
62. Savenko, I.A. et al.: The Radiation Situation in Outer Space on the Eve of the Launching of the Vostok 3 and Vostok 4 Spaceships (Radiatsionnaya obstanovka v kosmose nakanune poleta kosmicheskikh korabley "Vostok-3" i "Vostok-4"). Kosmich. Issled., Vol.I, No.1, 1963.
63. Samoylov, V.F. and Makoveyev, V.G.: Pulse Engineering (Impul'snaya tekhnika). Izd. "Svyaz", 1964.
64. Handbook on Dosimetric, Radiometric and Electron-Physics Instruments, Counters, Scintillators and Photomultipliers (Spravochnik po dozimetricheskim, radiometricheskim i elektronnofizicheskim priboram, schetchikam, stsintillyatoram i fotoumnozhitelyam). Gosatomizdat, Moscow, 1959.
65. Solar Corpuscular Fluxes and their Interaction with the Earth's Magnetic Field, edited by V.P.Shabanski (Solnechnyye korpuskulyarnyye potoki i ikh vzaimodeystviye s magnitnym polem Zemli, Pod red. V.P.Shabanskogo). Izd. Inostr. Lit., Moscow, 1962.
66. Solar Activity and Cosmic Rays (Solnechnaya aktivnost' i kosmicheskiye luchi). Izd. Inostr. Lit., Moscow, 1962.
67. Encyclopedic Dictionary of Physics (Fizicheskiy entsiklopedicheskiy slovar'). Moscow.
68. Frank, I.M. and Cherenkov, P.A.: Nobel Prize Lectures (Nobelevskiye lektsii). Moscow, 1960.
69. Frolkin, V.T.: Pulse Engineering (Impul'snaya tekhnika). Izd. "Sov. Radio", Moscow, 1960.
70. Chechik, N.O., Faynshteyn, S.M., and Pifshits, T.M.: Electron Multipliers (Elektronnyye umnozhiteli). Gostekhizdat, 1963.
71. Shafer, Yu.G. and Yarygin, A.V.: Measurements of Cosmic Rays by means of Geophysical Rockets (Izmereniya kosmicheskikh luchey na geofizicheskikh raketakh). Iskusstv. Sputniki Zemli, No.4, 1960.
72. Arnoldy, R., Hoffman, R., and Winckler, I.: Solar Cosmic Rays and Soft Radiation Observed at 5000000 Kilometers from Earth. J. Geophys. Res., Vol.65, p.3004, 1960.
73. Biermann, L.: Solar Corpuscular Radiation and the Interplanetary Gas. Observatory, Vol.77, p.109, 1957.
74. Denney, I.M.: Radiation Damage to Satellite Solar Cell Power Systems. Energy Conversion for Space Power, Vol.3, Academic Press, New York, 1961.
75. Van Allen, I.A.: The Geomagnetically Trapped Radiation. J. Geophys. Res., Vol.64, p.1683, 1959.
76. Winkler, I.: Balloon Study of High Altitude Radiations during the International Geophysical Year. J. Geophys. Res., Vol.65, p.1331, 1960.
77. Space Research. Proc. of the Space Science Symposium, Part I-III, N-H.P.C. (North-Holland Publ.Co.), 1960-1963.
78. Van Allen, I., Frank, L., and O'Brian, H.: Satellite Observations of the Artificial Radiation Belt of July 1962. J. Geophys. Res., Vol.68, No.3, 1963.
79. Freeman, I.W. and Van Allen, I.A.: Explorer 12 Observations of the Magnetospheric Boundary and the Associated Solar Plasma on September 13, 1961. J. Geophys. Res., Vol.68, No.8, 1963.
80. Brown, H.L. et al.: The Spacecraft Radiation Experiments. Bell System, Tech. J., Vol.42, No.4, pt.I, 1963.

CHAPTER VI

1. Burdo, R.E., Chapman, D., and Mayeda, K.: Studies of the Ionosphere by means of Rockets and Satellites (Issledovaniya ionosfery pri pomoshchi raket i sputnikov). Kosmich. Issled., Vol.III, No.1, 1965.
2. Granovskiy, V.L.: The Electrical Current in Gases (Elektricheskiy tok v gaze). Gostekhizdat, Moscow-Leningrad, 1952.
3. Krasovskiy, V.I. et al.: Certain Features of Geoactive Corpuscles (Nekotoryye osobennosti geoaktivnykh korpuskul). Geomagnetizm i Aeronomiya, Vol.III, No.3, 1963.
4. Gringauz, K.I., Bezrukikh, V.V., and Ozerov, V.D.: Results of Measurements of Positive Ion Concentration in the Ionosphere by the Ion Trap Method, Performed on the Third Soviet Earth's Satellite (Rezul'taty izmereniy kontsentratsii polozhitel'nykh ionov v ionosfere metodom ionnykh lovushek na tret'yem sovetskom sputnike Zemli). Iskusstv. Sputniki Zemli, No.6, 1961.
5. Gringauz, K.I.: Structure of Ionized Gaseous Envelope of the Earth according to Data on Direct Measurements of Local Charged Particle Concentrations, Performed in the USSR (Stroyeniye ionizovannoy gazovoy obolochki Zemli po dannym pryamykh izmereniy lokal'nykh kontsentratsiy zaryazhennykh chastits, provedennykh v SSSR). Iskusstv. Sputniki Zemli, No.12, 1962. /357
6. Gringauz, K.I.: Certain Results of Experiments Performed in Interplanetary Space with the Aid of Charged Particle Traps on Soviet Space Rockets (Nekotoryye rezul'taty opytov, provedennykh v mezhplanetnom prostranstve s pomoshch'yu lovushek zaryazhennykh chastits na sovetskikh kosmicheskikh raketakh). Iskusstv. Sputniki Zemli, No.12, 1962.
7. Gringauz, K.I. et al.: Direct Observations of Solar Plasma Fluxes at a Distance of the Order of 900,000 km from Earth on 17 February 1961 and Simultaneous Observations of the Geomagnetic Field (Pryamyye nablyudeniya potokov solnechnoy plazmy na rasstoyanii poryadka 900 000 km ot Zemli 17 fevralya 1961 g. i odnovremennyye nablyudeniya geomagnitnogo polya). Iskusstv. Sputniki Zemli, No.15, 1963.
8. Gringauz, K.I. et al.: Results of Experiments with Three-Electrode Charged Particle Traps in the Second Radiation Belt and in the Outermost Charged-Particle Belt (K rezul'tatam opytov s trekhelektrodnymi lovushkami zaryazhennykh chastits vo vtorom radiatsionnom poyase i v samom vneshnem poyase zaryazhennykh chastits). Iskusstv. Sputniki Zemli, No.15, 1963.
9. Gringauz, K.I. et al.: Study of the Interplanetary Ionized Gas, High-Energy Electrons and Corpuscular Radiation of the Sun by means of Three-Electrode Charged Particle Traps on the Second Soviet Space Rocket (Izucheniye mezhplanetnogo ionizovannogo gaza, energichnykh elektronov i korpuskulyarnogo izlucheniya Solntsa pri pomoshchi trekhelektrodnykh lovushek zaryazhennykh chastits na vtoroy sovetskoy kosmicheskoy rakete). Iskusstv. Sputniki Zemli, No.6, 1961.
10. Khok, G., Sitsinskiy, G.S., and Spenser, N.V.: Measurements of Temperature and Electron Concentration in the Ionosphere with the Aid of Langmuir's Probe (Izmereniya temperatury i elektronnoy kontsentratsii v ionosfere s pomoshch'yu zonda Langmyura). Nauchn. Ispol'z. Iskusstv. Sputnikov Zemli, Izd. Inostr. Lit., Moscow, 1960.
11. Bridge, S., Dilworth, C., and Rossi, B.: An Instrument for the Investigation of Interplanetary Plasma. J. Geophys. Res., Vol.65, No.10, 1960.

12. Bridge, H.S. et al.: Plasma Probe Instrumentation on Explorer X. Space Res., Proc. III Symposium, North Holland Publ. Co., 1963.
13. Boyd, R.L.F. and Willmore, A.P.: A Method of Studying the Energy Distributions of Sonospheric Ions and Electrons. Space Research, Proc. III Symposium, North Holland Publ. Co., 1963.
14. Bourdeau, R.E.: Ionospheric Results with Sounding Rockets and the Explorer VIII Satellite. Space Research, Proc. II Symposium, North Holland Publ. Co., 1961.
15. Johnson, J.: Two Stage Single Cycle Radio Frequency Mass Spectrometer. Space Research. Proc. III Symposium, North Holland Publ. Co., 1963.
16. Ichimiya, T., Takayama, K., and Aono, I.: A Probe for Measuring Ion Density in the Ionosphere. Space Research. Proc. I Symposium, North Holland Publ. Co., 1960.

CHAPTER VII

1. Aleksandrov, S.G. and Fedorov, R.Ye.: Soviet Satellites and Space Rockets (Sovetskiye sputniki i kosmicheskiye rakety). Izd. Akad. Nauk SSSR, Moscow, 1959.
2. Grinkhau, Dzh. and Lovell, A.: The Upper Atmosphere and Meteors, from "Physics of the Upper Atmosphere", edited by D.A.Ratklifa (Verkhnyaya atmosfera i meteory, Sb. "Fizika verkhney atmosfery", pod red. D.A. Ratklifa). Fizmatgiz, Moscow, 1963.
3. Micrometeorite Studies with the Aid of Instruments Installed in an Artificial Earth Satellite (Issledovaniye mikrometeoritov s pomoshch'yu apparatury, ustanovlennoy na iskusstvennom sputnike Zemli). Elektronika, Vol.34, No.34, 1961.
4. Isakovich, M.A. and Roy, N.A.: Acoustic Method of Measuring the Mechanical Parameters of Micrometeorites (Akusticheskiy metod izmereniya mekhanicheskikh parametrov meteoritov). Iskusstv. Sputniki Zemli, No.2, 1958.
5. The Utilization of Solar Energy in the Exploration of Space, edited by V.A.Baum (Ispol'zovaniye solnechnoy energii pri kosmicheskikh issledovaniyakh, red. V.A.Baum). "Mir", Moscow, 1964.
6. Karachevtsev, I.D.: The Effect of Micrometeor Particles on the Optical Surfaces of Telescopes beyond the Earth's Atmosphere (Vozdeystviye mikrometeornykh chastits na opticheskiye poverkhnosti teleskopov za atmosferoy Zemli). Iskusstv. Sputniki Zemli, No.15, 1963.
7. Komissarov, O.D. et al.: Rocket and Satellite Micrometeorite Studies (Issledovaniye mikrometeoritov na raketakh i sputnikakh). Iskusstv. Sputniki Zemli, No.2, 1958.
8. Kroshkin, M.G.: Geophysical Studies Conducted with the Aid of Rockets and Artificial Earth Satellites in the United States under the International Geophysical Year Program (Geofizicheskiye issledovaniya, provodimyye pri pomoshchi raket i iskusstvennykh sputnikov Zemli v SShA po programme mezhdunarodnogo geofizicheskogo goda). Inform. Byul. MGG. No.7. 1959.
9. Lavrent'yev, M.A.: The Problem of Breakdown at Escape Velocities (Problema probivaniya pri kosmicheskikh skorostyakh). Iskusstv. Sputniki Zemli, No.3, 1959.
10. Mirtov, B.A.: Meteoritic Matter and Problems of the Geophysics of the /358

Upper Layers of the Atmosphere (Meteornaya materiya i voprosy geofiziki vysokikh sloyev atmosfery). Iskusstv. Sputniki Zemli, No.4, 1960.
11. Nazarova, T.N.: Studies of Meteor Dust by means of Rockets and Artificial Earth Satellites (Issledovaniye meteornoy pyli na raketakh i iskusstvennykh sputnikakh Zemli). Iskusstv. Sputniki Zemli, No.12, 1962.
12. Nazarova, T.N.: Results of the Investigation of Meteoritic Matter by means of Instruments Installed in Space Rockets (Rezul'taty issledovaniya meteornogo veshchestva s pomoshch'yu priborov, ustanovlennykh na kosmicheskikh raketakh). Iskusstv. Sputniki Zemli, No.5, 1960.
13. Rez, I.S.: Correlation between Piezoelectric and Elastic Characteristics of Crystals (Korrelyatsiya mezhdu p'yezoelektricheskimi i uprugimi kharakteristikami kristallov). Vopr. Radioelektroniki, Ser.III, Radiodetali i Uzly, No.7, 1960.
14. Stanyukovich, K.P.: Elements of the Theory of the Collision of Solids at High (Cosmic) Velocities [Elementy teorii udara tverdykh tel s bol'shimi (kosmicheskimi) skorostyami]. Iskusstv. Sputniki Zemli, No.4, 1960.
15. Turichin, A.M.: Electrical Measurements of Non-Electric Quantities (Elektricheskiye izmereniya neelektricheskikh velichin). Gosenergoizdat, Moscow, 1959.
16. Dubin, M.: I.G.I. Micrometeorite Measurements. Space Research, Proc. I Symposium, North Holland Publ. Co., 1960.
17. Kornhauser, M.: Satellite Pressure Loses Caused by Meteoroid Impacts. ARS (Am. Rocket Soc.) J., Vol.30, No.5, 1960.

CHAPTER VIII

1. Amosov, A.P., Rotshteyn, A.Ya., and Tsirel', V.S.: The AYaAM-6 Nuclear Aeromagnetometer and the Results of its Preliminary In-Flight Tests (Yadernyy aeromagnitometr AYaAM-6 i rezul'taty yego predvaritel'nykh letnikh ispytaniy). Geofiz. Priborostr., No.6, 1960.
2. Afanas'yev, A.P.: The Possibilities for Constructing a Ferrosounding Magnetometer Operating on the Sum of Even Harmonics (O vozmozhnosti postroyeniya ferrozondovogo magnitometra, rabotayushchego na summe chetnykh garmonik). Sb. proizvodstvenno-tekhnicheskoy inform. po geofiz. priborostroeniyu, No.3, 1959.
3. Gdalevich, G.L.: Measurements of Electrostatic-Field Intensity at the Rocket Surface during Rocket Flights in the Ionosphere (Izmereniye napryazhennosti elektrostaticheskogo polya u poverkhnosti rakety vo vremya yeye poleta v ionosfere). Iskusstv. Sputniki Zemli, No.17, 1963.
4. Dolginov, Sh.Sh. and Pushkov, N.V.: Results of Measurements of the Earth's Magnetic Field from a Space Rocket (Rezul'taty izmereniya magnitnogo polya Zemli na kosmicheskoy rakete). Dokl. Akad. Nauk SSSR, Vol.129, No.1, 1959.
5. Dolginov, Sh.Sh. et al.: Study of the Moon's Magnetic Field (Issledovaniye magnitnogo polya Luny). Geomagnetizm i Aeronomiya, Vol.I, No.1, 1961.
6. Dolginov, Sh.Sh. et al.: Magnetic Measurements Performed by the Automatic Interplanetary Venus Probe (Magnitnyye izmereniya avtomaticheskoy mezhplanetnoy stantsii k Venere). Geomagnetizm i Aeronomiya, Vol.II, No.1, 1962.
7. Dolginov, Sh.Sh. and Pushkov, N.V.: Studies of the Magnetic Field of Outer

Space (Issledovaniye magnitnogo polya v kosmicheskom prostranstve). Kosmich. Issled., Vol.I, No.1, 1963.
8. Dolginov, Sh.Sh. et al.: Magnetic Measurements on the Second Space Rocket (Magnitnyye izmereniya na vtoroy kosmicheskoy rakete). Iskusstv. Sputniki Zemli, No.5, 1960.
9. Dolginov, Sh.Sh., Zhuzgov, L.N., and Selyutin, V.A.: Magnetometric Instruments of the Earth's Third Artificial Soviet Satellite (Magnitometricheskaya apparatura tret'yego sovetskogo iskusstvennogo sputnika Zemli). Iskusstv. Sputniki Zemli, No.4, 1960.
10. Imyanitov, I.M. and Shvarts, Ya.M.: Methods of Combatting the Interference Currents Arising at the Input of the Electrostatic Flux Meter during its Operation in a Conducting Medium (Metody bor'by s meshayushchimi tokami, voznikayushchimi na vkhode elektrostaticheskogo flyuksmetra pri yego rabote v provodyashchey srede). Iskusstv. Sputniki Zemli, No.3, 1959.
11. Imyanitov, I.M. and Shvarts, Ya.M.: Measurements of Electrostatic Field Intensity on the Third Artificial Earth Satellite (Izmereniye napryazhennosti elektrostaticheskogo polya na tret'yem iskusstvennom sputnike Zemli). Iskusstv. Sputniki Zemli, No.17, 1963.
12. Imyanitov, I.M., Gdalevich, G.L., and Shvarts, Ya.M.: Measurements of the Electrostatic Field Intensity at the Surface of the Geophysical Rockets Traveling in the Upper Layers of the Atmosphere (Izmereniye napryazhennosti elektrostaticheskogo polya u poverkhnosti geofizicheskikh raket, dvizhushchikhsya v verkhnikh sloyakh atmosfery). Iskusstv. Sputniki Zemli, No.17, 1963.
13. Imyanitov, I.M.: Instruments and Techniques for Investigating the Electricity of the Atmosphere (Pribory i metody dlya izucheniya elektrichestva atmosfery). Gostekhizdat, Moscow, 1957.
14. Imyanitov, I.M.: Measurements of Electrostatic Fields in the Upper Layers of the Earth's Atmosphere (Izmereniye elektrostaticheskikh poley v verkhnikh sloyakh zemnoy atmosfery). Usp. Fiz. Nauk, Vol.63, No.1, 1957.
15. Pushkov, N.V. and Dolginov, Sh.Sh.: Satellite and Rocket Studies of the Earth's Magnetic Field (Issledovaniye magnitnogo polya Zemli na iskusstvennykh sputnikakh i raketakh). Usp. Fiz. Nauk, Vol.63, No.4, 1957. /359
16. Pasynkov, V.V., Savel'yev, T.A., and Chirkin, L.K.: Nonlinear Semiconductor Resistors (Nelineynyye poluprovodnikovyye soprotivleniya). Sudpromgiz, Leningrad, 1962.
17. Rosenblatt, M.A.: Rectification in Nonlinear Symmetrical Electrical and Magnetic Circuits (Vypryamleniye v nelineynykh simmetrichnykh elektricheskikh i magnitnykh tsepyakh). Dokl. Akad. Nauk SSSR, Vol.68, No.3, 1949.
18. Shvarts, Ya.M.: On the Theory of the Operation of an Electrostatic Flux Meter in Plasma (K teorii raboty elektrostaticheskogo flyuksmetra v plazme). Radiotekhn. i Elektron., No.1, 1961.
19. Yanovskiy, B.M.: Terrestrial Magnetism, Part II (Zemnoy magnetizm, ch.II). Izd. Leningr. Gos. Univ., 1963.
20. Bloom, A.L. and Johnson, L.E.: A Magnetometer for the Satellite. Electronic Industr. and Tele. Techn., Vol.16, No.8, 1957.
21. Bourdeau, R.E. et al.: Ionospheric Measurements Using Environmental Sampling Techniques. Space Research, Proc. II Symposium, North Holland Publ. Co., 1960.
22. Ruddock, K.A.: Optically Pumped Rubidium Vapor Magnetometer for Space

Experiments. Space Research, Proc. II Symposium, North Holland Publ. Co., 1961.
23. Sonett, C.P. et al.: A Radial Rocket Survey of the Distant Geomagnetic Field. J. Geophys. Res., Vol.65, No.1, 1960.
24. Heppner, I.P., Skillman, T.L., and Cain, I.C.: Contributions of Rockets and Satellites to the World Magnetic Survey. Space Research, Proc. II Symposium, North Holland Publ. Co., 1961.

CHAPTER IX

1. Arkhangel'skaya, V.A. and Razumova, T.K.: Quantum Yield of the Thermoluminescence of Phosphorus (Kvantovyy vykhod termolyuminestsentsii fosfora). Sb. Statei "Optika i Spektroskopiya", Izd. Akad. Nauk SSSR, 1963.
2. Arkhangel'skaya, V.A., Vaynberg, B.I., and Razumova, T.K.: A Simple Method of Determining the Transmittance of Certain Optical Materials in the Schumann Region of the Spectrum (Prostoy sposob opredeleniya propuskaniya nekotorykh opticheskikh materialov v shumanovskoy oblasti spektra). Optika i Spektroskopiya, Vol.I, No.8, 1956.
3. Bruns, A.V. and Prokof'yev, V.K.: Measurement of Far Ultraviolet Emission of Helium on the Sun (Izmereniye dalekogo ul'trafioletovogo izlucheniya geliya na Solntse). Iskusstv. Sputniki Zemli, No.11, 1961.
4. Bruns, A.V. and Prokof'yev, V.K.: Spectrometer for Measuring Solar Radiation in the Far Ultraviolet (Spektrometr dlya izmereniya izlucheniya Solntsa v dalekom ul'trafiolete). Iskusstv. Sputniki Zemli, No.11, 1961.
5. Badinov, I.Ya.: A Three-Stage Transistorized Photoelectric Servosystem (Trekhstupenchataya fotoelektricheskaya sledyashchaya sistema na tranzistorakh). Iskusstv. Sputniki Zemli, No.14, 1962.
6. Harrison, D., Lord, R., and Lufburov, D.: Applied Spectroscopy (Prakticheskaya spektroskopiya). Izd. Inostr. Lit., Moscow, 1950.
7. Yefremov, A.I. et al.: Filter Apparatus for Investigating Solar Shortwave Radiation (Fil'trovaya apparatura dlya issledovaniya korotkovolnovoy radiatsii Solntsa). Iskusstv. Sputniki Zemli, No.10, 1961.
8. Yefremov, A.I. et al.: Investigation of the Shortwave Radiation of the Sun (Issledovaniye korotkovolnovoy radiatsii Solntsa). Iskusstv. Sputniki Zemli, No.10, 1961.
9. Utilization of Solar Energy in the Exploration of Space (Ispol'zovaniye solnechnoy energii pri kosmicheskikh issledovaniyakh). Izd. "Mir", Moscow, 1964.
10. Studies of the Upper Atmosphere with the Aid of Rockets and Artificial Earth Satellites (Issledovaniya verkhney atmosfery s pomoshch'yu raket i iskusstvennykh sputnikov Zemli). Translated by G.S.Ivanova-Kholodnyy, Izd. Inostr. Lit., Moscow, 1961.
11. Kazachevskaya, T.V. et al.: Measurements of X-Ray and Ultraviolet Radiation by means of Thermoluminescent Phosphorus (Izmereniye rentgenovskogo i ul'trafioletovogo izlucheniy s pomoshch'yu termolyuminestsentnogo fosfora). Iskusstv. Sputniki Zemli, No.15, 1963.
12. Kazachevskaya, T.V. and Ivanov-Kholodnyy, G.S.: Interpretation of the Data on Rocket Measurements in the Upper Atmosphere, Obtained with the Aid of Thermoluminescent Phosphorus (Interpretatsiya dannykh raketnykh izmereniy

v verkhney atmosfere, poluchennykh s pomoshch'yu termolyuminestsentnogo fosfora). Iskusstv. Sputniki Zemli, No.15, 1963.
13. Kondrat'yev, K.Ya.: The Radiant Energy of the Sun (Luchistaya energiya Solntsa). Gidrometeoizdat, Leningrad, 1954. /360
14. Lukirskiy, A.P., Savinov, Ye.P., and Shepelev, Yu.F.: Performance of Gold- and Titanium-Coated Echelles in Wavelength Range of from 23.6 to 113 Å (Rabota eshelletov s zolotym i titanovym pokrytiyami v oblasti dlin voln ot 23.6 do 113 Å). Optika i Spektroskopiya, Vol.XV, No.4, 1963.
15. Lukirskiy, A.P. et al.: Measurements of the Photoelectric Output for Ultrasoft X-Radiation (Izmereniye fotoelektricheskogo vykhoda dlya ul'tramyagkogo rentgenovskogo izlucheniya). Optika i Spektroskopiya, Vol.4, No.9, 1960.
16. Mandel'shtam, S.L. et al.: Studies of the X-Radiation of the Sun (Issledovaniye rentgenovskogo izlucheniya Solntsa). Iskusstv. Sputniki Zemli, Vols.I, II, and III, Nos.10, 11, and 15, 1961 to 1963.
17. Nikol'skiy, G.M.: Shortwave Radiation of the Sun (Korotkovolnovoye izlucheniye Solntsa). Geomagnetizm i Aeronomiya, Vol.II, No.1, 1962.
18. Nikole, M.: Aeronomy (Aeronomiya). "Mir", Moscow, 1964.
19. Rassudova, G.N. and Gerasimov, F.M.: Dispersion Gratings of GOI Echelle (Dispersionnyye reshetki eshelle GOI). Izv. Akad. Nauk SSSR, Ser. Fiz., Vol.XXVI, No.7, 1962.
20. Physics of the Upper Atmosphere, edited by A.Radclif (Fizika verkhney atmosfery, Pod red. Dzh.A.Ratklifa). Fizmatgiz, Moscow, 1963.
21. Shats, S.Ya.: Transistors in Pulse Engineering (Tranzistory v impul'snoy tekhnike). Sudpromgiz, Moscow, 1963.
22. Shuba, Yu.A., Tyutikov, A.M., and Sorokin, O.M.: Photocathodes for Investigating the Shortwave Radiation of the Sun (Fotokatody dlya issledovaniya korotkovolnovoy radiatsii Solntsa). Iskusstv. Sputniki Zemli, No.10, 1961.
23. Yakovleva, A.V. et al.: Spectrometric Investigation of the Ozone Layer up to 60 km Altitude (Spektrometricheskoye issledovaniye ozonnogo sloya do vysoty 60 km). Iskusstv. Sputniki Zemli, No.14, 1962.
24. Hinteregger, H.E. et al.: Telemetering Monochromator Measurements of Solar 304 Å Radiation. Space Research, Proc. I Symposium, North Holland Publ. Co., 1960.
25. Tousey, R., Watanabe, K., and Purcell, J.: Measurements of Solar Extreme Ultraviolet and X-Rays from Rockets by means of a $CaSO_4$(Mn) Phosphor. Phys. Rev., Vol.83, p.792, 1951.
26. Watanabe, K. et al.: Direct Measurements of Vertical Distribution of Atmospheric Ozone to 70 km Altitude. J. Geophys. Res., Vol.57, No.2, 1952.

CHAPTER X

1. Aver'yanov, I.P. et al.: Measurements from an Upper-Air Automatic Geophysical Station of the Thermal Radiation of the Earth into Outer Space during the Total Solar Eclipse of 15 February 1961 (Izmereniye s vysotnoy geofizicheskoy avtomaticheskoy stantsii teplovogo izlucheniya Zemli v kosmicheskoye prostranstvo vo vremya polnogo solnechnogo zatmeniya 15 fevralya 1961 g.). Iskusstv. Sputniki Zemli, No.14, 1962.

2. Allen, K.U.: Astrophysical Quantities (Astrofizicheskiye velichiny). Izd. Inostr. Lit., Moscow, 1960.
3. Andreyev, Yu.A. and Kobak, V.O.: Double T-Bridges in Selective Amplifiers (Dvoynyye T-obraznyye mosty v izbiratel'nykh usilitelyakh). Sudpromgiz, Leningrad, 1962.
4. Problems of Interpreting the Data of Weather Satellites (Voprosy interpretatsii dannykh meteorologicheskikh sputnikov). Tr. Gl. Geofiz. Observ., No.166, 1964.
5. Gushchin, G.P.: Investigation of Atmospheric Ozone (Issledovaniye atmosfernogo ozona). Gidrometeoizdat, Leningrad, 1963.
6. Ivanov, Yu.A. and Tyapkin, B.V.: Infrared Engineering and its Military Applications (Infrakrasnaya tekhnika v voyennom dele). Izd. "Sov. Radio", Moscow, 1963.
7. Infrared Searching and Tracking Head (Infrakrasnaya poiskovaya sledyashchaya golovka). Vopr. Raketnoy Tekhn., No.6, 1961.
8. Kasatkin, A.M.: Upper-Air Optical Station for Atmospheric Research (Vysotnaya opticheskaya stantsiya dlya issledovaniya atmosfery). Iskusstv. Sputniki Zemli, No.15, 1963.
9. Kellog, U. and Sagan, K.: The Atmosphere of Mars and Venus (Atmosfera Marsa i Venery). Izd. Inostr. Lit., Moscow, 1962.
10. Kondrat'yev, K.Ya.: Meteorological Satellites (Meteorologicheskiye sputniki). Gidrometeoizdat, Leningrad, 1963.
11. Kondrat'yev, K.Ya.: Radiation Energy of the Sun (Luchistaya energiya Solntsa). Gidrometeoizdat, Leningrad, 1954.
12. Liventsov, A.V. et al.: Experimental Determination of the Earth's Outgoing Radiation (Eksperimental'noye opredeleniye ukhodyashchego izlucheniya Zemli). Dokl. Akad. Nauk SSSR, Vol.146, No.2, 1962.
13. Malkevich, M.S., Pokras, V.M., and Yurkova, L.I.: Measurements of the /361
Radiation Balance on the Explorer VII Satellite (Ob izmereniyakh radiatsionnogo balansa na sputnike "Eksplorer-VII"). Iskusstv. Sputniki Zemli, No.14, 1962.
14. Mikirov, A.Ye.: Investigation of the Sky Brightness and of the Scattering Coefficient in the Upper Atmosphere (Issledovaniye yarkosti neba i koeffitsiyenta rasseyaniya verkhney atmosfery). Iskusstv. Sputniki Zemli, No.13, 1962.
15. Mirlin, D.N.: Semiconductor Bolometers (Poluprovodnikovyye bolometry). DNTP, Leningrad, 1956.
16. Moss, T.S.: Receptors of Infrared Radiation (Priyemniki infrakrasnogo izlucheniya). Usp. Fiz. Nauk, Vol.78, No.1, 1962.
17. Nasledov, D.N. and Smetannikova, Yu.S.: Semiconductor Receptors of Infrared Radiation (Poluprovodnikovyye priyemniki infrakrasnogo izlucheniya). Izd. "Znaniye", Leningrad, 1964.
18. Osherovich, A.L. and Rodionov, S.F.: Certain Parameters of Present-Day Telephotometric Systems (O nekotorykh parametrakh sovremennykh telefotometricheskikh sistem). Iskusstv. Sputniki Zemli, No.14, 1962.
19. Rockets and Artificial Satellites in Meteorology, edited by M.S.Malkevich (Rakety i iskusstvennyye sputniki v meteorologii, Sb. pod red. M.S. Malkevicha). Izd. Inostr. Lit., Moscow, 1963.
20. Safronov, Yu.P., Andrianov, Yu.G., and Lyevlev, D.S.: Infrared Engineering and Outer Space (Infrakrasnaya tekhnika v kosmose). Voyenizdat, Moscow, 1963.
21. Smith, D., Jones, F., and Chesmer, R.: Detection and Measurement of In-

frared Radiation (Obnaruzheniye i izmereniye infrakrasnogo izlucheniya). Izd. Inostr. Lit., Moscow, 1959.
22. Tverskoy, P.N.: A Course in Meteorology (Kurs meteorologii). Gidrometeoizdat, Leningrad, 1962.
23. Keppel, R. and York, D.: Results of Measurements Received from the Tiros II Weather Satellite (Rezul'taty izmereniy, poluchennyye s meteosputnika "Tayros-II"). Zarubezhnaya Radioelektronika, No.1, 1963.
24. Khekford, G.L.: Infrared Radiation (Infrakrasnoye izlucheniye). Izd. "Energiya", Moscow-Leningrad, 1964.
25. Chechik, N.O., Faynshteyn, S.M., and Lifshits, T.M.: Electron Multipliers (Elektronnyye umnozhiteli). Gostekhizdat, Moscow, 1957.
26. Shishlovskiy, A.A.: Applied Physical Optics (Prikladnaya fizicheskaya optika). Fizmatgiz, Moscow, 1961.
27. Estrkheymer, R., De Vaard, R., and Jackson, E.: Infrared Equipment of the Tiros II Weather Satellite (Infrakrasnaya apparatura meteosputnika "Tayros-II"). Zarubezhnaya Radioelektronika, No.1, 1963.
28. Dreyfus, M.G. and Hilleary, D.T.: Satellite Infrared Spectrometer. Aerospace Eng., Vol.21, No.22, 1962.
29. London, J.: A Study of the Atmospheric Heat Balance. New York Univ., 1957.
30. Schwarz, F.: Infrared Circuits in Tiros Satellites. Electronics, Vol.34, No.38, 1961.
31. Chase, S.C. and Schwarz, F.: Instrumentation Equipment of the Spacecraft Mariner II for Venus Study. Electronics, Vol.35, No.50, 1962.
32. Chase, S.C., Kaplan, L.D., and Neugebauer, G.: The Mariner II Infrared Radiometer Experiment. J. Geophys. Res., Vol.68, No.22, 1963.

CHAPTER XI

1. Ivanov, Yu.A. and Tyapkin, B.V.: Infrared Engineering and its Military Applications (Infrakrasnaya tekhnika v voyennom dele). Izd. "Sov. Radio", Moscow, 1963.
2. Kondrat'yev, K.Ya.: Meteorological Satellites (Meteorologicheskiye sputniki). Gidrometeoizdat, Leningrad, 1963.
3. Orlovskiy, Ye.L. et al.: Theoretical Foundations of the Electrical Transmission of Images (Teoreticheskiye osnovy elektricheskoy peredachi izobrazheniy). Izd. "Sov. Radio", Moscow, 1962.
4. Holter, M.R. and Wolfe, W.L.: Optical-Mechanical Scanning Techniques. Proc. IRE, Vol.47, No.9, 1959.
5. Press, H. and Michaels, I.V.: Nimbus Spacecraft Development. Astron. and Aerospace Eng., Vol.1, No.3, 1963.
6. Stampfl, R. and Press, H.: Nimbus Spacecraft System. Aerospace Eng., Vol.21, No.7, 1962.

CHAPTER XII

1. Aerial Photographic Surveying of Cities and Urban Settlements. A Reference Manual, edited by M.D.Bonch-Bruyevich (Aerofotos"yemka gorodov i gorodskikh poselkov, Spravochnoye rukovodstvo, pod red. M.D.Bonch-

Bruyevicha). Izd. Minkomkhoz RSFSR, Moscow, 1953.
2. Antonov, S.M. et al.: Photographic Processes Employed during the First /362 Photographing of the Far Side of the Moon (Fotograficheskiye protsessy, primenyavshiyesya pri pervom fotografirovanii obratnoy storony Luny). Iskusstv. Sputniki Zemli, No.9, 1961.
3. Barabashov, N.P. and Lipskiy, Yu.N.: First Results of Photographing the Far Side of the Moon (Pervyye rezul'taty fotografirovaniya nevidimoy s Zemli storony Luny). Dokl. Akad. Nauk SSSR, Vol.129, No.5, 1959.
4. Bugayets, Ye.A.: Photogrammetry (Fotogrammetriya). Gostekhizdat, Moscow, 1963.
5. Veselovskiy, N.N.: Aerial Photo Topography (Aerofototopografiya). Geodezizdat, Moscow, 1958.
6. Deyneko, V.D.: Aerial Photo Geodesy (Aerofotogeodeziya). Geodezizdat, Moscow, 1955.
7. Drobyshev, F.V.: Principles of Aerial Photographic Surveying and Photogrammetry (Osnovy aerofotos"yemki i fotogrammetrii). Gosgeoltekhizdat, Moscow, 1963.
8. Istomin, G.A.: Sensitometry of Aerial Photographic Materials and Aerial Photographic Exposure Metering (Sensitometriya aerofotomaterialov i aeroeksponometriya). Voyenizdat, Moscow, 1949.
9. Kasatkin, A.M.: Upper-Air Optical Station for Atmospheric Research (Vysotnaya opticheskaya stantsiya dlya issledovaniya atmosfery). Iskusstv. Sputniki Zemli, No.15, 1963.
10. Mikhaylov, V.Ya.: Aerial Photography and General Principles of Photography (Aerofotografiya i obshchiye osnovy fotografii). Geodezizdat, Moscow, 1959.
11. Orlovskiy, Ye.L. et al.: Theoretical Foundations of the Electrical Transmission of Images (Teoreticheskiye osnovy elektricheskoy peredachi izobrazheniy). Izd. "Sov. Radio", Moscow, 1962.
12. Optics and its Military Applications, Vol.I, edited by S.I.Vavilov and M.V.Sevast'yanov (Optika v voyennom dele, Sb. pod red. S.I.Vavilova i M.V.Sevast'yanovoy, Vol.I), Izd. Akad. Nauk SSSR, Moscow-Leningrad, 1945.
13. First Photographs of the Far Side of the Moon (Pervyye fotografii obratnoy storony Luny). Izd. Akad. Nauk SSSR, Moscow, 1959.
14. Perren, F.: Method for Evaluating Photographic Systems (Metody otsenki fotograficheskikh sistem). Usp. Fiz. Nauk, Vol.78, No.2, 1962.
15. Tsyganov, M.N.: General Photography and Special Types of Photography (Obshchaya fotografiya i spetsial'nyye vidy fotografii). Gosgeoltekhizdat, Moscow, 1963.
16. Katz, A.H.: Observation Satellites. Astronautics, Vol.5, No.9, 1960.

CHAPTER XIII

1. Antipin, M.V.: Evaluating the Quality of the Television Image (K otsenke kachestva televizionnogo izobrazheniya). Tekhn. Kino i Televideniya, No.9, 1963.
2. Artem'yev, N.L. and Seliverstova, N.P.: Television Converters of IR Image (Televizionnyye preobrazovateli IK-izobrazheniya). Tekhn. Kino i Televideniya, No.6, 1963.
3. Bogatov, G.B.: Television on Earth and in Outer Space (Televideniye na

Zemle i v kosmose). Izd. Akad. Nauk SSSR, Moscow, 1961.
4. Bende, Ya.Ya. et al.: The LI-407 Miniature Vidicon (Miniatyurnyy vidikon LI-407). Tekhn. Kino i Televideniya, No.5, 1963.
5. Gurevich, S.B.: Physical Processes in Television Pickup Tubes (Fizicheskiye protsessy v peredayushchikh televizionnykh trubkakh). Fizmatgiz, Moscow, 1958.
6. Zelenskiy, S.I.: Present Status and Future Prospects of Industrial Television in the Soviet Union (Sovremennoye sostoyaniye i perspektivy razvitiya promyshlennogo televideniya v Sovetskom Soyuze). Leningrad, 1960.
7. Zvorykin, V.K. and Morton, D.A.: Television (Televideniye). Izd. Inostr. Lit., Moscow, 1956.
8. Kondrat'yev, K.Ya.: Meteorological Satellites (Meteorologicheskiye sputniki). Gidrometeoizdat, Leningrad, 1963.
9. Kostykov, Yu.V. and Kryzhanovskiy, V.D.: The Principles of Television (Osnovy televideniya). Voyenizdat, Moscow, 1961.
10. Leytes, L.S.: Television-Broadcasting Techniques (Tekhnika televizionnogo veshchaniya). Svyaz'izdat, Moscow, 1963.
11. Mezon, I.: The Vidicon Pickup Camera with Electrostatic Deflection, Designed for Installation in the Ranger Interplanetary Probe (Televizionnaya peredayushchaya kamera na vidikone s elektrostaticheskim otkloneniyem dlya mezhplanetnoy stantsii "Reyndzher"). Elektronika, Vol.35, No.8, 1962.
12. Mezon, I.: Long-Range Plan for Space Research (Perspektivnyy plan issledovaniya kosmosa). Elektronika, Vol.36, No.8, 1963.
13. Milenin, N.K. and Suslonov, S.A.: General Objective Criterion for Evaluating the Quality of Television Systems and Images Reproduced by the Television System (Ob obobshchennom ob"yektivnom kriterii otsenki kachestva televizionnykh sistem i izobrazheniy, vosproizvodimykh televizionnoy sistemoy). Tekhn. Kino i Televideniya, No.2, 1964.
14. Orbital UV-System for Compiling Star Charts and Determining the Intensity of Air Glow (Orbital'naya UF-sistema dlya sostavleniya zvezdnykh kart i opredeleniya intensivnosti nebesnogo izlucheniya). Elektronika, Vol.35, No.8, 1962.
15. Orlovskiy, Ye.L. et al.: Theoretical Foundations of the Electrical Transmission of Images (Teoreticheskiye osnovy elektricheskoy peredachi izobrazheniy). Izd. "Sov. Radio", Moscow, 1962.
16. Polonik, V.S.: Applied Television (Prikladnoye televideniye). /363
Gosenergoizdat, Moscow, 1962.
17. Rockets and Artificial Satellites in Meteorology, edited by M.S.Malkevich (Rakety i iskusstvennyye sputniki v meteorologii, Sb. pod red. M.S. Malkevicha). Izd. Inostr. Lit., Moscow, 1963.
18. Handbook of Television Engineering, Parts I and II (Spravochnik po televizionnoy tekhnike, ch. I i II). Gosenergoizdat, Moscow, 1962.
19. Tables for Calculating Natural Illumination and Visibility, edited by V.V.Sharonov (Tablitsy dlya rascheta prirodnoy osveshchennosti i vidimosti, pod red. V.V.Sharonova). Izd. Akad. Nauk SSSR, 1956.
20. Television, a General Course edited by P.V.Shmakov (Televideniye, Obshchiy kurs pod red. P.V.Shmakova). Svyaz'izdat, Moscow, 1960.
21. Advanced Design Camera Tubes for Military Applications. Signal, Vol.15, No.9, 1961.
22. Airborne TV System to Help Guide Telescope Floating in Stratosphere.

Electr. Eng., Vol.80, No.5, 1961.
23. Alexander, G.: Nimbus Undergoes Tough Prelaunch Tests. Aviation Week, Vol.76, No.4, 1962.
24. Bang, A.: High-Sensitivity Television as an Aid to Low-Light-Level Photographic Recording. Journ. SMPTE (J. Soc. Motion Picture and Television Engrs.), Vol.70, No.9, 1961.
25. Beller, W.: Twelve Surveyors Now Planned for Moon Exploration. Missiles and Rockets, Vol.10, No.23, 1962.
26. Butber, C.: Tiros 8th APT System already Aids Cape Kennedy Weather Prediction. Missiles and Rockets, Vol.14, No.1, 1964.
27. Different Image Orticon Tubes. Electronics, Vol.35, No.14, 1962.
28. Goldberg, E. et al.: Key Equipment for Tiros I Meteorological Satellite. Astronautics, Vol.5, No.6, 1960.
29. Introducing OSO. Spaceflight, Vol.4, No.2, 1962.
30. Kapany, N.: Electro-Optical Systems Using Fiber Optics. Int. Journ. of Optica Acta, Vol.7, No.3, 1960.
31. Glass, P.: Nimbus will Test Electrostatic Camera. Aviat. Week and Space Techn., Vol.73, No.20, 1960.
32. Kenzer, B.: Electronic and Motion-Picture Systems in Space Age. Journ. SMPTE, Vol.70, No.12, 1961.
33. Press, H. and Michaels, I.V.: Nimbus Spacecraft Development. Astronautics and Aerospace Eng., Vol.1, No.3, 1963.
34. Project Ranger. Spaceflight, Vol.4, No.2, 1962.
35. Stampfe, R. and Press, H.: Nimbus Spacecraft System. Aerospace Eng., Vol.21, No.7, 1962.
36. Sternberg, S. and Strond, W.: Tiros I Meteorological Satellite. Astronautics, Vol.5, No.6, 196C.
37. Spaulding, S.: Television and Lunar Exploration. J. SMPTE., Vol.69, No.1, 1960.
38. Stereo-Color TV System may Guide Moon Robot. Electronics, Vol.34, No.41, 1961.
39. Sternberg, S. et al.: Roundup on Tiros I. Astronautics, Vol.5, No.6, 1960.
40. Tiros V Weather Satellite to Study Winter Area of Earth. Missiles and Rockets, Vol.10, No.25, 1962.
41. Weimer, P.K., Forgue, S.V., and Goodrich, R.R.: The Vidicon, a Photo-Conductive Camera Tube. Electronics, Vol.23, p.70, 1960.
42. Zastrow, R. and Ritchie, D.: Design Considerations of Television Satellite Reconnaissance Systems. IRE International Convention Record, Report 5, 1960.

Translated for the National Aeronautics and Space Administration by the O.W.Leibiger Research Laboratories, Inc.

"The aeronautical and space activities of the United States shall be conducted so as to contribute . . . to the expansion of human knowledge of phenomena in the atmosphere and space. The Administration shall provide for the widest practicable and appropriate dissemination of information concerning its activities and the results thereof."

—NATIONAL AERONAUTICS AND SPACE ACT OF 1958

NASA SCIENTIFIC AND TECHNICAL PUBLICATIONS

TECHNICAL REPORTS: Scientific and technical information considered important, complete, and a lasting contribution to existing knowledge.

TECHNICAL NOTES: Information less broad in scope but nevertheless of importance as a contribution to existing knowledge.

TECHNICAL MEMORANDUMS: Information receiving limited distribution because of preliminary data, security classification, or other reasons.

CONTRACTOR REPORTS: Scientific and technical information generated under a NASA contract or grant and considered an important contribution to existing knowledge.

TECHNICAL TRANSLATIONS: Information published in a foreign language considered to merit NASA distribution in English.

SPECIAL PUBLICATIONS: Information derived from or of value to NASA activities. Publications include conference proceedings, monographs, data compilations, handbooks, sourcebooks, and special bibliographies.

TECHNOLOGY UTILIZATION PUBLICATIONS: Information on technology used by NASA that may be of particular interest in commercial and other non-aerospace applications. Publications include Tech Briefs, Technology Utilization Reports and Notes, and Technology Surveys.

Details on the availability of these publications may be obtained from:

SCIENTIFIC AND TECHNICAL INFORMATION DIVISION

NATIONAL AERONAUTICS AND SPACE ADMINISTRATION

Washington, D.C. 20546